



UNIVERSITAT POLITÈCNICA DE CATALUNYA
BARCELONATECH

Escola Superior d'Enginyeries Industrial,
Aeroespacial i Audiovisual de Terrassa

PhD program in Mechanical Engineering, Fluids and Aeronautics

A new computational approach to topology optimization in solid mechanics problems

Doctoral thesis by Daniel Yago Llamas

Thesis advisors Dr. Juan Carlos Cante Terán
Dr. Oriol Lloberas-Valls

Research promoter Prof. Xavier Oliver Olivella

Article-based thesis

Physics Department. Aerospace Engineering Division.
Escola Superior d'Enginyeries Industrial, Aeroespacial i Audiovisual de
Terrassa - Universitat Politècnica de Catalunya · BarcelonaTech
Barcelona, January 2022

To my grandparents

Abstract

This doctoral thesis addresses topology optimization problems at a single scale. Based on this purpose, a new topology optimization approach is developed in order to improve existing and widespread techniques in the research community on the topic. The proposed technique presents several characteristics that overcome some of the well-known difficulties in topological optimization while maintaining a considerable degree of simplicity.

In the first place, the formulation of the topological optimization technique is presented, as well as its algorithm. The method is based on 4 fundamental features: (1) the use of a 1-0 characteristic function, as well as the precise identification of the material boundaries from a discrimination function (0-level-set function), (2) the definition of a topological derivative consistent with the ersatz method (used in the state problem), as an approximation to the exact topological derivative, (3) the inclusion of a Laplacian regularization with minimum size control of the different components, and (4) the formulation of an analytical optimality condition aiming at the optimal topology solution.

The approach is applied to different topology optimization problems, well-reported in the literature and used as numerical benchmarks (in structural and thermal problems), to examine their performance. In these fields, stiffness and conductivity maximization problems are considered for validation, respectively. In addition, different topological optimization problems of major engineering interest are tackled, including the design of compliant mechanisms within the structural field and thermal cloaking devices within the thermal field.

Finally, a comparison of the formulation with other existing topology optimization techniques is performed, including (1) SIMP, (2) ESO/BESO, and (3) Level-set with Hamilton-Jacobi as the updating equation. The analysis of the results provides a comparison in terms of the quality of the topology of each method, the computational cost of the optimal solutions, as well as the simplicity of implementation. The resulting study reveals the potential of the developed methodology in these specific comparison terms.

In an attempt to bring the method closer to other researchers and to promote its use, an educational version of the method (written in MATLAB) has been published in an online repository, together with documentation, facilitating its dissemination and subsequent use in other applications of interest.

Keywords: topology optimization technique, VARTOP, minimization, structural problems, thermal problems, optimality criteria, relaxed topological derivative, level-set function, characteristic function, Laplacian regularization, mesh size control, comparative study

Resumen

El objetivo de esta tesis doctoral es abordar el problema de optimización topológica a una única escala. En base a este propósito, se desarrolla una nueva técnica de optimización capaz de competir con técnicas ya existentes y extendidas entre la comunidad investigadora sobre el tema. Esta técnica presenta características que superan algunas de las dificultades bien conocidas en optimización topológica manteniendo un buen grado de simplicidad.

En primer lugar, se presenta la formulación de la técnica de optimización topológica, así como su algoritmia. El método se fundamenta en 4 aspectos básicos: (1) la utilización de una función característica 1-0, así como la definición precisa de las fronteras materiales a partir de una función de discriminación (isonivel 0 de la función level-set), (2) la definición de una derivada topológica coherente con el método ersatz (utilizado en la ecuación de estado), como aproximación a la derivada topológica exacta, (3) la inclusión de una regularización Laplaciana con control de tamaño mínimo de los diferentes componentes, y (4) la definición de una condición de optimalidad analítica para la determinación de la solución óptima de la topología.

La metodología se aplica a diferentes problemas de optimización topológica bien detallados en la literatura y utilizados como ensayos numéricos para examinar su respuesta frente a problemas estructurales y térmicos. En estos campos, se incluyen problemas de maximización de la rigidez y de la conductividad, respectivamente. Además, se resuelven diferentes problemas de optimización topológica con gran interés ingenieril en los campos estructurales con el diseño de mecanismos y térmicos con el diseño de dispositivos de camuflaje térmicos.

Finalmente, se realiza una comparación de la formulación con otras técnicas ya existentes, por ejemplo: (1) SIMP, (2) ESO/BESO, y (3) Level-set con Hamilton-Jacobi como ecuación de evolución. El análisis de los resultados permite comparar la calidad de la topología de cada método, el coste computacional de las soluciones óptimas, así como la simplicidad de implementación, demostrando el potencial de la metodología desarrollada principalmente en estos términos de comparación.

Con la finalidad de acercar el método a otros investigadores y de promover su utilización, se ha publicado una versión educativa del mismo (en MATLAB) en un repositorio online, junto a documentación, permitiendo así la divulgación del mismo y la posible utilización en otras aplicaciones de interés.

Palabras clave: técnica de optimización topológica, VARTOP, minimización, problema estructural, problema térmico, criterio de optimalidad, derivada topológica relajada, función level-set, función característica, regularización Laplaciana, control tamaño filamento, estudio comparativo

Preface

The ambition to learn and have a deeper understanding of the world that surrounds us drove my interest in the engineering field, culminating this process with higher studies in Aerospace Engineering. All these years of preparation have provided me with a solid background in engineering and numerical computation, leading me to pursue doctoral studies in this field.

The expansion of aviation in the 1990s represented a key event in the development of the industry as we know it today, as well as the current economical globalization, enabling cultural and knowledge exchange. However, this increase in aeronautical transport entails the consumption of tons of fuel and greenhouse emissions every year.

The existence of this serious problem for the industry gives rise to the need of developing new, cleaner transport models, improving engines or even replacing old combustion engines with new electric models, and designing new aircraft with better efficiencies. Starting from this last premise, a fundamental objective would be to reduce the weight of the aircraft without affecting their integrity.

With this purpose, this work aims at reducing the weight of the different structural components while maintaining the same structural stiffness, through the use of computational numerical tools such as topology optimization techniques. Therefore, the thesis focuses on developing, formulating, and implementing a new topology optimization approach capable of obtaining optimal topologies at a low-computational cost while including manufacturing constraints that could be used with the original objective in mind.

D. Yago,
Barcelona, December 2021.

Acknowledgments

I would like to acknowledge all those who have helped me or supported me over the years, which made possible the conclusion of this thesis.

First of all, I would like to recognize all the effort made by Professor Xavier Oliver for the development and fulfillment of this doctoral thesis. The hard work and dedication during months of formulation on the whiteboard have resulted in a satisfactory Ph.D. research. Throughout the duration of the doctoral thesis, Xavier has been a role model both in academia and research.

Secondly, I would like to thank my Ph.D. thesis directors, Oriol Lloberas and Juan Carlos Cante for their dedication and advice throughout the thesis to overcome any difficulties in the research. In particular, I would like to thank Juan Carlos for all the "lost hours" trying to share his knowledge and teach me the proper ways to do research.

On the other hand, I would like to thank all my colleagues in the office and at work with whom I have had the chance to work during this period. All of them have made the long working days more pleasant. In particular, Marcelo, Manuel, Lucia, Alejandro, and Sergio for the discussions and conversations during the coffee breaks. Finally, I would like to thank David and Laura for their support over the last few years, especially in the last year when we have shared concerns and hopes due to the pandemic situation. From all this experience, I get two good friends.

I would also like to sincerely express my gratitude to my family and especially to my grandparents, Juana and Francisco, for their lifelong efforts, thus providing their children and grandchildren with better living conditions. Thank you for all the support you have given me over the years.

Finally, I would like to thank the Spanish Ministry of Education for granting me an FPU fellowship (with reference number FPU17/03763) to pursue doctoral studies in Spain. The research leading from these results has received also funding from the European Research Council through the ERC PoC project "Computational design and prototyping of acoustic metamaterials for tailored insulation of noise" (METACOUSTIC / Proof of Concept Grant agreement n. 874481), and from the Spanish Ministry of Economy and Competitiveness through the project "Computational design of Acoustic and Mechanical Metamaterials" (METAMAT / Research Grant DPI2017-85521-P).

Article-based Thesis

This dissertation is submitted for the degree of Doctoral of Philosophy in Mechanical Engineering, Fluids and Aeronautics at Universitat Politècnica de Catalunya · BarcelonaTech. The research described herein was conducted under the supervision of Professors Juan Carlos Cante Teran, Oriol Lloberas-Valls, and Xavier Oliver Olivella in the Aerospace Engineering Division, Universitat Politècnica de Catalunya, between February 2018 and January 2022.

Thesis publications

All this work has been presented in the following scientific publications:

- [1] J. Oliver, D. Yago, J. Cante, and O. Lloberas-Valls, “Variational approach to relaxed topological optimization: Closed form solutions for structural problems in a sequential pseudo-time framework,” *Computer Methods in Applied Mechanics and Engineering*, vol. 355, pp. 779–819, Oct. 2019. DOI: [10.1016/j.cma.2019.06.038](https://doi.org/10.1016/j.cma.2019.06.038)
- [2] D. Yago, J. Cante, O. Lloberas-Valls, and J. Oliver, “Topology optimization of thermal problems in a nonsmooth variational setting: Closed-form optimality criteria,” *Computational Mechanics*, vol. 66, no. 2, pp. 259–286, Jun. 2020. DOI: [10.1007/s00466-020-01850-0](https://doi.org/10.1007/s00466-020-01850-0)
- [3] D. Yago, J. Cante, O. Lloberas-Valls, and J. Oliver, “Topology optimization using the unsmooth variational topology optimization (UNVARTOP) method: An educational implementation in MATLAB,” *Structural and Multidisciplinary Optimization*, vol. 63, pp. 955–981, Nov. 2020. DOI: [10.1007/s00158-020-02722-0](https://doi.org/10.1007/s00158-020-02722-0)
- [4] D. Yago, J. Cante, O. Lloberas-Valls, and J. Oliver, “Topology optimization methods for 3D structural problems: A comparative study,” *Archives of Computational Methods in Engineering*, Aug. 2021. DOI: [10.1007/s11831-021-09626-2](https://doi.org/10.1007/s11831-021-09626-2)

Article-based thesis

The set of articles presented above qualifies the requirements of the doctoral program to submit the thesis by compendium, as detailed in section 2 of the regulations for article-based thesis at Universitat Politècnica de Catalunya from January 12th, 2017. In particular, publications [2], [3] and [4] meet all the requirements of Article-based thesis of the Mechanical Engineering, Fluids and Aeronautics PhD program. Paper [1] is included in the thesis since it is directly related to the three articles included in the compendium (being the second author) and presents part of the results obtained in the development of the thesis.

Contents

1	Introduction	1
1.1	Motivation and Scope	1
1.2	Objective	2
1.3	Outline	2
2	State of the art	3
2.1	Topology optimization methodology	3
2.1.1	Non-Gradient-based techniques	4
2.1.2	Gradient-based techniques	4
2.2	Main issues of existing topology optimization techniques	7
3	Scientific contributions	8
3.1	Topology optimization technique	8
3.2	General formulation	8
3.2.1	Design domain and design variable	9
3.2.2	Topology optimization problem	10
3.2.3	Relaxed Topological Derivative (RTD)	10
3.2.4	Optimality criteria	13
3.2.5	Closed-form non-linear optimality criteria	13
3.2.6	Flowchart of the algorithm	17
3.3	Structural and thermal formulations	18
3.3.1	Structural topology optimization	19
3.3.2	Thermal topology optimization	21
3.4	Representative numerical examples	26
3.4.1	Representative examples in structural problems	26
3.4.2	Representative examples in thermal problems	29
3.5	Comparison	32
3.5.1	Guidelines for the comparison	33
3.5.2	Comparison analysis	34
3.5.3	Overall Performance	35
4	Conclusions	37
4.1	Discussion of the results	37
4.2	Future research lines	38
4.3	Research dissemination	39
5	Bibliography	40
A	Formulation. Structural Opt.	52
A.1	Abstract	53
A.2	Motivation	53
A.3	Problem set up	57
A.3.1	Relaxed characteristic function	57

A.3.2	Relaxed, bi-material, linear elastic problem	58
A.3.3	Finite element discretization	60
A.3.4	Relaxed Topological Derivative. Definition.	60
A.3.5	Examples of relaxed variational topological derivatives	62
A.4	Application to volume constrained topological optimization problems	65
A.4.1	Penalized functional for non-smooth optimization problems. Optimality criterion	66
A.4.2	Closed-form solution	67
A.5	Regularization	68
A.5.1	Regularization. Laplacian smoothing	69
A.6	Pseudo-time sequential approach for volume constrained optimization problem .	71
A.7	Algorithmic resolution	71
A.7.1	Iterative solving strategy	72
A.7.2	Lagrange multiplier resolution: bisection algorithm	73
A.7.3	Finite element implementation. Numerical aspects.	76
A.8	Structural compliance problems	77
A.8.1	Cost function topological sensitivity	77
A.9	Compliant mechanisms	79
A.9.1	Topological sensitivity	80
A.9.2	Closed-form solution	80
A.10	Representative numerical simulations	81
A.10.1	Mean compliance optimization. Cantilever beam.	81
A.10.2	Mean compliance optimization. 3D bridge design	84
A.10.3	Compliant mechanisms optimization.	86
A.10.4	Computational assessment. Variational closed-form solution vs. level-set method	87
A.11	Concluding remarks	89
A.A	Modified marching cubes strategy	91
A.B	Mixed finite element formulation for bi-material finite elements	92
A.C	A level set algorithm for relaxed bi-material topological optimization	93
A.C.1	Level set algorithm	93
B	Thermal Optimization	101
B.1	Abstract	102
B.2	Introduction	102
B.2.1	Motivation and background	102
B.3	Relaxed Variational Approach (RVA) to topology optimization: a summary . . .	104
B.3.1	Topology domain representation	104
B.3.2	Relaxed Topological Derivative (RTD)	106
B.3.3	Closed-form algebraic solutions	107
B.4	Formulation of the state problem	108
B.5	Optimization algorithm	110
B.6	Topology optimization problems	111
B.6.1	Thermal compliance problem	111
B.6.2	Thermal cloaking in terms of heat flux	113
B.6.3	Thermal cloaking in terms of temperature average and variance	116
B.7	Representative numerical simulations	122
B.7.1	Thermal compliance minimization. 3D thermal conductor.	122
B.7.2	Thermal cloaking optimization	124
B.7.3	Computational assessment. Variational closed-form solution vs. level set method	129
B.8	Concluding remarks	130
B.9	Acknowledgements	131

B.A	Finite element discretization	132
B.B	Thermal compliance minimization: cost function derivative	133
B.C	Thermal cloaking via heat flux manipulation: cost function derivative	133
B.D	Average temperature minimization: cost function derivative	135
B.E	Temperature variance minimization: cost function derivation	136
C	Educational implementation	140
C.1	Abstract	141
C.2	Introduction	141
C.3	Problem formulation	143
C.3.1	Unsmooth variational topology optimization	143
C.3.2	State problem	146
C.3.3	Finite element discretization	147
C.3.4	Algorithm	147
C.3.5	Mean compliance	148
C.3.6	Multi-load mean compliance	149
C.3.7	Compliant mechanisms	150
C.4	MATLAB implementation	151
C.4.1	Parameter definition	152
C.4.2	Geometry definition	152
C.4.3	Load and boundary definition	154
C.4.4	Material definition	154
C.4.5	Animation preparation	154
C.4.6	Finite element analysis preprocessing	154
C.4.7	Laplacian regularization preparation	156
C.4.8	Main program	156
C.4.9	Iso-surface plot	158
C.4.10	Cost function and volume vs. step plot	159
C.4.11	Topology evolution GUI	159
C.4.12	Multi-load mean compliance: code modification	160
C.4.13	Compliant mechanisms: code modification	161
C.5	Numerical examples	163
C.5.1	Cantilever beam	164
C.5.2	Messerschmitt-Bölkow-Blohm (MBB) beam	164
C.5.3	L-Shaped structure	165
C.5.4	Bridge	166
C.5.5	Gripper mechanism	166
C.5.6	Michell multi-load structure	167
C.6	Extensions	168
C.6.1	Bisection algorithm	168
C.6.2	Plane-strain assumption	169
C.6.3	Augmented Lagrangian to impose volume constraint	169
C.6.4	Thermal problem	170
C.6.5	3D extension	171
C.7	Conclusions	171
C.8	Acknowledgements	172
C.A	Matlab code	172
D	Comparative study	180
D.1	Abstract	181
D.2	Introduction	181
D.3	Theoretical aspects	186
D.3.1	Domain definition	186

D.3.2	The Topology Optimization problem. Contextual introduction	187
D.3.3	General algorithm	190
D.4	Topology Optimization methods	191
D.4.1	SIMP method	191
D.4.2	SOFTBESO method	195
D.4.3	VARTOP method	196
D.4.4	Level-set method via a Hamilton-Jacobi equation	198
D.5	Benchmark cases	200
D.5.1	Cantilever beam	200
D.5.2	L-shaped structure	200
D.5.3	Multi-load cantilever beam	201
D.5.4	Gripper compliant mechanism	202
D.6	Comparison of methods	202
D.6.1	Comparison settings	202
D.6.2	Results	206
D.7	Concluding remarks	219
D.A	Convergence criteria	221
D.B	Post-processing iteration	222
D.C	Parameter definition	222
D.D	Order of convergence	223
D.E	Robustness of L-shaped structure	224

List of Figures

3.1	Domain representation with optimal layout definition	9
3.2	Topological derivative computation	12
3.3	Laplacian regularization representation	14
3.4	Cutting and bisection iterative algorithm	15
3.5	Pareto Frontier of a topology optimization example	17
3.6	The general flowchart for the proposed topology optimization approach	18
3.7	Elastic problem sketch	20
3.8	Compliant mechanism sketch	21
3.9	Steady-state thermal problem sketch	22
3.10	Thermal cloaking problem	24
3.11	Average and variance temperature minimization problem	25
3.12	Cantilever beam setting	26
3.13	Cantilever beam topology optimization problem	27
3.14	Cantilever beam. Mesh-size objectivity results (τh)	27
3.15	Gripper design (compliant mechanism)	29
3.16	Thermal heat conductor	30
3.17	Thermal cloaking device: problem setup	31
3.18	Thermal cloaking device: temperature field on $\partial_c \Omega$	32
3.19	Topology optimization domains of the numerical benchmarks	33
3.20	Relative computational cost in terms of the number of iterations	36
3.21	Qualitative comparison of the studied methods	36
A.1	β -relaxed setting: bi-material design domain	57
A.2	Discrimination function ψ and the relaxed characteristic function χ_ψ	58
A.3	Topological derivative settings. Relaxed (RTD) and Exact (TD) Topological Derivatives	61
A.4	Design domain Ω with material-phase boundaries	63
A.5	Noisy modes removal and minimum phase-filament-thickness via Laplacian smoothing of the discrimination function $\psi(\mathbf{x})$	70
A.6	Pseudo-time evolutionary analysis. Typical evolution of the cost function and topology vs. time	72
A.7	Isoenergy (λ iso-level) contours of the spatial energy distribution ξ	74
A.8	Compliant mechanism topology optimization problem	79
A.9	Minimum compliance cantilever beam: problem setting	82
A.10	Cantilever beam. Mean structural compliance optimization for Mesh M1	82
A.11	Cantilever beam. Mesh-size objectivity results ($\epsilon = \tau \cdot h$)	83
A.12	Cantilever beam. Comparison of full 3D and $2^{1/2}D$ (extruded) optimal topologies for $t=0.85$ and mesh $M1$	84
A.13	Minimum compliance bridge design: problem setup	85
A.14	Bridge. Mean structural compliance optimization	85
A.15	Bridge. Mean structural compliance optimization. Topology for $t=0.94$	86
A.16	Compliant mechanism (gripper): problem setup	86

A.17	Compliant mechanism (gripper) design: original and auxiliary systems	87
A.18	3D-Gripper optimization	88
A.19	Cantilever beam. Variational closed-form solution vs. level set method	89
A.A.20	Marching cubes method: tessellation process	92
A.A.21	Marching cubes method: nodal values interpolation	92
A.B.22	Mixed finite element representation	94
A.C.23	Level-set problem definition	94
B.1	Representation of the analysis domain, Ω	105
B.2	Topology representation in terms of the discrimination function, $\psi(\mathbf{x})$	105
B.3	Thermal problem sketch	108
B.4	Cutting and bisection iterative algorithm. Visual representation for different λ . .	110
B.5	Thermal cloaking problem	113
B.6	Average and variance temperature minimization	117
B.7	Average temperature minimization	118
B.8	Thermal heat conductor: problem setup	123
B.9	Thermal heat conductor. Thermal compliance minimization	123
B.10	Thermal heat conductor. Thermal compliance minimization including heat source	124
B.11	Heat flux cloaking device: 3D problem setup	125
B.12	Heat flux cloaking device: optimization evolution	126
B.13	Heat flux cloaking device: optimal topologies and isothermal lines	126
B.14	Thermal cloaking device: 3D problem setup	127
B.15	Thermal cloaking device: optimization evolution	128
B.16	Thermal cloaking device: optimal topologies and temperature field	128
B.17	Thermal heat conductor. Non-smooth variational closed-form method vs level set method	130
C.1	Representation of the fixed design domain Ω	144
C.2	Topology representation in terms of the discrimination function ψ	144
C.3	The flowchart for the unsmooth variational topology optimization algorithm . . .	148
C.4	Cantilever beam: topology optimization domain and boundary conditions	151
C.5	Cantilever beam: topology optimization results	152
C.6	Cantilever beam: mesh discretization	153
C.7	GUI's design	159
C.8	Multi-load beam: topology optimization domain and boundary conditions	159
C.9	Multi-load beam: optimal topology layout	160
C.10	Multi-load beam: optimal topology layout when loads are applied at the same time	161
C.11	Inverter (compliant mechanism): topology optimization domain and boundary conditions	162
C.12	Inverter (compliant mechanism): optimal topology layout	162
C.13	Cantilever beam (load applied at the middle): optimal topology layout	165
C.14	Cantilever beam: topology evolution	165
C.15	MBB beam: optimal topology layout	165
C.16	L-shaped structure: optimal topology layout	166
C.17	Bridge: optimal topology layout	166
C.18	Gripper (compliant mechanism): optimal topology layout	167
C.19	Gripper (compliant mechanism): close-up view of the central hinge	167
C.20	Multi-load michell structure: optimal topology layout	168
C.21	Multi-load michell structure: optimal topology layout when loads are applied at the same time	168
D.1	Domain representation	186
D.2	Elastic problem sketch	187

D.3	The general flowchart for topology optimization approaches	191
D.4	Cantilever beam: topology optimization domain with boundary conditions and dimensions	200
D.5	L-shaped structure: topology optimization domain with boundary conditions . . .	201
D.6	Multi-load Cantilever beam: topology optimization domain with boundary conditions	201
D.7	Gripper (compliant mechanism): topology optimization domain with boundary conditions	202
D.8	Objective function value for each example and topology optimization approach normalized with $SIMP^{(I)}$	213
D.9	Relative computational cost in terms of the number of iterations	214
D.10	Evolution histories of the values of the objective function and volume fraction throughout the iterations of the Cantilever beam topology optimization	216
D.11	Evolution histories of the criteria values in the objective function and in the topology throughout iterations of the Cantilever beam topology optimization	217
D.12	Qualitative comparison of the studied methods: smoothness of the design, topology complexity, objective function and computational cost	218
D.13	Qualitative comparison of the studied methods: topology quality and computational efficiency	219
D.D.14	Iterative sequence of the objective function errors throughout the iterations of the Cantilever beam topology optimization	225
D.E.15	Evolution histories of the values of the objective function and volume fraction throughout the iterations of the L-shaped structure topology optimization	226
D.E.16	Evolution histories of the criteria values in the objective function and in the topology throughout iterations of the L-shaped structure topology optimization	227

List of Tables

3.1	Comparison of the results for the L-shaped structure	34
A.1	Relaxed topological derivative examples	66
C.1	List of fields used in the code	153
D.1	Comparison of the results of topology optimization methods for the Cantilever beam	208
D.2	Comparison of the results of topology optimization methods for the L-shaped structure	210
D.3	Comparison of the results of topology optimization methods for the Multi-load cantilever beam	211
D.4	Comparison of the results of topology optimization methods for the Gripper compliant mechanism	212
D.5	Comparison of computational cost in terms of iterations of the considered topology optimization methods	215
D.C.6	Global parameters and tolerances used for each benchmark case and topology optimization method	223
D.C.7	Parameters used for each benchmark case and topology optimization method . . .	224

Chapter 1

Introduction

1.1 Motivation and Scope

In the past three decades, topology optimization has become an active research field to seek new optimal counterintuitive designs in a wide range of problems governed by different physics, from which a reduction of the total weight can be obtained. As a result of this substantial effort, the optimal design obtained from the minimization of a given topology optimization problem can be used by engineers as a first approximation in the development of new products in a wide range of applications.

In particular, these methodologies can have a major impact in the automotive and aeronautical sectors, as they can be applied to achieve a reduction in the weight of automobiles or aircraft without losing the structural integrity or changing the physical properties. This can result in significant reductions in fuel consumption and greenhouse emissions, leading to million-dollar benefits in terms of reduced operating costs.

There is a multitude of material reduction strategies, most notably the use of lightweight composite materials. This material replacement has become more prevalent in recent years, especially with new-generation aircraft designs. By contrast, topology optimization techniques represent another alternative with the same objective, involving mainly the arrangement of a single material. These topology optimization techniques seek to optimize the topology by iteratively removing material from a full-domain object, under certain loads and boundary conditions. Therefore, the most important features of topology optimization strategies are both the location of the voids and the definition of their form, which will depend on the specific problem to minimize.

Topology optimization techniques have been applied to a large number of physical problems, including mechanical, thermal, acoustic, and electromagnetic, among others, with promising results. As a consequence, most commercial structural analysis (FEA) codes have developed specific computational modules to perform topology optimizations. Nonetheless, this software requires high computational resources to find optimal topologies, in addition to the adjustment of numerical parameters, which is one of the main reasons for its lack of popularity compared to other techniques.

The scope of this thesis will therefore focus on the development of mono-scale techniques targeting the minimization of an objective function subject to a volume constraint, for different physical problems including the most common ones: structural and thermal problems. In particular, optimal topologies of complex problems will be sought to be obtained at a reduced computational cost, so that they could be subsequently printed by additive manufacturing techniques.

1.2 Objective

The objective of this thesis is framed within the development and formulation of a new computational approach to topology optimization of macro-scale components in solid mechanics problems. This methodology must also consider the required manufacturability constraints enforced by modern additive manufacturing techniques.

Consequently, the topology optimization technique must be capable of finding new optimal topologies that minimize a certain objective function and are subject to some constraints. In addition, a robust and parameter-independent technique must be defined for solving the optimization problem, unlike the multiple parameters required by other existing methods. At the same time, the strategy must also intend to outperform or at least match the results in terms of topology quality, computational cost, and objective function, while addressing some of the numerical issues presented by other methods, such as checkerboard patterns, semi-dense elements, and mesh size dependence.

As a result, this thesis proposes a new topology optimization technique for minimizing several physical problems (e.g., structural and thermal) while prescribing the maximum volume and minimum bar size. Even though the mathematical complexity, the optimal topology is obtained in a low-computational procedure by computing the corresponding closed-form optimality condition of each optimization problem.

1.3 Outline

The remainder of this dissertation is organized as follows:

Chapter 2. The state of the art is described in this chapter. A review of the current state of topology optimization is carried out, pointing out the main topology optimization methods and their features. The review is focused on gradient-based topology methods, including SIMP-based techniques, ESO/BESO approaches, Phase-field methodologies, and Level-set techniques both with shape and topological derivatives. A section is finally devoted to discuss the most relevant technical challenges faced by all of them.

Chapter 3. This chapter is devoted to detail the scientific contributions made throughout the thesis. The developed topology optimization technique is first presented in a technical and general manner (Appendix A), to particularize in the next sections to structural and thermal topology optimization problems (detailed in Appendices A and B, respectively). Some representative numerical examples are carried out for each physical problem. Based on numerical benchmark cases, the topology optimization approach is compared with several relevant well-known techniques, including SIMP, BESO, and Level-set techniques, showing the potential of this methodology. Full details of this comparison are specified in Appendix D.

Chapter 4. The conclusions of this dissertation are summarized in this last chapter, including the achievements of this work and the dissemination carried out throughout the doctoral thesis. Potential future lines of research with some academic interest are also detailed.

Appendices A to D. Post-print editions of the supporting papers are included in the appendices. As mentioned before, Articles B, C, and D satisfy the minimum requirements for article-based thesis.

Chapter 2

State of the art

This chapter provides the reader with a state-of-the-art review of different topology optimization techniques, where their major advantages and disadvantages are highlighted. In addition to this literature review, an overview of some major ill-conditioning problems of the topology optimization problem is also presented. These well-known handicaps inherent to the optimization problem have a major impact on the formulation and convergence of each technique.

2.1 Topology optimization methodology

Topology optimization has gained increasing interest among researchers and engineers in the last years due to the need for demanding engineering solutions and the increasing computational performance of modern computers. In this context, topology optimization techniques play a major role in obtaining the best topology layouts (solutions) that satisfy any of the constraints imposed for a given application. These designs can be then used by engineers as a first approximation in the development of new products in a wide range of applications.

For instance, in the last three decades, topology optimization has been applied to a wide range of problems governed by different physics, i.e., solid mechanics [149, 124, 7, 20, 123, 27], fluid dynamics [16, 43, 46], thermal dynamics [67, 41, 141], acoustics [114, 33, 32, 70, 73, 99] and electromagnetism [53, 153, 152], among others. Furthermore, topology optimization of coupled multiphysics problems has been addressed in recent works, combining structural-thermal interaction [109, 107, 30], structural-fluid interaction [148, 82, 10, 56] or even thermal-fluid interaction [2, 19, 140, 78].

One can find a large variety of optimization techniques in the literature that make use of different design optimization strategies. These methodologies can be roughly classified into three main areas: (1) size optimization aims at finding the optimal size/thickness/cross-sectional area of the existing fixed components that minimizes a given functional, (2) shape optimization, on the other hand, modifies only the boundary of the (stiff) domain to find the optimal geometric definition of those boundaries that minimizes that functional, and finally (3) topology optimization seeks the optimal position and shape of a set of holes to be included in the design, thus reducing the amount of material while minimizing the objective function. In comparison to shape optimization, holes in the interior of the structure can be created in topology optimization. This thesis is mainly focused on shape and topology optimization, as will be explained in the following chapters.

According to the methodology used to update the optimal solution, the optimization techniques can be categorized into two blocks: (1) methods based on trial-and-error schemes that find the optimal topology by means of heuristic algorithms according to the objective function of the previous iteration, and (2) methods relying on a sensitivity (or gradient) of the objective function to determine the best way to update the topology, thus obtaining at each iteration a reduction of the objective function. Even though the former group may have some advantages for discrete applications, the latter methods are more suitable for the continuum applications.

The two previously listed groups are now briefly described in the following sections. For an in-depth review, the reader is referred to [102, 37, 29, 115, 31, 85].

2.1.1 Non-Gradient-based techniques

Nature-inspired optimization techniques are (meta)heuristic algorithms imitating natural phenomena and physical processes that seek the global minima through a global search strategy. These non-gradient-based or gradient-free (NGTO) techniques do not use any derivative, only the objective function values to determine the solution that provides the minimum one. Examples of such strategies are ant (AC) and bee (ABC) algorithms [58, 75], bat algorithm (BA) [147, 145, 55], cuckoo search (CS) [35], firefly algorithms (FA) [83, 129], genetic algorithms (GA) [60, 61, 126], differential evolution (DE) [127, 62], harmony search (HS) [64, 81], simulated annealing (SA) [134, 21], particle swarm optimizations (PSO) [76], and others. A detailed review of these methods can be found in [146].

In some circumstances, these NGTO approaches may be more competent in searching for high-performance designs by using global search techniques in combination with local search strategies. Nevertheless, the majority of these metaheuristic strategies are based on trial-and-error schemes to find or discover the best possible solution, thus requiring thousands of evaluations of the objective function for this purpose. In addition, there is no guarantee that optimal solutions will be reached, although one can expect to obtain solutions close enough to the global minimum when performing enough global searches in the feasible domain.

In particular, for continuum structures, the use of these methods implies solving the state equation thousands of times to test each configuration, as stated by Sigmund [113]. Up to this moment, NGTO approaches have been extensively used for (1) discrete size optimization, and (2) shape or topology optimization of extremely coarse problems, with great results. In addition, these algorithms are normally easier to implement and may scale on parallel computers without major issues. However, the number of evaluations of the state equation and the objective function increases exponentially with the number of unknowns of the problem, and hence the computational cost. Consequently, these strategies are not computationally feasible for fine-discretized problems with thousands or millions of elements, as it is intended here. For that reason, this entire family of approaches has been discarded as an option for this thesis.

2.1.2 Gradient-based techniques

According to the previous statement, Gradient-based (GTO) techniques are the only feasible group for optimizing large structures in a reasonable amount of time. These methods, however, require the computation of a size/shape/topology derivative for deciding where to modify the topology to minimize the objective function. Even though having to derive and compute the gradient of the objective function, the enormous reduction in the number of evaluations of the state equation justifies the additional mathematical difficulty against any other NGTO method. As a result, the computational cost significantly decreases, allowing to solve large problems.

As a consequence, in the continuum context, topology optimization has received extensive attention and experienced considerable progress over the past few years due to its great potential of application in many industrial areas. Up to now, various families of gradient-based techniques have been well-developed. The most widespread GTO algorithms are (a) topology optimization within homogenization theory [15], (b) density-based optimization (SIMP) techniques [13, 84, 14], (c) evolutionary methodologies (ESO) [132, 143], (d) Level-set approaches [6, 7, 124], (e) Topological Derivative method [116], and (f) Phase field approach [18, 122, 120], among others.

As mentioned above, all these topology optimization techniques require either the computation of a shape or topological derivative/gradient of the objective function with respect to a change in topology. For shape derivative strategies, the sensitivity is determined when a deformation is applied on a material boundary in the normal direction with unitary modulus. As the main drawback, methods based on shape derivative can not nucleate new voids, but only

modify the existing ones through their boundaries, thus being highly dependent on the initial configuration. In contrast, the topological derivative evaluates the change in the objective function when an infinitesimal perturbation is performed in the design domain, and can therefore modify any part of it, avoiding the initial layout dependence.

SIMP-based techniques

The seminal paper of Bendsøe and Kikuchi [15] propitiated the development of one of the most widespread streams of topology optimization methods, i.e., density-based approaches. In particular, the Solid Isotropic Material with Penalization (SIMP) method [13, 84, 14] is nowadays one of the most widely used topology optimization methods due to its computational efficiency and conceptual simplicity, and is considered a consolidated theory by the community.

The SIMP approach is based on a simple regularization of the discontinuous characteristic function χ , thus using an element-wise continuous density as the design variable instead of directly tackling the original 0 – 1 problem. As a consequence, semi-dense elements are allowed in the design domain, $\rho \in [0, 1]$. This density variable, penalized with an exponential factor p , is used to interpolate the material property (the constitutive tensor, for instance) and the objective function. According to this definition, a gradient of the objective function can be easily computed and used in continuous optimization algorithms. For instance, the density variable can be updated via a heuristic algorithm termed as optimality criteria (OC) method [15, 118], via the moving asymptotes (MMA) algorithm [119] or other mathematical programming-based optimization algorithms.

Although the topology almost leads to black-and-white designs once the penalization is applied, the SIMP method requires some type of filtering procedure to alleviate well-known numerical instabilities [108, 57] resulting from the ill-posedness of unconstrained topology optimization problems, e.g., gray areas (semi-dense intermediate elements), checkerboard patterns, and mesh-dependency issues. A large number of regularization schemes have been suggested to be used regarding topology optimization, including: (1) filtering, via the classical sensitivity [110, 111, 108] or density [17, 20] filters, projection techniques [44, 45], morphology-based filters [112, 121] or Helmholtz-type filters [63, 59], among others, and (2) geometric constraint techniques, e.g., perimeter constraint [48, 40] or gradient constraints [94].

This method has been extensively applied to structural [14, 155, 1], thermal [79, 128, 39] and acoustic [148, 34] topology optimization problems with promising results. However, gray elements are obtained in all these applications, and consequently, the method tends to converge to a local optimal topology with blurry boundaries. These non-optimal solutions require additional techniques to recover the full black-and-white configuration.

ESO/BESO techniques

Another recognized family of approaches is the one based on the evolutionary structural optimization (ESO) approach first introduced by Xie and Steven [132, 130]. ESO methods rely primarily on a simple heuristic criterion to gradually remove or hard-kill inefficient material from the initial full-stiff design domain after each finite element analysis. Contrary to SIMP, a discrete element design variable $\chi \in \{0, 1\}$ is now used to define the topology layout, thus avoiding gray elements from its definition. Despite being an intuitive and easy-to-code methodology, this change in design variables results in convergence issues and a high dependency on the initial configuration (and the sequence of element removal). In addition, there is no proof of optimality and may easily lead to non-optimal designs [151]. Despite these existing numerical problems, ESO has been applied to a large range of problems, from well-known structural problems [133, 131, 150, 26], including non-linear problems [96, 77], to thermal problems [66, 67, 95], and contact problems [68, 69].

To overcome these issues, the bidirectional evolutionary structural optimization (BESO) approach [97, 143, 98] was developed with the capability to add stiff material in certain areas of

the domain, thereby reducing the likelihood of finding non-optimal solutions. In an attempt to extend the number of potential applications, the BESO approach has been later combined with a density-based interpolation and a soft-kill strategy [154, 51]. An excellent overview of some recent developments in topology optimization using ESO/BESO is provided in [52].

As in density-based formulations, the design variable is normally regularized to reduce numerical instabilities such as mesh-dependency. For instance, these issues are mitigated via a checkerboard suppression filter [65], a mesh-independent filter [54] or a perimeter control [144], among others.

Phase-field techniques

On the other hand, Phase-field methods [8, 24, 38] continue to use the regularized model proposed in SIMP methods (using the density as design variable), but with the additional target of limiting the thickness of the interface between full and void material elements. Consequently, the resultant optimal solutions present smooth almost black-and-white domains separated by sharp thin finite thickness interfaces, reducing the total number of gray elements present in a given configuration and avoiding non-optimal solutions. Although different mathematical techniques tackle this problem, the gradient regularization of the density [18, 125, 23, 122] can be seen as the most straightforward one. This term is added to the objective function, thus minimizing the thickness of the interface.

In this spirit, Yamada *et al.* [142] has suggested a Phase-field approach based on a level-set function, used as the design variable, and a topological derivative incorporating a fictitious interface energy. This last mathematical technique allows controlling the complexity of the optimal layout. Although being applied to other problems [141, 71], it still resorts to a Hamilton-Jacobi equation to update the topology design, which may entail high computation resources to achieve convergence.

Level-set techniques (shape and topology optimization)

The last major stream is constituted by Level-set-based methods. In contrast to the previous topology optimization approaches, the optimal layout is implicitly defined by a scalar function ϕ , and the structural boundary of the design Γ is represented by the zero-level iso-contour (or iso-surface) of this function [92, 104, 91]. As a result, optimal designs with sharp and smooth edges are obtained, thus avoiding semi-dense (gray) elements and checkerboard patterns, like those observed in density-based methods. Due to this technical advantage, many formulations of Level-set-based approaches have been proposed over the years since Haber and Bendsoe [49] suggested its applications with topology optimization techniques, e.g., [105, 6, 124, 5]. The most important techniques are the Level-set (based on shape derivative) and the Topological Derivative methods.

The original Level-set methods are based on the classical shape sensitivity analysis of the objective function (for a deformation on the boundary) in combination, usually, with a Hamilton-Jacobi equation to update the level-set function [93, 6, 7, 124], where the shape derivative is used as a descent direction. As mentioned previously, the inability of nucleating holes and the large number of iterations make this approach limited and computationally inefficient. Nevertheless, these issues have been overcome through a set of mathematical techniques, e.g., nucleation strategies [36, 103], reinitializations, and alternative updating procedures. With the implementation of some of these modifications, the Level-set method has been applied to a broad range of design problems, including structural problems [4], vibration problems [93, 4], and thermal problems [47], among others.

The topological derivative [116, 25, 42] can also be employed in conjunction (or not) with shape derivatives in the Topological Derivative approach [22, 5, 86, 9, 50], overcoming, in this way, some limitations of classical Level-set methods. This set of improved methodologies avoids any stagnation or sub-optimal solution due to the capability of the sensitivity in determining how

to update the topology. The topological derivative provides information regarding the change in the objective function when an infinitesimal perturbation is created in the domain. However, this improvement entails a complex mathematical asymptotic analysis to obtain the exact topological derivative of each problem, narrowing then the number of potential applications. In addition, this family of methods still requires a large number of iterations to obtain the optimal layout as it normally leans on a Hamilton-Jacobi equation to update the level-set function.

2.2 Main issues of existing topology optimization techniques

The discrete topology optimization problem suffers from numerical instabilities, including the non-existence of optimal solution, mesh dependence, and checkerboard patterns. It is well-known that the 0-1 topology optimization problem subject to volume constraint lacks solutions in general, since the larger the number of holes in the domain (for the same volume fraction), the lower the objective function is (for instance, the compliance), i.e., there is a lack of determination of the set of feasible solutions. When this optimization problem is discretized in finite elements, the dependence in mesh is then observed, thus requiring regularization techniques as those discussed in the previous section, including relaxation, filtering techniques, and geometric constraints. On the other hand, checkerboard patterns are originated due to inaccurate modeling of the physical properties of the problem. These patterns can be removed from the admissible set of solutions by applying additional filtering techniques or constraints, or by using appropriate finite element interpolations for variables. For further information, the reader is referred to [108].

From the analysis of different topology optimization techniques, it can be concluded that, in most approaches, these numerical problems (mainly checkerboard patterns) are mitigated by using filtering techniques (e.g., sensitivity filtering) and regularization of the design variable (as implemented in SIMP). On the other hand, nodal-based design variables (level-set-based methods) can circumvent these difficulties, although these regularizations are also included to smooth the solutions while adding additional manufacturing constraints. Therefore, it makes sense that the combination of a method based on a characteristic function (resulting from the nodal level-set function) together with a manufacturing regularization of the solution will provide smooth mesh-independent solutions with no checkerboard patterns.

Chapter 3

Scientific contributions

3.1 Topology optimization technique

This doctoral thesis proposes a new topology optimization technique, termed as the Variational Topology Optimization (VARTOP) approach, as an alternative to other well-known and consolidated techniques. This methodology combines the mathematical simplicity of SIMP-based techniques while considering the characteristic function as the design variable from ESO/BESO methods. As a consequence, the topological design is defined as a binary configuration of two materials, describing then black-and-white designs. In particular, the boundary of the material domain is implicitly represented through a 0-level-set function (discrimination function) as in level-set-based methods, and the characteristic function can also be obtained from this function.

As opposed to other level-set-based methods, the proposed strategy does not require a Hamilton-Jacobi type function nor a Reaction-Diffusion function to update the discrimination function, but rather a closed-form optimality criterion, from which the optimal solution is obtained. This fixed-point system is obtained from the topological derivation of the optimization problem, leading to a result similar to that obtained in the OC method for SIMP approach. In contrast to more complex methods such as the Topological Derivative method where the exact topological derivative is considered, the VARTOP technique relies on the relaxed topological derivative, being consistent with the ersatz material approach while reducing the mathematical complexity.

The topology optimization problem is normally subjected to a volume constraint expressed in terms of a pseudo-time variable (volume fraction). This constraint equation is iteratively increased until the desired volume is achieved, thus obtaining converged topologies for intermediate volume fractions. By means of this procedure, referred to as time-advancing scheme, the corresponding Pareto Frontier between the objective function and the volume fraction is obtained. For each time-step, the closed-form optimality criteria have to be solved to compute both the Lagrange multiplier that fulfills the volume constraint and the optimal characteristic function.

As for the regularization, a Laplacian regularization, similar to those used in SIMP and Phase-field approaches, is applied to the discrimination function, providing not only smoothness in the optimal design but also mesh-size control. Consequently, two of the major existing problems in topology optimization are mitigated while limiting the complexity of the topology layout, as may be required by some manufacturing techniques.

3.2 General formulation

In the following sections, the general formulation of the proposed topology optimization technique is defined in a generic form without particularizing for any objective function and state problem. A volume constraint is assumed in all the optimization problems.

3.2.1 Design domain and design variable

The optimal topology layout of the design domain, Ω , is here defined in terms of the design variable, denoted by the characteristic function $\chi : \Omega \rightarrow \{0, 1\}$, $\chi \in L^\infty(\Omega)$ as follows

$$\begin{cases} \Omega^+ := \{\mathbf{x} \in \Omega / \chi(\mathbf{x}) = 1\} \\ \Omega^- := \{\mathbf{x} \in \Omega / \chi(\mathbf{x}) = 0\} \end{cases}, \quad (3.1)$$

where Ω^+ and Ω^- stand for the strong/hard and the void material domains, respectively. Alternatively, the topology can also be implicitly defined in terms of a discrimination function $\psi : \Omega \rightarrow \mathbb{R}$, $\psi \in H^1(\Omega)$ as

$$\begin{cases} \Omega^+ := \{\mathbf{x} \in \Omega / \psi(\mathbf{x}) > 0\} \\ \Omega^- := \{\mathbf{x} \in \Omega / \psi(\mathbf{x}) < 0\} \end{cases}, \quad (3.2)$$

similar to the level-set function definition. The topology definition (3.1) can be obtained from equation (3.2) by computing the Heaviside function of the discrimination function, i.e., $\chi(\mathbf{x}) = \mathcal{H}(\psi(\mathbf{x}))$, $\chi \in L^2(\Omega)$, this leading to a bi-material topology optimization problem.

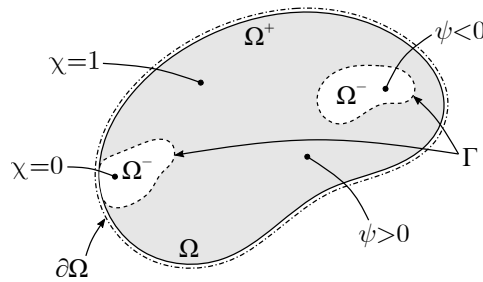


Figure 3.1: Domain representation: representation of the design domain, Ω , comprising two disjoint sub-domains Ω^+ (strong material domain) and Ω^- (void material domain) defined either via the characteristic function χ (equation (3.1)) or implicitly via the discrimination function ψ (equation (3.2)).

Instead of dealing with a theoretical 1-0 configuration, the void material is normally replaced by a weaker (or less conductive) material using a contrast factor α , in the so-called ersatz material approach [3, 28]. Accordingly to this modification, and considering equations (3.1) and (3.2), the relaxed characteristic function χ_β becomes

$$\chi_\beta(\psi(\mathbf{x})) = \begin{cases} 1 & \text{for } \psi(\mathbf{x}) > 0 \\ \beta & \text{for } \psi(\mathbf{x}) < 0 \end{cases}, \quad (3.3)$$

with β corresponding to the relaxation factor in the void sub-domain. This parameter can be easily correlated to the contrast factor used in the ersatz material approach. In particular, β is defined by

$$\beta = {}^m\sqrt{\alpha}, \quad (3.4)$$

m denoting an exponential factor, similar as the exponential factor p used in SIMP-based methods. As a result of this change of variables, it is possible to assign a small value α for the void subdomain and 1 for the remaining domain, when the relaxed characteristic function is raised to the exponent m .

3.2.2 Topology optimization problem

On a general basis, the topology optimization problem aims to obtain an optimal topology layout that minimizes a given target objective function \mathcal{J} subject to certain constraints \mathcal{C}_k (e.g., the volume constraint, the perimeter constraint, or even the maximum stress value) and governed by a linear or non-linear state equation. In the most straightforward case for the elastic or thermal problems, the compliance function would be used as the objective function, while the volume constraint as the constraint equation. In these situations, the stiffness or the conductivity of the structures are maximized for a certain volume (or weight) fraction. Nevertheless, different combinations of objective function and constraint equations can be found in the literature.

Based on this concept, the classical mathematical formulation of the corresponding topology optimization problem can be stated as follows

$$\left[\begin{array}{l} \min_{\chi \in \mathcal{U}_{ad}} \mathcal{J}(\mathbf{u}(\chi), \chi) \equiv \int_{\Omega} j(\mathbf{u}(\chi), \chi, \mathbf{x}) d\Omega \\ \text{subject to:} \\ \mathcal{C}_0(\chi) \equiv \int_{\Omega} c_0(\chi, \mathbf{x}) d\Omega \leq 0 \\ \text{governed by:} \\ \text{State equation} \end{array} \right. \quad \begin{array}{l} (a) \\ \\ (b) \\ (c) \end{array} \quad (3.5)$$

assuming the volume constraint \mathcal{C}_0 as the single constraint equation. The objective function $\mathcal{J} : (\chi, \Omega) \rightarrow \mathbb{R}$, $\mathcal{J} \in L^2(\Omega)$ and the volume constraint are expressed as volume integrals over the entire domain of local functions j or c_0 , respectively, in terms of the state variable \mathbf{u} , the design variable χ , and the position \mathbf{x} . Additionally, the integrands j and c_0 must be sufficiently smooth for differentiation purposes.

In particular, the volume constraint \mathcal{C}_0 can be expressed as an equality equation in terms of the void volume fraction, with respect to the design domain, through the relaxed characteristic function χ_{β} as

$$\mathcal{C}_0(\chi_{\beta}) \equiv \frac{|\overline{\Omega}^-|}{|\Omega|} - \frac{1}{|\Omega|} \int_{\Omega} \frac{1 - \chi_{\beta}(\mathbf{x})}{1 - \beta} d\Omega = t - \frac{|\Omega^-(\chi_{\beta})|}{|\Omega|} = 0, \quad (3.6)$$

where $|\Omega|$ and $|\overline{\Omega}^-|$ are the design domain and the target void material volumes (as illustrated in Figure 3.1), respectively. From the ratio of these two parameter, the pseudo-time variable t is defined as the target void volume fraction, which will subsequently be used to iteratively prescribe and increase the volume fraction. Henceforth, the subscript β from the characteristic function χ_{β} will be omitted.

3.2.3 Relaxed Topological Derivative (RTD)

Regardless of the optimization approach (from the most important group), a gradient (in case of using a continuous regularized design variable) or topological derivative must be derived to compute the sensitivities of the objective function and the volume constraint with respect to the design variable, χ . Such topological derivatives will then be used to define the optimality conditions for determining the optimal topology.

Generally speaking, the topological derivative measures the change in objective function (or volume constraint) when a small perturbation in the topology layout is performed at each point, i.e., when the material from a small region is exchanged from one material to the other (e.g., from stiff material to void material, or vice-versa).

In mathematical form, this idea can be expressed for the proposed approach via the following topological asymptotic expansion

$$\mathcal{J}(\chi + \eta_{\hat{\mathbf{x}}, \epsilon}) = \mathcal{J}(\chi) + \frac{\delta \mathcal{J}(\chi)}{\delta \chi}(\hat{\mathbf{x}}) \mu[\Omega_{\epsilon}(\hat{\mathbf{x}})] + o(\mu[\Omega_{\epsilon}(\hat{\mathbf{x}})]), \quad (3.7)$$

where $\eta_{\hat{\mathbf{x}},\epsilon}$ and $\mu[\Omega_\epsilon(\hat{\mathbf{x}})]$ correspond to the topology perturbation and the measure of the perturbation domain Ω_ϵ . In this context, the perturbation function $\eta_{\hat{\mathbf{x}},\epsilon}$ at point $\hat{\mathbf{x}}$ is defined as the exchange function

$$\Delta\chi(\hat{\mathbf{x}}) = \begin{cases} -(1 - \beta) < 0 & \text{for } \hat{\mathbf{x}} \in \Omega^+ \\ 1 - \beta > 0 & \text{for } \hat{\mathbf{x}} \in \Omega^- \end{cases} \quad (3.8)$$

evaluating the increment in the characteristic function χ due to the material exchange (as illustrated in Figure 3.2), and $\Omega_\epsilon(\hat{\mathbf{x}})$ is the circle or the sphere of center $\hat{\mathbf{x}}$ and radius ϵ , for 2D or 3D domains, which perturbation measure $\mu[\Omega_\epsilon(\hat{\mathbf{x}})]$ is a smooth positive function that tends to zero with ϵ .

According to the previous asymptotic expansion (3.7) and the exchange function (3.8), the relaxed topological derivative (RTD) of a functional \mathcal{J} at point $\hat{\mathbf{x}}$ can be computed as

$$\frac{\delta\mathcal{J}(\chi)}{\delta\chi}(\hat{\mathbf{x}}) = \lim_{\epsilon \rightarrow 0} \frac{1}{\mu[\Omega_\epsilon(\hat{\mathbf{x}})]} [\mathcal{J}(\chi + \eta_{\hat{\mathbf{x}},\epsilon}) - \mathcal{J}(\chi)] \quad (3.9)$$

when the material phase type is exchange (i.e., $\chi \rightarrow \chi + \Delta\chi(\hat{\mathbf{x}})$) at the perturbation domain $\Omega_\epsilon(\hat{\mathbf{x}})$. Unlike in the definition of the exact topological derivative [25, 117, 87, 88], here the perturbed (considering the material exchange, $\Omega^+ \setminus \Omega_\epsilon$) and original (Ω^+) domains remain the same domain. This fact reduces the mathematical complexity of solving analytically the corresponding asymptotic analysis of the objective function in the topological derivative approach. As a result, the relaxed topological derivative can be considered as a fast and easy-to-compute topological derivative, which approximates the exact one.

Relaxed Topological Derivative of the objective function

The relaxed topological derivative of the objective function \mathcal{J} (3.5a) at each point $\hat{\mathbf{x}}$ can be obtained from the corresponding topological asymptotic expansion in terms of the topology perturbation $\eta_{\hat{\mathbf{x}},\epsilon}$. The perturbed objective function $\mathcal{J}(\chi + \eta_{\hat{\mathbf{x}},\epsilon})$ can be then expressed as

$$\begin{aligned} \mathcal{J}(\chi + \eta_{\hat{\mathbf{x}},\epsilon}) &= \int_{\Omega} j(\chi + \eta_{\hat{\mathbf{x}},\epsilon}, \mathbf{x}) d\Omega = \int_{\Omega} \left(j(\chi, \mathbf{x}) + \frac{\partial j(\chi, \mathbf{x})}{\partial \chi} \eta_{(\hat{\mathbf{x}}),\epsilon} + o(\eta_{\hat{\mathbf{x}},\epsilon}) \right) d\Omega = \\ &= \mathcal{J}(\chi) + \int_{\Omega} \frac{\partial j(\chi, \mathbf{x})}{\partial \chi} \Delta\chi(\hat{\mathbf{x}}) d\Omega + o(\mu[\Omega_\epsilon(\hat{\mathbf{x}})]). \end{aligned} \quad (3.10)$$

By rearranging and replacing it into equation (3.9), the RTD of a generalized objective function $\mathcal{J}(\mathbf{u}(\chi), \chi)$ can be mathematically formulated as

$$\begin{aligned} \frac{\delta\mathcal{J}(\chi)}{\delta\chi}(\hat{\mathbf{x}}) &= \lim_{\epsilon \rightarrow 0} \frac{1}{\mu[\Omega_\epsilon(\hat{\mathbf{x}})]} \left(\int_{\Omega} \frac{\partial j(\chi, \mathbf{x})}{\partial \chi} \Delta\chi(\hat{\mathbf{x}}) d\Omega + o(\mu[\Omega_\epsilon(\hat{\mathbf{x}})]) \right) = \\ &= \lim_{\epsilon \rightarrow 0} \frac{|\Omega_\epsilon(\hat{\mathbf{x}})|}{\mu[\Omega_\epsilon(\hat{\mathbf{x}})]} \left[\frac{\partial j(\chi, \mathbf{x})}{\partial \chi} \Delta\chi(\hat{\mathbf{x}}) \right]_{\mathbf{x}=\hat{\mathbf{x}}} = \left[\frac{\partial j(\chi, \mathbf{x})}{\partial \chi} \right]_{\mathbf{x}=\hat{\mathbf{x}}} \Delta\chi(\hat{\mathbf{x}}), \end{aligned} \quad (3.11)$$

where the perturbation measure $\mu[\Omega_\epsilon]$ corresponds to the volume of the perturbation (i.e., $|\Omega_\epsilon|$) and lower order terms of the perturbation measure become 0 as the perturbation radius ϵ tends to 0.

As a result, the relaxed topological derivative of a functional $\mathcal{J}(\mathbf{u}(\chi), \chi)$ can be obtained from the product of the Fréchet derivative of the integrand j and the topology exchange function $\Delta\chi$ at each point $\hat{\mathbf{x}}$. Regarding the Fréchet derivative of the integrand, it is important to emphasize that the state variable \mathbf{u} also depends on the topology and must be derived with respect to χ through the chain rule, thus adding the derivative of the state variable with respect to the design variable. Instead of explicitly computing this term, the adjoint method is employed [72, 25], where the state equation and Lagrange multipliers are included in the original functional. The values of the Lagrange multipliers are found by solving an additional state equation. This will be considered in Section 3.3.

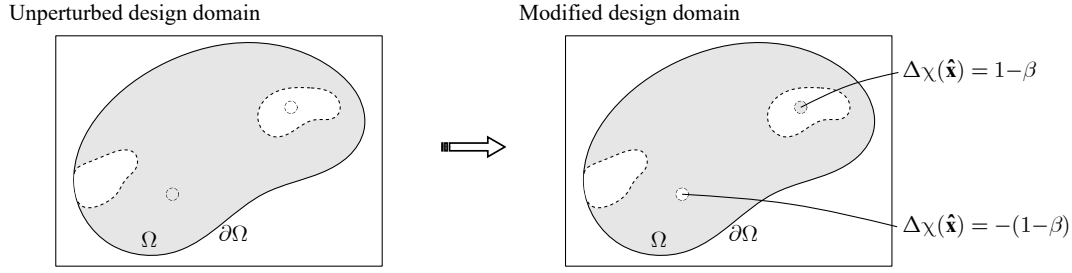
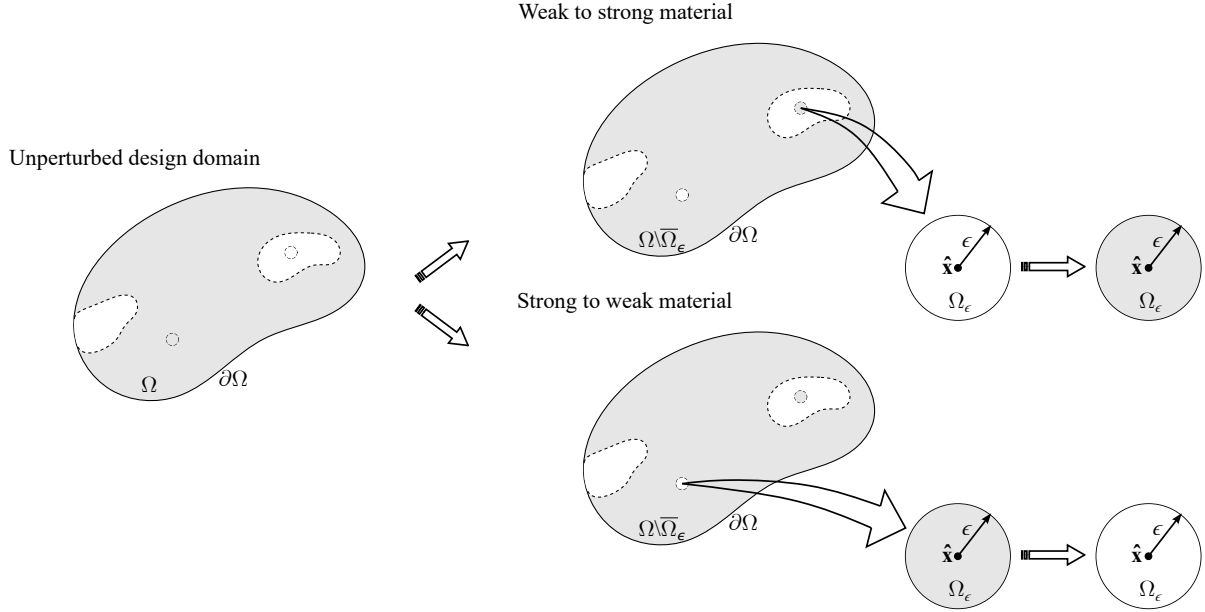
(a) Relaxed Topological Derivative (RTD)

(b) Exact Topological Derivative (TD)


Figure 3.2: Topological derivative computation: **(a)** Relaxed Topological Derivative (RTD) used in the proposed approach and **(b)** Exact Topological Derivative (TD) used in Topology Derivative methods.

Relaxed Topological Derivative of the volume constraint

In contrast of a generalized objective function, the volume constraint \mathcal{C}_0 (3.6) does not depend on the state variable \mathbf{u} , and its topological derivative can be easily derived from equation (3.11). The corresponding relaxed topological derivative can be computed as

$$\frac{\delta \mathcal{C}_0(\chi)}{\delta \chi}(\hat{\mathbf{x}}) = -\frac{1}{|\Omega|} \lim_{\epsilon \rightarrow 0} \frac{|\Omega_\epsilon(\hat{\mathbf{x}})|}{\mu[\Omega_\epsilon(\hat{\mathbf{x}})]} \left[\frac{\partial c_0(\chi, \mathbf{x})}{\partial \chi} \Delta \chi(\mathbf{x}) \right]_{\mathbf{x}=\hat{\mathbf{x}}} = -\frac{1}{|\Omega|} \left[\frac{\partial c_0(\chi, \mathbf{x})}{\partial \chi} \right]_{\mathbf{x}=\hat{\mathbf{x}}} \Delta \chi(\hat{\mathbf{x}}), \quad (3.12)$$

where the integrand c_0 corresponds to the volume of the void subdomain, as defined in equation (3.6). By replacing the integrand into the previous equation and considering the definition of the material exchange function (3.8), one obtains

$$\frac{\delta \mathcal{C}_0(\chi)}{\delta \chi}(\hat{\mathbf{x}}) = -\frac{1}{|\Omega|} \left[\frac{-1}{1 - \beta} \right]_{\mathbf{x}=\hat{\mathbf{x}}} \Delta \chi(\hat{\mathbf{x}}) = \frac{1}{|\Omega|} \frac{\Delta \chi(\hat{\mathbf{x}})}{1 - \beta} = \frac{\text{sgn}(\Delta \chi(\hat{\mathbf{x}}))}{|\Omega|}, \quad (3.13)$$

where the $\text{sgn}(\cdot)$ operator stands for the sign of the material exchange function, being equal to -1 for the hard material subdomain, and 1 elsewhere.

Understandably, the relaxed topological derivative of the volume constraint (normalized with respect to the volume of the design domain) corresponds to the sign function, being negative for those zones where hard material is replaced with weak material (i.e., material is removed from the topology layout), and positive for the opposite case (i.e., material is added to the configuration).

3.2.4 Optimality criteria

Once the topological derivatives of the objective function \mathcal{J} and the volume constraint \mathcal{C}_0 are defined, the optimality condition of the constrained topology optimization problem can be stated. From a logical perspective, the optimality condition has to state the condition for which any change in the topology leads to an increase in the objective function, hence no further changes will be of interest and the optimal topology will be obtained in the optimal condition. This condition can be mathematically defined in terms of the topological derivative of the Lagrangian function.

The Lagrangian function of the constrained problem (3.5) can be expressed as

$$\mathcal{L}(\mathbf{u}(\chi), \chi, \lambda) = \mathcal{J}(\mathbf{u}(\chi), \chi) + \lambda \mathcal{C}_0(\chi, t), \quad (3.14)$$

where the constraint equation \mathcal{C}_0 has been included in the original Lagrangian function by a Lagrange multiplier λ , which value must be computed to enforce the target volume fraction, t .

Consequently, the optimality condition for the constrained topology optimization problem, defined via the corresponding Lagrangian function (3.14), can be written as

$$\frac{\delta \mathcal{L}(\mathbf{u}(\chi), \chi, \lambda)}{\delta \chi}(\hat{\mathbf{x}}) = \frac{\delta \mathcal{J}(\mathbf{u}(\chi), \chi)}{\delta \chi}(\hat{\mathbf{x}}) + \lambda \frac{\delta \mathcal{C}_0(\chi, t)}{\delta \chi}(\hat{\mathbf{x}}) \geq 0 \quad \forall \hat{\mathbf{x}} \in \Omega, \quad (3.15)$$

which can be further simplified to

$$\frac{\delta \mathcal{L}(\mathbf{u}(\chi), \chi, \lambda)}{\delta \chi}(\hat{\mathbf{x}}) = \left(\left[\frac{\partial j(\mathbf{u}(\chi), \chi, \mathbf{x})}{\partial \chi} \right]_{\mathbf{x}=\hat{\mathbf{x}}} \Delta \chi(\hat{\mathbf{x}}) + \lambda \frac{\text{sgn}(\Delta \chi(\hat{\mathbf{x}}))}{|\Omega|} \right) \geq 0 \quad \forall \hat{\mathbf{x}} \in \Omega, \quad (3.16)$$

by replacing the topological derivative of the objective function (3.11) and the volume constraint (3.13). Specific details on the statement of this optimality criteria can be found in Paper A [89].

3.2.5 Closed-form non-linear optimality criteria

The closed-form non-linear optimality criteria rely on the enforcement, in strong form, of the original volume constraint \mathcal{C}_0 via the computation of the Lagrange multiplier, λ . As aforementioned, the exact value of this parameter is obtained using a bisection algorithm of the optimality criteria.

For the optimality criterion, the most crucial point is to determine its relation to the design variable of the optimization problem. As an intermediate point, the optimality condition in the whole design domain is related to the discrimination function ψ , and the latter to the characteristic function χ by means of the Heaviside function.

In this context, the optimality condition (3.16) particularized for a certain topology layout featuring two material subdomains Ω^+ and Ω^- reads as follows

$$\frac{\delta \mathcal{L}(\mathbf{u}(\chi), \chi, \lambda)}{\delta \chi}(\hat{\mathbf{x}}) = \begin{cases} \left(-(1 - \beta) \left[\frac{\partial j(\mathbf{u}(\chi), \chi, \mathbf{x})}{\partial \chi} \right]_{\mathbf{x}=\hat{\mathbf{x}}} - \frac{\lambda}{|\Omega|} \right) \geq 0 & \forall \hat{\mathbf{x}} \in \Omega^+ \\ \left((1 - \beta) \left[\frac{\partial j(\mathbf{u}(\chi), \chi, \mathbf{x})}{\partial \chi} \right]_{\mathbf{x}=\hat{\mathbf{x}}} + \frac{\lambda}{|\Omega|} \right) \geq 0 & \forall \hat{\mathbf{x}} \in \Omega^- \end{cases}, \quad (3.17)$$

from which one can identify a single expression that relates to the expression of the discrimination function ψ at each point $\hat{\mathbf{x}}$ of the design domain, being positive for points included in the strong material subdomain, and negative, in the void material subdomain.

As a result, for a given pseudo-time t and objective function derivative, the optimal topology layout can be found by solving the closed-form non-linear optimality criteria, i.e.,

$$\begin{cases} \psi(\chi, \hat{\mathbf{x}}, \lambda) := -(1 - \beta) \left[\frac{\partial j(\mathbf{u}(\chi), \chi, \mathbf{x})}{\partial \chi} \right]_{\mathbf{x}=\hat{\mathbf{x}}} - \frac{\lambda}{|\Omega|} \\ \chi(\hat{\mathbf{x}}, \lambda) = \mathcal{H}_\beta[\psi(\chi, \hat{\mathbf{x}}, \lambda)] \\ \mathcal{C}_0(\chi(\hat{\mathbf{x}}, \lambda), t) = t - \frac{|\Omega^-(\chi(\hat{\mathbf{x}}, \lambda))|}{|\Omega|} = 0 \end{cases}, \quad (3.18)$$

where equations (3.3), (3.6) and (3.17) have been considered.

Laplacian regularization

As any other technique, the proposed strategy requires some kind of filtering or regularization to mitigate the ill-posedness of the topology optimization problem, in terms of checkerboard patterns, mesh-dependency, and filament size control. In the literature, one can find a variety of techniques to reduce the effect of these problems, including the distance-based filter and the Tikhonov regularization [18, 63, 59, 142], among others.

In this approach, a Laplacian regularization is applied to the discrimination function ψ (3.18), thus obtaining a smooth scalar function ψ_τ . This smoothed function replaces the original discontinuous function in the closed-form optimality criteria. As a result, topology smoothness and mesh-independence are accomplished, and minimum bar-size can also be controlled, thus providing control over the complexity of topology layouts.

The smoothed discrimination function ψ_τ comes from the resolution of

$$\begin{cases} \psi_\tau - (\tau h_e)^2 \Delta_{\mathbf{x}} \psi_\tau = \psi & \text{in } \Omega \\ \nabla_{\mathbf{x}} \psi_\tau \cdot \mathbf{n} = 0 & \text{on } \partial\Omega \end{cases}, \quad (3.19)$$

where $\Delta_{\mathbf{x}}(\mathbf{x}, \cdot)$ and $\nabla_{\mathbf{x}}(\mathbf{x}, \cdot)$ are respectively the Laplacian and Gradient operators, and \mathbf{n} is the outward normal to the boundary of the design domain, $\partial\Omega$. τ and h_e stand for the dimensionless regularization parameter and the typical size of the finite element mesh, respectively.

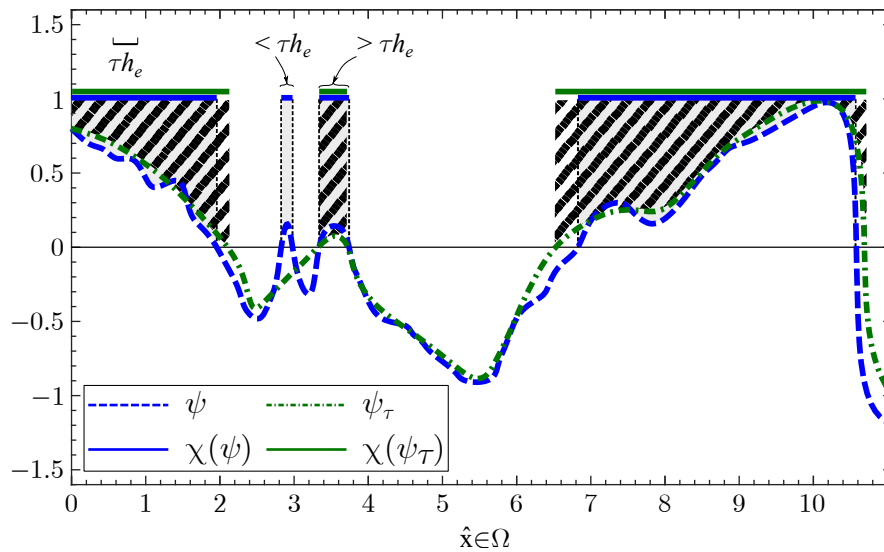


Figure 3.3: Laplacian regularization: the original discrimination function ψ and the corresponding characteristic function χ are illustrated in blue, while the smoothed ones (i.e., ψ_τ and $\chi(\psi_\tau)$) are drawn in green. The minimum characteristic size τh_e is displayed in the top left of the figure, representing the minimum size from which small bars are removed from the final design. The original topology layout ($\chi(\psi)$) is shaded in gray, and the final smoothed design ($\chi(\psi_\tau)$) is represented by a left-inclined lines pattern.

Note that, as an alternative to applying the Laplacian regularization to the discrimination function ψ including the topological derivative of the volume constraint \mathcal{C}_0 , the regularization can be directly applied to the derivative of the objective function \mathcal{J} , henceforth denoted as ξ . This term is known prior to solving the optimality criterion (3.18) and independent of the Lagrange multiplier, which is a constant value for the entire design domain. The resolution of equation (3.19) for the pseudo-energy ξ leads to the corresponding Laplacian-regularized version ξ_τ . From this function, the smoothed discrimination function ψ_τ can be computed together with the correct value of the Lagrange multiplier λ . As a consequence of this modification, the

regularization only needs to be applied once per iteration of equation (3.5) instead of equation (3.18), thus significantly reducing the computational cost of solving the optimality criteria.

Without going into details, the Laplacian filter manages to eliminate those wavelengths below the regularization parameter τ . Consequently, those bars or components with a thickness smaller than τh_e will be suppressed from the final design. In the case of imposing a zero τ parameter, a global smoothing would be applied to the pseudo-energy ξ with the mass matrix. Additionally, the regularization parameter τ can be defined as a tensor to impose different sizes for each direction, thus obtaining an anisotropic regularization, as tested in Article A.

Volume enforcement strategy

Cutting&bisection algorithm Considering a design topology χ and the corresponding sensitivity of the objective function ξ_τ , the resulting topology χ and the volume constraint \mathcal{C}_0 for each value of the Lagrange multiplier λ can be easily determined, as shown by the expression (3.18). The fulfillment of the constraint equation is achieved by computing the Lagrange multiplier that strongly satisfies the target volume fraction t using a bisection method.

According to the discrimination function ψ , for each value of the Lagrange multiplier λ , the new topology (strong material subdomain Ω^+) is defined as those points in the design domain with pseudo-energy greater than the Lagrange multiplier, i.e., $\Omega^+ = \{\mathbf{x} \in \Omega / \xi_\tau(\mathbf{u}(\chi), \chi, \mathbf{x}) > \lambda\}$ (equation (3.2)). Additionally, the material boundary Γ corresponds to the λ -isocontour of the pseudo-energy, defined by the zero level of that function, i.e., $\Gamma = \{\mathbf{x} \in \Omega / \xi_\tau(\mathbf{u}(\chi), \chi, \mathbf{x}) = \lambda\}$ (see Figure 3.1). As a consequence, each value of the Lagrange multiplier defines a new topology layout, which boundary is iso-energetic. By a slightly change in the Lagrange multiplier, a continuous change in the topology is obtained, allowing the boundary and the material domain to be precisely detailed.

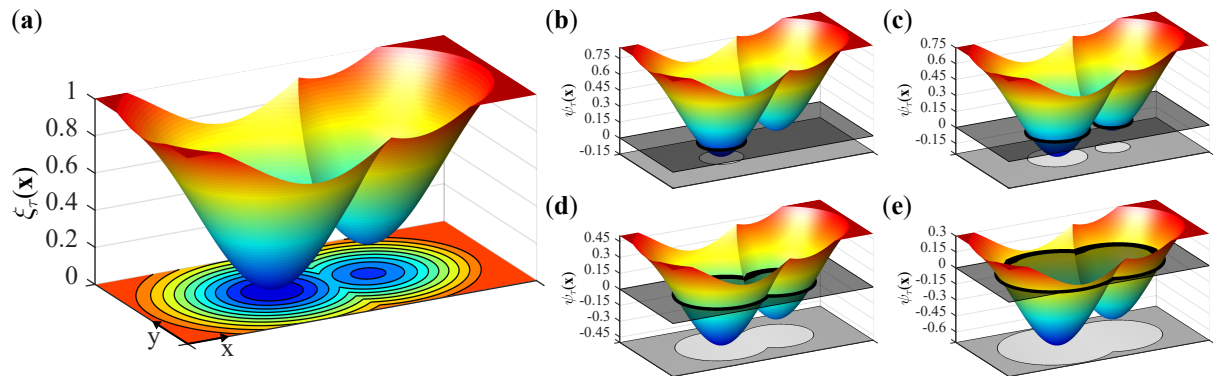


Figure 3.4: Cutting and bisection iterative algorithm: (a) Representation of the pseudo-energy ξ_τ in the design domain Ω with the corresponding λ -isocontours represented at the bottom, and (b)-(e) Visual representation of the corresponding discrimination function ψ_τ when the pseudo-energy is cut at different λ values. As the Lagrange multiplier increases, the material domain Ω^+ becomes smaller (hence the void domain Ω^- increases) and the constraint equation \mathcal{C}_0 varies accordingly, thus providing a solution to expression.

In this iso-contour context, the monotonically increasing relationship between the volume constraint $\mathcal{C}_0(\chi(\hat{\mathbf{x}}, \lambda), t)$ and the Lagrange multiplier λ can be determined for a given pseudo-time t . The value that satisfies this constraint can be accurately approximated, within a margin of error, by means of a bisection method as illustrated in Figure 3.4. The strategy used for

computing the Lagrange multiplier and obtaining the new topology can be formulated as follows

$$\left[\begin{array}{l} \text{Given } \chi_k, t, \text{ and the pseudo-energy} \\ \left\{ \begin{array}{l} \xi(\mathbf{u}(\chi_k), \chi_k, \hat{\mathbf{x}}) = -(1 - \beta) \left[\frac{\partial j(\mathbf{u}(\chi_k), \chi_k, \mathbf{x})}{\partial \chi} \right]_{\mathbf{x}=\hat{\mathbf{x}}} \\ \xi_\tau(\mathbf{u}(\chi_k), \chi_k, \hat{\mathbf{x}}) \leftarrow \text{solution to the Laplacian regularization (3.19) for } \xi \end{array} \right. \\ \text{find } \chi_{k+1} \text{ and } \lambda \text{ such that} \\ \left\{ \begin{array}{l} \psi_{k+1}(\chi_k, \hat{\mathbf{x}}, \lambda) = \xi_\tau(\mathbf{u}(\chi_k), \chi_k, \hat{\mathbf{x}}) - \frac{\lambda}{|\Omega|} \\ \chi_{k+1}(\hat{\mathbf{x}}, \lambda) = \mathcal{H}_\beta[\psi_{k+1}(\chi_k, \hat{\mathbf{x}}, \lambda)] \\ \mathcal{C}_0(\chi_{k+1}(\hat{\mathbf{x}}, \lambda), t) = t - \frac{|\Omega^-(\chi_{k+1}(\hat{\mathbf{x}}, \lambda))|}{|\Omega|} = 0 \rightarrow \|\mathcal{C}_0(\chi_{k+1}(\hat{\mathbf{x}}, \lambda), t)\| \leq \text{To}l_c \end{array} \right. \end{array} \right. \quad (3.20)$$

where the new topology χ_{k+1} is defined in terms of the topology of the previous iteration χ_k and the exact value of the Lagrange multiplier λ .

Augmented Lagrangian algorithm Note that as an alternative to explicitly imposing the volume using the fixed-point methodology, it is possible to impose the volume constraint using the augmented Lagrangian method [74]. In this context, the Lagrangian function (3.14) is modified to include the constraint equation \mathcal{C}_0 through a Lagrange multiplier λ and a penalty parameter ρ as follows

$$\mathcal{L}(\mathbf{u}(\chi), \chi, \lambda) = \mathcal{J}(\mathbf{u}(\chi), \chi) + \lambda \mathcal{C}_0(\chi, t) + \frac{1}{2} \rho \mathcal{C}_0(\chi, t)^2, \quad (3.21)$$

where per each topology iteration for minimizing the objective function, a λ -iteration for maximizing the objective function is performed, i.e., $\lambda_{k+1} = \lambda_k + \rho \mathcal{C}_0(\chi_k, t)$. In this strategy, the relaxed topological derivative of the Lagrangian function (3.15) is given by

$$\frac{\delta \mathcal{L}(\mathbf{u}(\chi), \chi, \lambda)}{\delta \chi}(\hat{\mathbf{x}}) = \frac{\delta \mathcal{J}(\mathbf{u}(\chi), \chi)}{\delta \chi}(\hat{\mathbf{x}}) + (\lambda + \rho \mathcal{C}_0(\chi, t)) \frac{\delta \mathcal{C}_0(\chi, t)}{\delta \chi}(\hat{\mathbf{x}}), \quad (3.22)$$

which is then used to iteratively update the discrimination function ψ via a Hamilton-Jacobi equation in an incremental scheme. The new topology χ_{k+1} is defined by

$$\left\{ \begin{array}{l} \psi_{k+1}(\chi_k, \hat{\mathbf{x}}, \lambda) = \psi_k(\chi_k, \hat{\mathbf{x}}, \lambda) + \Delta t \kappa \left(\xi(\mathbf{u}(\chi_k), \chi_k, \hat{\mathbf{x}}) - \frac{\lambda_k + \rho_k \mathcal{C}_0(\chi_k, t)}{|\Omega|} \right) \\ \psi_\tau(\chi_k, \hat{\mathbf{x}}, \lambda) \leftarrow \text{solution to the Laplacian regularization (3.19) for } \psi_{k+1} \\ \chi_{k+1}(\hat{\mathbf{x}}, \lambda) = \mathcal{H}_\beta[\psi_\tau(\chi_k, \hat{\mathbf{x}}, \lambda)] \end{array} \right., \quad (3.23)$$

where Δt and κ stand for a time-relaxation factor and a proportionally coefficient, respectively.

After updating the discrimination function via the Hamilton-Jacobi equation, a Laplacian regularization must be performed to remove undesired thin bars. The characteristic function can then be computed from this smooth discrimination function, ψ_τ . Without going into further detail, other technical modifications are required to prevent the process from stagnating, including limiting the discrimination function and normalizing the pseudo-energy function, among others. All required modifications are detailed in Appendix A.C of Article A.

In contrast to the proposed technique, the augmented Lagrangian methodology only imposes the volume constraint on the last converged iteration instead of on each iteration of the optimization problem, thus losing some global algorithmic robustness and requiring a large number of iterations to fulfill the volume constraint.

Time-advancing strategy

As aforementioned, the strategy to enforce the volume constraint \mathcal{C}_0 is by including a Lagrange multiplier λ in the Lagrangian function (3.14) of the optimization problem. In the proposed approach, unlike other techniques that impose a constant volume throughout the optimization, an incremental time-advancing scheme is implemented. The range of the constraint equation in terms of the pseudo-time $t \in [0, T]$, T being the final target volume fraction, is divided into n_{steps} steps, obtaining for each step the optimal solution. As a result of this strategy, the Pareto Frontier between the objective function and the volume constraint is obtained for different volume fractions t [12], as depicted in Figure 3.5 for a characteristic topology optimization problem.

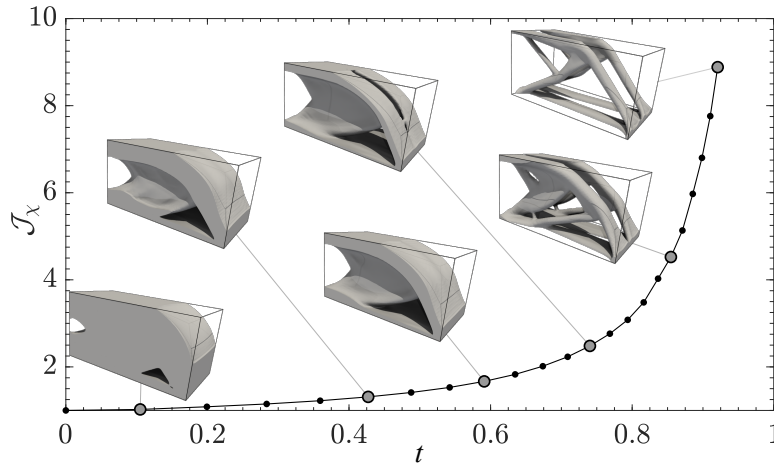


Figure 3.5: Pareto Frontier of a topology optimization example: the time interval $t \in [0, 0.92]$ has been divided into 22 steps, each step increasing the pseudo-time t exponentially.

Since the time interval $[0, T]$ is divided into a given number of time-steps, the optimal topology of the previous step can be used as a starting point to find the optimal configuration of the next step, assuming that the topology layouts are close enough for two consecutive steps. Consequently, the time-increment value Δt must be set by the user to a sufficiently small value so that the convergence of the topology optimization problem can be ensured. Despite requiring the resolution of multiple topology optimization problems, this incremental strategy increases the robustness of the resolution process and simultaneously obtains a set of converged solutions at a reduced computational cost, since a small number of iterations of the topology optimization problem (3.5) is required for a specific t value.

3.2.6 Flowchart of the algorithm

The flowchart of the general algorithm, used to obtain the optimal topology layouts, is illustrated in Figure 3.6. The main part of the algorithm consists in solving the state equation to obtain the unknown field \mathbf{u} , and computing the corresponding sensitivities along with the objective function value (3.5). After computing the relaxed topological derivatives of the objective function \mathcal{J} , the Laplacian regularization must be applied to the pseudo-energy ξ to improve numerical stability, ensure convergence, and control the complexity of the optimal solution. The topology layout, in terms of the discrimination function ψ or the characteristic function χ , is then updated according to the optimality criterion via the closed-form optimality criteria (3.20). Due to the time-advancing scheme, this topology optimization algorithm must be repeated for each time-step until the convergence criteria are met, thus obtaining a set of converged solutions over the Pareto Frontier of optimal solutions between the objective function and the volume constraint.

Compared to other techniques, the pseudo-energy ξ is first shifted and normalized, which

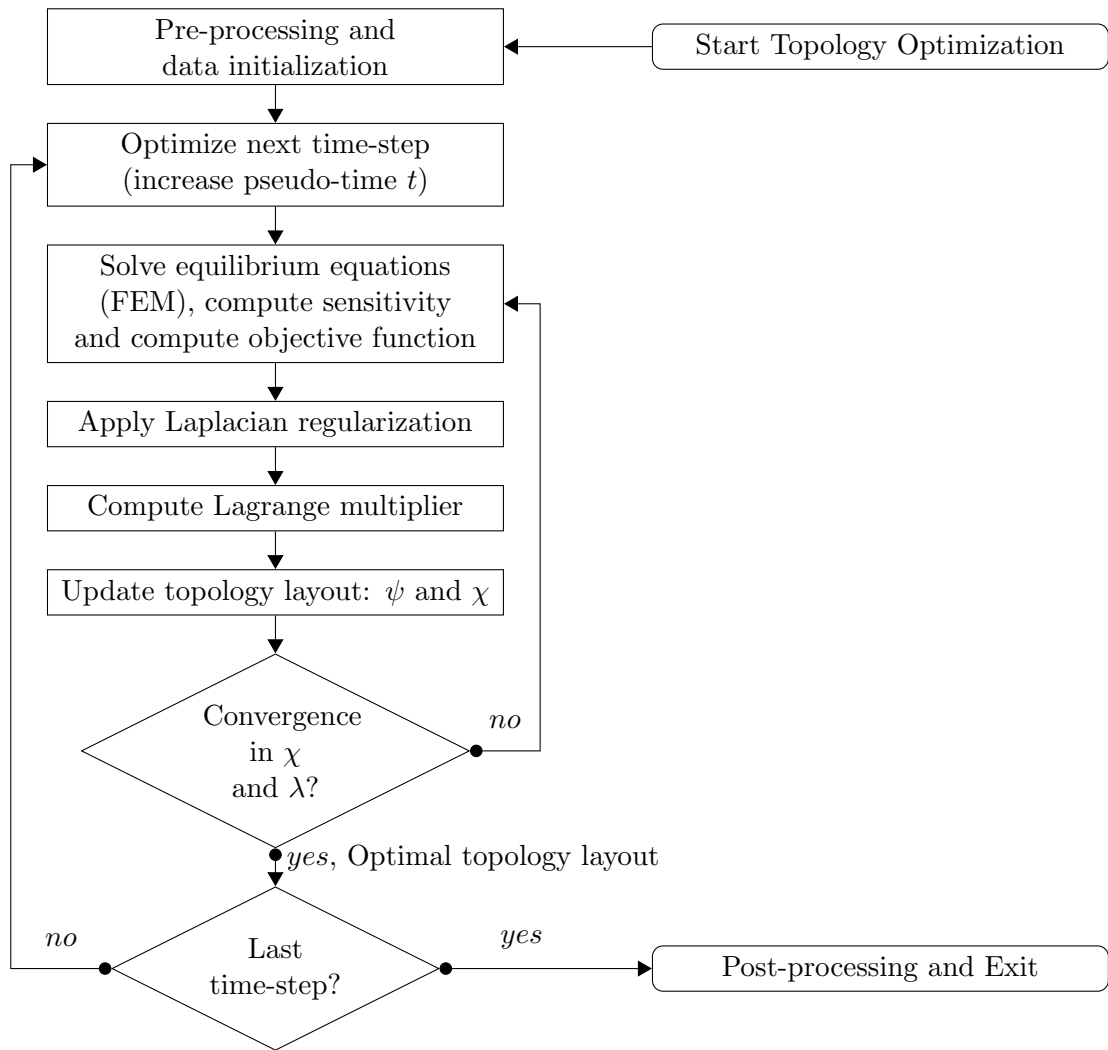


Figure 3.6: The general flowchart for the proposed topology optimization approach.

leads to the modified energy density defined as

$$\hat{\xi}(\hat{\mathbf{x}}) = \frac{\xi(\hat{\mathbf{x}}) - \chi(\hat{\mathbf{x}})\Delta_{shift}}{\Delta_{norm}}, \quad (3.24)$$

where Δ_{shift} and Δ_{norm} correspond to the shifting and normalization parameters defined at the first iteration as $\min(\xi_{\min}, 0)$ and $\max(\xi_{\max} - \xi_{\min}, \xi_{\max})$, respectively, with ξ_{\max} and ξ_{\min} being equal to $\max_{\mathbf{x} \in \Omega} \xi_0(\mathbf{x})$ and $\min_{\mathbf{x} \in \Omega} \xi_0(\mathbf{x})$. The constant shifting is applied in order to obtain positive pseudo-energy ξ in Ω at $t = 0$, thus providing algorithmic time consistency to the problem and ensuring a converged topology for this time-step. It can be proven that these operations do not alter the problem solution. This modified pseudo-energy replaces the original pseudo-energy term.

A detailed scheme of the proposed topology optimization technique is presented in Algorithm 1.

3.3 Structural and thermal formulations

The topology optimization technique presented in the previous section is now applied to different physical problems, including the structural problem (Section 3.3.1) and the thermal problem (Section 3.3.2). For each scenario, the state equation to be solved will be introduced, along with

Algorithm 1: Optimization algorithm of the proposed topology optimization technique

Data: Given the mesh, state equation, boundary conditions and objective function
Result: Find χ_n for $\mathcal{T} := \{t_0, t_1, \dots, t_n, \dots, T\}$
begin
 Initialization of the design variables;
 for $n \leftarrow 1$ **to** n_{steps} **do**
 Initialization of step n ;
 $k \leftarrow 0$;
 while $\|\Delta\chi\|_{L_2} > Tol_\chi$ **and** $\|\Delta\lambda\| > Tol_\lambda$ **do**
 Compute \mathbf{u} from the state equation using FEM;
 Compute the relaxed topological sensitivity ξ of the Lagrangian function from (3.15);
 Compute the modified pseudo-energy $\hat{\xi}$, via shifting and normalization, from (3.24);
 Regularize the modified pseudo-energy by a Laplacian smoothing ($\hat{\xi}_r$) from (3.19);
 $j \leftarrow 0$;
 while $\|\mathcal{C}_0(\chi_j(\hat{\mathbf{x}}, \lambda_j), t_n)\| \geq Tol_{\mathcal{C}}$ **do**
 Update the Lagrange multiplier λ_{j+1} from the bisection algorithm;
 Compute the corresponding discrimination function ψ_{j+1} from (3.20);
 Compute the corresponding characteristic function χ_{j+1} from (3.20);
 Compute the corresponding volume constraint $\mathcal{C}_0(\chi_{j+1}(\hat{\mathbf{x}}, \lambda_{j+1}), t_n)$ from (3.20);
 $j \leftarrow j + 1$;
 end
 Update the Lagrange multiplier $\lambda_{k+1} = \lambda_j$;
 Update the discrimination function ψ_{k+1} from (3.20);
 Update the characteristic function χ_{k+1} from (3.20);
 $k \leftarrow k + 1$;
 end
 Compute the converged optimal topology $\chi_n = \chi_k$;
 end
end

different objective functions to be minimized and the corresponding relaxed topological derivatives. The adjoint method will be used to avoid computing the relaxed topological derivative of the state field with respect to the design variable in equation (3.11).

3.3.1 Structural topology optimization

For the solid elastic problem, the state equation can be mathematically formulated in strong form as

$$\left[\begin{array}{l} \text{Find } \mathbf{u}(\chi, \mathbf{x}) \text{ such that} \\ \left\{ \begin{array}{ll} \nabla \cdot \boldsymbol{\sigma}(\chi, \mathbf{x}) + \mathbf{b}(\chi, \mathbf{x}) = \mathbf{0} & \text{in } \Omega \\ \boldsymbol{\sigma}(\chi, \mathbf{x}) \cdot \mathbf{n} = \mathbf{t}_n(\mathbf{x}) & \text{on } \partial_\sigma \Omega, \\ \mathbf{u}(\chi, \mathbf{x}) = \bar{\mathbf{u}}(\mathbf{x}) & \text{on } \partial_u \Omega \end{array} \right. \end{array} \right. \quad (3.25)$$

where $\boldsymbol{\sigma}(\chi, \mathbf{x})$ and $\mathbf{b}(\chi, \mathbf{x})$ stand for the second-order stress tensor field and the volumetric force, respectively, both depending on the topology layouts, and the unknown field $\mathbf{u}(\chi, \mathbf{x}) \in H^1(\Omega)$ corresponds to the displacement vector for a specific optimal design χ . As depicted in Figure 3.7, the boundary conditions are enforced as tractions $\mathbf{t}_n(\mathbf{x})$ and displacements $\bar{\mathbf{u}}(\mathbf{x})$ on $\partial_\sigma \Omega$ and $\partial_u \Omega$, respectively. The normal \mathbf{n} corresponds to the unit outward normal.

As for the material behavior, the elastic material is governed by the Hooke's law, i.e., $\boldsymbol{\sigma}(\mathbf{x}) = \mathbb{C}_\chi(\mathbf{x}) : \boldsymbol{\varepsilon}(\mathbf{x})$, with $\boldsymbol{\varepsilon}$ being the strain tensor ($\boldsymbol{\varepsilon}(\mathbf{x}) = \nabla^S \mathbf{u}_\chi(\mathbf{x})$) and \mathbb{C}_χ being the fourth-order, elastic constitutive tensor. The tensor \mathbb{C}_χ depends on the design variable χ via the material interpolation, in such a way as to represent the elastic properties of the stiff (\mathbb{C}^+) and weak ($\mathbb{C}^- = \alpha \mathbb{C}^+$) materials in the bi-material configuration presented in equation (3.3). From the expressions (3.3) and (3.4), the constitutive tensor \mathbb{C}_χ at each point \mathbf{x} is defined by

$$\mathbb{C}_\chi(\mathbf{x}) = \chi^m(\mathbf{x}) \mathbb{C}^+, \quad (3.26)$$

resulting in a constitutive tensor \mathbb{C}^+ in the stiff material subdomain for $\chi = 1$, and \mathbb{C}^- or $\alpha \mathbb{C}^+$ for $\chi = \beta$, otherwise.

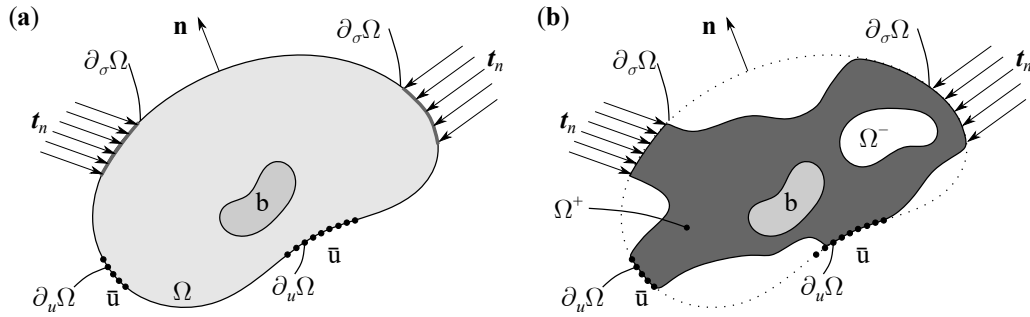


Figure 3.7: Elastic problem sketch: (a) fixed analysis domain Ω with boundary conditions (in which the displacement $\bar{\mathbf{u}}(\mathbf{x})$ or the traction $\mathbf{t}_n(\mathbf{x})$ can be prescribed at $\partial_u\Omega$ and $\partial_\sigma\Omega$, respectively) and (b) Bi-material configuration with stiff and soft material domains, Ω^+ and Ω^- , respectively, and the same boundary conditions.

Considering a Galerkin-based finite element discretization of equation (3.25), the resulting equation can be expressed in matrix form as

$$\begin{cases} \mathbb{K}_\chi \hat{\mathbf{u}}_\chi = \mathbf{f}_\chi & (3.27) \\ \text{with} \\ \mathbb{K}_\chi = \int_{\Omega} \mathbf{B}^T(\mathbf{x}) \mathbb{C}_\chi(\mathbf{x}) \mathbf{B}(\mathbf{x}) d\Omega, & (3.28) \\ \mathbf{f}_\chi = \int_{\partial_\sigma\Omega} \mathbf{N}_u^T(\mathbf{x}) \mathbf{t}_n(\mathbf{x}) d\Gamma + \int_{\Omega} \mathbf{N}_u^T(\mathbf{x}) \mathbf{b}_\chi(\mathbf{x}) d\Omega, & (3.29) \end{cases}$$

where \mathbb{K}_χ and \mathbf{f}_χ are the standard stiffness matrix and the external force vector, \mathbf{N}_u and \mathbf{B} are the shape function and the strain-displacement matrices, and $\hat{\mathbf{u}}_\chi$ is the nodal displacement vector. Henceforth, the dependence of external forces with respect to the design variable will be neglected.

Minimum mean compliance

The minimum mean compliance topology optimization problem seeks the optimal topology layout that maximizes the global stiffness of the structure, or equivalently, minimizes the external work on the structure. The objective function \mathcal{J} from equation (3.5a) can be written as

$$\mathcal{J}(\mathbf{u}(\chi), \chi) = \int_{\Omega} \hat{\mathbf{u}}_\chi^T \mathbf{B}^T(\mathbf{x}) \mathbb{C}_\chi(\mathbf{x}) \mathbf{B}(\mathbf{x}) \hat{\mathbf{u}}_\chi d\Omega = \mathbf{f}^T \hat{\mathbf{u}}_\chi, \quad (3.30)$$

with $j(\mathbf{u}(\chi), \chi, \mathbf{x})$ being $\nabla^S \mathbf{u}_\chi(\mathbf{x}) : \mathbb{C}_\chi(\mathbf{x}) : \nabla^S \mathbf{u}_\chi(\mathbf{x})$. The corresponding pseudo-energy ξ can be computed by applying the adjoint method to equation (3.30), which turns out to be self-adjoint, thus no requiring any additional state equation. The resultant sensitivity can be written in terms of the characteristic function χ and the nodal displacement vector $\hat{\mathbf{u}}$ as

$$\xi(\mathbf{u}(\chi), \chi, \hat{\mathbf{x}}) = -m\chi^{m-1}(\hat{\mathbf{x}}) \hat{\mathbf{u}}^T(\chi, \hat{\mathbf{x}}) \mathbf{B}^T(\hat{\mathbf{x}}) \mathbb{C}^+(\hat{\mathbf{x}}) \mathbf{B}(\hat{\mathbf{x}}) \hat{\mathbf{u}}(\chi, \hat{\mathbf{x}}) \Delta\chi(\hat{\mathbf{x}}). \quad (3.31)$$

The reader is referred to Article A for the complete derivation of this term.

Compliant mechanism synthesis

In this case, the topology optimization problem aims at maximizing the displacement at the output port due to an action (force or displacement) applied at the input port by designing a flexible structure. In other words, the objective is to design a flexible mechanism, e.g., a gripper,

providing a target displacement at the output port (the jaws of the gripper) from a given action performed at the input port. In the context of a finite element discretization, the corresponding objective function \mathcal{J} can be expressed as

$$\mathcal{J}(\mathbf{u}(\chi), \chi) = -\mathbf{1}^T \hat{\mathbf{u}}_\chi, \quad (3.32)$$

where $\mathbf{1}$ represents a dummy constant force vector applied only at the output port in the desired direction. Additional springs, denoted by K_{in} and K_{out} , must be considered in the input and output ports, respectively, to ensure convergence [111].

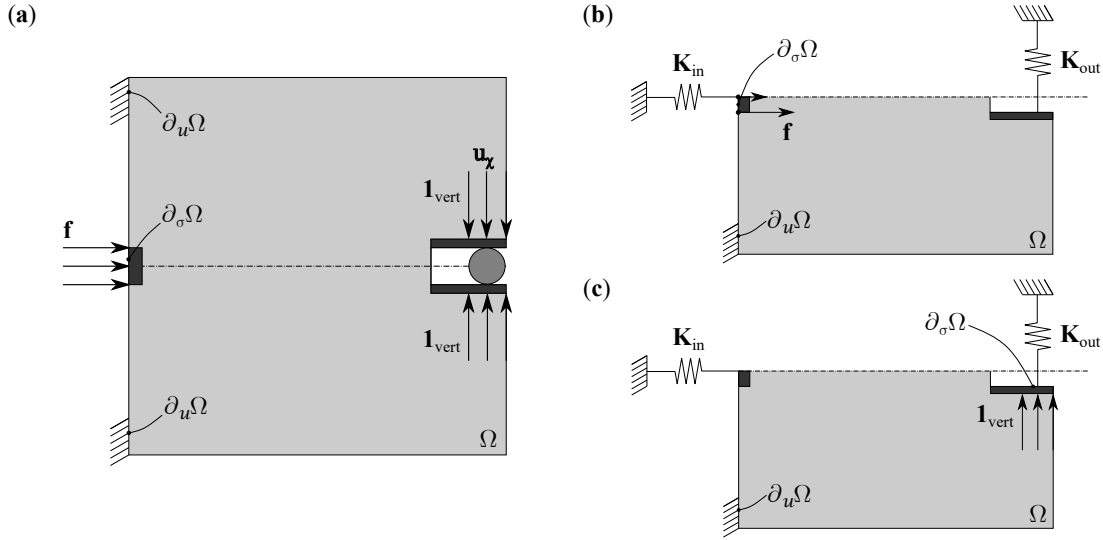


Figure 3.8: Compliant mechanism sketch: (a) topology optimization domain with an horizontal load applied on the left side (input port). The displacements at the jaws (output port) are maximized in the vertical direction. Figures (b) and (c) correspond to the problem settings for the original and auxiliary state equations, respectively. These problems are used to compute the state field $\hat{\mathbf{u}}^{(1)}$, and the relaxed topological derivative of the objective function, ξ .

As mentioned previously, the sensitivity is computed from equation (3.32) via the adjoint method. Nevertheless, the compliant mechanism problem is not self-adjoint, thus requiring the resolution of an additional state equation. The additional system presents the same stiffness matrix \mathbb{K}_χ from equation (3.28), but a different force vector $\mathbf{f}_\chi^{(2)}$ consisting in a dummy constant force at the output port (i.e., the force vector corresponds to $\mathbf{1}$). The resolution of this auxiliary equation leads to the state field $\hat{\mathbf{u}}_\chi^{(2)}$, which is subsequently used to compute the relaxed topological derivative of the objective function as

$$\xi(\mathbf{u}(\chi), \chi, \hat{\mathbf{x}}) = m\chi^{m-1}(\hat{\mathbf{x}}) \hat{\mathbf{u}}^{(2)T}(\chi, \hat{\mathbf{x}}) \mathbf{B}^T(\hat{\mathbf{x}}) \mathbb{C}^+(\hat{\mathbf{x}}) \mathbf{B}(\hat{\mathbf{x}}) \hat{\mathbf{u}}^{(1)}(\chi, \hat{\mathbf{x}}) \Delta\chi(\hat{\mathbf{x}}), \quad (3.33)$$

when volumetric forces are neglected. This term corresponds to the mutual potential energy.

In contrast to the previous example, the pseudo-energy is no longer always positive since $\hat{\mathbf{u}}^{(2)}$ may be different from $\hat{\mathbf{u}}^{(1)}$, which means that ξ may be either positive or negative in different areas of the design domain. In this particular situation, the shifting of the pseudo-energy ξ (3.24) results in the convergence of the optimization problem.

3.3.2 Thermal topology optimization

For the thermal problem, the state equation (3.25) now becomes the steady-state thermal problem, which states the heat energy balance in the design domain Ω . In this case, the unknown field $\mathbf{u}(\chi, \mathbf{x})$ corresponds to the temperature distribution $\theta(\chi, \mathbf{x})$ and can be obtained from solving

the following problem

$$\left[\begin{array}{l} \text{Find } \theta(\chi, \mathbf{x}), \text{ such that} \\ \left\{ \begin{array}{ll} -\nabla \cdot \mathbf{q}(\chi, \mathbf{x}) + r(\chi, \mathbf{x}) = 0 & \text{in } \Omega \\ \mathbf{q}(\chi, \mathbf{x}) \cdot \mathbf{n} = \bar{q}(\mathbf{x}) & \text{on } \partial_q \Omega \\ \theta(\chi, \mathbf{x}) = \bar{\theta}(\mathbf{x}) & \text{on } \partial_\theta \Omega \\ \mathbf{q}(\chi, \mathbf{x}) \cdot \mathbf{n} = h(\theta(\chi, \mathbf{x}) - \theta_{amb}(\mathbf{x})) & \text{on } \partial_h \Omega \end{array} \right. \end{array} \right. \quad (3.34)$$

where $\mathbf{q}(\chi, \mathbf{x})$ and $r(\chi, \mathbf{x})$ stand for the heat flux and the heat source function, $\bar{q}(\mathbf{x})$ and $\bar{\theta}(\mathbf{x})$ are the prescribed heat flux and temperature on the boundaries of Ω , and h and $\theta_{amb}(\mathbf{x})$ correspond to the heat transfer coefficient and the ambient temperature imposed at the convective boundary $\partial_h \Omega$. The thermal problem and the boundary conditions are illustrated in Figure 3.9.

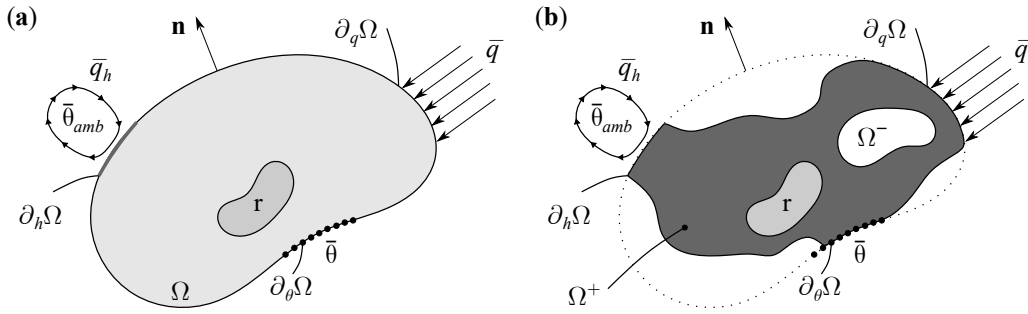


Figure 3.9: Steady-state thermal problem sketch: (a) fixed analysis domain Ω with boundary conditions (in which the temperature $\bar{\theta}(\mathbf{x})$, the normal heat flux $\bar{q}(\mathbf{x})$ or the convective heat flux $\bar{q}_h(\mathbf{x})$ can be prescribed at $\partial_\theta \Omega$, $\partial_q \Omega$ and $\partial_h \Omega$, respectively) and (b) Bi-material configuration with high and low-conductive material domains, Ω^+ and Ω^- , respectively, and the same boundary conditions.

In the thermal context, the conductive material is governed by the Fourier's law, which states that the heat flux field \mathbf{q} follows $\mathbf{q}(\chi, \mathbf{x}) = -\boldsymbol{\kappa}(\chi, \mathbf{x}) \cdot \nabla \theta_\chi(\mathbf{x})$. As in the structural problem, the conductive properties depend on the topology layout, i.e., the thermal conductivity $\boldsymbol{\kappa}$ and the heat source r are defined in terms of the characteristic function χ and the location in the design domain \mathbf{x} . Similar to the constitutive tensor \mathbb{C} for the structural problem, the symmetric second-order thermal conductivity tensor $\boldsymbol{\kappa}$ can be interpolated between the conductivity of the high-conductive material ($\boldsymbol{\kappa}^+$) and the property of the low-conductive material ($\boldsymbol{\kappa}^- = \alpha \boldsymbol{\kappa}^+$) in the bi-material topology layout. Mimicking the expression (3.26) for the constitutive tensor \mathbb{C} , the material interpolation can be written as

$$\boldsymbol{\kappa}_\chi(\mathbf{x}) = \chi^m(\mathbf{x}) \boldsymbol{\kappa}^+. \quad (3.35)$$

The finite element counterpart expressions to equations (3.27)-(3.29) of the structural problem can be written as

$$\left[\begin{array}{l} \mathbb{K}_\chi \hat{\boldsymbol{\theta}}_\chi = \mathbf{f}_\chi \\ \text{with} \end{array} \right. \quad (3.36)$$

$$\mathbb{K}_\chi = \int_\Omega \mathbf{B}^T(\mathbf{x}) \boldsymbol{\kappa}_\chi(\mathbf{x}) \mathbf{B}(\mathbf{x}) d\Omega - \int_{\partial_h \Omega} \mathbf{N}_\theta^T(\mathbf{x}) h \mathbf{N}_\theta(\mathbf{x}) d\Gamma, \quad (3.37)$$

$$\mathbf{f}_\chi = \int_\Omega \mathbf{N}_\theta^T(\mathbf{x}) r_\chi(\mathbf{x}) d\Omega - \int_{\partial_q \Omega} \mathbf{N}_\theta^T(\mathbf{x}) \bar{q}(\mathbf{x}) d\Gamma - \int_{\partial_h \Omega} \mathbf{N}_\theta^T(\mathbf{x}) h \theta_{amb}(\mathbf{x}) d\Gamma, \quad (3.38)$$

where the convective term has been included in the stiffness matrix \mathbb{K}_χ and the external force vector \mathbf{f}_χ . As in the previous problem, it is assumed that the force vector will not depend on

the topology, thus simplifying the derivation of the sensitivity. The complete derivation of the thermal equations, objective functions, and the corresponding relaxed topological derivatives are provided in Article B [139].

Maximum thermal diffusivity

Similarly to the minimum mean compliance problem (Section 3.3.1), the thermal compliance can now be minimized (in other words, the thermal diffusivity can be maximized) for the thermal problem. In this case, the objective function \mathcal{J} can be defined in terms of the total potential energy as

$$\begin{aligned} \mathcal{J}(\theta(\chi), \chi) &\equiv \frac{1}{2} \int_{\Omega} \hat{\boldsymbol{\theta}}_{\chi}^{\text{T}} \mathbf{B}^{\text{T}}(\mathbf{x}) \boldsymbol{\kappa}_{\chi}(\mathbf{x}) \mathbf{B}(\mathbf{x}) \hat{\boldsymbol{\theta}}_{\chi} d\Omega - \frac{1}{2} \int_{\partial_h \Omega} \hat{\boldsymbol{\theta}}_{\chi}^{\text{T}} \mathbf{N}_{\theta}^{\text{T}}(\mathbf{x}) h \mathbf{N}_{\theta}(\mathbf{x}) \hat{\boldsymbol{\theta}}_{\chi} d\Gamma = \\ &= \frac{1}{2} \mathbf{f}^{\text{T}} \hat{\boldsymbol{\theta}}_{\chi} \end{aligned}, \quad (3.39)$$

with $j(\chi, \mathbf{x}) \equiv \frac{1}{2} \nabla \theta_{\chi} \cdot \boldsymbol{\kappa}_{\chi}(\mathbf{x}) \cdot \nabla \theta_{\chi} = \mathcal{U}_{\chi}(\mathbf{x})$. Once the adjoint method is applied to the objective function, the resultant pseudo-energy can be computed as

$$\xi(\theta(\chi), \chi, \hat{\mathbf{x}}) = -\frac{1}{2} m \chi^{m-1}(\hat{\mathbf{x}}) \hat{\boldsymbol{\theta}}^{\text{T}}(\chi, \hat{\mathbf{x}}) \mathbf{B}^{\text{T}}(\hat{\mathbf{x}}) \boldsymbol{\kappa}^+(\hat{\mathbf{x}}) \mathbf{B}(\hat{\mathbf{x}}) \hat{\boldsymbol{\theta}}(\chi, \hat{\mathbf{x}}) \Delta \chi(\hat{\mathbf{x}}). \quad (3.40)$$

As in the structural case, no additional state equation is required since this topology optimization problem turns out to be self-adjoint. Note the similarity of the previous equation with equation (3.31) from the minimum mean compliance problem.

Thermal cloaking for minimizing heat flux deviation

Up to this point, some illustrative topology optimization problems, that are normally used by other researchers to prove the capabilities of their techniques to achieve optimal layouts, have been described for the structural and thermal problems. However, the proposed approach is now applied to a more complex and academic thermal problem.

The main objective is to hide an object, with different thermal properties, inside of a homogeneous structure from being detected by a thermal device measuring any perturbation in the heat flux field near the boundaries of the structure. Without any modification to the structure, the heat flux field will be highly perturbed when applying a temperature difference between the sides of the structure (with respect to the expected homogeneous one), thus revealing the existence of any external body inside the structure. The problem setting is depicted in Figure 3.10.

To avoid its detection or reduce the probability of the object being detected, it must be surrounded by a cloaking device, which should be optimized to recover the original heat flux field. The resultant cloaking device consists of a combination of high-conductive and low-conductive materials, which location and shape are given by solving a topology optimization problem. The corresponding objective function \mathcal{J} is written as the minimization of the deviation between the constant heat flux and the actual one in the domain surrounding the cloaking device (Ω_c), i.e.,

$$\mathcal{J}(\theta(\chi), \chi) = \|\mathbf{q}(\chi, \mathbf{x}) - \bar{\mathbf{q}}(\mathbf{x})\|_{L_2(\Omega_c)} = \left(\int_{\Omega_c} |\mathbf{q}(\chi, \mathbf{x}) - \bar{\mathbf{q}}(\mathbf{x})|^2 d\Omega \right)^{\frac{1}{2}}, \quad (3.41)$$

where $\bar{\mathbf{q}}(\mathbf{x})$ corresponds to the prescribed (original) heat flux at each point \mathbf{x} . The domain of integration Ω_c of the previous equation (3.41) is replaced by the entire design domain Ω via an indicator function of the subdomain Ω_c , i.e., $1_{\Omega_c} : \Omega \rightarrow \{0, 1\}$, $1_{\Omega_c} \in L^2(\Omega)$.

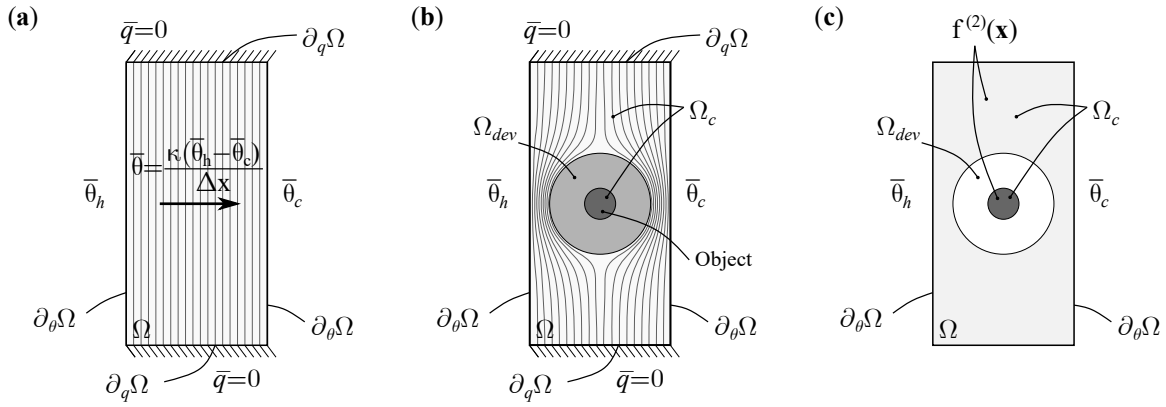


Figure 3.10: Thermal cloaking problem: **(a)** homogeneous problem setting where a constant uniform heat flux is observed over all the domain Ω , **(b)** topology optimization domain with boundary conditions of original state equation, and **(c)** topology optimization domain with boundary conditions of the auxiliary state equation. The objective is to minimize the perturbation of an object (in black) placed at the center of the domain Ω . For that reason, it is surrounded by a cloaking device, in dark gray, which must be optimized.

The resultant pseudo-energy ξ can be expressed as

$$\begin{aligned} \xi(\theta(\chi), \chi, \hat{\mathbf{x}}) = & -m\chi^{m-1}(\hat{\mathbf{x}}) \hat{\boldsymbol{\theta}}_{\chi}^{(1)\text{T}}(\hat{\mathbf{x}}) \mathbf{B}^{\text{T}}(\hat{\mathbf{x}}) \boldsymbol{\kappa}^+(\hat{\mathbf{x}}) \mathbf{B}(\hat{\mathbf{x}}) \hat{\boldsymbol{\theta}}_{\chi}^{(2)}(\hat{\mathbf{x}}) \Delta\chi(\hat{\mathbf{x}}) \\ & + m\chi^{m-1}(\hat{\mathbf{x}}) \frac{1_{\Omega_c}(\hat{\mathbf{x}})}{\mathcal{J}(\theta, \chi)} \hat{\boldsymbol{\theta}}_{\chi}^{(1)\text{T}}(\hat{\mathbf{x}}) \mathbf{B}^{\text{T}}(\mathbf{x}) \boldsymbol{\kappa}_{\chi}^{\text{T}}(\hat{\mathbf{x}}) \boldsymbol{\kappa}^+(\hat{\mathbf{x}}) \mathbf{B}(\hat{\mathbf{x}}) \hat{\boldsymbol{\theta}}_{\chi}^{(1)}(\hat{\mathbf{x}}) \Delta\chi(\hat{\mathbf{x}}) \quad (3.42) \\ & + m\chi^{m-1}(\hat{\mathbf{x}}) \frac{1_{\Omega_c}(\hat{\mathbf{x}})}{\mathcal{J}(\theta, \chi)} \hat{\mathbf{q}}^{\text{T}}(\hat{\mathbf{x}}) \mathbf{N}_{\theta}^{\text{T}}(\hat{\mathbf{x}}) \boldsymbol{\kappa}^+(\hat{\mathbf{x}}) \mathbf{B}(\hat{\mathbf{x}}) \hat{\boldsymbol{\theta}}_{\chi}^{(1)}(\hat{\mathbf{x}}) \Delta\chi(\hat{\mathbf{x}}), \end{aligned}$$

once the adjoint method has been employed. The adjoint state field $\hat{\boldsymbol{\theta}}_{\chi}^{(2)}$ is obtained from an auxiliary state equation (3.36) with

$$\mathbf{f}^{(2)} = - \int_{\Omega} \frac{1_{\Omega_c}(\mathbf{x})}{\mathcal{J}(\theta, \chi)} \mathbf{B}^{\text{T}}(\mathbf{x}) \boldsymbol{\kappa}_{\chi}^{\text{T}}(\mathbf{x}) \left(-\boldsymbol{\kappa}_{\chi}(\mathbf{x}) \mathbf{B}(\mathbf{x}) \hat{\boldsymbol{\theta}}_{\chi}^{(1)} - \hat{\mathbf{q}}(\mathbf{x}) \right) d\Omega. \quad (3.43)$$

Thermal cloaking for minimizing temperature

A similar topology optimization problem to the minimization of the heat flux deviation is now presented. However, in this case, the objective is not to hide an object with different properties, which could also be considered, but to cloak a high-temperature object from being detected by a thermal camera pointing at one side of the structure, referred to as the cloaking port $\partial_c\Omega$. The object, placed inside the structure, is once again surrounded by a cloaking device Ω_{dev} , which must distribute the heat toward the opposite boundary and toward the upper and lower parts of the left side of the domain. This goal can be addressed as a multi-objective topology optimization problem where both, the average temperature and the variance over the left surface are minimized. As a consequence of this objective function, the temperature field is optimized, reducing any temperature peaks while ensuring a uniform low-temperature field on the left side. The objective function \mathcal{J} , evaluated via a weighted sum of functionals [80], can be expressed as

$$\mathcal{J}(\theta(\chi), \chi) = \omega \frac{\mathcal{J}_{av}(\theta(\chi), \chi) - \mathcal{J}_{av}^{\circ}}{\mathcal{J}_{av}^{max} - \mathcal{J}_{av}^{\circ}} + (1 - \omega) \frac{\mathcal{J}_{vr}(\theta(\chi), \chi) - \mathcal{J}_{vr}^{\circ}}{\mathcal{J}_{vr}^{max} - \mathcal{J}_{vr}^{\circ}}, \quad (3.44)$$

where \mathcal{J}_{av} and \mathcal{J}_{vr} are the objective functions for the average temperature minimization and the temperature variance minimization, respectively, \mathcal{J}_i^{max} and \mathcal{J}_i° correspond to the maximum

objective function value \mathcal{J}_i obtained from the minimization of the other functional and the minimum value (utopia point) of the objective function \mathcal{J}_i when minimizing only the i -problem, and ω stands for the weighting factor between the two objective functions.

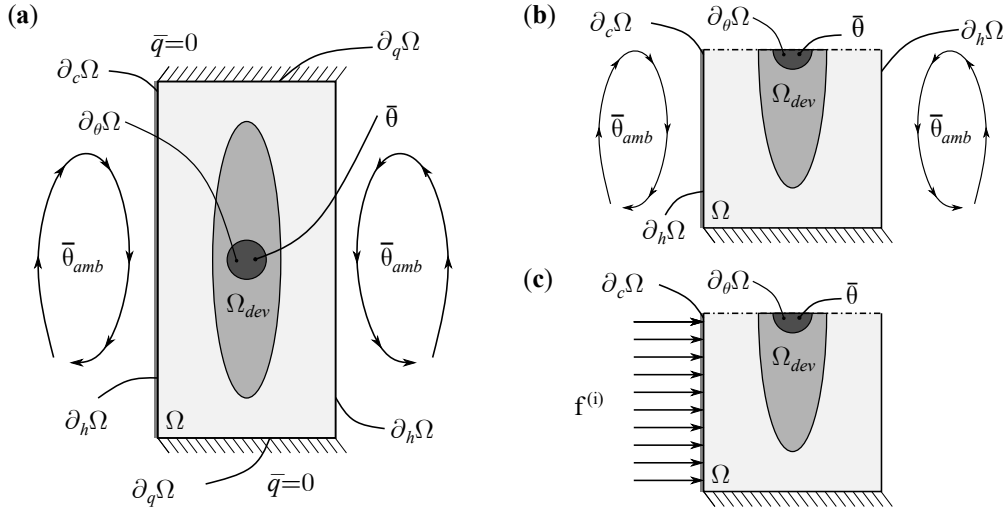


Figure 3.11: Average and variance temperature minimization problem: **(a)** homogeneous problem setting with boundary conditions. The object is prescribed at a high temperature $\bar{\theta}$, and the left and right sides are subject to convective boundary conditions, while adiabatic conditions are assumed on top and bottom sides of the domain. Figure **(b)** represents the topology optimization domain with boundary conditions of original state equation, and **(c)** illustrates the boundary conditions of the auxiliary state equations.

In this context, the objective functions \mathcal{J}_{av} and \mathcal{J}_{vr} are defined as

$$\begin{cases} \mathcal{J}_{av}(\theta(\chi), \chi) = C_2 \int_{\partial\Omega} 1_{\partial_c\Omega}(\mathbf{x}) \theta_\chi(\mathbf{x}) d\Gamma & (3.45) \\ \mathcal{J}_{vr}(\theta(\chi), \chi) = C_2 \int_{\partial\Omega} 1_{\partial_c\Omega}(\mathbf{x}) (\theta_\chi(\mathbf{x}) - \mathcal{J}_{av}(\theta(\chi), \chi))^2 d\Gamma & (3.46) \end{cases}$$

where C_2 corresponds to the inverse of the Lebesgue measure of the cloaking port and $1_{\partial_c\Omega}$ represents the indicator function of the subboundary $\partial_c\Omega$, i.e., $1_{\partial_c\Omega} : \Omega \rightarrow \{0, 1\}$, $1_{\partial_c\Omega} \in L^2(\Omega)$. The corresponding pseudo-energies ξ_{av} and ξ_{vr} are given by

$$\begin{cases} \xi_{av}(\theta(\chi), \chi, \hat{\mathbf{x}}) = C_2 m \chi^{m-1}(\hat{\mathbf{x}}) \hat{\boldsymbol{\theta}}_\chi^{(2)\top} \mathbf{B}^\top(\hat{\mathbf{x}}) \boldsymbol{\kappa}^+(\hat{\mathbf{x}}) \mathbf{B}(\hat{\mathbf{x}}) \hat{\boldsymbol{\theta}}_\chi^{(1)} \Delta\chi(\hat{\mathbf{x}}) & (3.47) \\ \xi_{vr}(\theta(\chi), \chi, \hat{\mathbf{x}}) = C_2 m \chi^{m-1}(\hat{\mathbf{x}}) \hat{\boldsymbol{\theta}}_\chi^{(3)\top} \mathbf{B}^\top(\hat{\mathbf{x}}) \boldsymbol{\kappa}^+(\hat{\mathbf{x}}) \mathbf{B}(\hat{\mathbf{x}}) \hat{\boldsymbol{\theta}}_\chi^{(1)} \Delta\chi(\hat{\mathbf{x}}) \\ \quad - 2C_2 \left(\hat{\boldsymbol{\theta}}_\chi^{(1)} - \mathbb{I} \mathcal{J}_{av}(\theta_\chi^{(1)}) \right)^\top \mathbf{N}_\theta^\top(\hat{\mathbf{x}}) 1_{\partial_c\Omega}(\hat{\mathbf{x}}) \xi_{av}(\theta(\chi), \chi, \hat{\mathbf{x}}), & (3.48) \end{cases}$$

where $\hat{\boldsymbol{\theta}}_\chi^{(2)}$ and $\hat{\boldsymbol{\theta}}_\chi^{(3)}$ correspond to the solution of two additional state equations (3.36). For these systems, the external force vectors are computed as

$$\begin{cases} \mathbf{f}^{(2)} = - \int_{\partial\Omega} \mathbf{N}^\top(\mathbf{x}) 1_{\partial_c\Omega}(\mathbf{x}) d\Gamma, & (3.49) \end{cases}$$

$$\begin{cases} \mathbf{f}^{(3)} = -2 \int_{\partial\Omega} \mathbf{N}^\top(\mathbf{x}) 1_{\partial_c\Omega}(\mathbf{x}) \left(\theta_\chi^{(1)}(\mathbf{x}) - \mathcal{J}_{av}(\theta_\chi^{(1)}) \right) d\Gamma. & (3.50) \end{cases}$$

The problem settings of the original state equation, and the two additional state equations are illustrated in Figure 3.11.

3.4 Representative numerical examples

The potential of the approach to find optimal solutions using the relaxed topological derivative as the sensitivity are shown through some representative numerical examples for the structural and thermal fields. In particular, the main advantage of the time-advancing strategy to obtain a set of converged solutions for intermediate volume fractions at a computational cost similar to the one required by other optimization techniques is exhibited.

3.4.1 Representative examples in structural problems

The focus will first be on the structural applications detailed in Section 3.3.1, both minimizing the mean compliance of a structure or designing compliant mechanism. The topology optimization problem (3.5) is subject to the volume constraint \mathcal{C}_0 (3.6) and the structural state equation (3.27).

For the following structural optimization problems, a linear elastic material with a Young's modulus $E^+ = 210GPa$ and a Poisson's ratio $\nu = 0.3$ is considered for the material in the stiff subdomain Ω^+ . The algorithmic tolerances Tol_χ , Tol_λ , and Tol_c , in Algorithm 1, are set to 10^{-1} , 10^{-1} , and 10^{-5} , respectively.

Cantilever beam: minimum mean compliance

This first numerical example refers to the minimization of the structural mean compliance (3.30) of a cantilever beam in a prismatic domain subjected to specific Dirichlet and Neumann boundary conditions. The displacements are prescribed on the left face of the design domain and a distributed vertical load is applied on the bottom-right edge of it. The analysis domain Ω , displayed in Figure 3.12a, corresponds to a prism of (relative) dimensions $2 \times 1 \times 1$, with the largest dimension oriented in the x -axis. The domain has been discretized using eight-node hexahedral (Q_1) finite elements while the time interval $[0, 0.92]$ has been divided into 22 time-steps using an exponential evolution of the pseudo-time t . Regarding the ersatz material approach, a contrast factor $\alpha = 10^{-6}$ and an exponential factor $m = 5$ are employed, thus leading to a relaxation factor β equal to $6.3 \cdot 10^{-2}$ and $E^- = 10^{-6}E^+$ for the void subdomain Ω^- .

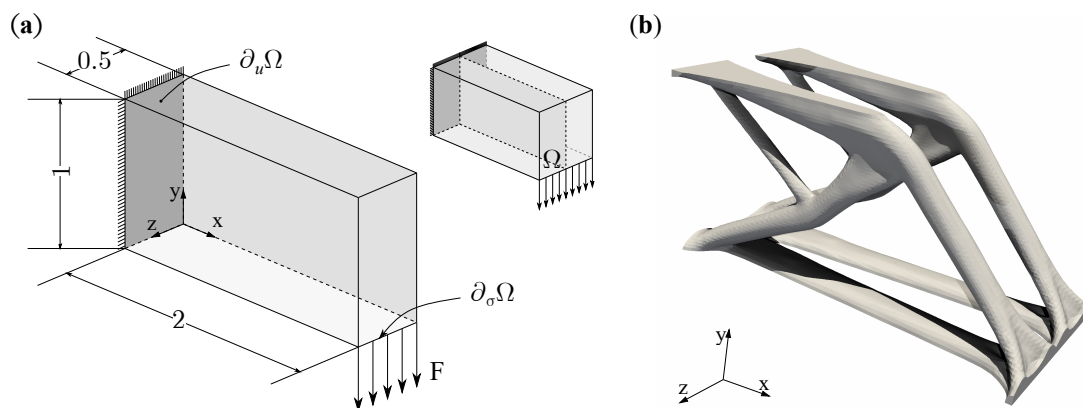


Figure 3.12: Cantilever beam: (a) topology optimization domain with boundary conditions and dimensions. A distributed vertical load F is applied on the bottom-right edge while the displacements \mathbf{u} are prescribed to $\mathbf{0}$ on the left surface of the domain. The rear surface of the domain, in soft gray, represents the surface of symmetry. Figure (b) illustrates the optimal topology for a volume fraction equal to $t = 0.92$, which corresponds to only 8% of initial stiff material.

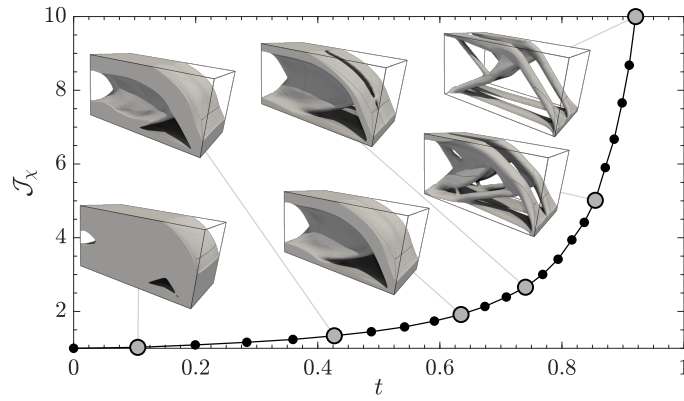


Figure 3.13: Cantilever beam topology optimization problem: the evolution of the objective function \mathcal{J} in terms of the pseudo-time t (Pareto Frontier) is illustrated here in conjunction with some relevant topologies for the time interval $t \in [0, 0.92]$.

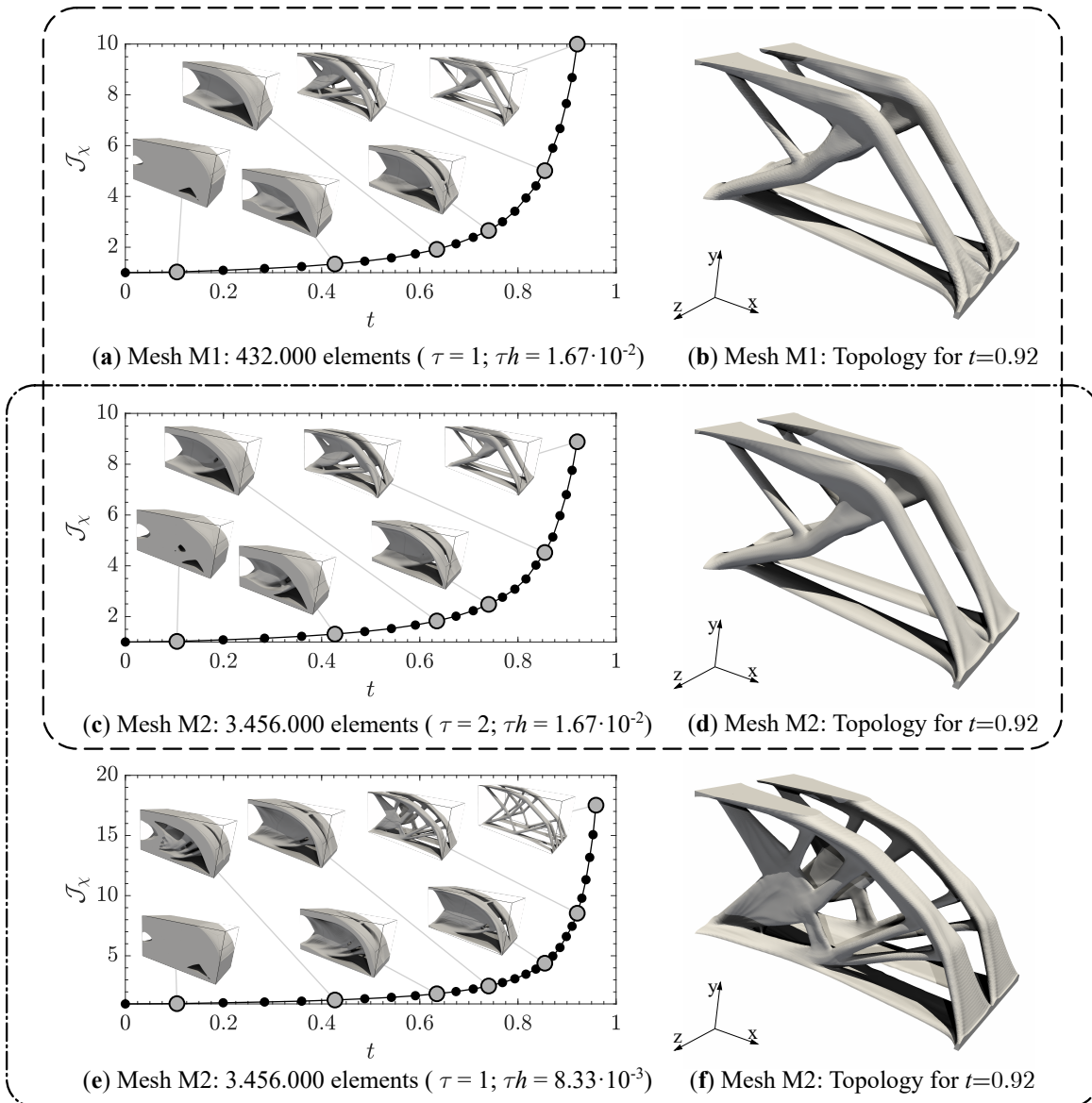


Figure 3.14: Cantilever beam. Mesh-size objectivity results via the Laplacian regularization (τh). Figures (a) to (d) display the results for meshes M1 and M2 with constant $\tau h = 1.67 \cdot 10^{-2}$, while Figures (c) to (f) corresponds to the results for the same mesh, M2, and different regularization values $\tau h = 1.67 \cdot 10^{-2}$ and $\tau h = 8.33 \cdot 10^{-3}$, respectively.

The Pareto Frontier in terms of the objective function \mathcal{J} and the pseudo-time t is displayed in Figure 3.13. As it can be observed, the mean compliance of the structure increases as the volume fraction of the void subdomain increases, thus reducing the global stiffness of the structure. The optimal layout gradually changes according to the volume fraction, although the minimum thickness, defined by the Laplacian filter (3.19), is always preserved. The final optimal topology for $t = 0.92$ is represented in Figure 3.12b via the discrimination function $\psi(\mathbf{x}) = 0$, showing smooth and crisp material boundaries.

In the context of mesh dependence, the Laplacian regularization may ensure almost the same optimal solution with two different meshes as long as the product τh is kept constant in both cases. This property of the regularization is illustrated by optimizing the design of the Cantilever beam using two different meshes: (a) a first reference mesh M1, displayed in Figure 3.12, and (b) a finer mesh M2, twice as dense in each direction. For this mesh M2, two different topology optimization are computed, one considering the same τh value as the mesh M1 and another prescribing the same τ value but different element size $h^{(M2)} = h^{(M1)}/2$. As depicted in Figure 3.14, the topology and objective function almost remain the same as the ones obtained with the reference mesh M1 for the first case, while maintaining just constant the regularization parameter τ leads to more complex optimal solutions with thinner bars, thus losing the objectivity in mesh size. As a result, the use of the Laplacian regularization overcomes one of the main inherent problems of topology optimization problems.

Other minimum mean compliance problems can be found in Articles A, C and D. For instance, a bridge structure is optimized in Article A, obtaining designs easily recognizable by bridge engineers for high volume fractions t . Other optimizations of structural benchmark cases are carried out in Article D, including an L-shaped structured and a multi-load cantilever beam.

Gripper: compliant mechanism synthesis

The last structural example corresponds to the design of a compliant mechanism (3.32). In this case, a 3D gripper is designed to maximize the vertical displacement at the output port (i.e., the jaws of the gripper) due to an action at the input port. The displacements are prescribed near the bottom edge at the left side of the domain. As illustrated in Figure 3.15a, a positive, horizontal distributed load \mathbf{f} is applied at the input port (i.e., on the left side of the domain) for the original state equation (Figure 3.15a-I), while a vertical upward dummy load $\mathbf{1}_{vert}$ is applied at the output port for the auxiliary state equation (Figure 3.15a-II). In addition to this dummy load, distributed springs are included in the input and output ports in the same direction as the input force and target displacements, respectively. As a result, the displacement amplitudes are limited at these areas, and both the input work of the actuator and the elastic reaction work are simulated at the input and output ports, respectively. The corresponding numerical values for the springs are $K_{in} = 3.19 \cdot 10^{14} N/m^3$ and $E_{out} = 10GPa$, while the distributed forces are $f_1 = 3.2 \cdot 10^{13} N/m^2$ and $f_2 = 3.2 \cdot 10^{10} N/m^2$, respectively.

Regarding the ersatz material approach, the contrast factor α is increased up to $\alpha = 10^{-2}$, while the exponential factor is set to $m = 3$ in order to improve the optimization convergence. The topology optimization is performed using a regularization parameter $\tau = 0.5$ and an exponential updating scheme for the pseudo-time t with 34 time-steps ranging between the full material layout (i.e., $t = 0$) and $t = 0.94$. Consequently, a large spectrum of optimal solutions can be observed.

As in the previous case, the Pareto Frontier between the objective function \mathcal{J} and the pseudo-time t is represented in Figure 3.15b. In contrast to the previous case where the mean compliance was minimized, the Pareto Frontier does not exhibit now an increasing monotonicity, but instead presents a global minima for a volume fraction $t = 0.48$. This condition does differ from the full material configuration for the minimum mean compliance problems. Thanks to the proposed time-advancing strategy, it is possible to obtain not only the optimal topology for the final volume fraction T , but the topology and volume fraction t for the global minimum of the optimization problem, too. Figures 3.15c to 3.15f show some optimal topologies for intermediate

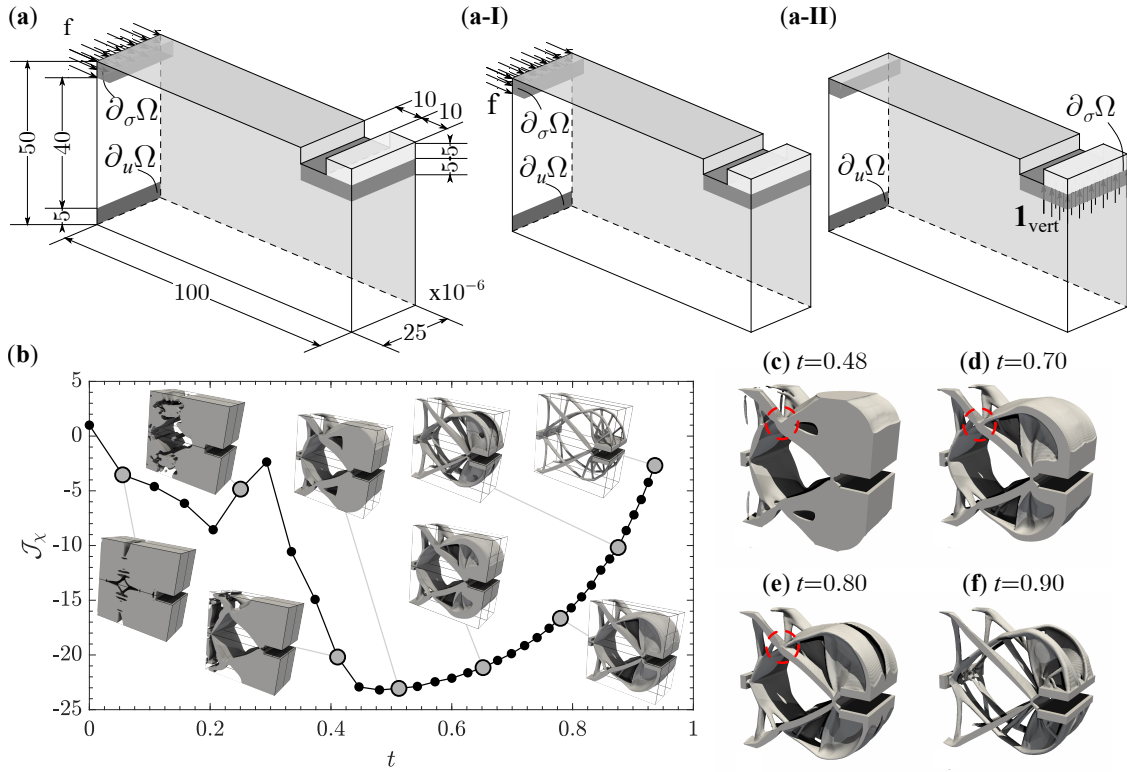


Figure 3.15: Gripper design (compliant mechanism). The topology optimization domain with boundary conditions and dimensions is depicted in Figure (a). The displacements are prescribed at the bottom part of the left surface of the domain, and a positive, horizontal distributed load is applied at the top of the left surface for the state equation (a-I), while a positive, vertical distributed dummy load is applied at the jaws of the gripper for the additional state equation (a-II). The top and rear surfaces correspond to the $x - y$ and $x - z$ symmetries, respectively. Figure (b) represents the evolution of the objective function \mathcal{J} in terms of the pseudo-time t with some relevant optimal configurations, while the optimal layouts for different pseudo-times are illustrated in Figure (c) to (f).

values of the pseudo-time t , in which the compression displacement in the jaws (output port) is obtained either from the presence of localized hinges (highlighted in red) or from the deformation (or distributed compliance) of slender bars (e.g., for $t = 0.90$).

3.4.2 Representative examples in thermal problems

The following numerical examples will be focused on the thermal problem, detailed in Section 3.3.2. Numerical results will be presented for two representative applications developed in this thesis: (a) thermal compliance minimization and (b) design of a thermal cloaking device by temperature control. In this case, the original topology optimization problem (3.5) is subject to the volume constraint \mathcal{C}_0 and the steady-state thermal equation (3.36). With respect to the algorithmic tolerances, the same values as in the structural problems are used here except for the tolerance in volume constraint, which is increased up to $Tol_{\mathcal{C}} = 10^{-3}$.

Thermal component: maximum thermal diffusivity

The first thermal example corresponds to the minimization of thermal compliance (3.39) in a thermal component, for instance, the topology optimization of the heat pipes for a CPU heat sink. The aim would therefore be to maximize heat diffusion through heat conduction from the heat sources (CPU's IHS) to the dissipation points (heat sink). From this concept, the design

domain Ω is defined as a one-meter cube with the heat sources placed on the left side and the cold spots, on the right side of the domain. However, in order to avoid trivial solutions in which these two areas would be directly connected in a straight line, a prismatic volume is removed from the center of the design domain, as shown in Figure 3.16a. The temperature on the four hot areas (colored in red) is prescribed to a high value $\bar{\theta}_h = 293K$ on the left boundary, while the nine circular regions (in blue) on the right side of the domain are set to $\bar{\theta}_c = 278K$. Adiabatic boundary conditions are assumed on the other boundaries of the design domain.

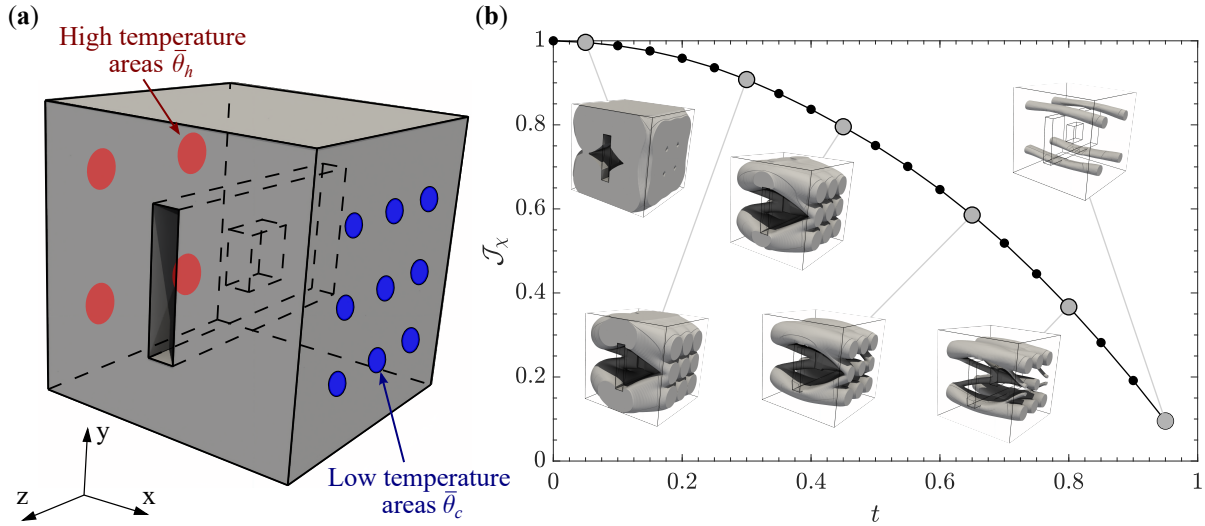


Figure 3.16: Thermal heat conductor. The design domain Ω is illustrated along with the boundary conditions in Figure (a). The temperature is prescribed to $\bar{\theta}_h$ at the four circular regions on the left face (colored in red) while a low temperature value $\bar{\theta}_c$ is prescribed at the nine circular regions on the right face (colored in blue). The other surfaces are assumed to be adiabatic. The evolution of the objective function \mathcal{J} with respect to the pseudo-time t is represented in Figure (b). Some relevant topologies are also included in the graphic for different volume fractions.

The design domain Ω is once again discretized with a structured mesh of eight-node hexahedral (Q_1) finite elements. According to this mesh, the regularization parameter τ from the Laplacian regularization is set to 1. Consequently, smooth optimal designs with thin filaments can be achieved, while the minimum size control is ensured. The interval of interest $[0, 0.95]$ is, on the other hand, discretized in 19 equally spaced time-steps.

The high-conductive subdomain Ω^+ is endowed with an isotropic material with normalized conductivity $\boldsymbol{\kappa}^+ = 1W/(Km)$ and zero heat sources $r = 0W/m^3$. Analogous to the structural problem, the parameters of the ersatz material approach are set to $\alpha = 10^{-3}$ and $m = 5$, thus obtaining a conductivity of $\boldsymbol{\kappa}^- = \alpha\boldsymbol{\kappa}^+ = 10^{-3}\boldsymbol{\kappa}^+$ for any material in the void subdomain Ω^- .

The evolution of the thermal diffusivity with respect to the pseudo-time parameter t is represented in Figure 3.16b, in addition to some illustrative topology layouts for intermediate volume fractions. Analogous to the minimum mean compliance problem (Section 3.4.1), the thermal diffusivity \mathcal{J} decreases as the volume fraction increases, though obtaining the maximum possible value for each pseudo-time t . From the topology evolution, it can be observed how the hot spots on the left surface are connected with the cold ones on the right side of the domain, thus minimizing the thermal compliance in the domain. For high volume fractions, i.e., $t \rightarrow 1$, the trivial topology configuration is recovered, in which the hot and cold spots are directly connected with four thin heat pipes.

Thermal cloaking device: temperature average and variance minimization

The last optimization example corresponds to the topology optimization of a thermal cloaking device, illustrated in Figure 3.17a. The optimization aims at cloaking an object at a different

temperature value $\bar{\theta}_h$, hidden inside a homogeneous structure, from being detected by a thermal camera pointing to the left surface of the domain $\partial_c\Omega$ measuring the temperature field, as detailed in Section 3.3.2. The heat generated by the object (in green) must be dissipated by the cloaking device Ω_{dev} (in orange) toward the upper and lower part of the left surface and toward the right surface of the domain, thus reducing the average temperature and the variance on the left surface. As a result, the corresponding objective function (3.44) is expressed as a multi-objective function that combines the minimization of the average temperature (3.45) and the minimization of the variance of the temperature (3.46) on the left surface when the object's temperature is set to $\bar{\theta}_h = 313K$ and thermal convection is considered for the left and right surfaces ($h = 1W/(K\ m^2)$ and $\theta_{amb} = 283.15K$). The other surfaces of the domain are assumed to be adiabatic.

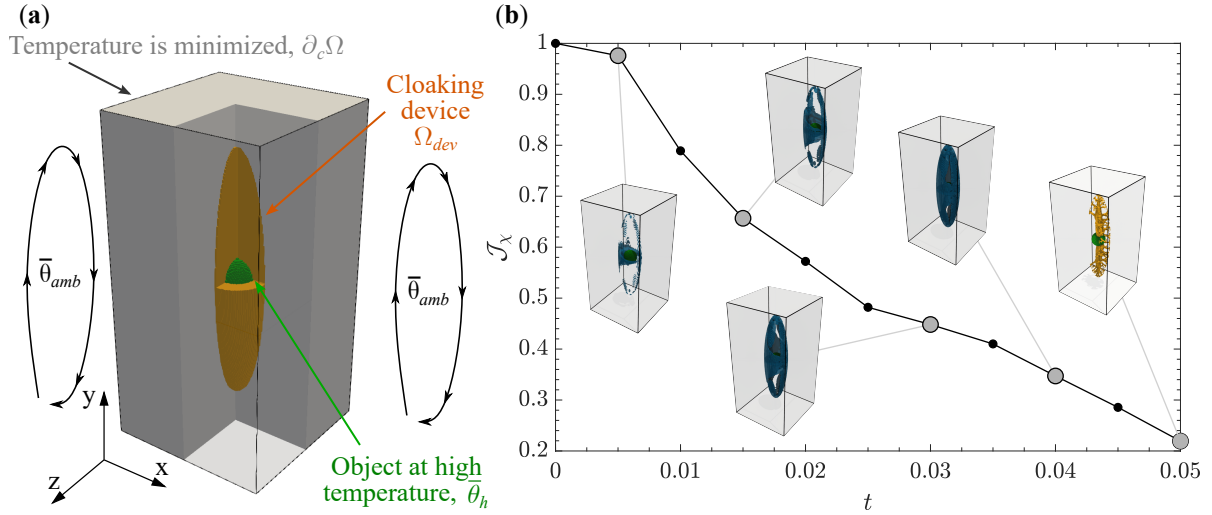


Figure 3.17: Thermal cloaking device. In Figure (a) the design domain Ω with the corresponding boundary conditions is depicted. The object to be cloaked (in green) is surrounded by the cloaking device Ω_{dev} (in orange). The temperature of the object is set to a high value $\bar{\theta}_h$ and convective boundary conditions are considered on the left and right surfaces of the domain. The other surfaces are assumed to be adiabatic. On the other hand, in Figure (b), the evolution of the objective function \mathcal{J} with respect to the pseudo-time t is displayed together with some optimal layouts for different volume fractions. The low-conductive material subdomain is highlighted in blue, and the high-conductive one has been omitted.

For this example, a conductivity of $\kappa = 0.57W/(mK)$ is considered for the surrounding material and the object, while the cloaking device Ω_{dev} results from the combination of two materials: (a) a material with a high conductivity equal to $\kappa^+ = 403W/(mK)$ and (b) a low-conductive material with $\kappa^- = 0.22W/(mK)$. In particular, this second low-conductive material represents the alternative material in the ersatz material approach, and is obtained from a contrast value of $\alpha = 5.46 \cdot 10^{-4}$. The regularization parameter τ is defined as $\tau = 0.1$, while the interval of interest $[0, 0.05]$ is discretized in 10 equally spaced steps. As detailed in Article B, the maximum and minimum values of each objective function are obtained from optimizing each term individually for $\omega = 1$ (average temperature) and $\omega = 0$ (variance of the temperature). These optimizations determine the values $\mathcal{J}_{av}^o = 308.6K$, $\mathcal{J}_{vr}^{max} = 7.4 \cdot 10^{-2}K^2$, $\mathcal{J}_{av}^{max} = 310.4K$ and $\mathcal{J}_{vr}^o = 9 \cdot 10^{-3}K^2$.

As in the other numerical examples, the evolution of the objective function \mathcal{J} is displayed in Figure 3.17b for $\omega = 0.5$, once the normalization of each term has been performed. As the volume fraction increases, the objective function decreases, resulting in designs with lower average temperature and lower temperature variance on the left side of the domain. Figure 3.18 (top) depicts the optimal topology layout of the cloaking device for different steps, in which the high-conductive material tends to adopt a spine-like design to distribute the heat toward the

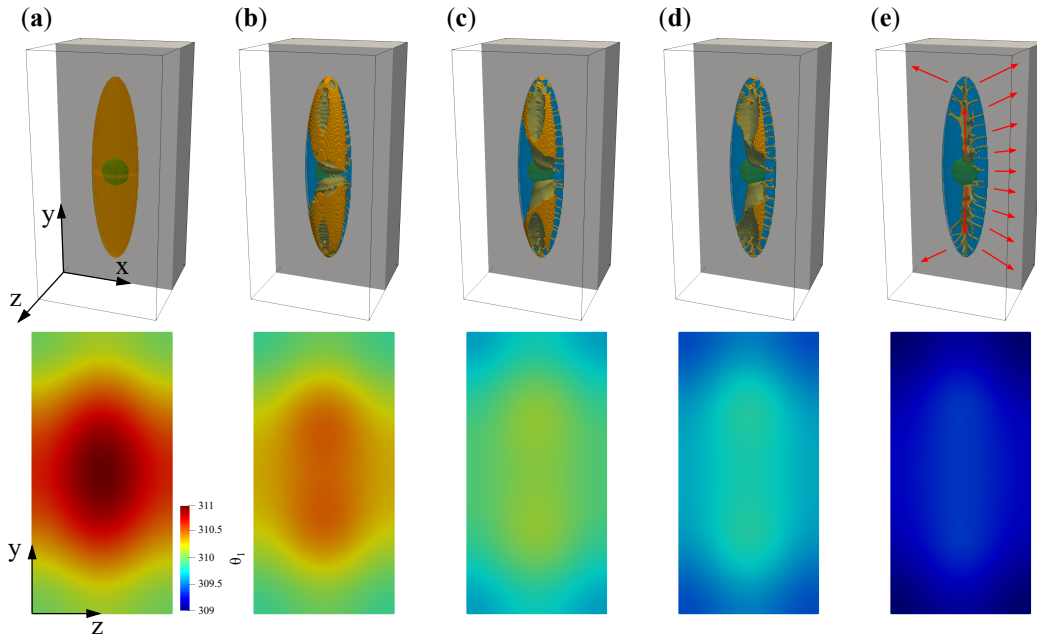


Figure 3.18: Thermal cloaking device: temperature field on $\partial_c\Omega$. The optimal layouts (on the top) and the temperature field of the left $y - z$ plane (on the bottom) are displayed in Figures (a) to (e) for steps 0, 3, 6, 8 and 10, respectively. As in the previous figure, the low-conductive and the high-conductive materials are colored in blue and orange, respectively, while the object is displayed in green at the center of the domain.

upper and lower part of the left side and toward the right side of the domain, sketched in Figure 3.18e. On these surfaces, the heat can be then dissipated by natural convection. Additionally, the effect of the topology can also be noticed in the temperature field over the control surface $\partial_c\Omega$. The temperature peak at the center and the high temperature difference between the central part and the corners in the initial configuration are minimized as the internal design is optimized, ultimately leading to a lower average value and higher homogeneity of the field.

The topology optimization of another cloaking device has also been performed, aiming to design a cloaking device that prevents an object (with different thermal properties, instead of different temperature values) from being detected by a thermal device measuring any perturbation in the heat flux field (as presented in Section 3.3.2). For more details on this numerical example, please refer to Article B.

3.5 Comparison

Up to this point, the proposed topology optimization approach has been formulated (Section 3.2) and applied to different numerical problems in the structural and thermal fields (Sections 3.3 and 3.4). Nonetheless, no information is available on how it compares with other well-known topology optimization techniques, leaving aside the comparisons shown in Articles A and B with respect to the level-set method using the Hamilton-Jacobi equation. Therefore, the proposed technique is now compared with different implementations of SIMP using the optimality criteria method [106, 11], BESO using a soft-kill criterion [52], and level-set approach with Hamilton-Jacobi updating equation (Section 3.2.5). In particular, the different SIMP implementations correspond to (a) SIMP with a Helmholtz-type PDE filter for the sensitivities [63, 11] (SIMP^(I)), (b) SIMP^(I) formulated now with an incremental time-advancing strategy (SIMP^(II)), and (c) SIMP using a radial sensitivity filter with a linear decaying kernel (SIMP^(III)). These three families of techniques have been selected among all existing ones due to their wide use on both the professional and research level, and for the convenience of implementation, thus facilitating

their verification and assuring a fair comparison among the approaches. A detailed description of each method, the specific conditions for the optimizations, as well as the numerical problems and their corresponding results are given in Article D [138].

3.5.1 Guidelines for the comparison

As a representative field, the structural problem is here considered for the comparison of the different topology optimization problems. With this objective in mind, four well-known benchmark cases have been addressed. In particular, two minimum mean compliance problems (Section 3.3.1), one multi-load mean compliance problem and a compliant mechanism topology optimization problem (Section 3.3.1) have been performed. The first two minimum compliance problems deal with the design of a cantilever beam and an L-shaped structure, the multi-load problem also aims at minimizing the mean compliance in a cantilever beam, but, in this case, two different loading conditions are considered: (1) a vertical distributed downward load at the right-bottom edge, and (2) a vertical distributed upward load at the right-top edge, and the last one involves the design of a compliant mechanism, a gripper. The corresponding problem setups are illustrated in Figure 3.19. The exact dimensions, finite element meshes, and the rest of details can be found in Article D.

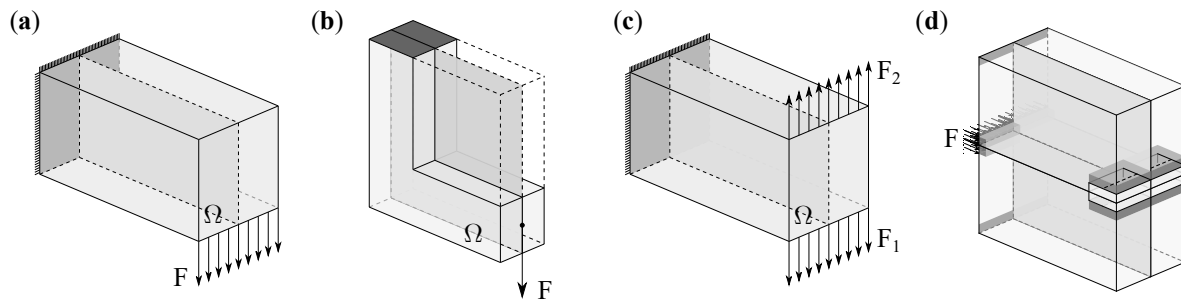


Figure 3.19: Topology optimization domains of the numerical benchmarks addressed in the comparison. The corresponding boundary conditions are illustrated in each figure. Figures (a) to (d) correspond to the cantilever beam (minimum mean compliance), the L-shaped structure (minimum mean compliance), the multi-load cantilever beam (multi-load minimum mean compliance), and the gripper mechanism (compliant mechanism synthesis), respectively. The symmetry surfaces are shaded in soft gray, while the areas where displacements are being imposed are shaded in dark gray.

This set of four numerical benchmark cases have been carefully selected to provide relevant information about each topology optimization strategy when designing optimal topologies with a high complexity degree (using industrial-like fine-discretization meshes). In this context, the comparison is focused on evaluating the computational cost (in terms of the number of iterations), the value of the objective function \mathcal{J} , and the topology quality of each method and benchmark case.

With the idea of ensuring a fair comparison among all methods, the same (or equivalent) convergence criteria must be used for the volume constraint \mathcal{C}_0 ($Tol_{\mathcal{C}} = 10^{-3}$), the objective function \mathcal{J} ($Tol_{\mathcal{J}} = 10^{-3}$) and the topology in terms of the characteristic function χ or the density value ρ ($Tol_{\chi,\rho} = 2.5 \cdot 10^{-3}$). For these last two criteria, convergence is evaluated along n consecutive iterations as a moving mean and as an L_2 norm between 2 consecutive iterations, respectively. Although the objective function \mathcal{J} plays an important role in topology optimization, it has been determined that convergence in this parameter does not provide an objective criterion for compliant mechanism design. Consequently, this convergence criterion is not considered in the last benchmark. For the other numerical examples, this criterion is still used since convergence in topology and in volume constraint guarantee the convergence of the optimization problem (and in the objective function, too).

On the other hand, it is particularly critical to ensure that the same replacement material is used in the ersatz material approach (or in the material interpolation) for all methods, as it can significantly impact the obtained results, e.g., the objective function and the convergence of the problem. For this reason, a constant contrast factor $\alpha = 10^{-6}$ is chosen for minimum mean compliance problems while this value is increased up to $\alpha = 10^{-2}$ for compliant mechanism synthesis. In addition to this consideration, an additional final iteration with an element-wise bi-material configuration (i.e., each element being represented with a single material) must also be performed to compare the objective functions among each method. That is mainly due to the effect that semi-dense elements have on the computation of the objective function.


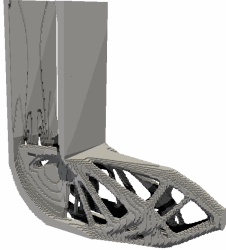
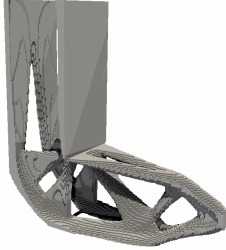
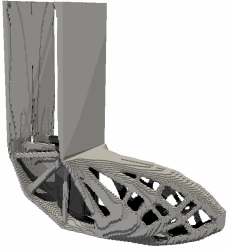
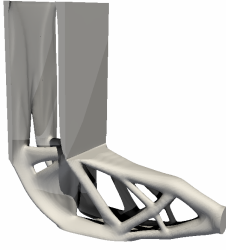
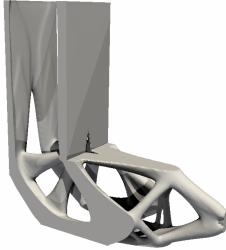
3.5.2 Comparison analysis

According to the previous guidelines, the results obtained from the different topology optimization approaches are now compared with each other for the four numerical benchmarks cases. As aforementioned, this comparison is carried out in terms of the optimal topology (quality/-complexity and minimum filament size \bar{h}), the objective function \mathcal{J} , and the computational cost (iterations). By considering all these aspects, an overall comparison of the different techniques can be made, thus assessing the potential of the proposed technique compared to other alternatives.

Optimal topologies

As a representative comparison solution, the resultant optimal topologies for the L-shaped structure are displayed in Table 3.1 for the required volume fraction $|\Omega^+|/|\Omega| = 0.1$. The results for the other benchmark cases are illustrated in Article D.

Table 3.1: Comparison of the results for the L-shaped structure.

SIMP ^(I)	SIMP ^(II)	SIMP ^(III)
		
SOFTBESO	VARTOP	Level-set
		

After analyzing all the results, it can be stated that topologies resulting from Level-set and VARTOP present low topology complexity and have smooth and accurate interfaces since the solution is defined via a level-set ϕ or a discrimination function ψ . On the contrary, SIMP-based and SOFTBESO methods produce element-wise discontinuous designs. In addition, SIMP-based approaches require special post-processing as semi-dense elements are found in the design, thus requiring an extra projection procedure to determine the density value that defines the material

interface. In this procedure, bars might be disconnected or broken up, giving as solution non-optimal topologies. Additionally, a smoothing post-processing should be performed to achieve crisp and smooth edges from these two families of approaches. Concerning the complexity of these two methods, the designs obtained from $\text{SIMP}^{(I)}$ and $\text{SIMP}^{(III)}$ present a much simpler design based on thicker bars (similar to those obtained with Level-set and VARTOP), while $\text{SIMP}^{(II)}$ and SOFTBESO exhibit higher topology complexity, with a larger number of thinner bars (lower minimum filament size \bar{h}). As the complexity of designs increases (i.e., the minimum filament size \bar{h} decreases), the difficulty to manufacture also increases, making the designs more susceptible to other phenomena such as buckling.

Objective function

From the analysis of the objective function \mathcal{J} (see Figure D.8 of Article D), it can be noticed that $\text{SIMP}^{(II)}$ achieves consistently optimal solutions with the lowest objective function as a consequence of the larger number of thinner straight bars, i.e., high topology complexity. However, the solution with the lowest objective function for the multi-load cantilever beam is obtained via the SOFTBESO approach, whose designs also exhibit high topology complexity with thinner or even continuous structures. As for the other topology optimization strategies, the objective function values does not differ much from one approach to another for each numerical case, and the values are just between a range of $\pm 15\%$ of the ones obtained using $\text{SIMP}^{(I)}$. In particular, the objective function values obtained from VARTOP, $\text{SIMP}^{(I)}$, and $\text{SIMP}^{(III)}$ are remarkably similar to each other, owing to the similarities observed in the topology layouts.

Computational cost

The computational cost is assessed in this paper according to the number of iterations instead of the computational time, thus obtaining the same results regardless of hardware, software, and solver, among others. The comparison of the computational cost is shown in Figure 3.20. As can be seen, the relative computational cost depends on each numerical example, although it keeps a certain tendency along the considered approaches for (multi-load) minimum mean compliance problems. $\text{SIMP}^{(I)}$, $\text{SIMP}^{(III)}$ and VARTOP exhibit similar computational cost with one approach being sometimes faster than the others, but all three are consistently faster than $\text{SIMP}^{(II)}$ and SOFTBESO, and up to an order of magnitude faster than Level-set technique. In particular, it is worth noting that VARTOP (and $\text{SIMP}^{(II)}$) not only provides the final optimal solution but also provides a set of converged solutions for different volume fractions (Pareto Frontier) at a similar computational cost as $\text{SIMP}^{(I)}$ or $\text{SIMP}^{(III)}$.

This tendency, however, does not hold true for the compliant mechanism problem. In this case, VARTOP is the fastest approach by far (almost an order of magnitude faster), followed by the Level-set and SOFTBESO approaches. Both methods require approximately half as many iterations as $\text{SIMP}^{(I)}$. In the case of $\text{SIMP}^{(III)}$ and $\text{SIMP}^{(II)}$, these techniques are respectively 20% and 10% faster than the reference method. This trend change in the computational cost may be caused by the change in the topology optimization problem.

3.5.3 Overall Performance

In addition to the quantitative results (objective function and computational cost) obtained up to this point, a more qualitative analysis of the results is now performed, comparing also the smoothness of the surface as well as the complexity of the optimal topology. The first aspect refers to the surface smoothness required by several manufacturing techniques, in which abrupt continuous changes must be avoided. On the other hand, the second criterion takes into account the complexity of the optimal design, and consequently the manufacturing time as well as other mechanical properties not included in the optimization. As a result, designs based on thick bars will have better structural behavior in buckling or fatigue compared to designs with a

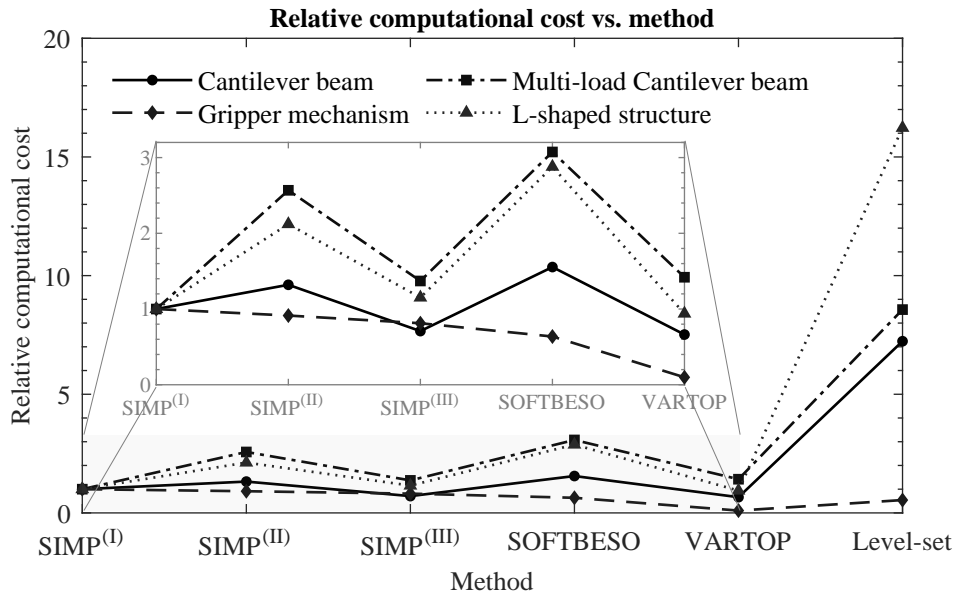


Figure 3.20: Relative computational cost in terms of the number of iterations. Each numerical example is normalized with the number of iterations of the SIMP^(I). Legend: (1) the Cantilever case is represented with a solid black line, (2) the L-shaped case, with a dotted black line, (3) the Cantilever multi-load case, with a dash-dotted line and (4) the Gripper mechanism with a dashed line.

greater number of thin bars. According to these four aspects, the different topology optimization approaches are rated in Figure 3.21 between A and D.

From this figure, it can be concluded that VARTOP, although not being the best approach in all considered aspects, is presented as a competitive technique to more conventional topology optimization approaches, such as SIMP^(I) and SIMP^(III). On the other hand, SOFTBESO and Level-set do not provide any significant advantages, exhibiting mostly deficiencies in topology complexity or computational cost, respectively, for these four benchmark cases. In conclusion, the VARTOP, SIMP^(I), and SIMP^(III) approaches present topology layouts with a higher topology quality than the other methods at a lower computational cost, even though their objective function is not minimized as much as in other approaches.

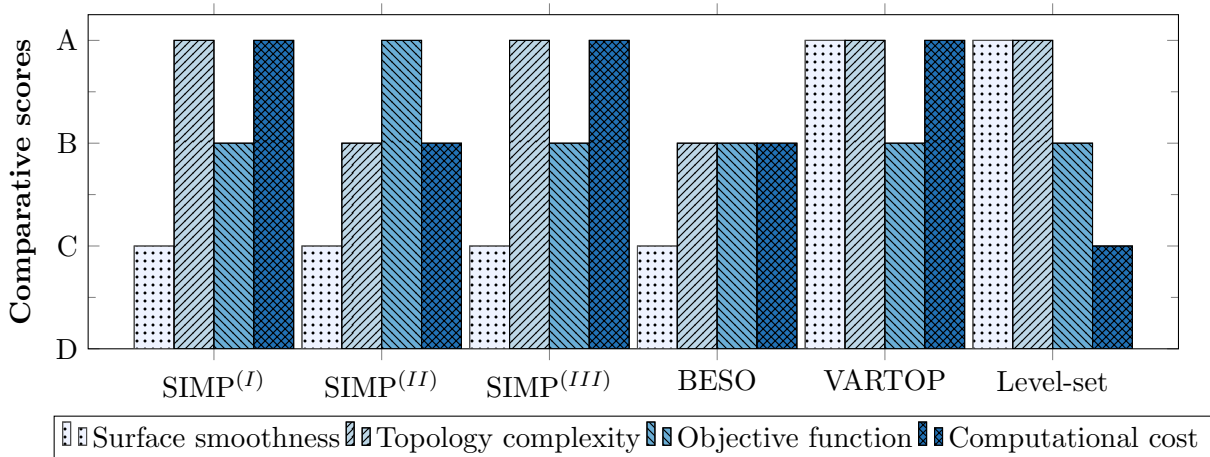


Figure 3.21: Qualitative comparison of the studied methods regarding the smoothness of the design, the topology complexity, the value of the objective function, and the computational cost in terms of iterations.

Chapter 4

Conclusions

4.1 Discussion of the results

This study addresses macro-scale topology optimization problems aiming to reduce the computational cost and the high mathematical complexity of up-to-date techniques. In order to achieve this goal, the main challenges hinge on the formulation of a topological derivative that contains all relevant topological information, and the development of an efficient and versatile topology updating strategy. This is achieved through the definition of the Relaxed Topological Derivative (RTD) and by proposing the resolution of the optimality criteria as a closed-form fixed-point problem. On top of that, the discrete properties of the characteristic function as a design variable are preserved throughout the approach.

The most relevant conclusions drawn from the development of this doctoral thesis are listed below.

- The adopted technique is essentially founded on a bi-material domain derived from the use of the ersatz material method, where the solid material is replaced by a weaker material (and vice-versa) instead of a void material. Consistently, based on this concept, a Relaxed Topological Derivative (RTD) with respect to the topology variable (characteristic function) can be defined as an approximation of the mathematically more complex exact Topological Derivative used in other methods. This definition leads to a simpler and faster way to compute the sensitivities while still providing numerical results of the same quality.
- The optimality condition in terms of the discrimination function is provided from the relaxed topological derivative (RTD) of the objective function and the volume constraint to calculate the corresponding sensitivities. This leads to the optimal topology as a solution to a closed-form algebraic non-linear equation, in which the volume constraint is imposed through the Lagrange multiplier. This parameter is then computed from a simple bisection algorithm, referred to as cutting&bisection algorithm. From this simple methodology, it is possible to impose the volume for the proposed problems in an exact and fast way.
- Adopting a pseudo-time advancing (volume-driven) strategy can be used to find the Pareto Frontier between the objective function and the volume constraint, thus returning a set of optimal solutions for intermediate volumes and providing the global minimum (minima) solution to the Pareto Frontier, at no extra computational cost. Despite the existence of other volume-enforcing methodologies, this one has shown promising results.
- The proposed technique has proven to be a versatile one in terms of applications and possible objective functions. Up to date, the strategy has been implemented and extended to structural problems (including minimum mean compliance and compliant mechanism) and thermal problems (maximum diffusivity and thermal cloaking problems), exploiting the relaxed topological derivative (RTD) to determine the sensitivity and a closed-form-solution time-advancing strategy. In addition, the proposed technique has been successfully applied to acoustic problems focused on resonance frequency fitting and bandgap maximization at the micro-scale [99].

- As a consequence of these features and in particular from the discrete property of the design variable, the proposed approach provides smooth black-and-white topology designs with sharp material boundaries. In those elements of the boundary, the characteristic function has been "relaxed" to capture the discontinuous stress field via a three-field mixed formulation ($\boldsymbol{\sigma} - \boldsymbol{\varepsilon} - \mathbf{u}$) in combination with the discrimination function, resulting in a density material interpolation similar to that found in SIMP techniques for this small number of elements. Mesh-size dependency and checkerboards effects are effectively mitigated via the Laplacian smoothing technique, ensuring also minimum material filament size control. As a result, other additional post-process filtering algorithms (e.g. Density filtering, Heaviside projections, morphological filters, among others) are not necessary, thus leading to a reduction in computational cost and mathematical complexity.
- The comparison with other techniques has confirmed that the proposed technique is at the same performance level (within an error margin) in terms of the objective function, computational cost, and robustness as some of the most relevant topological optimization techniques such as the SIMP method, and in most cases it outperforms the BESO and LS methods. On top of that, it has been proven that the pseudo-time incremental strategy does not represent any disadvantage compared to other techniques that impose a constant volume throughout the optimization, but rather it provides a full set of solutions with intermediate volumes.

In conclusion, the approach proposed throughout this study can be used as a starting point to optimize structures and engineering materials in different fields and achieve the envisaged targeted properties, while using an alternative technique to more established topology optimization methods. New strengths and features, as well as possible modifications to cover a larger number of examples, can be outlined by applying it to other problems.

4.2 Future research lines

The development and implementation of the proposed topology optimization technique can potentially provide the basis for future research lines in the field. Some relevant research topics are discussed below:

- *Extension to other applications or physical problems.* The proposed approach has been successfully applied in structural and thermal problems, as described in this dissertation. However, there are other interesting objective functions or even physical problems, e.g. in the electromagnetic field to develop and design new metamaterials, in which this method could be applied to with no major problems.
- *Implementation of other constitutive equations.* Up to this point, only linear materials have been employed in topology optimizations assuming small deformations. However, non-linear materials could be studied to analyze its effect when incorporated into the approach. In this case, new incremental strategies should be considered.
- *Multi-material optimizations.* Although two-material topology optimization can provide excellent results, it may also be one of the most important limitations in some situations. In contrast, multi-material topology optimization might lead to improved solutions by allowing for a wider range of possible applications.
- *Multi-scale concurrent topology optimization.* A concurrent topology optimization of multi-scales structures could be implemented to optimize both the macro-scale (as illustrated throughout this work) and the micro-scale at the same time. This strategy allows a double improvement in the objective function, by obtaining the optimal macro topology and the optimal micro-structure (e.g. optimal design and orientation) at each point of the macro-domain. Owing to the increase in the number of scales, the computational cost is exponentially increased. Hence, the proposed technique could be a suitable alternative to tackle these multi-scale problems, due to the satisfactory results in terms of computational cost.

4.3 Research dissemination

The dissemination of this work has been accomplished through the following scientific publications:

- [1] J. Oliver, D. Yago, J. Cante, and O. Lloberas-Valls, “Variational approach to relaxed topological optimization: Closed form solutions for structural problems in a sequential pseudo-time framework,” *Computer Methods in Applied Mechanics and Engineering*, vol. 355, pp. 779–819, Oct. 2019. DOI: [10.1016/j.cma.2019.06.038](https://doi.org/10.1016/j.cma.2019.06.038)
- [2] D. Yago, J. Cante, O. Lloberas-Valls, and J. Oliver, “Topology optimization of thermal problems in a nonsmooth variational setting: Closed-form optimality criteria,” *Computational Mechanics*, vol. 66, no. 2, pp. 259–286, Jun. 2020. DOI: [10.1007/s00466-020-01850-0](https://doi.org/10.1007/s00466-020-01850-0)
- [3] D. Yago, J. Cante, O. Lloberas-Valls, and J. Oliver, “Topology optimization using the unsmooth variational topology optimization (UNVARTOP) method: An educational implementation in MATLAB,” *Structural and Multidisciplinary Optimization*, vol. 63, pp. 955–981, Nov. 2020. DOI: [10.1007/s00158-020-02722-0](https://doi.org/10.1007/s00158-020-02722-0)
- [4] D. Yago, J. Cante, O. Lloberas-Valls, and J. Oliver, “Topology optimization methods for 3D structural problems: A comparative study,” *Archives of Computational Methods in Engineering*, Aug. 2021. DOI: [10.1007/s11831-021-09626-2](https://doi.org/10.1007/s11831-021-09626-2)

In particular, the online publication of an educational Matlab code in a public GitHub repository <https://github.com/DanielYago/UNVARTOP> (Paper C [136]) provides students and those new to the field (or to the proposed approach) with the theoretical basis for topology optimization and a better understanding in how this new topology optimization approach works. Specifically, the topology optimization code corresponds to the 2D structural implementation of the proposed technique for educational purposes to demonstrate its capabilities and effectiveness to tackle a large set of different problems subject to a volume constraint. Additionally, it can be easily extended to thermal problems or 3D problems.

As a long-term objective of this dissemination, it is expected that the availability of a set of publications and an open-source code will encourage researchers to conduct future research using the proposed technique in different fields, increasing the visibility of the technique among the topology optimization community.

In addition to the publications and the educational code, the work has been presented in the following conferences:

- [1] D. Roca, D. Yago, J. C. Cante, O. Lloberas-Valls, and J. Oliver, “Computational multiscale design of engineering metamaterials: Application to acoustic insulation panels,” in *6th European Conference on Computational Mechanics (Solids, Structures and Coupled Problems) / 7th European Computational Fluid Dynamics Conference*, Glasgow, Scotland, UK, Jun. 2018
- [2] J. Oliver, D. Yago, J. Cante, and O. Lloberas-Valls, “Variational approach to topological optimization problems: Closed-form solutions in a pseudo-time framework,” in *COMPLAS 2019 - XV International Conference on Computational Plasticity: Fundamentals and Applications*, Barcelona, Spain, Sep. 2019
- [3] D. Roca, D. Yago, J. Cante, O. Lloberas-Valls, and J. Oliver, “Computational procedure for optimal design of acoustic metamaterials,” in *COMPLAS 2019 - XV International Conference on Computational Plasticity: Fundamentals and Applications*, Barcelona, Spain, Sep. 2019
- [4] D. Yago, J. Cante, O. Lloberas-Valls, and J. Oliver, “Topology optimization of thermal problems: The closed-form solution method,” in *COMPLAS 2019 - XV International Conference on Computational Plasticity: Fundamentals and Applications*, Barcelona, Spain, Sep. 2019
- [5] D. Yago, J. Cante, O. Lloberas-Valls, and J. Oliver, “Nonsmooth variational approach to topology optimization (vartop),” in *14th World Congress on Computational Mechanics (WCCM XIV), 8th European Congress on Computational Methods in Applied Sciences and Engineering (ECCOMAS 2020)*, Paris, France, Jan. 2021

Chapter 5

Bibliography

- [1] N. Aage, E. Andreassen, B. S. Lazarov, and O. Sigmund, “Giga-voxel computational morphogenesis for structural design,” vol. 550, no. 7674, pp. 84–86, Oct. 2017. DOI: [10.1038/nature23911](https://doi.org/10.1038/nature23911).
- [2] J. Alexandersen, O. Sigmund, and N. Aage, “Large scale three-dimensional topology optimisation of heat sinks cooled by natural convection,” *International Journal of Heat and Mass Transfer*, vol. 100, pp. 876–891, Sep. 2016. DOI: [10.1016/j.ijheatmasstransfer.2016.05.013](https://doi.org/10.1016/j.ijheatmasstransfer.2016.05.013).
- [3] G. Allaire, E. Bonnetier, G. Francfort, and F. Jouve, “Shape optimization by the homogenization method,” *Numerische Mathematik*, vol. 76, no. 1, pp. 27–68, 1997. DOI: [10.1007/s002110050253](https://doi.org/10.1007/s002110050253).
- [4] G. Allaire, F. de gournay, F. Jouve, and A.-M. Toader, “Structural optimization using topological and shape sensitivity via a level set method,” *Control and Cybernetics*, vol. 34, 2005.
- [5] G. Allaire and F. Jouve, “A level-set method for vibration and multiple loads structural optimization,” *Computer Methods in Applied Mechanics and Engineering*, vol. 194, no. 30–33, pp. 3269–3290, 2005. DOI: [10.1016/j.cma.2004.12.018](https://doi.org/10.1016/j.cma.2004.12.018).
- [6] G. Allaire, F. Jouve, and A.-M. Toader, “A level-set method for shape optimization,” *Comptes Rendus Mathematique*, vol. 334, no. 12, pp. 1125–1130, Jan. 2002. DOI: [10.1016/s1631-073x\(02\)02412-3](https://doi.org/10.1016/s1631-073x(02)02412-3).
- [7] G. Allaire, F. Jouve, and A.-M. Toader, “Structural optimization using sensitivity analysis and a level-set method,” *Journal of Computational Physics*, vol. 194, no. 1, pp. 363–393, 2004. DOI: [10.1016/j.jcp.2003.09.032](https://doi.org/10.1016/j.jcp.2003.09.032).
- [8] S. M. Allen and J. W. Cahn, “A microscopic theory for antiphase boundary motion and its application to antiphase domain coarsening,” *Acta Metallurgica*, vol. 27, no. 6, pp. 1085–1095, Jun. 1979. DOI: [10.1016/0001-6160\(79\)90196-2](https://doi.org/10.1016/0001-6160(79)90196-2).
- [9] S. Amstutz and H. Andrä, “A new algorithm for topology optimization using a level-set method,” *Journal of Computational Physics*, vol. 216, no. 2, pp. 573–588, 2006. DOI: [10.1016/j.jcp.2005.12.015](https://doi.org/10.1016/j.jcp.2005.12.015).
- [10] C. S. Andreasen and O. Sigmund, “Topology optimization of fluid–structure-interaction problems in poroelasticity,” *Computer Methods in Applied Mechanics and Engineering*, vol. 258, pp. 55–62, May 2013. DOI: [10.1016/j.cma.2013.02.007](https://doi.org/10.1016/j.cma.2013.02.007).
- [11] E. Andreassen, A. Clausen, M. Schevenels, B. S. Lazarov, and O. Sigmund, “Efficient topology optimization in MATLAB using 88 lines of code,” *Structural and Multidisciplinary Optimization*, vol. 43, no. 1, pp. 1–16, Nov. 2010. DOI: [10.1007/s00158-010-0594-7](https://doi.org/10.1007/s00158-010-0594-7).

- [12] T. W. Athan and P. Y. Papalambros, “A note on weighted criteria methods for compromise solutions in multi-objective optimization,” *Engineering Optimization*, vol. 27, no. 2, pp. 155–176, Sep. 1996. DOI: [10.1080/03052159608941404](https://doi.org/10.1080/03052159608941404).
- [13] M. P. Bendsøe, “Optimal shape design as a material distribution problem,” *Structural Optimization*, vol. 1, no. 4, pp. 193–202, Dec. 1989. DOI: [10.1007/bf01650949](https://doi.org/10.1007/bf01650949).
- [14] M. P. Bendsøe and O. Sigmund, *Topology Optimization*. Springer Berlin Heidelberg, 2004. DOI: [10.1007/978-3-662-05086-6](https://doi.org/10.1007/978-3-662-05086-6).
- [15] M. P. Bendsøe and N. Kikuchi, “Generating optimal topologies in structural design using a homogenization method,” *Computer Methods in Applied Mechanics and Engineering*, vol. 71, no. 2, pp. 197–224, Nov. 1988. DOI: [10.1016/0045-7825\(88\)90086-2](https://doi.org/10.1016/0045-7825(88)90086-2).
- [16] T. Borrvall and J. Petersson, “Topology optimization of fluids in stokes flow,” *International Journal for Numerical Methods in Fluids*, vol. 41, no. 1, pp. 77–107, 2002. DOI: [10.1002/flid.426](https://doi.org/10.1002/flid.426).
- [17] B. Bourdin, “Filters in topology optimization,” *International Journal for Numerical Methods in Engineering*, vol. 50, no. 9, pp. 2143–2158, 2001. DOI: [10.1002/nme.116](https://doi.org/10.1002/nme.116).
- [18] B. Bourdin and A. Chambolle, “Design-dependent loads in topology optimization,” *ESAIM: Control, Optimisation and Calculus of Variations*, vol. 9, pp. 19–48, Jan. 2003. DOI: [10.1051/cocv:2002070](https://doi.org/10.1051/cocv:2002070).
- [19] T. E. Bruns, “Topology optimization of convection-dominated, steady-state heat transfer problems,” *International Journal of Heat and Mass Transfer*, vol. 50, no. 15-16, pp. 2859–2873, Jul. 2007. DOI: [10.1016/j.ijheatmasstransfer.2007.01.039](https://doi.org/10.1016/j.ijheatmasstransfer.2007.01.039).
- [20] T. E. Bruns and D. A. Tortorelli, “Topology optimization of non-linear elastic structures and compliant mechanisms,” *Computer Methods in Applied Mechanics and Engineering*, vol. 190, no. 26-27, pp. 3443–3459, Mar. 2001. DOI: [10.1016/s0045-7825\(00\)00278-4](https://doi.org/10.1016/s0045-7825(00)00278-4).
- [21] S. Bureerat and J. Limtragool, “Structural topology optimisation using simulated annealing with multiresolution design variables,” vol. 44, no. 12-13, pp. 738–747, Aug. 2008. DOI: [10.1016/j.finel.2008.04.002](https://doi.org/10.1016/j.finel.2008.04.002).
- [22] M. Burger, B. Hackl, and W. Ring, “Incorporating topological derivatives into level set methods,” *Journal of Computational Physics*, vol. 194, no. 1, pp. 344–362, 2004. DOI: [10.1016/j.jcp.2003.09.033](https://doi.org/10.1016/j.jcp.2003.09.033).
- [23] M. Burger and R. Stainko, “Phase-field relaxation of topology optimization with local stress constraints,” *SIAM Journal on Control and Optimization*, vol. 45, no. 4, pp. 1447–1466, Jan. 2006. DOI: [10.1137/05062723x](https://doi.org/10.1137/05062723x).
- [24] J. W. Cahn and J. E. Hilliard, “Free energy of a nonuniform system. I. interfacial free energy,” *The Journal of Chemical Physics*, vol. 28, no. 2, pp. 258–267, Feb. 1958. DOI: [10.1063/1.1744102](https://doi.org/10.1063/1.1744102).
- [25] J. C ea, S. Garreau, P. Guillaume, and M. Masmoudi, “The shape and topological optimizations connection,” *Computer Methods in Applied Mechanics and Engineering*, vol. 188, no. 4, pp. 713–726, 2000. DOI: [10.1016/s0045-7825\(99\)00357-6](https://doi.org/10.1016/s0045-7825(99)00357-6).
- [26] D. Chu, Y. Xie, A. Hira, and G. Steven, “Evolutionary structural optimization for problems with stiffness constraints,” *Finite Elements in Analysis and Design*, vol. 21, no. 4, pp. 239–251, Apr. 1996. DOI: [10.1016/0168-874x\(95\)00043-s](https://doi.org/10.1016/0168-874x(95)00043-s).
- [27] P. G. Coelho, P. R. Fernandes, J. M. Guedes, and H. C. Rodrigues, “A hierarchical model for concurrent material and topology optimisation of three-dimensional structures,” *Structural and Multidisciplinary Optimization*, vol. 35, no. 2, pp. 107–115, Jun. 2007. DOI: [10.1007/s00158-007-0141-3](https://doi.org/10.1007/s00158-007-0141-3).

- [28] M. Dambrine and D. Kateb, “On the ersatz material approximation in level-set methods,” *ESAIM: Control, Optimisation and Calculus of Variations*, vol. 16, no. 3, pp. 618–634, 2009. DOI: [10.1051/cocv/2009023](https://doi.org/10.1051/cocv/2009023).
- [29] J. D. Deaton and R. V. Grandhi, “A survey of structural and multidisciplinary continuum topology optimization: Post 2000,” *Structural and Multidisciplinary Optimization*, vol. 49, no. 1, pp. 1–38, 2013. DOI: [10.1007/s00158-013-0956-z](https://doi.org/10.1007/s00158-013-0956-z).
- [30] J. Deng, J. Yan, and G. Cheng, “Multi-objective concurrent topology optimization of thermoelastic structures composed of homogeneous porous material,” *Structural and Multidisciplinary Optimization*, vol. 47, no. 4, pp. 583–597, Nov. 2012. DOI: [10.1007/s00158-012-0849-6](https://doi.org/10.1007/s00158-012-0849-6).
- [31] N. P. van Dijk, K. Maute, M. Langelaar, and F. van Keulen, “Level-set methods for structural topology optimization: A review,” *Structural and Multidisciplinary Optimization*, vol. 48, no. 3, pp. 437–472, 2013. DOI: [10.1007/s00158-013-0912-y](https://doi.org/10.1007/s00158-013-0912-y).
- [32] H.-W. Dong, S.-D. Zhao, Y.-S. Wang, and C. Zhang, “Topology optimization of anisotropic broadband double-negative elastic metamaterials,” *Journal of the Mechanics and Physics of Solids*, vol. 105, pp. 54–80, Aug. 2017. DOI: [10.1016/j.jmps.2017.04.009](https://doi.org/10.1016/j.jmps.2017.04.009).
- [33] J. Du and N. Olhoff, “Minimization of sound radiation from vibrating bi-material structures using topology optimization,” *Structural and Multidisciplinary Optimization*, vol. 33, no. 4-5, pp. 305–321, Jan. 2007. DOI: [10.1007/s00158-006-0088-9](https://doi.org/10.1007/s00158-006-0088-9).
- [34] J. Du and N. Olhoff, “Topological design of vibrating structures with respect to optimum sound pressure characteristics in a surrounding acoustic medium,” vol. 42, no. 1, pp. 43–54, Jan. 2010. DOI: [10.1007/s00158-009-0477-y](https://doi.org/10.1007/s00158-009-0477-y).
- [35] İ. Durgun and A. R. Yildiz, “Structural design optimization of vehicle components using cuckoo search algorithm,” vol. 54, no. 3, pp. 185–188, Mar. 2012. DOI: [10.3139/120.110317](https://doi.org/10.3139/120.110317).
- [36] H. A. Eschenauer, V. V. Kobelev, and A. Schumacher, “Bubble method for topology and shape optimization of structures,” *Structural Optimization*, vol. 8, no. 1, pp. 42–51, Aug. 1994. DOI: [10.1007/bf01742933](https://doi.org/10.1007/bf01742933).
- [37] H. A. Eschenauer and N. Olhoff, “Topology optimization of continuum structures: A review,” *Applied Mechanics Reviews*, vol. 54, no. 4, pp. 331–390, Jul. 2001. DOI: [10.1115/1.1388075](https://doi.org/10.1115/1.1388075).
- [38] D. J. Eyre, “Systems of cahn–hilliard equations,” *SIAM Journal on Applied Mathematics*, vol. 53, no. 6, pp. 1686–1712, Dec. 1993. DOI: [10.1137/0153078](https://doi.org/10.1137/0153078).
- [39] V. D. Fachinotti, Á. A. Ciarbonetti, I. Peralta, and I. Rintoul, “Optimization-based design of easy-to-make devices for heat flux manipulation,” *International Journal of Thermal Sciences*, vol. 128, pp. 38–48, Jun. 2018. DOI: [10.1016/j.ijthermalsci.2018.02.009](https://doi.org/10.1016/j.ijthermalsci.2018.02.009).
- [40] P. Fernandes, J. M. Guedes, and H. Rodrigues, “Topology optimization of three-dimensional linear elastic structures with a constraint on “perimeter”,” *Computers & Structures*, vol. 73, no. 6, pp. 583–594, 1999. DOI: [10.1016/s0045-7949\(98\)00312-5](https://doi.org/10.1016/s0045-7949(98)00312-5).
- [41] T. Gao, W. H. Zhang, J. H. Zhu, Y. J. Xu, and D. H. Bassir, “Topology optimization of heat conduction problem involving design-dependent heat load effect,” *Finite Elements in Analysis and Design*, vol. 44, no. 14, pp. 805–813, Oct. 2008. DOI: [10.1016/j.finel.2008.06.001](https://doi.org/10.1016/j.finel.2008.06.001).
- [42] S. Garreau, P. Guillaume, and M. Masmoudi, “The topological asymptotic for PDE systems: The elasticity case,” *SIAM Journal on Control and Optimization*, vol. 39, no. 6, pp. 1756–1778, 2001. DOI: [10.1137/s0363012900369538](https://doi.org/10.1137/s0363012900369538).
- [43] A. Gersborg-Hansen, O. Sigmund, and R. Haber, “Topology optimization of channel flow problems,” *Structural and Multidisciplinary Optimization*, vol. 30, no. 3, pp. 181–192, Jun. 2005. DOI: [10.1007/s00158-004-0508-7](https://doi.org/10.1007/s00158-004-0508-7).

- [44] J. K. Guest, J. H. Prévost, and T. Belytschko, “Achieving minimum length scale in topology optimization using nodal design variables and projection functions,” *International Journal for Numerical Methods in Engineering*, vol. 61, no. 2, pp. 238–254, 2004. DOI: [10.1002/nme.1064](https://doi.org/10.1002/nme.1064).
- [45] J. K. Guest, A. Asadpoure, and S.-H. Ha, “Eliminating beta-continuation from heaviside projection and density filter algorithms,” *Structural and Multidisciplinary Optimization*, vol. 44, no. 4, pp. 443–453, Jul. 2011. DOI: [10.1007/s00158-011-0676-1](https://doi.org/10.1007/s00158-011-0676-1).
- [46] J. K. Guest and J. H. Prévost, “Topology optimization of creeping fluid flows using a darcy–stokes finite element,” *International Journal for Numerical Methods in Engineering*, vol. 66, no. 3, pp. 461–484, 2006. DOI: [10.1002/nme.1560](https://doi.org/10.1002/nme.1560).
- [47] S.-H. Ha and S. Cho, “Topological shape optimization of heat conduction problems using level set approach,” *Numerical Heat Transfer, Part B: Fundamentals*, vol. 48, no. 1, pp. 67–88, Jul. 2005. DOI: [10.1080/10407790590935966](https://doi.org/10.1080/10407790590935966).
- [48] R. B. Haber, C. S. Jog, and M. P. Bends Bendsøe, “A new approach to variable-topology shape design using a constraint on perimeter,” *Structural Optimization*, vol. 11, no. 1-2, pp. 1–12, 1996. DOI: [10.1007/bf01279647](https://doi.org/10.1007/bf01279647).
- [49] R. Haber and M. Bendsoe, “Problem formulation, solution procedures and geometric modeling - key issues in variable-topology optimization,” in *7th AIAA/USAF/NASA/ISSMO Symposium on Multidisciplinary Analysis and Optimization*, American Institute of Aeronautics and Astronautics, Sep. 1998. DOI: [10.2514/6.1998-4948](https://doi.org/10.2514/6.1998-4948).
- [50] L. He, C.-Y. Kao, and S. Osher, “Incorporating topological derivatives into shape derivatives based level set methods,” *Journal of Computational Physics*, vol. 225, no. 1, pp. 891–909, 2007. DOI: [10.1016/j.jcp.2007.01.003](https://doi.org/10.1016/j.jcp.2007.01.003).
- [51] X. Huang and Y. M. Xie, “Bi-directional evolutionary topology optimization of continuum structures with one or multiple materials,” *Computational Mechanics*, vol. 43, no. 3, pp. 393–401, Jul. 2008. DOI: [10.1007/s00466-008-0312-0](https://doi.org/10.1007/s00466-008-0312-0).
- [52] X. Huang and Y. M. Xie, *Evolutionary Topology Optimization of Continuum Structures*. John Wiley & Sons, Ltd, Apr. 2010. DOI: [10.1002/9780470689486](https://doi.org/10.1002/9780470689486).
- [53] X. Huang, Y. M. Xie, B. Jia, Q. Li, and S. W. Zhou, “Evolutionary topology optimization of periodic composites for extremal magnetic permeability and electrical permittivity,” *Structural and Multidisciplinary Optimization*, vol. 46, no. 3, pp. 385–398, Jan. 2012. DOI: [10.1007/s00158-012-0766-8](https://doi.org/10.1007/s00158-012-0766-8).
- [54] X. Huang and Y. Xie, “Convergent and mesh-independent solutions for the bi-directional evolutionary structural optimization method,” *Finite Elements in Analysis and Design*, vol. 43, no. 14, pp. 1039–1049, Oct. 2007. DOI: [10.1016/j.finel.2007.06.006](https://doi.org/10.1016/j.finel.2007.06.006).
- [55] A. A. Jaafer, M. Al-Bazoon, and A. O. Dawood, “Structural topology design optimization using the binary bat algorithm,” vol. 10, no. 4, p. 1481, Feb. 2020. DOI: [10.3390/app10041481](https://doi.org/10.3390/app10041481).
- [56] N. Jenkins and K. Maute, “Level set topology optimization of stationary fluid-structure interaction problems,” *Structural and Multidisciplinary Optimization*, vol. 52, no. 1, pp. 179–195, Mar. 2015. DOI: [10.1007/s00158-015-1229-9](https://doi.org/10.1007/s00158-015-1229-9).
- [57] C. S. Jog and R. B. Haber, “Stability of finite element models for distributed-parameter optimization and topology design,” *Computer Methods in Applied Mechanics and Engineering*, vol. 130, no. 3-4, pp. 203–226, Apr. 1996. DOI: [10.1016/0045-7825\(95\)00928-0](https://doi.org/10.1016/0045-7825(95)00928-0).
- [58] A. Kaveh, B. Hassani, S. Shojaee, and S. Tavakkoli, “Structural topology optimization using ant colony methodology,” vol. 30, no. 9, pp. 2559–2565, Sep. 2008. DOI: [10.1016/j.engstruct.2008.02.012](https://doi.org/10.1016/j.engstruct.2008.02.012).

- [59] A. Kawamoto, T. Matsumori, S. Yamasaki, T. Nomura, T. Kondoh, and S. Nishiwaki, “Heaviside projection based topology optimization by a PDE-filtered scalar function,” *Structural and Multidisciplinary Optimization*, vol. 44, no. 1, pp. 19–24, Aug. 2010. DOI: [10.1007/s00158-010-0562-2](https://doi.org/10.1007/s00158-010-0562-2).
- [60] H. Kawamura, H. Ohmori, and N. Kito, “Truss topology optimization by a modified genetic algorithm,” vol. 23, no. 6, pp. 467–473, Jul. 2002. DOI: [10.1007/s00158-002-0208-0](https://doi.org/10.1007/s00158-002-0208-0).
- [61] R. Kicinger, T. Arciszewski, and K. D. Jong, “Evolutionary computation and structural design: A survey of the state-of-the-art,” vol. 83, no. 23-24, pp. 1943–1978, Sep. 2005. DOI: [10.1016/j.compstruc.2005.03.002](https://doi.org/10.1016/j.compstruc.2005.03.002).
- [62] S. Kitayama, M. Arakawa, and K. Yamazaki, “Differential evolution as the global optimization technique and its application to structural optimization,” vol. 11, no. 4, pp. 3792–3803, Jun. 2011. DOI: [10.1016/j.asoc.2011.02.012](https://doi.org/10.1016/j.asoc.2011.02.012).
- [63] B. S. Lazarov and O. Sigmund, “Filters in topology optimization based on helmholtz-type differential equations,” *International Journal for Numerical Methods in Engineering*, vol. 86, no. 6, pp. 765–781, Dec. 2010. DOI: [10.1002/nme.3072](https://doi.org/10.1002/nme.3072).
- [64] K. S. Lee and Z. W. Geem, “A new structural optimization method based on the harmony search algorithm,” vol. 82, no. 9-10, pp. 781–798, Apr. 2004. DOI: [10.1016/j.compstruc.2004.01.002](https://doi.org/10.1016/j.compstruc.2004.01.002).
- [65] Q. Li, G. Steven, and Y. Xie, “A simple checkerboard suppression algorithm for evolutionary structural optimization,” *Structural and Multidisciplinary Optimization*, vol. 22, no. 3, pp. 230–239, Oct. 2001. DOI: [10.1007/s001580100140](https://doi.org/10.1007/s001580100140).
- [66] Q. Li, G. P. Steven, O. M. Querin, and Y. M. Xie, “Structural topology design with multiple thermal criteria,” *Engineering Computations*, vol. 17, no. 6, pp. 715–734, Sep. 2000. DOI: [10.1108/02644400010340642](https://doi.org/10.1108/02644400010340642).
- [67] Q. Li, G. P. Steven, O. M. Querin, and Y. Xie, “Shape and topology design for heat conduction by evolutionary structural optimization,” *International Journal of Heat and Mass Transfer*, vol. 42, no. 17, pp. 3361–3371, Sep. 1999. DOI: [10.1016/s0017-9310\(99\)00008-3](https://doi.org/10.1016/s0017-9310(99)00008-3).
- [68] W. Li, G. Steven, and Y. Xie, “Shape design for elastic contact problems by evolutionary structural optimization,” in *7th AIAA/USAF/NASA/ISSMO Symposium on Multidisciplinary Analysis and Optimization*, American Institute of Aeronautics and Astronautics, Sep. 1998. DOI: [10.2514/6.1998-4851](https://doi.org/10.2514/6.1998-4851).
- [69] W. Li, Q. Li, G. P. Steven, and Y. Xie, “An evolutionary shape optimization for elastic contact problems subject to multiple load cases,” *Computer Methods in Applied Mechanics and Engineering*, vol. 194, no. 30-33, pp. 3394–3415, Aug. 2005. DOI: [10.1016/j.cma.2004.12.024](https://doi.org/10.1016/j.cma.2004.12.024).
- [70] Y. fan Li, X. Huang, F. Meng, and S. Zhou, “Evolutionary topological design for phononic band gap crystals,” *Structural and Multidisciplinary Optimization*, vol. 54, no. 3, pp. 595–617, Mar. 2016. DOI: [10.1007/s00158-016-1424-3](https://doi.org/10.1007/s00158-016-1424-3).
- [71] S. Lim, T. Yamada, S. Min, and S. Nishiwaki, “Topology optimization of a magnetic actuator based on a level set and phase-field approach,” *IEEE Transactions on Magnetics*, vol. 47, no. 5, pp. 1318–1321, May 2011. DOI: [10.1109/tmag.2010.2097583](https://doi.org/10.1109/tmag.2010.2097583).
- [72] J. L. Lions, *Optimal Control of Systems Governed by Partial Differential Equations*. Springer Berlin Heidelberg, 1971, 416 pp., ISBN: 3642650260.
- [73] L. Lu, T. Yamamoto, M. Otomori, T. Yamada, K. Izui, and S. Nishiwaki, “Topology optimization of an acoustic metamaterial with negative bulk modulus using local resonance,” *Finite Elements in Analysis and Design*, vol. 72, pp. 1–12, Sep. 2013. DOI: [10.1016/j.finel.2013.04.005](https://doi.org/10.1016/j.finel.2013.04.005).

- [74] D. G. Luenberger and Y. Ye, *Linear and Nonlinear Programming*. Springer International Publishing, 2016. DOI: [10.1007/978-3-319-18842-3](https://doi.org/10.1007/978-3-319-18842-3).
- [75] G.-C. Luh and C.-Y. Lin, “Structural topology optimization using ant colony optimization algorithm,” vol. 9, no. 4, pp. 1343–1353, Sep. 2009. DOI: [10.1016/j.asoc.2009.06.001](https://doi.org/10.1016/j.asoc.2009.06.001).
- [76] G.-C. Luh, C.-Y. Lin, and Y.-S. Lin, “A binary particle swarm optimization for continuum structural topology optimization,” vol. 11, no. 2, pp. 2833–2844, Mar. 2011. DOI: [10.1016/j.asoc.2010.11.013](https://doi.org/10.1016/j.asoc.2010.11.013).
- [77] D. Manickarajah, Y. Xie, and G. Steven, “An evolutionary method for optimization of plate buckling resistance,” *Finite Elements in Analysis and Design*, vol. 29, no. 3-4, pp. 205–230, Jun. 1998. DOI: [10.1016/s0168-874x\(98\)00012-2](https://doi.org/10.1016/s0168-874x(98)00012-2).
- [78] G. Marck, M. Nemer, and J.-L. Harion, “Topology optimization of heat and mass transfer problems: Laminar flow,” *Numerical Heat Transfer, Part B: Fundamentals*, vol. 63, no. 6, pp. 508–539, Jun. 2013. DOI: [10.1080/10407790.2013.772001](https://doi.org/10.1080/10407790.2013.772001).
- [79] G. Marck, M. Nemer, J.-L. Harion, S. Russeil, and D. Bougeard, “Topology optimization using the SIMP method for multiobjective conductive problems,” *Numerical Heat Transfer, Part B: Fundamentals*, vol. 61, no. 6, pp. 439–470, Jun. 2012. DOI: [10.1080/10407790.2012.687979](https://doi.org/10.1080/10407790.2012.687979).
- [80] R. Marler and J. Arora, “Survey of multi-objective optimization methods for engineering,” *Structural and Multidisciplinary Optimization*, vol. 26, no. 6, pp. 369–395, Apr. 2004. DOI: [10.1007/s00158-003-0368-6](https://doi.org/10.1007/s00158-003-0368-6).
- [81] K. Martini, “Harmony search method for multimodal size, shape, and topology optimization of structural frameworks,” vol. 137, no. 11, pp. 1332–1339, Nov. 2011. DOI: [10.1061/\(asce\)st.1943-541x.0000378](https://doi.org/10.1061/(asce)st.1943-541x.0000378).
- [82] K. Maute and M. Allen, “Conceptual design of aeroelastic structures by topology optimization,” *Structural and Multidisciplinary Optimization*, vol. 27, no. 1-2, pp. 27–42, May 2004. DOI: [10.1007/s00158-003-0362-z](https://doi.org/10.1007/s00158-003-0362-z).
- [83] L. F. F. Miguel, R. H. Lopez, and L. F. F. Miguel, “Multimodal size, shape, and topology optimisation of truss structures using the firefly algorithm,” vol. 56, pp. 23–37, Feb. 2013. DOI: [10.1016/j.advengsoft.2012.11.006](https://doi.org/10.1016/j.advengsoft.2012.11.006).
- [84] H. P. Mlejnek, “Some aspects of the genesis of structures,” *Structural Optimization*, vol. 5, no. 1-2, pp. 64–69, Mar. 1992. DOI: [10.1007/bf01744697](https://doi.org/10.1007/bf01744697).
- [85] D. J. Munk, G. A. Vio, and G. P. Steven, “Topology and shape optimization methods using evolutionary algorithms: A review,” *Structural and Multidisciplinary Optimization*, vol. 52, no. 3, pp. 613–631, May 2015. DOI: [10.1007/s00158-015-1261-9](https://doi.org/10.1007/s00158-015-1261-9).
- [86] J. A. Norato, M. P. Bendsøe, R. B. Haber, and D. A. Tortorelli, “A topological derivative method for topology optimization,” *Structural and Multidisciplinary Optimization*, vol. 33, no. 4-5, pp. 375–386, 2007. DOI: [10.1007/s00158-007-0094-6](https://doi.org/10.1007/s00158-007-0094-6).
- [87] A. A. Novotny, R. A. Feijóo, E. Taroco, and C. Padra, “Topological sensitivity analysis,” *Computer Methods in Applied Mechanics and Engineering*, vol. 192, no. 7-8, pp. 803–829, 2003. DOI: [10.1016/s0045-7825\(02\)00599-6](https://doi.org/10.1016/s0045-7825(02)00599-6).
- [88] A. A. Novotny and J. Sokolowski, *Topological Derivatives in Shape Optimization*. Springer Berlin Heidelberg, 2013. DOI: [10.1007/978-3-642-35245-4](https://doi.org/10.1007/978-3-642-35245-4).
- [89] J. Oliver, D. Yago, J. Cante, and O. Lloberas-Valls, “Variational approach to relaxed topological optimization: Closed form solutions for structural problems in a sequential pseudo-time framework,” *Computer Methods in Applied Mechanics and Engineering*, vol. 355, pp. 779–819, Oct. 2019. DOI: [10.1016/j.cma.2019.06.038](https://doi.org/10.1016/j.cma.2019.06.038).

- [90] J. Oliver, D. Yago, J. Cante, and O. Lloberas-Valls, “Variational approach to topological optimization problems: Closed-form solutions in a pseudo-time framework,” in *COMPLAS 2019 - XV International Conference on Computational Plasticity: Fundamentals and Applications*, Barcelona, Spain, Sep. 2019.
- [91] S. Osher and R. Fedkiw, *Level Set Methods and Dynamic Implicit Surfaces*. Springer New York, 2003. DOI: [10.1007/b98879](https://doi.org/10.1007/b98879).
- [92] S. Osher and J. A. Sethian, “Fronts propagating with curvature-dependent speed: Algorithms based on hamilton-jacobi formulations,” *Journal of Computational Physics*, vol. 79, no. 1, pp. 12–49, 1988. DOI: [10.1016/0021-9991\(88\)90002-2](https://doi.org/10.1016/0021-9991(88)90002-2).
- [93] S. J. Osher and F. Santosa, “Level set methods for optimization problems involving geometry and constraints,” *Journal of Computational Physics*, vol. 171, no. 1, pp. 272–288, Jul. 2001. DOI: [10.1006/jcph.2001.6789](https://doi.org/10.1006/jcph.2001.6789).
- [94] J. Petersson and O. Sigmund, “Slope constrained topology optimization,” *International Journal for Numerical Methods in Engineering*, vol. 41, no. 8, pp. 1417–1434, Apr. 1998. DOI: [10.1002/\(sici\)1097-0207\(19980430\)41:8<1417::aid-nme344>3.0.co;2-n](https://doi.org/10.1002/(sici)1097-0207(19980430)41:8<1417::aid-nme344>3.0.co;2-n).
- [95] Y. M. X. Qing Li Grant P. Steven, “Thermoelastic topology optimization for problems with varying temperature fields,” *Journal of Thermal Stresses*, vol. 24, no. 4, pp. 347–366, Apr. 2001. DOI: [10.1080/01495730151078153](https://doi.org/10.1080/01495730151078153).
- [96] O. Querin, G. Steven, and Y. Xie, “Topology optimisation of structures with material and geometric non-linearities,” in *6th Symposium on Multidisciplinary Analysis and Optimization*, American Institute of Aeronautics and Astronautics, Sep. 1996. DOI: [10.2514/6.1996-4116](https://doi.org/10.2514/6.1996-4116).
- [97] O. Querin, G. Steven, and Y. Xie, “Evolutionary structural optimisation (ESO) using a bidirectional algorithm,” *Engineering Computations*, vol. 15, no. 8, pp. 1031–1048, Dec. 1998. DOI: [10.1108/02644409810244129](https://doi.org/10.1108/02644409810244129).
- [98] O. Querin, V. Young, G. Steven, and Y. Xie, “Computational efficiency and validation of bi-directional evolutionary structural optimisation,” *Computer Methods in Applied Mechanics and Engineering*, vol. 189, no. 2, pp. 559–573, Sep. 2000. DOI: [10.1016/s0045-7825\(99\)00309-6](https://doi.org/10.1016/s0045-7825(99)00309-6).
- [99] D. Roca, D. Yago, J. Cante, O. Lloberas-Valls, and J. Oliver, “Computational design of locally resonant acoustic metamaterials,” *Computer Methods in Applied Mechanics and Engineering*, vol. 345, pp. 161–182, Mar. 2019. DOI: [10.1016/j.cma.2018.10.037](https://doi.org/10.1016/j.cma.2018.10.037).
- [100] D. Roca, D. Yago, J. Cante, O. Lloberas-Valls, and J. Oliver, “Computational procedure for optimal design of acoustic metamaterials,” in *COMPLAS 2019 - XV International Conference on Computational Plasticity: Fundamentals and Applications*, Barcelona, Spain, Sep. 2019.
- [101] D. Roca, D. Yago, J. C. Cante, O. Lloberas-Valls, and J. Oliver, “Computational multi-scale design of engineering metamaterials: Application to acoustic insulation panels,” in *6th European Conference on Computational Mechanics (Solids, Structures and Coupled Problems) / 7th European Computational Fluid Dynamics Conference*, Glasgow, Scotland, UK, Jun. 2018.
- [102] G. I. N. Rozvany, “A critical review of established methods of structural topology optimization,” *Structural and Multidisciplinary Optimization*, vol. 37, no. 3, pp. 217–237, 2008. DOI: [10.1007/s00158-007-0217-0](https://doi.org/10.1007/s00158-007-0217-0).
- [103] A. Schumacher, “Topologieoptimierung von bauteilstrukturen unter verwendung von lochpositionierungskriterien,” Ph.D. dissertation, Forschungszentrum für Multidisziplinäre Analysen und Angewandte Strukturoptimierung, Institut für Mechanik und Regelungstechnik, Siegen, Germany, 1996.

- [104] J. A. Sethian, *Level Set Methods and Fast Marching Methods*. Cambridge University Press, 1999, 404 pp., ISBN: 0521645573.
- [105] J. A. Sethian and A. Wiegmann, “Structural boundary design via level set and immersed interface methods,” *Journal of Computational Physics*, vol. 163, no. 2, pp. 489–528, 2000. DOI: [10.1006/jcph.2000.6581](https://doi.org/10.1006/jcph.2000.6581).
- [106] O. Sigmund, “A 99 line topology optimization code written in matlab,” *Structural and Multidisciplinary Optimization*, vol. 21, no. 2, pp. 120–127, Apr. 2001. DOI: [10.1007/s001580050176](https://doi.org/10.1007/s001580050176).
- [107] O. Sigmund, “Design of multiphysics actuators using topology optimization – part i: One-material structures,” *Computer Methods in Applied Mechanics and Engineering*, vol. 190, no. 49–50, pp. 6577–6604, Oct. 2001. DOI: [10.1016/s0045-7825\(01\)00251-1](https://doi.org/10.1016/s0045-7825(01)00251-1).
- [108] O. Sigmund and J. Petersson, “Numerical instabilities in topology optimization: A survey on procedures dealing with checkerboards, mesh-dependencies and local minima,” *Structural Optimization*, vol. 16, no. 1, pp. 68–75, 1998. DOI: [10.1007/bf01214002](https://doi.org/10.1007/bf01214002).
- [109] O. Sigmund and S. Torquato, “Design of materials with extreme thermal expansion using a three-phase topology optimization method,” *Journal of the Mechanics and Physics of Solids*, vol. 45, no. 6, pp. 1037–1067, Jun. 1997. DOI: [10.1016/s0022-5096\(96\)00114-7](https://doi.org/10.1016/s0022-5096(96)00114-7).
- [110] O. Sigmund, “Design of material structures using topology optimization,” Ph.D. dissertation, Technical University of Denmark, 1994.
- [111] O. Sigmund, “On the design of compliant mechanisms using topology optimization,” *Mechanics of Structures and Machines*, vol. 25, no. 4, pp. 493–524, 1997. DOI: [10.1080/08905459708945415](https://doi.org/10.1080/08905459708945415).
- [112] O. Sigmund, “Morphology-based black and white filters for topology optimization,” *Structural and Multidisciplinary Optimization*, vol. 33, no. 4–5, pp. 401–424, Jan. 2007. DOI: [10.1007/s00158-006-0087-x](https://doi.org/10.1007/s00158-006-0087-x).
- [113] O. Sigmund, “On the usefulness of non-gradient approaches in topology optimization,” vol. 43, no. 5, pp. 589–596, Mar. 2011. DOI: [10.1007/s00158-011-0638-7](https://doi.org/10.1007/s00158-011-0638-7).
- [114] O. Sigmund and J. S. Jensen, “Systematic design of phononic band-gap materials and structures by topology optimization,” *Philosophical Transactions of the Royal Society of London. Series A: Mathematical, Physical and Engineering Sciences*, vol. 361, no. 1806, R. T. Bonnecaze and G. J. Rodin, Eds., pp. 1001–1019, Mar. 2003. DOI: [10.1098/rsta.2003.1177](https://doi.org/10.1098/rsta.2003.1177).
- [115] O. Sigmund and K. Maute, “Topology optimization approaches,” *Structural and Multidisciplinary Optimization*, vol. 48, no. 6, pp. 1031–1055, 2013. DOI: [10.1007/s00158-013-0978-6](https://doi.org/10.1007/s00158-013-0978-6).
- [116] J. Sokolowski and A. Zochowski, “On the topological derivative in shape optimization,” *SIAM Journal on Control and Optimization*, vol. 37, no. 4, pp. 1251–1272, Jan. 1999. DOI: [10.1137/s0363012997323230](https://doi.org/10.1137/s0363012997323230).
- [117] J. Sokolowski and A. Żochowski, “Topological derivative in shape optimization,” in *Encyclopedia of Optimization*, Springer US, 2001, pp. 2625–2626. DOI: [10.1007/0-306-48332-7_524](https://doi.org/10.1007/0-306-48332-7_524).
- [118] K. Suzuki and N. Kikuchi, “A homogenization method for shape and topology optimization,” *Computer Methods in Applied Mechanics and Engineering*, vol. 93, no. 3, pp. 291–318, Dec. 1991. DOI: [10.1016/0045-7825\(91\)90245-2](https://doi.org/10.1016/0045-7825(91)90245-2).
- [119] K. Svanberg, “The method of moving asymptotes—a new method for structural optimization,” *International Journal for Numerical Methods in Engineering*, vol. 24, no. 2, pp. 359–373, Feb. 1987. DOI: [10.1002/nme.1620240207](https://doi.org/10.1002/nme.1620240207).

- [120] A. Takezawa, S. Nishiwaki, and M. Kitamura, “Shape and topology optimization based on the phase field method and sensitivity analysis,” *Journal of Computational Physics*, vol. 229, no. 7, pp. 2697–2718, Apr. 2010. DOI: [10.1016/j.jcp.2009.12.017](https://doi.org/10.1016/j.jcp.2009.12.017).
- [121] F. Wang, B. S. Lazarov, and O. Sigmund, “On projection methods, convergence and robust formulations in topology optimization,” *Structural and Multidisciplinary Optimization*, vol. 43, no. 6, pp. 767–784, Dec. 2010. DOI: [10.1007/s00158-010-0602-y](https://doi.org/10.1007/s00158-010-0602-y).
- [122] M. Y. Wang, S. Zhou, and H. Ding, “Nonlinear diffusions in topology optimization,” *Structural and Multidisciplinary Optimization*, vol. 28, no. 4, pp. 262–276, 2004. DOI: [10.1007/s00158-004-0436-6](https://doi.org/10.1007/s00158-004-0436-6).
- [123] M. Y. Wang and X. Wang, ““Color” level sets: A multi-phase method for structural topology optimization with multiple materials,” *Computer Methods in Applied Mechanics and Engineering*, vol. 193, no. 6-8, pp. 469–496, Feb. 2004. DOI: [10.1016/j.cma.2003.10.008](https://doi.org/10.1016/j.cma.2003.10.008).
- [124] M. Y. Wang, X. Wang, and D. Guo, “A level set method for structural topology optimization,” *Computer Methods in Applied Mechanics and Engineering*, vol. 192, no. 1-2, pp. 227–246, 2003. DOI: [10.1016/s0045-7825\(02\)00559-5](https://doi.org/10.1016/s0045-7825(02)00559-5).
- [125] M. Y. Wang and S. Zhou, “Phase field: A variational method for structural topology optimization,” *Computer Modeling in Engineering and Sciences*, vol. 6, no. 6, pp. 547–566, 2004.
- [126] S. Y. Wang, K. Tai, and M. Y. Wang, “An enhanced genetic algorithm for structural topology optimization,” vol. 65, no. 1, pp. 18–44, 2005. DOI: [10.1002/nme.1435](https://doi.org/10.1002/nme.1435).
- [127] C.-Y. Wu and K.-Y. Tseng, “Topology optimization of structures using modified binary differential evolution,” vol. 42, no. 6, pp. 939–953, Jul. 2010. DOI: [10.1007/s00158-010-0523-9](https://doi.org/10.1007/s00158-010-0523-9).
- [128] S. Wu, Y. Zhang, and S. Liu, “Topology optimization for minimizing the maximum temperature of transient heat conduction structure,” *Structural and Multidisciplinary Optimization*, Jan. 2019. DOI: [10.1007/s00158-019-02196-9](https://doi.org/10.1007/s00158-019-02196-9).
- [129] Y. Wu, Q. Li, Q. Hu, and A. Borgart, “Size and topology optimization for trusses with discrete design variables by improved firefly algorithm,” vol. 2017, pp. 1–12, 2017. DOI: [10.1155/2017/1457297](https://doi.org/10.1155/2017/1457297).
- [130] Y. M. Xie and G. P. Steven, “A simple evolutionary procedure for structural optimization,” *Computers & Structures*, vol. 49, no. 5, pp. 885–896, Dec. 1993. DOI: [10.1016/0045-7949\(93\)90035-c](https://doi.org/10.1016/0045-7949(93)90035-c).
- [131] Y. M. Xie and G. P. Steven, “A simple approach to structural frequency optimization,” *Computers & Structures*, vol. 53, no. 6, pp. 1487–1491, Dec. 1994. DOI: [10.1016/0045-7949\(94\)90414-6](https://doi.org/10.1016/0045-7949(94)90414-6).
- [132] Y. M. Xie and G. P. Steven, *Evolutionary Structural Optimization*. Springer London, 1997. DOI: [10.1007/978-1-4471-0985-3](https://doi.org/10.1007/978-1-4471-0985-3).
- [133] Y. Xie and G. Steven, “Optimal design of multiple load case structures using an evolutionary procedure,” *Engineering Computations*, vol. 11, no. 4, pp. 295–302, Apr. 1994. DOI: [10.1108/02644409410799290](https://doi.org/10.1108/02644409410799290).
- [134] P. Y. Shim and S. Manoochehri, “Generating optimal configurations in structural design using simulated annealing,” vol. 40, no. 6, pp. 1053–1069, Mar. 1997. DOI: [10.1002/\(sici\)1097-0207\(19970330\)40:6<1053::aid-nme97>3.0.co;2-i](https://doi.org/10.1002/(sici)1097-0207(19970330)40:6<1053::aid-nme97>3.0.co;2-i).
- [135] D. Yago, J. Cante, O. Lloberas-Valls, and J. Oliver, “Topology optimization of thermal problems: The closed-form solution method,” in *COMPLAS 2019 - XV International Conference on Computational Plasticity: Fundamentals and Applications*, Barcelona, Spain, Sep. 2019.

- [136] D. Yago, J. Cante, O. Lloberas-Valls, and J. Oliver, “Topology optimization using the unsmooth variational topology optimization (UNVARTOP) method: An educational implementation in MATLAB,” *Structural and Multidisciplinary Optimization*, vol. 63, pp. 955–981, Nov. 2020. DOI: [10.1007/s00158-020-02722-0](https://doi.org/10.1007/s00158-020-02722-0).
- [137] D. Yago, J. Cante, O. Lloberas-Valls, and J. Oliver, “Nonsmooth variational approach to topology optimization (vartop),” in *14th World Congress on Computational Mechanics (WCCM XIV), 8th European Congress on Computational Methods in Applied Sciences and Engineering (ECCOMAS 2020)*, Paris, France, Jan. 2021.
- [138] D. Yago, J. Cante, O. Lloberas-Valls, and J. Oliver, “Topology optimization methods for 3D structural problems: A comparative study,” *Archives of Computational Methods in Engineering*, Aug. 2021. DOI: [10.1007/s11831-021-09626-2](https://doi.org/10.1007/s11831-021-09626-2).
- [139] D. Yago, J. Cante, O. Lloberas-Valls, and J. Oliver, “Topology optimization of thermal problems in a nonsmooth variational setting: Closed-form optimality criteria,” *Computational Mechanics*, vol. 66, no. 2, pp. 259–286, Jun. 2020. DOI: [10.1007/s00466-020-01850-0](https://doi.org/10.1007/s00466-020-01850-0).
- [140] K. Yaji, T. Yamada, S. Kubo, K. Izui, and S. Nishiwaki, “A topology optimization method for a coupled thermal–fluid problem using level set boundary expressions,” *International Journal of Heat and Mass Transfer*, vol. 81, pp. 878–888, Feb. 2015. DOI: [10.1016/j.ijheatmasstransfer.2014.11.005](https://doi.org/10.1016/j.ijheatmasstransfer.2014.11.005).
- [141] T. Yamada, K. Izui, and S. Nishiwaki, “A level set-based topology optimization method for maximizing thermal diffusivity in problems including design-dependent effects,” *Journal of Mechanical Design*, vol. 133, no. 3, p. 031011, 2011. DOI: [10.1115/1.4003684](https://doi.org/10.1115/1.4003684).
- [142] T. Yamada, K. Izui, S. Nishiwaki, and A. Takezawa, “A topology optimization method based on the level set method incorporating a fictitious interface energy,” *Computer Methods in Applied Mechanics and Engineering*, vol. 199, no. 45-48, pp. 2876–2891, 2010. DOI: [10.1016/j.cma.2010.05.013](https://doi.org/10.1016/j.cma.2010.05.013).
- [143] X. Y. Yang, Y. M. Xie, G. P. Steven, and O. M. Querin, “Bidirectional evolutionary method for stiffness optimization,” *AIAA Journal*, vol. 37, pp. 1483–1488, Jan. 1999. DOI: [10.2514/3.14346](https://doi.org/10.2514/3.14346).
- [144] X. Yang, Y. Xie, J. Liu, G. Parks, and P. Clarkson, “Perimeter control in the bidirectional evolutionary optimization method,” *Structural and Multidisciplinary Optimization*, vol. 24, no. 6, pp. 430–440, Dec. 2002. DOI: [10.1007/s00158-002-0256-5](https://doi.org/10.1007/s00158-002-0256-5).
- [145] X. S. Yang and X. He, “Bat algorithm: Literature review and applications,” vol. 5, no. 3, p. 141, 2013. DOI: [10.1504/ijbic.2013.055093](https://doi.org/10.1504/ijbic.2013.055093).
- [146] X.-S. Yang, *Nature-inspired optimization algorithms*. London England Waltham Massachusetts: Elsevier, 2014, ISBN: 9780124167438.
- [147] X.-S. Yang, M. Karamanoglu, and S. Fong, “Bat algorithm for topology optimization in microelectronic applications,” *IEEE*, Dec. 2012. DOI: [10.1109/fgct.2012.6476566](https://doi.org/10.1109/fgct.2012.6476566).
- [148] G. H. Yoon, J. S. Jensen, and O. Sigmund, “Topology optimization of acoustic–structure interaction problems using a mixed finite element formulation,” vol. 70, no. 9, pp. 1049–1075, 2007. DOI: [10.1002/nme.1900](https://doi.org/10.1002/nme.1900).
- [149] M. Yulin and W. Xiaoming, “A level set method for structural topology optimization and its applications,” *Advances in Engineering Software*, vol. 35, no. 7, pp. 415–441, 2004. DOI: [10.1016/j.advengsoft.2004.06.004](https://doi.org/10.1016/j.advengsoft.2004.06.004).
- [150] C. Zhao, G. Steven, and Y. Xie, “Evolutionary natural frequency optimization of two-dimensional structures with additional non-structural lumped masses,” *Engineering Computations*, vol. 14, no. 2, pp. 233–251, Mar. 1997. DOI: [10.1108/02644409710166208](https://doi.org/10.1108/02644409710166208).

- [151] M. Zhou and G. Rozvany, “On the validity of ESO type methods in topology optimization,” *Structural and Multidisciplinary Optimization*, vol. 21, no. 1, pp. 80–83, Mar. 2001. DOI: [10.1007/s001580050170](https://doi.org/10.1007/s001580050170).
- [152] S. Zhou, W. Li, Y. Chen, G. Sun, and Q. Li, “Topology optimization for negative permeability metamaterials using level-set algorithm,” *Acta Materialia*, vol. 59, no. 7, pp. 2624–2636, Apr. 2011. DOI: [10.1016/j.actamat.2010.12.049](https://doi.org/10.1016/j.actamat.2010.12.049).
- [153] S. Zhou, W. Li, G. Sun, and Q. Li, “A level-set procedure for the design of electromagnetic metamaterials,” *Optics Express*, vol. 18, no. 7, p. 6693, Mar. 2010. DOI: [10.1364/oe.18.006693](https://doi.org/10.1364/oe.18.006693).
- [154] J. H. Zhu, W. H. Zhang, and K. P. Qiu, “Bi-directional evolutionary topology optimization using element replaceable method,” *Computational Mechanics*, vol. 40, no. 1, pp. 97–109, Jun. 2006. DOI: [10.1007/s00466-006-0087-0](https://doi.org/10.1007/s00466-006-0087-0).
- [155] W. Zuo and K. Saitou, “Multi-material topology optimization using ordered SIMP interpolation,” vol. 55, no. 2, pp. 477–491, Jun. 2016. DOI: [10.1007/s00158-016-1513-3](https://doi.org/10.1007/s00158-016-1513-3).

Appendices: Articles included in the doctoral thesis

Article A

Variational approach to relaxed topological optimization: closed form solutions for structural problems in a sequential pseudo-time framework



Computer Methods in Applied Mechanics and
Engineering

Volume 355, 1 October 2019, Pages 779-819



Variational approach to relaxed topological optimization: Closed form solutions for structural problems in a sequential pseudo-time framework

J. Oliver^{a, c}, D. Yago^{a, b}, J. Cante^{a, b}, O. Lloberas-Valls^{a, c}

^a Centre Internacional de Mètodes Numèrics en Enginyeria (CIMNE), Campus Nord UPC, Mòdul C-1 101, c/ Jordi Girona 1-3, 08034 Barcelona, Spain

^b Escola Superior d'Enginyeries Industrial, Aeroespacial i Audiovisual de Terrassa (ESEIAAT), Technical University of Catalonia (UPC/Barcelona Tech), Campus Terrassa UPC, c/ Colom 11, 08222 Terrassa, Spain

^c E.T.S d'Enginyers de Camins, Canals i Ports de Barcelona (ETSECCPB), Technical University of Catalonia (UPC/Barcelona Tech), Campus Nord UPC, Mòdul C-1, c/ Jordi Girona 1-3, 08034 Barcelona, Spain

Received 18 February 2019, Revised 29 May 2019, Accepted 25 June 2019, Available online 11 July 2019.



Show less ^

+ Add to Mendeley Share Cite

<https://doi.org/10.1016/j.cma.2019.06.038>

[Get rights and content](#)

Variational approach to relaxed topological optimization: closed form solutions for structural problems in a sequential pseudo-time framework

J. Oliver^{b,c}, D. Yago^{a,b}, J. Cante^{a,b}, O. Lloberas-Valls^{b,c}

^a Escola Superior d'Enginyeries Industrial, Aeroespacial i Audiovisual de Terrassa (ES-EIAAT), Universitat Politècnica de Catalunya · BarcelonaTech (UPC), Campus Terrassa UPC, c/ Colom 11, 08222 Terrassa, Spain

^b Centre Internacional de Mètodes Numèrics en Enginyeria (CIMNE), Campus Nord UPC, Mòdul C-1 101, c/ Jordi Girona 1-3, 08034 Barcelona, Spain

^c Escola Tècnica Superior d'Enginyeria de Camins, Canals i Ports de Barcelona (ETSEC-CPB), Universitat Politècnica de Catalunya · BarcelonaTech (UPC), Campus Nord UPC, Mòdul C-1, c/ Jordi Girona 1-3, 08034 Barcelona, Spain

A.1 Abstract

The work explores a specific scenario for structural computational optimization based on the following elements: (a) a *relaxed optimization setting* considering the ersatz (bi-material) approximation, (b) a treatment based on a *non-smoothed characteristic function field* as a topological design variable, (c) the consistent derivation of a *relaxed topological derivative* whose determination is simple, general and efficient, (d) formulation of the *overall increasing cost function topological sensitivity* as a suitable optimality criterion, and (e) consideration of a pseudo-time framework for the problem solution, ruled by the problem constraint evolution.

In this setting, it is shown that the optimization problem can be analytically solved in a variational framework, leading to, nonlinear, *closed-form algebraic solutions for the characteristic function*, which are then solved, in every time-step, via fixed point methods based on a *pseudo-energy cutting algorithm* combined with the *exact fulfillment of the constraint*, at every iteration of the non-linear algorithm, via a bisection method. The issue of the ill-posedness (mesh dependency) of the topological solution, is then easily solved via a Laplacian smoothing of that pseudo-energy.

In the aforementioned context, a number of (3D) topological structural optimization benchmarks are solved, and the solutions obtained with the explored *closed-form solution method*, are analyzed, and compared, with their solution through an alternative level set method. Although the obtained results, in terms of the cost function and topology designs, are very similar in both methods, the associated computational cost is about five times smaller in the closed-form solution method this possibly being one of its advantages. Some comments, about the possible application of the method to other topological optimization problems, as well as envisaged modifications of the explored method to improve its performance close the work.

Keywords: Topological optimization, Variational approach, Closed-form solutions, Pseudo-time sequential analysis, Structural topological optimization

A.2 Motivation

Computational mechanics tools for solving topological optimization problems raise a large number of challenges, both from the mathematical and computational points of view. The problem is originally formulated in the context of a design domain, $\Omega \subset \mathbb{R}^3$, in which a *solid* domain, $\Omega^+ \subset \Omega$, whose topology is going to be designed, is embedded. Then, the *voids domain* is defined as $\Omega^- = \Omega \setminus \Omega^+$, and a cost function (typically the structural compliance or a related structural measure) is aimed at being optimized (minimized) in terms of some *design variables*, defining the material distribution (topology) in Ω , and subject to some constraints¹. This setting poses

¹Typically, but not necessarily, the volume occupied by the solid.

a number of difficulties, among which we will mention the following:

- (a) *Discrete character of the design variables.* The distribution of the material at every point, $\mathbf{x} \in \Omega$, is defined in terms of the characteristic function, $\chi : \Omega \rightarrow \{0, 1\}$; $\chi(\mathbf{x}) = 1 \forall \mathbf{x} \in \Omega^+$ (material) and $\chi(\mathbf{x}) = 0 \forall \mathbf{x} \in \Omega^-$ (voids). Therefore, the design variables $\chi(\mathbf{x})$ map into the *discrete image set* $\{0, 1\}$ and the optimization problem is highly non smooth.
- (b) *Number of design variables.* The design variable $\chi(\mathbf{x})$ is valued at all points $\mathbf{x} \in \Omega$. Therefore, unlike in standard discrete optimization problems [9], there are, in principle, an *infinite number* of design variables, $\chi(\mathbf{x}) \forall \mathbf{x} \in \Omega$, to be determined.
- (c) *The unknown characteristic function, $\chi(\mathbf{x})$, is non-Lipschitz and non-differentiable.* This translates into the fact that optimality conditions, based on standard differentiation of the cost functional, are not, in principle, applicable.

Along the last decades, a large number of approaches to computational topological optimization have been proposed. With no aim of exhaustiveness, two large *families* of methods to overcome those challenges have been proposed (see, for instance, [18, 40, 45] for exhaustive reviews on topological optimization methods):

- (I) *Regularize the characteristic function.* This is the choice of the most popular, and successful, of the current approaches: the *Solid Isotropic Material with Penalization* (SIMP) [8], in which the discrete characteristic function, χ , is replaced by a regularized (continuous) function, (*density-like function*), $\rho : \Omega \rightarrow [0, 1]$. The regularization domain, $\Omega^{reg} \subset \Omega$, (the set of points of Ω where $\rho(\mathbf{x}) \in (0, 1)$) is not necessarily small, and it requires to be covered by a, relatively large, number of *discretization domains* (finite elements or Voxels). The approach succeeds in breaking the challenge of continuity, and standard finite-dimensional optimization procedures² can be applied to the resulting optimization problem, now formulated in terms of a finite (but large) number of design variables³, which are, then, supplemented by additional constraints imposing $0 \leq \rho(\mathbf{x}_i) \leq 1$. The success of the method brings also some drawbacks, typically:
 - Intrinsic to the existence of the regularization domain, $\Omega^{reg} \subset \Omega$, is the appearance of *gray zones* (zones with *diffuse* material/voids coexistence, $0 < \rho < 1$) [10, 8], where the kind of material provided by the optimization is unclear. This requires to, subsequently, resort to *filtering* techniques to eliminate them.
 - The *mesh-dependence* [43] or *lack of mesh-size objectivity* of the results. Again these requires resorting to filtering techniques [54].
 - The appearance of *checkerboards* when using finite element discretizations. This type of problems is identified as a numerical instability (not fulfillment of the Ladyzhenskaya–Babuska–Brezzi stability conditions) and it should be solved by resorting to specific finite elements in modeling the problem [26].
- (II) *Change the design variable.* The so called *level-set methods* for topological optimization [17], overcome the difficulties inherent to the discrete character of the characteristic function, $\chi(\mathbf{x})$, by replacing it by a different, smoother, function (the level-set function $\phi \in H^1(\Omega) : \Omega \rightarrow \mathbb{R}$) related to each other through $\chi(\mathbf{x}) = \mathcal{H}(\phi(\mathbf{x}))$, where $\mathcal{H} : \mathbb{R} \rightarrow \{0, 1\}$ stands for the Heaviside function. The values of $\phi(\mathbf{x}_i)$ at the sampling points are the new design variables. The optimization problem is no longer solved through standard optimization methods, but by means of the solution of a Hamilton-Jacobi (pseudo-time evolutionary) equation [36, 50]. This family of methods have proven to be very robust in solving different types of topological optimization methods, albeit they suffer, also, from some drawbacks, e.g.:

²Typically based on efficient optimization techniques, like the Method for Moving Asymptotes (MMA).

³The value of $\rho(\mathbf{x}_i)$ at the sampling points $\mathbf{x}_i \in \Omega$.

- They also require regularization techniques, for instance Tikhonov-regularization based methods [53], to obtain a well posed (mesh-size objective) optimization problem.
- Their robustness, and rate of convergence, relies on the size of the pseudo time increment adopted, in turn depending on heuristic considerations. In general this translates into a high number of iterations and, thus, into a high computational cost. In some cases, these methods use initially the signed distance to the solid boundaries as level set function, and they may require re-initialization techniques during the analysis [54].
- A fundamental issue in this method is the selection of an appropriated *sensitivity* of the cost function to changes on the design variable (the level-set function) which was initially related to the *shape derivative concept* [3]. More recently, connections with the *topological derivative concept* were introduced (see for instance [3, 11, 53]).

The use of an appropriate sensitivity of the cost function to topological changes in the design domain, in front of the introduction of holes in the solid material, plays a fundamental role in the performance of this family of methods [30]. Indeed, derivation of analytical expressions for the topological derivative, in linear elastic problems, becomes crucial, and much work has been done in this sense ([33, 34, 23, 22, 5]). In these cases, the topological sensitivity is mathematically derived in terms of the perturbation of the cost function, after material removal (introduction of a hole) in a certain point of Ω , ruled by the elastic state problem in the perturbed solid. This analytical derivation, which specifically depends on the *type of optimization problem* and the *considered elastic material* (isotropic, orthotropic, anisotropic etc.), has to be previously derived via specific, and sometimes heavy, analytical methods, i.e. limit and asymptotic analysis to a null size of the hole. This could be also understood as a specific burden of the method.

On the light of the, so far, depicted situation, this work aims at exploring the impact and consequences of an alternative option for computational topological optimization: facing, as much as possible, the topological optimization problem in its original setting, i.e. considering the following scenario:

- A *non-smoothed characteristic function*, $\chi : \Omega \rightarrow \{\beta, 1\}$; $\beta \in (0, 1)$, as design variable.
- An *infinite-dimensional design space*, considering the values of the characteristic function $\chi(\mathbf{x})$ at all points of Ω , as design variables of the optimization problem.
- A *relaxed optimization setting*, which facilitates the obtainment of the topological derivative, not requiring a complex mathematical derivation.
- *Deriving* the corresponding *closed-form solutions*, for such a non-smooth optimization problem, *in a number of structural problems*⁴.

Then, an algorithmic setting for solving the obtained (highly non-linear) closed-form solutions is devised, consisting of:

- (1) A *relaxed, bi-material, topological optimization, setting*. The original *embedded-solid setting*, where a hard material (solid) domain Ω^+ is embedded into the design space, Ω , is relaxed to a *bi-material* (hard-phase + soft-phase, $\mathfrak{M}^+/\mathfrak{M}^-$) setting. This relaxed scenario is commonly found in current topological optimization approaches and it is, sometimes referenced as *ersatz material approximation* [2, 16]. Its main advantage is that it makes the optimization problem simpler than the alternatives, e.g. the *immersed boundary methods* [1, 41, 32]. In this way, *at all points of the design domain Ω , there exists (some type*

⁴As precursors of solutions, in the chosen context, for broader families of topological optimization problems.

of) *material*, and the classical concept of topological perturbation, initially understood as *solid material removal or addition*, is replaced by that of *material switching* or *material exchange* ($\mathfrak{M}^+(\mathbf{x}) \leftrightarrow \mathfrak{M}^-(\mathbf{x})$). A number of, non-trivial, consequences derive from this, apparently minor, modification: (a) the standard (solid + voids) setting is asymptotically approximated by assigning to the soft material, \mathfrak{M}^- , very weak elastic properties (characterized by the classical *contrast factor* $\alpha \rightarrow 0$), and (b) the sensitivity of the cost function to the topological perturbation at a given point $\mathbf{x} \in \Omega$, now understood as a *local material exchange* at the point.

- (2) *A consistent relaxed topological derivative (RTD)*. The aforementioned relaxed bi-material setting is used, not only for solving the *static elastic problem*, but also for the purposes of derivation of the topological sensitivity, this providing additional *consistence* to the approach. Derivation of this *consistent* topological sensitivity can be done, in a non-smooth variational setting, and computed, independently of the considered elastic material family, as a directional derivative of the cost functional. This derivation of RTD is extremely simple in comparison with the *exact topological derivative* classically used in the literature.
- (3) *Sequential pseudo-time framework*. In this framework, a pseudo-time parametrization is introduced. Solutions of the topological optimization problem are obtained for increasing values of the restriction (i.e. the soft-phase volume $|\Omega^-|$), that plays the role of a *pseudo-time*. In this context, *the time evolution* of the topology of the optimal solution (and the associate cost function values) is obtained at no additional computational cost. In this way the optimization process provides information, not only on the optimal topology at every pseudo-time-step and, thus, at the corresponding soft-phase volume level, but also on the *evolution of the minima* for a chosen set of times (volumes). In some cases this is a very useful information for the designer, who obtains, in a single run, additional information about, for instance, *the minimum of the minima* in the computed designs.
- (4) *Exact fulfillment of the restriction at every iteration of the algorithm*. This concept is borrowed from numerical techniques frequently used in non-linear analysis of structures: the so-called *load control, or arc-length* methods [15]. This substantially contributes to the robustness, and to the computational cost diminution, in the resolution of the resulting non-linear problem.
- (5) *Regularization of the obtained closed-form topological solutions* via Laplacian smoothing techniques. In order to prevent the aforementioned *ill-posedness of the problem*, leading to the mesh-size dependence, a Laplace-type smoothing is done, which removes from the solution the small (noisy) wavelengths below a predefined threshold. Distinctly from other approaches, this regularization is not done by introducing an additional contribution to the cost function [53], but by *smoothing the closed-form solution obtained from the original optimization problem*. Additionally, this allows: a) controlling the minimum attainable width/section of the *filaments of the solid material* in the obtained solutions topology and, b) obtaining $2\frac{1}{2}D$ (*extruded to the third dimension*) topological designs.

In next sections the theoretical and algorithmic aspects of the considered formulation are, first, presented in detail and, then, assessed by application to a set of representative examples. Comparisons of the obtained results, with those obtained with level-set (*Hamilton-Jacobi type*) techniques using the derived *relaxed topological derivative*, are done in order to check the performance of the analyzed approach, both in terms of the cost function values, and also in terms of the required computational cost.

A.3 Problem set up

A.3.1 Relaxed characteristic function

Let us consider the *design domain*, $\Omega \subset \mathbb{R}^n$; $n \in \{2, 3\}$, and the distribution over this domain of two different material phases: a) *hard-phase* (\mathfrak{M}^+) and b) *soft-phase* (\mathfrak{M}^-), the type of phase at every point, $\mathbf{x} \in \Omega$, being defined by the *characteristic function* χ as:

$$\chi : \Omega \rightarrow \{\beta, 1\} := \begin{cases} \chi(\mathbf{x}) = 1 & \text{if material phase at } \mathbf{x} \text{ is } \mathfrak{M}^+ \\ \chi(\mathbf{x}) = \beta & \text{if material phase at } \mathbf{x} \text{ is } \mathfrak{M}^- \end{cases} \quad (a) \quad (1)$$

$$0 < \beta < 1 \Rightarrow (1 - \beta) > 0 \quad (b)$$

In a second step we shall consider a *relaxed* version of the characteristic function, denoted as χ_ψ , in terms of the, here termed, *discrimination function* $\psi \in H^1(\Omega)$ which is assumed single-valued and defined as (see figure A.2)

$$\chi_\psi(\mathbf{x}) = \mathcal{H}_\beta(\psi(\mathbf{x})) \quad (2)$$

where $\mathcal{H}_\beta(\cdot)$ stands for a *relaxed* Heaviside function⁵, defined as

$$\begin{cases} \mathcal{H}_\beta(\psi) = 1 & \text{for } \psi > 0 \\ \mathcal{H}_\beta(\psi) = \beta & \text{for } \psi < 0 \end{cases} \quad (3)$$

Therefore, function $\psi(\mathbf{x})$ defines, through its value, two possible values of χ_ψ , i.e.

$$\begin{cases} \chi_\psi(\mathbf{x}) = \mathcal{H}_\beta(\psi(\mathbf{x})) = 1 & \text{for } \psi(\mathbf{x}) > 0 \\ \chi_\psi(\mathbf{x}) = \mathcal{H}_\beta(\psi(\mathbf{x})) = \beta & \text{for } \psi(\mathbf{x}) < 0 \end{cases} \quad (4)$$

and discriminates points $\mathbf{x} \in \Omega$ belonging either to the *hard-phase domain*, Ω^+ , or to the *soft-phase domain* Ω^- :

$$\begin{cases} \Omega^+(\chi_\psi) := \{\mathbf{x} \in \Omega ; \psi(\mathbf{x}) > 0\} \Rightarrow \chi_\psi(\mathbf{x}) = 1 & (a) \\ \Omega^-(\chi_\psi) := \{\mathbf{x} \in \Omega ; \psi(\mathbf{x}) < 0\} \Rightarrow \chi_\psi(\mathbf{x}) = \beta & (b) \end{cases} \quad (5)$$

Equations (5) define the *topology* of Ω .

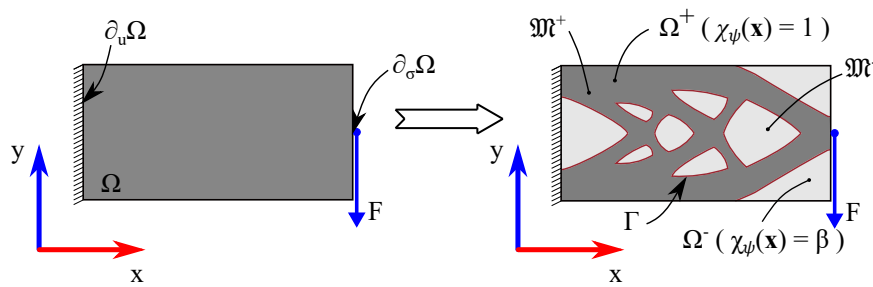


Figure A.1: β -relaxed setting: bi-material design domain.

Remark 1 Notice that, since only two different phases are considered, $\Omega^+ \cup \Omega^- = \Omega$, the description of the topology in equation (5) can be rephrased only in terms of the positive counterpart of the discrimination function, $\psi(\mathbf{x})$, i.e.

$$\begin{cases} \Omega^+(\chi_\psi) := \{\mathbf{x} \in \Omega ; \psi(\mathbf{x}) > 0\} & \Leftrightarrow \chi_\psi(\mathbf{x}) = 1 & (a) \\ \Omega^-(\chi_\psi) := \{\mathbf{x} \in \Omega ; \mathbf{x} \notin \Omega^+\} & \Leftrightarrow \chi_\psi(\mathbf{x}) = \beta & (b) \end{cases} \quad (6)$$

⁵Which recovers to the classical Heaviside function as $\beta \rightarrow 0$.

or, alternatively, in terms of the negative counterpart of $\psi(\mathbf{x})$ i.e.

$$\begin{cases} \Omega^-(\chi_\psi) := \{\mathbf{x} \in \Omega ; \psi(\mathbf{x}) < 0\} & \Rightarrow \chi_\psi(\mathbf{x}) = \beta & (a) \\ \Omega^+(\chi_\psi) := \{\mathbf{x} \in \Omega ; \mathbf{x} \notin \Omega^-\} & \Rightarrow \chi_\psi(\mathbf{x}) = 1 & (b) \end{cases} \quad (7)$$

From equations (6) or (7) the following equalities can be stated:

$$\begin{cases} |\Omega| = |\Omega^+(\chi_\psi)| + |\Omega^-(\chi_\psi)| & (a) \\ |\Omega^+(\chi_\psi)| = \int_{\Omega} \frac{\chi_\psi(\mathbf{x}) - \beta}{1 - \beta} d\Omega & (b) \\ |\Omega^-(\chi_\psi)| = \int_{\Omega} \frac{1 - \chi_\psi(\mathbf{x})}{1 - \beta} d\Omega & (c) \end{cases} \quad (8)$$

where $|\Omega|$, $|\Omega^+|$ and $|\Omega^-|$ stand, respectively, for the measure (surface/volume) of the design domain, Ω , the *hard-phase* domain, Ω^+ , and the *soft-phase* domain, Ω^- .

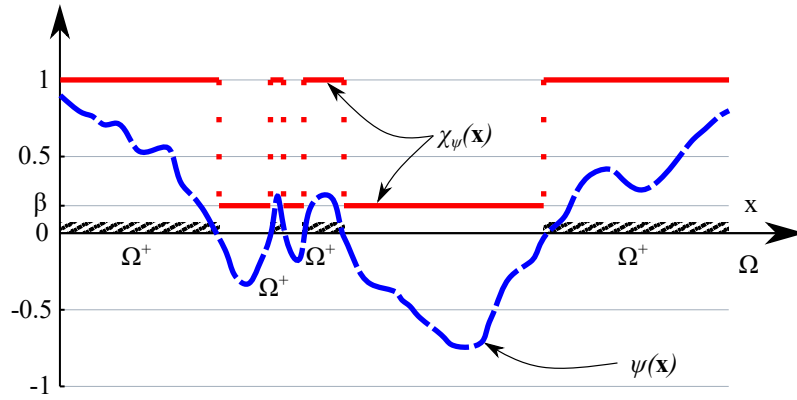


Figure A.2: Discrimination function, ψ and the corresponding relaxed characteristic function, χ_ψ .

A.3.2 Relaxed, bi-material, linear elastic problem

Let us now consider a *bi-material elastic solid* occupying the whole domain Ω . Then, the material distribution in Ω can be defined in terms of the relaxed characteristic function⁶, $\chi(\mathbf{x})$, in equations (1) to (5). The corresponding elastic problem reads

$$\begin{aligned} \nabla \cdot \boldsymbol{\sigma}_\chi(\mathbf{x}) + \mathbf{b}(\mathbf{x}) &= \mathbf{0}; & \begin{cases} \boldsymbol{\sigma}_\chi(\mathbf{x}) \equiv \boldsymbol{\sigma}(\mathbf{u}_\chi(\mathbf{x})) = \underbrace{\chi^m \mathbb{C}}_{\mathbb{C}_\chi(\mathbf{x})} : \boldsymbol{\varepsilon}(\mathbf{u}_\chi) & \forall \mathbf{x} \in \Omega & (a) \\ \boldsymbol{\varepsilon}(\mathbf{u}_\chi) \equiv (\nabla \otimes \mathbf{u}_\chi(\mathbf{x}))^{sym} & & (9) \end{cases} \\ \boldsymbol{\sigma}_\chi(\mathbf{x}) \cdot \mathbf{n} &= \mathbf{t}^*(\mathbf{x}) & \forall \mathbf{x} \in \partial_\sigma \Omega & (b) \\ \mathbf{u}_\chi(\mathbf{x}) &= \mathbf{0} & \forall \mathbf{x} \in \partial_u \Omega & (c) \end{aligned}$$

where $\mathbf{u}_\chi(\mathbf{x})$ is the displacement vector field, parametrized by the current topology, $\boldsymbol{\sigma}_\chi(\mathbf{x})$ stands for the second order stress tensor field, $\mathbf{b}(\mathbf{x})$, stands for the density of the body forces, $\mathbf{t}^*(\mathbf{x})$ stands for the boundary tractions and $\boldsymbol{\varepsilon}(\mathbf{u}_\chi)$ is the (infinitesimal) strain tensor. In equation (9)-(a), \mathbb{C} is the, fourth order, elastic constitutive tensor of the hard-phase (assumed constant), and the exponent m is typically taken $m > 1$. In addition, $\partial_u \Omega \subset \partial \Omega$ and $\partial_\sigma \Omega \subset \partial \Omega$, (where $\partial_u \Omega \cap \partial_\sigma \Omega = \emptyset$ and $\partial_u \Omega \cup \partial_\sigma \Omega = \partial \Omega$) are, respectively, those parts of the boundary, $\partial \Omega$, where

⁶From now on, subscript $(\cdot)_\psi$ will be omitted, unless it is strictly necessary.

displacements, \mathbf{u}_χ , and tractions, $\mathbf{t} = \boldsymbol{\sigma}_\chi \cdot \mathbf{n}$ or forces, are, prescribed (see figure A.1). In addition $\chi(\mathbf{x})$ is recalled, from equations (1) as:

$$\chi(\mathbf{x}) = \begin{cases} 1 & \forall \mathbf{x} \in \Omega^+ \\ \beta & \forall \mathbf{x} \in \Omega^- \end{cases} \quad (10)$$

where $0 < \beta < 1$ will be, from now on, termed *the relaxation factor*. Notice that, according to equations (9)-(a) and (10) the elastic constitutive tensor, $\mathbb{C}_\chi(\mathbf{x})$ can be specified for all the domain points as

$$\mathbb{C}_\chi(\mathbf{x}) \equiv \chi^m(\mathbf{x})\mathbb{C} = \begin{cases} \mathbb{C} & \forall \mathbf{x} \in \Omega^+(\chi) \\ \beta^m \mathbb{C} = \alpha \mathbb{C} \approx \mathbf{0} & \forall \mathbf{x} \in \Omega^-(\chi) \end{cases} \quad (a)$$

$$\alpha = \beta^m \in (0, 1); \quad \beta = \alpha^{\frac{1}{m}} \in (0, 1) \quad (b) \quad (11)$$

$$\frac{\partial \mathbb{C}_\chi}{\partial \chi} = m \chi^{m-1} \mathbb{C} = \begin{cases} m \mathbb{C} & \forall \mathbf{x} \in \Omega^+(\chi) \\ m \beta^{(m-1)} \mathbb{C} = m \alpha^{\frac{m-1}{m}} \mathbb{C} & \forall \mathbf{x} \in \Omega^-(\chi) \end{cases} \quad (c)$$

where the factor α and the exponent m will be, respectively, termed the *contrast stiffness factor* and the *contrast stiffness exponent*. For the standard isotropic case the elasticity tensor can be written [35]

$$\begin{cases} \mathbb{C} = \bar{\lambda} \mathbf{1} \otimes \mathbf{1} + 2\mu \mathbb{I} = \frac{\nu E}{(1+\nu)(1-2\nu)} \mathbf{1} + \frac{E}{(1+\nu)} \mathbb{I} \\ \mathbb{C}_{ijkl} = \bar{\lambda} \delta_{ij} \delta_{kl} + \mu [\delta_{ik} \delta_{jl} + \delta_{il} \delta_{jk}] ; \quad i, j, k, l \in \{1, 2, 3\} \end{cases} \quad (12)$$

where $\bar{\lambda}$ and μ are the Lamé coefficients and E and ν stand, respectively, for the Young modulus and the Poisson ratio. In addition, $\mathbf{1}$ and \mathbb{I} are, respectively, the second order unit tensor and the fourth order (symmetric) unit tensor. The problem in equations (9) can be alternatively written in a variational form as

$$\left[\begin{array}{l} \mathbf{Relaxed\ Bi-material\ Elastic\ Problem} \\ \text{Given: } \chi(\mathbf{x}), \mathbf{b}(\mathbf{x}), \mathbf{t}^*(\mathbf{x}), \quad (a) \\ \mathcal{V}_\eta := \left\{ \boldsymbol{\eta} \in \mathbf{H}^{(1)}(\Omega); \quad \boldsymbol{\eta} = \mathbf{0} \quad \text{on} \quad \partial_u \Omega \right\} \quad (b) \\ \text{Find: } \mathbf{u}(\chi, \mathbf{x}) \equiv \mathbf{u}_\chi(\mathbf{x}), \quad \mathbf{u}_\chi \in \mathcal{V}_\eta \quad (c) \\ \text{Fulfilling: } a_\chi(\mathbf{u}_\chi, \mathbf{w}) = l(\mathbf{w}) \quad \forall \mathbf{w} \in \mathcal{V}_\eta \quad (d) \\ \left\{ \begin{array}{l} a_\chi(\mathbf{u}_\chi, \mathbf{w}) \equiv \int_\Omega \boldsymbol{\varepsilon}(\mathbf{u}_\chi) : \mathbb{C}_\chi : \boldsymbol{\varepsilon}(\mathbf{w}) d\Omega ; \quad \boldsymbol{\varepsilon}(\boldsymbol{\eta}) = (\nabla \otimes \boldsymbol{\eta})^{sym} \\ l(\mathbf{w}) = \int_\Omega \mathbf{b} \cdot \mathbf{w} d\Omega + \int_{\partial_\sigma \Omega} \mathbf{t}^* \cdot \mathbf{w} d\Gamma \end{array} \right. \quad (e) \end{array} \right. \quad (13)$$

where, $a_\chi(\mathbf{u}_\chi, \mathbf{w})$ is a symmetric bilinear form ($a_\chi(\mathbf{u}_\chi, \mathbf{w}) = a_\chi(\mathbf{w}, \mathbf{u}_\chi)$).

Remark 2 Notice that, unlike in the strong form of the relaxed elastic problem, in equations (9), no derivative of the, spatially discontinuous, constitutive tensor \mathbb{C}_χ appears in the variational form of problem in equations (13). The problem description in these equations will be the one considered, from now on, and termed the (relaxed) state problem (or equation). With the boundary conditions appropriately precluding the rigid body motions, it has a unique solution.

Remark 3 Additionally, it is assumed that, as the relaxation factor $\beta \rightarrow 0$ (and, thus, $\alpha \rightarrow 0$), the relaxed elastic problem, in equations (9) to (13), asymptotically converges, to the solution of

the single material ($\mathfrak{M}^+ \equiv \text{solid}$ and $\mathfrak{M}^- \equiv \text{voids}$) elastic problem defined as:

$$\left[\begin{array}{l}
 \textbf{Single-material Elastic Problem} \\
 \text{Given: } \Omega, \Omega^+, \mathbf{b}(\mathbf{x}), \mathbf{t}^*(\mathbf{x}), \quad (a) \\
 \mathcal{V}_\eta := \left\{ \boldsymbol{\eta} \in \mathbf{H}^{(1)}(\Omega^+); \quad \boldsymbol{\eta} = \mathbf{0} \quad \text{on} \quad \partial_u \Omega \cap \partial \Omega^+ \right\} \quad (b) \\
 \text{Find: } \mathbf{u}(\mathbf{x}) \in \mathcal{V}_\eta \quad (c) \\
 \text{Fulfilling: } a(\mathbf{u}, \mathbf{w}) = l(\mathbf{w}) \quad \forall \mathbf{w} \in \mathcal{V}_\eta \quad (d) \\
 \left\{ \begin{array}{l}
 a(\mathbf{u}, \mathbf{w}) \equiv \int_{\Omega^+} \boldsymbol{\varepsilon}(\mathbf{u}) : \mathbb{C} : \boldsymbol{\varepsilon}(\mathbf{w}) d\Omega ; \quad \boldsymbol{\varepsilon}(\boldsymbol{\eta}) = (\nabla \otimes \boldsymbol{\eta}(\mathbf{x}))^{sym} \\
 l(\mathbf{w}) = \int_{\Omega^+} \mathbf{b} \cdot \mathbf{w} d\Omega + \int_{\partial_\sigma \Omega^+} \mathbf{t}^* \cdot \mathbf{w} d\Gamma
 \end{array} \right. \quad (e)
 \end{array} \right. \quad (14)$$

i.e. the linear elastic solution of the (non-relaxed or embedded) solid/voids problem.

The fact that the relaxed bi-material version (in equations (13)) is considered here as the target state problem for the subsequent developments, is emphasized.

A.3.3 Finite element discretization

So far, no mention has been made of the numerical method used to solve the elastic state problem in equation (13). If the finite element method is chosen, the state-equation (13)-(d) yields⁷, after discretization,

$$\begin{aligned}
 \mathbb{K}_\chi \mathbf{d}_\chi &= \mathbf{f}; \quad \mathbb{K}_\chi = \int_{\Omega} \mathbf{B}^T(\mathbf{x}) \mathbb{D}_\chi(\mathbf{x}) \mathbf{B}(\mathbf{x}) d\Omega; \quad \mathbb{D}_\chi(\mathbf{x}) = (\chi(\mathbf{x}))^m \mathbb{D} \quad (a) \\
 \boldsymbol{\sigma}_\chi(\mathbf{x}) &= \mathbb{D}_\chi \boldsymbol{\varepsilon}_\chi(\mathbf{x}); \quad \boldsymbol{\varepsilon}_\chi(\mathbf{x}) = \mathbf{B}(\mathbf{x}) \mathbf{d}_\chi; \quad \mathbf{u}_\chi(\mathbf{x}) = \mathbf{N}_u(\mathbf{x}) \mathbf{d}_\chi \quad (b)
 \end{aligned} \quad (15)$$

where \mathbb{K}_χ stands for the stiffness matrix, \mathbf{f} for the external forces vector and \mathbf{d}_χ is the nodal displacement vector. In addition, $\boldsymbol{\sigma}_\chi(\mathbf{x})$ and $\boldsymbol{\varepsilon}_\chi(\mathbf{x})$ stand, respectively, for the stress and strain vectors, $\mathbf{B}(\mathbf{x})$ is the strain matrix, \mathbb{D} is the matrix version of the hard-phase constitutive tensor \mathbb{C} , and $\mathbf{N}_u(\mathbf{x})$ is the, displacement, interpolation (shape-function) matrix.

A.3.4 Relaxed Topological Derivative. Definition.

Let us consider the function space of solutions, $\mathcal{V}_{\mathbf{u}_\chi}$, of the relaxed state problem in equation (13) for all possible topologies $\chi(\mathbf{x})$, i.e.

$$\left\{ \begin{array}{l}
 \mathcal{V}_\chi := \{ \chi : \Omega \rightarrow \{\beta, 1\} \} \\
 \mathcal{V}_{\mathbf{u}_\chi} := \{ \mathbf{u}_\chi / \mathbf{u}_\chi : \Omega \rightarrow \mathbb{R}^n, n \in \{2, 3\}; \quad \chi \in \mathcal{V}_\chi; \quad a_\chi(\mathbf{u}_\chi, \mathbf{w}) = l(\mathbf{w}) \quad \forall \mathbf{w} \in \mathcal{V}_\eta \}
 \end{array} \right. \quad (16)$$

and the function space, \mathcal{V}_Ω , of L^2 -integrable mappings $G(\chi(\mathbf{x}), \mathbf{u}_\chi(\mathbf{x}), \mathbf{x})$, in \mathbb{R} , and the corresponding functional $\mathcal{J}(\chi)$ i.e.

$$\left\{ \begin{array}{l}
 \mathcal{V}_\Omega := \{ G / G : \mathcal{V}_\chi \times \mathcal{V}_{\mathbf{u}_\chi} \times \Omega \rightarrow \mathbb{R} \} \\
 \mathcal{J}(\chi) \equiv \mathcal{J}_\chi : \mathcal{V}_\Omega \rightarrow \mathbb{R}; \quad \mathcal{J}_\chi = \int_{\Omega} \underbrace{G(\chi, \mathbf{u}_\chi(\mathbf{x}), \mathbf{x})}_{F(\chi, \mathbf{x})} d\Omega = \int_{\Omega} F(\chi, \mathbf{x}) d\Omega
 \end{array} \right. \quad (17)$$

Let us now consider a specific point, $\hat{\mathbf{x}} \in \Omega$, and a sequence of balls⁸, $\Omega_\epsilon(\hat{\mathbf{x}})$ of radius ϵ , (the perturbation domain), surrounding $\hat{\mathbf{x}}$, i.e. $\hat{\mathbf{x}} \in \Omega_\epsilon \subset \Omega$, where $\epsilon \in \mathbb{R}^+$ and $\epsilon \rightarrow 0$ is a regularization parameter (see figure A.3). Let us finally consider the space of perturbations, due

⁷In the following, matrix (Voigt's) notation is used for discrete finite element formulations.

⁸ $\Omega_\epsilon(\mathbf{x})$ is a circle (in 2D) or a sphere in (3D).

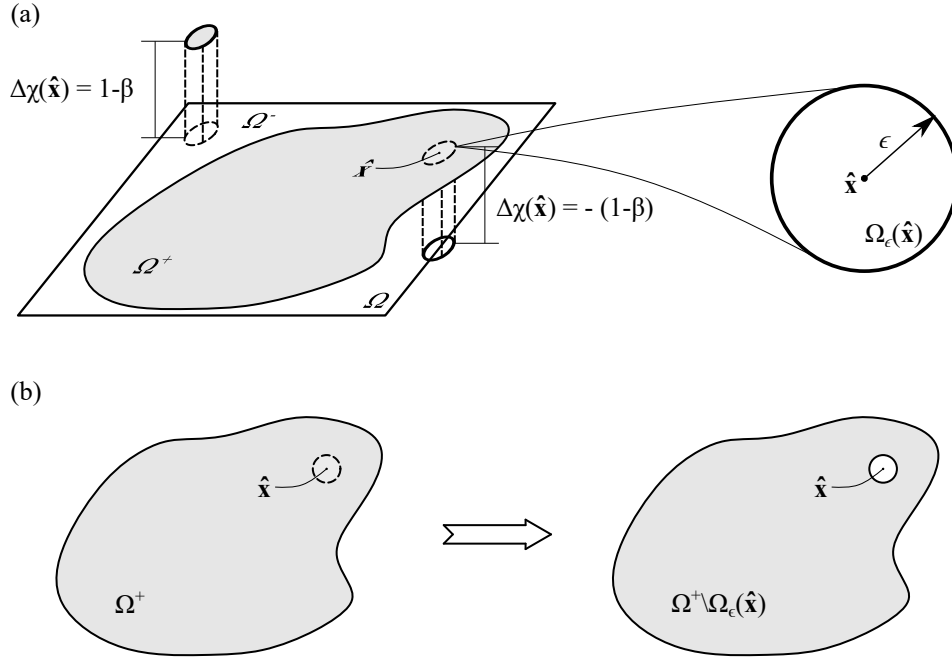


Figure A.3: Topological derivative settings: (a) *Relaxed Topological Derivative (RTD)*, (b) *Exact Topological Derivative (TD)*.

to material phase exchange *only at points of the domain* $\Omega_\epsilon(\hat{\mathbf{x}})$,

$$\Delta \mathcal{V}_{\hat{\mathbf{x}}, \epsilon} := \{ \eta_{\hat{\mathbf{x}}, \epsilon}; \quad \eta_{\hat{\mathbf{x}}, \epsilon}(\mathbf{x}) = \Delta \chi(\mathbf{x}) \quad \forall \mathbf{x} \in \Omega_\epsilon(\hat{\mathbf{x}}); \quad \eta_{\hat{\mathbf{x}}, \epsilon}(\mathbf{x}) = 0 \quad \forall \mathbf{x} \in \Omega \setminus \Omega_\epsilon(\hat{\mathbf{x}}) \} \quad (18)$$

where $\Delta \chi(\mathbf{x})$ stands for the increment in the value of $\chi(\mathbf{x})$ due to exchange of the type of material phase at point \mathbf{x} . In view of equation (5), the value $\Delta \chi(\mathbf{x})$, is:

$$\Delta \chi(\mathbf{x}) = \begin{cases} -(1 - \beta) < 0 & \text{for } \mathbf{x} \in \Omega^+ \\ 1 - \beta > 0 & \text{for } \mathbf{x} \in \Omega^- \end{cases} \quad (19)$$

Let us now consider the following *asymptotic expansion* of the functional $\mathcal{J}(\chi)$ in equation (17), in terms of the perturbation $\eta_{\hat{\mathbf{x}}, \epsilon} \in \Delta \mathcal{V}_{\hat{\mathbf{x}}, \epsilon}$

$$\mathcal{J}(\chi + \eta_{\hat{\mathbf{x}}, \epsilon}) = \mathcal{J}(\chi) + \frac{\delta \mathcal{J}(\chi)}{\delta \chi}(\hat{\mathbf{x}}) \mu[\Omega_\epsilon(\hat{\mathbf{x}})] + o(\mu[\Omega_\epsilon(\hat{\mathbf{x}})]) \quad (20)$$

where, $\mu[\Omega_\epsilon(\hat{\mathbf{x}})]$ is an appropriate measure⁹ of the perturbation domain $\Omega_\epsilon(\hat{\mathbf{x}})$, fulfilling the following conditions

$$\begin{cases} 1) \mu[\Omega_\epsilon(\hat{\mathbf{x}})] > 0 & (a) \\ 2) \lim_{\epsilon \rightarrow 0} \mu[\Omega_\epsilon(\hat{\mathbf{x}})] = 0 & (b) \\ 3) \text{ makes } \frac{\delta \mathcal{J}(\chi)}{\delta \chi}(\hat{\mathbf{x}}) \text{ nonzero valued and bounded} & (c) \end{cases} \quad (21)$$

Specific mathematical aspects of the previous derivations are out of the scope of this work and left to be proven in specialized contexts. From equation (20), and conditions in equation (21), we define the Relaxed Topological Derivative (RTD) of the functional $\mathcal{J}(\chi)$ at point $\hat{\mathbf{x}}$ as

$$\frac{\delta \mathcal{J}(\chi)}{\delta \chi}(\hat{\mathbf{x}}) = \lim_{\epsilon \rightarrow 0} \frac{1}{\mu[\Omega_\epsilon(\hat{\mathbf{x}})]} [\mathcal{J}(\chi + \eta_{\hat{\mathbf{x}}, \epsilon}) - \mathcal{J}(\chi)] \quad (22)$$

⁹For practical purposes, it will be the volume or the surface (depending on the case) of the perturbation domain $\mu[\Omega_\epsilon(\hat{\mathbf{x}})]$.

In view of the previous derivations the RTD can be conceptually defined as

Definition 1 (RTD) *The (relaxed) topological derivative (RTD) of functional $\mathcal{J}(\chi)$, at point $\hat{\mathbf{x}} \in \Omega$, is a finite measure of the sensitivity of $\mathcal{J}(\chi)$ to the change of topology at that point, in the α -relaxed setting described in sections A.3.1 and A.3.2. It is computed as the limit, as $\alpha \rightarrow 0$; $\beta \rightarrow 0$, of the change of $\mathcal{J}(\chi)$, when the material phase type is exchanged ($\chi \leftrightarrow \chi + \Delta\chi(\hat{\mathbf{x}})$) at the neighborhood, $\Omega_\epsilon(\hat{\mathbf{x}})$ per unit of the perturbation measure, $\mu[\Omega_\epsilon(\hat{\mathbf{x}})]$.*

Notice in the previous derivations the similarity of the procedure for obtainment of the topological derivative, here acronymized as (RTD), in the *relaxed bi-material setting* in equations (22), and that in the *embedded/single-material setting*: the *exact* Topological Derivative (TD) [12, 47, 33, 34]. The fundamental difference is that, in the second case the TD is considered in the context of a *single (solid) phase*, occupying the domain $\Omega^+ \subset \Omega$, the corresponding functional being $\mathcal{J}(\Omega^+) = \int_{\Omega^+} (\cdot)(\mathbf{x}) d\Omega$. This functional is perturbed by *removing* the material in an infinitesimal neighborhood, $\Omega_\epsilon(\hat{\mathbf{x}})$, around point $\hat{\mathbf{x}}$, so that the *perturbed solid domain* becomes $\Omega^+ \setminus \Omega_\epsilon(\hat{\mathbf{x}})$ (see figure A.3).

Then the topological derivative is defined as:

$$\mathcal{D}_T(\hat{\mathbf{x}}) := \lim_{\epsilon \rightarrow 0} \frac{\int_{\Omega^+ \setminus \Omega_\epsilon(\hat{\mathbf{x}})} (\cdot)(\mathbf{x}) d\Omega - \int_{\Omega^+} (\cdot)(\mathbf{x}) d\Omega}{\mu[\Omega_\epsilon(\hat{\mathbf{x}})]} \quad (23)$$

Unlike in the RTD derivation, in the TD case the integration domains, $\Omega^+ \setminus \Omega_\epsilon$ and Ω^+ , in equation (23) are not the same, and it is not possible to establish a homeomorphism between both domains [33]. This motivates a subsequent analytical procedure that involves some additional, and problem dependent, limit and asymptotic analyzes [22].

Along this work, it will be assumed that the RTD is a convenient approximation of the TD, requesting much simpler calculations, and it will be checked it provides a *sufficient approximation of the cost sensitivity* to lead to accurate solutions for a number of engineering problems.

A.3.5 Examples of relaxed variational topological derivatives

In the following sections, some results for relaxed topological derivatives, used in this work, are presented.

Relaxed topological derivative of an integral over the design domain

For the functional, \mathcal{J}_χ , defined as in equation (17), the asymptotic expansion in the direction of the perturbation $\eta_{\hat{\mathbf{x}},\epsilon}$ reads

$$\begin{aligned} \mathcal{J}(\chi + \eta_{\hat{\mathbf{x}},\epsilon}) &= \int_{\Omega} F(\chi + \eta_{\hat{\mathbf{x}},\epsilon}, \mathbf{x}) d\Omega = \int_{\Omega} \left(F(\chi, \mathbf{x}) + \frac{\partial F(\chi, \mathbf{x})}{\partial \chi} \eta_{\hat{\mathbf{x}},\epsilon} + o(\eta_{\hat{\mathbf{x}},\epsilon}) \right) d\Omega = \\ &= \mathcal{J}(\chi) + \int_{\Omega} \frac{\partial F(\chi, \mathbf{x})}{\partial \chi} \eta_{\hat{\mathbf{x}},\epsilon} d\Omega + o(\mu[\Omega_\epsilon(\hat{\mathbf{x}})]) = \\ &= \mathcal{J}(\chi) + \int_{\Omega} \left(\frac{\partial G(\chi, \mathbf{u}_\chi(\mathbf{x}), \mathbf{x})}{\partial \chi} + \frac{\partial G(\chi, \mathbf{u}_\chi(\mathbf{x}), \mathbf{x})}{\partial \mathbf{u}_\chi} \cdot \frac{\partial \mathbf{u}_\chi}{\partial \chi} \right) d\Omega + o(\mu[\Omega_\epsilon(\hat{\mathbf{x}})]) \end{aligned} \quad (24)$$

where, when necessary, the displacement derivatives $\partial \mathbf{u}_\chi / \partial \chi$ are obtained from the relaxed elastic problem (the state equation) in equations (13), either directly by χ -differentiation of its solution, or indirectly, by using the adjoint-problem method [12]. Then, the topological

derivative of the functional \mathcal{J}_χ is obtained by replacing equation (24) into equation (22), as

$$\begin{aligned} \frac{\delta \mathcal{J}(\chi)}{\delta \chi}(\hat{\mathbf{x}}) &= \frac{\delta}{\delta \chi} \left[\int_{\Omega} F(\chi, \mathbf{x}) d\Omega \right] (\hat{\mathbf{x}}) = \lim_{\epsilon \rightarrow 0} \frac{1}{\mu[\Omega_\epsilon(\hat{\mathbf{x}})]} [\mathcal{J}(\chi + \eta_{\hat{\mathbf{x}}, \epsilon}) - \mathcal{J}(\chi)] = \\ &= \lim_{\epsilon \rightarrow 0} \frac{1}{\mu[\Omega_\epsilon(\hat{\mathbf{x}})]} \left(\int_{\Omega} \frac{\partial F(\chi, \mathbf{x})}{\partial \chi} \eta_{\hat{\mathbf{x}}, \epsilon} d\Omega + o(\mu[\Omega_\epsilon(\hat{\mathbf{x}})]) \right) = \\ &= \lim_{\epsilon \rightarrow 0} \frac{1}{\mu[\Omega_\epsilon(\hat{\mathbf{x}})]} \int_{\Omega_\epsilon(\hat{\mathbf{x}})} \frac{\partial F(\chi, \mathbf{x})}{\partial \chi} \Delta \chi(\hat{\mathbf{x}}) d\Omega = \\ &= \lim_{\epsilon \rightarrow 0} \frac{|\Omega_\epsilon(\hat{\mathbf{x}})|}{\mu[\Omega_\epsilon(\hat{\mathbf{x}})]} \left[\frac{\partial F(\chi(\mathbf{x}), \mathbf{x})}{\partial \chi} \Delta \chi(\mathbf{x}) \right]_{\mathbf{x}=\hat{\mathbf{x}}} \end{aligned} \quad (25)$$

where equations (22) and (24), and the definition of the perturbation $\eta_{\hat{\mathbf{x}}, \epsilon}$ in equation (18), have been taken into account. In order to fulfill condition in equation (21)-(c), a suitable choice for $\mu[\Omega_\epsilon(\hat{\mathbf{x}})]$ is

$$\mu[\Omega_\epsilon(\hat{\mathbf{x}})] = |\Omega_\epsilon(\hat{\mathbf{x}})| = \frac{4}{3} \pi \epsilon^3 \quad (26)$$

this yielding, in terms of the descriptions $F(\cdot)$ and $G(\cdot)$ in equation (17)

$$\begin{aligned} \frac{\delta \mathcal{J}(\chi)}{\delta \chi}(\hat{\mathbf{x}}) &= \frac{\delta}{\delta \chi} \left[\int_{\Omega} F(\chi, \mathbf{x}) d\Omega \right] (\hat{\mathbf{x}}) = \left[\frac{\partial F(\chi, \mathbf{x})}{\partial \chi} \right]_{\mathbf{x}=\hat{\mathbf{x}}} \Delta \chi(\hat{\mathbf{x}}) = \\ &= \left[\frac{\partial G(\chi, \mathbf{u}_\chi, \mathbf{x})}{\partial \chi} + \frac{\partial G(\chi, \mathbf{u}_\chi, \mathbf{x})}{\partial \mathbf{u}_\chi} \cdot \frac{\partial \mathbf{u}_\chi}{\partial \chi} \right]_{\mathbf{x}=\hat{\mathbf{x}}} \Delta \chi(\hat{\mathbf{x}}) \end{aligned} \quad (27)$$

Remark 4 Notice that the linear character of the integration and differentiation operations, involved in the determination of the relaxed variational topological derivative in equations (25) to (27), confers to the RTD the same linear character, i.e.

$$\frac{\delta (\mathcal{J}(\chi) + \lambda \mathcal{K}(\chi))}{\delta \chi}(\hat{\mathbf{x}}) = \frac{\delta \mathcal{J}(\chi)}{\delta \chi}(\hat{\mathbf{x}}) + \lambda \frac{\delta \mathcal{K}(\chi)}{\delta \chi}(\hat{\mathbf{x}}); \quad \mathcal{J}(\chi), \mathcal{K}(\chi) \in \mathcal{V}_\Omega; \quad \lambda \in \mathbb{R} \quad (28)$$

Relaxed topological derivative of a material phase volume

Let us consider the functional defining the volume of phase \mathfrak{M}^+ (see figure A.4)

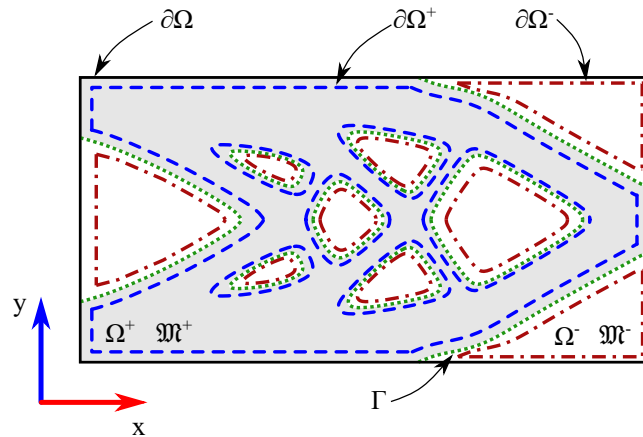


Figure A.4: Design domain Ω : material-phase domains (Ω^+ and Ω^-), material-phase boundaries ($\partial\Omega^+$ and $\partial\Omega^-$), and phase interfaces (Γ).

$$\mathcal{J}(\chi) \equiv |\Omega^+(\chi)| = \int_{\Omega^+(\chi)} d\Omega; \quad \mathcal{J}(\chi) \in \mathcal{V}_\Omega \quad (29)$$

and the identity

$$\lim_{\epsilon \rightarrow 0} \mathcal{J}(\chi + \eta_{\hat{\mathbf{x}}, \epsilon}) = \lim_{\epsilon \rightarrow 0} |\Omega^+(\chi + \eta_{\hat{\mathbf{x}}, \epsilon})| = \lim_{\epsilon \rightarrow 0} (|\Omega^+(\chi)| + \text{sgn}(\Delta\chi(\hat{\mathbf{x}}))|\Omega_\epsilon(\hat{\mathbf{x}})|) \quad (30)$$

where $\text{sgn}(\Delta\chi(\hat{\mathbf{x}})) = -1 \ \forall \hat{\mathbf{x}} \in \Omega^+$ and $\text{sgn}(\Delta\chi(\hat{\mathbf{x}})) = 1 \ \forall \hat{\mathbf{x}} \in \Omega^-$ (see equation (19)).

The corresponding topological derivative, at point $\hat{\mathbf{x}} \in \Omega$, can be now computed from equations (22) and (30) as

$$\begin{aligned} \frac{\delta \mathcal{J}(\chi)}{\delta \chi}(\hat{\mathbf{x}}) &= \lim_{\epsilon \rightarrow 0} \frac{1}{\mu[\Omega_\epsilon(\hat{\mathbf{x}})]} [\mathcal{J}(\chi + \eta_{\hat{\mathbf{x}}, \epsilon}) - \mathcal{J}(\chi)] = \lim_{\epsilon \rightarrow 0} \frac{|\Omega^+(\chi + \eta_{\hat{\mathbf{x}}, \epsilon})| - |\Omega^+(\chi)|}{\mu[\Omega_\epsilon(\hat{\mathbf{x}})]} = \\ &= \lim_{\epsilon \rightarrow 0} \frac{|\Omega^+(\chi)| + \text{sgn}(\Delta\chi(\hat{\mathbf{x}}))|\Omega_\epsilon(\hat{\mathbf{x}})| - |\Omega^+(\chi)|}{\mu[\Omega_\epsilon(\hat{\mathbf{x}})]} = \\ &= \text{sgn}(\Delta\chi(\hat{\mathbf{x}})) \lim_{\epsilon \rightarrow 0} \frac{|\Omega_\epsilon(\hat{\mathbf{x}})|}{\mu[\Omega_\epsilon(\hat{\mathbf{x}})]} = \text{sgn}(\Delta\chi(\hat{\mathbf{x}})) \end{aligned} \quad (31)$$

where the choice for $\mu[\Omega_\epsilon(\hat{\mathbf{x}})]$, to fulfill the condition in equation (21)-(c), is

$$\mu[\Omega_\epsilon(\hat{\mathbf{x}})] = |\Omega_\epsilon(\hat{\mathbf{x}})| = \frac{4}{3}\pi\epsilon^3 \quad (32)$$

In summary

$$\frac{\delta |\Omega^+(\chi)|}{\delta \chi}(\hat{\mathbf{x}}) = \text{sgn}(\Delta\chi(\hat{\mathbf{x}})) = \begin{cases} -1 & \forall \hat{\mathbf{x}} \in \Omega^+ \\ +1 & \forall \hat{\mathbf{x}} \in \Omega^- \end{cases} \quad (33)$$

For the RTD of the soft-phase \mathfrak{M}^- case we consider the identity

$$|\Omega^+(\chi)| + |\Omega^-(\chi)| = |\Omega| \quad (34)$$

which yields

$$\frac{\delta |\Omega^-(\chi)|}{\delta \chi}(\hat{\mathbf{x}}) = -\frac{\delta |\Omega^+(\chi)|}{\delta \chi}(\hat{\mathbf{x}}) = -\text{sgn}(\Delta\chi(\hat{\mathbf{x}})) = \begin{cases} +1 & \forall \hat{\mathbf{x}} \in \Omega^+ \\ -1 & \forall \hat{\mathbf{x}} \in \Omega^- \end{cases} \quad (35)$$

An alternative procedure to obtain the RTD of the functional in equation (29), consists of rephrasing it, considering equation (10), and applying the result in equation (27) (see also Table A.1), i.e.

$$\left\{ \begin{aligned} |\Omega^+(\chi)| &= \int_{\Omega^+} d\Omega = \int_{\Omega} \underbrace{\frac{\chi - \beta}{1 - \beta}}_{F(\chi)} d\Omega \\ F(\chi) &\equiv \frac{\chi - \beta}{1 - \beta} \Rightarrow \frac{\partial F(\chi)}{\partial \chi} = \frac{1}{1 - \beta} \\ \frac{\delta |\Omega^+(\chi)|}{\delta \chi}(\hat{\mathbf{x}}) &= \left[\frac{\partial F(\chi)}{\partial \chi} \right]_{\mathbf{x}=\hat{\mathbf{x}}} \Delta\chi(\hat{\mathbf{x}}) = \frac{1}{1 - \beta} \underbrace{(1 - \beta)(\text{sgn}(\Delta\chi(\hat{\mathbf{x}})))}_{\Delta\chi(\hat{\mathbf{x}})} = \text{sgn}(\Delta\chi(\hat{\mathbf{x}})) \end{aligned} \right. \quad (36)$$

which, as expected, coincides with the result in equation (33).

Relaxed topological derivative of a phase perimeter

We now consider the functional corresponding to the perimeter of the hard-phase, $\mathcal{P}^+(\chi)$, defined as (see figure A.4)

$$\mathcal{J}(\chi) = \mathcal{P}^+(\chi) = \int_{\partial\Omega^+(\chi)} d\Gamma = |\partial\Omega^+(\chi)| \quad (37)$$

and the identity

$$\lim_{\epsilon \rightarrow 0} \mathcal{J}(\chi + \eta_{\hat{\mathbf{x}}, \epsilon}) = \lim_{\epsilon \rightarrow 0} |\partial\Omega^+(\chi + \eta_{\hat{\mathbf{x}}, \epsilon})| = \lim_{\epsilon \rightarrow 0} (|\partial\Omega^+(\chi)| + |\partial\Omega_\epsilon(\hat{\mathbf{x}})|) \quad (38)$$

The corresponding topological derivative, at point $\hat{\mathbf{x}} \in \Omega$, can be now computed from equations (22) and (38) as:

$$\begin{aligned} \frac{\delta \mathcal{J}(\chi)}{\delta \chi}(\hat{\mathbf{x}}) &= \lim_{\epsilon \rightarrow 0} \frac{1}{\mu[\Omega_\epsilon(\hat{\mathbf{x}})]} [\mathcal{J}(\chi + \eta_{\hat{\mathbf{x}}, \epsilon}) - \mathcal{J}(\chi)] = \lim_{\epsilon \rightarrow 0} \frac{|\partial\Omega^+(\chi + \eta_{\hat{\mathbf{x}}, \epsilon})| - |\partial\Omega^+(\chi)|}{\mu[\Omega_\epsilon(\hat{\mathbf{x}})]} = \\ &= \lim_{\epsilon \rightarrow 0} \frac{|\partial\Omega^+(\chi)| + |\partial\Omega_\epsilon(\hat{\mathbf{x}})| - |\partial\Omega^+(\chi)|}{\mu[\Omega_\epsilon(\hat{\mathbf{x}})]} = \lim_{\epsilon \rightarrow 0} \frac{|\partial\Omega_\epsilon(\hat{\mathbf{x}})|}{\mu[\Omega_\epsilon(\hat{\mathbf{x}})]} = 1 \end{aligned} \quad (39)$$

where the choice for $\mu[\Omega_\epsilon(\hat{\mathbf{x}})]$, in equation (21)-(c), is

$$\mu[\Omega_\epsilon(\hat{\mathbf{x}})] = |\partial\Omega_\epsilon(\hat{\mathbf{x}})| = 4\pi\epsilon^2 \quad (40)$$

From the previous derivation it is evident that the same result would be found for the perimeter of the soft-phase domain $\mathcal{P}^-(\chi)$. Therefore, in summary,

$$\begin{cases} \mathcal{P}^+(\chi) := |\partial\Omega^+(\chi)| & \Rightarrow \frac{\delta \mathcal{P}^+(\chi)}{\delta \chi}(\hat{\mathbf{x}}) = 1 \\ \mathcal{P}^-(\chi) := |\partial\Omega^-(\chi)| & \Rightarrow \frac{\delta \mathcal{P}^-(\chi)}{\delta \chi}(\hat{\mathbf{x}}) = 1 \end{cases} \quad (41)$$

Remark 5 (Interface measure) *A measure frequently considered in the topological optimization literature [19] is the measure of the phases interface $\Gamma(\chi)$ (see figure A.4), which does not correspond to any of the phase perimeters, \mathcal{P}^+ and \mathcal{P}^- , in equation (41), but to the measure, $|\Gamma(\chi)|$, of the geometric interface, $\Gamma := (\partial\Omega^+ \cup \partial\Omega^-)$, shared by both phases (thus, excluding the boundary $\partial\Omega$, see figure A.4).*

The RTD of $\Gamma(\chi)$ can be readily obtained from the following identity

$$\underbrace{|\partial\Omega^+(\chi)|}_{\mathcal{P}^+(\chi)} + \underbrace{|\partial\Omega^-(\chi)|}_{\mathcal{P}^-(\chi)} = 2|\Gamma(\chi)| + |\partial\Omega| \quad (42)$$

and the RTD of equation (42) yields

$$\frac{\delta |\Gamma(\chi)|}{\delta \chi}(\hat{\mathbf{x}}) = \frac{1}{2} \left(\frac{\delta \mathcal{P}^+(\chi)}{\delta \chi}(\hat{\mathbf{x}}) + \frac{\delta \mathcal{P}^-(\chi)}{\delta \chi}(\hat{\mathbf{x}}) \right) = 1 \quad (43)$$

where equations (41) have been taken into account.

In Table A.1, examples of commonly used RTD derivatives are summarized.

A.4 Application to volume constrained topological optimization problems

Let us consider the following topological optimization problem in the design domain Ω

$$\left[\begin{array}{l} \text{Find: } \chi(\mathbf{x}) = \mathcal{H}_\beta(\psi(\mathbf{x})) ; \quad \chi : \Omega \rightarrow \{\beta, 1\} ; \quad \psi \in H^1(\Omega) \\ \text{Fulfilling:} \\ \quad \chi^* = \underset{\chi}{\operatorname{argmin}} \quad \mathcal{J}(\chi) \equiv \int_{\Omega} F(\chi, \mathbf{x}) d\Omega \quad (a) \quad (44) \\ \text{Subject to:} \\ \quad \mathcal{C}(\chi) \equiv |\Omega^+(\chi)| - \bar{V} = |\Omega| - |\Omega^-(\chi)| - \bar{V} = 0 \quad (b) \end{array} \right.$$

where, in equation (44)-(b), \bar{V} is the target volume for the material *hard-phase* (\mathfrak{M}^+) and the equality $|\Omega^+(\chi)| = |\Omega| - |\Omega^-(\chi)|$ has been used.

Table A.1: Relaxed topological derivative examples. $\Delta\chi(\hat{\mathbf{x}}) = -(1 - \beta) \forall \hat{\mathbf{x}} \in \Omega^+$, $\Delta\chi(\hat{\mathbf{x}}) = (1 - \beta) \forall \hat{\mathbf{x}} \in \Omega^-$.

Functional \mathcal{J}_χ	RTD $(\delta\mathcal{J}_\chi/\delta\chi)(\hat{\mathbf{x}})$	Perturbation measure $\mu[\Omega_\epsilon(\hat{\mathbf{x}})]$
$\int_\Omega F(\chi, \mathbf{x}) d\Omega$	$\left[\frac{\partial F(\chi(\mathbf{x}), \mathbf{x})}{\partial \chi} \right]_{\mathbf{x}=\hat{\mathbf{x}}} \Delta\chi(\hat{\mathbf{x}})$	$ \Omega_\epsilon(\hat{\mathbf{x}}) $
$ \Omega^+(\chi) := \int_{\Omega^+(\chi)} d\Omega$	$\text{sgn}(\Delta\chi(\hat{\mathbf{x}}))$	$ \Omega_\epsilon(\hat{\mathbf{x}}) $
$ \Omega^-(\chi) := \int_{\Omega^-(\chi)} d\Omega$	$\text{sgn}(\Delta\chi(\hat{\mathbf{x}}))$	$ \Omega_\epsilon(\hat{\mathbf{x}}) $
$\mathcal{P}^+(\chi) := \int_{\partial\Omega^+(\chi)} d\Gamma$	1	$ \partial\Omega_\epsilon(\hat{\mathbf{x}}) $
$\mathcal{P}^-(\chi) := \int_{\partial\Omega^-(\chi)} d\Gamma$	1	$ \partial\Omega_\epsilon(\hat{\mathbf{x}}) $
$\Gamma(\chi) := \int_{(\partial\Omega^+ \cap \partial\Omega^-)(\chi)} d\Gamma$	1	$ \partial\Omega_\epsilon(\hat{\mathbf{x}}) $

A.4.1 Penalized functional for non-smooth optimization problems. Optimality criterion

In order to face the difficulty to impose the minimization, accounting for the constraint in equation (44)-(b) in non-differentiable function spaces, we will resort to a sequence of penalized problems (see [9]), by means of the parameter $\frac{1}{k}$, penalizing the values of χ that violate the constraint $\mathcal{C}(\chi) = 0$. Therefore, we start from the following penalized problem, in terms of the *extended* functional, \mathcal{J}^{ext} ,

$$\begin{cases}
 \text{Find: } \chi_k(\mathbf{x}) = \mathcal{H}_\beta(\psi_k(\mathbf{x})) : \Omega \rightarrow \{\beta, 1\}; & \psi_k \in H^1(\Omega) \\
 \text{Fulfilling:} \\
 \chi_k^* = \underset{\chi_k}{\text{argmin}} \quad \mathcal{J}^{ext}(\chi_k) \equiv \mathcal{J}(\chi_k) + \frac{1}{2k}(\mathcal{C}(\chi_k))^2 & (a) \\
 \text{Subject to:} \\
 \mathcal{C}(\chi_k) \equiv |\Omega^+(\chi_k)| - \bar{V} = 0 & (b) \\
 \chi^* = \lim_{k \rightarrow 0} \chi_k^* & (b)
 \end{cases} \quad (45)$$

In order to solve the problem in equation (45) we impose the following *optimality criterion*

$$\begin{aligned}
 \frac{\delta\mathcal{J}^{ext}(\chi_k)}{\delta\chi_k}(\mathbf{x}) &= \frac{\delta\mathcal{J}(\chi_k)}{\delta\chi}(\mathbf{x}) + \frac{\mathcal{C}(\chi_k)}{k} \frac{\delta\mathcal{C}(\chi_k)}{\delta\chi_k}(\mathbf{x}) = \\
 &= \left(\frac{\partial F(\chi_k, \mathbf{x})}{\partial \chi_k} \Delta\chi(\mathbf{x}) + \frac{\mathcal{C}(\chi_k)}{k} \text{sgn}(\Delta\chi(\mathbf{x})) \right) > 0; \quad \forall \mathbf{x} \in \Omega
 \end{aligned} \quad (46)$$

where the topological derivation rules in equations (27) and (29) have been applied.

Remark 6 (Overall-increasing cost function sensitivity) Condition in equation (46) arises from the following argument (inspired by the one in [7]): by definition, the RTD, $(\delta\mathcal{J}^{ext}(\chi_k)/\delta\chi_k(\mathbf{x}))$, measures the sensitivity to topological changes of the functional $\mathcal{J}^{ext}(\chi_k)$ in front of local phase exchanges, $\Delta\chi(\mathbf{x})$ at point \mathbf{x} , per unit of measure of the perturbed domain (see definition 1). Therefore, denoting $\hat{\Omega}$ the subset of Ω where these exchanges take place, i.e.

$$\begin{aligned}
 \hat{\Omega} \subset \Omega &\rightarrow \hat{\Omega} := \{\mathbf{x} \in \Omega; \Delta\chi_k(\mathbf{x}) = \Delta\chi \neq 0\} \\
 \Omega \setminus \hat{\Omega} \subset \Omega &\rightarrow \Omega \setminus \hat{\Omega} := \{\mathbf{x} \in \Omega; \Delta\chi_k(\mathbf{x}) = 0\}
 \end{aligned} \quad (47)$$

such that

$$\Delta\chi_k(\mathbf{x}) = \begin{cases} 0 \rightarrow \text{no phase exchange at point } \mathbf{x} \\ \Delta\chi \neq 0 \rightarrow \text{actual phase exchange at point } \mathbf{x} \end{cases} \quad (48)$$

If condition in equation (46) is fulfilled everywhere, for a given topology, $\chi_k(\mathbf{x})$, and for all possible phase changes of that topology ($\Delta\chi_k(\mathbf{x}); \forall \mathbf{x} \in \hat{\Omega}; \forall \hat{\Omega} \subset \Omega$) then, the increment of the functional $\Delta\mathcal{J}^{ext}(\chi_k)$ for material phase exchange at any finite subset $\hat{\Omega}(\chi_k) \subset \Omega$ is:

$$\Delta\mathcal{J}^{ext}(\chi_k) = \int_{\hat{\Omega}(\chi_k)} \underbrace{\frac{\delta\mathcal{J}^{ext}(\chi_k, \Delta\chi)}{\delta\chi_k}(\mathbf{x})}_{> 0} d\Omega > 0 \quad \forall \hat{\Omega}(\chi_k) \subset \Omega \quad (49)$$

this indicating that χ_k is a local minimizer of $\mathcal{J}^{ext}(\chi_k)$. This proves that equation (46) is a sufficient condition for minimization of the problem in equation (45).

A.4.2 Closed-form solution

Replacing equation (19) into equation (46) yields:

$$\begin{aligned} \frac{\partial F(\chi_k, \mathbf{x})}{\partial \chi_k} \Delta\chi(\mathbf{x}) + \frac{C(\chi_k)}{k} \text{sgn}(\Delta\chi(\mathbf{x})) &= \\ &= \begin{cases} -(1-\beta) \frac{\partial F(\chi_k, \mathbf{x})}{\partial \chi_k} - \frac{C(\chi_k)}{k} > 0 & \text{for } \mathbf{x} \in \Omega^+(\chi_k) \\ (1-\beta) \frac{\partial F(\chi_k, \mathbf{x})}{\partial \chi_k} + \frac{C(\chi_k)}{k} > 0 & \text{for } \mathbf{x} \in \Omega^-(\chi_k) \end{cases} \end{aligned} \quad (50)$$

Comparing equation (50) with equations (5) and (6), and since $(1-\beta) > 0$ (see equation (1)-(a)), we can identify the closed-form solution of the penalized problem through

$$\begin{cases} \psi_k(\mathbf{x}) := -(1-\beta) \frac{\partial F(\chi_k, \mathbf{x})}{\partial \chi_k} - \frac{C(\chi_k)}{k} \\ \chi_k^*(\mathbf{x}) := \mathcal{H}_\beta[\psi_k(\mathbf{x})] \end{cases} \quad (51)$$

where equation (2), has been considered. Finally, taking to the limit equation (51), as indicated in equation (45)-(b), yields

$$\chi^*(\mathbf{x}) = \lim_{k \rightarrow 0} \chi_k^*(\mathbf{x}) \quad (52)$$

The drawback of the penalty method, considered so far, is that, for getting accurate and robust solutions in equations (52) the penalty parameter, k , has to be taken very close to the limit ($k \rightarrow 0$). This issue can be circumvented by rephrasing equations (45) and (46) through definition of a new variable λ (see [9]),

$$\begin{cases} \lambda := \lim_{k \rightarrow 0} \frac{C(\chi_k)}{k} \quad \left(= \frac{0}{0} \right) & (a) \\ \lim_{k \rightarrow 0} C(\chi_k) = 0 & (b) \end{cases} \quad (53)$$

where the new unknown, $\lambda : \Omega \rightarrow \mathbb{R}$, arising from the (undetermined) equation (53)-(a) is solved by imposing, in strong form, the original restriction, $\mathcal{C}(\chi) = 0$ in equation (53)-(b). Taking the limit $k \rightarrow 0$ in equations (45) to (52), and replacing $\lim_{k \rightarrow 0} \frac{C(\chi_k)}{k}$ by λ , yields the following *closed-form solution*.

Box I: Volume constrained topological optimization problem. Closed form solution.

Problem:

$$\begin{cases} \chi^* = \underset{\chi}{\operatorname{argmin}} \mathcal{J}(\chi) = \underset{\chi}{\operatorname{argmin}} \int_{\Omega} F(\chi, \mathbf{x}) d\Omega \\ \text{s.t. } \mathcal{C}(\chi) \equiv |\Omega^+(\chi)| - \bar{V} = 0 \end{cases} \quad (a)$$

$$\text{Lagrangian: } \mathcal{L}(\chi, \lambda) = \mathcal{J}(\chi) + \lambda \mathcal{C}(\chi) \quad (b)$$

Optimality criterion:

$$\begin{cases} \frac{\delta \mathcal{L}(\chi, \lambda)}{\delta \chi}(\mathbf{x}) = \frac{\partial F(\chi, \mathbf{x})}{\partial \chi} \Delta \chi(\mathbf{x}) + \lambda \operatorname{sgn}(\Delta \chi(\mathbf{x})) > 0 \quad \forall \mathbf{x} \in \Omega \\ \mathcal{C}(\chi) = 0 \end{cases} \quad (c)$$

Closed-form solution:

$$\begin{aligned} \psi_{\chi}(\mathbf{x}, \lambda) &:= -(1 - \beta) \frac{\partial F(\chi, \mathbf{x})}{\partial \chi} - \lambda > 0 \quad \text{for } \mathbf{x} \in \Omega^+ \\ \Rightarrow \begin{cases} \psi_{\chi}(\mathbf{x}, \lambda) := -(1 - \beta) \frac{\partial F(\chi, \mathbf{x})}{\partial \chi} - \lambda \\ \chi(\mathbf{x}, \lambda) = \mathcal{H}_{\beta}[\psi_{\chi}(\mathbf{x}, \lambda)] \rightarrow \chi_{\lambda}(\mathbf{x}) \quad (\mathbf{d-1}) \\ \mathcal{C}(\chi_{\lambda}, \lambda) = 0 \quad (\mathbf{d-2}) \end{cases} \rightarrow \lambda^* \rightarrow \chi^*(\mathbf{x}) =: \chi_{\lambda^*}(\mathbf{x}) \end{aligned} \quad (d)$$

Topology:

$$\begin{cases} \Omega^+(\chi) := \{\mathbf{x} \in \Omega; \psi_{\chi}(\mathbf{x}, \lambda) > 0\} \\ \Omega^-(\chi) := \{\mathbf{x} \in \Omega; \mathbf{x} \notin \Omega^+\} \\ \Gamma(\chi) := \{\mathbf{x} \in \Omega; \psi_{\chi}(\mathbf{x}, \lambda) = 0\} \end{cases} \quad (54)$$

Equation (54)-(d-1) provides, at any point $\mathbf{x} \in \Omega$ and for a given value of λ , a closed-form (fixed-point type) scalar equation¹⁰, whose solution is $\chi_{\lambda}(\mathbf{x})$. When this is set for all points $\mathbf{x} \in \Omega$, the spatial description of a topology can be parametrized in terms of the current value of λ , i.e.: $\chi_{\lambda} \equiv \chi(\mathbf{x}, \lambda)$. Substitution into the constraint equation (54)-(d-2) yields a scalar equation supplying the solutions λ^* , and $\chi^*(\mathbf{x}) = \chi_{\lambda^*}(\mathbf{x})$, and the solution of the original problem in equations (44)-(a) and (54)-(a), is retrieved.

A.5 Regularization

It is well known that the topological optimization problem may be ill-posed [43, 8]. For instance, in case of the restriction in equation (45)-(b), in terms of the material *hard-phase* (\mathfrak{M}^+) volume, $|\Omega^+(\chi)|$, i.e.

$$\mathcal{C}(\chi) \equiv |\Omega^+(\chi)| - \bar{V} = 0 \quad (55)$$

the infimum of the problem corresponds to a topology made of infinite number of inclusions of the *soft-phase* (\mathfrak{M}^-), of infinitesimal size each, embedded into a matrix of *hard-phase* (\mathfrak{M}^+). Since, for solving the problem numerically, one uses meshes with cells (voxels or finite elements) of typical size, h , this determines the minimum inclusion size that can be captured by the mesh. Therefore, a *local minimum* is achieved with the inclusion's size in terms of h . However, when finer meshes are used ($h \rightarrow 0$) finer topologies (with smaller inclusion's size) are obtained, providing different and unbounded lower minima of the cost function $\mathcal{J}(\chi)$. No convergence is achieved in this process in terms of h (lack of mesh size objectivity).

¹⁰Of the type $y = \mathcal{G}(y)$, in the argument $y \equiv \chi$.

Although this issue does not appear for some other type of restrictions (like perimeter restrictions [4, 19]), this fact sets serious limits to the type of applications in the topological derivative optimization based methods, unless some remedy to the *ill-posed-problem/mesh-size-unobjectivity issue* is introduced. In the literature some of them can be found, typically based on introducing some modifications on the original cost function \mathcal{J} that *regularize* the problem (like the Tikhonov regularization, [53]), by using Fourier series-based regularizations [51], or by a combination of topological and shape derivatives [11, 3].

A.5.1 Regularization. Laplacian smoothing

Here we resort to a very simple and efficient regularization procedure, based on a Laplacian smoothing of the discrimination function $\psi(\mathbf{x}, \lambda)$, derived in equation (54)-(d). This function, which in principle might be discontinuous due to the characteristic function $\chi \in \{\beta, 1\}$, is here *regularized* through the solution of a Laplace-type smoothing equation, that returns a smooth field $\psi_\tau(\mathbf{x}, \lambda)$ to be inserted in equation (54)-(d):

$$\psi(\mathbf{x}, \lambda) \leftarrow \psi_\tau(\mathbf{x}, \lambda) \quad (56)$$

the smooth field $\psi_\tau(\mathbf{x})$ being the solution of

$$\begin{cases} \psi_\tau(\mathbf{x}, \lambda) - \epsilon^2 \Delta_{\mathbf{x}} \psi_\tau(\mathbf{x}, \lambda) = \psi(\mathbf{x}, \lambda) & \forall \mathbf{x} \in \Omega \\ \nabla_{\mathbf{x}} \psi_\tau(\mathbf{x}, \lambda) \cdot \mathbf{n} = 0 & \forall \mathbf{x} \in \partial\Omega \end{cases} \quad (57)$$

where, $\Delta_{\mathbf{x}}(\mathbf{x}, \cdot)$ and $\nabla_{\mathbf{x}}(\mathbf{x}, \cdot)$ stand for the Laplacian and gradient operators, respectively, \mathbf{n} is the outwards normal to the boundary, $\partial\Omega$, of the design domain. Therefore, the closed-form solution of the problem in equation (45) reads:

$$\chi(\mathbf{x}) \rightarrow \text{solution of } \begin{cases} \chi(\mathbf{x}, \lambda) = \mathcal{H}_\beta[\psi_\tau(\mathbf{x})] \\ \mathcal{C}(\chi(\mathbf{x}, \lambda)) = 0 \end{cases} \quad \forall \mathbf{x} \in \Omega \quad (58)$$

where $\psi_\tau(\mathbf{x})$ is the solution of equation (57), which can be solved in the context of any spatial numerical discretization method. In a finite element context, it yields:

$$\begin{cases} \psi_\tau(\mathbf{x}) = \mathbf{N}(\mathbf{x})\{\hat{\psi}_\tau\}; & \hat{\psi}_\tau = \tilde{\mathbb{G}}^{-1}\mathbf{f}; & \tilde{\mathbb{G}} = \tilde{\mathbb{M}} + \epsilon^2\tilde{\mathbb{K}} & (a) \\ \tilde{\mathbb{M}} = \int_{\Omega} \mathbf{N}^T(\mathbf{x})\mathbf{N}(\mathbf{x}); & \tilde{\mathbb{K}} = \int_{\Omega} \nabla\mathbf{N}(\mathbf{x})^T\nabla\mathbf{N}(\mathbf{x}) d\Omega; & \mathbf{f}(\psi) = \int_{\Omega} \mathbf{N}^T(\mathbf{x})\psi(\mathbf{x}) d\Omega & (b) \end{cases} \quad (59)$$

where $\mathbf{N}(\mathbf{x})$ stands for the standard interpolation matrix and $\hat{\psi}_\tau$ is the vector of nodal values of the field $\psi_\tau(\mathbf{x})$. Notice that matrix $\tilde{\mathbb{G}}_\tau$, in equation (59)-(a), needs to be built, and inverted, only once for ever, and that it can be used as many times as the Laplacian smoothing is required in the optimization problem. This translates into a low computational cost of the procedure.

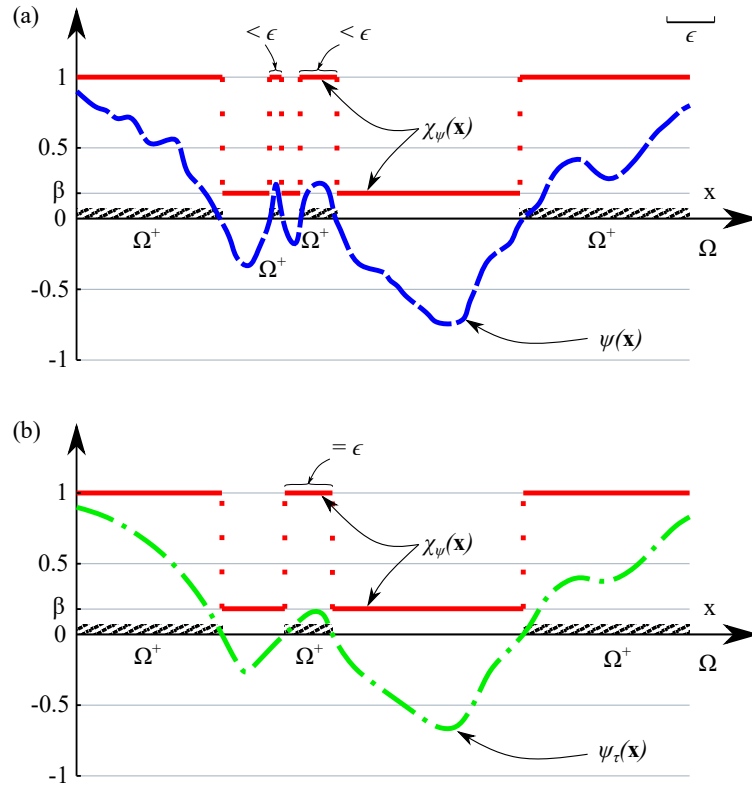


Figure A.5: Noisy modes removal and minimum phase-filament-thickness, via Laplacian smoothing of the discrimination function $\psi(\mathbf{x})$. (a) Before smoothing and (b) After smoothing.

The regularization parameter, $\epsilon \geq 0$, in equations (56) to (59), is indirectly defined through the mesh/voxel size, h , and the non-dimensional parameter, τ , i.e.

$$\epsilon = \tau h; \quad \tau \in \mathbb{R}^+ \quad (60)$$

where, for every mesh, τ , describes the *number of elements* that typically cover the filtering measure ϵ . The Laplacian smoothing procedure in equations (57) and (59) is frequently used in digital image processing [49, 37] to remove the short wavelength spectral components (*noisy components*) of the original field $\psi(\mathbf{x})$, in such a way that the smoothed field, $\psi_\tau(\mathbf{x})$, does not exhibit oscillation wavelengths shorter than ϵ . Therefore, the value of ϵ , approximately defines a lower bound for *the minimum hard-phase filaments width* (separating soft-phase inclusions) that appear in the optimized topology emerging from equations (57) (see figure A.5). Consequently, in equation (60), τ defines, for a given uniform-size mesh, the number of elements covering the width of the thinnest hard-phase filaments [24]. This strategy breaks down the mesh-size dependency of the obtained topologies and the aforementioned ill-condition paradigm. Now, the resulting soft-phase (inclusions/voids) cannot be closer to each other than the distance defined by ϵ , disregard the size and number of the finite elements covering this width. In some way this is equivalent to establishing a *perimeter constraint*¹¹ in the optimization problem to remove those shortcomings [25]. From another point of view, the need for a regularization can be related to *manufacturing constraints*, related to manufacturing issues [31], ϵ defining the minimum hard-phase \mathfrak{M}^+ filament width that the manufacturing technology can produce.

¹¹Actually, perimeter constraint in topology optimization is a deep question whose discussion can be found in [6].

A.6 Pseudo-time sequential approach for volume constrained optimization problem

Introduction of a *pseudo-time*, t , as an additional increasing scalar parameter in the problem, allows connecting the strategy of resolution of the topological optimization problem, with some well known algorithmic time-advancing techniques in computational mechanics. For instance, *control* methods in non-linear solid mechanics problems (i.e. displacement control, arc-length methods, in which one additional algebraic equation (equivalent to the restriction in equation (44)-(b)) is used to limit/control the evolution of the problem unknowns¹², in order to increase the robustness of the resolution process [15].

In this context, the pseudo-time parameter $t \in [0, T]$ is introduced in the constraint, which is now rewritten as:

$$\mathcal{C}(\chi, t) \equiv \frac{|\Omega^+(\chi)|}{|\Omega|} - \frac{\bar{V}}{|\Omega|} = \frac{|\Omega| - |\Omega^-(\chi)|}{|\Omega|} - \underbrace{\frac{\bar{V}}{|\Omega|}}_{1-t} = t - \frac{|\Omega^-(\chi)|}{|\Omega|}; \quad t \in [0, 1] \quad (61)$$

so that all variables become *parametrized* in terms of t , and the original problem in equation (44) now reads:

$$\left[\begin{array}{l} \text{Find: } \psi : \Omega \times [0, T] \rightarrow \mathbb{R}; \quad \psi(\cdot, t) \in H^{(1)}(\Omega) \quad \text{and} \\ \quad \chi : \Omega \times [0, 1] \rightarrow \{\beta, 1\}; \quad \chi(\mathbf{x}, t) = \mathcal{H}_\beta(\psi(\mathbf{x}, t)) \\ \text{Fulfilling:} \\ \quad \chi_t^* = \underset{\chi}{\operatorname{argmin}} \quad \mathcal{J}_t(\chi) \equiv \int_{\Omega} F(\chi, \mathbf{x}, t) d\Omega \\ \text{Subject to:} \\ \quad \mathcal{C}(\chi, t) \equiv t - \frac{|\Omega^-(\chi)|}{|\Omega|} = 0 \end{array} \right. \quad \begin{array}{l} (a) \\ (b) \quad (62) \\ (c) \end{array}$$

A.7 Algorithmic resolution

The time-discretized version of the closed-form problem and solution in equations (62) can be now written as:

$$\left[\begin{array}{l} \text{Given: } \left\{ \begin{array}{l} \mathcal{T} := \{t_0 = 0, t_1, t_2, \dots, T \leq 1\} \quad (\text{time discretization}) \\ \chi(\mathbf{x}, t_n) \equiv \chi_n(\mathbf{x}) \quad (\text{topology at time } t_n) \\ \text{and } [t_n, t_{n+1}] \quad (\text{time interval}) \end{array} \right. \\ \text{Find: } \chi_{n+1} : \Omega \rightarrow \{\beta, 1\}, \text{ and } \lambda(t_{n+1}) \equiv \lambda_{n+1} \in \mathbb{R} \\ \text{Fulfilling:} \\ \quad \psi_\tau(\mathbf{x}, \lambda_{n+1}) := \text{solution of } \left\{ \begin{array}{l} \psi_\tau(\mathbf{x}, \lambda_{n+1}) - \epsilon^2 \Delta \psi_\tau(\mathbf{x}, \lambda_{n+1}) = \psi(\mathbf{x}, \lambda_{n+1}) \quad \forall \mathbf{x} \in \Omega \\ \nabla \psi_\tau(\mathbf{x}, \lambda_{n+1}) \cdot \mathbf{n} = \mathbf{0} \quad \forall \mathbf{x} \in \partial\Omega \\ \psi(\mathbf{x}, \lambda_{n+1}) := - \left((1 - \beta) \frac{\partial F(\chi_{n+1}, \mathbf{x})}{\partial \chi} + \lambda_{n+1} \right) \end{array} \right. \quad (a) \\ \chi_{n+1}(\mathbf{x}) = \mathcal{H}_\beta[\psi_\tau(\chi_{n+1}, \mathbf{x}, \lambda_{n+1})] \quad (b) \\ \mathcal{C}(\chi_{n+1}, t_{n+1}) \equiv t_{n+1} - \frac{|\Omega^-(\chi_{n+1})|}{|\Omega|} = 0 \quad (c) \end{array} \right. \quad (63)$$

Equations (63) define a discrete time-advancing problem providing the solution $(\chi_{n+1}(\mathbf{x}), \lambda_{n+1})$, at pseudo-time t_{n+1} , in terms of results at previous times (see figure A.6). Equations (63)-(a) are

¹²The time interval $[0, T]$ is subdivided into a number of *time-steps*, each one defining an independent optimization problem, with a sufficiently small length, Δt , so as to ensure that the solution of the problem, at the beginning of the time step, is close enough to the solution at its end; this helping the convergence of the solving iterative process.

associated to determination of the *topology*, χ_{n+1} , whereas solution of equation (63)-(c) provides the value of the *Lagrange multiplier* λ_{n+1} . Therefore, they can be numerically solved by means of an iterative algorithm at every time step. At time step $[t_n, t_{n+1}]$ the iterative problem to be solved is defined by the coupled system of equations involving as unknowns *the topological field*, $\chi_{n+1}(\mathbf{x})$, and the (spatially constant) *Lagrange multiplier*, λ_{n+1} .

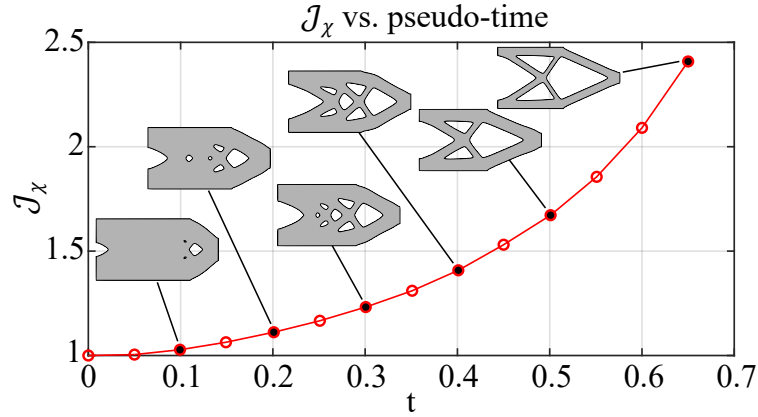


Figure A.6: Pseudo-time evolutionary analysis. Typical evolution of the cost function and topology vs. time.

A.7.1 Iterative solving strategy

The problem to be solved, at the representative iteration $(i + 1)$ of the considered time step $[t_n, t_{n+1}]$, can be then sketched as:

$$\left[\begin{array}{l} \text{Given } \chi_{n+1}^{(i)} : \Omega \rightarrow \{\beta, 1\} \\ \text{Solve } \begin{cases} \chi_{n+1}^{(i+1)} = \mathcal{F}(\chi_{n+1}^{(i)}, \lambda_{n+1}) & \forall \mathbf{x} \in \Omega \quad (\text{topology problem}) & (a) \\ \lambda_{n+1} = \mathcal{G}(\chi_{n+1}^{(i+1)}, \lambda_{n+1}) & (\text{restriction problem}) & (b) \end{cases} \\ \text{Until } \left\| \chi_{n+1}^{(i+1)} - \chi_{n+1}^{(i)} \right\|_{L^2(\Omega)} = \left[\int_{\Omega} \left(\chi_{n+1}^{(i+1)}(\mathbf{x}) - \chi_{n+1}^{(i)}(\mathbf{x}) \right)^2 d\Omega \right]^{\frac{1}{2}} \leq \text{Toler}_{\chi} \end{array} \right. \quad (64)$$

Notice that the *topology problem*, in equation (64)-(a), sketching equations (63)-(a) involves as unknown the *space field*, $\chi_{n+1}^{(i+1)}(\mathbf{x})$, which is iteratively updated, in terms of its value at the previous iteration, $\chi_{n+1}^{(i)}(\mathbf{x})$, until convergence is achieved according to the tolerance Toler_{χ} . On the contrary, the *restriction problem* in equation (64)-(b), corresponding to equation (63)-(c), which involves the scalar unknown λ_{n+1} , is *exactly enforced at every iteration* $(i + 1)$ of the time step. This goal is achieved via a specific method for resolution of scalar equations e.g.: a bisection algorithm. Details on the procedure are given in next sections.

Topology problem: cutting algorithm

The problem reads as follows

$$\left[\begin{array}{l} \text{Given } \chi^{(i)}(\mathbf{x}) \text{ (topology at the end of iteration "i")} \\ \text{Solve } \chi^{(i+1)}(\mathbf{x}) \left\{ \begin{array}{l} \xi_\tau(\chi^{(i)}, \mathbf{x}) := \text{solution of } \begin{cases} \xi_\tau(\chi^{(i)}, \mathbf{x}) - \epsilon^2 \Delta \xi_\tau(\chi^{(i)}, \mathbf{x}) = \xi(\chi^{(i)}, \mathbf{x}) & \forall \mathbf{x} \in \Omega \\ \nabla \xi_\tau(\chi^{(i)}, \mathbf{x}) \cdot \mathbf{n} = \mathbf{0} & \forall \mathbf{x} \in \partial\Omega \end{cases} \quad (a) \\ \psi_\tau(\chi^{(i)}, \mathbf{x}, \lambda) = \xi_\tau(\chi^{(i)}, \mathbf{x}) - \lambda \quad (b) \\ \chi^{(i+1)}(\mathbf{x}) = \mathcal{H}_\beta \left[\psi_\tau(\chi^{(i)}, \mathbf{x}, \lambda) \right] \quad (c) \end{array} \right. \\ \text{Until } \|\chi^{(i+1)} - \chi^{(i)}\| \leq \text{Toler}_\chi \end{array} \right. \quad (65)$$

where the Laplacian smoothing of variable $\xi_\tau(\chi^{(i)}, \mathbf{x})$, in equation (65)-(a), (from now on termed the *spatial energy distribution*), provides equivalent results¹³ to the smoothing of variable $\psi_\tau(\mathbf{x}, \lambda_{n+1})$ in equation (63)-(a).

Remark 7 *In view of equation (65)-(c), iteration $i + 1$ can be regarded as performing a spatial cut, at level λ , of the spatial energy distribution, $\xi_\tau(\chi^{(i)}(\mathbf{x}), \mathbf{x})$, to obtain the corresponding λ -contour (line/surface), $\Gamma^{(i+1)}$, defining the topological boundaries (see figure A.7) i.e.*

$$\left[\Gamma(\chi^{(i)}, \lambda) \right]^{(i+1)} := \left\{ \mathbf{x} \in \Omega ; \quad \xi_\tau(\chi^{(i)}(\mathbf{x}), \mathbf{x}) = \lambda \right\} \quad (66)$$

Therefore, equation (66) proves that, for the optimal topology solution corresponding to any of the sequential problems in equations (63), the material phase boundaries are, iso-energetic, λ -contours of the smoothed spatial energy distribution $\xi_\tau(\mathbf{x})$ ¹⁴.

From the result in equation (66), the *hard-phase* (matrix) domain, $|\Omega^+|(\lambda)$, and the *soft-phase* (inclusions) domain, $|\Omega^-|(\lambda)$, are finally obtained as (accordingly with equation (6))

$$\begin{aligned} \left(\Omega^+(\chi^{(i)}, \lambda) \right)^{(i+1)} &:= \left\{ \mathbf{x} \in \Omega ; \quad \xi_\tau(\chi^{(i)}(\mathbf{x}), \mathbf{x}) > \lambda \right\} \\ \left(\Omega^-(\chi^{(i)}, \lambda) \right)^{(i+1)} &:= \left\{ \mathbf{x} \in \Omega ; \quad \mathbf{x} \notin \left(\Omega^+ \right)^{(i+1)} \right\} \end{aligned} \quad (67)$$

and, finally, from equations (65), the updated characteristic function

$$\chi^{(i+1)}(\mathbf{x}) = \mathcal{H}_\beta \left[\xi_\tau(\chi^{(i)}(\mathbf{x}), \mathbf{x}) - \lambda \right] \quad (68)$$

can be calculated (see figure A.2). Calculations in equations (65) to (68) are repeated until convergence is achieved ($\|\chi^{(i+1)} - \chi^{(i)}\|_{L^2(\Omega)} \leq \text{Toler}_\chi$).

A.7.2 Lagrange multiplier resolution: bisection algorithm

The algorithm consists in determining, for the (i -th) iteration characteristic function, $\chi^{(i)}(\mathbf{x})$ and the corresponding spatial energy distribution, $\xi_\tau(\chi^{(i)}, \mathbf{x})$, the cutting level, λ , in equation (66), that fulfills the volume constraint (62)-(c), i.e.

$$\phi(\lambda) \equiv \mathcal{C}(\chi^{(i+1)}, \lambda, t) \equiv t - \frac{|\Omega^-(\chi^{(i+1)}, \lambda)|}{|\Omega|} = 0 \quad (69)$$

The bisection algorithm is based on the following stages:

¹³Since the spatially constant variable λ is not affected by the smoothing procedure.

¹⁴This concept is also retrieved in the context of regularized methods (SIMP) for the regularized domain Ω^{reg} , see [8].

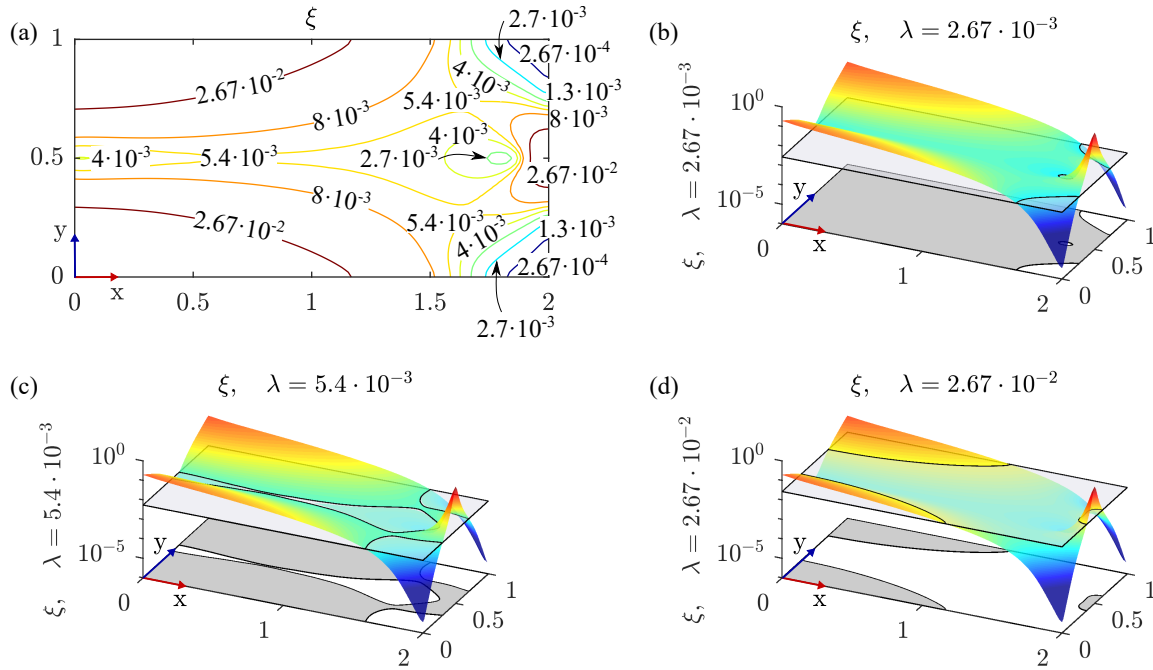


Figure A.7: Isoenergy (λ iso-level) contours of the *spatial energy distribution* ξ : (a) contour-lines of ξ ; (b)-(c)-(d) ξ iso-levels for different values of λ .

- 1) Explore the appropriate range of $\lambda \in \mathbb{R}$ and find in a sequence $\{0, \lambda^{(1)}, \dots, \lambda^{(j)}, \lambda^{(j+1)}\}$ a *bracket* $\{\lambda_+^{(j+1)}, \lambda_-^{(j)}\}$, for the sign change of function $\phi(\lambda^j)$, in equation (69):

$$\begin{aligned} \phi\left(\lambda_+^{(j+1)}\right) &\equiv t - \frac{|\Omega^-(\chi, \lambda^{(j+1)})|}{|\Omega|} ; & \phi\left(\lambda_-^{(j)}\right) &\equiv t - \frac{|\Omega^-(\chi, \lambda^{(j)})|}{|\Omega|} \\ \phi\left(\lambda_+^{(j+1)}\right) &> 0 ; & \phi\left(\lambda_-^{(j)}\right) &< 0 \end{aligned} \quad (70)$$

- 2) When the bracket is found, decrease the bracket's size by iteration and interpolation (*regula falsi method*) [39] until

$$\left\| \lambda_+^{(j+1)} - \lambda_-^{(j)} \right\| \leq \text{Toler}_\lambda \Rightarrow \lambda \leftarrow \lambda_+^{(j+1)} \quad (71)$$

or, equivalently,

$$\left| \phi\left(\lambda_+^{(j+1)}\right) \right| \leq \text{Toler}_c \quad (72)$$

Once the value of λ is determined, the topology domains $(\Omega^+)^{(i+1)}$ and $(\Omega^-)^{(i+1)}$ are computed, according to equations (67) and the new characteristic function, $\chi^{(i+1)}$, is obtained according to equation (68).

Remark 8 A specific feature of the proposed algorithm is that, unlike in alternative options (i.e. augmented Lagrangian methods), the restriction $\mathcal{C}(\chi)$, in equation (63)-(c) is not fulfilled only at the end (convergence) of the iterative process. Instead, that constraint is exactly fulfilled (up to a small tolerance, Toler_c) at every iteration "i" of the algorithm. This provides, in comparison with some alternative procedures¹⁵, additional control on the evolution of topologies along iterations, which translates into global algorithmic robustness.

¹⁵Like augmented Lagrangian methods, where λ is iteratively updated until convergence to the exact final value.

Algorithm initialization

As commented above, a relevant issue for convergence of the topology problem algorithm in equation (65), is the fact that the value of the unknown field at the beginning of the current time interval, $\chi_{n+1}^{(0)}(\mathbf{x})$, has to be *close enough* to the final one (converged) at the end of the time step ($\chi_{n+1}^{(converged)}(\mathbf{x})$).

In the pseudo-time sequential approach chosen here (see sections A.6 and A.7), this could be *conceptually* achieved by choosing a sufficiently small time-step length, $\Delta t = t_{n+1} - t_n$, which places the iterative values into the suitable range of convergence. However, the Δt -proportional distance, between consecutive solutions, requires that the algorithm initiates (i.e. at time $t = 0 \equiv t_0$), at a *solution* of the problem: i.e. fulfilling the equations of the algorithm¹⁶.

$$t_0 = 0 \rightarrow \begin{cases} \lambda_{t_0} = 0 & (a) \\ \mathcal{C}(\chi_{t_0}) = \frac{|\Omega^+(\chi_{t_0})|}{|\Omega|} = 1 \Rightarrow |\Omega^+(\chi_{t_0})| = |\Omega| \Rightarrow \chi_{t_0}(\mathbf{x}) = 1 \quad \forall \mathbf{x} \in \Omega & (b) \\ \xi_{t_0}(\mathbf{x}) - \lambda_{t_0} > 0 \quad \forall \mathbf{x} \in \Omega \Rightarrow \min_{\mathbf{x} \in \Omega} \xi_{t_0}(\mathbf{x}) \geq \lambda_{t_0} = 0 & (c) \end{cases} \quad (73)$$

where equations (73)-(a) and (73)-(b) state the initial conditions in terms of $\lambda = 0$, and a *full hard-phase* \mathfrak{M}^+ distribution for the initial design ($\Omega^+(\chi_{t_0}) = \Omega$; $\Omega^-(\chi_{t_0}) = \{\emptyset\}$). However, under these initial conditions, equation (73)-(c) is not automatically fulfilled in some problems: typically those in which the *initial energy*, ξ_{t_0} , is not intrinsically positive definite (i.e. $\exists \mathbf{x} \in \Omega; \xi(\mathbf{x}) < 0$). In these cases, convergence in the first time interval is not achievable (or robustly achievable) disregard the considered time-step size¹⁷ Δt . A remedy for this problem, is to perform a *constant shift*¹⁸, of value Δ_{shift} , of both unknown fields: $\xi(\chi(\mathbf{x}))$ (*only at the Ω^+ domain*) and λ i.e.

$$\Delta_{shift} = \min_{\mathbf{x} \in \Omega} \xi_{t_0}(\mathbf{x}) \rightarrow \begin{cases} \hat{\xi}_{t_n}^{(i)}(\mathbf{x}) = \xi_{t_n}(\mathbf{x}) - \Delta_{shift} & \forall \mathbf{x} \in (\Omega^+)^{(i)} & (a) \\ \hat{\xi}_{t_n}^{(i)}(\mathbf{x}) = \xi_{t_n}(\mathbf{x}) & \forall \mathbf{x} \in (\Omega^-)^{(i)} & (b) \\ \hat{\lambda}_{t_n}^{(i)} = \lambda_{t_n} - \Delta_{shift} & & (c) \end{cases} \quad \forall i \quad \forall t_n \quad (74)$$

In addition, a *normalization* of the resulting energy field, $\xi(\mathbf{x}^{(i)})$, is done, in terms of a positive factor, $\Delta_{norm} > 0$ (again constant for all iterations and time steps), in order to keep its value inside convenient ranges, i.e.

$$\Delta_{norm} = \left| \max_{\mathbf{x} \in \Omega} \xi_{t_0}(\mathbf{x}) - \min_{\mathbf{x} \in \Omega} \xi_{t_0}(\mathbf{x}) \right| \rightarrow \begin{cases} \hat{\xi}_{t_n}^{(i)}(\mathbf{x}) = \frac{\xi_{t_n}(\mathbf{x}) - \Delta_{shift}}{\Delta_{norm}} & \forall \mathbf{x} \in (\Omega^+)^{(i)} & (a) \\ \hat{\xi}_{t_n}^{(i)}(\mathbf{x}) = \frac{\xi_{t_n}(\mathbf{x})}{\Delta_{norm}} & \forall \mathbf{x} \in (\Omega^-)^{(i)} & (b) \\ \hat{\lambda}_{t_n}^{(i)} = \frac{\lambda_{t_n} - \Delta_{shift}}{\Delta_{norm}} & & (c) \end{cases} \quad \forall i \quad \forall t_n \quad (75)$$

Therefore, the topology is updated, according to the cutting algorithm in section A.7.1, in terms of the values of the corrected fields, $\hat{\xi}_{\tau, t_n}^{(i)}(\mathbf{x}) - \hat{\lambda}_{t_n}^{(i)}$, at the domain, Ω^+ , instead of the original ones, $\xi_{\tau, t_n}^{(i)}(\mathbf{x}) - \lambda_{t_n}^{(i)}$, (see equations (65) to (67)):

$$\begin{aligned} (\Omega_{t_n}^+)^{(i+1)} &:= \left\{ \mathbf{x} \in \Omega; \psi_{t_n} := \hat{\xi}_{\tau, t_n}^{(i)}(\mathbf{x}) - \hat{\lambda}_{t_n}^{(i)} > 0 \right\} & (a) \\ (\Omega_{t_n}^-)^{(i+1)} &:= \left\{ \mathbf{x} \in \Omega; \mathbf{x} \notin [\Omega_{t_n}^+]^{(i+1)} \right\} & (b) \end{aligned} \quad (76)$$

¹⁶Here it is assumed that the algorithm is initiated at a *full hard-phase* \mathfrak{M}^+ design ($\Omega_{t_0}^+ = \Omega$).

¹⁷Even for $\Delta t = 0$.

¹⁸Constant for all time-steps and iterations of the optimization algorithm.

where $\hat{\xi}_{\tau,t_n}^{(i)}(\mathbf{x})$ is the result of applying the Laplacian smoothing, in equations (65)-(a), to the normalized energy $\hat{\xi}_{t_n}^{(i)}(\mathbf{x})$ in equations (75).

Remark 9 Notice that the shifted and normalized fields, $\hat{\xi}_{t_n}^{(i)}(\mathbf{x})$ and $\hat{\lambda}_{t_n}^{(i)}$, in equation (75) fulfill the following properties:

- a) By construction, at the initial time t_0 , $\min_{\mathbf{x} \in \Omega} \hat{\xi}_{t_0}(\mathbf{x}) = 0$. Therefore, if $\Omega_{t_0}^+ \equiv \Omega$, equations (73) are fulfilled for $\xi_{t_0} \equiv \hat{\xi}_{t_0}$ and $\lambda_{t_0} \equiv \hat{\lambda}_{t_0} = 0$.
- b) Since the shift, Δ_{shift} , is applied to both fields, $\xi_{t_n}^{(i)}(\mathbf{x})$ and $\lambda_{t_n}^{(i)}$, their difference, $\psi_{t_n}^{(i)} \equiv \xi_{t_n}^{(i)}(\mathbf{x}) - \lambda_{t_n}^{(i)}$, and the corresponding topology, $\chi_{t_n}^{(i)} = \mathcal{H}_\beta(\psi_{t_n}^{(i)})$, is not affected by that shift. Also the normalization in equation (75) does not affect neither the sign of $\psi_{t_n}^{(i)}$ nor the topology.
- c) The Laplacian smoothing, $\hat{\xi}_{t_n}^{(i)} \leftarrow \hat{\xi}_{\tau,t_n}^{(i)}$, is neither affected by the initialization operations¹⁹.
- d) In consequence, if the discrimination function $\psi_{t_n}^{(i)}$, in equation (76)-(a), is applied in terms of the shifted and normalized entities, $\hat{\xi}_{\tau,t_n}^{(i)}(\mathbf{x})$ and $\hat{\lambda}_{t_n}^{(i)}$ at Ω^+ (see equation (76)), the topology, at convergence, is not affected. However, the robustness of the iterative process is remarkably increased.

A.7.3 Finite element implementation. Numerical aspects.

In the examples presented in section A.10, the design space, Ω , has been discretized in uniform structured meshes (labeled $M_i, i = 1, 2, \dots$) made of regular hexahedra, i.e. elements, e , occupying the domain $\Omega^{(e)} \subset \Omega$, with typical size $h^{(e)}$. These finite element meshes have been used both for solving the state bi-material elastic problem, in equation (9), and for obtaining the geometrical data (typically the volume of the soft-phase Ω^-) necessary for the cutting and bisection algorithm in sections A.7.1 and A.7.2. In general, the integration (Gauss) points of regular elements have been used as *sampling points*, \mathbf{x}_i , to evaluate the necessary data i.e. *characteristic function* $\chi(\mathbf{x}_i)$, *discrimination function* $\psi(\chi, \mathbf{x}_i)$, etc.

Topology properties determination. Modified marching cubes strategy

Determination of the volumes, Ω^+ or Ω^- , in the cutting algorithm (equation (67), see also figure A.7) has been performed via the classic strategy of *marching cubes* [28]. In appendix A.A, additional details on the method are provided.

Bi-material elements. Three field mixed displacement-strain-stress formulation

A specific issue arises in the treatment of the finite element formulation of *bi-material elements*, i.e. those elements containing both the hard-phase, \mathfrak{M}^+ , and soft-phase, \mathfrak{M}^- . They are identified during the marching cubes strategy and the subset of bi-material elements $\Omega^{(+,-)} \subset \Omega$ is determined, as well as the portions $\Omega^{(e,+)} \subset \Omega^{(e)}$ and $\Omega^{(e,-)} \subset \Omega^{(e)}$ ($\Omega^{(e,+)} \cup \Omega^{(e,-)} = \Omega^{(e)}$) containing hard and soft material phases in every element (e).

$$\begin{cases} \Omega^{(e,+)} := \{\mathbf{x} \in \Omega^{(e)} ; \mathbf{x} \in \Omega^+\} \\ \Omega^{(e,-)} := \{\mathbf{x} \in \Omega^{(e)} ; \mathbf{x} \in \Omega^-\} \\ \Omega^{(+,-)} := \left\{ \bigcup_{e=1}^{e=n_{elem}} \left(\Omega^{(e,+)} \cup \Omega^{(e,-)} \right) \right\} \end{cases} \quad (77)$$

Details on the derivation of this formulation are given in Appendix A.B.

¹⁹Except for the error associated to the (assumed small) parameter ϵ in the smoothing procedure (see equations (65)).

A.8 Structural compliance problems

Let us now specify the equations for the *minimal compliance* topological optimization in a linear elastic problem, e.g.:

$$\begin{cases} \chi(\mathbf{x}, t) = \underset{\chi}{\operatorname{argmin}} \mathcal{J}(\mathbf{u}_\chi(\mathbf{x}, t)) = \underset{\chi}{\operatorname{argmin}} l(\mathbf{u}_\chi(\mathbf{x}, t)) & (a) \\ \text{subject to: } \mathcal{C}(\chi, t) := t - \frac{|\Omega^-|(\chi)}{|\Omega|} = 0; \quad t \in [0, 1] & (b) \end{cases} \quad (78)$$

The problem above, belongs to the class of problems considered in equation (62) with

$$\begin{aligned} \mathcal{J}(\mathbf{u}_\chi) = l(\mathbf{u}_\chi) &= \int_{\Omega} \mathbf{b} \cdot \mathbf{u}_\chi \, d\Omega + \int_{\partial\sigma\Omega} \mathbf{t}^* \cdot \mathbf{u}_\chi \, d\Gamma = a_\chi(\mathbf{u}_\chi, \mathbf{u}_\chi) = \\ &= \int_{\Omega} \boldsymbol{\varepsilon}(\mathbf{u}_\chi) : \mathbb{C}_\chi : \boldsymbol{\varepsilon}(\mathbf{u}_\chi) \, d\Omega = \int_{\Omega} 2\mathcal{U}_\chi \, d\Omega \end{aligned} \quad (79)$$

where equations (13)-(d)-(e) have been considered for $\mathbf{w} \equiv \mathbf{u}$, and \mathcal{U}_χ can be identified as the *actual elastic energy density* ($\mathcal{U}_\chi = \frac{1}{2}\boldsymbol{\varepsilon} : \mathbb{C}_\chi : \boldsymbol{\varepsilon}$). Comparing equations (79) and (44) we can identify

$$F(\chi, \mathbf{x}) \equiv \boldsymbol{\varepsilon}(\mathbf{u}_\chi(\mathbf{x})) : \mathbb{C}_\chi : \boldsymbol{\varepsilon}(\mathbf{u}_\chi(\mathbf{x})) = 2\mathcal{U}_\chi(\mathbf{x}) \quad (80)$$

The corresponding finite element discretization counterpart of the problem in equation (78) reads

$$\begin{cases} \chi(\mathbf{x}, t) = \underset{\chi}{\operatorname{argmin}} \mathcal{J}^{(h)}(\mathbf{d}_\chi(t)) = \underset{\chi}{\operatorname{argmin}} \mathbf{f}^T \mathbf{d}_\chi(t) & (a) \\ \text{subject to: } \mathcal{C}(\chi, t) := t - \frac{|\Omega^-|(\chi)}{|\Omega|} = 0; \quad t \in [0, 1] & (b) \end{cases} \quad (81)$$

where h stands for the typical size of the finite element mesh, and the term $\mathbf{f}^T \mathbf{d}_\chi(t)$, in equation (81)-(a) corresponds to the structural compliance value.

A.8.1 Cost function topological sensitivity

The *adjoint equation method* [12] for sensitivity analysis is mimicked here for the case of RTD. The goal is to compute the variational topological derivative (RTD) of the cost-function²⁰, $\mathcal{J}^{(h)}(\mathbf{d}_\chi)$, in equation (81)-(a), without explicitly computing the sensitivity of the nodal displacement field ($\partial\mathbf{d}_\chi/\partial\chi$). The sensitivity of $\mathcal{J}^{(h)}(\chi)$ can be, then, obtained through the following steps:

1. Rephrase the cost function accounting for the state equation (15)-(a)

$$\mathcal{J}^{(h)}(\chi) = \mathbf{f}^T \mathbf{d}_\chi = \mathbf{f}^T \mathbf{d}_\chi - \mathbf{w}^T \underbrace{(\mathbb{K}_\chi \mathbf{d}_\chi - \mathbf{f})}_{= \mathbf{0}} \quad (82)$$

where \mathbf{w} is a vector to be chosen.

2. Compute the RTD of the equation (82)

$$\frac{\delta \mathcal{J}^{(h)}(\chi)}{\delta \chi}(\hat{\mathbf{x}}) = (\mathbf{f}^T - \mathbf{w}^T \mathbb{K}_\chi) \frac{\delta \mathbf{d}_\chi}{\delta \chi}(\hat{\mathbf{x}}) - \mathbf{w}^T \frac{\delta \mathbb{K}_\chi}{\delta \chi}(\hat{\mathbf{x}}) \mathbf{d}_\chi \quad (83)$$

3. Choose $\mathbf{w} \equiv \mathbf{d}_\chi$ and replace it into equation (83)

$$\frac{\delta \mathcal{J}^{(h)}(\chi)}{\delta \chi}(\hat{\mathbf{x}}) = \underbrace{(\mathbf{f}^T - \mathbf{d}_\chi^T \mathbb{K}_\chi)}_{= \mathbf{0}} \frac{\delta \mathbf{d}_\chi}{\delta \chi}(\hat{\mathbf{x}}) - \mathbf{d}_\chi^T \frac{\delta \mathbb{K}_\chi}{\delta \chi}(\hat{\mathbf{x}}) \mathbf{d}_\chi = - \left[\mathbf{d}_\chi^T \frac{\delta \mathbb{K}_\chi}{\delta \chi}(\mathbf{x}) \mathbf{d}_\chi \right]_{\mathbf{x} \equiv \hat{\mathbf{x}}} \quad (84)$$

²⁰Omitting time dependencies.

where equations (15) and the symmetry of \mathbb{K}_χ ($\mathbb{K}_\chi = \mathbb{K}_\chi^\top$) have been considered, yielding the final result

$$\begin{aligned} \frac{\delta \mathcal{J}^{(h)}(\chi)}{\delta \chi}(\hat{\mathbf{x}}) &= - \underbrace{\mathbf{d}_\chi^\top \mathbf{B}^\top(\hat{\mathbf{x}})}_{\boldsymbol{\varepsilon}_\chi^\top(\hat{\mathbf{x}})} \frac{\partial \mathbb{D}_\chi}{\partial \chi}(\hat{\mathbf{x}}) \underbrace{\mathbf{B}(\hat{\mathbf{x}}) \mathbf{d}_\chi}_{\boldsymbol{\varepsilon}_\chi(\hat{\mathbf{x}})} \Delta \chi(\hat{\mathbf{x}}) = - \left[\boldsymbol{\varepsilon}_\chi^\top(\mathbf{x}) \frac{\partial \mathbb{D}_\chi}{\partial \chi} \boldsymbol{\varepsilon}_\chi(\mathbf{x}) \right]_{\mathbf{x}=\hat{\mathbf{x}}} \Delta \chi(\hat{\mathbf{x}}) = \\ &= - [m\chi^{m-1} \boldsymbol{\varepsilon}_\chi^\top(\mathbf{x}) \mathbb{D} \boldsymbol{\varepsilon}_\chi(\mathbf{x})]_{\mathbf{x}=\hat{\mathbf{x}}} \Delta \chi(\hat{\mathbf{x}}) \end{aligned} \quad (85)$$

where the result, in matrix form, in equation (11) has been considered. The result in equation (85) can be then written as

$$\begin{cases} \frac{\delta(\mathbf{f}^\top \mathbf{d}_\chi)}{\delta \chi} = \frac{\delta \mathcal{J}^{(h)}(\mathbf{u}_\chi)}{\delta \chi}(\hat{\mathbf{x}}) = - [m\chi^{m-1} \boldsymbol{\varepsilon}^\top(\mathbf{d}_\chi) \mathbb{D} : \boldsymbol{\varepsilon}(\mathbf{d}_\chi)]_{\mathbf{x}=\hat{\mathbf{x}}} \Delta \chi(\hat{\mathbf{x}}) = \\ \hspace{15em} = -2m(\chi(\hat{\mathbf{x}}))^{m-1} \bar{\mathcal{U}}(\hat{\mathbf{x}}) \Delta \chi(\hat{\mathbf{x}}) \end{cases} \quad (a) \quad (86)$$

$$\bar{\mathcal{U}}(\hat{\mathbf{x}}) = \frac{1}{2} (\boldsymbol{\varepsilon}^\top(\mathbf{d}_\chi) \mathbb{D} \boldsymbol{\varepsilon}(\mathbf{d}_\chi))(\hat{\mathbf{x}}) \quad (b)$$

where $\bar{\mathcal{U}}_\chi(\hat{\mathbf{x}})$ is the *nominal elastic energy density*²¹. The result in equation (86) is close to the one obtained for the sensitivity in the (regularized/smoothed) method SIMP [8], except for the *material exchange term* $\Delta \chi(\hat{\mathbf{x}})$ (see equation (19)).

Now the original compliance functional $\mathcal{J}^{(h)}$, in equation (81)-(a) can be extended to account for the restriction in equation (81)-(b). Following the methodology in section A.4, and accounting for the RTD results in Table (A.1) one arrives to

Box II: Topological optimization for mean compliance problems

Problem:

$$\begin{cases} \chi^* = \underset{\chi}{\operatorname{argmin}} \mathcal{J}^{(h)}(\chi) := \mathbf{f}^\top \mathbf{d}_\chi \\ s.t. \quad \mathcal{C}(\chi) \equiv |\Omega^+(\chi)| - \bar{V} = 0 \end{cases} \quad (a)$$

$$\text{Lagrangian: } \mathcal{L}(\chi, \lambda) = \mathcal{J}^{(h)}(\chi) + \lambda \mathcal{C}(\chi) \quad (b)$$

Optimality criterion:

$$\begin{cases} \frac{\delta \mathcal{L}(\chi, \lambda)}{\delta \chi}(\mathbf{x}) = -2m\chi^{m-1}(\mathbf{x}) \bar{\mathcal{U}}(\mathbf{x}) \Delta \chi(\mathbf{x}) + \lambda \operatorname{sgn}(\Delta \chi(\mathbf{x})) > 0 \quad \forall \mathbf{x} \in \Omega \\ \mathcal{C}(\chi) = 0 \end{cases} \quad (c)$$

Closed-form solution:

$$\begin{cases} \psi_\chi(\mathbf{x}, \lambda) := 2m(1 - \beta)\chi^{m-1}(\mathbf{x}) \bar{\mathcal{U}}(\mathbf{x}) - \lambda; \quad \bar{\mathcal{U}}(\hat{\mathbf{x}}) = \frac{1}{2} (\boldsymbol{\varepsilon}^\top(\mathbf{d}_\chi) \mathbb{D} \boldsymbol{\varepsilon}(\mathbf{d}_\chi))(\hat{\mathbf{x}}) \geq 0 \\ \left\{ \begin{array}{l} \chi(\mathbf{x}, \lambda) = \mathcal{H}_\beta[\psi_\chi(\mathbf{x}, \lambda)] \rightarrow \chi_\lambda(\mathbf{x}) \quad (\mathbf{d-1}) \\ \mathcal{C}(\chi_\lambda, \lambda) = 0 \quad (\mathbf{d-2}) \end{array} \right\} \rightarrow \lambda^* \rightarrow \chi^*(\mathbf{x}) =: \chi_{\lambda^*}(\mathbf{x}) \end{cases} \quad (d)$$

Topology:

$$\begin{cases} \Omega^+(\chi) := \{\mathbf{x} \in \Omega; \quad \psi_\chi(\mathbf{x}, \lambda) > 0\} \\ \Omega^-(\chi) := \{\mathbf{x} \in \Omega; \quad \mathbf{x} \notin \Omega^+\} \\ \Gamma(\chi) := \{\mathbf{x} \in \Omega; \quad \psi_\chi(\mathbf{x}, \lambda) = 0\} \end{cases} \quad (87)$$

²¹Notice the difference of the *nominal elastic energy density* $\bar{\mathcal{U}}(\hat{\mathbf{x}}) = \frac{1}{2} (\boldsymbol{\varepsilon}^\top(\mathbf{d}_\chi) \mathbb{D} \boldsymbol{\varepsilon}(\mathbf{d}_\chi))(\hat{\mathbf{x}})$ (in terms of \mathbb{D}), in equation (86)-(b), and the *actual elastic energy density*, $\mathcal{U}(\hat{\mathbf{x}}) = \frac{1}{2} (\boldsymbol{\varepsilon}^\top(\mathbf{d}_\chi) \mathbb{D}_\chi \boldsymbol{\varepsilon}(\mathbf{d}_\chi))(\hat{\mathbf{x}})$ (in terms of $\mathbb{D}_\chi = \chi^m \mathbb{D}$).

A.9 Compliant mechanisms

We consider now the optimal design of the compliant mechanism sketched in figure A.8. The goal is to design the topology of a gripper, so as to maximize the compressive displacement of a spring placed at *port (out)*, with stiffness \mathbf{K}_{out} (standing for the stiffness of the gripped object), under the action of a force acting on *port (in)*, \mathbf{f} , also applied by means of spring of stiffness \mathbf{K}_{in} (see figure A.8) [44, 29, 21]. Therefore the structural system is constituted by the gripper and the two springs (at ports *in* and *out*). In the context of a finite element discretization, like in section A.3.3, the problem is expressed as

$$\begin{cases} \min_{\chi} \mathcal{J}^{(h)}(\mathbf{d}_{\chi}) = -\mathbf{d}_{\chi}^T \mathbf{1}_{\text{vert}} & (a) \\ \text{subject to : } C(\chi, t) := t - \frac{|\Omega^{-}|(\chi)}{|\Omega|} = 0 ; \quad t \in [0, 1] & (b) \end{cases} \quad (88)$$

where, in equation (88)-(a), $\mathbf{1}_{\text{vert}}$ stands for that nodal vector force corresponding to uniform vertical components (*in the spring stretching sense*) acting on the gripper jaws²².

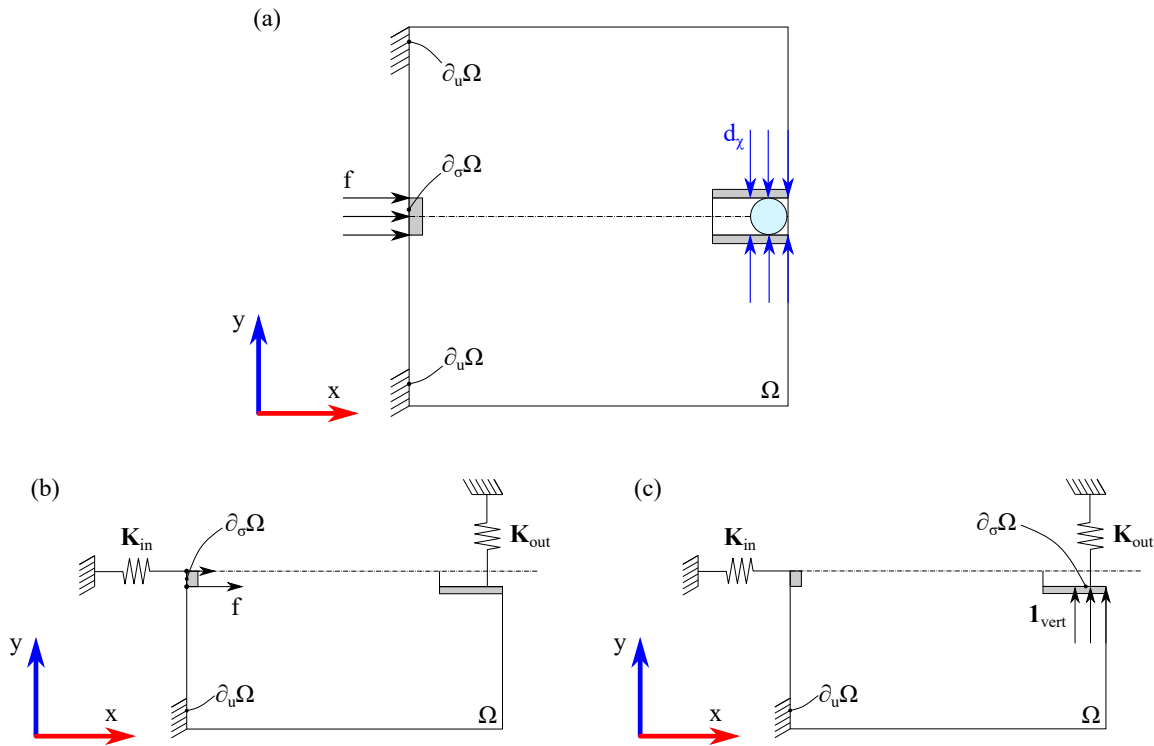


Figure A.8: Compliant mechanism: (a) problem setting, (b) system (1) (half domain), (c) system (2) (half domain).

The *original elastic system (1)* is supplemented with an *auxiliary elastic system (2)*, subject only to the forces $\mathbf{1}_{\text{vert}}$ (see figure A.8). Both of them are ruled by the elastic problem in equations (15), with the same stiffness matrix \mathbb{K}_{χ} and *different actions*, with solutions $\mathbf{d}_{\chi}^{(1)}$ and $\mathbf{d}_{\chi}^{(2)}$, respectively, i.e.:

$$\begin{cases} \mathbb{K} \mathbf{d}_{\chi}^{(1)} = \mathbf{f} ; \quad \mathbf{d}_{\chi} = \mathbf{d}_{\chi}^{(1)} & (a) \\ \mathbb{K} \mathbf{d}_{\chi}^{(2)} = \mathbf{1}_{\text{vert}} & (b) \end{cases} \quad (89)$$

²²Therefore, its components are zero everywhere excepting at the gripper jaws nodes.

Standard algebraic manipulations allow replacing the cost function in equation (88)-(a) by

$$\mathcal{J}^{(h)}(\mathbf{u}_\chi) \equiv - \int_{\Omega} \boldsymbol{\varepsilon}(\mathbf{d}_\chi^{(1)}) : \mathbb{C}_\chi : \boldsymbol{\varepsilon}(\mathbf{d}_\chi^{(2)}) d\Omega = - \int_{\Omega} 2\mathcal{U}_\chi(\mathbf{x}) d\Omega \quad (90)$$

where, again, \mathcal{U}_χ is defined as a *pseudo elastic energy* of the combined system.

$$\begin{cases} \mathcal{U}_\chi(\mathbf{x}) = \frac{1}{2} \boldsymbol{\varepsilon}^T(\mathbf{d}_\chi^{(1)}(\mathbf{x})) \mathbb{D}_\chi \boldsymbol{\varepsilon}(\mathbf{d}_\chi^{(2)}(\mathbf{x})) \equiv \frac{1}{2} \left(\boldsymbol{\varepsilon}_\chi^{(1)}(\mathbf{x}) \right)^T \mathbb{D}_\chi \boldsymbol{\varepsilon}_\chi^{(2)}(\mathbf{x}) \\ \boldsymbol{\varepsilon}(\mathbf{d}_\chi^{(1)}(\mathbf{x})) \equiv \boldsymbol{\varepsilon}_\chi^{(1)}(\mathbf{x}) = \mathbf{B}(\mathbf{x}) \mathbf{d}_\chi^{(1)}; \quad \boldsymbol{\varepsilon}(\mathbf{d}_\chi^{(2)}(\mathbf{x})) \equiv \boldsymbol{\varepsilon}_\chi^{(2)}(\mathbf{x}) = \mathbf{B}(\mathbf{x}) \mathbf{d}_\chi^{(2)} \end{cases} \quad (91)$$

A.9.1 Topological sensitivity

The sensitivity of $\mathcal{J}^{(h)}(\chi)$ is then obtained through the following steps

1. Rephrase the cost function accounting for the state equation (89)-(a) (adjoint equation method)

$$\mathcal{J}^{(h)}(\chi) = -\mathbf{1}_{\text{vert}}^T \mathbf{d}_\chi = -\mathbf{1}_{\text{vert}}^T \mathbf{d}_\chi^{(1)} = -\mathbf{1}_{\text{vert}}^T \mathbf{d}_\chi^{(1)} + \underbrace{\mathbf{w}^T \left(\mathbb{K}_\chi \mathbf{d}_\chi^{(1)} - \mathbf{f} \right)}_{= \mathbf{0}} \quad (92)$$

where \mathbf{w} is a vector to be chosen.

2. Compute the RTD of the equation (92)

$$\frac{\delta \mathcal{J}^{(h)}(\chi)}{\delta \chi}(\hat{\mathbf{x}}) = - \left(\mathbf{1}_{\text{vert}}^T - \mathbf{w}^T \mathbb{K}_\chi \right) \frac{\delta \mathbf{d}_\chi^{(1)}}{\delta \chi}(\hat{\mathbf{x}}) + \mathbf{w}^T \frac{\delta \mathbb{K}_\chi}{\delta \chi}(\hat{\mathbf{x}}) \mathbf{d}_\chi^{(1)} \quad (93)$$

3. Choose $\mathbf{w} \equiv \mathbf{d}_\chi^{(2)}$ and replace it into equation (93)

$$\begin{aligned} \frac{\delta \mathcal{J}^{(h)}(\chi)}{\delta \chi}(\hat{\mathbf{x}}) &= - \underbrace{\left(\mathbf{1}_{\text{vert}}^T - \left(\mathbf{d}_\chi^{(2)} \right)^T \mathbb{K}_\chi \right)}_{= \mathbf{0}} \frac{\delta \mathbf{d}_\chi^{(1)}}{\delta \chi}(\hat{\mathbf{x}}) + \left(\mathbf{d}_\chi^{(2)} \right)^T \frac{\delta \mathbb{K}_\chi}{\delta \chi}(\hat{\mathbf{x}}) \mathbf{d}_\chi^{(1)} = \\ &= \left(\mathbf{d}_\chi^{(1)} \right)^T \frac{\delta \mathbb{K}_\chi}{\delta \chi}(\hat{\mathbf{x}}) \mathbf{d}_\chi^{(2)} \end{aligned} \quad (94)$$

where equation (89)-(b) and the symmetry of \mathbb{K} ($\mathbb{K} = \mathbb{K}^T$) have been considered, yielding the final result

$$\begin{aligned} \frac{\delta \left(-\mathbf{1}_{\text{vert}}^T \mathbf{d}_\chi \right)}{\delta \chi}(\hat{\mathbf{x}}) &= \frac{\delta \mathcal{J}^{(h)}(\chi)}{\delta \chi}(\hat{\mathbf{x}}) = \underbrace{\left(\mathbf{d}_\chi^{(1)} \right)^T \mathbf{B}^T(\hat{\mathbf{x}})}_{\left(\boldsymbol{\varepsilon}_\chi^{(1)} \right)^T(\hat{\mathbf{x}})} \frac{\delta \mathbb{D}_\chi}{\delta \chi}(\hat{\mathbf{x}}) \underbrace{\mathbf{B}(\hat{\mathbf{x}}) \mathbf{d}_\chi^{(2)}}_{\boldsymbol{\varepsilon}_\chi^{(2)}(\hat{\mathbf{x}})} = \left[\left(\boldsymbol{\varepsilon}_\chi^{(1)} \right)^T \frac{\delta \mathbb{D}_\chi}{\delta \chi} \boldsymbol{\varepsilon}_\chi^{(2)} \right]_{\mathbf{x}=\hat{\mathbf{x}}} = \\ &= \left[m \chi^{m-1} \left(\boldsymbol{\varepsilon}_\chi^{(1)} \right)^T \mathbb{D} \boldsymbol{\varepsilon}_\chi^{(2)} \right]_{\mathbf{x}=\hat{\mathbf{x}}} \Delta \chi(\hat{\mathbf{x}}) = 2m \left(\chi(\hat{\mathbf{x}}) \right)^{m-1} \bar{\mathcal{U}}(\hat{\mathbf{x}}) \Delta \chi(\hat{\mathbf{x}}) \end{aligned} \quad (95)$$

where equations (15)-(b) ($\mathbb{D}_\chi = \chi^m \mathbb{D}$) has been considered. From equation (95) the *nominal pseudo elastic strain energy density* of the combined system, $\bar{\mathcal{U}}(\mathbf{x})$ ²³, is defined as

$$\bar{\mathcal{U}}(\hat{\mathbf{x}}) := \frac{1}{2} \left(\boldsymbol{\varepsilon}_\chi^{(1)}(\hat{\mathbf{x}}) \right)^T \mathbb{D} \boldsymbol{\varepsilon}_\chi^{(2)}(\hat{\mathbf{x}}) \quad (96)$$

A.9.2 Closed-form solution

Following the methodology in section A.4, and accounting for the RTD results in table A.1, one arrives to

²³Notice that, unlike in equation (86)-(b), for the mean structural compliance problem, now $\bar{\mathcal{U}}(\hat{\mathbf{x}})$ may be positive or negative. This makes a substantial difference in the sign of the RTD in equation (95).

Box III: Topological optimization of compliant mechanisms

Problem:

$$\begin{cases} \min_{\chi} \mathcal{J}^{(h)}(\chi) = -\mathbf{d}_{\chi}^T \mathbf{1}_{\text{vert}} & \text{(a-1)} \\ s.t. \quad \mathcal{C}(\chi) \equiv |\Omega^+(\chi)| - \bar{V} = 0 & \text{(a-2)} \end{cases} \quad (a)$$

$$\text{Lagrangian: } \mathcal{L}(\chi, \lambda) = \mathcal{J}^{(h)}(\chi) + \lambda \mathcal{C}(\chi) \quad (b)$$

Optimality criterion:

$$\begin{cases} \frac{\delta \mathcal{L}(\chi, \lambda)}{\delta \chi}(\mathbf{x}) = 2m\chi^{m-1}(\mathbf{x})\bar{U}(\mathbf{x})\Delta\chi(\mathbf{x}) + \lambda \text{sign}(\Delta\chi(\mathbf{x})) \quad \forall \mathbf{x} \in \Omega \\ \mathcal{C}(\chi) = 0 \end{cases} \quad (c)$$

Closed-form solution:

$$\begin{cases} \psi_{\chi}(\mathbf{x}, \lambda) := -(1 - \beta)2m\chi^{m-1}(\mathbf{x})\bar{U}(\mathbf{x}) - \lambda; \quad \bar{U}(\mathbf{x}) := \frac{1}{2} \left(\boldsymbol{\varepsilon}_{\chi}^{(1)}(\mathbf{x}) \right)^T \mathbb{D} \boldsymbol{\varepsilon}_{\chi}^{(2)}(\mathbf{x}) \\ \left\{ \begin{array}{l} \chi(\mathbf{x}, \lambda) = \mathcal{H}_{\beta}[\psi_{\chi}(\mathbf{x}, \lambda)] \rightarrow \chi_{\lambda}(\mathbf{x}) \quad \text{(d-1)} \\ \mathcal{C}(\chi_{\lambda}, \lambda) = 0 \quad \text{(d-2)} \end{array} \right\} \rightarrow \lambda^* \rightarrow \chi^*(\mathbf{x}) =: \chi_{\lambda^*}(\mathbf{x}) \end{cases} \quad (d)$$

Topology:

$$\begin{cases} \Omega^+(\chi) := \{\mathbf{x} \in \Omega; \quad \psi_{\chi}(\mathbf{x}, \lambda) > 0\} \\ \Omega^-(\chi) := \{\mathbf{x} \in \Omega; \quad \mathbf{x} \notin \Omega^+\} \\ \Gamma(\chi) := \{\mathbf{x} \in \Omega; \quad \psi_{\chi}(\mathbf{x}, \lambda) = 0\} \end{cases} \quad (97)$$

A.10 Representative numerical simulations

In the following a set of 3D numerical simulations are presented, in order to display the performance of the proposed approach. Unless it is differently indicated, the following material properties for the isotropic elastic material are considered:

$$\begin{aligned} \text{Young modulus } E &= 210 \text{ GPa}; \text{ Poisson ratio } \nu = 0.3; \text{ Stiffness contrast factor } \alpha = 1.0 \cdot 10^{-6} \\ \text{Stiffness contrast exponent } m &= 5 \text{ (see eq. (11))} \Rightarrow \text{Relaxation factor } \beta = \alpha^{\frac{1}{m}} = 6.3 \cdot 10^{-2} \end{aligned} \quad (98)$$

The following additional algorithmic data used for running the proposed algorithm is

$$\begin{aligned} \text{Tolerance error for topology} & \quad Tol_{\chi} = 10^{-1} \\ \text{Tolerance error for Lagrange multiplier} & \quad Tol_{\lambda} = 10^{-1} \\ \text{Tolerance error for bisection} & \quad Tol_{\mathcal{C}} = 10^{-5} \end{aligned} \quad (99)$$

A.10.1 Mean compliance optimization. Cantilever beam.

The 3D design domain, in figure A.9, is used. A first mesh, M1, (made of 432000 bi-linear hexahedral finite elements), displayed in figure A.9-(b), is used to mesh one-half of the design domain Ω (see figure A.9-(a)). The mean compliance design of the structure is done for the distributed loading forces at the right, lower, boundary of the design domain (see figure A.9-(d)).

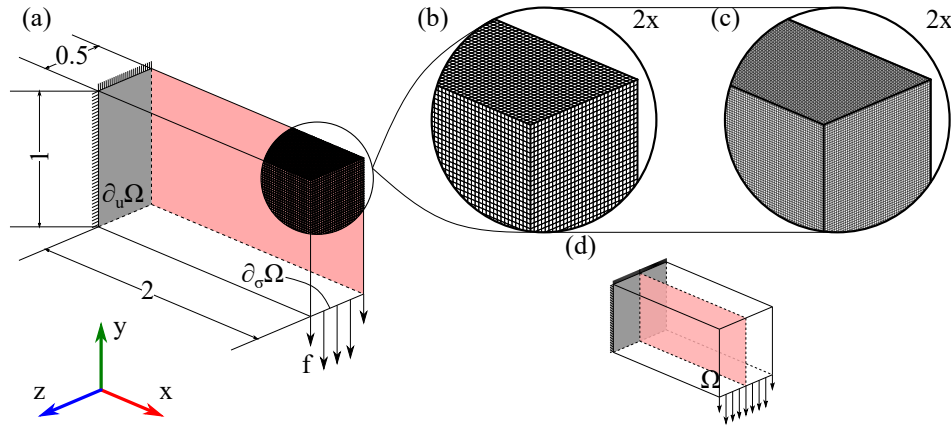


Figure A.9: Minimum compliance cantilever beam: (a) Meshed domain, (b) Detailed mesh M1, (c) Detailed mesh M2, (d) Symmetrized design domain Ω .

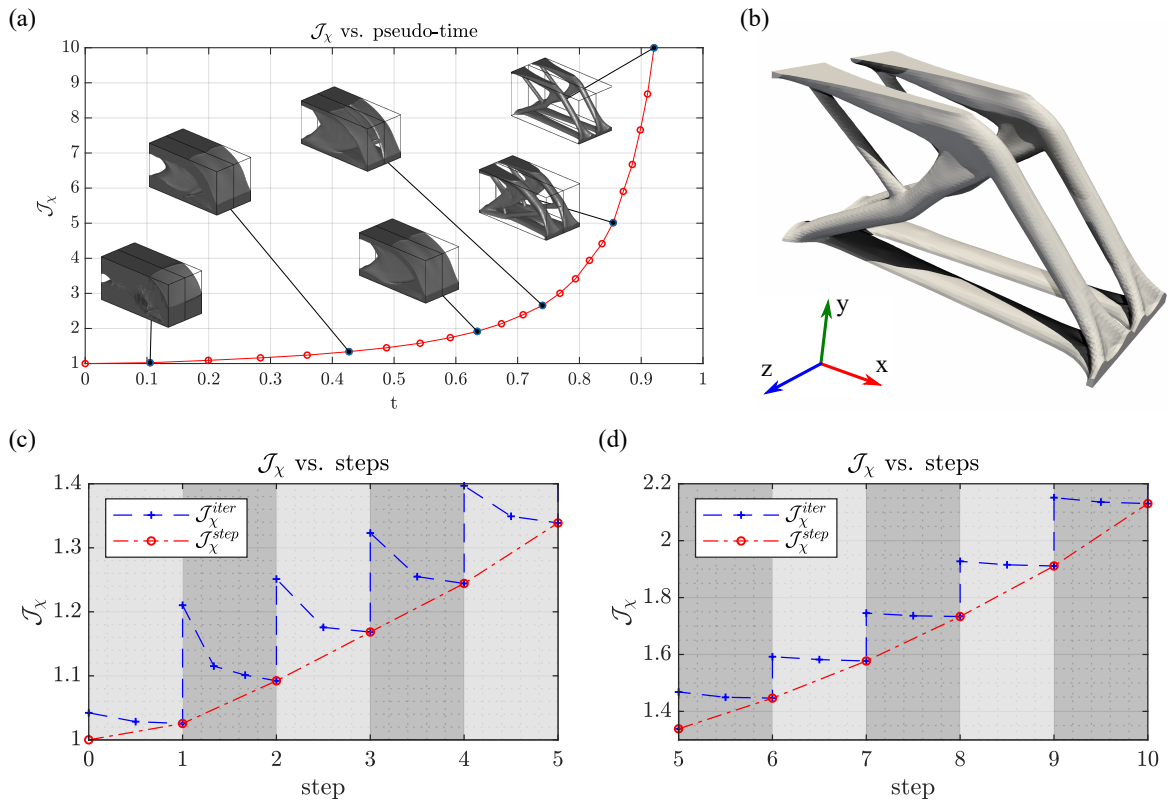


Figure A.10: Cantilever beam. Mean structural compliance optimization for Mesh M1: 432.000 elements and $\tau = 1$ ($\epsilon = \tau \cdot h = 1.67 \cdot 10^{-2}$) (a) Cost function and topology evolution, (b) Topology for $t = \frac{|\Omega^-|}{|\Omega|} = 0.92$, $\frac{|\Omega^+|}{|\Omega|} = 0.08$, (c-d) In-step convergence of the cost function for steps 1 to 10. Vertical stripes correspond to steps, and crosses inside them correspond to step-iterations.

In figure A.10-(a), the pseudo-time, ($t = \frac{|\Omega^-|}{|\Omega|}$), evolution of the analysis is shown, both in terms of the cost-function and the topology. In figure A.10-(b), the final design, when the hard-phase (solid material) equals 8% of the initial one (100%), is depicted. Figures A.10-(c) and A.10-(d) illustrate the convergence rate of the cost function, \mathcal{J}_χ , for the first ten steps. As it can be observed, the objective function tends to a local optimal value in a few iterations for each step.

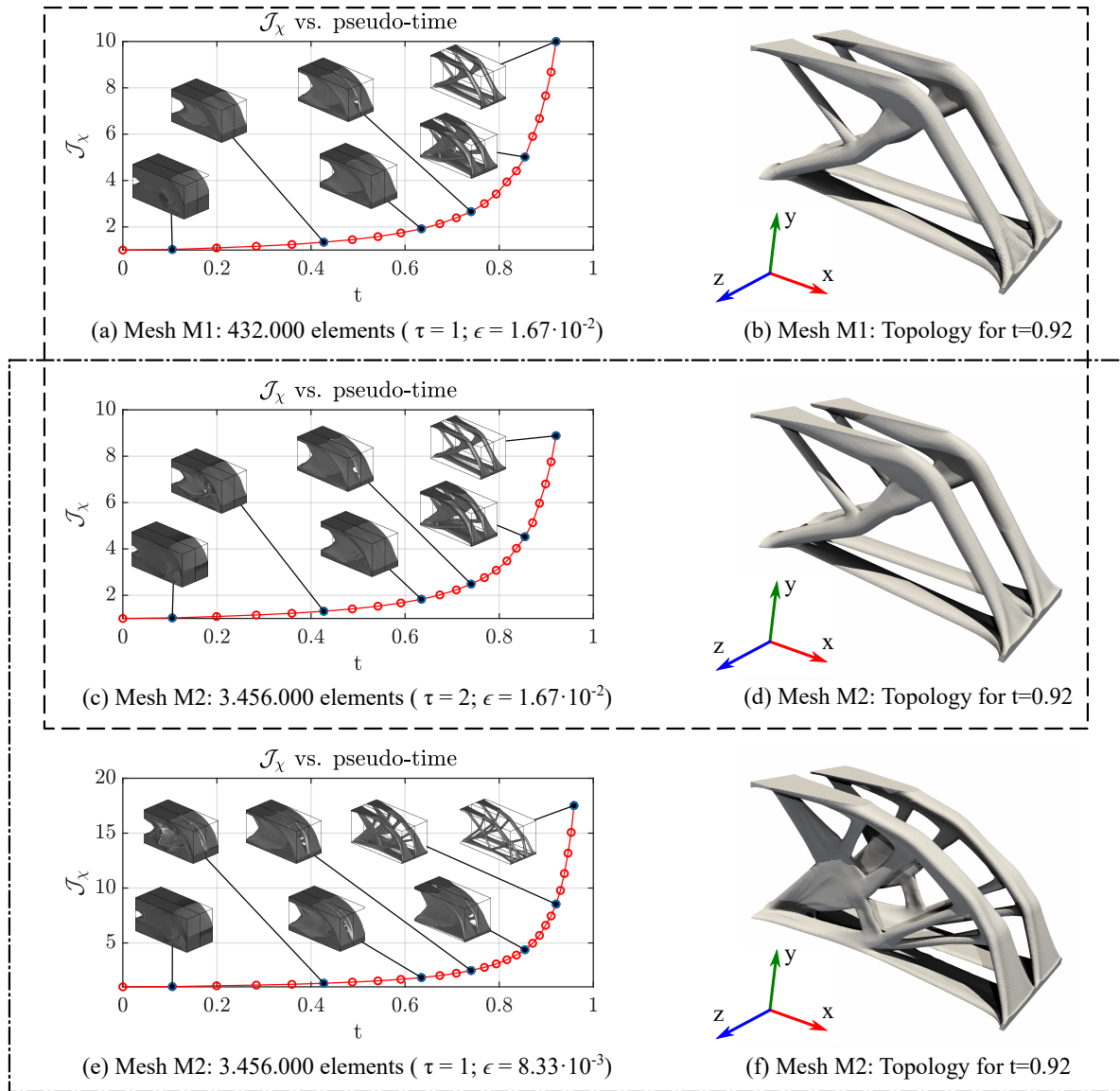


Figure A.11: Cantilever beam. Mesh-size objectivity results ($\epsilon = \tau \cdot h$). (a) to (d): results for meshes M1 and M2 and the *same regularization parameter* ($\epsilon = 1.67 \cdot 10^{-2}$), (c) to (f): results for the same mesh, M2, and different regularization values ($\epsilon = 1.67 \cdot 10^{-2}$ and $\epsilon = 8.33 \cdot 10^{-3}$).

Mesh size objectivity

The effects of the regularization parameter, ϵ , in the Laplacian smoothing equations (56) to (60), are examined, now for two different meshes in the design domain Ω . Mesh M1 ($120 \times 60 \times 30 = 216.000$ elements, with size $h^{(1)}$), and mesh M2 (obtained by doubling the number of elements in every direction $\{x, y, z\}$, this leading to a total of 1.728.000 elements $\Rightarrow h^{(2)} = h^{(1)}/2$, see figure A.9-(c)).

Mesh size objectivity is assessed in figures A.11-(a)-(b)-(c)-(d), when the *value of the regularization parameter* $\epsilon = 1.67 \cdot 10^{-2}$ is kept constant for the original, M1, and direction-doubled, M2, meshes, giving rise to very similar cost-function and topological design evolution. If, instead, *no action is taken to keep this parameter constant in mesh M2* ($\epsilon^{(2)} = 8.33 \cdot 10^{-3} = 1/2\epsilon^{(1)}$), thus keeping $\tau = \text{constant}$ in equation $\epsilon^{(i)} = \tau h^{(i)}$, the results, in figures A.11-(e)-(f), substantially change with respect to the ones in the figure above, and *they become strongly dependent on the finite element mesh size* $h^{(i)}$.

2-1/2D extruded design

Following the steps in [53] (where a *Tikhonov-like* regularization was used) we show here that, changing the tensor order of the Laplacian smoothing regularization parameter ϵ , from scalar to orthotropic second order tensor or, equivalently, the parameter $\tau = \frac{\epsilon}{h}$ in equations (56) to (60), one can obtain *2-1/2D extruded designs* in a selected direction.

For instance, let us replace the scalar value ϵ , in these equations, by an orthotropic second order tensor, ϵ , defined through,

$$\epsilon := \begin{bmatrix} \epsilon_x & 0 & 0 \\ 0 & \epsilon_y & 0 \\ 0 & 0 & \epsilon_z \end{bmatrix} = \begin{bmatrix} 1 & 0 & 0 \\ 0 & 1 & 0 \\ 0 & 0 & \eta \end{bmatrix} \tau h = \underbrace{\begin{bmatrix} \tau_x & 0 & 0 \\ 0 & \tau_x & 0 \\ 0 & 0 & \tau_z \end{bmatrix}}_{\tau} h = \tau h ; \quad \eta \gg 1 \quad (100)$$

where the second order tensor $\epsilon = \tau h$ ($\tau_z = \eta\tau \gg \tau_x = \tau_y$) is an orthotropic tensor defining the *minimum filament width size* (see section A.5.1) in the directions $\{x, y, z\}$. The value $\eta \gg 1$ sets the length of the *minimum solid filament width in the z-direction* (=filtered wavelength in the z -direction) much larger than in the other two orthogonal directions, this resulting in z -extruded designs (see figure A.12). This action was performed in the mean compliance optimization of the cantilever beam, in section A.10.1, with the only modification of considering the orthotropic character of the filtering tensor ϵ in equation (100). The corresponding results are shown in figure A.12.

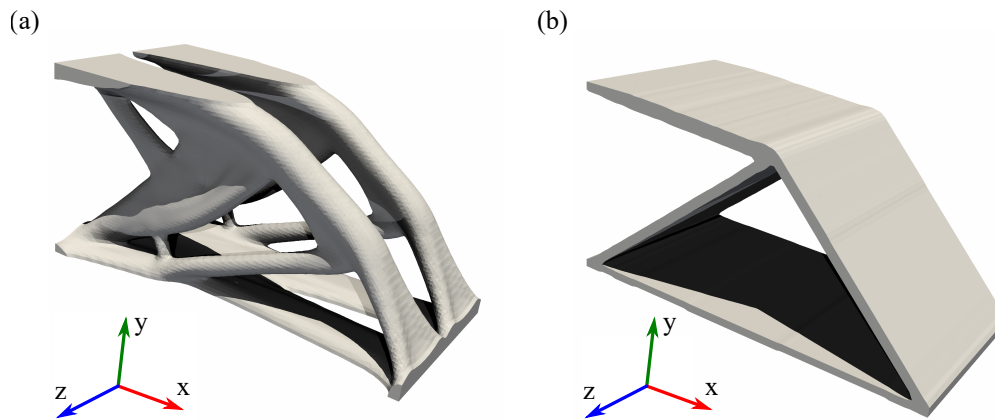


Figure A.12: Cantilever beam. Comparison of full 3D and $2^{1/2}D$ (extruded) optimal topologies for $t=0.85$ and mesh $M1$. (a) full 3D optimal topology ($\tau = 1; \epsilon = 1.67 \cdot 10^{-2}$); (b) Extruded optimal topology ($\tau = 1; \epsilon_x = \epsilon_y = 1.67 \cdot 10^{-2}; \epsilon_z = 1.67 \cdot 10^3$).

A.10.2 Mean compliance optimization. 3D bridge design

The problem of minimum compliance design of a bridge is tackled here. The design domain, Ω , is depicted in figure A.13. For symmetry reasons, only one fourth of the domain is discretized in a structured mesh of $240 \times 204 \times 40$, which leads to 1.084.800 hexahedra (see figure A.13-(a)). A uniform load on the bridge deck, $\partial_\sigma \Omega$, is prescribed, as well as, the position for the eventual support at boundary, $\partial_u \Omega$.

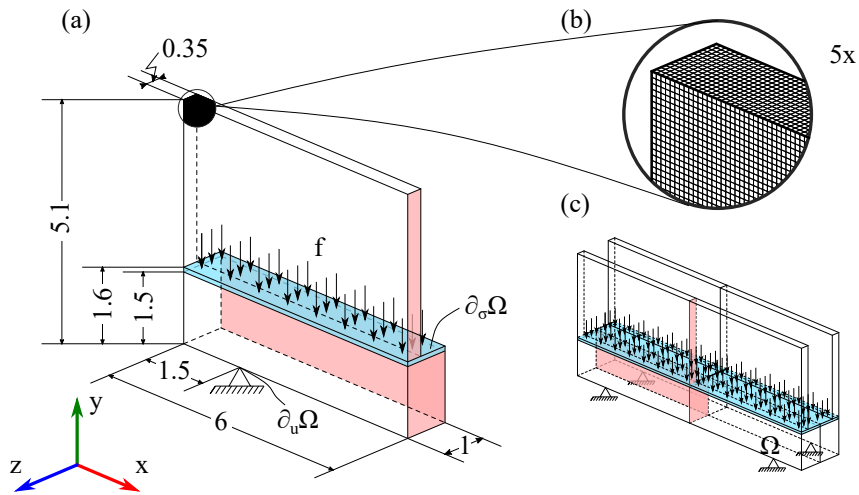
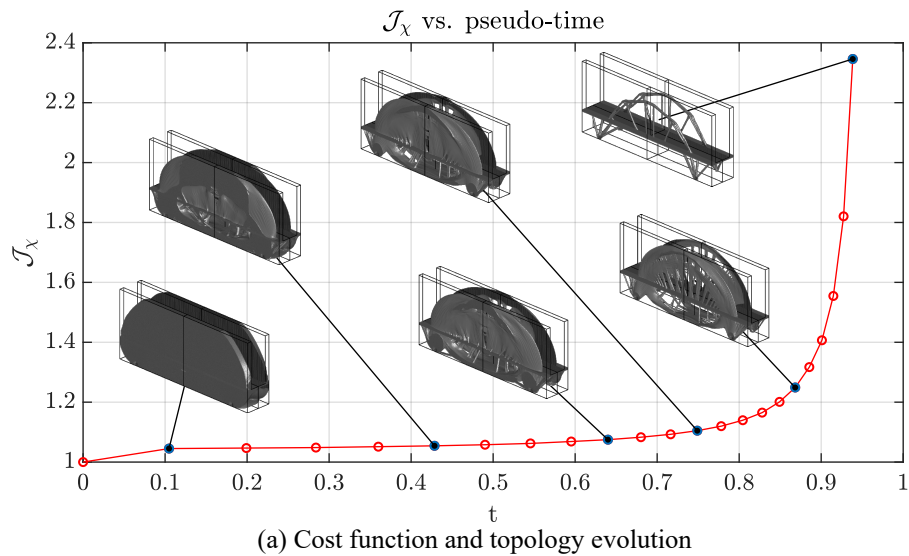
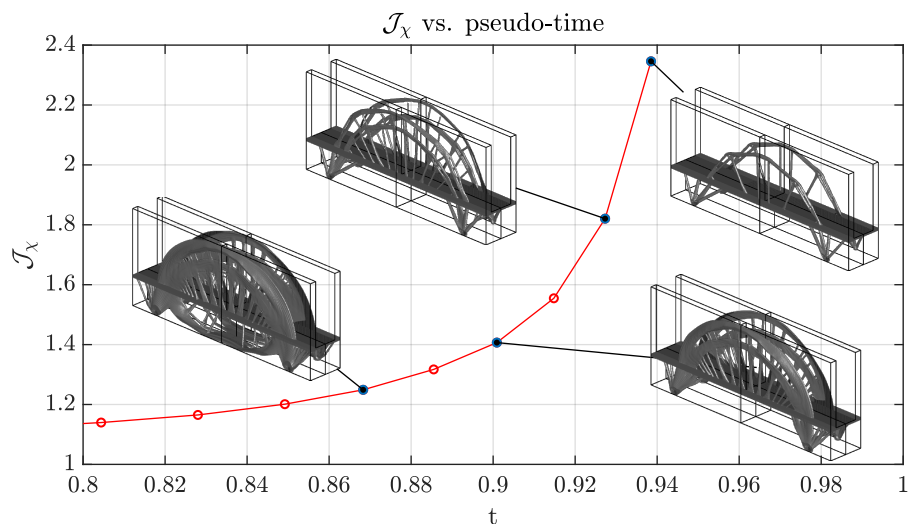


Figure A.13: Minimum compliance bridge design: (a) Meshed domain, (b) Detailed mesh, (c) Symmetrized design domain Ω .



(a) Cost function and topology evolution



(b) Detailed view of the optimization process evolution

Figure A.14: Bridge. Mean structural compliance optimization. $\tau = 0.316$ ($\epsilon = \tau \cdot h = 7.9 \cdot 10^{-3}$).

Then, the pseudo-time evolving optimization process, starting from a design at $t = 0$ made of *hard-phase* material over all Ω , evolves along the increasing pseudo time $t = \frac{|\Omega^-|}{|\Omega|}$. In figure A.14, the cost function and the topology evolution are shown. Finally, in figure A.15 the final topology, for $|\Omega^+| = 0.06|\Omega|$, is displayed in detail. Amazingly, subtle structural design details, for the structural family of *arch bridges*, well known by structural designers, are captured by the numerically obtained optimized solution.



Figure A.15: Bridge. Mean structural compliance optimization. Topology for $t=0.94$ ($|\Omega^+| = 6\%|\Omega|$).

A.10.3 Compliant mechanisms optimization.

The computational design of compliant mechanisms is another example of structural optimization problem for which the approach considered in this work is evaluated. The RTD and closed form solution derived in section A.9 (see equation (97) and figure A.8) is applied here to the design of a compliant 3D gripper.

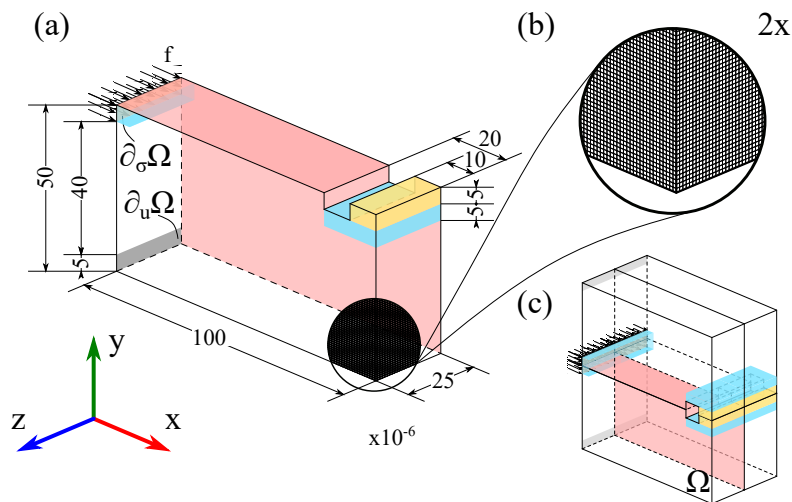


Figure A.16: Compliant mechanism (gripper). (a) Design domain Ω , (b) detailed mesh, (c) symmetrized design domain.

The problem is inspired in that in [53] using a Tikhonov-regularized level set method, and

the mechanical properties considered here are²⁴,

Young modulus $E = 210GPa$; Poisson ratio $\nu = 0.31$; Stiffness contrast factor $\alpha = 1.0 \cdot 10^{-2}$
 Stiffness contrast exponent $m = 3$ (see equation (11))

$$\mathbf{K}_{in} = 3.19 \cdot 10^{14} \frac{N}{m^3} ; \quad E_{out} = 10GPa ; \quad \nu_{out} = 0 ; \quad \mathbf{f}_{in} = 3.2 \cdot 10^{13} \frac{N}{m^2} ; \quad \mathbf{f}_{out} = 3.2 \cdot 10^{10} \frac{N}{m^2} \quad (101)$$

Due to symmetry considerations only one fourth of the design domain, Ω , is meshed with a structured hexahedra with $160 \times 80 \times 40$, which leads to 506.880 elements (see figure A.16).

In figure A.17, the state problem (system (1)) and the adjoint state problem (system (2)) are also presented.

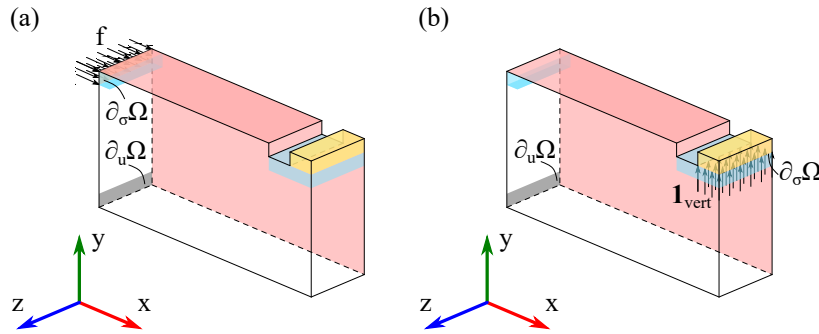


Figure A.17: Compliant mechanism (gripper): (a) system (1) (1/4th-domain), (b) system (2) (1/4th-domain).

In figure A.18-(a), results concerning the cost-function (opening displacement of the gripper jaws is minimized, therefore the closing motion is maximized) are presented, as well as the topology evolution. It is worth noting here that, unlike in the mean structural compliance case, the cost function is not monotonously increasing, and a *minimum of the minima* compliant design can be identified for $t = \frac{|\Omega^-|}{|\Omega|} \approx 0.48$. In addition, one can identify a sudden change of the topology, around $t = 0.3$, translating into a change of trend of the cost function to, subsequently, fall into a new local minimum.

Also notice that the chosen value for τ ($\tau = 0.5$) corresponds to $\epsilon = \frac{1}{2}h$, i.e. one half of the element size, in order to allow the formation of hinges (thin solid-phase filaments) typical of this problem in some stages of the optimization process (see figure A.18-(b)-(c)-(d)).

A.10.4 Computational assessment. Variational closed-form solution vs. level-set method

To assess the performance of the variational closed-form approach used in this work, in this section we compare the results for the cantilever beam, obtained in section A.10.1 with the so far described setting, with those using a level-set method driven by the relaxed topological derivative (RTD) in equation (87)-(c). Details on the level-set numerical algorithm and its properties are given in Appendix A.C.

In order to have a fair comparison, in both methods (*variational closed-form solution* and *level set method*) the same sequence of time steps, t_i , has been imposed along the pseudo-time interval $[0, T] \equiv [0, 1]$, i.e. 22 exponentially spaced time steps from $t = 0$ to $t = 0.92$ as indicated in equation (62). The pseudo-time, t , evolution is, then, defined according to the following

²⁴At the output port, the existence of a *gripped material mass* has been considered. Therefore, it has been equipped with elastic material properties, softer than the design solid material.

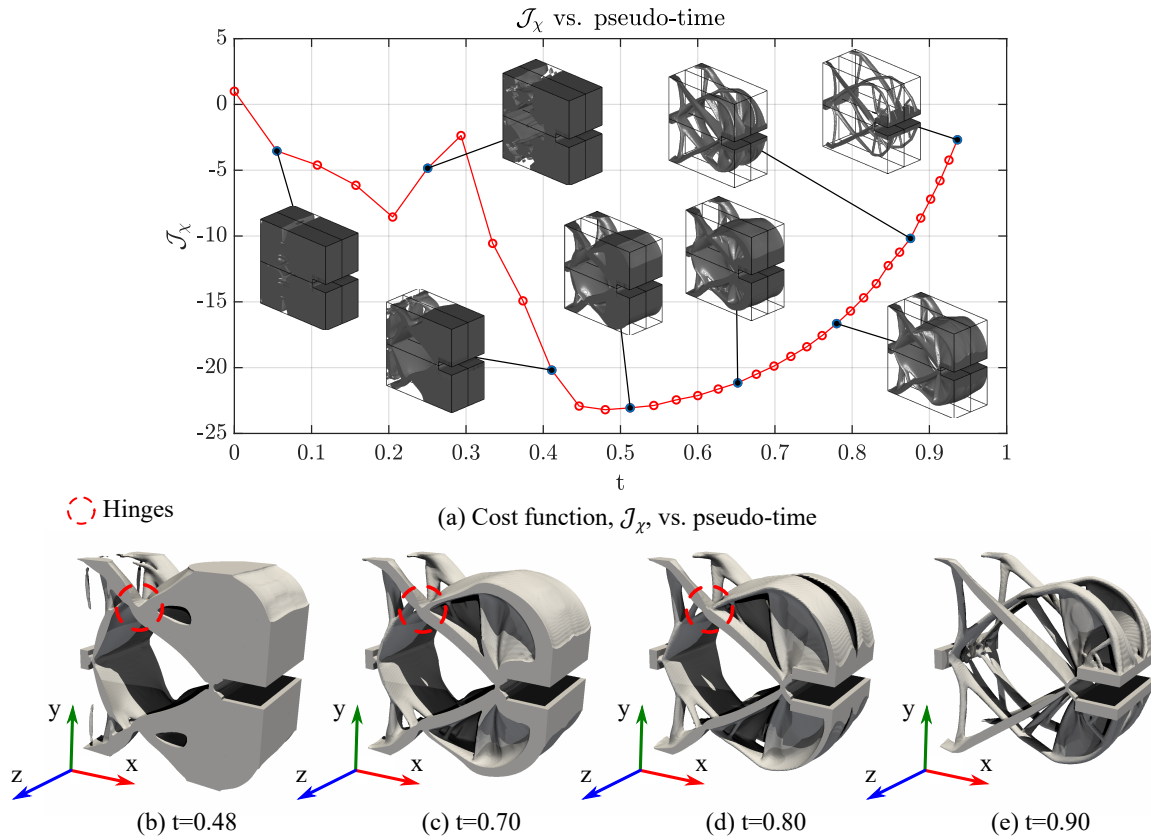


Figure A.18: 3D-Gripper optimization: (a) cost function evolution, (b) to (e) optimal topologies at different pseudo-times. ($\tau = 0.5$; $\epsilon = \tau \cdot h = 3.125 \cdot 10^{-7}$). Notice, in figures (b) to (d) the appearance of hinges, in terms of thin short-bars, to provide additional compliance to the design.

exponential law

$$t_i = t_0 + \frac{T - t_0}{1 - e^K} \left(1 - e^{K(i/n)}\right); \quad i \in \{0, 1, \dots, n\} \quad (102)$$

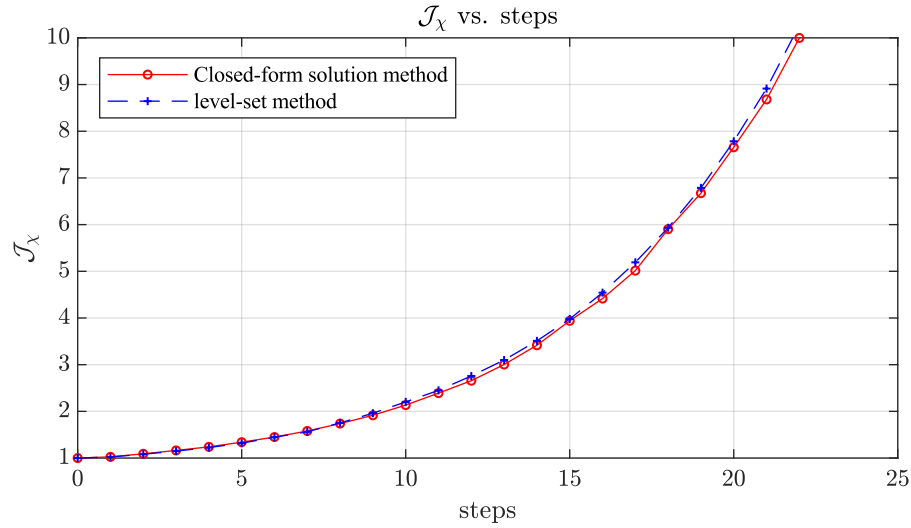
where $n = 40$ denotes the number of steps required to reach the time $t_n = T = 1$, and the constant K is set to obtain the desired exponential function ($K = -4.5$).

Then, both algorithms are run until convergence in terms of the topology (with the same tolerance $Tol_\chi = 10^{-1}$). Their relative computational cost, is evaluated in terms of the number of iterations required to converge for each of the methods²⁵.

In figure A.19-(a), the cost function evolution is displayed, showing a very similar quantitative performance of both methods. As for the computational cost (number of required iterations) the variational closed-form solution is about 5 times (in average) cheaper to obtain than in the level-set method (see figure A.19-(b)). The fact that the volume restriction is enforced at every iteration, in the variational closed-form method, plays, in opinion of the authors, a relevant role in this cost reduction. On the other hand, the number of requested iterations tends to be almost constant, along time intervals, in the variational closed-form solution, whereas, in the level-set method it exhibits a large increase in the required number of iterations for high values of the pseudo-time (i.e. small volumes of the solid-phase $|\Omega^+|$).

Similar trends, to those specifically emphasized here, has been observed in other optimization problems solved using both methods. In summary, lower computational cost, in front of level-set

²⁵In fact, the solution of the state (equilibrium) problem dominates the computational cost in both methods. Therefore, the computational cost is closely proportional to the number of required iterations to converge.



(a) Variational closed-form solution method vs. level-set method: cost-function evolution



(b) Variational closed-form method vs. level-set method: computational cost

Figure A.19: Cantilever beam. Variational closed-form solution vs. level set method for $\varepsilon = \tau \cdot h = 1.67 \cdot 10^{-2}$.

methods, while providing similar quantitative results, seems to be an argument in favor of the approach in the present work.

A.11 Concluding remarks

Along this work a variational approach to relaxed topological optimization has been explored, and assessed through its application to a number of structural problems. The conclusions to be highlighted by the authors, about this work, are the following:

- Though *the relaxed character of the optimization setting* is not specific of the present approach, the formulation of a *relaxed topological derivative* (RTD), clarifies the issue of using a topological sensitivity *consistent with the relaxed setting in which the optimization is performed*. This is in contrast with the frequent use, in relaxed optimization settings, of the *exact topological derivative* (TD), derived in an *immersed setting* at the cost of heavy, and problem dependent, mathematical derivations. Although, from the mathematical

point of view, it could be argued that the TD represents the exact sensitivity with respect to singular domain perturbations whereas the RTD is just an approximation of it, the results obtained using the later, for practical applications as the ones in this work, are manifestly similar to those obtained with the TD. In consequence, the RTD can be considered a powerful and, at the same time very simple tool, for topological optimization in engineering applications.

- The difficulties inherent to the discrete (discontinuous) character of the design variable (the characteristic function $\chi(\mathbf{x})$), and the resulting non-smoothness of the cost function, have traditionally suggested detouring the formulation from the original variational scenario; either by resorting to regularization of the characteristic function (like in SIMP) or by totally abandoning the variational formulation when facing the impossibility to obtain the stationarity conditions based on differentiation of that cost function (like in level-set methods). Surprisingly enough, the difficulties arising from that non-smooth character of the problem can be easily overcome. Indeed, the analysis of the sensitivity of the cost function, in front of topology perturbations, via the aforementioned expressions of the RTD, yields an *inequality-type optimality criterion: the overall-increasing cost function sensitivity*. Amazingly, the emerging inequality, in terms of the, here termed, *discrimination function* $\psi(\mathbf{x})$, leads straightforwardly to *closed-form solutions of the topological optimization problem in the form of simple algebraic non-linear equations*. These equations, involving the characteristic function, $\chi(\mathbf{x})$, can be solved, in turn, via simple non-linear algorithms. This is a very specific result of the proposed approach, which suggests possible extensions of the technique to further methods and applications. In the cases studied here, typically the mean structural compliance and compliant mechanisms problems, the resulting optimality solutions are interpreted as fixed-point equations, to be solved by combination of a cutting algorithm, of energy-like surfaces, and the exact imposition of the volume restriction (via bisection methods).
- Since the presented approach is not regularized in terms of the characteristic function, the obtained topological designs are completely *black and white designs*, and there is no need of subsequent filtering techniques to eliminate gray-scales.
- Besides, the characteristic function, $\chi(\mathbf{x})$, is never regularized, even for the treatment of bi-material elements. Instead, three-field *mixed formulations* $(\boldsymbol{\sigma} - \boldsymbol{\varepsilon} - \mathbf{u})$ [55] in hexahedral finite elements, detailed in appendix A.B, are used for accurately capturing the discontinuous stress field in those bi-material elements. Albeit, the LBB stability condition is not fulfilled in those elements, numerical instabilities do not appear, thus not leading to the classical *checkerboards*, due to their isolate position, in a mesh of *regular elements*, which avoids propagation of the possible instability modes. Also the marching cubes strategy, with the specific variant of *marching tetrahedra method* (see appendix A.A) has provided the expected robustness and accuracy in the determination of volumes and surfaces on the finite element mesh.
- An *evolving pseudo-time framework* can be naturally inserted in the considered setting. Albeit this is not an exclusive feature of the proposed approach, and it can be used, for instance, in combination with the level set methods, it is worth mentioning some of the benefits provided by this framework, i.e. the fact that a number of *intermediate optimal designs for a set of values of the volume restriction* are obtained "for free" and, in some problems, like compliant mechanisms design, information of the *minimum of the minima* designs in the explored range can be obtained.
- The approach considered here has proven to provide results, in the considered structural examples, very similar to the ones obtained with other methods, the main difference being that the computational cost is smaller (about five times in a benchmark test checked in

the work) when compared with the level-set method, using the same code, the same RTD and the same computational setting.

- The explored approach allows envisaging new computational strategies for topological optimization, which could overcome some of the classical drawbacks of relaxed optimization settings, e.g. the *necessity of using high dense meshes in the design domain involving millions of elements* and the application to new topological design problems (e.g. multiscale topological design [27, 20, 38, 14], immersed boundary methods combined with XFEM techniques [42], convected methods [52], etc.). This is an issue to be explored in a subsequent research.

Acknowledgements

This research has received funding from the European Research Council (ERC) under the European Union’s Horizon 2020 research and innovation programme (Proof of Concept Grant agreement n 779611) through the project “Computational catalog of multiscale materials: a plugin library for industrial finite element codes” (CATALOG). The authors also acknowledge the funding received from the Spanish Ministry of Science, Innovation and Universities through the research grant DPI2017-85521-P for the project “Computational design of Acoustic and Mechanical Metamaterials” (METAMAT).

A.A Modified marching cubes strategy

Different strategies can be found in the literature to extract the zero-level surface, $\Gamma := \{\mathbf{x} \in \Omega^{(e)} ; \psi(\mathbf{x}) = 0\}$, from a scalar field, $\psi(\mathbf{x})$. Among them, the marching cubes (MC) approach, see [28], has been the most popular technique used for volume visualization. However, the classical MC-method implementation requires the analysis of 15 different cases in every cubic cell, and the corresponding rotations and symmetries. In spite of this, it does not guarantee the topology correctness of the isosurface of a trilinear function.

For this reason, a modified algorithm, which takes into account 33 topologically different configurations to correctly treat topological ambiguities, both on the faces and inside the cell, was subsequently developed in [13]. Nevertheless, this algorithm is heavy to code and difficult to verify its faultlessness.

In this work, an alternative *marching tetrahedra method* (MT) has been implemented, which overcomes the aforementioned obstacles while avoiding ambiguities. The proposed strategy is based on an adaptive cube tessellation, see [48], which ensures topologically correct isosurfaces in case of ambiguities. Furthermore, this tessellation preserves the symmetries in the domain. The method is briefly sketched next.

The cubic cell is divided into six pyramids, a central extra-node, \mathbf{x}_C , is added to the cell and the value $\psi_C \equiv \psi(\mathbf{x}_C)$ is computed by interpolation from the regular nodes. In turn, each pyramid is split into four tetrahedra, including an extra-node, \mathbf{x}_{Fi} , on each face, and the value $\psi_{Fi} \equiv \psi(\mathbf{x}_{Fi})$ is computed, by interpolation, from its value at the vertices, see figure A.A.20. Therefore, seven extra values must be computed based on the trilinear approximation (green and red dots in figure A.A.21-(b)).

Then, each tetrahedron is treated as usually in marching tetrahedra, where triangular surfaces and tetrahedral volumes are computed. This procedure readily allows the geometrical computation of the perimeter and volume of the cell.

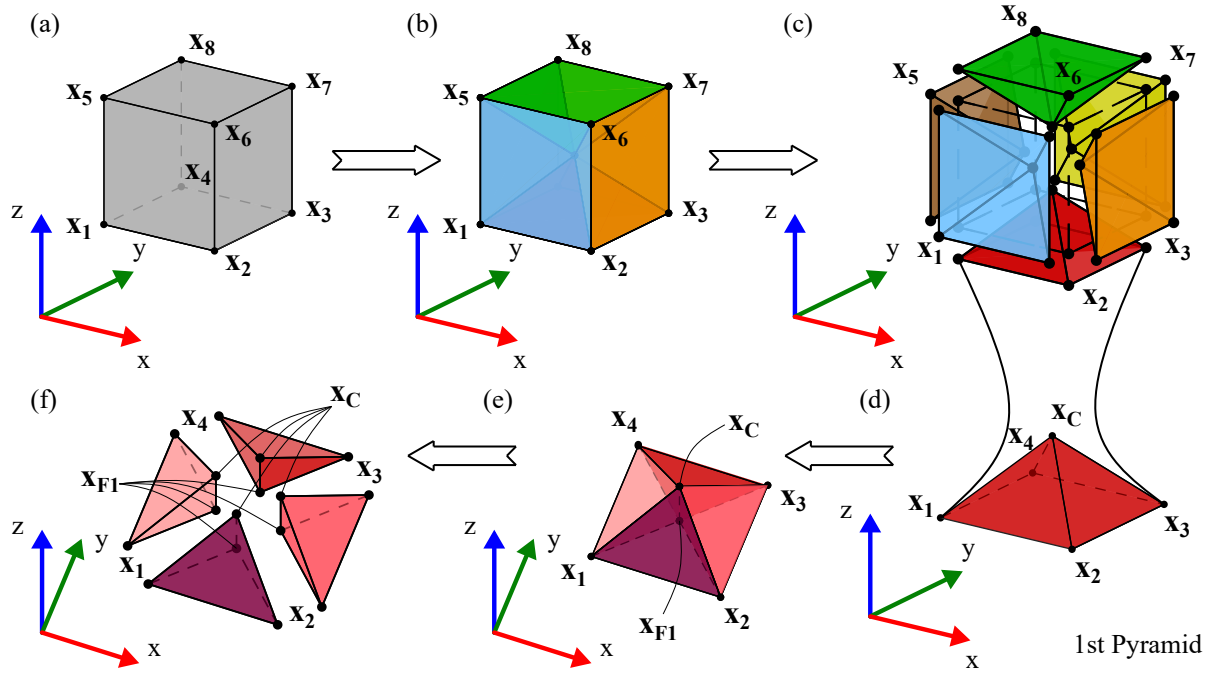


Figure A.A.20: Marching cubes method: tessellation process.

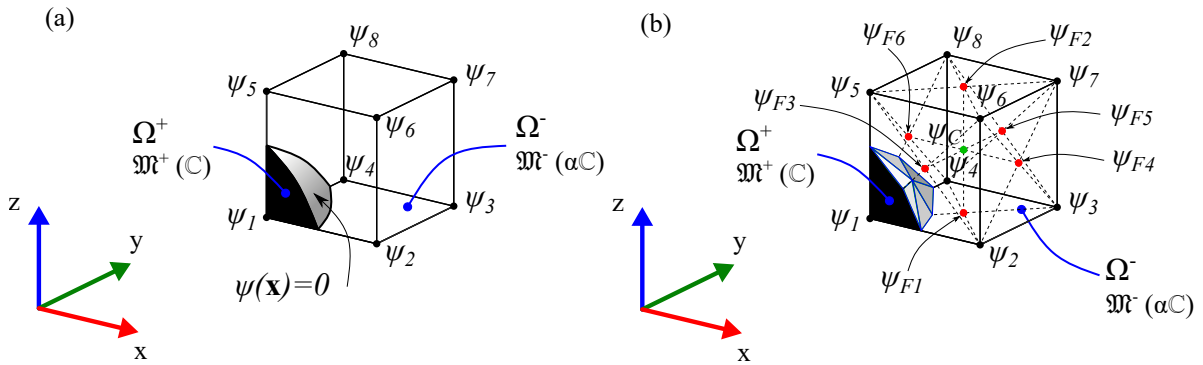


Figure A.A.21: Marching cubes method: nodal values interpolation.

A.B Mixed finite element formulation for bi-material finite elements

Let us consider the subset of bi-material elements $\Omega^{(+,-)} \subset \Omega$ as well as the portions $\Omega^{(e,+)} \subset \Omega^{(e)}$ and $\Omega^{(e,-)} \subset \Omega^{(e)}$ ($\Omega^{(e,+)} \cup \Omega^{(e,-)} = \Omega^{(e)}$) containing hard and soft material phases, in every element e . This subset of elements is treated considering a specific *discontinuous elemental material approach* based on a *three field mixed* stress-strain-displacement $(\boldsymbol{\sigma}_\chi - \boldsymbol{\varepsilon}_\chi - \mathbf{d}_\chi)$ finite element formulation [55]. The elemental stresses, $\boldsymbol{\sigma}_\chi^{(e)}(\mathbf{x})$, strains, $\boldsymbol{\varepsilon}_\chi^{(e)}(\mathbf{x})$, and displacements, $\mathbf{u}_\chi^{(e)}(\mathbf{x})$, are independently interpolated inside the element e . For the case of hexahedral elements, we will consider element-wise constant stresses and strains. Therefore, following the notation in equation (15), they read

$$\begin{cases} \mathbf{u}_\chi^{(e)}(\mathbf{x}) = [\mathbf{N}_u^{(e)}(\mathbf{x})]\mathbf{d}_\chi^{(e)}; & [\mathbf{N}_u^{(e)}(\mathbf{x})] = [\mathbf{N}_1^{(e)}(\mathbf{x}), \dots, \mathbf{N}_8^{(e)}(\mathbf{x})]; & \mathbf{d}_\chi^{(e)} = [\mathbf{d}_1^{(e)}, \dots, \mathbf{d}_8^{(e)}]^T & (a) \\ \boldsymbol{\varepsilon}_\chi^{(e)}(\mathbf{x}) = \boldsymbol{\varepsilon}^{(e)} = \text{constant} & \forall \mathbf{x} \in \Omega^{(e)} & & (b) \\ \boldsymbol{\sigma}_\chi^{(e)}(\mathbf{x}) = \boldsymbol{\sigma}^{(e)} = \text{constant} & \forall \mathbf{x} \in \Omega^{(e)} & & (c) \end{cases} \quad (103)$$

where $\mathbf{N}_u^{(e)}(\mathbf{x})$ is the elemental displacement bilinear interpolation matrix, and $\mathbf{d}_\chi^{(e)}$ the corresponding nodal vectors. The nodal displacement interpolation matrices $\mathbf{N}_i^{(e)}(\mathbf{x})$ $i \in \{1, \dots, 8\}$ have a standard nodal support, and the nodal displacements $\mathbf{d}_i^{(e)}$ $i \in \{1, \dots, 8\}$ correspond to the displacements at the element nodes. As for the strain and stress interpolation, due to their element-wise discontinuous character, they can be associated to one *fictitious* internal element node in the center of every element $\Omega^{(e)}$, with coordinates \mathbf{x}_C , (see figure A.B.22), where the (constant) elemental strain vector, $\boldsymbol{\varepsilon}^{(e)}$, is defined. The elemental strain, $\boldsymbol{\varepsilon}^{(e)}$, is, then, determined via the following additional variational equation (uncoupled for every element in $\Omega^{(+,-)}$)

$$\left[\begin{array}{l} \text{Given} \\ \mathcal{V}_\varepsilon^{(e)} := \left\{ \boldsymbol{\eta}_\varepsilon^{(e)} \in \mathbb{R}^6 \right\} ; \quad \mathcal{V}_\sigma^{(e)} := \left\{ \boldsymbol{\eta}_\sigma^{(e)} \in \mathbb{R}^6 \right\} \\ \text{Find: } \boldsymbol{\varepsilon}^{(e)} \in \mathcal{V}_\varepsilon^{(e)} \text{ and } \boldsymbol{\sigma}^{(e)} \in \mathcal{V}_\sigma^{(e)} \\ \text{Fulfilling:} \\ \int_{\Omega^{(e)}} \left(\boldsymbol{\eta}_\varepsilon^{(e)} \right)^T \left(\boldsymbol{\varepsilon}^{(e)} - \boldsymbol{\varepsilon}_\chi^{(e)}(\mathbf{x}) \right) d\Omega = \left(\boldsymbol{\eta}_\varepsilon^{(e)} \right)^T \int_{\Omega^{(e)}} \left(\boldsymbol{\varepsilon}^{(e)} - \boldsymbol{\varepsilon}_\chi^{(e)}(\mathbf{x}) \right) d\Omega = 0 \quad \forall \boldsymbol{\eta}_\varepsilon^{(e)} \in \mathcal{V}_\varepsilon^{(e)} \\ \int_{\Omega^{(e)}} \left(\boldsymbol{\eta}_\sigma^{(e)} \right)^T \left(\boldsymbol{\sigma}^{(e)} - \mathbb{D}^{(e)}(\mathbf{x})\boldsymbol{\varepsilon}^{(e)} \right) d\Omega = \left(\boldsymbol{\eta}_\sigma^{(e)} \right)^T \int_{\Omega^{(e)}} \left(\boldsymbol{\sigma}^{(e)} - \mathbb{D}^{(e)}(\mathbf{x})\boldsymbol{\varepsilon}^{(e)} \right) d\Omega = 0 \quad \forall \boldsymbol{\eta}_\sigma^{(e)} \in \mathcal{V}_\sigma^{(e)} \\ \boldsymbol{\varepsilon}_\chi^{(e)}(\mathbf{x}) = \mathbf{B}^{(e)}(\mathbf{x})\mathbf{d}_\chi^{(e)} \end{array} \right. \quad (104)$$

where $\mathbf{B}(\mathbf{x})^{(e)}$ and $\mathbb{D}^{(e)}(\mathbf{x})$ stand, respectively, for the elemental deformation matrix and the elastic constitutive matrix in equation (15). Equation (104) can be solved for $\boldsymbol{\varepsilon}^{(e)}$ and $\boldsymbol{\sigma}^{(e)}$ yielding

$$\left\{ \begin{array}{l} \boldsymbol{\varepsilon}^{(e)} = \frac{1}{|\Omega^{(e)}|} \int_{\Omega^{(e)}} \boldsymbol{\varepsilon}_\chi^{(e)}(\mathbf{x}) d\Omega = \int_{\Omega^{(e)}} \mathbf{B}^{(e)}(\mathbf{x})\mathbf{d}_\chi^{(e)} d\Omega = \underbrace{\int_{\Omega^{(e)}} \mathbf{B}^{(e)}(\mathbf{x}) d\Omega}_{\overline{\mathbf{B}}^{(e)}(\mathbf{x})} \mathbf{d}_\chi^{(e)} = \overline{\mathbf{B}}^{(e)}(\mathbf{x}) \mathbf{d}_\chi^{(e)} \quad (a) \\ \overline{\mathbf{B}}^{(e)}(\mathbf{x}) \simeq \mathbf{B}^{(e)}(\mathbf{x}_C) \quad (b) \end{array} \right. \quad (105)$$

where $\overline{(\cdot)}$ stands for the *mean value* of $(\cdot)(\mathbf{x})$ in $\Omega^{(e)}$, and equation (105)-(b) stems from the bi-linear character of the element. Now, considering the stress problem in equation (104), and solving for $\boldsymbol{\sigma}^{(e)}$ yields

$$\left\{ \begin{array}{l} \boldsymbol{\sigma}^{(e)} = \frac{1}{|\Omega^{(e)}|} \int_{\Omega^{(e)}} \mathbb{D}(\mathbf{x})\boldsymbol{\varepsilon}^{(e)} d\Omega = \frac{1}{|\Omega^{(e)}|} \underbrace{\int_{\Omega^{(e)}} \mathbb{D}(\mathbf{x}) d\Omega}_{\overline{\mathbb{D}}(\mathbf{x})} \boldsymbol{\varepsilon}^{(e)} = \overline{\mathbb{D}}(\mathbf{x}) \boldsymbol{\varepsilon}^{(e)} \quad (a) \\ \overline{\mathbb{D}}(\mathbf{x}) = \frac{|\Omega^{(e,+)}|}{|\Omega^{(e)}|} \mathbb{D}_\chi^+ + \frac{|\Omega^{(e,-)}|}{|\Omega^{(e)}|} \mathbb{D}_\chi^- = \left(\frac{|\Omega^{(e,+)}|}{|\Omega^{(e)}|} + \alpha \frac{|\Omega^{(e,-)}|}{|\Omega^{(e)}|} \right) \mathbb{D} \quad (b) \end{array} \right. \quad (106)$$

where the values of the elastic constitutive tensor in Ω^+ (\mathbb{D}_χ^+) and in Ω^- (\mathbb{D}_χ^-) in equations (11) and (15) have been considered.

A.C A level set algorithm for relaxed bi-material topological optimization

A.C.1 Level set algorithm

Let us consider the topological optimization problem in equation (54)-(a) for the design domain Ω , and the *hard-material phase*, Ω_t^+ and *soft-material phase*, Ω_t^- , corresponding to a pseudo-time, t , in turn associated to an iteration procedure. The interface between the two phases is denoted by Γ_t , and \mathbf{n} denotes the unit normal to Γ_t pointing to Ω^+ (see figure A.C.23).

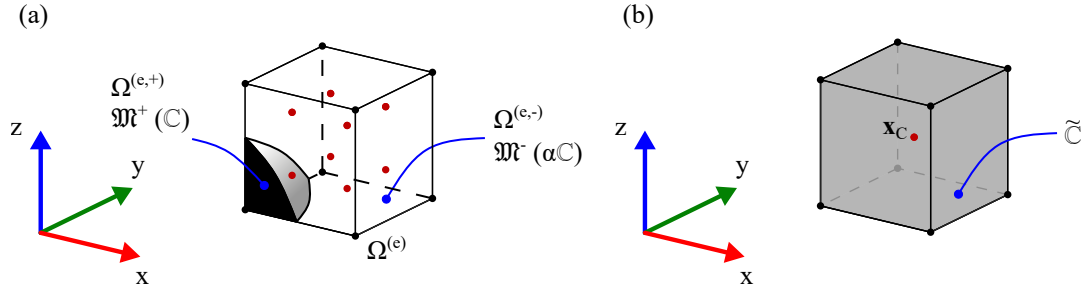


Figure A.B.22: Mixed finite element representation: (a) Hexahedra element with 8 integration points (b) Mixed element with 1 pseudo-integration point.

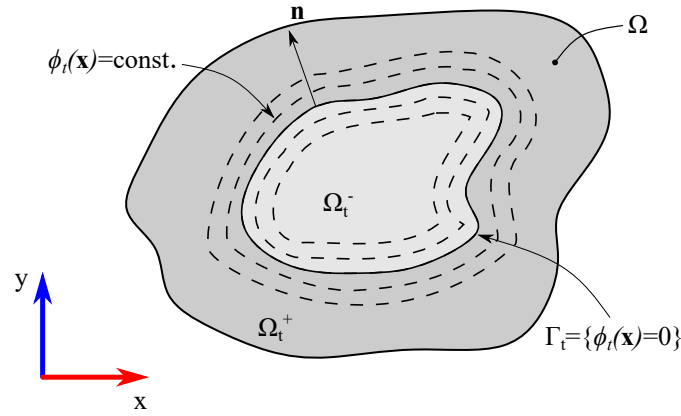


Figure A.C.23: Level-set problem definition. The zero level-set ($\phi_t(\mathbf{x}) = 0$) defines, at time t , the position of the material phase interface, Γ_t , in the design domain, Ω , and, therefore, the phase domains Ω_t^+ and Ω_t^- .

Let $\phi_t \in \mathcal{V}_\phi$ be the level set function, considered as the actual unknown of the problem, through which the characteristic function, $\chi_t(\mathbf{x})$, is defined (see equations (1) to (3)). Let us also consider $\phi_t(\mathbf{x})$ defined through a time-evolving (Hamilton-Jacobi) equation [3] i.e.

$$\begin{aligned} \mathcal{V}_\phi &\in H^1(\Omega) := \{\phi : \Omega \times [0, T] \rightarrow \mathbb{R}\} \\ \left\{ \begin{aligned} \dot{\phi}_t(\mathbf{x}, \lambda) &\equiv \dot{\phi}(\mathbf{x}, \lambda_t) = -k \frac{1}{\Delta\chi_t(\mathbf{x})} \frac{\delta\mathcal{L}(\chi_t, \lambda_t)}{\delta\chi_t}(\mathbf{x}); \quad k > 0; \quad -1 \leq \phi_t \leq 1; \quad \forall \mathbf{x} \in \Omega & (a) \\ \mathcal{L}_t(\phi, \lambda) &\equiv \mathcal{L}(\chi(\phi_t), \lambda_t) = \mathcal{J}(\chi(\phi_t)) + \lambda_t \mathcal{C}(\chi(\phi_t)) & (b) \\ \chi_t(\mathbf{x}) &= \mathcal{H}_\beta(\phi_t(\mathbf{x})) & (c) \end{aligned} \right. & (107) \end{aligned}$$

where the relaxed topological derivative of the Lagrange functional $\mathcal{L}_t(\phi, \lambda)$ in equation (107) is given by (see equations (97)-(a)-(b)-(c))

$$\left\{ \begin{aligned} \frac{\delta\mathcal{L}_t(\chi, \lambda)}{\delta\chi}(\mathbf{x}) &= 2m\chi_t^{m-1}(\mathbf{x})\bar{u}_t(\mathbf{x})\Delta\chi_t(\mathbf{x}) + \lambda_t \text{sign}(\Delta\chi_t(\mathbf{x})) \quad \forall \mathbf{x} \in \Omega & (a) \\ \bar{u}_t(\mathbf{x}) &:= \frac{1}{2} \left(\epsilon_\chi^{(1)}(\mathbf{x}, t) \right)^T \mathbb{D} \epsilon_\chi^{(2)}(\mathbf{x}, t) & (b) \end{aligned} \right. & (108)$$

The Lagrange multiplier, λ_t , is determined via the augmented Lagrange method (see reference [46]) i.e

$$\left\{ \begin{aligned} \lambda_t &\leftarrow \lambda_t + \rho \mathcal{C}(\chi(\phi_t)) & (a) \\ \mathcal{C}(\chi(\phi_t)) &\equiv t - \frac{|\Omega^-(\chi(\phi_t))|}{|\Omega|} & (b) \end{aligned} \right. & (109)$$

where $\rho \in \mathbb{R}^+$ is a suitable penalty value.

The discrete time-evolution form of equations (107)-(a) and (109)-(a) is obtained after time integration, giving rise to the following iterative update, from iteration i to $i + 1$, accounting for equation (107)-(c),

$$\begin{cases} \phi^{(i+1)}(\mathbf{x}) = \phi^{(i)}(\mathbf{x}) - k \frac{1}{\Delta\chi^{(i)}(\mathbf{x})} \frac{\delta\mathcal{L}(\chi^{(i)}, \lambda^{(i)})}{\delta\chi^{(i)}}(\mathbf{x}) \Rightarrow \chi^{(i+1)} = \mathcal{H}_\beta(\phi^{(i+1)}(\mathbf{x})) & \forall \mathbf{x} \in \Omega \\ \lambda^{(i+1)} = \lambda^{(i)} + \rho \mathcal{C}(\chi(\phi^{(i)})) \end{cases} \quad (110)$$

The iterative update in equation (110) is stopped when the steady state solution of the problem is achieved, determined in terms of some given tolerances on the variation of the unknowns $\chi(\phi(\mathbf{x}))$ and λ , i.e.

$$\begin{aligned} \|\chi^{(i+1)} - \chi^{(i)}\|_{L^2(\Omega)} &\leq \text{Toler}_\chi \\ |\lambda^{(i+1)} - \lambda^{(i)}| &\leq \text{Toler}_\lambda \end{aligned} \quad (111)$$

The corresponding characteristic function, $\chi(i + 1)(\mathbf{x})$ is then determined through equation (110).

Descending character of the algorithm

The algorithm in equations (107) to (110) leads to a continuous descent, along pseudo-time or iterations, of the Lagrange functional to be minimized. This warrants that, when a steady state is reached, the solution is a local minimum of the problem. The proof is readily achieved through the following sequence of propositions. Let us consider the time-evolutionary problem in equation (107)

$$\begin{aligned} \mathcal{V}_\phi &:= \{\phi / \phi : \Omega \times [0, T] \rightarrow \mathbb{R}\} \\ \begin{cases} \dot{\phi}_t(\mathbf{x}) = -k \frac{1}{\Delta\chi(\mathbf{x})} \frac{\delta\mathcal{L}(\chi, \lambda)}{\delta\chi}(\mathbf{x}); & k \in \mathbb{R}^+; \quad -1 \leq \phi_t \leq 1 \\ \mathcal{L}_t(\phi, \lambda) \equiv \mathcal{L}(\chi(\phi_t), \lambda) = \mathcal{J}(\chi(\phi_t)) + \lambda\mathcal{C}(\chi(\phi_t)) \end{cases} \end{aligned} \quad (a) \quad (112)$$

(b)

Lemma 1 *Given the functional*

$$\mathcal{L}(\chi) = \int_{\Omega} G(\mathbf{u}(\mathbf{x}), \mathbf{x}) d\Omega \equiv \int_{\Omega} F(\chi, \mathbf{x}) d\Omega \quad (113)$$

and considering the function derivative of $\mathcal{L}(\chi)$ as a, parameter- χ -dependent, integral, the following equality is fulfilled

$$\frac{\partial\mathcal{L}(\chi)}{\partial\chi} = \int_{\Omega} \frac{1}{\Delta\chi(\mathbf{x})} \frac{\delta\mathcal{L}(\chi)}{\delta\chi}(\mathbf{x}) d\Omega \quad (114)$$

Proof 1 *The function derivative of $\mathcal{L}(\chi)$, in equation (113), with respect to χ reads*

$$\frac{\partial\mathcal{L}(\chi)}{\partial\chi} = \int_{\Omega} \frac{\partial F(\chi, \mathbf{x})}{\partial\chi} d\Omega \quad (115)$$

and, equation (27) (replacing \mathcal{J} by \mathcal{L}), yields

$$\begin{cases} \left[\frac{\partial F(\chi, \mathbf{x})}{\partial\chi} \right]_{\mathbf{x}=\hat{\mathbf{x}}} \Delta\chi(\hat{\mathbf{x}}) = \frac{\delta}{\delta\chi} \left[\int_{\Omega} F(\chi, \mathbf{x}) d\Omega \right] (\hat{\mathbf{x}}) & \forall \hat{\mathbf{x}} \in \Omega \Rightarrow \\ \Rightarrow \frac{\partial F(\chi, \hat{\mathbf{x}})}{\partial\chi} = \frac{1}{\Delta\chi(\hat{\mathbf{x}})} \frac{\delta\mathcal{L}(\chi)}{\delta\chi}(\hat{\mathbf{x}}) & \forall \hat{\mathbf{x}} \in \Omega \end{cases} \quad (a) \quad (116)$$

(b)

Substitution of the result in equation (116)-(b) into equation (115) yields the proposition in equation (114).

Lemma 2

$$\frac{\partial \chi(\phi_t(\mathbf{x}))}{\partial \phi_t} \equiv \frac{\partial \chi(\phi_t)}{\partial \phi_t}(\mathbf{x}) = (1 - \beta) \|\nabla \phi_t(\mathbf{x})\|^{-1} \delta_{\Gamma_t}(\mathbf{x}) \quad (117)$$

where $\delta_{\Gamma_t}(\mathbf{x})$ stands for the line/surface Dirac's-delta function, shifted to Γ_t (see figure A.C.23) thus fulfilling

$$\int_{\Omega} \delta_{\Gamma_t}(\mathbf{x}) \varphi(\mathbf{x}) d\Omega = \int_{\Gamma_t} \varphi(\mathbf{x}) d\Gamma \quad (118)$$

for any sufficiently regular $\varphi(\mathbf{x})$.

Proof 2

$$\begin{aligned} \chi(\phi_t(\mathbf{x})) = \mathcal{H}_{\beta}(\phi_t(\mathbf{x})) &\Rightarrow \begin{cases} \nabla \chi(\phi_t(\mathbf{x})) = \nabla \mathcal{H}_{\beta}(\phi_t(\mathbf{x})) = (1 - \beta) \delta_{\Gamma_t}(\mathbf{x}) \otimes \mathbf{n}(\mathbf{x}); & \mathbf{n}(\mathbf{x}) = \frac{\nabla \phi_t(\mathbf{x})}{\|\nabla \phi_t(\mathbf{x})\|} \\ \nabla \chi(\phi_t(\mathbf{x})) = \frac{\partial \chi(\phi_t(\mathbf{x}))}{\partial \phi_t} \nabla \phi_t(\mathbf{x}) = \frac{\partial \chi(\phi_t(\mathbf{x}))}{\partial \phi_t} \|\nabla \phi_t(\mathbf{x})\| \otimes \mathbf{n}(\mathbf{x}) \end{cases} \\ \Rightarrow \frac{\partial \chi(\phi_t(\mathbf{x}))}{\partial \phi_t} \|\nabla \phi_t(\mathbf{x})\| &= (1 - \beta) \delta_{\Gamma_t}(\mathbf{x}) \Rightarrow \frac{\partial \chi(\phi_t(\mathbf{x}))}{\partial \phi_t} = (1 - \beta) \|\nabla \phi_t(\mathbf{x})\|^{-1} \delta_{\Gamma_t}(\mathbf{x}) \end{aligned} \quad (119)$$

Theorem 1 Time evolution of the Lagrangian functional $\mathcal{L}_t(\phi, \lambda) \equiv \mathcal{L}(\chi(\phi_t), \lambda)$, in equation (112), is always negative i.e. $\dot{\mathcal{L}}(\chi(\phi_t), \lambda) < 0$.

Proof 3 Time differentiation of $\mathcal{L}(\phi_t, \lambda)$, in equation (112)-(b), yields

$$\begin{aligned} \frac{\partial \mathcal{L}(\chi(\phi_t(\mathbf{x}), \lambda))}{\partial t} &\equiv \dot{\mathcal{L}}(\chi(\phi_t(\mathbf{x}), \lambda)) = \int_{\Omega} \frac{\partial (\mathcal{J}(\chi(\phi_t)) + \lambda \mathcal{C}(\chi(\phi_t)))}{\partial \chi} \frac{\partial \chi(\phi_t)}{\partial \phi_t} \dot{\phi}_t(\mathbf{x}) d\Omega = \\ &= \int_{\Omega} (1 - \beta) \|\nabla \phi_t(\mathbf{x})\|^{-1} \delta_{\Gamma_t}(\mathbf{x}) \frac{\partial (\mathcal{J}(\chi(\phi_t)) + \lambda \mathcal{C}(\chi(\phi_t)))}{\partial \chi} \dot{\phi}_t(\mathbf{x}) d\Omega = \\ &= \int_{\Omega} (1 - \beta) \|\nabla \phi_t(\mathbf{x})\|^{-1} \frac{1}{\Delta \chi(\mathbf{x})} \frac{\delta \mathcal{L}(\chi(\phi_t), \lambda)}{\delta \chi}(\mathbf{x}) \delta_{\Gamma_t}(\mathbf{x}) \dot{\phi}_t(\mathbf{x}) d\Omega = \\ &= \int_{\Gamma_t} (1 - \beta) \|\nabla \phi_t(\mathbf{x})\|^{-1} \frac{1}{\Delta \chi(\mathbf{x})} \frac{\delta \mathcal{L}(\chi(\phi_t), \lambda)}{\delta \chi}(\mathbf{x}) \dot{\phi}_t(\mathbf{x}) d\Gamma \end{aligned} \quad (120)$$

where results in equations (114), (117) and (118) have been used. Replacement of equation (112) into equation (120) yields

$$\begin{aligned} \begin{cases} \dot{\mathcal{L}}(\chi(\phi_t), \lambda) = \int_{\Gamma_t} (1 - \beta) \|\nabla \phi_t(\mathbf{x})\|^{-1} \frac{1}{\Delta \chi(\mathbf{x})} \frac{\delta \mathcal{L}(\chi(\phi_t), \lambda)}{\delta \chi}(\mathbf{x}) \dot{\phi}_t(\mathbf{x}) d\Gamma \\ \dot{\phi}_t(\mathbf{x}) = -k \frac{1}{\Delta \chi(\mathbf{x})} \frac{\delta \mathcal{L}(\chi, \lambda)}{\delta \chi}(\mathbf{x}); & k \in \mathbb{R}^+ \end{cases} \\ \Rightarrow \dot{\mathcal{L}}(\chi(\phi_t), \lambda) = -k \int_{\Gamma_t} \underbrace{(1 - \beta) \|\nabla \phi_t(\mathbf{x})\|^{-1}}_{> 0} \underbrace{\left(\frac{1}{\Delta \chi(\mathbf{x})} \frac{\delta \mathcal{L}(\chi(\phi_t), \lambda)}{\delta \chi}(\mathbf{x}) \right)^2}_{> 0} d\Gamma < 0 \quad \forall t \end{aligned} \quad (121)$$

Corollary 1.1 Therefore, at the stationarity of the characteristic function ($\dot{\chi}(\phi_t(\mathbf{x})) = 0 \forall \mathbf{x} \in \Omega$) the achieved, topology $\chi(\mathbf{x}, t)$, defines a (local) minimum of $\mathcal{L}_t(\phi, \lambda) \equiv \mathcal{L}(\chi(\phi_t), \lambda)$ in equation (112).

References

- [1] G. Allaire, *Shape optimization by the homogenization method*. Springer New York, Dec. 6, 2012.
- [2] G. Allaire, E. Bonnetier, G. Francfort, and F. Jouve, “Shape optimization by the homogenization method,” *Numerische Mathematik*, vol. 76, no. 1, pp. 27–68, 1997. DOI: [10.1007/s002110050253](https://doi.org/10.1007/s002110050253).
- [3] G. Allaire, F. de gournay, F. Jouve, and A.-M. Toader, “Structural optimization using topological and shape sensitivity via a level set method,” *Control and Cybernetics*, vol. 34, 2005.
- [4] L. Ambrosio and G. Buttazzo, “An optimal design problem with perimeter penalization,” *Calculus of Variations and Partial Differential Equations*, vol. 1, no. 1, pp. 55–69, 1993. DOI: [10.1007/bf02163264](https://doi.org/10.1007/bf02163264).
- [5] S. Amstutz, S. M. Giusti, A. A. Novotny, and E. A. de Souza Neto, “Topological derivative for multi-scale linear elasticity models applied to the synthesis of microstructures,” *International Journal for Numerical Methods in Engineering*, vol. 84, no. 6, pp. 733–756, 2010. DOI: [10.1002/nme.2922](https://doi.org/10.1002/nme.2922).
- [6] S. Amstutz, “Regularized perimeter for topology optimization,” *SIAM Journal on Control and Optimization*, vol. 51, no. 3, pp. 2176–2199, 2013. DOI: [10.1137/100816997](https://doi.org/10.1137/100816997).
- [7] S. Amstutz and H. Andrä, “A new algorithm for topology optimization using a level-set method,” *Journal of Computational Physics*, vol. 216, no. 2, pp. 573–588, 2006. DOI: [10.1016/j.jcp.2005.12.015](https://doi.org/10.1016/j.jcp.2005.12.015).
- [8] M. P. Bendsoe and O. Sigmund, *Topology optimization*. Springer Berlin Heidelberg, Dec. 1, 2003, 388 pp., ISBN: 3540429921.
- [9] D. P. Bertsekas, D. P. Bertsekas, and D. P. Bertsekas, *Constrained Optimization and Lagrange Multiplier Methods (Optimization and neural computation series)*. Athena Scientific, 1996, ISBN: 1-886529-04-3.
- [10] B. Bourdin, “Filters in topology optimization,” *International Journal for Numerical Methods in Engineering*, vol. 50, no. 9, pp. 2143–2158, 2001. DOI: [10.1002/nme.116](https://doi.org/10.1002/nme.116).
- [11] M. Burger, B. Hackl, and W. Ring, “Incorporating topological derivatives into level set methods,” *Journal of Computational Physics*, vol. 194, no. 1, pp. 344–362, 2004. DOI: [10.1016/j.jcp.2003.09.033](https://doi.org/10.1016/j.jcp.2003.09.033).
- [12] J. C ea, S. Garreau, P. Guillaume, and M. Masmoudi, “The shape and topological optimizations connection,” *Computer Methods in Applied Mechanics and Engineering*, vol. 188, no. 4, pp. 713–726, 2000. DOI: [10.1016/s0045-7825\(99\)00357-6](https://doi.org/10.1016/s0045-7825(99)00357-6).
- [13] E. Chernyaev, “Marching cubes 33: Construction of topologically correct isosurfaces,” Tech. Rep., 1995.
- [14] P. G. Coelho, J. M. Guedes, and J. B. Cardoso, “Topology optimization of cellular materials with periodic microstructure under stress constraints,” *Structural and Multidisciplinary Optimization*, vol. 59, no. 2, pp. 633–645, 2018. DOI: [10.1007/s00158-018-2089-x](https://doi.org/10.1007/s00158-018-2089-x).
- [15] M. A. Crisfield, “An arc-length method including line searches and accelerations,” *International Journal for Numerical Methods in Engineering*, vol. 19, no. 9, pp. 1269–1289, 1983. DOI: [10.1002/nme.1620190902](https://doi.org/10.1002/nme.1620190902).
- [16] M. Dambrine and D. Kateb, “On the ersatz material approximation in level-set methods,” *ESAIM: Control, Optimisation and Calculus of Variations*, vol. 16, no. 3, pp. 618–634, 2009. DOI: [10.1051/cocv/2009023](https://doi.org/10.1051/cocv/2009023).

- [17] N. P. van Dijk, K. Maute, M. Langelaar, and F. van Keulen, “Level-set methods for structural topology optimization: A review,” *Structural and Multidisciplinary Optimization*, vol. 48, no. 3, pp. 437–472, 2013. DOI: [10.1007/s00158-013-0912-y](https://doi.org/10.1007/s00158-013-0912-y).
- [18] H. A. Eschenauer and N. Olhoff, “Topology optimization of continuum structures: A review,” *Applied Mechanics Reviews*, vol. 54, no. 4, pp. 331–390, 2001.
- [19] P. Fernandes, J. M. Guedes, and H. Rodrigues, “Topology optimization of three-dimensional linear elastic structures with a constraint on “perimeter”,” *Computers & Structures*, vol. 73, no. 6, pp. 583–594, 1999. DOI: [10.1016/s0045-7949\(98\)00312-5](https://doi.org/10.1016/s0045-7949(98)00312-5).
- [20] A. Ferrer, J. C. Cante, J. A. Hernández, and J. Oliver, “Two-scale topology optimization in computational material design: An integrated approach,” *International Journal for Numerical Methods in Engineering*, vol. 114, no. 3, pp. 232–254, 2018. DOI: [10.1002/nme.5742](https://doi.org/10.1002/nme.5742).
- [21] M. I. Frecker, G. K. Ananthasuresh, S. Nishiwaki, N. Kikuchi, and S. Kota, “Topological synthesis of compliant mechanisms using multi-criteria optimization,” *Journal of Mechanical design*, vol. 119, no. 2, pp. 238–245, 1997.
- [22] S. M. Giusti, A. Ferrer, and J. Oliver, “Topological sensitivity analysis in heterogeneous anisotropic elasticity problem. theoretical and computational aspects,” *Computer Methods in Applied Mechanics and Engineering*, vol. 311, pp. 134–150, 2016. DOI: [10.1016/j.cma.2016.08.004](https://doi.org/10.1016/j.cma.2016.08.004).
- [23] S. M. Giusti, A. A. Novotny, and C. Padra, “Topological sensitivity analysis of inclusion in two-dimensional linear elasticity,” *Engineering Analysis with Boundary Elements*, vol. 32, no. 11, pp. 926–935, 2008. DOI: [10.1016/j.enganabound.2007.12.007](https://doi.org/10.1016/j.enganabound.2007.12.007).
- [24] J. K. Guest, J. H. Prévost, and T. Belytschko, “Achieving minimum length scale in topology optimization using nodal design variables and projection functions,” *International Journal for Numerical Methods in Engineering*, vol. 61, no. 2, pp. 238–254, 2004. DOI: [10.1002/nme.1064](https://doi.org/10.1002/nme.1064).
- [25] R. B. Haber, C. S. Jog, and M. P. Bends Bendsøe, “A new approach to variable-topology shape design using a constraint on perimeter,” *Structural Optimization*, vol. 11, no. 1-2, pp. 1–12, 1996. DOI: [10.1007/bf01279647](https://doi.org/10.1007/bf01279647).
- [26] G.-W. Jang, J. H. Jeong, Y. Y. Kim, D. Sheen, C. Park, and M.-N. Kim, “Checkerboard-free topology optimization using non-conforming finite elements,” *International Journal for Numerical Methods in Engineering*, vol. 57, no. 12, pp. 1717–1735, 2003. DOI: [10.1002/nme.738](https://doi.org/10.1002/nme.738).
- [27] J. Kato, D. Yachi, K. Terada, and T. Kyoya, “Topology optimization of micro-structure for composites applying a decoupling multi-scale analysis,” *Structural and Multidisciplinary Optimization*, vol. 49, no. 4, pp. 595–608, 2013. DOI: [10.1007/s00158-013-0994-6](https://doi.org/10.1007/s00158-013-0994-6).
- [28] W. E. Lorensen and H. E. Cline, “Marching cubes: A high resolution 3d surface construction algorithm,” *ACM SIGGRAPH Computer Graphics*, vol. 21, no. 4, pp. 163–169, 1987. DOI: [10.1145/37402.37422](https://doi.org/10.1145/37402.37422).
- [29] S. Nishiwaki, M. I. Frecker, S. Min, and N. Kikuchi, “Topology optimization of compliant mechanisms using the homogenization method,” *International journal for numerical methods in engineering*, vol. 42, no. 3, pp. 535–559, 1998.
- [30] J. Norato, R. Haber, D. Tortorelli, and M. P. Bendsøe, “A geometry projection method for shape optimization,” *International Journal for Numerical Methods in Engineering*, vol. 60, no. 14, pp. 2289–2312, 2004. DOI: [10.1002/nme.1044](https://doi.org/10.1002/nme.1044).

- [31] J. A. Norato, B. K. Bell, and D. A. Tortorelli, “A geometry projection method for continuum-based topology optimization with discrete elements,” *Computer Methods in Applied Mechanics and Engineering*, vol. 293, pp. 306–327, 2015. DOI: [10.1016/j.cma.2015.05.005](https://doi.org/10.1016/j.cma.2015.05.005).
- [32] J. A. Norato, M. P. Bendsøe, R. B. Haber, and D. A. Tortorelli, “A topological derivative method for topology optimization,” *Structural and Multidisciplinary Optimization*, vol. 33, no. 4-5, pp. 375–386, 2007. DOI: [10.1007/s00158-007-0094-6](https://doi.org/10.1007/s00158-007-0094-6).
- [33] A. A. Novotny, R. A. Feijóo, E. Taroco, and C. Padra, “Topological sensitivity analysis,” *Computer Methods in Applied Mechanics and Engineering*, vol. 192, no. 7-8, pp. 803–829, 2003. DOI: [10.1016/s0045-7825\(02\)00599-6](https://doi.org/10.1016/s0045-7825(02)00599-6).
- [34] A. A. Novotny and J. Sokolowski, *Topological Derivatives in Shape Optimization*. Springer Berlin Heidelberg, 2013. DOI: [10.1007/978-3-642-35245-4](https://doi.org/10.1007/978-3-642-35245-4).
- [35] J. Oliver and C. Agelet de Saracibar, *Continuum mechanics for engineers. Theory and problems (first edition, september 2016)*, en. 2016. DOI: [10.13140/rg.2.2.25821.20961](https://doi.org/10.13140/rg.2.2.25821.20961).
- [36] S. Osher and J. A. Sethian, “Fronts propagating with curvature-dependent speed: Algorithms based on hamilton-jacobi formulations,” *Journal of Computational Physics*, vol. 79, no. 1, pp. 12–49, 1988. DOI: [10.1016/0021-9991\(88\)90002-2](https://doi.org/10.1016/0021-9991(88)90002-2).
- [37] G. Patané and B. Falcidieno, “Computing smooth approximations of scalar functions with constraints,” *Computers & Graphics*, vol. 33, no. 3, pp. 399–413, 2009.
- [38] J. M. Podestá, C. G. Méndez, S. Toro, A. E. Huespe, and J. Oliver, “Material design of elastic structures using voronoi cells,” *International Journal for Numerical Methods in Engineering*, vol. 115, no. 3, pp. 269–292, 2018. DOI: [10.1002/nme.5804](https://doi.org/10.1002/nme.5804).
- [39] W. H. Press, S. A. Teukolsky, W. T. Vetterling, and B. P. Flannery, *Numerical Recipes*. Cambridge University Pr., Sep. 6, 2007, 1248 pp., ISBN: 0521880688.
- [40] G. I. N. Rozvany, “A critical review of established methods of structural topology optimization,” *Structural and Multidisciplinary Optimization*, vol. 37, no. 3, pp. 217–237, 2008. DOI: [10.1007/s00158-007-0217-0](https://doi.org/10.1007/s00158-007-0217-0).
- [41] J. A. Sethian and A. Wiegmann, “Structural boundary design via level set and immersed interface methods,” *Journal of Computational Physics*, vol. 163, no. 2, pp. 489–528, 2000. DOI: [10.1006/jcph.2000.6581](https://doi.org/10.1006/jcph.2000.6581).
- [42] A. Sharma and K. Maute, “Stress-based topology optimization using spatial gradient stabilized XFEM,” *Structural and Multidisciplinary Optimization*, vol. 57, no. 1, pp. 17–38, 2017. DOI: [10.1007/s00158-017-1833-y](https://doi.org/10.1007/s00158-017-1833-y).
- [43] O. Sigmund and J. Petersson, “Numerical instabilities in topology optimization: A survey on procedures dealing with checkerboards, mesh-dependencies and local minima,” *Structural Optimization*, vol. 16, no. 1, pp. 68–75, 1998. DOI: [10.1007/bf01214002](https://doi.org/10.1007/bf01214002).
- [44] O. Sigmund, “On the design of compliant mechanisms using topology optimization,” *Mechanics of Structures and Machines*, vol. 25, no. 4, pp. 493–524, 1997. DOI: [10.1080/08905459708945415](https://doi.org/10.1080/08905459708945415).
- [45] O. Sigmund and K. Maute, “Topology optimization approaches,” *Structural and Multidisciplinary Optimization*, vol. 48, no. 6, pp. 1031–1055, 2013. DOI: [10.1007/s00158-013-0978-6](https://doi.org/10.1007/s00158-013-0978-6).
- [46] J. C. Simo and T. A. Laursen, “An augmented lagrangian treatment of contact problems involving friction,” *Computers & Structures*, vol. 42, no. 1, pp. 97–116, 1992. DOI: [10.1016/0045-7949\(92\)90540-g](https://doi.org/10.1016/0045-7949(92)90540-g).
- [47] J. Sokolowski and A. Żochowski, “Topological derivative in shape optimization,” in *Encyclopedia of Optimization*, Springer US, 2001, pp. 2625–2626. DOI: [10.1007/0-306-48332-7_524](https://doi.org/10.1007/0-306-48332-7_524).

- [48] F. Velasco, J. C. Torres, A. Léon, and F. Soler, *Adaptive cube tessellation for topologically correct isosurfaces*, en, 2008. DOI: [10.20385/1860-2037/5.2008.3](https://doi.org/10.20385/1860-2037/5.2008.3).
- [49] L. J. van Vliet, I. T. Young, and G. L. Beckers, “A nonlinear laplace operator as edge detector in noisy images,” *Computer Vision, Graphics, and Image Processing*, vol. 45, no. 2, pp. 167–195, 1989. DOI: [10.1016/0734-189x\(89\)90131-x](https://doi.org/10.1016/0734-189x(89)90131-x).
- [50] M. Y. Wang, X. Wang, and D. Guo, “A level set method for structural topology optimization,” *Computer Methods in Applied Mechanics and Engineering*, vol. 192, no. 1-2, pp. 227–246, 2003. DOI: [10.1016/s0045-7825\(02\)00559-5](https://doi.org/10.1016/s0045-7825(02)00559-5).
- [51] D. A. White, M. L. Stowell, and D. A. Tortorelli, “Topological optimization of structures using fourier representations,” *Structural and Multidisciplinary Optimization*, vol. 58, no. 3, pp. 1205–1220, 2018. DOI: [10.1007/s00158-018-1962-y](https://doi.org/10.1007/s00158-018-1962-y).
- [52] K. Yaji, M. Otomori, T. Yamada, K. Izui, S. Nishiwaki, and O. Pironneau, “Shape and topology optimization based on the convected level set method,” *Structural and Multidisciplinary Optimization*, vol. 54, no. 3, pp. 659–672, 2016. DOI: [10.1007/s00158-016-1444-z](https://doi.org/10.1007/s00158-016-1444-z).
- [53] T. Yamada, K. Izui, S. Nishiwaki, and A. Takezawa, “A topology optimization method based on the level set method incorporating a fictitious interface energy,” *Computer Methods in Applied Mechanics and Engineering*, vol. 199, no. 45-48, pp. 2876–2891, 2010. DOI: [10.1016/j.cma.2010.05.013](https://doi.org/10.1016/j.cma.2010.05.013).
- [54] S. Yamasaki, S. Nishiwaki, T. Yamada, K. Izui, and M. Yoshimura, “A structural optimization method based on the level set method using a new geometry-based re-initialization scheme,” *International Journal for Numerical Methods in Engineering*, vol. 83, no. 12, pp. 1580–1624, 2010. DOI: [10.1002/nme.2874](https://doi.org/10.1002/nme.2874).
- [55] O. C. Zienkiewicz and R. L. Taylor, *The finite element method for solid and structural mechanics*. Butterworth-Heinemann, 2005, ISBN: 978-0-7506-6321-2.

Article B

Topology optimization of thermal problems in a nonsmooth variational setting: closed-form optimality criteria



Original Paper | [Published: 19 June 2020](#)

Topology optimization of thermal problems in a nonsmooth variational setting: closed-form optimality criteria

[Daniel Yago](#), [Juan Cante](#), [Oriol Lloberas-Valls](#) & [Javier Oliver](#) 

[Computational Mechanics](#) **66**, 259–286 (2020) | [Cite this article](#)

404 Accesses | 2 Citations | 1 Altmetric | [Metrics](#)

Abstract

This paper extends the nonsmooth Relaxed Variational Approach (RVA) to topology optimization, proposed by the authors in a preceding work, to the solution of thermal optimization problems. First, the RVA topology optimization method is briefly discussed and, then, it is applied to a set of representative problems in which the thermal compliance, the deviation of the heat flux from a given field and the average temperature are minimized. For each optimization problem, the relaxed topological derivative and the corresponding adjoint equations are presented. This set of expressions are then discretized in the context of the finite element method and used in the optimization algorithm to update the characteristic function. Finally, some representative (3D) thermal topology optimization examples are presented to assess the performance of the proposed method and the Relaxed Variational Approach solutions are compared with the ones obtained with the *level set method* in terms of the cost function, the topology design and the computational cost.

Topology optimization of thermal problems in a nonsmooth variational setting: closed-form optimality criteria

D. Yago^{a,b}, J. Cante^{a,b}, O. Lloberas-Valls^{b,c}, J. Oliver^{b,c}

^a Escola Superior d'Enginyeries Industrial, Aeroespacial i Audiovisual de Terrassa (ES-EIAAT), Universitat Politècnica de Catalunya · BarcelonaTech (UPC), Campus Terrassa UPC, c/ Colom 11, 08222 Terrassa, Spain

^b Centre Internacional de Mètodes Numèrics en Enginyeria (CIMNE), Campus Nord UPC, Mòdul C-1 101, c/ Jordi Girona 1-3, 08034 Barcelona, Spain

^c Escola Tècnica Superior d'Enginyeria de Camins, Canals i Ports de Barcelona (ETSEC-CPB), Universitat Politècnica de Catalunya · BarcelonaTech (UPC), Campus Nord UPC, Mòdul C-1, c/ Jordi Girona 1-3, 08034 Barcelona, Spain

B.1 Abstract

This paper extends the nonsmooth Relaxed Variational Approach (RVA) to topology optimization, proposed by the authors in a preceding work, to the solution of thermal optimization problems. First, the RVA topology optimization method is briefly discussed and, then, it is applied to a set of representative problems in which the thermal compliance, the deviation of the heat flux from a given field and the average temperature are minimized. For each optimization problem, the relaxed topological derivative (RTD) and the corresponding adjoint equations are presented. This set of expressions are then discretized in the context of the finite element method (FEM) and used in the optimization algorithm to update the characteristic function.

Finally, some representative (3D) thermal topology optimization examples are presented to assess the performance of the proposed method and the Relaxed Variational Approach solutions are compared with the ones obtained with the *level set method* in terms of the cost function, the topology design and the computational cost.

keywords: Thermal Topology Optimization, Relaxed Variational Approach, Relaxed Topological Derivative, Closed-form optimality criteria, Pseudo-time sequential analysis

B.2 Introduction

B.2.1 Motivation and background

During the last decades, a variety of topology optimization methods have been proposed in the literature. With no aim of being exhaustive, we could classify them into (i) homogenization methods, (ii) density based optimization (SIMP) methods, (iii) level set approaches, and (iv) evolutionary methods, among others. For further information the reader is addressed to reviews in [7, 22, 23, 6]. Albeit these techniques were initially focused on structural problems, along time several of them have been extended to other problems, thus including thermal problems and a number of different applications in this field, e.g.:

- (a) *Thermal compliance minimization:* focused on maximizing thermal diffusion in steady-state problems. Bendsoe and Sigmund [3] implemented the SIMP method for thermal optimization problem as an extension of structural optimization. This same problem was also addressed with ESO-based methods by Li *et al.* [15]. Subsequently, Ha and Cho [12] suggested a level set method for the minimization of the thermal compliance via a Hamilton-Jacobi equation. Later, Zhuang *et al.* [30] implemented the aforementioned problem using a topological derivative method. Alternatively, Gersborg-Hansen *et al.* [10], for the Finite Volume Method (FVM) together with a SIMP method, Gao *et al.* [9], for the ESO method, and Giusti *et al.* [11], for the topological derivative method,

have developed the corresponding algorithms to include design-dependent effects of heat sources.¹ Furthermore, Iga *et al.* [13] and Yamada *et al.* [26] included the heat convection effects in the design for maximizing thermal diffusivity using a homogenization design method and the modified phase-field method reported in [27], respectively.

- (b) *Maximum/average temperature minimization*: looking for designs that reduce the temperature of thermal devices, while increasing their durability. With this goal in mind, researchers have proposed different objective functions to minimize either the average temperature or the maximum temperature in the design domain. Zhang and Liu [28] reported that the p -norm of the temperature field in the design domain, approximates reasonably well the maximum temperature for a large enough p . Marck *et al.* [17] proposed the minimization of the average temperature and its variance, via a SIMP method, by creating the Pareto front of the multi-objective thermal problem, thus leading to a reduction in the achieved temperature while avoiding temperature peaks. On the other side, Burger *et al.* [4] minimized the average internal temperature in the whole design domain, by dissipating the generated heat through the introduction of distributed heat sources within the design domain. For the transient case, the minimization of the maximum temperature throughout the entire operating period was analyzed by Wu *et al.* [25] via the SIMP method.
- (c) *Multiple heat actions optimization*: which can be regarded as multi-objective problems where the cost function corresponds to the weighted sum of individual cost functions for each of the heat actions. In this context Li *et al.* [15, 14] optimized some printed circuit boards (PCB) with the ESO method subjected to multiple heat source, by considering a functional proportional to the heat flux. Years later, Zhuang *et al.* [30] proposed the optimization of some thermally conductive structures via a level set method by optimizing the weighted average of the quadratic temperature gradient.
- (d) *Multi-material thermal optimization*: thermal topology optimization has been also carried out taking into account three or more different materials. Zhuang *et al.* [31] proposed a multi-material topology optimization for the heat conduction problem via a level set method. Later, Zhuang and Xiong [29] used the SIMP method to optimize transient heat conduction problems.
- (e) *Heat flux manipulation optimization problems*: a precursor work on the field is the one by Narayana and Sato [19], where multilayered optimized designs for thermal problems were presented. Later, Dede *et al.* [5] proposed a homogenization-based method which optimizes the orientation of a micro-structure by modifying the effective conductivity tensor at each point. Following this line, Peralta *et al.* [21] suggested a homogenization-based optimization, where the error in guiding the heat flux in given path is minimized, and successfully accomplished the optimization of a thermal concentrator. Finally, Fachinotti *et al.* [8] extended the idea to *black-and-white designs* via a SIMP optimization.

This work focuses on applying the Relaxed Variational Approach (RVA) to topology optimization, proposed by the authors in a previous work [20], to thermal problems. The distinctive feature of RVA is that it keeps the original nonsmooth character of the characteristic function, the design variable, describing the material topology ($\chi : \Omega \rightarrow \{0, 1\}$) but, in spite of this, a variational analysis can be conducted and, then, *closed-form solutions* of the problem (equivalent to the Euler equations in smooth variational problems) can be readily obtained. The approach relies on the use of a specific topological sensitivity, *the Relaxed Topological Derivative* (RTD), as an efficient and simple approximation to the geometrical (or exact) topological derivative (TD), which is consistently derived in the considered relaxed optimization setting.² Then, a robust and efficient *Cutting&Bisection algorithm* is proposed for solving the obtained algebraic, non-linear, solutions in a sequential pseudo-time framework.

The goal here is, thus, to explore the possible extension of the benefits of the RVA, reported in [20] for structural problems, to the realm of thermal problems, typically:

¹The magnitude of the heat source changes according to the material of the point.

²based on a bi-material (soft/hard) approximation, or ersatz approach.

- Avoid *checkerboard patterns* and *mesh-dependency* in the optimized solution.
- Display *black-and-white solutions*, instead of *blurry black-gray-and-white* solutions, for the material distribution, without resorting to *a posteriori filtering techniques*.
- Achieve precise local optima, in a reduced number of iterations of the non-linear solution algorithm, thus leading to relevant diminutions of the associated computational cost.
- Involve *general and easy-to-derive* sensitivities of the cost function in the resulting optimization algorithm.
- Allow the control of the *minimum width* of the material filaments in the optimized layout, thus incorporating *manufacturing constraints* in the designs and precluding classical *element/cell-size-dependence* in the obtained solutions, thus removing the well-known ill-posedness of the problem.

For this purpose three representative thermal optimization problems are explored in this work a) maximization of thermal diffusion, without boundary dependent properties, in steady-state thermal scenarios, b) thermal cloaking based on minimization of the deviation of the heat flux with respect to a target one and c) thermal cloaking based on minimizing the average temperature on a surface around the cloaked object.

The remaining of this paper is structured as follows: in Section B.3, the considered Relaxed Variational Approach (RVA) to topology optimization is summarized in order to, both, supply to the reader the indispensable information and providing the work with the necessary completeness. Then, in Section B.4, a detailed specification of the RVA for thermal optimization problems is presented. Subsequently, a general optimization algorithm is described in Section B.5. The resulting formulation is then assessed, by its application to a set of thermal problems, first in terms of their formulation, in Section B.6 and, then, in terms of their numerical application to specific 3D problems in Section B.7. Finally, Section B.8 concludes with some final remarks.

B.3 Relaxed Variational Approach (RVA) to topology optimization: a summary

B.3.1 Topology domain representation

Let the *analysis domain*³, Ω , denote a fixed smooth open domain of \mathbb{R}^n ($n = 2$ or 3), whose boundary $\partial\Omega$ is also smooth, composed in turn by two smooth open subdomains, $\Omega^+, \Omega^- \subset \Omega$, with $\overline{\Omega^+} \cup \overline{\Omega^-} = \overline{\Omega}$ and $\Omega^+ \cap \Omega^- = \emptyset$.⁴ The first subdomain, Ω^+ , stands for the *hard material* domain, made of a hard (*high-conductive*) material (\mathfrak{M}^+), while subdomain, Ω^- , denoted as the *soft material* domain, is occupied by a soft (*low-conductive*) material (\mathfrak{M}^-). These two subdomains are surrounded by their respective boundaries, $\partial\Omega^+$ and $\partial\Omega^-$, with $\partial\Omega^+ \cap \partial\Omega^- = \Gamma$ (see Figure B.1).

The standard nonsmooth *characteristic function*, $\chi(\mathbf{x}) : \Omega \rightarrow \{0, 1\}$, defining the topology of the analysis domain,⁵ is then defined as

$$\begin{cases} \Omega^+ := \{\mathbf{x} \in \Omega / \chi(\mathbf{x}) = 1\} \\ \Omega^- := \{\mathbf{x} \in \Omega / \chi(\mathbf{x}) = 0\} \end{cases} . \quad (1)$$

Alternatively, the topology can be implicitly defined through a smooth function (termed

³Albeit the name *design domain* is commonly used in topology optimization for Ω , in this work distinction is made of the *analysis domain*, the whole domain considered in the analysis, and the *design domain*, the subset of Ω where the topology is going to be optimized (therefore changed from an initial layout). The reason is that, in some of the considered problems, a certain part of Ω is endowed with a fixed, predetermined, topology thus not being properly part of the design domain.

⁴ $\overline{(\cdot)}$ denotes the closure of the open domain (\cdot) .

⁵The characteristic function, χ , is considered as the design variable in the topology optimization problem.

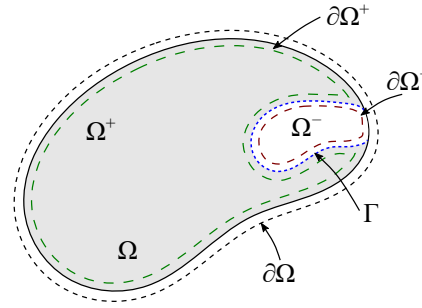


Figure B.1: Representation of the analysis domain, Ω , comprising two disjoint sub-domains Ω^+ and Ω^- . The external boundary of Ω , $\partial\Omega$, is represented by a black dashed line, while the sub-domains boundaries, $\partial\Omega^+$ and $\partial\Omega^-$, are, respectively, depicted by long green and short red dashed lines. Finally, the common sub-domains border, Γ , is represented by a blue dotted line.

discrimination function in Oliver *et al.* [20]) $\psi(\mathbf{x}) : \Omega \rightarrow \mathbb{R}$, $\psi \in H^1(\Omega)$, defined as

$$\begin{cases} \psi(\mathbf{x}) > 0 \iff \mathbf{x} \in \Omega^+ \\ \psi(\mathbf{x}) < 0 \iff \mathbf{x} \in \Omega^- \end{cases} . \quad (2)$$

Then, the two aforementioned subdomains are implicitly defined through $\psi(\mathbf{x})$ (see Figure B.2) as

$$\begin{cases} \Omega^+ := \{\mathbf{x} \in \Omega / \psi(\mathbf{x}) > 0\} \\ \Omega^- := \{\mathbf{x} \in \Omega / \psi(\mathbf{x}) < 0\} \end{cases} , \quad (3)$$

and the *characteristic function*, $\chi_\psi(\mathbf{x}) : \Omega \rightarrow \{0, 1\}$, defining the topology of the analysis domain, can be then expressed as

$$\chi_\psi(\mathbf{x}) = \mathcal{H}(\psi(\mathbf{x})) , \quad (4)$$

where $\mathcal{H}(\cdot)$ stands for the Heaviside function evaluated at (\cdot) .⁶

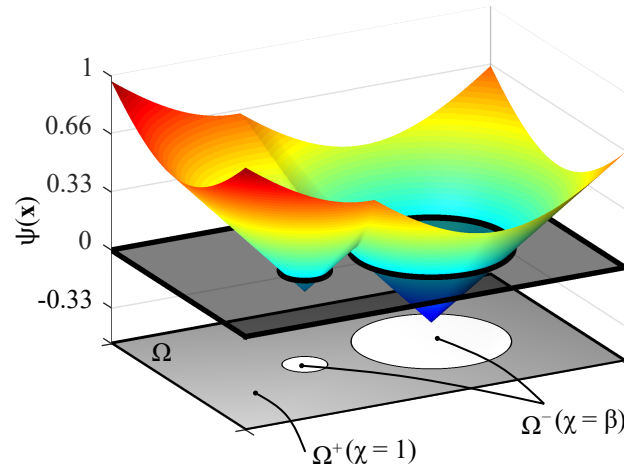


Figure B.2: Topology representation in terms of the discrimination function, $\psi(\mathbf{x})$.

According to equations (3) and (4), the bi-valued *characteristic function*, $\chi(\mathbf{x})$, takes the value 1 when the discrimination function is positive ($\psi(\mathbf{x}) > 0$), i.e. when $\mathbf{x} \in \Omega^+$, and the value 0 when $\psi(\mathbf{x}) < 0$, i.e. when $\mathbf{x} \in \Omega^-$. This *bi-valued (black-and-white)* (black=1, white=0)

⁶Henceforth, the subindex ψ of the characteristic function, χ_ψ , will be omitted.

character of χ , is a fundamental feature of the RVA, and it is always held along the mathematical derivations keeping the nonsmooth character of the design variable. However, the image-set $\{1, 0\}$ is modified to $\{1, \beta\}$, by introducing the, here termed, *relaxed Heaviside function*

$$\mathcal{H}_\beta(x) = \begin{cases} 1 & \text{for } x > 0 \\ \beta & \text{for } x < 0 \end{cases} \quad x \in \mathbb{R}; \quad \beta \ll 1. \quad (5)$$

Remark 1 In *single-material topology optimization*, the value $\chi(\mathbf{x})$ is commonly used to define the material property value \mathbb{E} , at point \mathbf{x} , in terms of the *reference material property value* E , through $\mathbb{E}(\mathbf{x}) = \chi(\mathbf{x})^m E$; with $m > 1$. Then, $\chi = 1$ in Ω^+ naturally defines a *solid material* with properties $\mathbb{E} = \chi^m E = E$, whereas the value $\chi = 0$ in Ω^- , *made of no-material (voids)*, defines null material properties $\mathbb{E}(\mathbf{x}) = \chi(\mathbf{x})^m E = 0$ in that domain. In the present relaxed variational approach, instead, the shift of the low limit of χ to β ($0 < \beta \ll 1$), in equation (5), relaxes that setting to a *bi-material approach*, with Ω containing *two different solid materials*: 1) a *hard material*, in Ω^+ , with regular solid properties $\mathbb{E} = \chi^m E = E$, and 2) a *soft material*, in Ω^- , with very low material properties $\mathbb{E} = \chi^m E = \beta^m E$, which are scaled to values close to zero by the factor $\chi = \beta \ll 1$.⁷ This qualifies the RVA as a *relaxed* or *ersatz/bi-material* approach. This fact will be retrieved later on in this work (see, for instance, equations (14) and (15)).

The topology optimization goal is, then, to minimize a functional or cost function $\mathcal{J}(\chi)$ subjected to one or more constraints and governed by the state equation, i.e.

$$\left[\begin{array}{l} \min_{\chi \in \mathcal{U}_{ad}} \quad \mathcal{J}(\chi) \equiv \int_{\Omega} j(\chi, \mathbf{x}) d\Omega \quad (a) \\ \text{subject to:} \\ \quad \mathcal{C}(\chi) \equiv \int_{\Omega} c(\chi, \mathbf{x}) d\Omega = 0 \quad (b) \quad (6) \\ \text{governed by:} \\ \quad \text{state equation} \quad (c) \end{array} \right.$$

where \mathcal{U}_{ad} stands for the set of admissible solutions for χ . Furthermore, $\mathcal{C}(\chi)$ represents the constraint functional, which, in all the examples in this paper, will be the volume constraint,⁸ and the state equation will correspond to the energy balance in the domain Ω , which will be described later in this paper (see equation (13)). Functionals (6)-(a-b) are assumed to pertain to the following family

$$\mathcal{F}(\chi) : L^2(\Omega) \rightarrow \mathbb{R}; \quad \mathcal{F}(\chi) \equiv \int_{\Omega} f(\chi, \mathbf{x}) d\Omega, \quad (7)$$

the kernel $f(\cdot, \cdot)$ being sufficiently smooth, for differentiation purposes.

B.3.2 Relaxed Topological Derivative (RTD)

The RVA defines the *Relaxed Topological Derivative* (RTD), as the sensitivity of the functional in equation (7). The RTD is derived as the change of the functional in terms of $\chi(\hat{\mathbf{x}})$, as the material at point $\hat{\mathbf{x}}$ is exchanged, per unit of the measure of a perturbed domain around $\hat{\mathbf{x}}$. It can be computed in terms of the classical Fréchet derivative, $\frac{\partial(\cdot)}{\partial\chi}(\hat{\mathbf{x}})$, of the integral kernel, i.e.

$$\frac{\delta\mathcal{F}(\chi)}{\delta\chi}(\hat{\mathbf{x}}) = \left[\frac{\partial f(\chi, \mathbf{x})}{\partial\chi} \right]_{\mathbf{x}=\hat{\mathbf{x}}} \Delta\chi(\hat{\mathbf{x}}), \quad (8)$$

⁷Thus, the single-material and the bi-material formulations converge asymptotically as $\beta \rightarrow 0$.

⁸The present *Cutting&Bisection* algorithm is only intended for single constrained topology optimization problems. Furthermore, along this paper, only equality, pseudo-time evolving volume constraints are considered.

where $\Delta\chi(\hat{\mathbf{x}})$ is termed the *exchange function* and stands for the signed variation of $\chi(\hat{\mathbf{x}})$, due to that material exchange, i.e.

$$\Delta\chi(\hat{\mathbf{x}}) = \begin{cases} -(1 - \beta) < 0 & \text{for } \hat{\mathbf{x}} \in \Omega^+ \\ (1 - \beta) > 0 & \text{for } \hat{\mathbf{x}} \in \Omega^- \end{cases}. \quad (9)$$

Details on the derivations can be found in Oliver *et al.* [20].

B.3.3 Closed-form algebraic solutions

After some algebraic operations, the optimality condition for the *constrained topology optimization problem* can be written as

$$\begin{aligned} \frac{\delta\mathcal{L}(\chi, \lambda)}{\delta\chi}(\mathbf{x}) &= \frac{\delta\mathcal{J}(\chi)}{\delta\chi}(\mathbf{x}) + \lambda \frac{\delta\mathcal{C}(\chi)}{\delta\chi}(\mathbf{x}) = \\ &= \left(\frac{\partial j(\chi, \mathbf{x})}{\partial\chi} \Delta\chi(\mathbf{x}) + \lambda \operatorname{sgn}(\Delta\chi(\mathbf{x})) \right) > 0 \quad \forall \mathbf{x} \in \Omega, \end{aligned} \quad (10)$$

where λ stands for a Lagrange multiplier enforcing restriction $\mathcal{C}(\chi) = 0$, and \mathcal{L} stands for the *Lagrangian function* of the optimization problem (see Oliver *et al.* [20] for additional information). Then, a *closed-form* solution for the topology in equation (4) can be computed as

$$\begin{cases} \psi(\mathbf{x}) := \xi(\chi, \mathbf{x}) - \lambda \\ \chi(\mathbf{x}) = \mathcal{H}_\beta(\psi(\mathbf{x})) \end{cases} \quad \text{in } \Omega, \quad (11)$$

where $\xi(\chi, \mathbf{x})$ is termed the *pseudo-energy*⁹ and it shall be specifically derived for each considered problem. Equations (11) constitute a *closed-form-algebraic* (non-linear fixed-point equation) solution of the problem, which are solved, for $\chi(\mathbf{x})$ and λ , via the *Cutting&Bisection algorithm* proposed in [20]. The resulting global algorithm is sketched in Box I, where the constraint equation is expressed in terms of the pseudo-time $t \in [0, T]$, in the context of a time advancing strategy. Notice that the parameter T stands for the pseudo-time corresponding to the final volume of the proposed topology optimization (pseudo-time dependent) procedure and must be set by the user.

Remark 2 The discrimination function $\psi(\mathbf{x})$ in equation (11) is subsequently smoothed through a *Laplacian smoothing*, whose parameter ϵ determines the *minimum filament width* of the resulting topology, thus removing the possible mesh dependency of the results and the ill-posedness of the problem. The reader is addressed to reference [20] for further details.

Box I: Topology optimization: closed-form solution method

Problem¹⁰:

$$\begin{cases} \chi^* = \operatorname{argmin}_{\chi \in \mathcal{U}_{ad}} \mathcal{J}^{(he)}(\chi) \\ s.t. \quad \mathcal{C}(\chi) \equiv t - \frac{|\Omega^-(\chi\psi)|}{|\Omega|} = 0; \quad t \in [0, T] \\ \text{state equation} \end{cases} \quad (a)$$

Lagrangian:

$$\mathcal{L}(\chi, \lambda) = \mathcal{J}^{(he)}(\chi) + \lambda\mathcal{C}(\chi) \quad (b)$$

Optimality criterion:

⁹The pseudo-energy, $\xi(\mathbf{x}, \chi)$, has normally dimensions of energy.

$$\begin{cases} \frac{\delta \mathcal{L}(\chi, \lambda)}{\delta \chi}(\mathbf{x}) = (\xi(\mathbf{x}, \chi) - \lambda) \\ \mathcal{C}(\chi) = 0 \end{cases} \quad (c)$$

Shifting and normalization¹¹:

$$\begin{cases} \hat{\xi}(\mathbf{x}) = \frac{\xi(\mathbf{x}) - \Delta_{shift}}{\Delta_{norm}} & \forall \mathbf{x} \in \Omega^+ \\ \hat{\xi}(\mathbf{x}) = \frac{\xi(\mathbf{x})}{\Delta_{norm}} & \forall \mathbf{x} \in \Omega^- \end{cases} \quad (d)$$

Closed-form solution:

$$\begin{cases} \psi_\chi(\mathbf{x}, \lambda) := \hat{\xi}(\mathbf{x}, \chi) - \lambda \\ \chi(\mathbf{x}, \lambda) = \mathcal{H}_\beta[\psi_\chi(\mathbf{x}, \lambda)] \\ \mathcal{C}(\chi(\mathbf{x}, \lambda)) = 0 \end{cases} \quad (e)$$

Topology:

$$\begin{cases} \Omega^+(\chi) := \{\mathbf{x} \in \Omega / \psi_\chi(\mathbf{x}, \lambda) > 0\} \\ \Omega^-(\chi) := \{\mathbf{x} \in \Omega / \psi_\chi(\mathbf{x}, \lambda) < 0\} \\ \Gamma(\chi) := \{\mathbf{x} \in \Omega / \psi_\chi(\mathbf{x}, \lambda) = 0\} \end{cases} \quad (12)$$

B.4 Formulation of the state problem

In the context of the relaxed (bi-material) approach referred to in Remark 1, both the unknowns (temperatures) and data of the optimization problem (material properties) depend on the topology layout, that is, on the characteristic function, χ . Then, let Ω be the analysis domain, whose boundary $\partial\Omega$ is made of three mutually disjoint subsets, $\partial\Omega = \partial_\theta\Omega \cup \partial_q\Omega \cup \partial_h\Omega$, as depicted in Figure B.3, with $\partial_\theta\Omega$ of nonzero Lebesgue measure. Boundaries $\partial_\theta\Omega$, $\partial_q\Omega$ and $\partial_h\Omega$ are, respectively, those subsets of $\partial\Omega$, where temperature, $\bar{\theta}(\mathbf{x})$, heat fluxes, $\bar{q}(\mathbf{x}) = \mathbf{q}(\mathbf{x}) \cdot \mathbf{n}$ and convective heat fluxes, $h(\theta(\mathbf{x}) - \theta_{amb}(\mathbf{x})) = \mathbf{q}(\mathbf{x}) \cdot \mathbf{n}$, are prescribed.

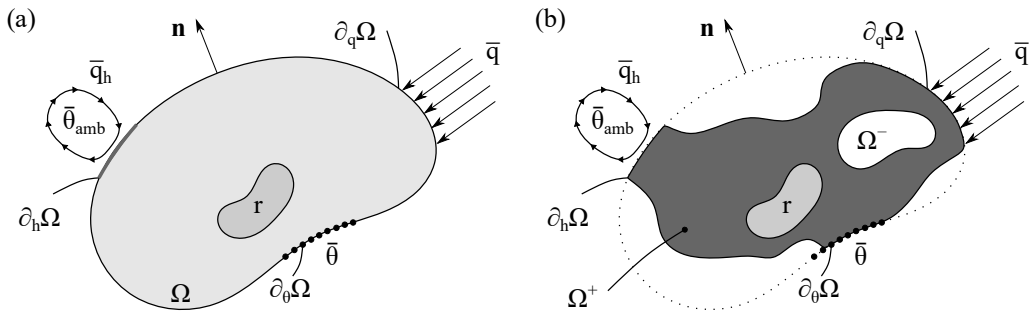


Figure B.3: Thermal problem sketch: (a) fixed analysis domain Ω with boundary conditions (in which the temperature $\bar{\theta}(\mathbf{x})$, the normal heat flux $\bar{q}(\mathbf{x})$ or the convective heat flux $\bar{q}_h(\mathbf{x})$ can be prescribed at $\partial_\theta\Omega$, $\partial_q\Omega$ and $\partial_h\Omega$, respectively) and (b) Hard and soft material domains, Ω^+ and Ω^- , respectively, with the same boundary conditions.

The steady-state thermal problem, for the temperature distribution $\theta(\mathbf{x}, \chi)$, states the heat

¹⁰From now on, superscript $(\cdot)^{(he)}$ refers to results obtained from approximations via finite element calculations of typical mesh-size h_e .

¹¹Shifting and normalization operations in terms of Δ_{shift} and Δ_{norm} (standing, respectively, for the minimum value and the range of ξ at $t = 0$) are introduced for the purposes of providing *algorithmic time consistency* to the problem at $t = 0$. It can be proven that those operations do not alter the problem solution.

energy balance in the analysis domain, Ω , and it can be formulated as

$$\left[\begin{array}{l} \text{Find } \theta(\mathbf{x}, \chi), \text{ such that} \\ \left\{ \begin{array}{ll} -\nabla \cdot \mathbf{q}(\mathbf{x}, \chi) + r(\mathbf{x}, \chi) = 0 & \text{in } \Omega \\ \mathbf{q}(\mathbf{x}, \chi) \cdot \mathbf{n} = \bar{q}(\mathbf{x}) & \text{on } \partial_q \Omega \\ \theta(\mathbf{x}, \chi) = \bar{\theta}(\mathbf{x}) & \text{on } \partial_\theta \Omega \\ \mathbf{q}(\mathbf{x}, \chi) \cdot \mathbf{n} = h (\theta(\mathbf{x}, \chi) - \theta_{amb}(\mathbf{x})) & \text{on } \partial_h \Omega \end{array} \right. \end{array} \right. , \quad (13)$$

where $\mathbf{q}(\mathbf{x}, \chi)$ stands for the heat flux, $r(\mathbf{x}, \chi)$ is the heat source function and $\bar{q}(\mathbf{x})$ stands for the prescribed heat flux on the boundaries of Ω . Additionally, h denotes the heat transfer coefficient, $\theta_{amb}(\mathbf{x})$ corresponds to the ambient temperature imposed at $\partial_h \Omega$ and \mathbf{n} defines the unit outwards normal.

The conductive material is governed by the Fourier's law, i.e. $\mathbf{q}(\mathbf{x}, \chi) = -\boldsymbol{\kappa}(\mathbf{x}, \chi) \cdot \nabla \theta_\chi(\mathbf{x})$, where $\boldsymbol{\kappa}$ stands for the symmetric second order thermal conductivity tensor and $\nabla \theta_\chi(\mathbf{x})$ is the thermal gradient tensor.¹² Both, the conductivity, $\boldsymbol{\kappa}(\mathbf{x}, \chi)$, and the heat source, $r(\mathbf{x}, \chi)$, are postulated, in terms of the characteristic function, χ , (see Remark 1) as follows:

$$\left\{ \begin{array}{l} \boldsymbol{\kappa}_\chi(\mathbf{x}) = \chi_\kappa^{m_\kappa}(\mathbf{x}) \boldsymbol{\kappa}(\mathbf{x}) ; \quad m_\kappa > 1 \\ r_\chi(\mathbf{x}) = \chi_r^{m_r}(\mathbf{x}) r(\mathbf{x}) ; \quad m_r \geq 1 \end{array} \right. \quad (14)$$

$$(15)$$

with

$$\left\{ \begin{array}{l} \chi_\kappa(\mathbf{x}) = \mathcal{H}_{\beta_\kappa}(\chi) := \begin{cases} 1 & \text{if } \mathbf{x} \in \Omega^+ \\ \beta_\kappa & \text{if } \mathbf{x} \in \Omega^- \end{cases} \\ \chi_r(\mathbf{x}) = \mathcal{H}_{\beta_r}(\chi) := \begin{cases} 1 & \text{if } \mathbf{x} \in \Omega^+ \\ \beta_r & \text{if } \mathbf{x} \in \Omega^- \end{cases} \end{array} \right. , \quad (16)$$

$$(17)$$

where χ_κ and χ_r stand for the *relaxed characteristic functions* for the thermal conductivity, $\boldsymbol{\kappa}$, and the heat source, r , respectively. Associated to the *relaxation factor*, β , of every property, we define the contrast factor, α , through $\beta_{(\cdot)} = \alpha_{(\cdot)}^{1/m_{(\cdot)}} \implies \alpha_{(\cdot)} = \beta_{(\cdot)}^{m_{(\cdot)}}$. Different values of $m_{(\cdot)}$ may be required for the topology optimization procedure, depending on the material interpolation.

Alternatively, the thermal problem stated in equation (13) can be written in variational form as

$$\left[\begin{array}{l} \text{Find the temperature field } \theta_\chi \in \mathcal{U}(\Omega) \text{ such that} \\ a(w, \theta_\chi) = l(w) \quad \forall w \in \mathcal{V}(\Omega) \end{array} \right. \quad (18)$$

$$\left[\begin{array}{l} \text{where} \\ a(w, \theta_\chi) = \int_\Omega \nabla w(\mathbf{x}) \cdot \boldsymbol{\kappa}_\chi(\mathbf{x}) \cdot \nabla \theta_\chi(\mathbf{x}) d\Omega + \int_{\partial_h \Omega} h w(\mathbf{x}) \theta_\chi(\mathbf{x}) d\Gamma, \end{array} \right. \quad (19)$$

$$\left[\begin{array}{l} l(w) = - \int_{\partial_q \Omega} w(\mathbf{x}) \bar{q}(\mathbf{x}) d\Gamma + \int_{\partial_h \Omega} h w(\mathbf{x}) \theta_{amb}(\mathbf{x}) d\Gamma + \int_\Omega w(\mathbf{x}) r_\chi(\mathbf{x}) d\Omega, \end{array} \right. \quad (20)$$

where the set of admissible temperature fields is $\mathcal{U}(\Omega) := \{\theta(\mathbf{x}) / \theta \in H^1(\Omega), \theta = \bar{\theta} \text{ on } \partial_\theta \Omega\}$, and the space of admissible virtual temperature fields is given by $\mathcal{V}(\Omega) := \{w(\mathbf{x}) / w \in H^1(\Omega), w = 0 \text{ on } \partial_\theta \Omega\}$. Equations (18) to (20) are discretized via the Finite Element Method as shown in Appendix B.A.

¹² $\boldsymbol{\kappa} = \kappa \mathbf{I}$ for isotropic conductive materials.

B.5 Optimization algorithm

The algorithm to obtain the optimal characteristic function distribution, $\chi(\mathbf{x})$,¹³ is based on the *Cutting&Bisection technique*, shown in Algorithm 3, in the context of the *pseudo-time-advancing strategy*. The strategy, described in Oliver *et al.* [20], is sketched in Algorithm 2. The number of time-steps of this methodology is related to the robustness and computational cost of the problem: the more time-steps, the more robust the solution is, although the computational cost of the optimization is higher. Then, it is up to the user to impose a feasible time evolution based on his/her own experience.

Algorithm 2: Optimization algorithm

Data: Given the mesh, state equation, boundary conditions and objective function
Result: Find χ_n for $\mathcal{T} := \{t_0, t_1, \dots, t_n, \dots, T\}$
begin
 Initialization of the design variables;
 for $n \leftarrow 1$ **to** n_{steps} **do**
 Initialization of step n ;
 $i \leftarrow 0$;
 while *Topology and Lagrange multiplier tolerances are not satisfied* **do**
 Solve the equilibrium equation using FEM;
 Compute the relaxed topological sensitivity (RTD) using the adjoint method;
 Modify the sensitivity (*Shifting and normalization*);
 Regularize the sensitivity by a Laplacian smoothing;
 Compute the Lagrangian multiplier using a *bisection algorithm* (algorithm 3);
 Update the discrimination function;
 Update the characteristic function;
 $i \leftarrow i + 1$;
 end
 $\chi_n \leftarrow$ current characteristic function;
 end
end

For practical purposes, the *Laplacian regularization* is applied to the *pseudo-energy density*, ξ (sensitivity), instead of the *discrimination function*, $\psi = \xi - \lambda$, since the regularization does not affect the (constant) Lagrange multiplier λ . In this way, it is required only once for each iteration of the algorithm 2 (outer loop), instead of at every iteration of the *Cutting&Bisection* algorithm 3 (inner loop). This minor modification translates into a significant reduction in the computational cost of the *bisection algorithm*.

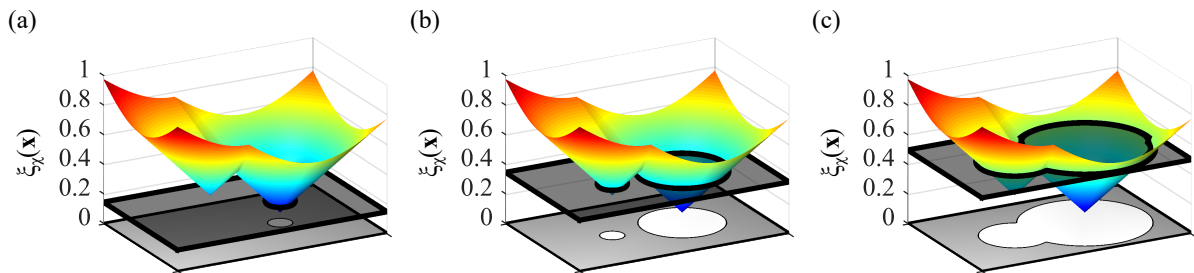


Figure B.4: Cutting and bisection iterative algorithm. Visual representation for different λ : (a) cutting plane at $\lambda_1 = 0.15$, (b) Cutting plane at $\lambda_2 = 0.35$ and (c) Cutting plane at $\lambda_3 = 0.50$. As it can be observed, the ratio of soft domain, $\frac{|\Omega^-|}{|\Omega|}$, increases with the Lagrange multiplier. Therefore, $|\Omega^-(\lambda_1)| < |\Omega^-(\lambda_2)| < |\Omega^-(\lambda_3)|$.

In addition, the procedure to compute the Lagrange multiplier, imposing the constraint equation of (12)-(a), is illustrated in Figure B.4. A modified Marching Cubes method, detailed in Oliver *et al.* [20], is used to numerically compute the 0-level iso-surface of the *discrimination*

¹³The solution χ , resulting from the optimization process, must lie in the subset of admissible solutions, \mathcal{U}_{ad} , corresponding to the tackled single-material (state) thermal problem (i.e. for $\beta \rightarrow 0$). Then, the subset is defined as $\mathcal{U}_{ad} = \{\chi / \Omega^+(\chi) \subset \Omega, \partial_\theta \Omega \cap \partial \Omega^+(\chi) \neq \emptyset, \partial_q \Omega \subset \partial \Omega^+(\chi), \partial_h \Omega \subset \partial \Omega^+(\chi)\}$.

function, ψ . Through this technique, the element hard-phase volume can be obtained, along with the constraint value, \mathcal{C} .

Algorithm 3: Cutting&Bisection iterative algorithm

Data: Given the mesh, the regularized energy density $\xi_\tau(\mathbf{x}, \chi)$ and the pseudo-time t_n

Result: Find λ_n such that the constraint equation is fulfilled

begin

$j \leftarrow 0$;

while *Volume constraint is not satisfied* **do**

 Update the Lagrangian multiplier;

 Compute the corresponding discrimination function;

 Compute the corresponding characteristic function;

 Compute the corresponding volume constraint;

$j \leftarrow j + 1$;

end

end

B.6 Topology optimization problems

B.6.1 Thermal compliance problem

Let us now consider the *maximal thermal diffusivity (minimal thermal compliance)* topology optimization problem. This goal can be achieved by minimizing the negative of the total potential energy, i.e.:

$$\left[\begin{array}{l} \min_{\chi \in \mathcal{U}_{ad}} \mathcal{J}(\theta_\chi(\mathbf{x}, t)) \equiv - \left(\frac{1}{2} a_\chi(\theta_\chi, \theta_\chi) - l(\theta_\chi) \right) \equiv \frac{1}{2} l(\theta_\chi(\mathbf{x}, t)) \quad (a) \\ \text{subject to:} \\ \mathcal{C}(\chi, t) := t - \frac{|\Omega^-|(\chi)}{|\Omega|} = 0; \quad t \in [0, 1] \quad (b) \\ \text{governed by:} \\ a(w, \theta_\chi) = l(w) \quad \forall w \in \mathcal{V}(\Omega), \forall \theta_\chi \in \mathcal{U}(\Omega) \quad (c) \end{array} \right. \quad (21)$$

This problem belongs to the class of problems considered in equation (6) with

$$\begin{aligned} \mathcal{J}(\theta_\chi) &\equiv \frac{1}{2} l(\theta_\chi) = \frac{1}{2} \left(\int_{\Omega} r \theta_\chi \, d\Omega - \int_{\partial_q \Omega} \bar{q} \theta_\chi \, d\Gamma - \int_{\partial_h \Omega} h \theta_{amb} \theta_\chi \, d\Gamma \right) = \frac{1}{2} a_\chi(\theta_\chi, \theta_\chi) \equiv \\ &\equiv \frac{1}{2} \left(\int_{\Omega} \nabla \theta_\chi \cdot \boldsymbol{\kappa}_\chi \cdot \nabla \theta_\chi \, d\Omega - \int_{\partial_h \Omega} h \theta_\chi \theta_\chi \, d\Gamma \right) = \int_{\Omega} \mathcal{U}_\chi \, d\Omega - \int_{\partial_h \Omega} h \theta_\chi \theta_\chi \, d\Gamma \end{aligned} \quad (22)$$

where equations (19) and (20) have been considered for $w \equiv \theta_\chi$, and \mathcal{U}_χ can be identified as the *actual thermal energy density* ($\mathcal{U}_\chi = \frac{1}{2} \nabla \theta_\chi \cdot \boldsymbol{\kappa}_\chi \cdot \nabla \theta_\chi$). Comparing equations (22) and (6), we can identify

$$j(\chi, \mathbf{x}) \equiv \frac{1}{2} \nabla \theta_\chi \cdot \boldsymbol{\kappa}_\chi(\mathbf{x}) \cdot \nabla \theta_\chi = \mathcal{U}_\chi(\mathbf{x}). \quad (23)$$

The corresponding finite element discretization counterpart of the problem in equation (21) reads

$$\left[\begin{array}{l} \min_{\chi \in \mathcal{U}_{ad}} \mathcal{J}^{(h_e)}(\theta_\chi(t)) \equiv \frac{1}{2} \mathbf{f}^T \hat{\boldsymbol{\theta}}_\chi(t) \quad (a) \\ \text{subject to:} \\ \mathcal{C}(\chi, t) := t - \frac{|\Omega^-|(\chi)}{|\Omega|} = 0; \quad t \in [0, 1] \quad (b) \\ \text{governed by:} \\ \mathbb{K}_\chi \hat{\boldsymbol{\theta}}_\chi = \mathbf{f} \quad (c) \end{array} \right. \quad (24)$$

where h_e stands for the typical size of the finite element mesh, and $\mathbf{f}^T \hat{\boldsymbol{\theta}}_\chi(t)$ denotes the thermal compliance. Bear in mind that the discretization of the state equation for the thermal problem (73) has been also considered in the previous minimization problem.

Topological sensitivity of the cost function

The *adjoint method* [16] for sensitivity analysis is used in this paper to compute the relaxed topological derivative (RTD) of the cost-function, $\mathcal{J}^{(h_e)}(\theta_\chi)$, in equation (24)-(a), without explicitly computing the sensitivity of the nodal temperature field ($\partial\theta_\chi/\partial\chi$).

Let $\bar{\mathcal{J}}^{(h_e)}(\chi)$ be the extended cost function of $\mathcal{J}^{(h_e)}(\chi)$ defined as

$$\bar{\mathcal{J}}^{(h_e)}(\chi) = \frac{1}{2} \mathbf{f}^T \hat{\boldsymbol{\theta}}_\chi - \hat{\mathbf{w}}^T \left(\mathbb{K}_\chi \hat{\boldsymbol{\theta}}_\chi - \mathbf{f} \right), \quad (25)$$

where $\hat{\mathbf{w}}$ stands for the solution of the adjoint state problem. Then, the sensitivity of the cost function results, after using the RTD, in the following

$$\begin{aligned} \frac{\delta \bar{\mathcal{J}}^{(h_e)}(\chi)}{\delta \chi}(\hat{\mathbf{x}}) &= \left(\frac{1}{2} \mathbf{f}^T - \hat{\mathbf{w}}^T \mathbb{K}_\chi \right) \frac{\delta \hat{\boldsymbol{\theta}}_\chi}{\delta \chi}(\hat{\mathbf{x}}) \\ &+ \left(\frac{1}{2} \frac{\delta \mathbf{f}_\chi^T}{\delta \chi}(\hat{\mathbf{x}}) \hat{\boldsymbol{\theta}}_\chi - \hat{\mathbf{w}}^T \frac{\delta \mathbb{K}_\chi}{\delta \chi}(\hat{\mathbf{x}}) \hat{\boldsymbol{\theta}}_\chi + \hat{\mathbf{w}}^T \frac{\delta \mathbf{f}_\chi}{\delta \chi}(\hat{\mathbf{x}}) \right). \end{aligned} \quad (26)$$

After some algebraic manipulation, accounting for the adjoint state equation, one arrives to

$$\frac{\delta \bar{\mathcal{J}}^{(h_e)}(\chi)}{\delta \chi}(\hat{\mathbf{x}}) = \left[\frac{\delta \mathbf{f}_\chi^T}{\delta \chi}(\mathbf{x}) \hat{\boldsymbol{\theta}}_\chi - \frac{1}{2} \hat{\boldsymbol{\theta}}_\chi^T \frac{\delta \mathbb{K}_\chi}{\delta \chi}(\mathbf{x}) \hat{\boldsymbol{\theta}}_\chi \right]_{\mathbf{x}=\hat{\mathbf{x}}}. \quad (27)$$

Finally, equation (27) is discretized using the FEM expressions of equations (78)-(81), as detailed in Appendix B.B, as

$$\frac{\delta \bar{\mathcal{J}}^{(h_e)}(\theta_\chi)}{\delta \chi}(\hat{\mathbf{x}}) = m_r (\chi_r(\hat{\mathbf{x}}))^{m_r-1} \bar{U}_r(\hat{\mathbf{x}}) \Delta \chi_r(\hat{\mathbf{x}}) - m_\kappa (\chi_\kappa(\hat{\mathbf{x}}))^{m_\kappa-1} \bar{U}(\hat{\mathbf{x}}) \Delta \chi_\kappa(\hat{\mathbf{x}}), \quad (28)$$

where $\bar{U}(\hat{\mathbf{x}})$ is the *nominal heat conduction energy density* and $\bar{U}_r(\hat{\mathbf{x}})$ is the *nominal heat source energy density*, which are respectively written as

$$\begin{cases} \bar{U}(\hat{\mathbf{x}}) = \frac{1}{2} (\nabla \theta_\chi \cdot \boldsymbol{\kappa} \cdot \nabla \theta_\chi)(\hat{\mathbf{x}}) & (a) \\ \bar{U}_r(\hat{\mathbf{x}}) = (r \theta_\chi)(\hat{\mathbf{x}}) & (b) \end{cases}. \quad (29)$$

Closed-form solution

In Box II, the *pseudo-energy density*, $\xi(\mathbf{x}, \chi)$, to be considered for the closed-form solution in Box I, is presented.

Box II: Topology optimization of thermal compliance problems

Problem:

$$\begin{cases} \chi^* = \underset{\chi \in \mathcal{A}_{ad}}{\operatorname{argmin}} \mathcal{J}^{(h_e)}(\chi) := \frac{1}{2} \mathbf{f}^T \hat{\boldsymbol{\theta}}_\chi \\ \text{s.t. } \mathcal{C}(\chi, t) := t - \frac{|\Omega^-|(\chi)}{|\Omega|} = 0; \quad t \in [0, 1] \\ \mathbb{K}_\chi \hat{\boldsymbol{\theta}}_\chi = \mathbf{f} \end{cases} \quad (a)$$

Energy density:

$$\xi(\hat{\mathbf{x}}, \chi) = \gamma_1(\hat{\mathbf{x}}, \chi) \bar{U}(\hat{\mathbf{x}}) - \gamma_2(\hat{\mathbf{x}}, \chi) \bar{U}_r(\hat{\mathbf{x}}) \quad (b)$$

where

$$\begin{cases} \bar{U}(\hat{\mathbf{x}}) = \frac{1}{2} (\nabla \theta_\chi \cdot \boldsymbol{\kappa} \cdot \nabla \theta_\chi)(\hat{\mathbf{x}}) \geq 0; \\ \bar{U}_r(\hat{\mathbf{x}}) = (r \theta_\chi)(\hat{\mathbf{x}}) \\ \gamma_1 = 2m_\kappa (\chi_\kappa(\hat{\mathbf{x}}))^{m_\kappa - 1} (1 - \beta_\kappa) \\ \gamma_2 = m_r (\chi_r(\hat{\mathbf{x}}))^{m_r - 1} (1 - \beta_r) \end{cases} \quad (30)$$

B.6.2 Thermal cloaking in terms of heat flux

We now consider an object whose thermal properties may differ from the properties of the surrounding material Ω . Then, the main objective is to thermally cloak the object, colored in black (see Figure B.5), from being detected by an external thermal detecting device, measuring the deviation between the constant heat flux, theoretically observed on the 3D homogeneous domain Ω , and the actual flux in the non-homogeneous domain containing the cloaked object. Under the assumption that there is no body that alters the flux, the heat flux entering across the left face of Ω should be constant and equal to that exiting across the right face. In addition, the unperturbed domain presents a known homogeneous heat flux field. Thus, the goal of this topology optimization problem is to find the optimal topology of the surrounding cloaking device, Ω_{dev} , displayed in dark gray, that mitigates the perturbation of the object in the heat flux field so as to resemble the original homogeneous heat-flux.

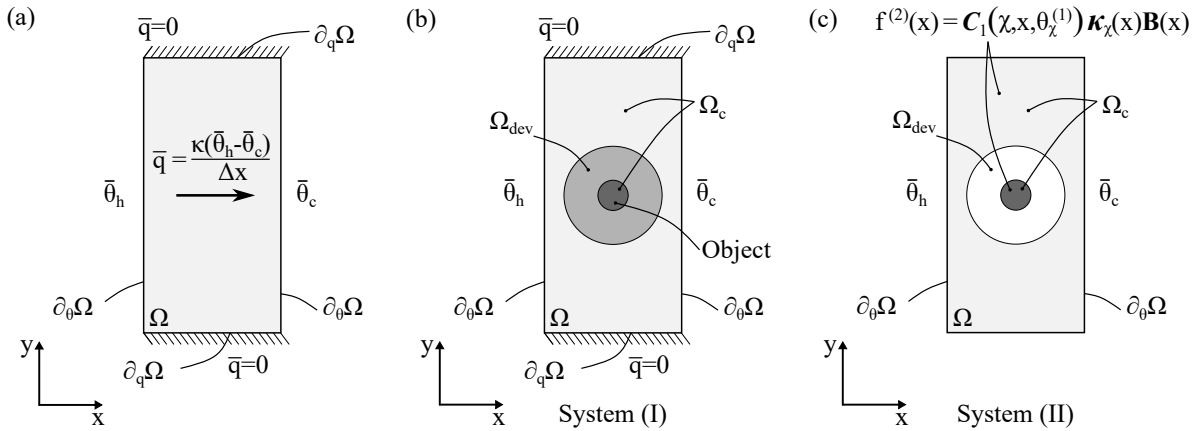


Figure B.5: Thermal cloaking problem: (a) homogeneous problem setting where a constant uniform heat flux over all the domain Ω is observed, (b) topology optimization domain with boundary conditions of system (I), and (c) topology optimization domain with boundary conditions of system (II). The objective is to minimize the perturbation of an object placed in the center of the domain Ω . For that reason, it is surrounded by a cloaking device, in dark gray, which must be optimized.

The problem setting is illustrated in Figure B.5, in which the constant given heat flux is prescribed via the equivalent Dirichlet conditions on both vertical sides, i.e. the temperature is prescribed to a high value, $\bar{\theta}_h$, and a low value, $\bar{\theta}_c$, at the left and right sides, respectively (see Figure B.5-(a)). Adiabatic conditions are assumed on the other two boundaries. Figure B.5-(b) depicts the setting and boundary conditions when the object to be hidden is placed inside the analysis domain, Ω . The corresponding topology optimization problem is written as the minimization of the deviation (measured through a L2-norm) between the constant heat flux

and the actual heat flux in domain $\Omega_c \equiv \Omega \setminus \Omega_{dev}$, which reads as

$$\left[\begin{array}{l} \min_{\chi \in \mathcal{U}_{ad}} \mathcal{J}(\theta_\chi(\mathbf{x}, t)) = \|\mathbf{q}_\chi(\mathbf{x}, \theta_\chi) - \bar{\mathbf{q}}(\mathbf{x})\|_{L_2(\Omega_c)} = \left(\int_{\Omega_c} |\mathbf{q}_\chi(\mathbf{x}, \theta_\chi) - \bar{\mathbf{q}}(\mathbf{x})|^2 d\Omega \right)^{\frac{1}{2}} \quad (a) \\ \text{subject to :} \\ \mathcal{C}(\chi, t) := t - \frac{|\Omega^-(\chi)}{|\Omega|} = 0; \quad t \in [0, 1] \quad (b) \\ \text{governed by:} \\ a(w, \theta_\chi) = l(w) \quad \forall w \in \mathcal{V}(\Omega), \forall \theta_\chi \in \mathcal{U}(\Omega) \quad (c) \end{array} \right. \quad (31)$$

where, in equation (31)-(a), $\mathbf{q}_\chi(\mathbf{x}, \theta_\chi)$ stands for the heat flux vector, which depends on the topology, whereas $\bar{\mathbf{q}}(\mathbf{x})$ corresponds to the prescribed (original) heat flux at the same point.

This problem belongs to the class of problems with the functional considered in equation (7), which can be generalized as

$$\mathcal{F}_\chi \equiv \left(\int_{\Omega} f(\chi, \mathbf{x}) d\Omega \right)^p \quad (32)$$

where $p > 0$ stands for an exponential factor. Then, the relaxed topological derivative (RTD) proposed in equation (8) can be rewritten as

$$\frac{\delta \mathcal{F}(\chi)}{\delta \chi}(\hat{\mathbf{x}}) = p \mathcal{F}(\chi)^{p-1} \left[\frac{\partial f(\chi, \mathbf{x})}{\partial \chi} \right]_{\mathbf{x}=\hat{\mathbf{x}}} \Delta \chi(\hat{\mathbf{x}}). \quad (33)$$

Therefore, the functional (31)-(a) is related to (32) by

$$\begin{aligned} \mathcal{J}(\theta_\chi) &\equiv \left(\int_{\Omega_c} |\mathbf{q}_\chi(\mathbf{x}, \theta_\chi) - \bar{\mathbf{q}}(\mathbf{x})|^2 d\Omega \right)^{\frac{1}{2}} = \\ &= \left(\int_{\Omega} 1_{\Omega_c}(\mathbf{x}) |-\boldsymbol{\kappa}_\chi(\mathbf{x}) \cdot \nabla \theta_\chi(\mathbf{x}) - \bar{\mathbf{q}}(\mathbf{x})|^2 d\Omega \right)^{\frac{1}{2}} \end{aligned} \quad (34)$$

with $p = 1/2$. Comparing equations (34), (32) and (6) we can readily identify

$$j(\chi, \mathbf{x}) \equiv 1_{\Omega_c}(\mathbf{x}) |\mathbf{q}_\chi(\mathbf{x}, \theta_\chi) - \bar{\mathbf{q}}(\mathbf{x})|^2 \quad \forall \mathbf{x} \in \Omega, \quad (35)$$

with $1_{\Omega_c}(\mathbf{x}) : \Omega \rightarrow \{0, 1\}$ being the indicator function of the subdomain $\Omega_c \subset \Omega$, which is equal to 1 for any point contained in Ω_c , and 0 for any point outside the subdomain Ω_c .

Let us now discretize the cost function, $\mathcal{J}(\theta_\chi(t))$, using the FEM expressions defined in Appendix B.A, which yields to

$$\min_{\chi \in \mathcal{U}_{ad}} \mathcal{J}^{(he)}(\theta_\chi(t)) \equiv \left(\int_{\Omega} 1_{\Omega_c}(\mathbf{x}) \left| -\boldsymbol{\kappa}_\chi(\mathbf{x}) \mathbf{B}(\mathbf{x}) \hat{\boldsymbol{\theta}}_\chi^{(1)} - \bar{\mathbf{q}}(\mathbf{x}) \right|^2 d\Omega \right)^{\frac{1}{2}}, \quad (36)$$

where the constraint equation and the state equation are identical to those shown in equation (31)-(b-c).

Topological sensitivity of the cost function

Mimicking the procedure described in Section B.6.1, we include the discretized version of the state equation (31)-(c) into the discretized cost function (36), in order to express the extended cost function, $\bar{\mathcal{J}}^{(he)}(\chi)$, as

$$\bar{\mathcal{J}}^{(he)}(\chi) = \left(\int_{\Omega} 1_{\Omega_c}(\mathbf{x}) \left| -\boldsymbol{\kappa}_\chi(\mathbf{x}) \mathbf{B}(\mathbf{x}) \hat{\boldsymbol{\theta}}_\chi^{(1)} - \bar{\mathbf{q}}(\mathbf{x}) \right|^2 d\Omega \right)^{\frac{1}{2}} - \hat{\mathbf{w}}^T \left(\mathbb{K}_\chi \hat{\boldsymbol{\theta}}_\chi^{(1)} - \mathbf{f}^{(1)} \right), \quad (37)$$

where $\hat{\mathbf{w}}$ is the solution of the adjoint state problem. Once the extended cost function is defined, we proceed to derive it using the Relaxed Topological Derivative as

$$\begin{aligned} \frac{\delta \bar{\mathcal{J}}^{(h_e)}(\chi)}{\delta \chi}(\hat{\mathbf{x}}) = & - (\hat{\mathbf{w}}^T \mathbb{K}_\chi + \mathbf{C}_1 \boldsymbol{\kappa}_\chi \nabla) \frac{\delta \hat{\boldsymbol{\theta}}_\chi^{(1)}}{\delta \chi}(\hat{\mathbf{x}}) - \mathbf{C}_1 \frac{\delta \boldsymbol{\kappa}_\chi(\chi)}{\delta \chi}(\hat{\mathbf{x}}) \nabla \theta_\chi^{(1)}(\hat{\mathbf{x}}) \\ & - \hat{\mathbf{w}}^T \frac{\delta \mathbb{K}_\chi}{\delta \chi}(\hat{\mathbf{x}}) \hat{\boldsymbol{\theta}}_\chi^{(1)} + \hat{\mathbf{w}}^T \frac{\delta \mathbf{f}_\chi^{(1)}}{\delta \chi}(\hat{\mathbf{x}}) \end{aligned} \quad (38)$$

where $\mathbf{C}_1(\chi, \hat{\mathbf{x}}, \theta_\chi^{(1)})$ is

$$\mathbf{C}_1(\chi, \hat{\mathbf{x}}, \theta_\chi^{(1)}) = \frac{1_{\Omega_c}(\hat{\mathbf{x}}) \left(\mathbf{q}_\chi(\hat{\mathbf{x}}, \theta_\chi^{(1)}) - \bar{\mathbf{q}}(\hat{\mathbf{x}}) \right)^T}{\mathcal{J}^{(h_e)}(\chi)}. \quad (39)$$

We must now solve the *adjoint state problem* of equation (38) for $\hat{\mathbf{w}} = \hat{\boldsymbol{\theta}}_\chi^{(2)}$. Thus, in contrast to the first optimization problem, that has been shown in Section B.6.1, the *original thermal system (I)* has to be supplemented with an *auxiliary thermal system (II)* (see Figure B.5). Both systems are governed by the thermal problem (equation (73)) with the same stiffness matrix \mathbb{K}_χ but different actions and solutions $\hat{\boldsymbol{\theta}}_\chi^{(1)}$ and $\hat{\boldsymbol{\theta}}_\chi^{(2)}$, respectively, defined as

$$\begin{cases} \mathbb{K}_\chi \hat{\boldsymbol{\theta}}_\chi^{(1)} = \mathbf{f}^{(1)} & \text{(system I)} \\ \mathbb{K}_\chi \hat{\boldsymbol{\theta}}_\chi^{(2)} = \mathbf{f}^{(2)} & \text{(system II)} \end{cases} \quad (40)$$

where

$$\mathbf{f}^{(2)T} = - \int_\Omega \mathbf{N}^T(\mathbf{x}) \frac{\delta \mathcal{J}^{(h_e)}(\theta_\chi^{(1)})}{\delta \theta_\chi}(\mathbf{x}) d\Omega = - \int_\Omega \mathbf{N}^T(\mathbf{x}) \mathbf{C}_1(\chi, \mathbf{x}, \theta_\chi^{(1)}) \boldsymbol{\kappa}_\chi(\mathbf{x}) \mathbf{B}(\mathbf{x}) d\Omega. \quad (41)$$

By simplifying the first term of equation (38), and after some algebraic manipulations, detailed in Appendix B.C, the relaxed topological sensitivity of the cost function can be expressed as a sum of *energy densities*, i.e.

$$\frac{\delta \bar{\mathcal{J}}^{(h_e)}(\chi)}{\delta \chi}(\hat{\mathbf{x}}) = + 2\gamma_1(\hat{\mathbf{x}}, \chi) \bar{U}_{1-2}(\hat{\mathbf{x}}) - \gamma_2(\hat{\mathbf{x}}, \chi) \bar{U}_r(\hat{\mathbf{x}}) + \gamma_1(\hat{\mathbf{x}}, \chi) \bar{U}_q(\hat{\mathbf{x}}), \quad (42)$$

where $\bar{U}_{1-2}(\hat{\mathbf{x}})$, $\bar{U}_r(\hat{\mathbf{x}})$ and $\bar{U}_q(\hat{\mathbf{x}})$ are, respectively, *the nominal heat conduction energy density*, *the nominal heat source energy density* and *the nominal heat flux energy density*, which are given by

$$\begin{cases} \bar{U}_{1-2}(\hat{\mathbf{x}}) = \frac{1}{2} \left(\nabla \theta_\chi^{(1)} \cdot \boldsymbol{\kappa} \cdot \nabla \theta_\chi^{(2)} \right) (\hat{\mathbf{x}}) & (a) \\ \bar{U}_r(\hat{\mathbf{x}}) = \left(r \theta_\chi^{(2)} \right) (\hat{\mathbf{x}}) & (b) \\ \bar{U}_q(\hat{\mathbf{x}}) = \left(\mathbf{C}_1 \cdot \boldsymbol{\kappa} \cdot \nabla \theta_\chi^{(1)} \right) (\hat{\mathbf{x}}) & (c) \end{cases} \quad (43)$$

and

$$\begin{cases} \gamma_1(\hat{\mathbf{x}}, \chi) = (1 - \beta_\kappa) m_\kappa (\chi_\kappa(\hat{\mathbf{x}}))^{m_\kappa - 1} \\ \gamma_2(\hat{\mathbf{x}}, \chi) = (1 - \beta_r) m_r (\chi_r(\hat{\mathbf{x}}))^{m_r - 1} \end{cases}. \quad (44)$$

Closed-form solution

The *problem-dependent energy density*, $\xi(\hat{\mathbf{x}}, \chi)$, of the original functional $\mathcal{J}^{(h_e)}$ (equation (36)) is illustrated in Box III, analogously to Box II.

Box III: Topology optimization of heat flux cloaking

Problem:

$$\left[\begin{array}{l} \chi^* = \underset{\chi \in \mathcal{A}_{ad}}{\operatorname{argmin}} \mathcal{J}^{(he)}(\chi) = \left(\int_{\Omega} 1_{\Omega_c}(\mathbf{x}) \left| -\boldsymbol{\kappa}_{\chi}(\mathbf{x}) \mathbf{B}(\mathbf{x}) \hat{\boldsymbol{\theta}}_{\chi}^{(1)} - \bar{\mathbf{q}}(\mathbf{x}) \right|^2 d\Omega \right)^{\frac{1}{2}} \\ s.t. \quad \mathcal{C}(\chi, t) := t - \frac{|\Omega^-|(\chi)}{|\Omega|} = 0; \quad t \in [0, 1] \\ \mathbb{K}_{\chi} \hat{\boldsymbol{\theta}}_{\chi}^{(i)} = \mathbf{f}^{(i)}; \quad i = \{1, 2\} \end{array} \right. \quad (a)$$

Energy density:

$$\xi(\hat{\mathbf{x}}, \chi) = \gamma_1(\hat{\mathbf{x}}, \chi) (2\bar{U}_{1-2}(\hat{\mathbf{x}}) + \bar{U}_{\mathbf{q}}(\hat{\mathbf{x}})) - \gamma_2(\hat{\mathbf{x}}, \chi) \bar{U}_r(\hat{\mathbf{x}}) \quad (b)$$

where

$$\left\{ \begin{array}{l} \bar{U}_{1-2}(\hat{\mathbf{x}}) = \frac{1}{2} \left(\nabla \theta_{\chi}^{(1)} \cdot \boldsymbol{\kappa} \cdot \nabla \theta_{\chi}^{(2)} \right) (\hat{\mathbf{x}}); \\ \bar{U}_r(\hat{\mathbf{x}}) = \left(r \theta_{\chi}^{(2)} \right) (\hat{\mathbf{x}}); \\ \bar{U}_{\mathbf{q}}(\hat{\mathbf{x}}) = \left(\frac{1_{\Omega_c}(\hat{\mathbf{x}}) \left(\mathbf{q}_{\chi} \left(\theta_{\chi}^{(1)} \right) - \bar{\mathbf{q}} \right) \cdot \boldsymbol{\kappa} \cdot \nabla \theta_{\chi}^{(1)}}{\mathcal{J}^{(he)} \left(\chi, \theta_{\chi}^{(1)} \right)} \right) (\hat{\mathbf{x}}) \\ \gamma_1(\hat{\mathbf{x}}, \chi) = (1 - \beta_{\kappa}) m_{\kappa} (\chi_{\kappa}(\hat{\mathbf{x}}))^{m_{\kappa}-1} \\ \gamma_2(\hat{\mathbf{x}}, \chi) = (1 - \beta_r) m_r (\chi_r(\hat{\mathbf{x}}))^{m_r-1} \end{array} \right. \quad (45)$$

B.6.3 Thermal cloaking in terms of temperature average and variance

Let us now consider a hot object whose temperature is higher than the environment temperature, θ_{amb} . The goal is to cloak the object for an external thermal detecting device, located at some distance from it (like a thermal camera). The cloaked object might be then easily detected if the temperature along a virtual plane, between the object and the observer, changes significantly with respect to the ambient temperature. Thus, the goal is to find the optimal layout of a surrounding cloaking device, which minimizes the perturbation of the temperature on this plane.

The setting of the problem is sketched in Figure B.6, in which Ω represents the region of concern, the small black region, placed at the center, represents the object to be cloaked, and the surrounding ellipsoid, colored in gray, corresponds to the cloaking device, Ω_{dev} . In addition, the vertical left edge, referred as the *cloaking port*, $\partial_c \Omega$, illustrates the plane where the temperatures are measured by the observer. The temperature of the object is prescribed at a high temperature $\bar{\theta} > \theta_{amb}$ on its surface, $\partial_{\theta} \Omega$, and natural convective boundary conditions are applied on the left and right edges, $\partial_h \Omega$. On the other two faces, adiabatic conditions are considered.

The optimal topology will be achieved with a *multi-objective optimization* via two cost functionals. The first functional addresses the minimization of the average temperature on the cloaking port, $\partial_c \Omega$, while the second is responsible of minimizing the variance of the temperature on the same face, ensuring an homogeneous temperature on the left edge. The topological optimization problem, evaluated via a *weighted sum* of the functionals, is expressed as

$$\left[\begin{array}{l} \min_{\chi \in \mathcal{A}_{ad}} \mathcal{J}(\theta_{\chi}) = \omega \mathcal{J}_{av}(\theta_{\chi}) + (1 - \omega) \mathcal{J}_{vr}(\theta_{\chi}) \\ \text{subject to :} \\ \mathcal{C}(\chi, t) := t - \frac{|\Omega^-|(\chi)}{|\Omega|} = 0; \quad t \in [0, 1] \\ \text{governed by :} \\ a(w, \theta_{\chi}) = l(w) \quad \forall w \in \mathcal{V}(\Omega), \forall \theta_{\chi} \in \mathcal{U}(\Omega) \end{array} \right. \quad (a) \quad (b) \quad (c) \quad (46)$$

where $\mathcal{J}_{av}(\theta_{\chi})$ corresponds to the objective function of the *average temperature minimization*,

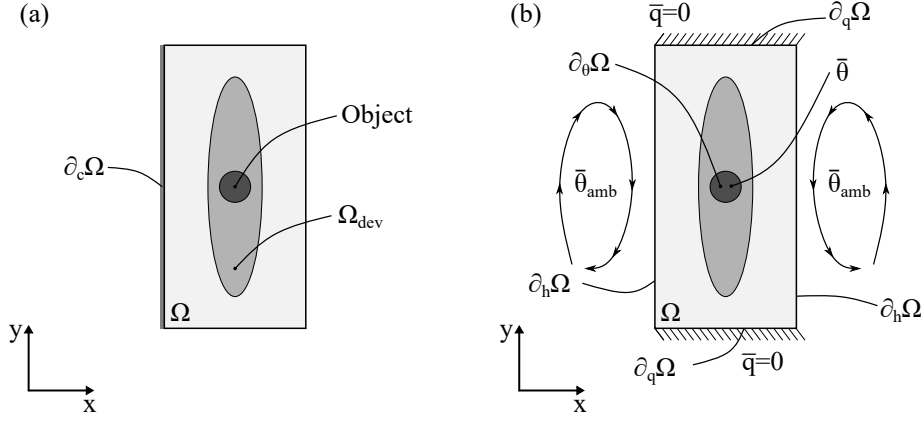


Figure B.6: Average and variance temperature minimization: (a) representation of the subdomains surrounding the object to be cloaked (the cloaking device, Ω_{dev} , is displayed in dark gray, while the left edge, where the average value and the variance of the temperature are minimized, is denoted by $\partial_c \Omega$) and (b) problem setting with boundary conditions. The domain, Ω , corresponds to the control volume in which optimization will be carried out, which includes the object prescribed at a high temperature, $\bar{\theta}$. The left and right sides are subject to convective boundary conditions, while adiabatic conditions are assumed on top and bottom sides of the domain.

while $\mathcal{J}_{vr}(\theta_\chi)$ corresponds to the objective function of the *temperature variance minimization*. The coefficient ω represents the weight between these two objective functions. Therefore, we are simultaneously optimizing, for a given weighting coefficient ω , both functionals and achieving an *optimal trade-off* from these objective functions. If this weight is changed, a different optimal solution will be obtained. Thus, given a set of weight values, the optimal solutions of each optimization problem define the classical Pareto front [2].

According to Marler and Arora [18], a convenient transformation of the original objective functions is through its ranges. This *normalization* is given as follows

$$\tilde{\mathcal{J}}_i(\chi) = \frac{\mathcal{J}_i(\chi) - \mathcal{J}_i^\circ}{\mathcal{J}_i^{max} - \mathcal{J}_i^\circ} \quad \text{for } i = \{\text{av}, \text{vr}\} \quad (47)$$

where $\tilde{\mathcal{J}}_i(\chi)$ represents the transformed objective function, \mathcal{J}_i° denotes the utopia point¹⁴ and \mathcal{J}_i^{max} corresponds to the maximum objective function value.¹⁵ This *normalization* yields non-dimensional objective functions values between zero and one. We have chosen to normalize the functionals with respect to the minimum value when minimizing only each objective functional $\mathcal{J}_i(\chi)$ (Utopia point) and the maximum value obtained from the minimization of the other functional $\mathcal{J}_i(\chi_j^*)$. Therefore, two extra optimization problems must be done for $\omega = 1$ and $\omega = 0$. From the first problem, \mathcal{J}_{av}° and \mathcal{J}_{vr}^{max} are obtained, and from the second, \mathcal{J}_{av}^{max} and \mathcal{J}_{vr}° .

According to this scalarization approach, the transformed optimization problem is written

¹⁴The utopia point \mathcal{J}_i° defined as $\mathcal{J}_i^\circ = \min_{\chi} \mathcal{J}_i(\chi) \quad \forall \chi \in \mathcal{U}_{ad}$ is an unattainable optimal point and it may be prohibitively expensive to compute. In these cases, an approximation is used.

¹⁵The maximum objective function value corresponds either to the maximum value that minimizes the other objective functions, $\mathcal{J}_i^{max} = \max_j \mathcal{J}_i(\chi_j^*) \quad j \neq i$, or the absolute maximum of $\mathcal{J}_i(\chi)$.

as follows

$$\begin{cases} \min_{\chi \in \mathcal{U}_{ad}} \tilde{\mathcal{J}}(\theta_\chi) = \omega \frac{\mathcal{J}_{av}(\theta_\chi) - \mathcal{J}_{av}^\circ}{\mathcal{J}_{av}^{max} - \mathcal{J}_{av}^\circ} + (1 - \omega) \frac{\mathcal{J}_{vr}(\theta_\chi) - \mathcal{J}_{vr}^\circ}{\mathcal{J}_{vr}^{max} - \mathcal{J}_{vr}^\circ} & (a) \\ \text{subject to :} & \\ \mathcal{C}(\chi, t) := t - \frac{|\Omega^-|(\chi)}{|\Omega|} = 0; t \in [0, 1] & (b) \quad (48) \\ \text{governed by :} & \\ a(w, \theta_\chi) = l(w) \quad \forall w \in \mathcal{V}(\Omega), \forall \theta_\chi \in \mathcal{U}(\Omega) & (c) \end{cases}$$

Thanks to the use of a multi-objective scheme, the topological sensitivity of both terms may be computed independently, as it will be shown below.

Average temperature minimization

Let us now focus on the first objective function which deals with the minimization of the average temperature over the cloaking port, $\partial_c \Omega$, by designing the cloaking device (drawn in gray in Figure B.7). The corresponding optimization problem, subjected to the same constraint equation and ruled by the thermal state equation of equation (46), is given as

$$\min_{\chi \in \mathcal{U}_{ad}} \mathcal{J}_{av}(\theta_\chi) = C_2 \int_{\partial_c \Omega} \theta_\chi(\mathbf{x}) d\Gamma = C_2 \int_{\partial \Omega} 1_{\partial_c \Omega}(\mathbf{x}) \theta_\chi(\mathbf{x}) d\Gamma, \quad (49)$$

where the integrated temperature is normalized with the corresponding Lebesgue measure, $C_2 = \left(\int_{\partial_c \Omega} d\Gamma \right)^{-1}$, and $1_{\partial_c \Omega}(\mathbf{x})$ stands for the indicator function on the subset $\partial_c \Omega$, to enforce the minimization over the whole boundary.

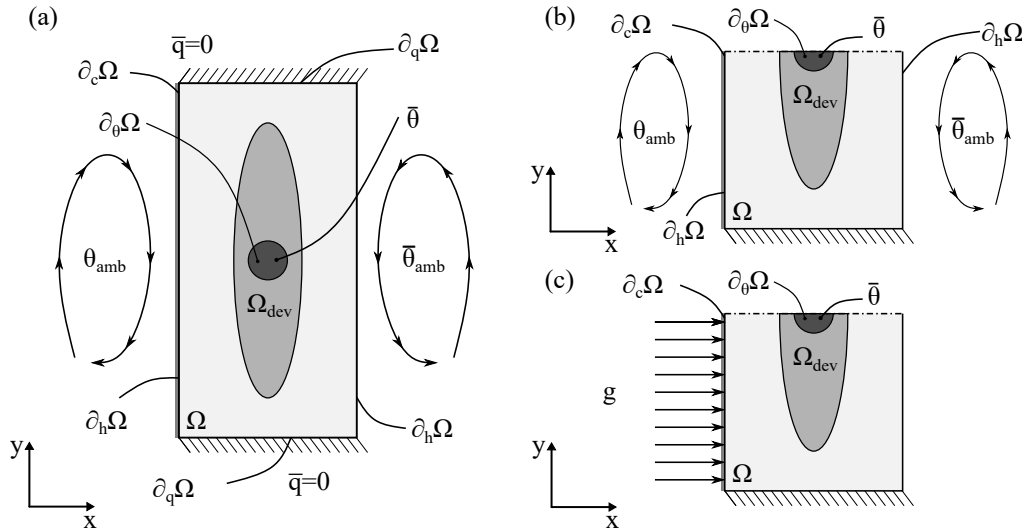


Figure B.7: Average temperature minimization: (a) problem setting, (b) system (I) (half-domain), and (c) system (II), where $g := f^{(2)}$ (half-domain). The optimal design of the cloaking device, in gray, must achieve a reduction in the average temperature of the left surface, $\partial_c \Omega$.

Discretizing the topology optimization problem (49) via the finite element method, we finally obtain

$$\min_{\chi \in \mathcal{U}_{ad}} \mathcal{J}_{av}^{(h_e)}(\theta_\chi) = C_2 \int_{\partial \Omega} 1_{\partial_c \Omega}(\mathbf{x}) \mathbf{N}(\mathbf{x}) \hat{\theta}_\chi^{(1)} d\Gamma = C_2 \mathbf{1}_{\partial_c \Omega}^T \hat{\theta}_\chi^{(1)}, \quad (50)$$

whose extended functional is then derived according to Section B.3.2 in order to compute the topological sensitivity of the cost function. Following the same steps as in Section B.6.1, and

applying the *adjoint method* with $\hat{\mathbf{w}} = -C_2 \hat{\boldsymbol{\theta}}_\chi^{(2)}$ to avoid computing the temperature derivative with respect to the design variable, one finds that problem (50) also requires the resolution of an *auxiliary state equation* (system (II)) in addition to the *original state equation* (system (I)), which read as

$$\begin{cases} \mathbb{K}_\chi \hat{\boldsymbol{\theta}}_\chi^{(1)} = \mathbf{f}^{(1)} & \text{(system I)} \\ \mathbb{K}_\chi \hat{\boldsymbol{\theta}}_\chi^{(2)} = \mathbf{f}^{(2)} & \text{(system II)} \end{cases} \quad (51)$$

where

$$\mathbf{f}^{(2)} = -\mathbf{1}_{\partial_c \Omega} = - \int_{\partial \Omega} \mathbf{N}^T(\mathbf{x}) \mathbf{1}_{\partial_c \Omega}(\mathbf{x}) d\Gamma. \quad (52)$$

Introducing the solution of the two state equations, $\hat{\boldsymbol{\theta}}_\chi^{(1)}$ and $\hat{\boldsymbol{\theta}}_\chi^{(2)}$, into the corresponding relaxed topological derivative of the cost function, and after some algebraic manipulations, detailed in Appendix B.D, one obtains the expression of the *pseudo-energy density*, expressed as

$$\xi_{\text{av}}(\hat{\mathbf{x}}, \chi) = \gamma_1(\hat{\mathbf{x}}, \chi) \bar{U}_{1-2}(\hat{\mathbf{x}}) + \gamma_2(\hat{\mathbf{x}}, \chi) \bar{U}_{r-2}(\hat{\mathbf{x}}), \quad (53)$$

where $\bar{U}_{1-2}(\hat{\mathbf{x}})$ and $\bar{U}_{r-2}(\hat{\mathbf{x}})$ correspond respectively to *the nominal heat conduction energy density* and *the nominal heat source energy density*, and $\gamma_1(\hat{\mathbf{x}}, \chi)$ and $\gamma_2(\hat{\mathbf{x}}, \chi)$ are respectively the coefficient of these *energy densities*, which depend on the *characteristic function* and the properties of the material. In summary

$$\begin{cases} \bar{U}_{1-2}(\hat{\mathbf{x}}) = \frac{1}{2} \left(\nabla \theta_\chi^{(2)} \cdot \boldsymbol{\kappa} \cdot \nabla \theta_\chi^{(1)} \right) (\hat{\mathbf{x}}) & (a) \\ \bar{U}_{r-2}(\hat{\mathbf{x}}) = \left(r \theta_\chi^{(2)} \right) (\hat{\mathbf{x}}) & (b) \\ \gamma_1(\hat{\mathbf{x}}, \chi) = -2C_2(1 - \beta_\kappa) m_\kappa (\chi_\kappa(\hat{\mathbf{x}}))^{m_\kappa - 1} & (c) \\ \gamma_2(\hat{\mathbf{x}}, \chi) = C_2(1 - \beta_r) m_r (\chi_r(\hat{\mathbf{x}}))^{m_r - 1} & (d) \end{cases} \quad (54)$$

Temperature variance minimization

The second objective function deals with the minimization of the temperature variance over the cloaking port, $\partial_c \Omega$, so the main goal is to design a cloaking device that *homogenizes the temperature on a desired surface*. This optimization problem is written as follows

$$\begin{aligned} \min_{\chi \in \mathcal{U}_{\text{ad}}} \mathcal{J}_{\text{vr}}(\theta_\chi) &= C_3 \int_{\partial_c \Omega} (\theta_\chi(\mathbf{x}) - \mathcal{J}_{\text{av}}(\theta_\chi))^2 d\Gamma = \\ &= C_3 \int_{\partial \Omega} \mathbf{1}_{\partial_c \Omega}(\mathbf{x}) (\theta_\chi(\mathbf{x}) - \mathcal{J}_{\text{av}}(\theta_\chi))^2 d\Gamma, \end{aligned} \quad (55)$$

where the coefficient C_3 is equal to the inverse of the measure of the surface, i.e. $C_3 = \left(\int_{\partial_c \Omega} d\Gamma \right)^{-1}$, and, as commented before, the temperature variance is only minimized on a part of the boundary of the domain described by the indicator function of the surface $\partial_c \Omega$, $\mathbf{1}_{\partial_c \Omega}(\mathbf{x})$.

Applying the FEM discretization (70) to expression (55), we finally reach to

$$\begin{aligned} \min_{\chi \in \mathcal{U}_{\text{ad}}} \mathcal{J}_{\text{vr}}^{(h_e)}(\theta_\chi) &= C_3 \int_{\partial \Omega} \mathbf{1}_{\partial_c \Omega}(\mathbf{x}) \left(\mathbf{N}(\mathbf{x}) \hat{\boldsymbol{\theta}}_\chi^{(1)} - \mathbf{N}(\mathbf{x}) \mathbb{I} \mathcal{J}_{\text{av}}^{(h_e)} \left(\theta_\chi^{(1)} \right) \right)^2 d\Gamma = \\ &= C_3 \left(\hat{\boldsymbol{\theta}}_\chi^{(1)} - \mathbb{I} \mathcal{J}_{\text{av}}^{(h_e)} \left(\theta_\chi^{(1)} \right) \right)^T \mathbb{M}_{\partial_c \Omega} \left(\hat{\boldsymbol{\theta}}_\chi^{(1)} - \mathbb{I} \mathcal{J}_{\text{av}}^{(h_e)} \left(\theta_\chi^{(1)} \right) \right) \end{aligned} \quad (56)$$

with

$$\mathbb{M}_{\partial_c \Omega} = \int_{\partial \Omega} \mathbf{N}^T(\mathbf{x}) \mathbf{1}_{\partial_c \Omega}(\mathbf{x}) \mathbf{N}(\mathbf{x}) d\Gamma, \quad (57)$$

where \mathbb{I} represents an all-ones vector with the same length as $\hat{\boldsymbol{\theta}}_\chi^{(1)}$. Equation (56) is subject to the volume constraint in equation (46)-(b) and governed by the thermal state equation (46)-(c). Now, mimicking the procedure followed for the first functional of equation (46)-(a) in Section B.6.3, we proceed to compute the RTD of the expression (56) via the *adjoint method* with $\hat{\mathbf{w}} = -C_3 \hat{\boldsymbol{\theta}}_\chi^{(3)}$, and introducing the RTD of the average temperature $\mathcal{J}_{\text{av}}^{(h_e)}(\theta_\chi^{(1)})$ with the corresponding *adjoint state problem*, equation (51)-(system (II)).

Finally, one can obtain three *state equations*, being the first two equations mutual to both optimizations problems. Thus, the *original thermal system (I)* is supplemented with two *auxiliary thermal system*: (II) and (III) (where g in Figure B.7 corresponds to $f^{(2)}$ for the *first auxiliary system*, while it is equal to $f^{(3)}$ for the *second auxiliary system*), which are described by

$$\mathbb{K}_\chi \hat{\boldsymbol{\theta}}_\chi^{(i)} = \mathbf{f}^{(i)} ; \quad i = \{1, 2, 3\} \quad (58)$$

with

$$\mathbf{f}^{(3)} = -2\mathbb{M}_{\partial_c\Omega}^T \mathcal{T}_\chi(\theta_\chi^{(1)}) = -2 \int_{\partial_c\Omega} \mathbf{N}^T 1_{\partial_c\Omega}(\mathbf{x}) \left(\theta_\chi^{(1)}(\mathbf{x}) - \mathcal{J}_{\text{av}}^{(h_e)}(\theta_\chi^{(1)}) \right) d\Gamma, \quad (59)$$

where $\mathcal{T}_\chi(\theta_\chi^{(1)})$ corresponds to $\hat{\boldsymbol{\theta}}_\chi^{(1)} - \mathbb{I} \mathcal{J}_{\text{av}}^{(h_e)}(\theta_\chi^{(1)})$.

After replacing the solutions of both *auxiliary systems*, $\hat{\boldsymbol{\theta}}_\chi^{(2)}$ and $\hat{\boldsymbol{\theta}}_\chi^{(3)}$, into the RTD of $\mathcal{J}_{\text{vr}}^{(h_e)}(\theta_\chi)$ and simplifying the consequent terms, the corresponding *spatial energy density*, $\xi(\hat{\mathbf{x}}, \chi)$, can be written as

$$\xi_{\text{vr}}(\hat{\mathbf{x}}, \chi) = \gamma_3 \bar{\mathcal{U}}_{1-2}(\hat{\mathbf{x}}) + \gamma_4 \bar{\mathcal{U}}_{r-2}(\hat{\mathbf{x}}) + \gamma_5 \bar{\mathcal{U}}_{1-3}(\hat{\mathbf{x}}) + \gamma_6 \bar{\mathcal{U}}_{r-3}(\hat{\mathbf{x}}) \quad (60)$$

where $\bar{\mathcal{U}}_{i-j}(\hat{\mathbf{x}})$ is the *nominal heat conduction energy density* for i -th and j -th temperature fields ($i, j = \{1, 2, 3\}$) and $\bar{\mathcal{U}}_{r-k}(\hat{\mathbf{x}})$ corresponds to the *nominal heat source energy density* for the k -th temperature field ($k = \{1, 2, 3\}$), which are respectively written as

$$\begin{cases} \bar{\mathcal{U}}_{1-2}(\hat{\mathbf{x}}) = \frac{1}{2} \left(\nabla \theta_\chi^{(2)} \cdot \boldsymbol{\kappa} \cdot \nabla \theta_\chi^{(1)} \right) (\hat{\mathbf{x}}) \\ \bar{\mathcal{U}}_{r-2}(\hat{\mathbf{x}}) = \left(r \theta_\chi^{(2)} \right) (\hat{\mathbf{x}}) \\ \bar{\mathcal{U}}_{1-3}(\hat{\mathbf{x}}) = \frac{1}{2} \left(\nabla \theta_\chi^{(3)} \cdot \boldsymbol{\kappa} \cdot \nabla \theta_\chi^{(1)} \right) (\hat{\mathbf{x}}) \\ \bar{\mathcal{U}}_{r-3}(\hat{\mathbf{x}}) = \left(r \theta_\chi^{(3)} \right) (\hat{\mathbf{x}}) \end{cases}, \quad (61)$$

and γ_i for $i = \{3, 4, 5, 6\}$ are the corresponding coefficients, defined as

$$\begin{cases} \gamma_3(\hat{\mathbf{x}}, \chi) = 4C_3 C_2 (1 - \beta_\kappa) m_\kappa (\chi_\kappa(\hat{\mathbf{x}}))^{m_\kappa - 1} \mathcal{A} & (a) \\ \gamma_4(\hat{\mathbf{x}}, \chi) = -C_3 C_2 (1 - \beta_r) m_r (\chi_r(\hat{\mathbf{x}}))^{m_r - 1} \mathcal{A} & (b) \\ \gamma_5(\hat{\mathbf{x}}, \chi) = -2C_3 (1 - \beta_\kappa) m_\kappa (\chi_\kappa(\hat{\mathbf{x}}))^{m_\kappa - 1} & (c) \\ \gamma_6(\hat{\mathbf{x}}, \chi) = C_3 (1 - \beta_r) m_r (\chi_r(\hat{\mathbf{x}}))^{m_r - 1} & (d) \end{cases}, \quad (62)$$

where

$$\mathcal{A} = \left(\mathcal{T}_\chi(\theta_\chi^{(1)}) \right)^T \mathbb{M}_{\partial_c\Omega} \mathbb{I}. \quad (63)$$

For additional details, the reader is addressed to Appendix B.E where intermediate steps are presented.

Temperature multi-objective minimization

Topological sensitivity of the cost function Taking into account the expressions obtained in Sections B.6.3 and B.6.3, we can define the *energy distribution* of the original problem (equation (46)) as a linear combination of equations (53) and (60), yielding to

$$\xi(\hat{\mathbf{x}}, \chi) = \omega \xi_{\text{av}}(\hat{\mathbf{x}}, \chi) + (1 - \omega) \xi_{\text{vr}}(\hat{\mathbf{x}}, \chi), \quad (65)$$

where the parameter ω adjusts the weight of each objective function (or sensitivity). As previously mentioned, the sensitivity corresponds to the *weighted sum* of the sensitivities of the two problems.

Since each term of the original multi-objective problem (46) has been normalized with its range (equation (47)), the sensitivity of the scalarized multi-objective problem (48)-(a) includes some extra terms with respect to equation (65) to account for it, i.e. the sensitivity is expressed as

$$\tilde{\xi}(\hat{\mathbf{x}}, \chi) = \omega C_4 \xi_{\text{av}}(\hat{\mathbf{x}}, \chi) + (1 - \omega) C_5 \xi_{\text{vr}}(\hat{\mathbf{x}}, \chi), \quad (66)$$

Box IV: Topology optimization for average and variance temperature minimization

Problem:

$$\left[\begin{array}{l} \chi^* = \underset{\chi \in \mathcal{U}_{ad}}{\operatorname{argmin}} \tilde{\mathcal{J}}^{(he)}(\chi) = \omega \tilde{\mathcal{J}}_{\text{av}}^{(he)}(\chi) + (1 - \omega) \tilde{\mathcal{J}}_{\text{vr}}^{(he)}(\chi) \\ \text{s.t. } \mathcal{C}(\chi, t) := t - \frac{|\Omega^-|(\chi)}{|\Omega|} = 0; \quad t \in [0, 1] \\ \mathbb{K}_\chi \hat{\theta}_\chi^{(i)} = \mathbf{f}^{(i)}; \quad i = \{1, 2, 3\} \end{array} \right. \quad (a)$$

Energy density:

$$\begin{aligned} \xi(\hat{\mathbf{x}}, \chi) = & \omega C_4 [\gamma_1 \bar{U}_{1-2}(\hat{\mathbf{x}}) + \gamma_2 \bar{U}_{r-2}(\hat{\mathbf{x}})] \\ & + (1 - \omega) C_5 [\gamma_3 \bar{U}_{1-2}(\hat{\mathbf{x}}) + \gamma_4 \bar{U}_{r-2}(\hat{\mathbf{x}}) + \gamma_5 \bar{U}_{1-3}(\hat{\mathbf{x}}) + \gamma_6 \bar{U}_{r-3}(\hat{\mathbf{x}})] \end{aligned} \quad (b)$$

where

$$\left\{ \begin{array}{l} \bar{U}_{1-2}(\hat{\mathbf{x}}) = \frac{1}{2} \left(\nabla \theta_\chi^{(2)} \cdot \boldsymbol{\kappa} \cdot \nabla \theta_\chi^{(1)} \right) (\hat{\mathbf{x}}); \\ \bar{U}_{1-3}(\hat{\mathbf{x}}) = \frac{1}{2} \left(\nabla \theta_\chi^{(3)} \cdot \boldsymbol{\kappa} \cdot \nabla \theta_\chi^{(1)} \right) (\hat{\mathbf{x}}) \\ \bar{U}_{r-2}(\hat{\mathbf{x}}) = \left(r \theta_\chi^{(2)} \right) (\hat{\mathbf{x}}); \\ \bar{U}_{r-3}(\hat{\mathbf{x}}) = \left(r \theta_\chi^{(3)} \right) (\hat{\mathbf{x}}) \\ \gamma_1(\hat{\mathbf{x}}, \chi) = -2C_2(1 - \beta_\kappa) m_\kappa (\chi_\kappa(\hat{\mathbf{x}}))^{m_\kappa - 1}; \\ \gamma_2(\hat{\mathbf{x}}, \chi) = +C_2(1 - \beta_r) m_r (\chi_r(\hat{\mathbf{x}}))^{m_r - 1} \\ \gamma_3(\hat{\mathbf{x}}, \chi) = +4C_3 C_2 (1 - \beta_\kappa) m_\kappa (\chi_\kappa(\hat{\mathbf{x}}))^{m_\kappa - 1} \mathcal{A} \\ \gamma_4(\hat{\mathbf{x}}, \chi) = -C_3 C_2 (1 - \beta_r) m_r (\chi_r(\hat{\mathbf{x}}))^{m_r - 1} \mathcal{A} \\ \gamma_5(\hat{\mathbf{x}}, \chi) = -2C_3 (1 - \beta_\kappa) m_\kappa (\chi_\kappa(\hat{\mathbf{x}}))^{m_\kappa - 1} \\ \gamma_6(\hat{\mathbf{x}}, \chi) = +C_3 (1 - \beta_r) m_r (\chi_r(\hat{\mathbf{x}}))^{m_r - 1} \\ \mathcal{A} = \left(\mathcal{T}_\chi \left(\theta_\chi^{(1)} \right) \right)^\top \mathbb{M}_{\partial_c \Omega} \mathbb{I}; \end{array} \right. \quad (64)$$

where

$$\begin{cases} C_4 = \frac{1}{\mathcal{J}_{av}^{max} - \mathcal{J}_{av}^o} \\ C_5 = \frac{1}{\mathcal{J}_{vr}^{max} - \mathcal{J}_{vr}^o} \end{cases} \quad (67)$$

As explained before, each topology optimization problem requires *auxiliary thermal systems*. We must solve two and three thermal systems for the average temperature minimization and the temperature variance minimization, respectively. However, *the auxiliary thermal system* of the first minimization problem (50) is included into the second minimization problem (56). Therefore, only the following 3 thermal systems must be solved,

$$\begin{cases} \mathbb{K}_\chi \hat{\boldsymbol{\theta}}_\chi^{(1)} = \mathbf{f}^{(1)} & (a) \\ \mathbb{K}_\chi \hat{\boldsymbol{\theta}}_\chi^{(2)} = \mathbf{f}^{(2)} = -\mathbf{1}_{\partial_c \Omega} & (b) \\ \mathbb{K}_\chi \hat{\boldsymbol{\theta}}_\chi^{(3)} = \mathbf{f}^{(3)} = -2\mathbb{M}_{\partial_c \Omega}^T \left(\hat{\boldsymbol{\theta}}_\chi^{(1)} - \mathbb{I} \mathcal{J}_{av}^{(h_e)} \left(\boldsymbol{\theta}_\chi^{(1)} \right) \right) & (c) \end{cases} \quad (68)$$

Closed-form solution The *energy distribution*, $\xi(\hat{\mathbf{x}}, \chi)$, of this topology optimization problem is stated in Box IV. This function combines the *energy distributions* presented in equations (53) and (60).

B.7 Representative numerical simulations

In this section, a number of 3D numerical examples to assess the performance of the proposed methodology are presented. Unless otherwise specified, all simulations are done using an isotropic thermal material with a normalized conductivity $\kappa = 1W/(Km)$ and a null heat source ($r = 0W/m^3$). When needed, the heat transfer coefficient is set to $h = 1W/(Km^2)$ and the ambient temperature is fixed to $\theta_{amb} = 283.15K$. The material contrast factor and the corresponding exponent are set to $\alpha = 10^{-3}$ and $m = 5^{16}$, respectively. The used relaxation factor is $\beta = 2.51 \cdot 10^{-1}$. $Tol_\chi = 10^{-1}$, $Tol_\lambda = 10^{-1}$ and $Tol_c = 10^{-3}$ are the used tolerances. In all cases, eight-node hexahedral (Q_1) finite elements are used in the solution of the thermal state equation.

B.7.1 Thermal compliance minimization. 3D thermal conductor.

This example refers to the minimization of the thermal compliance, as explained in Section B.6.1, in a thermal component, e.g. heat pipes for a CPU heat sink, in a cubic domain subject to specific Dirichlet conditions. The aim is to display the potential of the present methodology for obtaining the optimal topology for heat conduction in a complex analysis domain.

The analysis domain, illustrated in Figure B.8, is a cube, $1 \times 1 \times 1$ m, with a rectangular hole all the way across it, with dimensions $0.1 \times 0.5 \times 1$ m, located in the center and oriented in the z direction. A small prismatic volume, $0.1 \times 0.2 \times 0.2$ m, is set in the center of the domain as part of the initial domain. The radii of the left and right circular areas, highlighted in Figure B.8-(c), are $R_h = 0.075$ m and $R_c = 0.05$ m, respectively. The domain is discretized with a structured mesh of $120 \times 120 \times 120$ hexahedral elements (mesh size $h_e = 8.3 \cdot 10^{-3}$ m), which leads to 1.648.512 hexahedra (see Figure B.8-(b)).

It is assumed that the four areas, colored in red and located on the left surface, with a prescribed temperature of $\bar{\theta}_h = 293$ K are connected with four CPU's IHS. The other nine areas, at temperature $\bar{\theta}_c = 278$ K, colored in blue, and located on the right face, are coupled to the cooling system (heat sink). Adiabatic boundary conditions are assumed on the other faces.

¹⁶The exponential parameters m_i are set on the basis of the authors' experience.

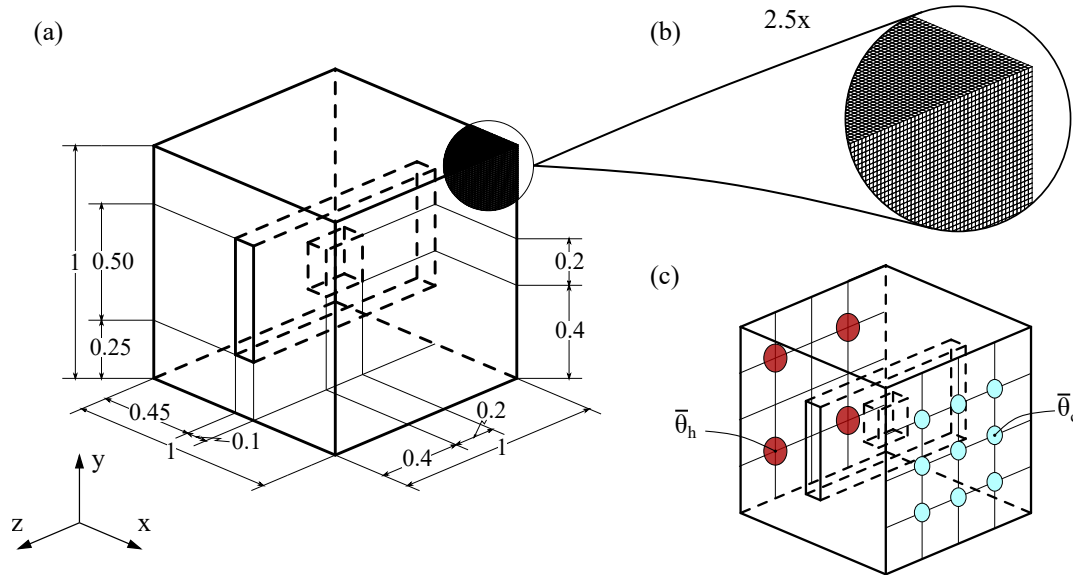


Figure B.8: Thermal heat conductor: (a) Setup of the analysis domain, (b) Detailed mesh based on hexahedral finite elements and (c) Boundary conditions of the problem. The temperature is prescribed to $\bar{\theta}_h$ at the four circular regions on the left face (colored in red) while it is set to $\bar{\theta}_c$ at the nine circular regions on the right face (colored in blue). The other surfaces are assumed to be adiabatic.

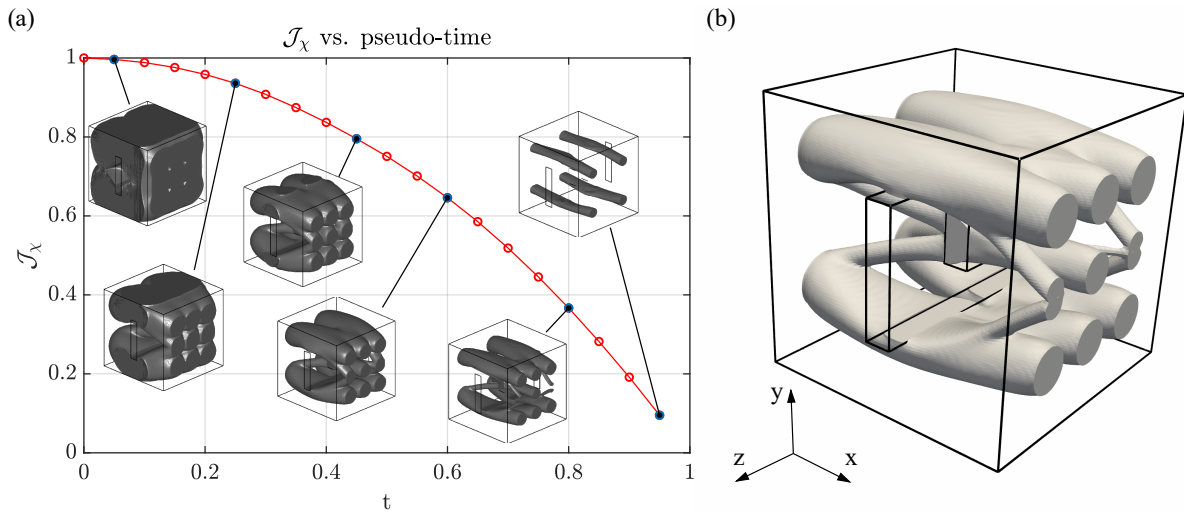


Figure B.9: Thermal heat conductor. Thermal compliance minimization: (a) Cost function and topology evolution, (b) Topology for $t = \frac{|\Omega^-(x)|}{|\Omega|} = 0.75$.

For the Laplacian smoothing (see Appendix B.A), a value of $\tau = 1$ is used, resulting in a parameter $\varepsilon = 8.3 \cdot 10^{-3}$ m. The time interval of interest $[0, 0.95]$ is discretized in 19 equally spaced steps.

In Figure B.9-(a), the evolution of the cost-function, \mathcal{J}_x , and some representative optimal topologies are illustrated in terms of the pseudo-time, ($t = \frac{|\Omega^-(x)|}{|\Omega|}$). As it could be expected, while the soft material increases, the cost function decreases. In Figure B.9-(b), an intermediate optimal design, when the hard material is the 25% of the total analysis domain, is presented. The topologies in Figure B.9-(a) show how the hot regions are connected with the cold ones, minimizing the thermal compliance. In the limit case of imposing very little conductive material

(high values of t), the obtained optimal topology connects the hot and cold faces with only four (thin) heat pipes (see also Online Resource 1).

Let us now modify this numerical example in order to consider a not null heat source ($r \neq 0$) inside the design domain, Ω . Then, a heat source of $r = 1kW/m^3$ is considered in the small prismatic volume, located at the center of the domain (see Figure B.8), which cannot be removed from the hard material domain. The contrast factor for the heat source is set to $\alpha = 1e - 3$, and the exponent is set to $m = 1$. Both the boundary conditions and the mesh discretization are kept unchanged with respect to the definition of the example. In addition, the same value of τ is used for the Laplacian smoothing. Nevertheless, the time interval of interest $[0, 0.85]$, in this case, is discretized in 17 equally spaced steps.

Mimicking Figure B.9, Figure B.10-(a) illustrates the evolution of the cost-function throughout the topology optimization in terms of the pseudo-time, t , along with some optimal topologies. The optimal topology for $t = 0.8$ is displayed in Figure B.10-(b). Due to the incorporation of the heat source in the central prismatic volume, a major change in the optimal topologies between the two presented situations is observed. In the last situation, the volume, in which the heat source is added, is also connected to the cold regions on the right side of the domain in order to dissipate as much heat as possible. In addition, the connection between hot and cold regions, observed in Figure B.9 for high values of t , gets removed in favor of a better connection to the heat source.

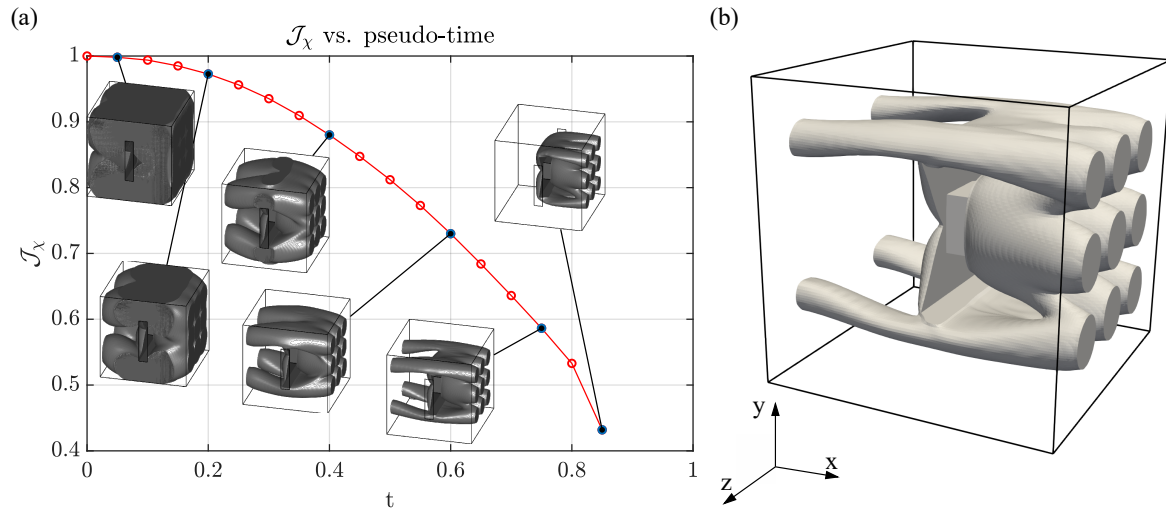


Figure B.10: Thermal heat conductor. Thermal compliance minimization including heat source: (a) Cost function and topology evolution, (b) Topology for $t = \frac{|\Omega^-(\chi)|}{|\Omega|} = 0.8$.

B.7.2 Thermal cloaking optimization

Thermal cloaking via heat flux manipulation. 3D heat flux cloaking device.

The optimization of a 3D thermal cloaking device, surrounding the object to be cloaked, is now addressed. The goal is to design the optimal topology of the cloaking device by means of the manipulation of the heat flux around it, as detailed in Section B.6.2. This problem, inspired in the pioneering work by Fachinotti *et al.* [8], can be considered a 3D extension of this work, with the heat flux prescribed to a given constant value. For the solution of the problem, a square prismatic domain Ω , with dimensions $0.09 \times 0.18 \times 0.09$ (in meters), is defined and discretized with a structured mesh of $100 \times 200 \times 100$ hexahedral elements (Figure B.11). The non-dimensional regularization parameter τ is equal to 0.1 and the pseudo-time interval $[0, 0.08]$ is discretized in 8 steps.

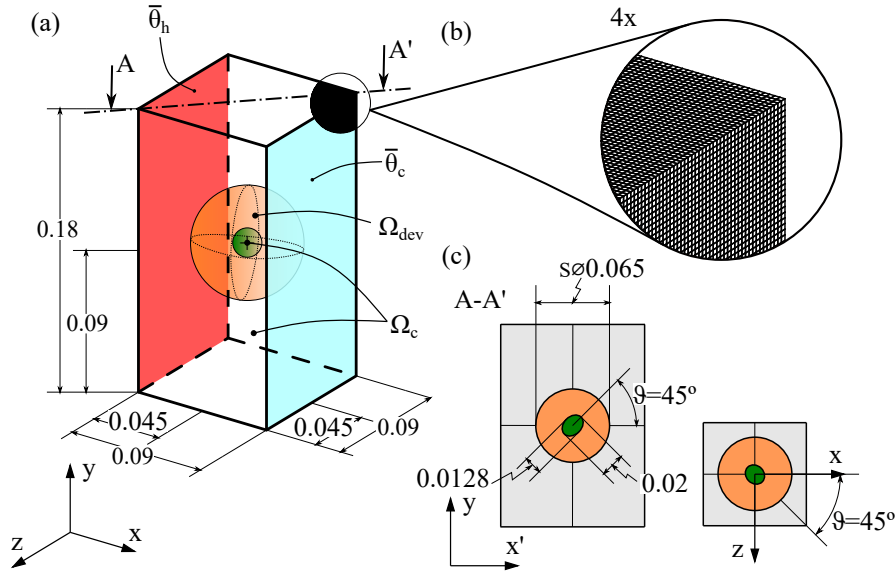


Figure B.11: Heat flux cloaking device: (a) Analysis domain, with boundary conditions and dimensions, (b) Detailed mesh and (c) Dimensional details. The cloaked object in green, placed at the center of the domain, is surrounded by the cloaking device, Ω_{dev} , in orange, whose design is optimized. The temperature on the left surface is set to $\bar{\theta}_h$, while the right one is set to $\bar{\theta}_c$.

Domain, Ω , is partitioned in three distinct regions, as illustrated in Figure B.11: 1) the cloaked object is an ellipsoid, colored in green, located at the center of the analysis domain (the principal axes of the ellipsoid are $d_1 = 0.02m$ and $d_2 = d_3 = 0.0128m$, the main axis being oriented 45° with respect to the x and y axes); b) a sphere of diameter $d = 0.065m$, shaded in orange, corresponding to the cloaking device to be designed (design domain, Ω_{dev}), and c) the remaining part of the analysis domain, colored in gray in Figure B.11-(c). Regions 1 and 3 correspond to domain $\Omega_c \equiv \Omega \setminus \Omega_{dev}$, and the optimization goal is to keep the original homogeneous heat flux constant and unaffected by the cloaking device in these regions.

The conductivity in Ω_c and Ω_{dev} is $\kappa = 0.57 W/(mK)$ and $\kappa = 403W/(mK)$, respectively. In order to obtain a conductivity of $\kappa = 0.22W/(mK)$ in the soft phase of region 2, a contrast factor of $\alpha = 5.459 \cdot 10^{-4}$ is considered, equivalently, $m = 5$ and $\beta = 0.886$ are also considered.

The temperatures on the left and right surfaces of the domain are prescribed to $\bar{\theta}_h = 321.85K$ and $\bar{\theta}_c = 283.15K$, respectively. The other surfaces are assumed to be adiabatic. Under these boundary conditions and assuming an homogeneous isotropic thermal material of $\kappa = 0.57W/(mK)$ for the whole domain, the homogeneous temperature gradient in the x -direction results in a constant horizontally heat flux $\bar{q} = [245.1, 0, 0] W/m^2$, which corresponds to the target heat flux in Ω_c .

In Figure B.12-(a), the evolution of the cost function, including some representative optimal topologies, is presented. A detail of the optimal layout for $t = 8\%$ is illustrated in Figure B.12-(b). In Figures B.13-(a-d), the topology design evolution of the cloaking device is plotted for different intermediate time steps¹⁷(see also Online Resource 2). Figures B.13-(e-h) represent the isotherms and the optimal topology layout of both material phases, obtained at the slice parallel to the x - y plane, and centered along z -axis. As it can be observed in the figure, isotherms tend to reach an homogeneous temperature gradient configuration¹⁸ as t increases (and, thus, more low-conductivity material is used in the cloaked domain). Also it can be observed that the optimal design of the cloaking device, and the way it works, are, by no means, obvious. The incoming horizontal heat flux is modified, by the combination of the low and high conductive materials

¹⁷removing an octant of the total domain as well as the hard material for a better visualization of the topology.

¹⁸The isotherms for the homogeneous case are vertical, equally spaced, isolines from $\bar{\theta}_h$ to $\bar{\theta}_c$.

in Ω_{dev} , into two different structures: a low-conductive shell and a low-conductive toroid-like domain. The thickness of the shell structure increases along time, and strongly modifies the heat flux near the left and right faces of the cloaking device Ω_{dev} , as it can be observed in Figures B.13-(f) and B.13-(g). The toroid surrounds the cloaked object and controls the heat flux inside it, see Figure B.13-(b).

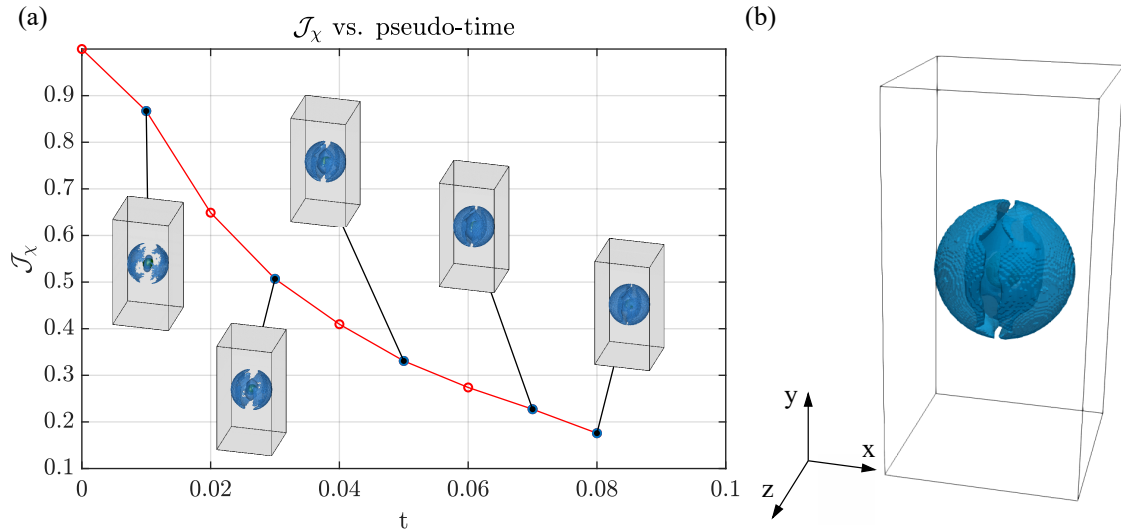


Figure B.12: Heat flux cloaking device: (a) Cost function and topology evolution, and (b) Topology for $t = \frac{|\Omega^-|}{|\Omega|} = 0.08$.

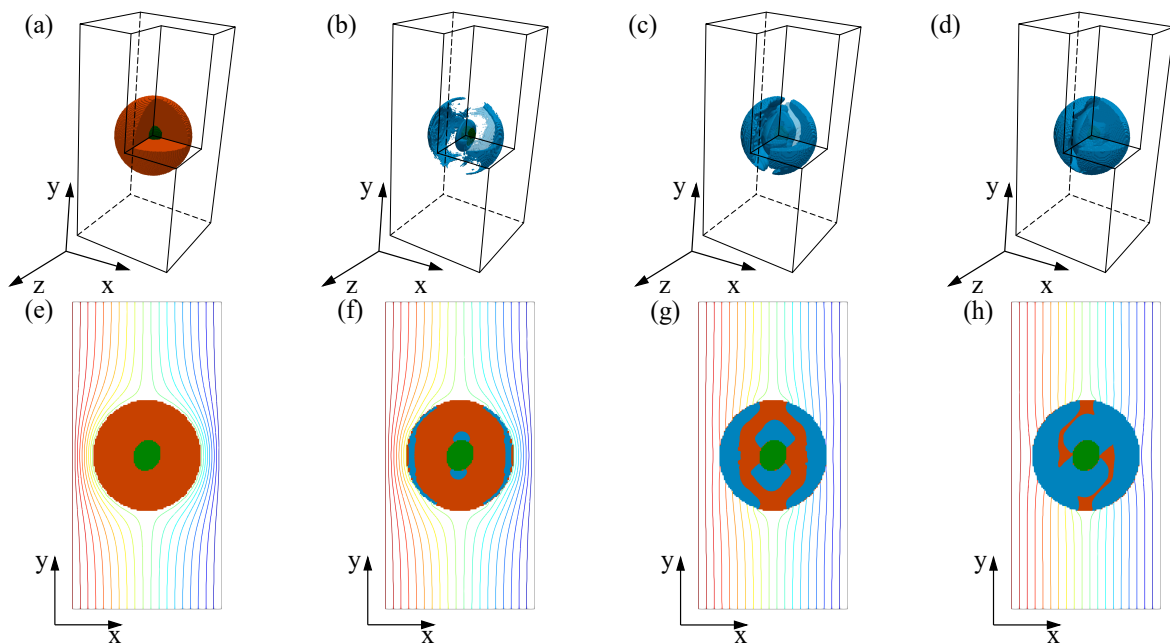


Figure B.13: Heat flux cloaking device: figures (a)-(d): 3D view of intermediate topologies, in terms of the soft (low conductive) material counterpart, at steps 0, 1, 5 and 8, respectively. Figures (e)-(h): evolution of the isotherms and layout of the cloaking device at the middle x-y plane, for the same representative steps. (Color legend: blue→soft material, orange→hard material and green→cloaked object).

Thermal cloaking via average and variance temperature minimization. 3D thermal cloaking device.

Now, a thermal cloaking device is again designed but, this time, aiming at minimizing the average and variance temperature, on a virtual plane at the surface of the analysis domain, in which the values and distribution of temperature are measured by an external device (a thermal camera, for instance). The cloaking device, in Ω_{dev} , should mitigate the distortion produced on the virtual plane by the (hot) cloaked object. The setup of the problem is displayed in Figure B.14. The dimensions of the prismatic domain, Ω , are the same than in the previous example, but a slightly finer finite element mesh is used (150x300x150 linear hexahedral elements). Taking advantage of the symmetries, only a quarter of the domain is discretized.

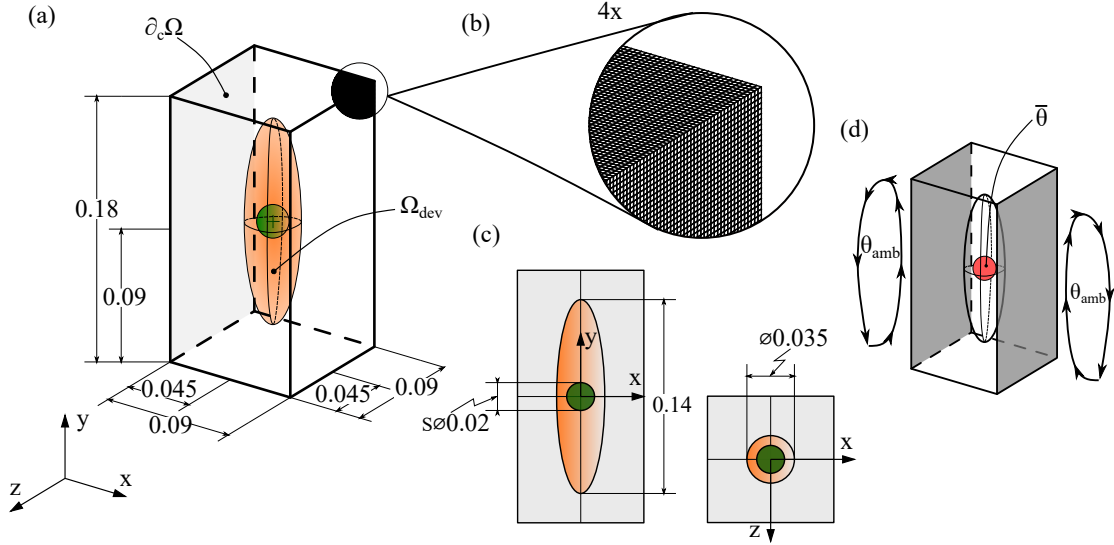


Figure B.14: Thermal cloaking device: (a) Analysis domain with its dimensions, (b) Detail of the mesh, (c) Details of dimensions and (d) Boundary conditions. The cloaked object, in green, prescribed to a high temperature $\bar{\theta}$ is surrounded by the cloaking device, in orange, which must distribute the heat to minimize the average and the variance of the temperature on the left face, $\partial_c \Omega$.

The domain is again partitioned in three different regions, see Figure B.14-(c). The innermost region is a sphere of radius $R = 0.01m$ (the hot object to be cloaked, colored in green), which is completely surrounded by region 2, an ellipsoid shaded in orange (the cloaking device, Ω_{dev}), of dimensions $d_x = d_z = 0.035m$ and $d_y = 0.14m$ (see Figure B.14). The remaining volume of Ω defines region 3. The material properties of each region are the same as the ones described in Section B.7.2. The conductivity of regions 1 and 3 is set to $\kappa = 0.57 W/(mK)$, while it is set to $\kappa = 403W/(mK)$ for the hard material in Ω_{dev} . The contrast factor in Ω_{dev} is $\alpha = 5.459 \cdot 10^{-4}$. The temperature of the cloaked object is set to $\bar{\theta} = 313K$. Left and right surfaces are subjected to a convective flux described by $h = 1W/(Km^2)$ and $\theta_{amb} = 283K$. The other surfaces are assumed to be adiabatic (see Figure B.14-(d)). The regularization parameter is $\tau = 0.1$, and the time interval $[0, 0.05]$ is split into 10 equally spaced pseudo-time steps.

Following the scheme detailed in Section B.6.3, the optimization problem (46) has to be solved three times (for $\omega = 0$, $\omega = 1$, and $\omega = 0.5$, respectively). From the results of the first two optimizations, the values of $\mathcal{J}_{av}^o = 308.6K$, $\mathcal{J}_{vr}^{max} = 7.4 \cdot 10^{-2}K^2$, $\mathcal{J}_{av}^{max} = 310.4K$ and $\mathcal{J}_{vr}^o = 9 \cdot 10^{-3}K^2$, have been determined. In this specific case, the results of the second problem are not required, since the maximum average temperature is obtained in the first iteration and the utopia point of the variance can be approximated as $\mathcal{J}_{vr}^o = 0K^2$. Finally, completing the objective function (48) with the previous parameters, the third optimization problem is solved for $\omega = 0.5$.

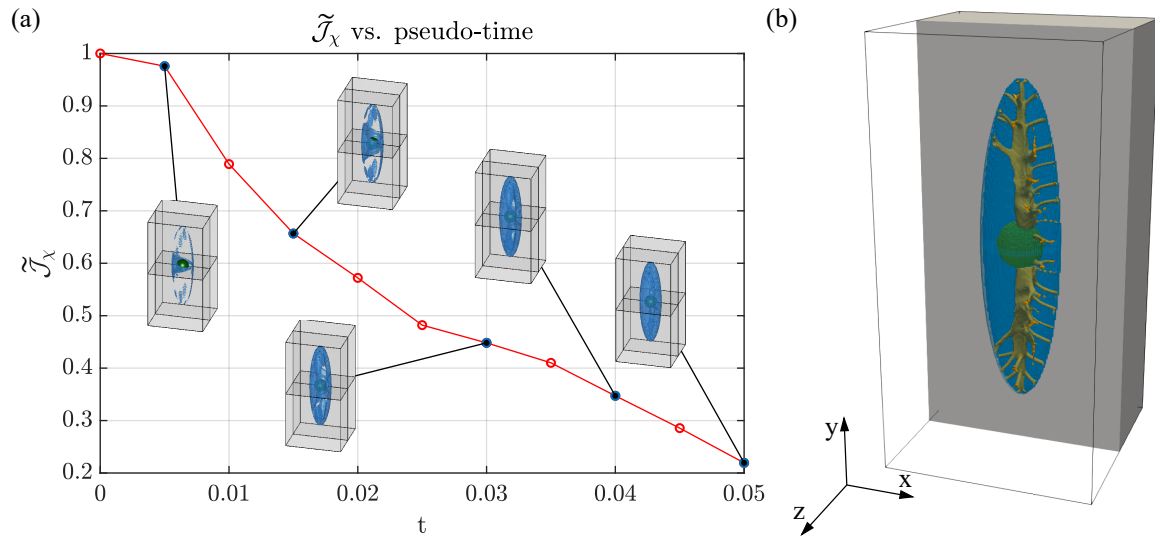


Figure B.15: Thermal cloaking device: (a) Cost function and topology evolution, and (b) Topology for $t = \frac{|\Omega^-|}{|\Omega|} = 0.05$.

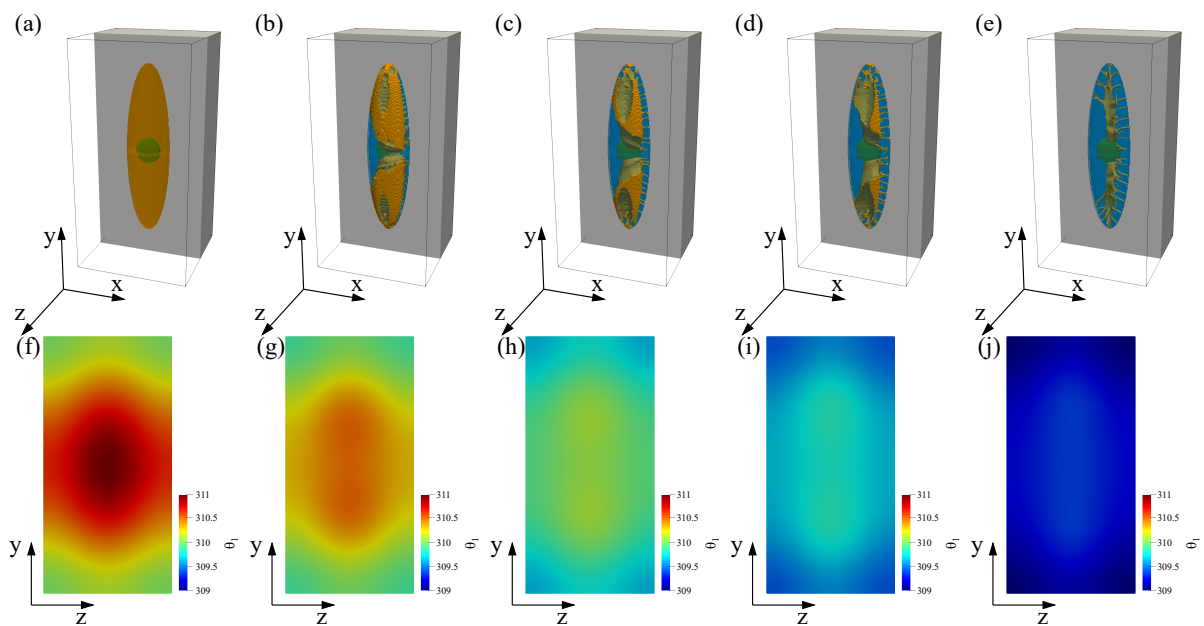


Figure B.16: Thermal cloaking device: figures (a)-(e): 3D view of intermediate configurations, illustrated by the soft and hard materials of the cloaking device, for steps 0, 3, 6, 8 and 10. Figures (f)-(j): Evolution of the temperature field of the left y-z plane, for the same representative pseudo-time steps. (Color legend: blue→soft material, orange→hard material and green→sphere).

The cost function evolution and intermediate topologies are displayed in Figures B.15 and B.16. In Figures B.16-(a) to B.16-(e), the design evolution of the cloaking device shows how the hard material (colored in orange), which initially completely fills the design domain, is progressively replaced by an insulating material (the low-conductive, soft, material colored in blue), see also Online Resource 3. The final optimal layout of the cloaking device, presented in Figure B.15-(b), where half of the domain has been removed for the sake of clarity, resembles a sort of "spine", linked with the rest of the domain at its right side while the links at the left side are scarce and limited to the top and bottom of the "spine". Therefore, the internal heat

generated by the cloaked object is, on one hand, transmitted to the top and bottom regions of the left surface ($\partial_c\Omega$) and, on the other, to the complete right surface where the heat is dissipated by natural convection. The distribution of temperatures obtained on the left surface, see Figures B.16-(f) to B.16-(j), confirms that as the hard (high-conductive) material tends to vanish, the temperature resulting in an uniform temperature distribution approaching the ambient temperature, θ_{amb} . This "a posteriori" analysis, explains the role of that, by no means obvious, resulting thermal cloaking analysis.

B.7.3 Computational assessment. Variational closed-form solution vs. level set method

This section, is devoted to analyze the computational performance of the *nonsmooth relaxed variational approach* to topology optimization, based on the Relaxed Topological Derivative (RTD), used in this work for thermal problems, with respect to a *level set method* driven by the same Relaxed Topological Derivative. To illustrate the comparison, the example described in Section B.7.1 is analyzed with both methods. The comparisons are established in terms of the cost function values and the relative computational cost, which, in turn, is evaluated in terms of the number of iterations that each method requires to converge with the same tolerances ($Tol_\chi = 10^{-1}$ and $Tol_C = 10^{-3}$).¹⁹ For a fair comparison, the time interval $[0, 0.9]$ and the number of steps, 18, are used for both methods.

The level set function, $\phi(\mathbf{x})$, in the level set method, is updated through a time-evolving (Hamilton-Jacobi) equation [1], while the volume constraint is satisfied by means of a Lagrangian multiplier updating scheme²⁰ [24]. The time evolution process continues until both the topology, defined via the characteristic function, and volume tolerances are satisfied. Therefore, the level set function is iteratively updated as follows (see [20] for more details)

$$\begin{cases} \phi^{(i+1)}(\mathbf{x}) = \phi^{(i)}(\mathbf{x}) - \frac{\Delta t}{\Delta\chi^{(i)}(\mathbf{x})} \frac{\delta\mathcal{L}(\chi^{(i)}, \lambda^{(i)})}{\delta\chi^{(i)}}(\mathbf{x}) & (a) \\ \chi^{(i+1)} = \mathcal{H}_\beta\left(\phi^{(i+1)}(\mathbf{x})\right) & (b) \\ \lambda^{(i+1)} = \lambda^{(i)} + \rho \mathcal{C}(\chi(\phi^{(i)})) & (c) \end{cases}, \quad (69)$$

where $\frac{\delta\mathcal{L}(\chi^{(i)}, \lambda^{(i)})}{\delta\chi^{(i)}}(\mathbf{x})$ corresponds to the relaxed topological derivative (RTD) of the Lagrangian and $\rho \in \mathbb{R}^+$ is a suitable penalty value.

We emphasize that the parameter Δt , in equation (69)-(a), has a remarkable effect in the convergence rate of this method. For very small values, the method will require many iterations until convergence is achieved while, for large values of Δt , results oscillate or even diverge. This parameter has to be tuned for every problem to find the optimal (convergent and large enough) value of Δt . After this, a value of $\Delta t = 1 \cdot 10^{-1}$ has been established for the considered problem as the optimal one for the comparison purposes. The penalty is set to $\rho = 5 \cdot 10^{-2}$.

The results of the comparison, as for the cost function is concerned, are depicted in Figure B.17. The cost function evolution, displayed in Figure B.17-(a), shows close results for both methods, although the result for some steps may be slightly different. However, significant improvements, in terms of the total computational cost, are obtained using the closed-form solutions of the proposed approach, with respect to level set method. This is represented in Figure B.17-(b), where the accumulative number of iterations is illustrated. From these results, it can be concluded that the nonsmooth variational approach, is more than an order of magnitude

¹⁹The comparison is done in terms of the number of iterations, instead of the computational time, as the computational cost per iteration is almost equivalent for the two approaches. Additionally, the number of iterations remains independent of the platform.

²⁰The *Cutting&Bisection* algorithm in Section B.5 is then replaced by the standard Augmented Lagrangian update, see equation (69)-(c). At convergence, the volume constraint is fulfilled at he prescribed tolerance.

(up to 15 times) faster than the level set method, while obtaining similar results in terms of optimal topologies and cost function. Moreover, the computational cost (number of required iterations) seems to be uniform along the steps for the *nonsmooth closed-form solution approach*.

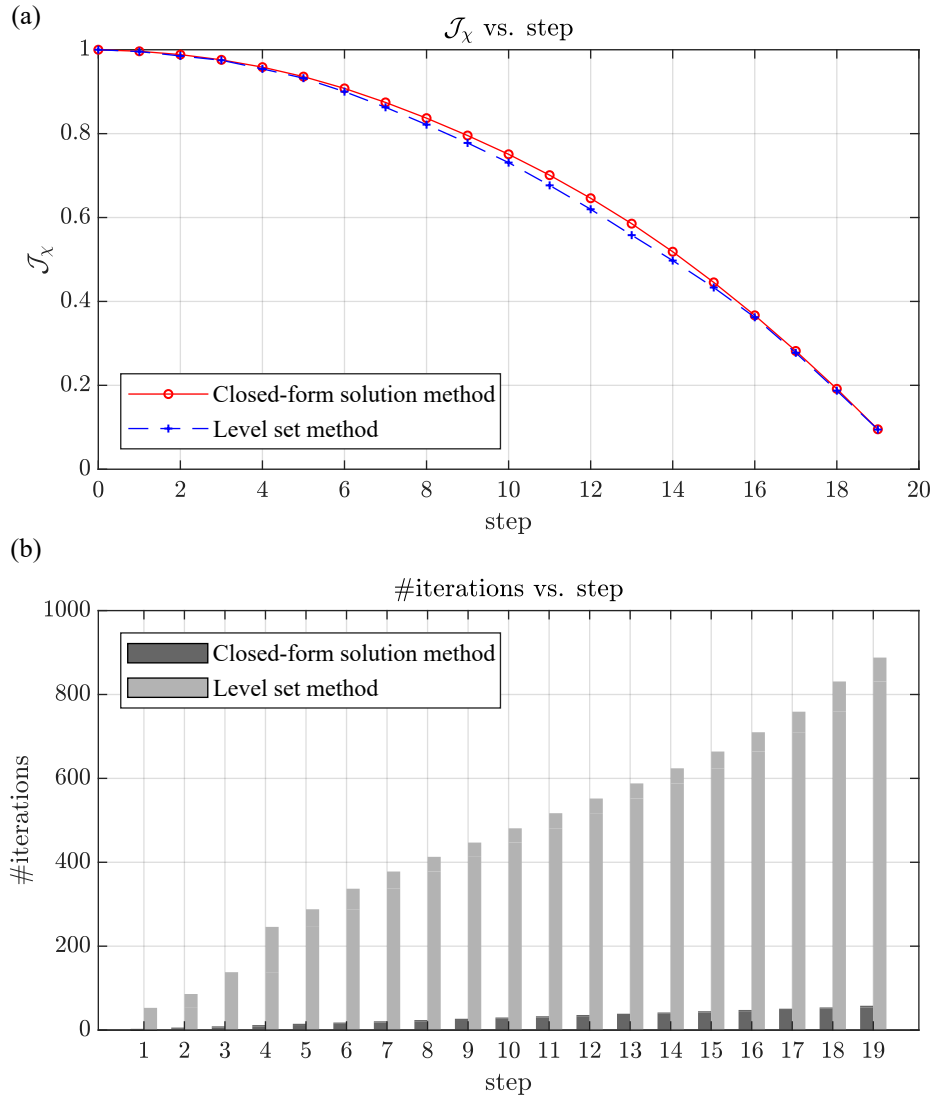


Figure B.17: Thermal heat conductor. Non-smooth variational closed-form method vs level set method: (a) Cost-function evolution, and (b) Computational cost in terms of the number of iterations.

B.8 Concluding remarks

In this paper, the nonsmooth variational approach to relaxed topology optimization, proposed in Oliver *et al.* [20] for structural problems, has been extended and applied to solve thermal topology optimization problems involving the analysis of 3D heat conducting components and thermal cloaking devices. From this work the following conclusions can be displayed:

- The RVA technique can be readily extended from structural problems to thermal ones. One, evident, reason for this is that, in spite that the physics, and technical applications in both sets of problems are very different, the mathematical settings in which they are inserted are similar. However, problems like thermal cloaking, tackled in this work, which have not a clear counterpart in structural analysis, have been successfully solved here.

- The *Cutting&Bisection* technique used to solve the resulting, fixed point algebraic closed-form, equations has been tested here beyond the original structural scenario, in which they were overall positive or negative. Here, the technique has proven to efficiently work both for constant-sign *energy densities* (Section B.6.1) but, also, in sign-changing cases (Sections B.6.2 and B.6.3). This dissipates one of the unknowns pending on this subject. The success of this algorithm strongly relies on the unique-valued character of the energy functions, ξ , as it happens in all considered problems of this work.
- As in the structural problems case, the obtainment of the *closed-form optimality criteria solutions* only requires the *formulation of the cost function*, the corresponding *energy density*, and a *pseudo-time* (volume-driven) *advancing scheme*. The Relaxed Topological Derivative, as sensitivity for the optimization problem, can be systematically and simply derived via the classical *adjoint method*, as proven in the presented applications.
- The presented numerical examples confirm that the proposed approach provides *smooth black-and-white topology designs*, also for thermal optimization problems. Mesh-size dependency and checkerboards effects are effectively removed by the the minimum material filament size control via the *Laplacian smoothing technique*, so that post-process filtering algorithms are not necessary.
- In Sections B.7.2 and B.7.2 the approach proves amenable to achieve complex non-trivial topology layouts, far from being intuitive, and even impossible to obtain without suitable numerical computational methods.
- In alignment with what was reported in [20] for structural optimization, the computational cost of the considered method for thermal optimization problems turns out to be much smaller (more than 15 times for the test considered here) when compared with an, equivalent, level set method (Hamilton-Jacobi update scheme based on the same Relaxed Topology Derivative).

In summary, the considered topological optimization methodology, based on

- 1) Optimizing the distribution of the nonsmooth characteristic function in a variational setting,
- 2) Resorting the easy-to-derive Relaxed Topological Derivative as sensitivity, and
- 3) Obtaining closed-form optimality criteria, to be numerically solved using a robust *Cutting&Bisection* algorithm, in a pseudo-time advancing scheme.

When applied to complex thermal problems, the proposed methodology exhibits the same encouraging features than in structural problems. Its extension to other families of topology optimization problems is an ongoing research that will be presented in future works.

B.9 Acknowledgements

This research has received funding from the European Research Council (ERC) under the European Union’s Horizon 2020 research and innovation programme (Proof of Concept Grant agreement n 874481) through the project “Computational design and prototyping of acoustic metamaterials for target ambient noise reduction” (METACOUSTIC). The authors also acknowledge financial support from the Spanish Ministry of Economy and Competitiveness, through the research grant DPI2017-85521-P for the project “Computational design of Acoustic and Mechanical Metamaterials” (METAMAT) and through the “Severo Ochoa Programme for Centres of Excellence in R&D” (CEX2018-000797-S). D. Yago acknowledges the support received from the Spanish Ministry of Education through the FPU program for PhD grants.

B.A Finite element discretization

The finite element method (FEM) is used to discretize and solve the state-equation (18) and the required adjoint problems. The temperature field in Ω is approximated via C_0 shape functions as follows²¹:

$$\theta_\chi(\mathbf{x}) \equiv \mathbf{N}_\theta(\mathbf{x})\hat{\boldsymbol{\theta}}_\chi \quad (70)$$

where $\mathbf{N}_\theta(\mathbf{x})$ is the, temperature, shape-function matrix and $\hat{\boldsymbol{\theta}}_\chi$ corresponds to the nodal temperature vector. Equivalently, the gradient of $\theta_\chi(\mathbf{x})$ is expressed as

$$\nabla\theta_\chi(\mathbf{x}) \equiv \mathbf{B}(\mathbf{x})\hat{\boldsymbol{\theta}}_\chi \quad (71)$$

where $\mathbf{B}(\mathbf{x})$ denotes the gradient matrix. Then, introducing expressions (70) and (71) into the Fourier's law, the heat flux, $\mathbf{q}_\chi(\mathbf{x})$, can be written as

$$\mathbf{q}_\chi(\mathbf{x}) \equiv -\boldsymbol{\kappa}_\chi(\mathbf{x}) \mathbf{B}(\mathbf{x})\hat{\boldsymbol{\theta}}_\chi. \quad (72)$$

Finally, the state equation (18), once the previous expressions are replaced, yields to

$$\mathbb{K}_\chi\hat{\boldsymbol{\theta}}_\chi = \mathbf{f} \quad (73)$$

with

$$\begin{cases} \mathbb{K}_\chi = \int_{\Omega} \mathbf{B}^T(\mathbf{x}) \boldsymbol{\kappa}_\chi(\mathbf{x}) \mathbf{B}(\mathbf{x}) d\Omega - \int_{\partial_h\Omega} \mathbf{N}_\theta^T(\mathbf{x}) h \mathbf{N}_\theta(\mathbf{x}) d\Gamma \\ \mathbf{f} = \int_{\Omega} \mathbf{N}_\theta^T(\mathbf{x}) r_\chi(\mathbf{x}) d\Omega - \int_{\partial_q\Omega} \mathbf{N}_\theta^T(\mathbf{x}) \bar{q}(\mathbf{x}) d\Gamma - \int_{\partial_h\Omega} \mathbf{N}_\theta^T(\mathbf{x}) h \theta_{amb}(\mathbf{x}) d\Gamma \end{cases}, \quad (74)$$

where \mathbb{K}_χ and \mathbf{f} stand for the stiffness matrix and the external forces vector, respectively.²²

A Laplacian smoothing is used to smooth the topology, control the filament size and avoid checkerboard patterns. The smooth discrimination function, ψ_τ , corresponds to the solution of

$$\begin{cases} \psi_\tau(\mathbf{x}) - \epsilon^2 \Delta_{\mathbf{x}} \psi_\tau(\mathbf{x}) = \psi(\mathbf{x}) & \text{in } \Omega \\ \nabla_{\mathbf{x}} \psi_\tau(\mathbf{x}) \cdot \mathbf{n} = 0 & \text{on } \partial\Omega \end{cases}, \quad (75)$$

where, $\Delta_{\mathbf{x}}(\mathbf{x}, \cdot)$ and $\nabla_{\mathbf{x}}(\mathbf{x}, \cdot)$ stand for the Laplacian and gradient operators, respectively, and \mathbf{n} is the outwards normal to the boundary of the analysis domain, $\partial\Omega$. The FE discretization of equation (75), considering $\psi_\tau(\mathbf{x}) = \mathbf{N}(\mathbf{x})\hat{\boldsymbol{\psi}}_\tau$, leads to the following system

$$\hat{\boldsymbol{\psi}}_\tau = \tilde{\mathbb{G}}^{-1} \mathbf{f}(\psi) \quad (76)$$

with

$$\begin{cases} \tilde{\mathbb{G}} = \tilde{\mathbb{M}} + \epsilon^2 \tilde{\mathbb{K}} & \rightarrow & \begin{cases} \tilde{\mathbb{M}} = \int_{\Omega} \mathbf{N}^T(\mathbf{x}) \mathbf{N}(\mathbf{x}) d\Omega; \\ \tilde{\mathbb{K}} = \int_{\Omega} \nabla \mathbf{N}^T(\mathbf{x}) \nabla \mathbf{N}(\mathbf{x}) d\Omega; \end{cases} & (a) \\ \mathbf{f}(\psi) = \int_{\Omega} \mathbf{N}^T(\mathbf{x}) \psi(\mathbf{x}) d\Omega & & & (b) \end{cases} \quad (77)$$

where $\mathbf{N}(\mathbf{x})$ stands for the standard interpolation matrix and $\hat{\boldsymbol{\psi}}_\tau$ is the vector of nodal values of the field $\psi_\tau(\mathbf{x})$.

²¹Voigt's vector/matrix notation is used in what follows.

²²From now on, the sub-index θ of \mathbf{N}_θ shall be omitted.

B.B Thermal compliance minimization: cost function derivative

The topological sensitivity of the thermal compliance optimization problem (equation (24)) is computed in detail in this section via the *adjoint method* and the Relaxed Topological Derivative (RTD). Let first rephrase the objective function, $\mathcal{J}^{(h_e)}(\chi)$, to incorporate the state equation (73)

$$\overline{\mathcal{J}}^{(h_e)}(\chi) = \frac{1}{2} \mathbf{f}^T \hat{\boldsymbol{\theta}}_\chi - \hat{\mathbf{w}}^T \underbrace{\left(\mathbb{K}_\chi \hat{\boldsymbol{\theta}}_\chi - \mathbf{f} \right)}_{= \mathbf{0}}, \quad (78)$$

where $\hat{\mathbf{w}}$ corresponds to the solution of the *adjoint state problem*, as aforementioned. Computing the RTD of equation (78) and reordering terms, one arrives to

$$\begin{aligned} \frac{\delta \overline{\mathcal{J}}^{(h_e)}(\chi)}{\delta \chi}(\hat{\mathbf{x}}) &= \left(\frac{1}{2} \mathbf{f}^T - \hat{\mathbf{w}}^T \mathbb{K}_\chi \right) \frac{\delta \hat{\boldsymbol{\theta}}_\chi}{\delta \chi}(\hat{\mathbf{x}}) \\ &+ \left(\frac{1}{2} \frac{\delta \mathbf{f}_\chi^T}{\delta \chi}(\hat{\mathbf{x}}) \hat{\boldsymbol{\theta}}_\chi - \hat{\mathbf{w}}^T \frac{\delta \mathbb{K}_\chi}{\delta \chi}(\hat{\mathbf{x}}) \hat{\boldsymbol{\theta}}_\chi + \hat{\mathbf{w}}^T \frac{\delta \mathbf{f}_\chi}{\delta \chi}(\hat{\mathbf{x}}) \right). \end{aligned} \quad (79)$$

Substituting $\hat{\mathbf{w}} \equiv \frac{1}{2} \hat{\boldsymbol{\theta}}_\chi$ in equation (79), and considering the state equation (73), the expression can be simplified to

$$\begin{aligned} \frac{\delta \overline{\mathcal{J}}^{(h_e)}(\chi)}{\delta \chi}(\hat{\mathbf{x}}) &= \frac{1}{2} \underbrace{\left(\mathbf{f}^T - \hat{\boldsymbol{\theta}}_\chi^T \mathbb{K}_\chi \right)}_{= \mathbf{0}} \frac{\delta \hat{\boldsymbol{\theta}}_\chi}{\delta \chi}(\hat{\mathbf{x}}) + \left(\frac{\delta \mathbf{f}_\chi^T}{\delta \chi}(\hat{\mathbf{x}}) \hat{\boldsymbol{\theta}}_\chi - \frac{1}{2} \hat{\boldsymbol{\theta}}_\chi^T \frac{\delta \mathbb{K}_\chi}{\delta \chi}(\hat{\mathbf{x}}) \hat{\boldsymbol{\theta}}_\chi \right) = \\ &= \left[\frac{\delta \mathbf{f}_\chi^T}{\delta \chi}(\mathbf{x}) \hat{\boldsymbol{\theta}}_\chi - \frac{1}{2} \hat{\boldsymbol{\theta}}_\chi^T \frac{\delta \mathbb{K}_\chi}{\delta \chi}(\mathbf{x}) \hat{\boldsymbol{\theta}}_\chi \right]_{\mathbf{x}=\hat{\mathbf{x}}}. \end{aligned} \quad (80)$$

Then, considering equations (14)-(17) and replacing the corresponding terms into equation (80), the Relaxed Topological Derivative of equation (78) can be expressed as

$$\begin{aligned} \frac{\delta \overline{\mathcal{J}}^{(h_e)}(\chi)}{\delta \chi}(\hat{\mathbf{x}}) &= \frac{\partial r_\chi}{\partial \chi}(\hat{\mathbf{x}}) \mathbf{N}(\hat{\mathbf{x}}) \hat{\boldsymbol{\theta}}_\chi \Delta \chi_r(\hat{\mathbf{x}}) - \frac{1}{2} \hat{\boldsymbol{\theta}}_\chi^T \mathbf{B}^T(\hat{\mathbf{x}}) \frac{\partial \boldsymbol{\kappa}_\chi}{\partial \chi}(\hat{\mathbf{x}}) \mathbf{B}(\hat{\mathbf{x}}) \hat{\boldsymbol{\theta}}_\chi \Delta \chi_\kappa(\hat{\mathbf{x}}) = \\ &= \left[\frac{\partial r_\chi}{\partial \chi} \mathbf{N}(\mathbf{x}) \hat{\boldsymbol{\theta}}_\chi \right]_{\mathbf{x}=\hat{\mathbf{x}}} \Delta \chi_r(\hat{\mathbf{x}}) - \left[\frac{1}{2} \boldsymbol{\nabla} \theta_\chi^T(\mathbf{x}) \frac{\partial \boldsymbol{\kappa}_\chi}{\partial \chi} \boldsymbol{\nabla} \theta_\chi(\mathbf{x}) \right]_{\mathbf{x}=\hat{\mathbf{x}}} \Delta \chi_\kappa(\hat{\mathbf{x}}) = \\ &= \left[m_r \chi^{m_r-1}(\mathbf{x}) r(\mathbf{x}) \mathbf{N}(\mathbf{x}) \hat{\boldsymbol{\theta}}_\chi \right]_{\mathbf{x}=\hat{\mathbf{x}}} \Delta \chi_r(\hat{\mathbf{x}}) \\ &- \left[\frac{1}{2} m_\kappa \chi^{m_\kappa-1}(\mathbf{x}) \boldsymbol{\nabla} \theta_\chi^T(\mathbf{x}) \boldsymbol{\kappa}(\mathbf{x}) \boldsymbol{\nabla} \theta_\chi(\mathbf{x}) \right]_{\mathbf{x}=\hat{\mathbf{x}}} \Delta \chi_\kappa(\hat{\mathbf{x}}), \end{aligned} \quad (81)$$

which is then written in terms of *energy densities*, to recover equation (28), as

$$\frac{\delta \overline{\mathcal{J}}^{(h_e)}(\chi)}{\delta \chi}(\hat{\mathbf{x}}) = m_r (\chi_r(\hat{\mathbf{x}}))^{m_r-1} \overline{U}_r(\hat{\mathbf{x}}) \Delta \chi_r(\hat{\mathbf{x}}) - m_\kappa (\chi_\kappa(\hat{\mathbf{x}}))^{m_\kappa-1} \overline{U}(\hat{\mathbf{x}}) \Delta \chi_\kappa(\hat{\mathbf{x}}), \quad (82)$$

where $\overline{U}(\hat{\mathbf{x}})$ is the *nominal heat conduction energy density* and $\overline{U}_r(\hat{\mathbf{x}})$ is the *nominal heat source energy density*, as described in equation (29).

B.C Thermal cloaking via heat flux manipulation: cost function derivative

This section describes step-by-step the topological sensitivity computation of the thermal cloaking optimization problem (34), mimicking the procedure explained in Appendix B.B. Let us

then define the extended cost function, $\overline{\mathcal{J}}^{(he)}(\chi)$, i.e.

$$\overline{\mathcal{J}}^{(he)}(\chi) = \left(\underbrace{\int_{\Omega} 1_{\Omega_c}(\mathbf{x}) \left| \mathbf{q}_{\chi}(\mathbf{x}, \theta_{\chi}^{(1)}) - \overline{\mathbf{q}}(\mathbf{x}) \right|^2 d\Omega}_{E(\chi, \theta_{\chi}^{(1)})} \right)^{\frac{1}{2}} - \hat{\mathbf{w}}^T \underbrace{\left(\mathbb{K}_{\chi} \hat{\boldsymbol{\theta}}_{\chi}^{(1)} - \mathbf{f}^{(1)} \right)}_{= \mathbf{0}}, \quad (83)$$

which is subsequently derived through the RTD, yielding to

$$\begin{aligned} \frac{\delta \overline{\mathcal{J}}^{(he)}(\chi)}{\delta \chi}(\hat{\mathbf{x}}) &= \frac{1}{2} \frac{1}{\mathcal{J}^{(he)}(\chi)} \frac{\delta E(\chi)}{\delta \chi}(\hat{\mathbf{x}}) - \hat{\mathbf{w}}^T \frac{\delta \mathbb{K}_{\chi}}{\delta \chi}(\hat{\mathbf{x}}) \hat{\boldsymbol{\theta}}_{\chi}^{(1)} \\ &\quad - \hat{\mathbf{w}}^T \mathbb{K}_{\chi} \frac{\delta \hat{\boldsymbol{\theta}}_{\chi}^{(1)}}{\delta \chi}(\hat{\mathbf{x}}) + \hat{\mathbf{w}}^T \frac{\delta \mathbf{f}_{\chi}^{(1)}}{\delta \chi}(\hat{\mathbf{x}}) \end{aligned} \quad (84)$$

where

$$\begin{cases} \frac{\delta E(\chi)}{\delta \chi}(\hat{\mathbf{x}}) = \left[2 \, 1_{\Omega_c}(\mathbf{x}) \left(\mathbf{q}_{\chi}(\mathbf{x}, \theta_{\chi}^{(1)}) - \overline{\mathbf{q}}(\mathbf{x}) \right)^T \frac{\delta \mathbf{q}_{\chi}(\chi)}{\delta \chi}(\mathbf{x}) \right]_{\mathbf{x}=\hat{\mathbf{x}}}, \\ \frac{\delta \mathbf{q}_{\chi}(\chi)}{\delta \chi}(\hat{\mathbf{x}}) = - \frac{\delta \boldsymbol{\kappa}_{\chi}(\chi)}{\delta \chi}(\hat{\mathbf{x}}) \nabla \theta_{\chi}^{(1)}(\hat{\mathbf{x}}) - \boldsymbol{\kappa}_{\chi} \nabla \frac{\delta \theta_{\chi}^{(1)}}{\delta \chi}(\hat{\mathbf{x}}). \end{cases} \quad (85)$$

Introducing expressions (85) into equation (84), and manipulating the terms, we obtain

$$\begin{aligned} \frac{\delta \overline{\mathcal{J}}^{(he)}(\chi)}{\delta \chi}(\hat{\mathbf{x}}) &= \underbrace{\left(-\hat{\mathbf{w}}^T \mathbb{K}_{\chi} - \mathbf{C}_1(\chi, \hat{\mathbf{x}}, \theta_{\chi}^{(1)}) \boldsymbol{\kappa}_{\chi} \nabla \right)}_{= \mathbf{0}} \frac{\delta \hat{\boldsymbol{\theta}}_{\chi}^{(1)}}{\delta \chi}(\hat{\mathbf{x}}) \\ &\quad - \mathbf{C}_1(\chi, \hat{\mathbf{x}}, \theta_{\chi}^{(1)}) \frac{\delta \boldsymbol{\kappa}_{\chi}(\chi)}{\delta \chi}(\hat{\mathbf{x}}) \nabla \theta_{\chi}^{(1)}(\hat{\mathbf{x}}) \\ &\quad - \hat{\mathbf{w}}^T \frac{\delta \mathbb{K}_{\chi}}{\delta \chi}(\hat{\mathbf{x}}) \hat{\boldsymbol{\theta}}_{\chi}^{(1)} + \hat{\mathbf{w}}^T \frac{\delta \mathbf{f}_{\chi}^{(1)}}{\delta \chi}(\hat{\mathbf{x}}), \end{aligned} \quad (86)$$

with

$$\mathbf{C}_1(\chi, \hat{\mathbf{x}}, \theta_{\chi}^{(1)}) = \frac{1_{\Omega_c}(\hat{\mathbf{x}}) \left(\mathbf{q}_{\chi}(\hat{\mathbf{x}}, \theta_{\chi}^{(1)}) - \overline{\mathbf{q}}(\hat{\mathbf{x}}) \right)^T}{\mathcal{J}^{(he)}(\chi)}. \quad (87)$$

Now, the adjoint problem of equation (86) is solved for $\hat{\mathbf{w}} \equiv \hat{\boldsymbol{\theta}}_{\chi}^{(2)}$, leading to

$$\begin{aligned} \frac{\delta \overline{\mathcal{J}}^{(he)}(\chi)}{\delta \chi}(\hat{\mathbf{x}}) &= - \mathbf{C}_1(\chi, \hat{\mathbf{x}}, \theta_{\chi}^{(1)}) \frac{\delta \boldsymbol{\kappa}_{\chi}(\chi)}{\delta \chi}(\hat{\mathbf{x}}) \nabla \theta_{\chi}^{(1)}(\hat{\mathbf{x}}) \\ &\quad - \left(\hat{\boldsymbol{\theta}}_{\chi}^{(2)} \right)^T \frac{\delta \mathbb{K}_{\chi}}{\delta \chi}(\hat{\mathbf{x}}) \hat{\boldsymbol{\theta}}_{\chi}^{(1)} + \left(\hat{\boldsymbol{\theta}}_{\chi}^{(2)} \right)^T \frac{\delta \mathbf{f}_{\chi}^{(1)}}{\delta \chi}(\hat{\mathbf{x}}). \end{aligned} \quad (88)$$

After applying the RTD to the corresponding terms, equation (88) reads as

$$\begin{aligned} \frac{\delta \overline{\mathcal{J}}^{(he)}(\chi)}{\delta \chi}(\hat{\mathbf{x}}) &= \left[\left(\hat{\boldsymbol{\theta}}_{\chi}^{(2)} \right)^T \mathbf{N}^T(\mathbf{x}) \frac{\partial r_{\chi}}{\partial \chi}(\mathbf{x}) \right]_{\mathbf{x}=\hat{\mathbf{x}}} \Delta \chi_r(\hat{\mathbf{x}}) \\ &\quad - \left[\left(\hat{\boldsymbol{\theta}}_{\chi}^{(1)} \right)^T \mathbf{B}^T(\mathbf{x}) \frac{\partial \boldsymbol{\kappa}_{\chi}}{\partial \chi}(\mathbf{x}) \mathbf{B}(\mathbf{x}) \hat{\boldsymbol{\theta}}_{\chi}^{(2)} \right]_{\mathbf{x}=\hat{\mathbf{x}}} \Delta \chi_{\kappa}(\hat{\mathbf{x}}) \\ &\quad - \left[\mathbf{C}_1(\chi, \mathbf{x}, \theta_{\chi}^{(1)}) \frac{\partial \boldsymbol{\kappa}_{\chi}}{\partial \chi}(\mathbf{x}) \mathbf{B}(\mathbf{x}) \hat{\boldsymbol{\theta}}_{\chi}^{(1)} \right]_{\mathbf{x}=\hat{\mathbf{x}}} \Delta \chi_{\kappa}(\hat{\mathbf{x}}). \end{aligned} \quad (89)$$

Subsequently, relations (14) and (15) are considered in equation (89), which yields to

$$\begin{aligned} \frac{\delta \bar{\mathcal{J}}^{(he)}(\chi)}{\delta \chi}(\hat{\mathbf{x}}) &= \left[m_r \chi^{m_r-1} \left(\hat{\boldsymbol{\theta}}_\chi^{(2)} \right)^\top \mathbf{N}^\top(\mathbf{x}) r(\mathbf{x}) \right]_{\mathbf{x}=\hat{\mathbf{x}}} \Delta \chi_r(\hat{\mathbf{x}}) \\ &\quad - \left[m_\kappa \chi^{m_\kappa-1} \left(\nabla \theta_\chi^{(1)} \right)^\top(\mathbf{x}) \boldsymbol{\kappa}(\mathbf{x}) \nabla \theta_\chi^{(2)}(\mathbf{x}) \right]_{\mathbf{x}=\hat{\mathbf{x}}} \Delta \chi_\kappa(\hat{\mathbf{x}}) \\ &\quad - \left[m_\kappa \chi^{m_\kappa-1} \mathbf{C}_1 \left(\chi, \mathbf{x}, \theta_\chi^{(1)} \right) \boldsymbol{\kappa}(\mathbf{x}) \mathbf{B}(\mathbf{x}) \hat{\boldsymbol{\theta}}_\chi^{(1)} \right]_{\mathbf{x}=\hat{\mathbf{x}}} \Delta \chi_\kappa(\hat{\mathbf{x}}). \end{aligned} \quad (90)$$

Finally, equation (90) can be reformulated, in terms of *pseudo-energies*, as

$$\begin{aligned} \frac{\delta \bar{\mathcal{J}}^{(he)}(\chi)}{\delta \chi}(\hat{\mathbf{x}}) &= m_r (\chi_r(\hat{\mathbf{x}}))^{m_r-1} \bar{\mathcal{U}}_r(\hat{\mathbf{x}}) \Delta \chi_r(\hat{\mathbf{x}}) \\ &\quad - 2 m_\kappa (\chi_\kappa(\hat{\mathbf{x}}))^{m_\kappa-1} \bar{\mathcal{U}}_{1-2}(\hat{\mathbf{x}}) \Delta \chi_\kappa(\hat{\mathbf{x}}) \\ &\quad - m_\kappa (\chi_\kappa(\hat{\mathbf{x}}))^{m_\kappa-1} \bar{\mathcal{U}}_q(\hat{\mathbf{x}}) \Delta \chi_\kappa(\hat{\mathbf{x}}), \end{aligned} \quad (91)$$

where $\bar{\mathcal{U}}_{1-2}(\hat{\mathbf{x}})$ is the nominal heat conduction energy density, $\bar{\mathcal{U}}_r(\hat{\mathbf{x}})$ is the nominal heat source energy density and $\bar{\mathcal{U}}_q(\hat{\mathbf{x}})$ corresponds to the nominal heat flux energy density, as defined in equation (43).

B.D Average temperature minimization: cost function derivative

Let us now proceed with the computation of the topological sensitivity of the average temperature minimization problem (50). As before, let $\bar{\mathcal{J}}_{\text{av}}^{(he)}(\chi)$ be the extended cost function, considering the *state equation* through the Lagrange multiplier vector, $\hat{\mathbf{w}}$, defined as

$$\bar{\mathcal{J}}_{\text{av}}^{(he)}(\chi) = C_2 \mathbf{1}_{\partial_c \Omega}^\top \hat{\boldsymbol{\theta}}_\chi^{(1)} - \hat{\mathbf{w}}^\top \underbrace{\left(\mathbb{K}_\chi \hat{\boldsymbol{\theta}}_\chi^{(1)} - \mathbf{f}^{(1)} \right)}_{= \mathbf{0}}, \quad (92)$$

where $C_2 = \left(\int_{\partial_c \Omega} d\Gamma \right)^{-1}$.

Applying the RTD to equation (92) and reordering its terms, one obtains

$$\frac{\delta \bar{\mathcal{J}}_{\text{av}}^{(he)}(\chi)}{\delta \chi}(\hat{\mathbf{x}}) = \left(-\hat{\mathbf{w}}^\top \mathbb{K}_\chi + C_2 \mathbf{1}_{\partial_c \Omega}^\top \right) \frac{\delta \hat{\boldsymbol{\theta}}_\chi^{(1)}}{\delta \chi}(\hat{\mathbf{x}}) - \hat{\mathbf{w}}^\top \frac{\delta \mathbb{K}_\chi}{\delta \chi}(\hat{\mathbf{x}}) \hat{\boldsymbol{\theta}}_\chi^{(1)} + \hat{\mathbf{w}}^\top \frac{\delta \mathbf{f}_\chi^{(1)}}{\delta \chi}(\hat{\mathbf{x}}), \quad (93)$$

which is then simplified by choosing $\hat{\mathbf{w}} \equiv -C_2 \hat{\boldsymbol{\theta}}_\chi^{(2)}$, yielding to

$$\begin{aligned} \frac{\delta \bar{\mathcal{J}}_{\text{av}}^{(he)}(\chi)}{\delta \chi}(\hat{\mathbf{x}}) &= C_2 \underbrace{\left(\left(\hat{\boldsymbol{\theta}}_\chi^{(2)} \right)^\top \mathbb{K}_\chi + \mathbf{1}_{\partial_c \Omega}^\top \right)}_{= \mathbf{0}} \frac{\delta \hat{\boldsymbol{\theta}}_\chi^{(1)}}{\delta \chi}(\hat{\mathbf{x}}) + C_2 \left(\hat{\boldsymbol{\theta}}_\chi^{(2)} \right)^\top \frac{\delta \mathbb{K}_\chi}{\delta \chi}(\hat{\mathbf{x}}) \hat{\boldsymbol{\theta}}_\chi^{(1)} \\ &\quad - C_2 \left(\hat{\boldsymbol{\theta}}_\chi^{(2)} \right)^\top \frac{\delta \mathbf{f}_\chi^{(1)}}{\delta \chi}(\hat{\mathbf{x}}) = \\ &= C_2 \left(\left(\hat{\boldsymbol{\theta}}_\chi^{(2)} \right)^\top \frac{\delta \mathbb{K}_\chi}{\delta \chi}(\hat{\mathbf{x}}) \hat{\boldsymbol{\theta}}_\chi^{(1)} - \left(\hat{\boldsymbol{\theta}}_\chi^{(2)} \right)^\top \frac{\delta \mathbf{f}_\chi^{(1)}}{\delta \chi}(\hat{\mathbf{x}}) \right). \end{aligned} \quad (94)$$

Equation (94) is finally discretized using the expressions in Section B.A, which then reads as

$$\frac{\delta \bar{\mathcal{J}}_{\text{av}}^{(he)}(\chi)}{\delta \chi}(\hat{\mathbf{x}}) = C_2 \left(\hat{\boldsymbol{\theta}}_\chi^{(2)} \right)^\top \mathbf{B}^\top(\hat{\mathbf{x}}) \frac{\partial \boldsymbol{\kappa}_\chi}{\partial \chi}(\hat{\mathbf{x}}) \mathbf{B}(\hat{\mathbf{x}}) \hat{\boldsymbol{\theta}}_\chi^{(1)} \Delta \chi_\kappa(\hat{\mathbf{x}})$$

$$\begin{aligned}
& - C_2 \left(\hat{\boldsymbol{\theta}}_{\chi}^{(2)} \right)^{\text{T}} \mathbf{N}^{\text{T}}(\hat{\mathbf{x}}) \frac{\partial r_{\chi}}{\partial \chi}(\hat{\mathbf{x}}) \Delta \chi_r(\hat{\mathbf{x}}) = \\
& = C_2 \left[m_{\kappa} \chi^{m_{\kappa}-1}(\mathbf{x}) \left(\hat{\boldsymbol{\theta}}_{\chi}^{(2)} \right)^{\text{T}} \mathbf{B}^{\text{T}}(\mathbf{x}) \boldsymbol{\kappa}(\mathbf{x}) \mathbf{B}(\mathbf{x}) \hat{\boldsymbol{\theta}}_{\chi}^{(1)} \right]_{\mathbf{x}=\hat{\mathbf{x}}} \Delta \chi_{\kappa}(\hat{\mathbf{x}}) \\
& - C_2 \left[m_r \chi^{m_r-1}(\mathbf{x}) \left(\hat{\boldsymbol{\theta}}_{\chi}^{(2)} \right)^{\text{T}} \mathbf{N}^{\text{T}}(\mathbf{x}) r(\mathbf{x}) \right]_{\mathbf{x}=\hat{\mathbf{x}}} \Delta \chi_r(\hat{\mathbf{x}}). \tag{95}
\end{aligned}$$

The Relaxed Topological Derivative of the cost function (50) can be finally expressed in terms of *energy densities* as

$$\begin{aligned}
\frac{\delta \bar{\mathcal{J}}_{\text{av}}^{(h_e)}(\chi)}{\delta \chi}(\hat{\mathbf{x}}) & = 2C_2 m_{\kappa} (\chi_{\kappa}(\hat{\mathbf{x}}))^{m_{\kappa}-1} \bar{\mathcal{U}}_{1-2}(\hat{\mathbf{x}}) \Delta \chi_{\kappa}(\hat{\mathbf{x}}) \\
& - C_2 m_r (\chi_r(\hat{\mathbf{x}}))^{m_r-1} \bar{\mathcal{U}}_{r-2}(\hat{\mathbf{x}}) \Delta \chi_r(\hat{\mathbf{x}}), \tag{96}
\end{aligned}$$

where $\bar{\mathcal{U}}_{1-2}(\hat{\mathbf{x}})$ and $\bar{\mathcal{U}}_{r-2}(\hat{\mathbf{x}})$ are, respectively, *the nominal heat conduction energy density* and *the nominal heat source energy density*, both defined in equation (54).

B.E Temperature variance minimization: cost function derivation

Let us now address the corresponding RTD computation of the cost function for the minimization of the temperature variance (equation (56)), starting by defining the extended cost function as

$$\bar{\mathcal{J}}_{\text{vr}}^{(h_e)}(\chi) = C_3 \left(\mathcal{T}_{\chi} \left(\theta_{\chi}^{(1)} \right) \right)^{\text{T}} \mathbb{M}_{\partial_e \Omega} \mathcal{T}_{\chi} \left(\theta_{\chi}^{(1)} \right) - \hat{\mathbf{w}}^{\text{T}} \underbrace{\left(\mathbb{K}_{\chi} \hat{\boldsymbol{\theta}}_{\chi}^{(1)} - \mathbf{f}^{(1)} \right)}_{= \mathbf{0}}, \tag{97}$$

where $\mathcal{T}_{\chi} \left(\theta_{\chi}^{(1)} \right)$ and $\mathbb{M}_{\partial_e \Omega}$ are respectively defined as

$$\begin{aligned}
\mathcal{T}_{\chi} \left(\theta_{\chi}^{(1)} \right) & = \hat{\boldsymbol{\theta}}_{\chi}^{(1)} - \mathbb{I} \mathcal{J}_{\text{av}}^{(h_e)} \left(\theta_{\chi}^{(1)} \right), \\
\mathbb{M}_{\partial_e \Omega} & = \int_{\partial \Omega} \mathbf{N}^{\text{T}}(\mathbf{x}) 1_{\partial_e \Omega}(\mathbf{x}) \mathbf{N}(\mathbf{x}) d\Gamma.
\end{aligned}$$

Applying the RTD to equation (97) and rearranging the expression, one arrives to

$$\begin{aligned}
\frac{\delta \bar{\mathcal{J}}_{\text{vr}}^{(h_e)}(\chi)}{\delta \chi}(\hat{\mathbf{x}}) & = \overbrace{\left(-\hat{\mathbf{w}}^{\text{T}} \mathbb{K}_{\chi} + 2C_3 \left(\mathcal{T}_{\chi} \left(\theta_{\chi}^{(1)} \right) \right)^{\text{T}} \mathbb{M}_{\partial_e \Omega} \right)}^{= \mathbf{0}} \frac{\delta \hat{\boldsymbol{\theta}}_{\chi}^{(1)}}{\delta \chi}(\hat{\mathbf{x}}) \\
& - 2C_3 \left(\mathcal{T}_{\chi} \left(\theta_{\chi}^{(1)} \right) \right)^{\text{T}} \mathbb{M}_{\partial_e \Omega} \mathbb{I} \frac{\delta \mathcal{J}_{\text{av}}^{(h_e)}(\chi)}{\delta \chi}(\hat{\mathbf{x}}) \\
& - \hat{\mathbf{w}}^{\text{T}} \frac{\delta \mathbb{K}_{\chi}}{\delta \chi}(\hat{\mathbf{x}}) \hat{\boldsymbol{\theta}}_{\chi}^{(1)} + \hat{\mathbf{w}}^{\text{T}} \frac{\delta \mathbf{f}_{\chi}^{(1)}}{\delta \chi}(\hat{\mathbf{x}}). \tag{98}
\end{aligned}$$

Then, the *adjoint state equation* can be readily identified from equation (98) and solved for $\hat{\mathbf{w}} \equiv -C_3 \hat{\boldsymbol{\theta}}_{\chi}^{(3)}$, resulting in

$$\begin{aligned}
\frac{\delta \bar{\mathcal{J}}_{\text{vr}}^{(h_e)}(\chi)}{\delta \chi}(\hat{\mathbf{x}}) & = -2C_3 \left(\mathcal{T}_{\chi} \left(\theta_{\chi}^{(1)} \right) \right)^{\text{T}} \mathbb{M}_{\partial_e \Omega} \mathbb{I} \frac{\delta \mathcal{J}_{\text{av}}^{(h_e)}(\chi)}{\delta \chi}(\hat{\mathbf{x}}) \\
& + C_3 \left(\hat{\boldsymbol{\theta}}_{\chi}^{(3)} \right)^{\text{T}} \frac{\delta \mathbb{K}_{\chi}}{\delta \chi}(\hat{\mathbf{x}}) \hat{\boldsymbol{\theta}}_{\chi}^{(1)} - C_3 \left(\hat{\boldsymbol{\theta}}_{\chi}^{(3)} \right)^{\text{T}} \frac{\delta \mathbf{f}_{\chi}^{(1)}}{\delta \chi}(\hat{\mathbf{x}}), \tag{99}
\end{aligned}$$

which can be, after inserting the RTD of $\mathcal{J}_{\text{av}}^{(h_e)}(\chi)$ (94), expressed as

$$\begin{aligned} \frac{\delta \overline{\mathcal{J}}_{\text{vr}}^{(h_e)}(\chi)}{\delta \chi}(\hat{\mathbf{x}}) = & -2C_3 \left(\mathcal{T}_\chi \left(\theta_\chi^{(1)} \right) \right)^\top \mathbb{M}_{\partial_c \Omega} \mathbb{I} \left(C_2 \left(\hat{\theta}_\chi^{(2)} \right)^\top \frac{\delta \mathbb{K}_\chi}{\delta \chi}(\hat{\mathbf{x}}) \hat{\theta}_\chi^{(1)} - C_2 \left(\hat{\theta}_\chi^{(2)} \right)^\top \frac{\delta \mathbf{f}_\chi^{(1)}}{\delta \chi}(\hat{\mathbf{x}}) \right) \\ & + C_3 \left(\hat{\theta}_\chi^{(3)} \right)^\top \frac{\delta \mathbb{K}_\chi}{\delta \chi}(\hat{\mathbf{x}}) \hat{\theta}_\chi^{(1)} - C_3 \left(\hat{\theta}_\chi^{(3)} \right)^\top \frac{\delta \mathbf{f}_\chi^{(1)}}{\delta \chi}(\hat{\mathbf{x}}). \end{aligned} \quad (100)$$

Replacing the RTD of the stiffness matrix and the force vector into equation (100), one arrives to

$$\begin{aligned} \frac{\delta \overline{\mathcal{J}}_{\text{vr}}^{(h_e)}(\chi)}{\delta \chi}(\hat{\mathbf{x}}) = & -2C_3 \mathcal{A} \left(\theta_\chi^{(1)} \right) \left(C_2 \left(\hat{\theta}_\chi^{(2)} \right)^\top \mathbf{B}^\top(\hat{\mathbf{x}}) \frac{\partial \boldsymbol{\kappa}_\chi}{\partial \chi}(\hat{\mathbf{x}}) \mathbf{B}(\hat{\mathbf{x}}) \hat{\theta}_\chi^{(1)} \Delta \chi_\kappa(\hat{\mathbf{x}}) \right. \\ & \left. - C_2 \left(\hat{\theta}_\chi^{(2)} \right)^\top \mathbf{N}^\top(\hat{\mathbf{x}}) \frac{\partial r_\chi}{\partial \chi}(\hat{\mathbf{x}}) \Delta \chi_r(\hat{\mathbf{x}}) \right) \\ & + C_3 \left(\hat{\theta}_\chi^{(3)} \right)^\top \mathbf{B}^\top(\hat{\mathbf{x}}) \frac{\partial \boldsymbol{\kappa}_\chi}{\partial \chi}(\hat{\mathbf{x}}) \mathbf{B}(\hat{\mathbf{x}}) \hat{\theta}_\chi^{(1)} \Delta \chi_\kappa(\hat{\mathbf{x}}) \\ & - C_3 \left(\hat{\theta}_\chi^{(3)} \right)^\top \mathbf{N}^\top(\hat{\mathbf{x}}) \frac{\partial r_\chi}{\partial \chi}(\hat{\mathbf{x}}) \Delta \chi_r(\hat{\mathbf{x}}), \end{aligned} \quad (101)$$

where $\mathcal{A} \left(\theta_\chi^{(1)} \right)$ is equal to $\left(\mathcal{T}_\chi \left(\theta_\chi^{(1)} \right) \right)^\top \mathbb{M}_{\partial_c \Omega} \mathbb{I}$. Now we introduce the definition of the conductivity and the heat source with respect to the topology (equations (14) and (15)) into expression (101), yielding to

$$\begin{aligned} \frac{\delta \overline{\mathcal{J}}_{\text{vr}}^{(h_e)}(\chi)}{\delta \chi}(\hat{\mathbf{x}}) = & -2C_3 \mathcal{A} \left(\theta_\chi^{(1)} \right) \left(C_2 \left[m_\kappa \chi^{m_\kappa - 1} \left(\hat{\theta}_\chi^{(2)} \right)^\top \mathbf{B}^\top(\mathbf{x}) \boldsymbol{\kappa}(\mathbf{x}) \mathbf{B}(\mathbf{x}) \hat{\theta}_\chi^{(1)} \right]_{\mathbf{x}=\hat{\mathbf{x}}} \Delta \chi_\kappa(\hat{\mathbf{x}}) \right. \\ & \left. - C_2 \left[m_r \chi^{m_r - 1} \left(\hat{\theta}_\chi^{(2)} \right)^\top \mathbf{N}^\top(\mathbf{x}) r(\mathbf{x}) \right]_{\mathbf{x}=\hat{\mathbf{x}}} \Delta \chi_r(\hat{\mathbf{x}}) \right) \\ & + C_3 \left[m_\kappa \chi^{m_\kappa - 1} \left(\hat{\theta}_\chi^{(3)} \right)^\top \mathbf{B}^\top(\mathbf{x}) \boldsymbol{\kappa}(\mathbf{x}) \mathbf{B}(\mathbf{x}) \hat{\theta}_\chi^{(1)} \right]_{\mathbf{x}=\hat{\mathbf{x}}} \Delta \chi_\kappa(\hat{\mathbf{x}}) \\ & - C_3 \left[m_r \chi^{m_r - 1} \left(\hat{\theta}_\chi^{(3)} \right)^\top \mathbf{N}^\top(\mathbf{x}) r(\mathbf{x}) \right]_{\mathbf{x}=\hat{\mathbf{x}}} \Delta \chi_r(\hat{\mathbf{x}}). \end{aligned} \quad (102)$$

Finally, the sensitivity $\frac{\delta \overline{\mathcal{J}}_{\text{vr}}^{(h_e)}(\chi)}{\delta \chi}$ at point $\hat{\mathbf{x}}$ can be written as a sum of *actual energies*, which yields to

$$\begin{aligned} \frac{\delta \overline{\mathcal{J}}_{\text{vr}}^{(h_e)}(\chi)}{\delta \chi}(\hat{\mathbf{x}}) = & -4C_3 C_2 m_\kappa (\chi_\kappa(\hat{\mathbf{x}}))^{m_\kappa - 1} \mathcal{A} \left(\theta_\chi^{(1)} \right) \overline{\mathcal{U}}_{1-2}(\hat{\mathbf{x}}) \Delta \chi_\kappa(\hat{\mathbf{x}}) \\ & + C_3 C_2 m_r (\chi_r(\hat{\mathbf{x}}))^{m_r - 1} \mathcal{A} \left(\theta_\chi^{(1)} \right) \overline{\mathcal{U}}_{r-2}(\hat{\mathbf{x}}) \Delta \chi_r(\hat{\mathbf{x}}) \\ & + 2C_3 m_\kappa (\chi_\kappa(\hat{\mathbf{x}}))^{m_\kappa - 1} \overline{\mathcal{U}}_{1-3}(\hat{\mathbf{x}}) \Delta \chi_\kappa(\hat{\mathbf{x}}) \\ & - C_3 m_r (\chi_r(\hat{\mathbf{x}}))^{m_r - 1} \overline{\mathcal{U}}_{r-3}(\hat{\mathbf{x}}) \Delta \chi_r(\hat{\mathbf{x}}), \end{aligned} \quad (103)$$

where $\overline{\mathcal{U}}_{i-j}(\hat{\mathbf{x}})$ is the *nominal heat conduction energy density* for i -th and j -th temperature fields ($i, j = \{1, 2, 3\}$) and $\overline{\mathcal{U}}_{r-k}(\hat{\mathbf{x}})$ corresponds to the *nominal heat source energy density* for the k -th temperature field ($k = \{1, 2, 3\}$).

References

- [1] G. Allaire, F. de gournay, F. Jouve, and A.-M. Toader, "Structural optimization using topological and shape sensitivity via a level set method," *Control and Cybernetics*, vol. 34, 2005.

- [2] T. W. Athan and P. Y. Papalambros, “A note on weighted criteria methods for compromise solutions in multi-objective optimization,” *Engineering Optimization*, vol. 27, no. 2, pp. 155–176, Sep. 1996. DOI: [10.1080/03052159608941404](https://doi.org/10.1080/03052159608941404).
- [3] M. P. Bendsøe and O. Sigmund, *Topology Optimization*. Springer Berlin Heidelberg, 2004. DOI: [10.1007/978-3-662-05086-6](https://doi.org/10.1007/978-3-662-05086-6).
- [4] F. H. Burger, J. Dirker, and J. P. Meyer, “Three-dimensional conductive heat transfer topology optimisation in a cubic domain for the volume-to-surface problem,” *International Journal of Heat and Mass Transfer*, vol. 67, pp. 214–224, Dec. 2013. DOI: [10.1016/j.ijheatmasstransfer.2013.08.015](https://doi.org/10.1016/j.ijheatmasstransfer.2013.08.015).
- [5] E. M. Dede, T. Nomura, and J. Lee, “Thermal-composite design optimization for heat flux shielding, focusing, and reversal,” *Structural and Multidisciplinary Optimization*, vol. 49, no. 1, pp. 59–68, Jul. 2013. DOI: [10.1007/s00158-013-0963-0](https://doi.org/10.1007/s00158-013-0963-0).
- [6] N. P. van Dijk, K. Maute, M. Langelaar, and F. van Keulen, “Level-set methods for structural topology optimization: A review,” *Structural and Multidisciplinary Optimization*, vol. 48, no. 3, pp. 437–472, 2013. DOI: [10.1007/s00158-013-0912-y](https://doi.org/10.1007/s00158-013-0912-y).
- [7] H. A. Eschenauer and N. Olhoff, “Topology optimization of continuum structures: A review,” *Applied Mechanics Reviews*, vol. 54, no. 4, pp. 331–390, Jul. 2001. DOI: [10.1115/1.1388075](https://doi.org/10.1115/1.1388075).
- [8] V. D. Fachinotti, Á. A. Ciarbonetti, I. Peralta, and I. Rintoul, “Optimization-based design of easy-to-make devices for heat flux manipulation,” *International Journal of Thermal Sciences*, vol. 128, pp. 38–48, Jun. 2018. DOI: [10.1016/j.ijthermalsci.2018.02.009](https://doi.org/10.1016/j.ijthermalsci.2018.02.009).
- [9] T. Gao, W. H. Zhang, J. H. Zhu, Y. J. Xu, and D. H. Bassir, “Topology optimization of heat conduction problem involving design-dependent heat load effect,” *Finite Elements in Analysis and Design*, vol. 44, no. 14, pp. 805–813, Oct. 2008. DOI: [10.1016/j.finel.2008.06.001](https://doi.org/10.1016/j.finel.2008.06.001).
- [10] A. Gersborg-Hansen, M. P. Bendsøe, and O. Sigmund, “Topology optimization of heat conduction problems using the finite volume method,” *Structural and Multidisciplinary Optimization*, vol. 31, no. 4, pp. 251–259, Mar. 2006. DOI: [10.1007/s00158-005-0584-3](https://doi.org/10.1007/s00158-005-0584-3).
- [11] S. M. Giusti, A. A. Novotny, and J. Sokółowski, “Topological derivative for steady-state orthotropic heat diffusion problem,” *Structural and Multidisciplinary Optimization*, vol. 40, no. 1-6, pp. 53–64, Feb. 2009. DOI: [10.1007/s00158-009-0359-3](https://doi.org/10.1007/s00158-009-0359-3).
- [12] S.-H. Ha and S. Cho, “Topological shape optimization of heat conduction problems using level set approach,” *Numerical Heat Transfer, Part B: Fundamentals*, vol. 48, no. 1, pp. 67–88, Jul. 2005. DOI: [10.1080/10407790590935966](https://doi.org/10.1080/10407790590935966).
- [13] A. Iga, S. Nishiwaki, K. Izui, and M. Yoshimura, “Topology optimization for thermal conductors considering design-dependent effects, including heat conduction and convection,” *International Journal of Heat and Mass Transfer*, vol. 52, no. 11-12, pp. 2721–2732, May 2009. DOI: [10.1016/j.ijheatmasstransfer.2008.12.013](https://doi.org/10.1016/j.ijheatmasstransfer.2008.12.013).
- [14] Q. Li, G. P. Steven, O. M. Querin, and Y. M. Xie, “Structural topology design with multiple thermal criteria,” *Engineering Computations*, vol. 17, no. 6, pp. 715–734, Sep. 2000. DOI: [10.1108/02644400010340642](https://doi.org/10.1108/02644400010340642).
- [15] Q. Li, G. P. Steven, O. M. Querin, and Y. Xie, “Shape and topology design for heat conduction by evolutionary structural optimization,” *International Journal of Heat and Mass Transfer*, vol. 42, no. 17, pp. 3361–3371, Sep. 1999. DOI: [10.1016/s0017-9310\(99\)00008-3](https://doi.org/10.1016/s0017-9310(99)00008-3).
- [16] J. L. Lions, *Optimal Control of Systems Governed by Partial Differential Equations*. Springer Berlin Heidelberg, 1971, 416 pp., ISBN: 3642650260.

- [17] G. Marck, M. Nemer, J.-L. Harion, S. Russeil, and D. Bougeard, “Topology optimization using the SIMP method for multiobjective conductive problems,” *Numerical Heat Transfer, Part B: Fundamentals*, vol. 61, no. 6, pp. 439–470, Jun. 2012. DOI: [10.1080/10407790.2012.687979](https://doi.org/10.1080/10407790.2012.687979).
- [18] R. Marler and J. Arora, “Survey of multi-objective optimization methods for engineering,” *Structural and Multidisciplinary Optimization*, vol. 26, no. 6, pp. 369–395, Apr. 2004. DOI: [10.1007/s00158-003-0368-6](https://doi.org/10.1007/s00158-003-0368-6).
- [19] S. Narayana and Y. Sato, “Heat flux manipulation with engineered thermal materials,” *Physical Review Letters*, vol. 108, no. 21, May 2012. DOI: [10.1103/physrevlett.108.214303](https://doi.org/10.1103/physrevlett.108.214303).
- [20] J. Oliver, D. Yago, J. Cante, and O. Lloberas-Valls, “Variational approach to relaxed topological optimization: Closed form solutions for structural problems in a sequential pseudo-time framework,” *Computer Methods in Applied Mechanics and Engineering*, vol. 355, pp. 779–819, Oct. 2019. DOI: [10.1016/j.cma.2019.06.038](https://doi.org/10.1016/j.cma.2019.06.038).
- [21] I. Peralta, V. D. Fachinotti, and Á. A. Ciarbonetti, “Optimization-based design of a heat flux concentrator,” *Scientific Reports*, vol. 7, no. 1, Jan. 2017. DOI: [10.1038/srep40591](https://doi.org/10.1038/srep40591).
- [22] G. I. N. Rozvany, “A critical review of established methods of structural topology optimization,” *Structural and Multidisciplinary Optimization*, vol. 37, no. 3, pp. 217–237, 2008. DOI: [10.1007/s00158-007-0217-0](https://doi.org/10.1007/s00158-007-0217-0).
- [23] O. Sigmund and K. Maute, “Topology optimization approaches,” *Structural and Multidisciplinary Optimization*, vol. 48, no. 6, pp. 1031–1055, 2013. DOI: [10.1007/s00158-013-0978-6](https://doi.org/10.1007/s00158-013-0978-6).
- [24] J. C. Simo and T. A. Laursen, “An augmented lagrangian treatment of contact problems involving friction,” *Computers & Structures*, vol. 42, no. 1, pp. 97–116, 1992. DOI: [10.1016/0045-7949\(92\)90540-g](https://doi.org/10.1016/0045-7949(92)90540-g).
- [25] S. Wu, Y. Zhang, and S. Liu, “Topology optimization for minimizing the maximum temperature of transient heat conduction structure,” *Structural and Multidisciplinary Optimization*, Jan. 2019. DOI: [10.1007/s00158-019-02196-9](https://doi.org/10.1007/s00158-019-02196-9).
- [26] T. Yamada, K. Izui, and S. Nishiwaki, “A level set-based topology optimization method for maximizing thermal diffusivity in problems including design-dependent effects,” *Journal of Mechanical Design*, vol. 133, no. 3, p. 031011, 2011. DOI: [10.1115/1.4003684](https://doi.org/10.1115/1.4003684).
- [27] T. Yamada, K. Izui, S. Nishiwaki, and A. Takezawa, “A topology optimization method based on the level set method incorporating a fictitious interface energy,” *Computer Methods in Applied Mechanics and Engineering*, vol. 199, no. 45-48, pp. 2876–2891, 2010. DOI: [10.1016/j.cma.2010.05.013](https://doi.org/10.1016/j.cma.2010.05.013).
- [28] Y. Zhang and S. Liu, “The optimization model of the heat conduction structure,” *Progress in Natural Science*, vol. 18, no. 6, pp. 665–670, Jun. 2008. DOI: [10.1016/j.pnsc.2008.01.010](https://doi.org/10.1016/j.pnsc.2008.01.010).
- [29] C. Zhuang and Z. Xiong, “Temperature-constrained topology optimization of transient heat conduction problems,” *Numerical Heat Transfer, Part B: Fundamentals*, vol. 68, no. 4, pp. 366–385, Jun. 2015. DOI: [10.1080/10407790.2015.1033306](https://doi.org/10.1080/10407790.2015.1033306).
- [30] C. Zhuang, Z. Xiong, and H. Ding, “A level set method for topology optimization of heat conduction problem under multiple load cases,” *Computer Methods in Applied Mechanics and Engineering*, vol. 196, no. 4-6, pp. 1074–1084, Jan. 2007. DOI: [10.1016/j.cma.2006.08.005](https://doi.org/10.1016/j.cma.2006.08.005).
- [31] C. Zhuang, Z. Xiong, and H. Ding, “Topology optimization of multi-material for the heat conduction problem based on the level set method,” *Engineering Optimization*, vol. 42, no. 9, pp. 811–831, Jun. 2010. DOI: [10.1080/03052150903443780](https://doi.org/10.1080/03052150903443780).

Article C

Topology Optimization using the UNsmooth VARIational Topology OPTimization (UNVARTOP) method: an educational implementation in Matlab



Educational Paper | Published: 03 November 2020

Topology optimization using the unsmooth variational topology optimization (UNVARTOP) method: an educational implementation in MATLAB

Daniel Yago, Juan Cante, Oriol Lloberas-Valls & Javier Oliver

Structural and Multidisciplinary Optimization **63**, 955–981 (2021) | [Cite this article](#)

876 Accesses | 3 Citations | 1 Altmetric | [Metrics](#)

Abstract

This paper presents an efficient and comprehensive MATLAB code to solve two-dimensional structural topology optimization problems, including minimum mean compliance, compliant mechanism synthesis, and multi-load compliance problems. The unsmooth variational topology optimization (UNVARTOP) method, developed by Oliver et al. (*Comput Methods Appl Mech Eng* 355:779–819, [2019](#)), is used in the topology optimization code, based on the finite element method (FEM), to compute the sensitivity and update the topology. The paper also includes instructions to improve the *bisection algorithm*, modify the computation of the Lagrangian multiplier by using an Augmented Lagrangian to impose the constraint, implement heat conduction problems, and extend the code to three-dimensional topology optimization problems. The code, intended for students and newcomers in topology optimization, is included as an appendix (Appendix [A](#)) and it can be downloaded from <https://github.com/DanielYago/UNVARTOP> together with supplementary material.

Topology Optimization using the UNsmooth VARIational Topology OPTimization (UNVARTOP) method: an educational implementation in Matlab

D. Yago^{a,b}, J. Cante^{a,b}, O. Lloberas-Valls^{b,c}, J. Oliver^{b,c}

^a Escola Superior d'Enginyeries Industrial, Aeroespacial i Audiovisual de Terrassa (ES-EIAAT), Universitat Politècnica de Catalunya · BarcelonaTech (UPC), Campus Terrassa UPC, c/ Colom 11, 08222 Terrassa, Spain

^b Centre Internacional de Mètodes Numèrics en Enginyeria (CIMNE), Campus Nord UPC, Mòdul C-1 101, c/ Jordi Girona 1-3, 08034 Barcelona, Spain

^c Escola Tècnica Superior d'Enginyeria de Camins, Canals i Ports de Barcelona (ETSEC-CPB), Universitat Politècnica de Catalunya · BarcelonaTech (UPC), Campus Nord UPC, Mòdul C-1, c/ Jordi Girona 1-3, 08034 Barcelona, Spain

C.1 Abstract

This paper presents an efficient and comprehensive MATLAB code to solve two-dimensional structural topology optimization problems, including minimum mean compliance, compliant mechanism synthesis and multi-load compliance problems. The Unsmooth Variational Topology Optimization (UNVARTOP) method, developed by Oliver *et al.* [22], is used in the topology optimization code, based on the finite element method (FEM), to compute the sensitivity and update the topology. The paper also includes instructions to improve the *bisection algorithm*, modify the computation of the Lagrangian multiplier by using an Augmented Lagrangian to impose the constraint, implement heat conduction problems and extend the code to three-dimensional topology optimization problems. The code, intended for students and newcomers in topology optimization, is included as an appendix (Appendix C.A) and it can be downloaded from <https://github.com/DanielYago/UNVARTOP> together with supplementary material.

Keywords: Structural Topology optimization, Relaxed Topological Derivative, Compliance, Compliant Mechanism, Education, MATLAB code

C.2 Introduction

The dissemination of the Matlab code, included in this paper, is intended for education purposes, in order to provide students and those new to the field with the theoretical basis for topology optimization of structural problems as well as to familiarize a wider audience with the new technique. This article is inspired by similar ones (e.g. [27] and [5]) which presented a Matlab implementation and possible extensions of other topology optimization approaches for structural problems.

A wide variety of topology optimization approaches and the corresponding Matlab implementations can be found in the literature, including the *Solid Isotropic Material with Penalization* (SIMP) method ([6, 7] and [27]), the *Bidirectional Evolutionary Structural Optimization* (BESO) method ([39, 42] and [45]), the *Level-set* method using a shape derivative ([2, 3, 34] and [10, 35]), the parameterized Level-set method using Radial basis functions ([37, 36] and [38]), the *Topology Derivative* method ([29, 21] and [30]) and the *Phase-field* approaches ([31, 34, 41] and [24]), among others. Along years, researchers have adapted or combined some features of these techniques to propose alternative approaches. Nevertheless, some limitations remain in any of them.

The *Unsmooth Variational Topology Optimization* approach, first developed by Oliver *et al.* [22], appears to be an alternative to other well-established approaches due to the mathematical simplicity and robustness of the present method. So far, the UNVARTOP approach has been

applied in a wide range of linear applications, including static structural [22] and steady-state thermal applications [40], considering the volume constraint as a single constraint equation, with promising results, essentially in terms of computational cost.

The domain, in the present approach, is implicitly represented through a 0-level-set function [23], using the so-called *discrimination function* ψ , to define a discrete *characteristic function*, χ , at each point of the domain, \mathbf{x} . This variable, used as design variable, is related to the *discrimination function* with the Heaviside function by $\chi(\mathbf{x}) = \mathcal{H}(\psi(\mathbf{x}))$, defining, thus, a *black-and-white design*, i.e. a binary configuration with two domains: a void and a material domain. This definition is in contrast to that used by density-based methods, such as SIMP method, where the relative density, ρ_e , in each element is used as design variable see Bendsøe and Sigmund [7]. In addition, this change in the design variable, typically from *Level-set methods*, allows smooth representation of the topology (void and material domains) and the corresponding boundary using the 0-level iso-surface of the *discrimination function*.

The *black-and-white design* is relaxed via the *ersatz material approach* to a bi-material setting, where the void material is replaced with a soft material, as proposed by Allaire *et al.* [1]. Despite this relaxation, the discrete nature of the *characteristic function* is maintained. However, this is not true for density-based methods¹, which have to be relaxed via a power-law interpolation function to intermediate values (i.e. between void and solid), leading thus to the SIMP method, in order to avoid the ill-conditioning of the topology optimization problem obtaining then blurry interfaces with semi-dense elements, as stated in Sigmund and Petersson [28].

The aim of a topology optimization must be defined by means of a cost function, which will be minimized. For each specific cost function, a sensitivity evaluating the variation of it to topological perturbations must be derived. This derivation may be mathematically challenging for some topology optimization approaches. For example, the *Topology Derivative* method requires heavy analytical derivation methods, dependent on the type of the topology optimization problem and the considered material in the optimization [14, 21]. However, in the current method, a consistent *relaxed topological derivative* is formulated within the *ersatz material approach*, and evaluated as a directional derivative of the cost function. Additionally, it can be interpreted as an approximation of the exact topological derivative, used in *Topology Derivative* method, resulting in a simpler and less time-consuming derivation.

Apart from the problem setting and the cost function, the procedure of updating the design variable is a crucial feature of each approach. Most of the topology optimization methods, that use a *level-set* function to define the topology layout at each iteration, update the design variable via a Hamilton-Jacobi equation using an appropriate velocity at boundaries (in terms of the precomputed sensitivity) [2, 34]. Despite using an equivalent level-set function (*discrimination function*), the topology is not updated neither via a Hamilton-Jacobi [36, 3, 41] nor a Reaction-Diffusion [24] equations, but it is updated via the solution of a *fixed-point, non-linear, closed-form algebraic system*. The fulfillment of the volume constraint is ensured within the closed-form solution by means of a *Lagrange multiplier*, similar to the one used with Optimality Criteria (OC) in SIMP methods, computed through an efficient bisection algorithm.

Almost every technique require some kind of filtering in order to avoid or at least mitigate the inherent ill-posedness of the topology optimization problem [28]. Through this filtering, the lack of mesh-independency is overcome. Density-based methods resort to density or sensitivity filtering, extensively used in density-based approaches. Nevertheless, alternative filters have been formulated in the last two decades. For instance, projection methods [15] or a Helmholtz filter [16] are also used for this purpose. This last filter, so called the *Laplacian regularization* [25, 33] is applied to the *discrimination function* to control the filament width. A similar approach is used by Yamada *et al.* [41] to control the complexity of the optimal design.

Finally, the last key feature is related with the volume constraint and how the requested

¹The density-based methods appear also in literature as Variable Density Methods and they should be understood as synonyms throughout the text.

volume percentage is achieved. An incremental time-advancing scheme is adopted in the present methodology for the volume percentage, as a control parameter, obtaining, then, intermediate converged, optimal topologies. The optimization procedure starts from a domain fully filled with stiff material. Then, the topology optimization for a given small volume percentage is performed, obtaining a converged, optimal topology. Subsequently, the volume percentage (*pseudo-time* in the algorithm) is increased and the new optimal topology is found. This procedure is repeated until the desired volume fraction is achieved, similar to the Pareto frontier-optimal tracing approach proposed by Suresh [30]. Although this implementation is not unique of the current approach, it differs from SIMP and Level-set based methods, since they directly seek the optimal topology for the requested volume fraction. Similar iterative schemes can be found in ESO/BESO approaches, where the volume fraction is incremented at each iteration until the final volume is achieved. However, optimal conditions are not fulfilled at these intermediate volumes.

Thanks to this set of features, the methodology proposed in this manuscript presents a lower computational cost, around 5 times, when it is compared with other methods, e.g. a Level-set method with the RTD, while obtaining very similar results, as reported in Oliver *et al.* [22] and Yago *et al.* [40]. In addition, intermediate converged optimal topologies are obtained for different volume values at no additional computational cost, allowing further decisions once the topology optimization optimization has finalized.

The remainder of the paper is organized as follows. The unsmooth variational topology optimization approach is briefly described in section C.3 along with the particularities for minimum mean compliance, multi-load compliance and compliant mechanisms problems. In section C.4, the code implementation of the present methodology, provided in Appendix C.A, is discussed in detail. Several numerical examples are addressed in section C.5 to show the potential in the three optimization problems. Additionally, in section C.6, possible extensions and enhancements of the code are discussed. Finally, section C.7 concludes with some final remarks.

C.3 Problem formulation

C.3.1 Unsmooth variational topology optimization

Let us define a fixed rectangular design domain, $\Omega \subset \mathbb{R}^2$, composed by two smooth subdomains, Ω^+ and Ω^- , as depicted in Figure C.1. These two domains, made respectively of solid and void materials, are defined via the nonsmooth *characteristic function*, $\chi(\mathbf{x}) : \Omega \rightarrow \{0, 1\}$, as

$$\begin{cases} \Omega^+ := \{\mathbf{x} \in \Omega / \chi(\mathbf{x}) = 1\} \\ \Omega^- := \{\mathbf{x} \in \Omega / \chi(\mathbf{x}) = 0\} \end{cases} . \quad (1)$$

The topology layout can also be implicitly represented by the smooth *discrimination function*, $\psi(\mathbf{x}) : \Omega \rightarrow \mathbb{R}$, $\psi \in H^1(\Omega)$, (see Figure C.2) defined as

$$\begin{cases} \Omega^+ := \{\mathbf{x} \in \Omega / \psi(\mathbf{x}) > 0\} \\ \Omega^- := \{\mathbf{x} \in \Omega / \psi(\mathbf{x}) < 0\} \end{cases} . \quad (2)$$

In addition, the *characteristic function*, $\chi_\psi(\mathbf{x}) : \Omega \rightarrow \{0, 1\}$, can be expressed in terms of the *discrimination function* by

$$\chi_\psi(\mathbf{x}) = \mathcal{H}(\psi(\mathbf{x})), \quad (3)$$

where $\mathcal{H}(\cdot)$ stands for the Heaviside function evaluated at (\cdot) . The *characteristic function*, used as the design variable, is now relaxed to $\chi_\psi(\mathbf{x}) : \Omega \rightarrow \{\beta, 1\}$, where the void material is replaced with a soft material with low stiffness (ersatz material approach), with β being the *relaxation factor*.

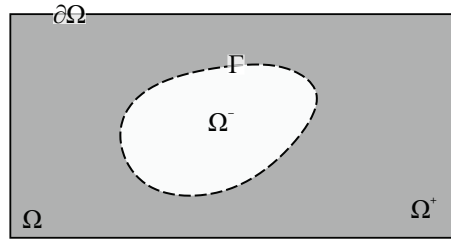


Figure C.1: Representation of the fixed design domain Ω .

The topology optimization goal is to minimize a cost function $\mathcal{J}(\chi)$ subjected to one constraint, typically the volume, and governed by the state equations. The classic mathematical formulation of the corresponding topology optimization problem can be expressed as

$$\left[\begin{array}{l} \min_{\chi \in \mathcal{U}_{ad}} \quad \mathcal{J}(\chi) \equiv \int_{\Omega} j(\chi, \mathbf{x}) d\Omega \\ \text{subject to:} \\ \quad \mathcal{C}(\chi) \equiv \int_{\Omega} c(\chi, \mathbf{x}) d\Omega = 0 \\ \text{governed by:} \\ \quad \text{Equilibrium equation} \end{array} \right. \quad \begin{array}{l} (a) \\ \\ (b) \text{ , } (4) \\ (c) \end{array}$$

where \mathcal{U}_{ad} stands for the set of admissible solutions for χ and $\mathcal{C}(\chi)$ represents the constraint functional (e.g. the volume constraint).

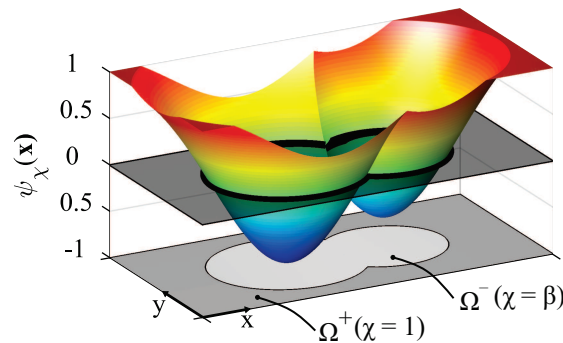


Figure C.2: Topology representation in terms of the *discrimination function*, ψ .

Following Oliver *et al.* [22], the *Relaxed Topological Derivative* (RTD), specific characteristic of the proposed approach, evaluated as

$$\frac{\delta \mathcal{J}(\chi)}{\delta \chi}(\hat{\mathbf{x}}) = \left[\frac{\partial j(\chi, \mathbf{x})}{\partial \chi} \right]_{\mathbf{x}=\hat{\mathbf{x}}} \Delta \chi(\hat{\mathbf{x}}), \quad (5)$$

measures the sensitivity of the functional (4)-a, in terms of the classical Fréchet derivative $\frac{\partial(\cdot)}{\partial \chi}(\hat{\mathbf{x}})$ of the integral kernel, when a material exchange is made at point $\hat{\mathbf{x}}$. The term $\Delta \chi(\hat{\mathbf{x}})$, denoted as the *exchange function*, corresponds to the signed variation of $\chi(\hat{\mathbf{x}})$, due to that material exchange, i.e.

$$\Delta \chi(\hat{\mathbf{x}}) = \begin{cases} -(1 - \beta) < 0 & \text{for } \hat{\mathbf{x}} \in \Omega^+ \\ (1 - \beta) > 0 & \text{for } \hat{\mathbf{x}} \in \Omega^- \end{cases} . \quad (6)$$

Notice that the RTD of equation (5) will depend on each specific cost function, as detailed in sections C.3.5 to C.3.7. Mimicking equation (5), the RTD of the volume constraint ((4)-b) is computed as

$$\frac{\delta \mathcal{C}(\chi, t)}{\delta \chi}(\hat{\mathbf{x}}) = \left[\frac{\partial c(\chi, \mathbf{x})}{\partial \chi} \right]_{\mathbf{x}=\hat{\mathbf{x}}} \Delta \chi(\hat{\mathbf{x}}) = \frac{1}{|\Omega|} \text{sgn}(\Delta \chi(\hat{\mathbf{x}})), \quad (7)$$

where $\mathcal{C}(\chi, t) := t - \frac{|\Omega^-(\chi)|}{|\Omega|} = 0$ and $|\Omega^-(\chi)| = \int_{\Omega} \frac{1-\chi}{1-\beta} d\Omega$. Additionally, the $\text{sgn}(\cdot)$ corresponds to the sign function of (\cdot) , while the term $t \in [0, T]$ corresponds to the *pseudo-time* parameter, given by the user, used in the *pseudo-time-advancing strategy*. Notice that the parameter T stands for the *pseudo-time* corresponding to the final volume.

The *Lagrangian function* of the optimization problem (4) can be commonly expressed as

$$\mathcal{L}(\chi) = \mathcal{J}(\chi) + \lambda \mathcal{C}(\chi, t), \quad (8)$$

where the *constraint equation*, \mathcal{C} , multiplied with a Lagrange multiplier, λ , is added to the original cost function \mathcal{J} . The value of λ is such that the volume constraint is fulfilled.

Finally, applying the RTD to equation (8) and considering equations (5) and (7), the optimality condition of the *original topology optimization problem* can be written as

$$\begin{aligned} \frac{\delta \mathcal{L}(\chi, \lambda)}{\delta \chi}(\hat{\mathbf{x}}) &= \left(\frac{\partial j(\chi, \hat{\mathbf{x}})}{\partial \chi} \Delta \chi(\hat{\mathbf{x}}) + \lambda \text{sgn}(\Delta \chi(\hat{\mathbf{x}})) \right) = \\ &= \psi(\hat{\mathbf{x}}, \chi) = \xi(\hat{\mathbf{x}}, \chi) - \lambda \quad \forall \hat{\mathbf{x}} \in \Omega, \end{aligned} \quad (9)$$

where $\psi(\hat{\mathbf{x}}, \chi)$ corresponds to the *discrimination function* and $\xi(\hat{\mathbf{x}}, \chi)$ is termed the *pseudo-energy* and must be computed for each optimization problem, thus obtaining a similar updating expression to other topology optimization techniques². Compared to other techniques, the *pseudo-energy* is first shifted³ and normalized, yielding to the *modified energy density* defined as

$$\hat{\xi}(\hat{\mathbf{x}}) = \frac{\xi(\hat{\mathbf{x}}) - \chi(\hat{\mathbf{x}}) \Delta_{shift}}{\Delta_{norm}}, \quad (10)$$

where Δ_{shift} and Δ_{norm} correspond to the shifting and normalization parameters defined at the first iteration as $\min(\xi_0, 0)$ and $\max(\text{range}(\xi_0), \max(\xi_0))$, respectively. The resultant ψ , after replacing equation (10) into (9), is subsequently smoothed through a *Laplacian regularization*, in contrast to other distance-based filters used in methods such as SIMP or ESO, in order to mitigate mesh-dependency along with controlling the minimum filament's size. The *smooth discrimination function*, ψ_{τ} , corresponds to the solution of

$$\begin{cases} \psi_{\tau} - (\tau h_e)^2 \Delta_{\mathbf{x}} \psi_{\tau} = \psi & \text{in } \Omega \\ \nabla_{\mathbf{x}} \psi_{\tau} \cdot \mathbf{n} = 0 & \text{on } \partial \Omega \end{cases}, \quad (11)$$

where, $\Delta_{\mathbf{x}}(\mathbf{x}, \cdot)$ and $\nabla_{\mathbf{x}}(\mathbf{x}, \cdot)$ are respectively the Laplacian and gradient operators, and \mathbf{n} is the outwards normal to the boundary of the design domain, $\partial \Omega$. τ and h_e stand for the dimensionless *regularization parameter* and the typical size of the finite element mesh, respectively.

The topology layout, χ , is updated by means of the *Cutting&Bisection* algorithm⁴, in which the value of λ , which enforces volume constraint (equation (4)-b), is computed. Then, a *closed-*

²Note that, since $|\Omega|$ is constant, it can be included in the Lagrange multiplier, λ , in the second term of the equation (9).

³The shifting is applied in order to obtain positive *pseudo-energy*, ξ , in Ω at $t = 0$, thus, ensuring a converged topology for this time-step.

⁴The present *Cutting&Bisection* algorithm has been so far applied to single constrained topology optimization problems subject to equality, pseudo-time evolving volume constraints. Further development is required to extend it to other constraints.

form solution of the topology optimization problem (4) can be written as

$$\begin{cases} \psi(\hat{\mathbf{x}}) := \hat{\xi}(\hat{\mathbf{x}}, \chi) - \lambda \\ \chi(\hat{\mathbf{x}}) = \mathcal{H}(\psi_\tau(\hat{\mathbf{x}})) & \text{in } \Omega, \\ \mathcal{C}(\chi(\lambda), t) = 0 \end{cases} \quad (12)$$

where $\psi_\tau(\hat{\mathbf{x}})$ corresponds to the solution of equation (11) that must be applied at each iteration. Equation (12) constitutes a fundamental feature of the UNVARTOP method, as aforementioned in section C.2. Nonetheless, the *Laplacian regularization* only affects the *modified energy density*, $\hat{\xi}(\hat{\mathbf{x}}, \chi)$, since the term λ is constant, thus leading equation (12) to

$$\begin{cases} \psi_\tau(\hat{\mathbf{x}}) := \hat{\xi}_\tau(\hat{\mathbf{x}}, \chi) - \lambda \\ \chi(\hat{\mathbf{x}}) = \mathcal{H}(\psi_\tau(\hat{\mathbf{x}})) & \text{in } \Omega, \\ \mathcal{C}(\chi(\lambda), t) = 0 \end{cases} \quad (13)$$

where $\hat{\xi}_\tau$ is the solution of equation (11) for the *modified energy density*. Due to this modification, the computational cost of the bisection algorithm is significantly reduced.

For more details on the formulation, the reader is referred to Oliver *et al.* [22] and Yago *et al.* [40], where in-depth discussions are made on each subject.

C.3.2 State problem

The governing variational problem for linear elasticity, in terms of the displacement field (\mathbf{u}_χ) and the virtual displacement field (\mathbf{w}), can be written as

$$\left[\begin{array}{l} \text{Find the displacement field } \mathbf{u}_\chi \in \mathcal{U}(\Omega) \text{ such that} \\ a(\mathbf{w}, \mathbf{u}_\chi) = l(\mathbf{w}) \quad \forall \mathbf{w} \in \mathcal{V}(\Omega) \end{array} \right. \quad (14)$$

where

$$a(\mathbf{w}, \mathbf{u}_\chi) = \int_{\Omega} \nabla^S \mathbf{w}(\mathbf{x}) : \mathbb{C}_\chi(\mathbf{x}) : \nabla^S \mathbf{u}_\chi(\mathbf{x}) \, d\Omega, \quad (15)$$

$$l(\mathbf{w}) = \int_{\partial_\sigma \Omega} \mathbf{w}(\mathbf{x}) \cdot \bar{\boldsymbol{\sigma}}(\mathbf{x}) \, d\Gamma + \int_{\Omega} \mathbf{w}(\mathbf{x}) \cdot \mathbf{b}_\chi(\mathbf{x}) \, d\Omega, \quad (16)$$

where \mathbb{C}_χ and \mathbf{b}_χ correspond to the fourth order elastic constitutive tensor and the volumetric force, respectively. In addition, $\bar{\boldsymbol{\sigma}}(\mathbf{x})$ stands for the boundary tractions applied on $\partial_\sigma \Omega \subset \partial\Omega$, while the term $\nabla^S(\cdot)$ corresponds to the symmetrical gradient of (\cdot) . Finally, the set of admissible displacement fields, $\mathcal{U}(\Omega)$, is defined as $\mathcal{U}(\Omega) := \{\mathbf{u}(\mathbf{x}) / \mathbf{u} \in H^1(\Omega), \mathbf{u} = \bar{\mathbf{u}} \text{ on } \partial_u \Omega\}$, while the space of admissible virtual displacement fields is given by $\mathcal{V}(\Omega) := \{\mathbf{w}(\mathbf{x}) / \mathbf{w} \in H^1(\Omega), \mathbf{w} = 0 \text{ on } \partial_u \Omega\}$.

As in any other topology optimization approach, the constitutive tensor⁵, \mathbb{C}_χ , and the volumetric force, \mathbf{b}_χ , depend on the topology. Thus, they are mathematically defined in terms of the *characteristic function* as follows

$$\begin{cases} \mathbb{C}_\chi(\mathbf{x}) = \chi_k^{m_k}(\mathbf{x}) \bar{\mathbb{C}}(\mathbf{x}); & m_k > 1 \\ \mathbf{b}_\chi(\mathbf{x}) = \chi_b^{m_b}(\mathbf{x}) \bar{\mathbf{b}}(\mathbf{x}); & m_b > 1 \end{cases} \quad (17)$$

$$\quad (18)$$

where $m_{(\cdot)}$ stands for the *exponential factor* of property (\cdot) . The lower limit of the *relaxed characteristic function*, χ_β , is defined through the *contrast factor*, $\alpha_{(\cdot)}$, and $m_{(\cdot)}$ by $\beta_{(\cdot)} = \alpha_{(\cdot)}^{1/m_{(\cdot)}}$. Both $\bar{\mathbb{C}}$ and $\bar{\mathbf{b}}$ denote the corresponding nominal property of the stiff material.

⁵The constitutive tensor is governed by Hooke's law, i.e. $\boldsymbol{\sigma} = \mathbb{C}\boldsymbol{\varepsilon}$, with $\boldsymbol{\varepsilon}$ being the strain tensor ($\boldsymbol{\varepsilon} = \nabla^S u_\chi(\mathbf{x})$).

Assuming plane-stress condition, the constitutive tensor $\bar{\mathbb{C}}$ is given by

$$\bar{\mathbb{C}}^{Pstress} = \frac{E}{1-\nu^2} \begin{bmatrix} 1 & \nu & 0 \\ \nu & 1 & 0 \\ 0 & 0 & \frac{1-\nu}{2} \end{bmatrix}, \quad (19)$$

with E representing the Young's modulus of the *stiff material* and ν , the Poisson's ratio of the isotropic material.

C.3.3 Finite element discretization

The state equation (14) is now discretized using the standard finite element method [44, 26]. The displacement field and its gradient are approximated as follows

$$\mathbf{u}_\chi(\mathbf{x}) \equiv \mathbf{N}_u(\mathbf{x}) \hat{\mathbf{u}}_\chi \quad (20)$$

$$\nabla^S u_\chi(\mathbf{x}) \equiv \mathbf{B}(\mathbf{x}) \hat{\mathbf{u}}_\chi \quad (21)$$

where $\mathbf{N}_u(\mathbf{x})$ and $\mathbf{B}(\mathbf{x})$ stand for the displacement, shape function matrix and the strain-displacement matrix, respectively, and $\hat{\mathbf{u}}_\chi$ corresponds to the nodal displacement vector.

Introducing equations (17)-(18) and (20)-(21) into equations (14)-(16), the resultant state equation reads

$$\mathbb{K}_\chi \hat{\mathbf{u}}_\chi = \mathbf{f} \quad (22)$$

with

$$\left\{ \begin{array}{l} \mathbb{K}_\chi = \int_{\Omega} \mathbf{B}^T(\mathbf{x}) \mathbb{C}_\chi(\mathbf{x}) \mathbf{B}(\mathbf{x}) d\Omega \\ \mathbf{f} = \int_{\partial\sigma\Omega} \mathbf{N}_u^T(\mathbf{x}) \bar{\boldsymbol{\sigma}}(\mathbf{x}) d\Gamma + \int_{\Omega} \mathbf{N}_u^T(\mathbf{x}) \mathbf{b}_\chi(\mathbf{x}) d\Omega \end{array} \right., \quad (23)$$

where \mathbb{K}_χ and \mathbf{f} stand for the stiffness matrix and the external forces vector, respectively. The element stiffness matrix and the volumetric term of the force vector are numerically integrated inside each element, Ω_e , employing several quadrature points. Subsequently, these terms are assembled to obtain the global stiffness matrix and force vector.

C.3.4 Algorithm

The flowchart of the algorithm used to obtain the optimal topology layouts in terms of the *characteristic function*, χ , is illustrated in Figure C.3.

The algorithm is based on a two-steps procedure: 1) data initialization and FE analysis pre-processing, e.g. mesh generation, creation of figures, computation of element FE matrices, assembly of Laplacian regularization matrix, along others, and 2) a topology optimization loop over time-steps. For each step, the state equation (22) is solved to obtain the displacement vector, and the corresponding sensitivities are computed (equations (5) and (7)), obtaining then the *pseudo-energy*, ξ , dependent on each topology optimization problem defined in subsequent sections, and the corresponding *modified energy density*, $\hat{\xi}$ (equation (10)). The cost function is then computed via equation (4)-a using the previously computed displacement vector. Then, the *Laplacian regularization* is applied to $\hat{\xi}$ (equation (11)) while the Lagrange multiplier is obtained by means of a *bisection algorithm* (equation (13)), thus obtaining the new optimal topology (in terms of the *discrimination function* ψ and the corresponding *characteristic function* χ). If tolerances are fulfilled⁶, the topology is considered as converged and then the *pseudo-time*, t , is increased. Otherwise, an iteration is carried out with the new topology.

⁶The L2-norm of the *characteristic function* and the L ∞ -norm of the Lagrange multiplier are checked.

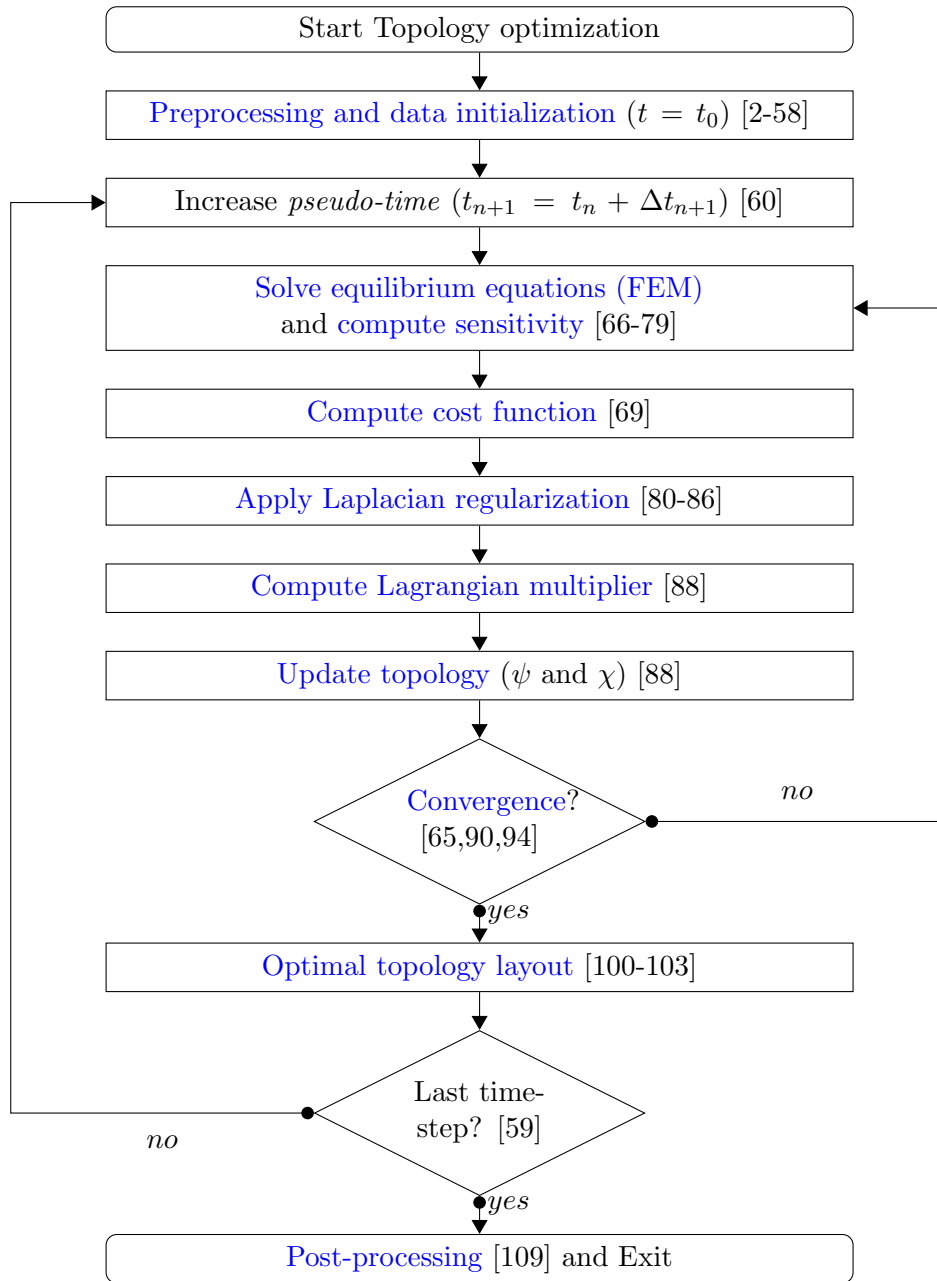


Figure C.3: The flowchart for the unsmooth variational topology optimization algorithm with the corresponding code lines in brackets.

C.3.5 Mean compliance

The main goal of the minimum mean compliance problems is to seek the *optimal topology layout*, in terms of the *characteristic function*, χ , that maximizes the global stiffness of the structure given specific boundary conditions. That is, the external work produced by applied forces is minimized. The objective function is written as

$$\mathcal{J}(\mathbf{u}_\chi) \equiv l(\mathbf{u}_\chi) \equiv a_\chi(\mathbf{u}_\chi, \mathbf{u}_\chi) \equiv 2 \int_{\Omega} \frac{1}{2} \nabla^S \mathbf{u}_\chi : \mathbb{C}_\chi : \nabla^S \mathbf{u}_\chi d\Omega = 2 \int_{\Omega} \mathcal{U}_\chi d\Omega, \quad (24)$$

where \mathcal{U}_χ can be identified as the *actual strain energy density* ($\mathcal{U}_\chi = \frac{1}{2} \nabla^S \mathbf{u}_\chi : \mathbb{C}_\chi : \nabla^S \mathbf{u}_\chi$), and $a_\chi(\mathbf{u}_\chi, \mathbf{u}_\chi)$ and $l(\mathbf{u}_\chi)$ are the bilinear forms of the elastic problem (14) for $\mathbf{w} = \mathbf{u}_\chi$.

Considering equations (22) and (24), the corresponding finite element discretization coun-

terpart of problem (4) reads

$$\left[\begin{array}{l} \min_{\chi \in \mathcal{U}_{ad}} \mathcal{J}^{(he)}(\mathbf{u}_\chi(t)) \equiv \mathbf{f}^T \hat{\mathbf{u}}_\chi(t) \\ \text{subject to:} \\ \mathcal{C}(\chi, t) := t - \frac{|\Omega^-(\chi)|}{|\Omega|} = 0; \quad t \in [0, 1] \\ \text{governed by:} \\ \mathbb{K}_\chi \hat{\mathbf{u}}_\chi = \mathbf{f} \end{array} \right. \quad \begin{array}{l} (a) \\ \\ (b) \\ \\ (c) \end{array} \quad (25)$$

where $\mathbf{f}^T \hat{\mathbf{u}}_\chi$ denotes the structural compliance.

According to Oliver *et al.* [22], the *relaxed topological derivative* with respect to $\chi(\mathbf{x})$, using the adjoint method⁷, is defined as

$$\frac{\delta \bar{\mathcal{J}}^{(he)}(\chi)}{\delta \chi}(\hat{\mathbf{x}}) = \left[2 \frac{\delta \mathbf{f}^T}{\delta \chi}(\mathbf{x}) \hat{\mathbf{u}}_\chi - \hat{\mathbf{u}}_\chi^T \frac{\delta \mathbb{K}_\chi}{\delta \chi}(\mathbf{x}) \hat{\mathbf{u}}_\chi \right]_{\mathbf{x}=\hat{\mathbf{x}}} . \quad (26)$$

Assuming that no volumetric forces are applied on the domain and substituting the definition of the relaxed topological derivative of each term (5), equation (26) can be expressed as

$$\frac{\delta \bar{\mathcal{J}}^{(he)}(\mathbf{u}_\chi)}{\delta \chi}(\hat{\mathbf{x}}) = -2m_k (\chi_k(\hat{\mathbf{x}}))^{m_k-1} \bar{\mathcal{U}}(\hat{\mathbf{x}}) \Delta \chi_k(\hat{\mathbf{x}}), \quad (27)$$

where the *nominal energy density*, $\bar{\mathcal{U}}(\hat{\mathbf{x}})$, is given by

$$\bar{\mathcal{U}}(\hat{\mathbf{x}}) = \frac{1}{2} (\nabla^S \mathbf{u}_\chi : \bar{\mathbb{C}} : \nabla^S \mathbf{u}_\chi)(\hat{\mathbf{x}}) \geq 0. \quad (28)$$

Finally, comparing equation (27) with equation (9), the *pseudo-energy*, $\xi(\hat{\mathbf{x}}, \chi)$, of topology problem (25) reads

$$\xi(\hat{\mathbf{x}}, \chi) = 2m_k (\chi_k(\hat{\mathbf{x}}))^{m_k-1} \bar{\mathcal{U}}(\hat{\mathbf{x}}) (1 - \beta(\hat{\mathbf{x}})), \quad (29)$$

which must be then modified as detailed in equation (10). Discretizing the terms in equation (29), and after some mathematical manipulations, it can be numerically computed as

$$\xi(\hat{\mathbf{x}}, \chi) = \gamma_1 \hat{\mathbf{u}}(\hat{\mathbf{x}})^T \left[\mathbf{B}(\hat{\mathbf{x}})^T \bar{\mathbb{C}} \mathbf{B}(\hat{\mathbf{x}}) \right] \hat{\mathbf{u}}(\hat{\mathbf{x}}), \quad (30)$$

with $\gamma_1 = 2m_k (\chi_k(\hat{\mathbf{x}}))^{m_k-1} (1 - \beta(\hat{\mathbf{x}}))$.

C.3.6 Multi-load mean compliance

Multi-load compliance problems are considered a specific case of minimum compliance problems (see section C.3.5), in which a set of elastic problems with different loading conditions are solved independently. The objective function (24) is replaced with the weighted average sum of all the cases, i.e.

$$\mathcal{J}(\mathbf{u}_\chi) \equiv \sum_{i=1}^{n_l} l(\mathbf{u}_\chi^{(i)}) \equiv \sum_{i=1}^{n_l} \int_{\Omega} \nabla^S \mathbf{u}_\chi^{(i)} : \mathbb{C}_\chi : \nabla^S \mathbf{u}_\chi^{(i)} d\Omega = \sum_{i=1}^{n_l} 2 \int_{\Omega} \mathcal{U}_\chi^{(i)} d\Omega, \quad (31)$$

⁷The adjoint method is used to avoid explicitly compute the sensitivities of the displacements. The minimum mean compliance problem is self-adjoint.

where n_l stands for the number of loading states and $\mathcal{U}_\chi^{(i)}$ corresponds to the *actual energy density* of the i -th loading state. Then, according to this new definition, equation (25) is rewritten as

$$\left[\begin{array}{l} \min_{\chi \in \mathcal{U}_{ad}} \mathcal{J}^{(h_e)}(\mathbf{u}_\chi(t)) \equiv \sum_{i=1}^{n_l} \mathbf{f}^{(i)\text{T}} \hat{\mathbf{u}}_\chi^{(i)}(t) \\ \text{subject to:} \\ \mathcal{C}(\chi, t) := t - \frac{|\Omega^-|(\chi)}{|\Omega|} = 0; \quad t \in [0, 1] \\ \text{governed by:} \\ \mathbb{K}_\chi \hat{\mathbf{u}}_\chi^{(i)} = \mathbf{f}^{(i)} \quad \forall i \in [1, n_l] \end{array} \right. \quad \begin{array}{l} (a) \\ \\ (b) \\ \\ (c) \end{array} \quad (32)$$

Equations (26) to (29) are consequently modified to account multiple loading cases, leading to

$$\xi(\hat{\mathbf{x}}, \chi) = \gamma_1 \sum_{i=1}^{n_l} \hat{\mathbf{u}}^{(i)}(\hat{\mathbf{x}})^{\text{T}} \left[\mathbf{B}(\hat{\mathbf{x}})^{\text{T}} \bar{\mathbf{C}} \mathbf{B}(\hat{\mathbf{x}}) \right] \hat{\mathbf{u}}^{(i)}(\hat{\mathbf{x}}). \quad (33)$$

Bear in mind that the optimal topology layout will considerably differ from the single minimum compliance problem with all the loads applied at the same time. Multi-load optimization problems are employed to find a trade-off between optimal topologies for each loading state.

C.3.7 Compliant mechanisms

Compliant mechanisms are flexible structures that transfer an action (force or displacement) at the *input port* to the *output port*, obtaining a desired force or displacement at that port. The objective function, \mathcal{J} , can be expressed in terms of the displacement at the output port, when maximum displacement is sought, as

$$\mathcal{J}(\mathbf{u}_\chi) \equiv \mathbf{1}^{\text{T}} \hat{\mathbf{u}}_\chi, \quad (34)$$

where $\mathbf{1}$ represents a dummy constant force vector applied only on the *output port* at the desired direction. Additional springs, denoted by K_{in} and K_{out} , must be considered in the *input* and *output ports*, respectively.

In the context of finite element discretization, like in equation (25), the *topology optimization problem* (4) can be expressed as

$$\left[\begin{array}{l} \min_{\chi \in \mathcal{U}_{ad}} \mathcal{J}^{(h_e)}(\mathbf{u}_\chi(t)) \equiv -\mathbf{1}^{\text{T}} \hat{\mathbf{u}}_\chi(t) \\ \text{subject to:} \\ \mathcal{C}(\chi, t) := t - \frac{|\Omega^-|(\chi)}{|\Omega|} = 0; \quad t \in [0, 1] \\ \text{governed by:} \\ \mathbb{K}_\chi \hat{\mathbf{u}}_\chi = \mathbf{f} \end{array} \right. \quad \begin{array}{l} (a) \\ \\ (b) \\ \\ (c) \end{array} \quad (35)$$

where the cost function (34) has been defined as a minimization problem by changing its sign.

Contrary to the problem of minimal compliance (section C.3.5), the compliant mechanism problem is not self-adjoint. Thus, an *auxiliary state problem* must be solved in addition to the *original state problem* (22). Both systems present the same stiffness matrix \mathbb{K}_χ but different actions and solutions $\hat{\mathbf{u}}_\chi^{(1)}$ and $\hat{\mathbf{u}}_\chi^{(2)}$, respectively, defined as

$$\left\{ \begin{array}{l} \mathbb{K}_\chi \hat{\mathbf{u}}_\chi^{(1)} = \mathbf{f}^{(1)} \quad (\text{system I}) \\ \mathbb{K}_\chi \hat{\mathbf{u}}_\chi^{(2)} = \mathbf{1} \quad (\text{system II}) \end{array} \right. \quad (36)$$

Following Oliver *et al.* [22], the *relaxed topological derivative* of the optimization problem (35), once the *adjoint state equation* (36) has been substituted in, can be expressed as

$$\frac{\delta \bar{\mathcal{J}}^{(he)}(\chi)}{\delta \chi}(\hat{\mathbf{x}}) = \left[\hat{\mathbf{u}}_{\chi}^{(2)T} \frac{\delta \mathbb{K}_{\chi}}{\delta \chi}(\mathbf{x}) \hat{\mathbf{u}}_{\chi}^{(1)} - \hat{\mathbf{u}}_{\chi}^{(2)T} \frac{\delta \mathbf{f}_{\chi}^{(1)}}{\delta \chi}(\mathbf{x}) \right]_{\mathbf{x}=\hat{\mathbf{x}}} . \quad (37)$$

As proceeded in section C.3.5, equation (37) can be simplified and expressed in terms of a *pseudo-energy density*, yielding to

$$\frac{\delta \bar{\mathcal{J}}^{(he)}(\mathbf{u}_{\chi})}{\delta \chi}(\hat{\mathbf{x}}) = 2m_k (\chi_k(\hat{\mathbf{x}}))^{m_k-1} \bar{\mathcal{U}}_{1-2}(\hat{\mathbf{x}}) \Delta \chi_k(\hat{\mathbf{x}}), \quad (38)$$

when volumetric forces are neglected. The corresponding *nominal pseudo-energy density* can be determined as

$$\bar{\mathcal{U}}_{1-2}(\hat{\mathbf{x}}) = \frac{1}{2} \left(\nabla^S \mathbf{u}_{\chi}^{(2)} : \bar{\mathbb{C}} : \nabla^S \mathbf{u}_{\chi}^{(1)} \right) (\hat{\mathbf{x}}). \quad (39)$$

Finally, mimicking equation (30), the *pseudo-energy*, $\xi(\hat{\mathbf{x}}, \chi)$, can be obtained as

$$\xi(\hat{\mathbf{x}}, \chi) = -\gamma_1 \hat{\mathbf{u}}^{(2)}(\hat{\mathbf{x}})^T \left[\mathbf{B}(\hat{\mathbf{x}})^T \bar{\mathbb{C}} \mathbf{B}(\hat{\mathbf{x}}) \right] \hat{\mathbf{u}}^{(1)}(\hat{\mathbf{x}}). \quad (40)$$

C.4 MATLAB implementation

The user can run the code from the Matlab prompt with the following Matlab call

```
UNVARTOP_2D_compliance (nelx, nely, nsteps, Vol0, Vol1, k, tau)
```

where `nelx` and `nely` stand for the number of quadrilateral elements in the horizontal and vertical directions, respectively.⁸ The following four parameters define the time evolution of the optimization procedure, being `nsteps` the number of increments to get from the initial void volume (`vol0`) to the final void volume (`vol1`), and parameter `k` defines the curvature of the exponential function, in case this type of time-advancing sequence is preferred. For an equally-spaced pseudo-time advance, set `k` to 0. The remaining input variable, `tau`, rules the minimum filament's width of the optimal design. Other variables related with the topology optimization algorithm and the numerical example (geometry and boundary conditions) are defined inside the function (see Appendix C.A), and can be modified if needed.

For instance, the code can be called with the input line

```
UNVARTOP_2D_compliance (100, 50, 10, 0, 0.5, 0, 0.5)
```

⁸The design domains are assumed to be rectangular domains discretized with quadrilateral unit square finite elements.

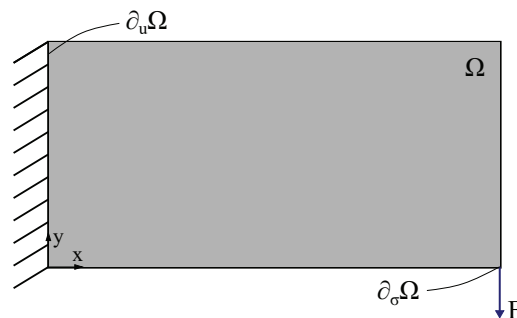


Figure C.4: Cantilever beam: topology optimization domain and boundary conditions.

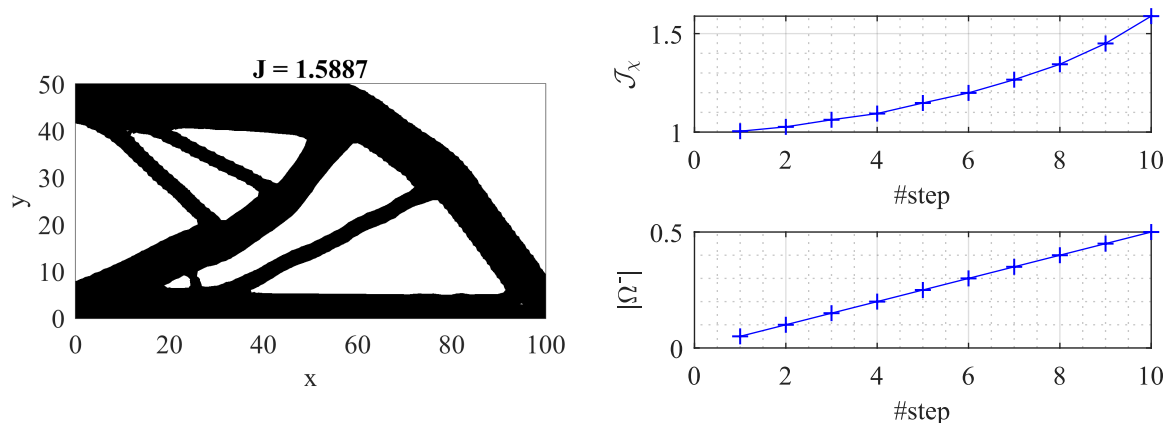


Figure C.5: Cantilever beam: topology optimization results.

for the default example, which corresponds to a cantilever beam with a vertical load applied on the bottom-right corner of Ω , and the displacements are prescribed on the left side of it, as illustrated in Figure C.4. The algorithm generates two output figures, the first one displays the optimal topology for each iteration, and the second one shows the evolution of the cost function J_x and the void volume, $|\Omega^-|$ along the time-steps, as depicted in Figure C.5. At the end, a graphical user interface (GUI) with topology evolution, animated in [Online Resource 1](#), is shown.

Relevant details of the Matlab code are explained in the following subsections for the minimum mean compliance problem (section C.3.5), referring to the code in Appendix C.A, along with the required modifications to solve the topology optimization problems defined in sections C.3.6 and C.3.7.

C.4.1 Parameter definition: lines 2-4

Table C.1 shows the list of variables and fields required by the program and used along it, excluding the variables already defined in the previous section. These parameters can be grouped in three blocks: all the parameters of the first block are related to the physical problem and the finite element used in the FEM analysis, the next three parameters conform the second block, which define the threshold iterations of the algorithm, and the last one defines a structure of optional parameters to choose which graphics are displayed and which solver is used to solve the *Laplacian regularization*.

C.4.2 Geometry definition: lines 5-9

The design domain, as aforementioned, is assumed to be rectangular and discretized with square elements. The FE mesh is defined via the coordinates and connectivities arrays, named `coord` and `connect` in the code. A coarse example mesh of the default example, see Figure C.4, is illustrated in Figure C.6, consisting of 15 nodes and 8 elements, numbered in column-wise (top to bottom) from left to right. The position of each node is defined respect to Cartesian coordinate system with origin at the left-bottom corner.

The `coord` matrix is generated using Matlab's `meshgrid` function and then, the obtained `x,y` matrices are reshaped into the coordinates matrix, which dimensions are $[n \times n_dim]$, i.e.

$$\text{coord} = \begin{bmatrix} 0 & 0 & 0 & 1 & 1 & \dots & 4 & 4 & 4 \\ 2 & 1 & 0 & 2 & 1 & \dots & 2 & 1 & 0 \end{bmatrix}^T. \quad (41)$$

The connectivity matrix, `connect`, is constructed following the same procedure for computing the degree of freedom connectivity matrix, `edofMat`, described by Andreassen *et al.* [5]. First,

Table C.1: List of fields used in the code.

Variable	Value	Definition
<code>n_dim</code>	2	number of dimensions of the problem
<code>n_unkn</code>	2	number of unknown per node
<code>n_nodes</code>	4	number of nodes per element (e.g. 4 nodes for the quadrilateral element)
<code>n_gauss</code>	{1, 4}	total number of quadrature points of the quadrilateral element
<code>n</code>	$(nelx+1)*(nely+1)$	total number of nodes
<code>h_e</code>	1	element's size
<code>alpha0</code>	1e-3	Prescribed value of ψ for active/passive nodes
<code>iter_max_step</code>	20	maximum number of in-step iterations
<code>iter_min_step</code>	4	minimum number of in-step iterations
<code>iter_max</code>	500	maximum number of iterations
<code>opt.Plot_top_iso</code>	{true, false}	Boolean variable to plot the topology along iterations
<code>opt.Plot_vol_step</code>	{true, false}	Boolean variable to plot the evolution of the volume along iterations
<code>opt.EdgeColor</code>	{'none', RGB-color}	RGB color of the sides of the quadrilateral elements
<code>opt.Solver_Lap</code>	{'direct', 'iterative'}	method to solve the Laplacian regularization

matrix `nodenrs` is created with node IDs in a $(nely+1) \times (nelx+1)$ matrix in line 7, mimicking the numbering in Figure C.6. Next, the left-bottom node ID of each element is stored in `nodeVec` vector, by using matrix `nodenrs`. For the given example, this variables are defined as follows:

$$\text{nodenrs} = \begin{bmatrix} 1 & 4 & 7 & 10 & 13 \\ 2 & 5 & 8 & 11 & 14 \\ 3 & 6 & 9 & 12 & 15 \end{bmatrix} \rightarrow \text{nodeVec} = [2, 3, 5, 6, 8, 9, 11, 12]^T. \quad (42)$$

Finally, thanks to the repetitive structure of the grid, the connectivity table, `connect`, can be constructed using only `nodeVec` and numbering within an element in anticlockwise order starting

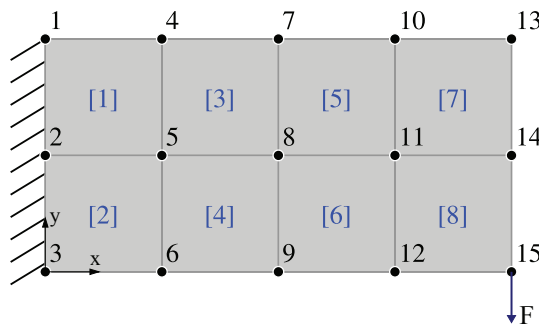


Figure C.6: Cantilever beam: mesh discretization.

from the left-bottom node, which reads as

$$\text{connect} = \begin{bmatrix} 2 & 5 & 4 & 1 \\ 3 & 6 & 5 & 2 \\ \vdots & \vdots & \vdots & \vdots \\ 11 & 14 & 13 & 10 \\ 12 & 15 & 14 & 11 \end{bmatrix}. \quad (43)$$

C.4.3 Load and boundary definition: lines 10-17

Lines 11-17 define the boundary conditions for the displacement and force field. First, the force vector, \mathbb{F} , and the displacement vector, \mathbf{u} , are initialized in lines 11 and 12, respectively. Next, line 13 assigns the imposed force to the force vector, which corresponds to a downwards force applied at the bottom right corner, as illustrated in Figure C.4, with a small value to limit the maximum displacement of the structure. The next line defines the prescribed degrees of freedom, and stores them in `fixed_dofs`.

Parameters `active_node` and `passive_node` of line 15 are used to force some nodes to be included in the stiff (Ω^+) and soft (Ω^-) material domains, respectively. It is done via the modification of the *discrimination function*, `psi`, as in line 54 for the initialization of the *discrimination function* or in the *bisection algorithm* (line 149), by imposing the value `alpha0` or `-alpha0`.

Finally, the list with free degrees of freedom is generated and stored in `free_dofs` (line 16), and the displacement of `fixed_dofs` are prescribed to the corresponding value, e.g. 0.

C.4.4 Material definition: lines 18-19

The material used for the analysis is defined in terms of the Young's modulus \mathbb{E}_0 , of the stiff phase (material domain) and the Poisson's ratio ν , ν (see section C.3.2). In addition, and as a specific parameter of the algorithm, the coefficient `m` is defined and prescribed to `m=5` for the minimum mean compliance problem. This coefficient in conjunction with the *contrast factor*, `alpha`, is used to compute the corresponding *relaxation factor*, `beta`. Notice that a noticeably small *contrast factor* can be imposed for compliance problem.

C.4.5 Animation preparation: lines 20-23

Lines 21-23 initialize the vectors `psi_vec`, `chi_vec` and `u_vec` to 0, which correspond respectively to the *discrimination function*, the *characteristic function* and the displacement vector. This vectors are used to store the corresponding variables at the convergence of each time-step (line 103), and are later called by the `Topology_evolution` GUI.

C.4.6 Finite element analysis preprocessing: lines 24-40

As already mentioned, the regularity in the mesh is highly exploited when computing the global stiffness matrix, \mathbb{K} , to reduce the computational time inside the optimization loop. For that reason, only two element stiffness matrices are required, one for the mixed elements⁹ and another for the other elements. The first one, is computed with a central quadrature point `posgp1`, while the second one requires at least 4 quadrature points to be correctly integrated, `posgp4`. The weights of each point are stored in `w1` and `w4`, respectively. This information is computed by evoking `gauss_points` function (lines 111-114) with the total number of point inside the quadrilateral element, as will be later explained.

Next, the nominal constitutive tensor `DE` for \mathbb{E}_0 and ν , assuming plane-stress (equation (19)), is computed in line 27, by calling `D_matrix_stress` function. The element stiffness matrix,

⁹The elements bisected by the zero-level of the *discrimination function* are sub-integrated with a single quadrature point according a three-field ($\boldsymbol{\varepsilon}$ - $\boldsymbol{\sigma}$ - $\hat{\mathbf{u}}$) mixed element. Further details can be found in [22].

evaluated as

$$K_e = \int_{\Omega_e} \mathbf{B}^T \bar{\mathbf{C}} \mathbf{B} d\Omega = \sum_{i=1}^{n_{gauss}} w_i |J_i| \mathbf{B}_i^T \bar{\mathbf{C}}_i \mathbf{B}_i, \quad (44)$$

is computed in lines 28-34 for solid and void elements, `KE`. The equivalent nominal matrix, for bisected elements, `KE_cut` is computed in lines 35-37. The strain-displacement matrix \mathbf{B} , defined in lines 119-124 (`B_matrix`), is evaluated in each gauss point along with the corresponding determinant of the Jacobian. Moreover, the product $\mathbf{B}^T \bar{\mathbf{C}} \mathbf{B}$ for the i -th gauss point is stored in `KE_i` and `K_cut`, respectively.

Finally, the connectivity table of DOFs, `edofMat`, is generated in line 38 using built-in `kron` and `repmat` functions. Each row represents the degrees of freedom of a different element, e.g.

$$\text{edofMat} = \begin{bmatrix} 3 & 4 & 9 & 10 & 7 & 8 & 1 & 2 \\ 5 & 6 & 11 & 12 & 9 & 10 & 3 & 4 \\ \vdots & \vdots & \vdots & \vdots & \vdots & \vdots & \vdots & \vdots \\ 21 & 22 & 27 & 28 & 25 & 26 & 19 & 20 \\ 23 & 24 & 29 & 30 & 27 & 28 & 21 & 22 \end{bmatrix}. \quad (45)$$

This matrix is now used to compute the indices `iK` and `jK` used to generate the global stiffness matrix as a sparse matrix from the triplets `iK`, `jK` and `sK`, as will be explained later.

Gauss points, Shape function and Cartesian derivatives: lines 110-125

The bilinear quadrilateral element is used in the FE analysis, which consists of four nodes. Its numerical implementation can be found in the literature [44, 26].

This element is correctly integrated when 4 quadrature points are employed. The position and weights are computed in `gauss_points` function (lines 111-114), where the gauss quadrature points in one direction (parent dimension) are extended to two dimensions, using Matlab's `meshgrid` function. `posgp` defines the position $[\xi, \eta]$ in the parent square element, where each column represent a different point. The weight values are stored in `w` as a row vector.

The shape matrix, \mathbf{N} , (size `n_nodes` x `n_gauss`) is computed in lines 116-117 inside `N_matrix` function, as explained in [44, 26].

Last, the shape derivatives (size `n_dim` x `n_nodes`), the Jacobian matrix J (size `n_dim` x `n_dim`) and the Cartesian derivatives (size `n_dim` x `n_nodes`) are obtained in `B_matrix` for a given `gauss_points` (lines 119-124), assuming a square unit element. Finally, the strain-displacement matrix \mathbf{B} for the case of interest is computed (size `3` x `n_nodes*n_unkn`).

Element Stiffness matrix: lines 125-135

The constitutive tensor of each element depends on the material properties, which are common to all the elements, and the *characteristic function*. Due to this regularity, the nominal constitutive tensor, $\bar{\mathbf{C}}$, is computed only once for the stiff material properties, in lines 126 and 127, and the corresponding stiffness matrix is later multiplied by the term χ_β^m , which depends on each element. The *relaxed characteristic function* is calculated in lines 129-131, inside `interp_property` function, as follows

$$\text{coeff} = \begin{cases} (\chi + (1 - \chi)\beta)^m & \text{for stiffness} \\ m(\chi + (1 - \chi)\beta)^{m-1}(1 - \beta) & \text{for sensitivity} \end{cases}$$

with $\chi \in [0, 1]$.

The global stiffness matrix is assembled at each iteration inside the optimization loop using Matlab's `sparse` function to addition the components with same i -th (`iK`) and j -th (`jK`) degree of freedom, calling `assembly_stiff_mat`. Its definition is written in lines 133-135, where the third

component (`sK`) for the `sparse` function is computed. Each column of the `sK` matrix corresponds to the stiffness matrix of element `e`. It is worth emphasizing that the bisected elements must be multiplied by `KE_cut`.

C.4.7 Laplacian regularization preparation: lines 41-52

Mimicking the preprocessing procedure of the global stiffness matrix (see section C.4.6), the lhs matrix of equation (11) can be computed just once (lines 42-48), since it does not depend on the topology but on the mesh, which is regular. Thus, the terms $\nabla \mathbf{N}^T \nabla \mathbf{N}$ and $\mathbf{N}^T \mathbf{N}$, which correspond to `KE_Lap` and `ME_Lap` defined in lines 42 and 43, are analytically computed and defined as

$$KE_{Lap} = \int_{\Omega} \mathbf{B}^T \mathbf{B} d\Omega \rightarrow KE_{Lap} = \frac{1}{6} \begin{bmatrix} 4 & -1 & -2 & -1 \\ -1 & 4 & -1 & -2 \\ -2 & -1 & 4 & -1 \\ -1 & -2 & -1 & 4 \end{bmatrix}$$

$$ME_{Lap} = \int_{\Omega} \mathbf{N}^T \mathbf{N} d\Omega \rightarrow ME_{Lap} = \frac{1}{36} \begin{bmatrix} 4 & 2 & 1 & 2 \\ 2 & 4 & 2 & 1 \\ 1 & 2 & 4 & 2 \\ 2 & 1 & 2 & 4 \end{bmatrix}.$$

Next, combining both matrices and the *regularization parameter* τ , the lhs matrix is generated and saved in `KE_Lap` (line 44). Lines 45 to 47 define the triplets `i_KF`, `j_KF` and `s_KF`, which are then used to obtain the sparse matrix `K_Lap` in line 48.

Depending on `opt_solver_Lap`, the Laplacian regularization will be solved using a direct or an iterative method. This procedure can be sped up by computing the Cholesky factorization of the lhs (`chol(K_Lap, 'lower')`) if the direct method is chosen, or computing the incomplete Cholesky factorization (`ichol(K_Lap, opts)`, with `opts = struct('type', 'ict', 'droptol', 1e-3, 'diagcomp', 0.1)`) in case an iterative algorithm is desired. It will be later used as a preconditioner.

The rhs must be computed at each iteration, since it depends on the *discrimination function*, `psi`, as detailed in section C.4.8. Nevertheless, the resolution procedure of equation (11) can be prepared by computing both the shape matrix, `N_T`, of size `n_nodes` x `n_gauss`¹⁰, and the indexes of the element nodes `i_xi` (reshaping the connectivity matrix into a column vector). The assembly is carried out in lines 83 and 85 evoking `accumarray` function.

C.4.8 Main program: lines 53-107

The main optimization procedure starts by initializing the topology via the *discrimination function* to `alpha0`, constant to all the nodes, except for those listed in `passive_node`. Next, the *characteristic function* is obtained via `compute_volume` function. Line 57 is used to initialize several vectors, which will accumulate the convergence variables (cost function, volume and lambda), and other essential variables. The initial topology is displayed in the next line by means of `plot_isosurface`.

The optimization starts in line 59, where the loop over time-steps is defined. As explained in section C.3.4, the *reference pseudo-time* is iteratively increased following a linear or exponential expression, which definition is written through lines 186-188, and for each time-step the optimization loop is repeated until convergence is achieved. The optimization loop (lines 65-99) consists of five parts: finite element analysis, sensitivity computation, Laplacian regularization, topology update and convergence check.

Finally, at each iteration, the topology is plotted (line 92), the intermediate results are printed in display (line 96) and the iteration counters are increased (line 97).

¹⁰The matrix is transposed with respect to the common one.

Finite element code: lines 66-69

The global stiffness matrix, κ , is assembled inside `assembly _stiff_mat` function using the `sparse` function, where `sK` is computed considering the corresponding *relaxed characteristic function* for each element. Next, in line 68, the equilibrium equation (22) is solved using a direct method. The displacements are stored in `u`. Next, the cost function, J , normalized with the one of the first iteration (`J_ref`), can be obtained at the current topology layout.

Sensitivity computation: lines 70-79

According to equation (9), the *energy density* is defined as the partial derivative of the cost objective's kernel multiplied by the exchange function, $\Delta\chi$. The *energy density* is computed in two parts, in the first one (lines 72 to 75) the sensitivity of non-bisected elements is obtained for the 4 quadrature points, while the sensitivity for the mixed elements is calculated in the second part (lines 76 to 78).

The element sensitivity, as detailed in section C.3.5 for the minimum compliance problem, is computed as $m\chi_\beta^{m-1} \mathbf{u}_e^T K_{e,i} \mathbf{u}_e (1-\beta)$ for the e -th element and the i -th gauss point (see equation (30)). However, for the bisected elements, the element stiffness matrix $K_{e,i}$ is replaced by κ_{cut} , and the resultant value is copied to the four gauss points.

At the first iteration, the parameters `xi_shift` and `xi_norm` are defined as

```
xi_shift = min(0, min(Energy(:)))
xi_norm = max([range(Energy(:)); Energy(:)])
```

and will be used to obtain the *modified energy density*, $\hat{\xi}(\mathbf{x})$, described in equation (10).

Laplacian regularization: lines 80-86

As aforementioned, instead of applying the *Laplacian regularization* (11) to the resultant *discrimination function*, at each iteration of the *bisection algorithm* and since it does not affect constant fields such as λ , the *Laplacian regularization* is only implemented for $\hat{\xi}$. The corresponding system is defined as

$$\begin{cases} \xi_\tau - (\tau h_e)^2 \Delta_{\mathbf{x}} \xi_\tau = \hat{\xi} & \text{in } \Omega \\ \nabla_{\mathbf{x}} \xi_\tau \cdot \mathbf{n} = 0 & \text{on } \partial\Omega \end{cases}, \quad (46)$$

where $\hat{\xi}$ and ξ_τ stand for the *modified unfiltered energy density* and the *smooth energy density*, respectively. As commented in section C.3.1, the lhs has been precomputed (see section C.4.7) and the rhs is now computed based on the *modified energy density* (field on gauss points). FE discretization of the rhs leads to

$$rhs = \int_{\Omega} \mathbf{N}^T \hat{\xi}(\mathbf{x}) d\Omega, \quad (47)$$

which can be rewritten in matrix form, defined in line 81, as

```
s1 xi_int = N_T*(Energy-xi_shift*chi)/xi_norm;
```

The nodal contribution of this integral is later constructed by means of the built-in `accumarray` Matlab function.

The system of linear equations (46), as mentioned, can be solved using the Cholesky factorization and a direct solver (line 83) or an iterative solver (e.g. `minres` solver) applying the incomplete Cholesky factorization as the preconditioner of the system, as described in section C.4.7.

It is worth to mention that for low number of elements, as it is the case of this paper since it is for academic purposes, the *Laplacian regularization* may generate boundary waves for thin filaments, as displayed in some figures. This undesirable effect should vanish if finer meshes are used.

Update of χ and ψ : line 88

The topology layout, satisfying the constraint equation, is obtained by means of a *bisection algorithm* (solution of equation (13)) called in line 88. The `find_volume` functions computes the Lagrange multiplier λ (`lambda`), the new *discrimination function* ψ (`psi`) and the corresponding *characteristic function* χ (`chi`).

Bisection algorithm: lines 137-152 The *bisection algorithm* consists of a search for a suitable bracket, and the subsequent root finding. The left and right extremes of the interval are easily defined by the minimum and maximum value of the energy density field, and stored as 11 and 12, respectively. The corresponding constraint values are saved as `c1` and `c2`. Lines 139-141 tests the last λ as a trial extreme of the interval, by means of `compute_volume_lambda`, to reduce the number of iterations. The bisection loop is written in lines 142 to 146, where the root of the constraint equation is estimated as the midpoint of the bracketing interval (line 143).

At each iteration of the bisection, given a *density function* `xi` and a trial `lambda`, the *discrimination function* is obtained at line 149. The active and passive nodes are considered by modifying the `psi` function, as aforementioned. The void volume ratio `vol` and the *characteristic function* `chi` are obtained from `compute_volume` in line 150. Next, the constraint equation is evaluated in line 151, and the extremes of the interval are updated accordingly. This procedure is repeated until the void volume is within 10^{-4} of the reference time.

Volume computation: lines 153-161 The computation of the volume is done by means of an integration with 36 quadrature points. This methodology differs for simplicity of the implementation from the one used in Oliver *et al.* [22], where a modified marching squares was employed.

The position and weights of the 36 quadrature points are assigned as defined in [26]. First, line 158 determines which elements are bisected by the internal boundary through the nodal value of the *discrimination function*. In case they all have the same sign, the boundary will not cross throughout the element. Then, the element nodal ψ , `psi_n`, is evaluated in the quadrature points for the bisected elements and saved as `psi_x`. The *characteristic function* is obtained as the dot product of `w` and `psi_x > 0`. Finally, the void volume ratio is computed in line 161.

Convergence check: lines 90 and 94

Lines 90 and 94 compute the convergence tolerances of the algorithm, along with the constraint tolerance `Tol_constr`. The convergence is checked inside the while condition at line 65, and it only converges when the number of in-step iterations (`iter_step`) is in between `iter_min_step` and `iter_max_step`, and the three following conditions are satisfied: the L2-norm of the *characteristic function* is less than 0.1, the relative difference of the Lagrange multiplier with respect the previous one is less than 0.1, and the volume magnitude is within 10^{-4} of the desired *pseudo-time*, `t_ref`.

The optimization terminates if the maximum number of iterations, `iter_max`, or the maximum number of in-step iterations are achieved, showing a warning message in command window.

C.4.9 Iso-surface plot: lines 92 (162-172)

The `plot_isosurface` function shows the optimal topology via the *discrimination function* `psi` in a black-and-white design, as seen in Figure C.5 (top view). The behavior of this function depends on the iteration, i.e. the first time it is called, a figure is generated and its handle saved as `fig_handle`. In addition, the topology is represented using built-in `patch` function, the handle of which is stored as `obj_handle`, by means of the coordinates matrix, connectivity matrix and the nodal *discrimination function*. However, only `psi` field is updated in the other iterations using `set(obj_handle, 'FaceVertexCData', psi);`.

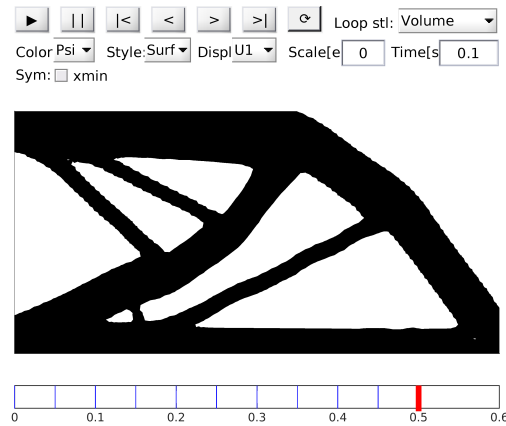


Figure C.7: GUI's design.

C.4.10 Cost function and volume vs. step plot: line 102 (173-184)

The definition of `plot_volume_iter` function is similar to that of `plot_isosurface` function. At iteration 1, it creates the figure, and two axes using `subplot` function. The cost function evolution is illustrated in the top subplot, while the volume evolution is displayed at the bottom. At other iterations, the lines are updated using `set` function, with the updated `J_vec` and `vol_vec` vectors, respectively.

C.4.11 Topology evolution GUI: lines 108-109

Once the Topology Optimization problem has been solved, the results can be graphically post-processed by means of a graphical user interface (GUI), where the topology and displacement fields are displayed for the set of time-steps. It is created by the following function call:

```
Topology_evolution(coord, connect, [Vol0, vol_vec], psi_vec, chi_vec, U_vec);
```

where `vol_vec` corresponds to the set of *pseudo-time* values for which the topology has been optimized. Then, `psi_vec` and `chi_vec` correspond respectively to the *discrimination function* (nodal scalar field) and the *characteristic function* (element scalar field), each column corresponding to a different time-step. Similarly, `U_vec` correspond to the displacement field, where each column and layer of the array represent a different loading condition and a different time-step, respectively.

The interface allows to select the field to display (psi, chi or the norm of the displacement for any load condition) and the style of the representation (surface only, wireframe only and surface plus wireframe). The user can also choose the scale factor and the displacement field to deform the mesh as it can be observed in Figure C.7.

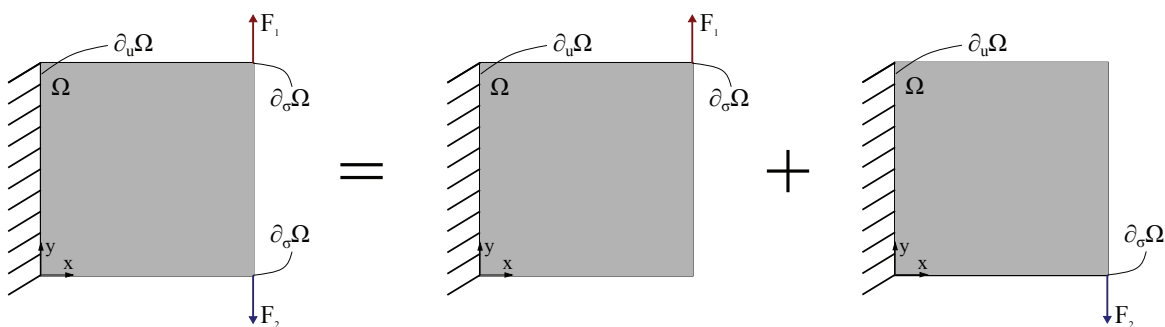


Figure C.8: Multi-load beam: topology optimization domain and boundary conditions.

The set of push-buttons on the top-left area controls the animation of the topology along the *pseudo-time*, the time between time-steps can be modified in the *dt* text edit field. The last button corresponds to a toggle-button, which animates indefinitely the topology until it is clicked. Depending on the chosen loop style option, the topology is animated along the time-steps (Volume) or along the scale factor for a given time-step (Scale linear and Scale sine).

The possibility to mirror/symmetrize the topology is the last relevant feature of this figure. A set of checkboxes allow to symmetrize the mesh and its properties on any of the sides of the domain.

C.4.12 Multi-load mean compliance: code modification

According to section C.3.6, the program can be easily adapted to optimize multi-load problems, as shown in Figure C.8. Then, the cost function as well as the sensitivity are evaluated as weighted averages of each individual optimization problem.

First, the loads and boundary conditions are changed to include the second loading state¹¹, defined in the second column of **F**:

```
11 F = sparse(n_unkn*n,2);
12 U = zeros(n_unkn*n,2);
13-1 F(n_unkn*find(coord(:,2)==nelx & coord(:,1)==nelx),1) = 0.01*nelx;
13-2 F(n_unkn*find(coord(:,2)==0 & coord(:,1)==nelx),2) = -0.01*nelx;
```

Furthermore, an additional column is added to **U_vec** by replacing line 23 with

```
23 U_vec = zeros(n_unkn*size(coord,1),size(U,2),nsteps+1);
```

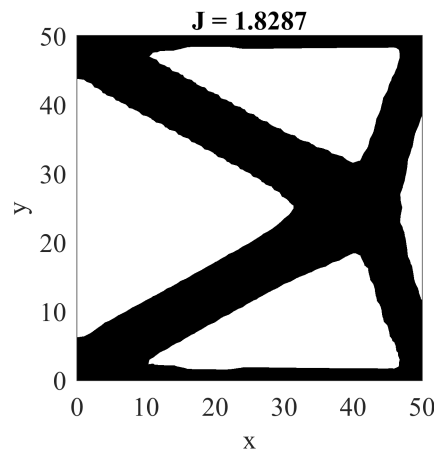


Figure C.9: Multi-load beam: optimal topology layout.

Next, the sensitivity computation must be adapted to include multiple loading states, via a **for** loop. Then, lines 73-75 are substituted with

```
73-1 for i_load=1:size(F,2)
73-2   u_e = reshape(U(edofMat(id,:)',i_load),n_nodes*n_unkn,[]); w_e = u_e;
74   for i=1:n_gauss; Energy(i,id) = Energy(i,id) + sum(w_e.*(KE_i(:, :, i)*u_e),1); end
75 end; Energy(:,id) = int_chi.*Energy(:,id);
```

and equivalently, lines 77 and 78 are replaced by

```
77-1 for i_load=1:size(F,2)
77-2   u_e = reshape(U(edofMat(id,:)',i_load),n_nodes*n_unkn,[]); w_e = u_e;
78-1   Energy(:,id) = Energy(:,id) + repmat(sum(w_e.*(K_cut*u_e),1),n_gauss,1);
78-2 end; Energy(:,id) = int_chi.*Energy(:,id);
```

This example can be simulated by the following line

¹¹More than one additional loading state can be considered.

```
UNVARTOP_2D_multiload (50,50,11,0,0.55,0,0.5)
```

The resultant optimal topology, at $t_{ref} = 0.55$, is displayed in Figure C.9, while the topology evolution is shown in [Online Resource 2](#). It can be observed in Figure C.10 how much the topology differs from the single loading condition, when the two loads of Figure C.8 are applied at the same time.

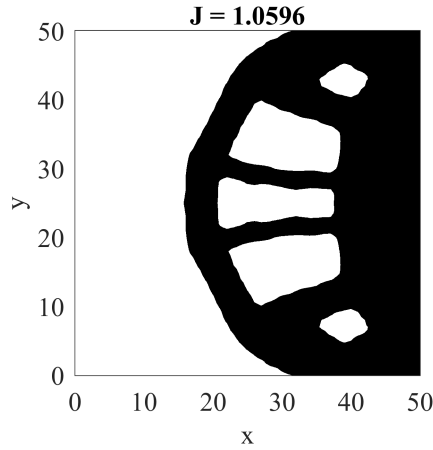


Figure C.10: Multi-load beam: optimal topology layout when loads are applied at the same time.

C.4.13 Compliant mechanisms: code modification

Mimicking the previous section, the base code in Appendix C.A also requires some modifications in order to optimize compliant mechanisms, as depicted in Figure C.11. A second loading state must be solved to compute the *adjoint state* \mathbf{w} , which is later used in the sensitivity computation. This second state is loaded with a dummy constant load applied in the *output nodes* in the same direction as the desired displacement. Then, the loads and boundary conditions are modified to

```
11 F = sparse(n_unkn*n,2);
12 U = zeros(n_unkn*n,2);
13-1 F(n_unkn*find(coord(:,2)>=0.9*nely & coord(:,1)==0)-1,1) = 0.0001*nely;
13-2 F(n_unkn*find(coord(:,2)>=0.9*nely & coord(:,1)==nelx)-1,2) = -0.0001*nely;
14-1 fixed_dofs = [reshape(n_unkn*find(coord(:,2)==nely),1,[]),...
14-2 reshape(n_unkn*find(coord(:,1)==0 & coord(:,2)<=0.1*nely)+(-n_unkn+1:0)
,1,[])];
15-1 active_node = find(coord(:,2)>0.9*nely&(coord(:,1)<0.05*nely|coord(:,1)
>0.95*nely));
15-2 passive_node = [];
```

Notice that the force is applied along a segment, and not only in a single node. Furthermore, only half of the design is computed thanks to the symmetry of the design and some nodes surrounding the *input* and *output ports* are forced to remain as stiff material.

The properties of the material (line 19) should be also changed to `m=3` and `alpha=1e-2`. This adjustment increases convergence.

To ensure fast convergence, external springs must be included in the *input* and *output ports* at the same degrees of freedom as the applied forces. These degrees are obtained by means of the following lines:

```
id_in = find(F(:,1)); id_in = sub2ind(n_unkn*(nely+1)*(nelx+1)*[1 1],id_in
,id_in);
id_out = find(F(:,2)); id_out = sub2ind(n_unkn*(nely+1)*(nelx+1)*[1 1],
id_out,id_out);
```

which must be inserted between lines 17 and 18. These two lists are used inside `assembly_stiff_mat`, thus its call has to be replaced by

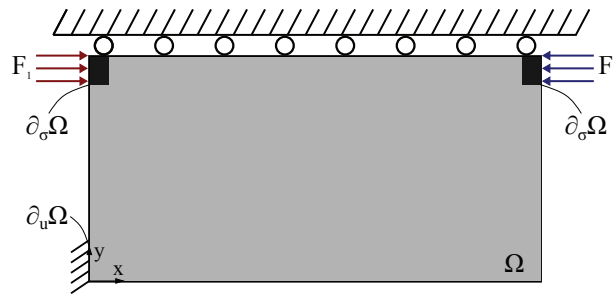


Figure C.11: Inverter (compliant mechanism): topology optimization domain and boundary conditions.

```
67 [K] = assmably_stiff_mat (chi,KE,KE_cut,beta,m,iK,jK,n_unkn,nelx,nely,
    id_in,id_out);
```

as well as its definition at line 133

```
133 function [K] = assmably_stiff_mat (chi,KE,KE_cut,beta,m,iK,jK,n_unkn,nelx,
    nely,id_in,id_out)
```

The external springs, using `id_in` and `id_out`, are added to the global stiffness matrix after line 135:

```
K(id_in) = K(id_in) + 0.002;
K(id_out) = K(id_out) + 0.002;
```

The prescribed value for the springs must be adjusted for each individual example.

The cost function must be also replaced by the corresponding work at the *output port*, since the cost function is defined as the maximization of the output displacement. It is implemented by the following line:

```
69 if iter == 1; U_vec(:, :, 1)=U; J_ref = -abs(F(:,2) '*U(:,1)); end; J = F
    (:,2) '*U(:,1)/J_ref;
```

As in section C.4.12, `U_vec` must be substituted by

```
23 U_vec = zeros(n_unkn*size(coord,1),2,nsteps+1);
```

Finally, the displacements of the *adjoint system*, used in the calculation of the sensitivity, must be replaced by the corresponding displacements of the second system. Thus, these lines are now defined as

```
73-1 u_e = reshape(U(edofMat(id,:),1),n_nodes*n_unkn,[]);
73-2 w_e = -reshape(U(edofMat(id,:),2),n_nodes*n_unkn,[]);
```

and

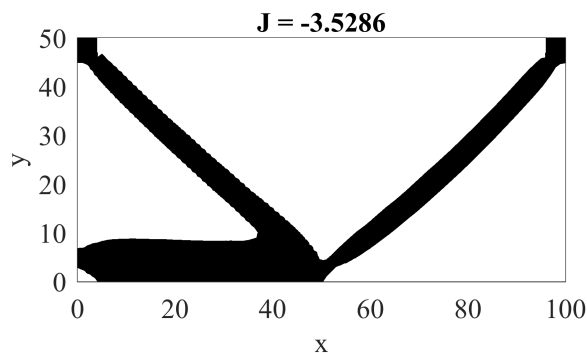


Figure C.12: Inverter (compliant mechanism): optimal topology layout.


```

77-1 u_e = reshape(U(edofMat(id,:),1),n_nodes*n_unkn,[]);
77-2 w_e = -reshape(U(edofMat(id,:),2),n_nodes*n_unkn,[]);

```


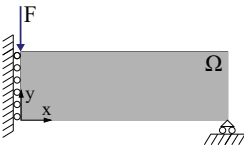
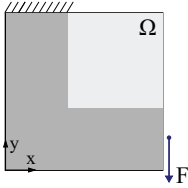
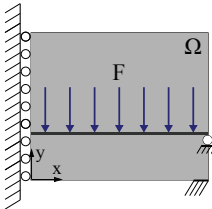
The optimal topology, for the given boundary conditions, illustrated in Figure C.12 can be performed with

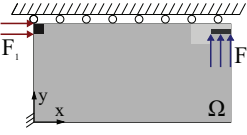
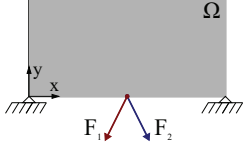
```
UNVARTOP_2D_complmechanism (100,50,10,0,0.8,-2,0.5)
```

The resultant compliant mechanism is animated in [Online Resource 3](#).

C.5 Numerical examples

The following numerical examples exhibit the potential of the unsmooth variational topology optimization technique in 2D problems. Unless otherwise stated, the parameters and material properties are left as the default examples, for each of the three optimization problems described in this work. The design domain, the function call and the boundary conditions for each example are defined in Table C.2.

Domain	Matlab's call	Boundary conditions
	<pre>UNVARTOP_2D_compliance (100, 50, 12, 0, 0.65, 0, 0.5)</pre>	<pre>F(n_unkn*find(coord(:,2)==round(0.5* nely) & coord(:,1)==nelx),1) = -0.01*nelx; fixed_dofs = reshape(n_unkn*find(coord (:,1)==0)+(-n_unkn+1:0),1,[]); active_node = []; passive_node = [];</pre>
	<pre>UNVARTOP_2D_compliance (150, 50, 10, 0, 0.6, 0, 1)</pre>	<pre>F(n_unkn*find(coord(:,2)==nely & coord (:,1)==0),1) = -0.01*nelx; fixed_dofs = [reshape(n_unkn*find(coord (:,1)==0)-1,1,[]),... reshape(n_unkn*find(coord(:,1)== nelx & coord(:,2)==0),1,[])]; active_node = []; passive_node = [];</pre>
	<pre>UNVARTOP_2D_compliance (100, 100, 12, 0.36, 0.75, 0, 0.5)</pre>	<pre>F(n_unkn*find(coord(:,2)==round(0.2* nely) & coord(:,1)==nelx),1) = -0.01*nelx; fixed_dofs = reshape(n_unkn*find(coord (:,1)<=0.4*nelx & coord(:,2)==nely) +(-n_unkn+1:0),1,[]); active_node = []; passive_node = find(coord(:,1)>ceil(nelx*0.4) & coord(:,2)>ceil(nely *0.4));</pre>
	<pre>UNVARTOP_2D_compliance (240, 200, 32, 0, 0.775, 0, 0.5)</pre>	<pre>F(n_unkn*find(coord(:,2)==floor(nely *1.6/5),1) = -0.01*nelx; fixed_dofs = [reshape(n_unkn*find(coord (:,1)==0)-1,1,[]),... shape(n_unkn*find(coord(:,1)>=5.75/6* nelx & coord(:,2)==0)+(-n_unkn+1:0) ,1,[]),... shape(n_unkn*find(coord(:,1)==nelx & coord(:,2)==floor(nely*1.5/5) ,1,[])]; active_node = find(coord(:,2)>=nely *1.5/5 & coord(:,2)<=nely*1.6/5); passive_node = [];</pre>

Domain	Matlab's call	Boundary conditions
	<pre>UNVARTOP_2D_ complmechanism (150, 75, 14, 0, 0.85, -2, 0.5)</pre>	<pre>F(n_unkn*find(coord(:,2)>=0.9*nely & coord(:,1)==0)-1,1) = 0.0001*nelx; F(n_unkn*find(coord(:,2)==round(0.9* nely) & coord(:,1)>=0.9*nelx),2) = 0.0001*nelx; fixed_dofs = [reshape(n_unkn*find(coord (:,2)==nely),1,[]), reshape(n_unkn* find(coord(:,1)==0 & coord(:,2) <=0.1*nely)+(-n_unkn+1:0),1,[])]; active_node = [find(coord(:,2)>0.9*nely & coord(:,1)<0.05*nelx); find(coord (:,2)>0.9*nely&coord(:,2)<=0.95* nely&coord(:,1)>=0.9*nelx)]; passive_node = [find(coord(:,1)>0.8* nelx & coord(:,1)<0.9*nelx & coord (:,2)>0.8*nely); find(coord(:,1) >=0.9*nelx & coord(:,2)>0.95*nely)];</pre>
	<pre>UNVARTOP_2D_multiload (200, 100, 24, 0, 0.6, 0, 0.5)</pre>	<pre>F(n_unkn*find(coord(:,2)==0 & coord (:,1)==round(nelx/2))-1,1) = -0.01* nelx; F(n_unkn*find(coord(:,2)==0 & coord (:,1)==round(nelx/2)),1) = -2*0.01* nelx; F(n_unkn*find(coord(:,2)==0 & coord (:,1)==round(nelx/2))-1,2) = 0.01* nelx; F(n_unkn*find(coord(:,2)==0 & coord (:,1)==round(nelx/2)),2) = -2*0.01* nelx; fixed_dofs = reshape(n_unkn*find((coord (:,1)==0 & coord(:,2)==0) (coord (:,1)==nelx & coord(:,2)==0))+(- n_unkn+1:0),1,[]); active_node = []; passive_node = [];</pre>

C.5.1 Cantilever beam

A variation of the initial examples is now performed. In this case, the load is not applied at the bottom-right corner but in the middle of the right side of the domain, as depicted in the first row of Table C.2. Dirichlet conditions are not modified, i.e. the displacements are prescribed on the left boundary of the domain. The optimal topology layout, for the last time-step, is illustrated in Figure C.13, with the values from Table C.2. That is, the interval of interest $[0, 0.65]$ is discretized with 12 equally spaced steps and the regularization parameter is prescribed to $\tau = 0.5$. In addition, the topology evolution, shown in the animation (Online Resource 4), is displayed in Figure C.14 for time-steps 2, 4, 7, and 10. Similar results obtained with other optimization techniques can be found in [30, 8, 43, 11].

C.5.2 Messerschmitt-Bölkow-Blohm (MBB) beam

Half of the MBB-beam, with an aspect ratio of 3:1, is optimized in the second example. Symmetry is assumed on the left side of the domain and the vertical displacement at the bottom-right corner is constrained, as observed in Table C.2, and only a point-wise load is applied at the top-left corner. The last requested $t_{ref} = 0.6$ is achieved in 10 time steps. Figure C.15 depicts the resulting optimal topology layout using the provided code, adapted with the corresponding boundary conditions (see second row of Table C.2). Additionally, Online Resource 5 displays the animation of optimal topologies for the given time-steps. The results are comparable to those presented by [27, 5, 32, 43, 11], among others.

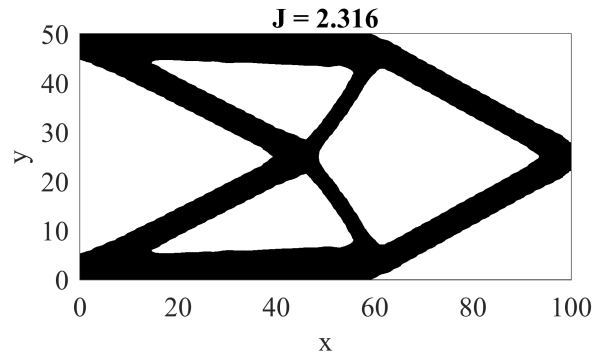


Figure C.13: Cantilever beam (load applied at the middle): optimal topology layout.

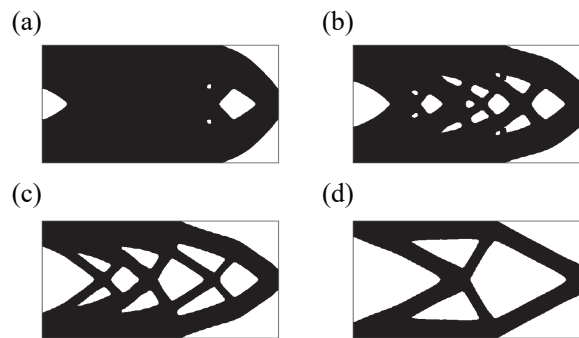


Figure C.14: Cantilever beam: topology evolution. (a) optimal topology at $t_{ref} = 0.11$, (b) optimal topology at $t_{ref} = 0.22$, (c) optimal topology at $t_{ref} = 0.38$ and (d) optimal topology at $t_{ref} = 0.54$.

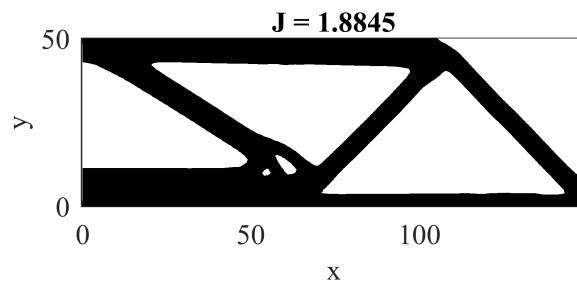


Figure C.15: MBB beam: optimal topology layout.

C.5.3 L-Shaped structure

The L-Shaped structure, shown in Table C.2, represents a simplified version of a hook. The domain has a prescribed void zone in the top right area, defined by $x_i \geq 0.4$ and $y_i \geq 0.4$. All the nodes contained in this area are listed in `passive_node`. A single vertical load is applied on the right side of the domain at $y = 0.2$.¹² The nodes on the top-left boundary ($y = 1$ and $x < 0.4$) are fixed. The optimal configuration, shown in Figure C.16, is obtained by the inputs described in Table C.2. As in previous examples, the topology evolution is animated in [Online Resource 6](#). Similar optimal designs are obtained by Biyikli and To [8] and Liu and Tovar [18], for 2D and 3D problems, respectively.

¹²All measures are relative to the dimensions of the domain.

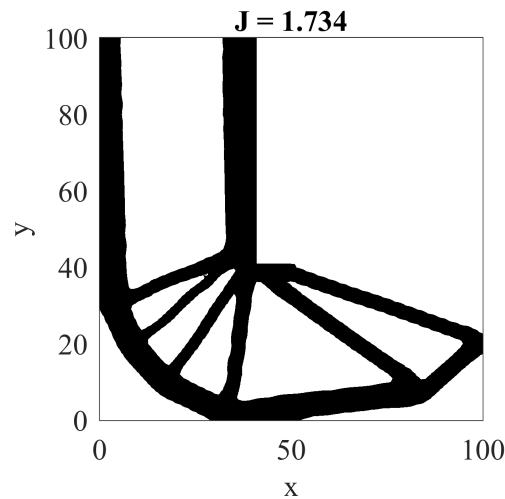


Figure C.16: L-shaped structure: optimal topology layout.

C.5.4 Bridge

The fourth numerical example in Table C.2 corresponds to a bridge, which domain is given by 12x5 rectangle. However, only half of it is optimized thanks to the central symmetry. Then, the horizontal displacement on the left side of the domain is prescribed to 0. In addition, the domain is supported by a small segment on the bottom-right corner of it and the vertical displacement is prescribed at the right side of the road. A distributed vertical downside load is applied on the road, which does not change throughout the optimization procedure (i.e. it can not be removed since all its nodes are included in `active_node` list). The corresponding boundary conditions of this problem are listed in Table C.2.

The optimal topology, at $t_{ref} = 0.775$, is displayed in Figure C.17, along with the corresponding animation in [Online Resource 7](#). The topology in Figure C.17 is closely similar to that obtained by Feijoo *et al.* [13] and Liang and Steven [17]. Furthermore, the design can be compared with the solution of a multi-load problem done by [19].

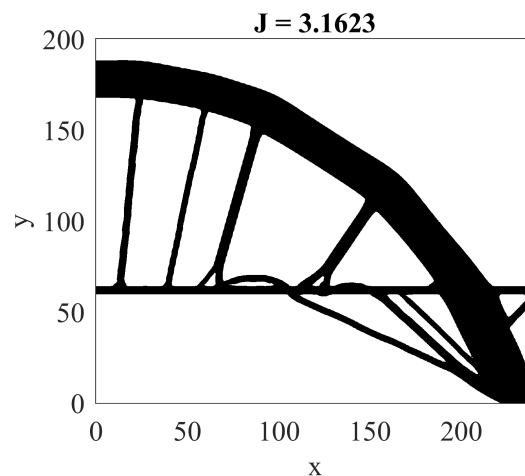


Figure C.17: Bridge: optimal topology layout.

C.5.5 Gripper mechanism

Let us now consider a compliant mechanism different from the one explained in section C.4.13 and inspired by [22, 41]. The goal of this optimization is to maximize the compressive displacement at the *output port* (vertical displacement at the top-right side) when an horizontal force is applied at the *input port* (top-left side of the domain). The domain is supported by a small area in

the bottom-left corner and symmetry is applied on the top side of Ω , as it can be observed in Table C.2 (fifth row). A small area in the *output port* is set to soft material (i.e. included in *passive_node* list) in order to represent the gap in the jaws of the gripper. Furthermore, some stiff material areas are restricted in both ports, and the corresponding spring stiffness values must be replaced by 0.01.

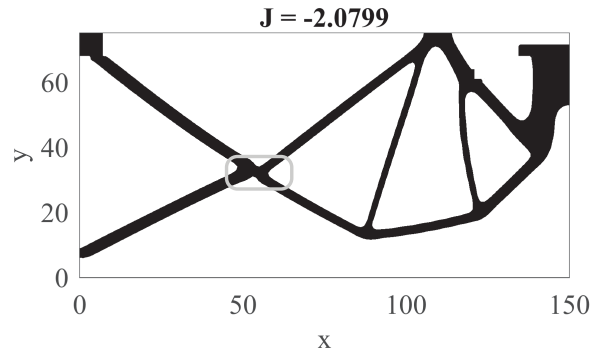


Figure C.18: Gripper (compliant mechanism): optimal topology layout. The central hinge is highlighted with a gray square.

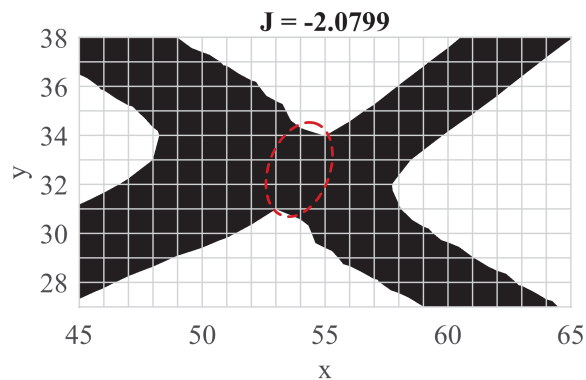


Figure C.19: Gripper (compliant mechanism): close-up view of the central hinge.

The *pseudo-time* is updated following an exponential expression in 14 time steps. The given optimal topology of Figure C.18 is obtained evoking `UNVARTOP_2D_compl_mechanism` function with the appropriate boundary conditions. A close-up view of the central hinge is illustrated in Figure C.19, where the flexible (thin) material, circled in red, performs as a hinge. The compliant mechanism of Figure C.18 is animated in [Online Resource 8](#), where the displacements are updated following a sinus function.

C.5.6 Michell multi-load structure

The last numerical example corresponds to a multi-load mean compliance problem with two loading states. The 2×1 rectangular domain is supported by its two bottom corners and subjected to a pair of forces in the middle of the bottom side at an angle of 30° with respect to the vertical. The desired *pseudo-time* is prescribed to 0.6, which optimal topology is illustrated in Figure C.20. The topology animation is given in [Online Resource 9](#).

The topology layout, as already noted, deviates from the corresponding optimal topology when both loads are applied at the same time, as shown in Figure C.21. In this setting, the bottom bars, which connect the supporting nodes with the central node, have been removed. The problem definition is based on [19]. Other variations can be found in [10, 32].

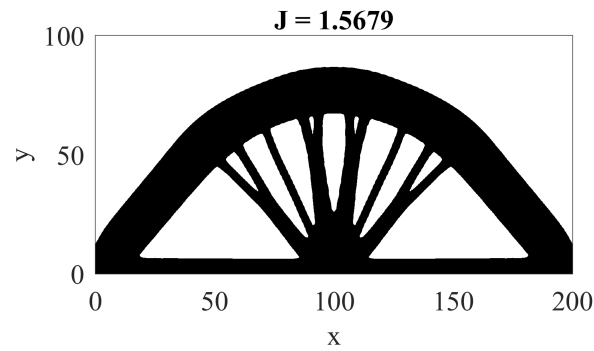


Figure C.20: Multi-load michell structure: optimal topology layout.

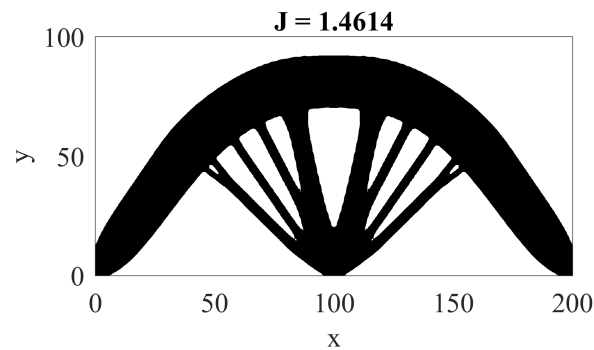


Figure C.21: Multi-load michell structure: optimal topology layout when loads are applied at the same time.

C.6 Extensions

C.6.1 Bisection algorithm

The bisection algorithm of the *cutting&bisection* algorithm, which estimates the solution as the midpoint of the bracketing interval (see section C.4.8), can be easily improved by introducing either a *regula falsi method* [9] or a more sophisticated method, like the *Anderson-Björk with Illinois algorithm* [4]. These two mathematical techniques reduce the number of iterations required to find the root of the *constraint equation* ((25)-b), C .

Regula falsi

In order to compute the test `lambda`¹³ through the *regula falsi* approximation inside the *bisection algorithm* [9], line 143 must be replaced by

```
143 lambda = 11 - c1*(12-11)/(c2-c1);
```

where 11 and 12 stand for the left and right λ brackets, while c_1 and c_2 are respectively the corresponding constraint values. The linear interpolation with the endpoints of the bracketing interval is used to find the value of the root, i.e. the root is approximated as the intersecting point between the line joining the extremes and the x-axis. Next, the subinterval is updated by checking the sign of the constraint equation at `lambda`, as mentioned in section C.4.8, until the tolerance is attained.

¹³The *Lagrange multiplier* is denoted as `lambda` in the code.

Anderson-Björck with Illinois algorithm

The *regula falsi* method usually converges faster than the regular *bisection algorithm*. However, for some specific situations, it can show slower convergence. To avoid these numerical instabilities, the *Anderson-Björck algorithm with an Illinois algorithm* [4] is implemented. ¹⁴ Lines 143 and 152 are changed to:

```

143 lambda = l1 - c1*(l2-l1)/(c2-c1);
and
152-1 if c2*Tol_constr<=0; l1=l2; c1=c2; l2=lambda; c2=Tol_constr;
152-2 else; g=1-Tol_constr/c2; g=(g-0.5)*(g>0)+0.5; l2=lambda; c1=g*c1; c2=
Tol_constr; end

```

With these changes, the number of iterations and the computational cost/time of the optimization procedure is reduced.

C.6.2 Plane-strain assumption

The corresponding constitutive tensor, $\bar{\mathbb{C}}$, for the plane-strain assumption

$$\bar{\mathbb{C}}^{Pstrain} = \frac{E}{(1-\nu)(1-2\nu)} \begin{bmatrix} 1-\nu & \nu & 0 \\ \nu & 1-\nu & 0 \\ 0 & 0 & \frac{1-2\nu}{2} \end{bmatrix} \quad (48)$$

can be easily used by replacing the definition of the constitutive tensor of the plane-stress assumption, see section C.3.2, in lines 126-127 with the following

```

126 function [DE] = D_matrix_strain(E,nu) %Planestrain
127 DE = E/((1+nu)*(1-2*nu))*[(1-nu) nu 0;nu (1-nu) 0;0 0 (1-2*nu)/2];

```

Line 27 must be also modified, to call the `D_matrix_strain` function, to

```

27 [DE] = D_matrix_stress(E0,nu);

```

C.6.3 Augmented Lagrangian to impose volume constraint

The constraint equation (25)-b, \mathcal{C} , can be also imposed through an Augmented Lagrangian method [20], which updates the lagrangian multiplier according the following definition

$$\lambda_{i+1} = \lambda_i + \rho \mathcal{C}_i, \quad (49)$$

to prescribed an equality constraint. The penalty value, ρ , can be either set to a constant value or increased along iterations, which improves convergence rate. Then, the penalty coefficient is updated as

$$\rho_{i+1} = \begin{cases} \min(1.02\rho_i, 100\rho_0) & \text{for } |\mathcal{C}_{i+1} - \mathcal{C}_i| < 10^{-3} \\ \rho_i & \text{otherwise,} \end{cases} \quad (50)$$

where ρ_0 corresponds to the initial penalty value and i represents the i -th iteration. The values 1.02 and 100 can be modified at the user's discretion, and will highly depend on each specific numerical example. In this implementation, the Lagrangian equation (8) is defined as

$$\mathcal{L} = J + \lambda \mathcal{C} + \frac{1}{2} \rho \mathcal{C}^2. \quad (51)$$

¹⁴On one hand, the *Illinois* method [12] seeks to eliminate the ill-condition generated by permanently retaining one of the end-points (always set to the left bracket in the code). This issue is fixed by multiplying the retained extreme point by $g = 0.5$. On the other hand, *Anderson-Björck algorithm* improves the *regula falsi approach* by combining linear interpolation (when the left bracket should be replaced) with parabolic interpolation (when the right bracket should be replaced). Furthermore, it includes an *Illinois-scheme* with $g = 1 - \frac{\mathcal{C}(\lambda)}{\mathcal{C}(\lambda_2)}$, when g is positive, or 0.5, otherwise.

In order to impose the constraint with this methodology, a few changes need to be made to the original code of Appendix C.A. First, the initialization of constraint vector and the penalty value must be initialized by inserting

```
Tol_constr_vec = []; rho = rho0;
```

between lines 57 and 58, and the constraint must be computed before starting the optimization loop, just below line 64:

```
Tol_constr = t_ref - vol;
```

and stored in the corresponding vector after line 95

```
Tol_constr_vec = [Tol_constr_vec, abs(Tol_constr)];
```

The convergence criteria of line 65 must be also changed to include the constraint equation as an extra convergence condition by introducing `abs(Tol_constr)>1e-3`.

Second, the *bisection algorithm* (lines 137-146) and its function call in the optimization loop (line 88) must be replaced with the corresponding updating of λ and ρ (equations (49) and (50)), defined as

```
function [lambda,rho,chi,psi,vol,Tol_constr] = find_volume (iter,xi,connect,
    active_node,passive_node,t_ref,lambda,rho,rho0,alpha0,Tol_constr,
    Tol_constr_vec)
lambda = lambda + rho * Tol_constr;
psi = xi - lambda; psi(passive_node) = -alpha0; psi(active_node) = alpha0;
[vol,chi] = compute_volume (psi,connect);
Tol_constr = -(vol-t_ref);
if iter>=3; rho = min(0.02*rho*(abs(diff(Tol_constr_vec(end-1:end))))<1e-3) +
    rho,100*rho0); end
```

and

```
88 [lambda,rho,chi_n,psi,vol,Tol_constr] = find_volume (iter,xi,connect,
    active_node,passive_node,t_ref,lambda,rho,rho0,alpha0,Tol_constr,
    Tol_constr_vec);
```

Last, the cost function must be computed according equation (51), which takes into account the constraint equation. The additional terms are summed in one extra line under line 69:

```
J = J + nelx*nely*(lambda*Tol_constr + rho*Tol_constr^2)/J_ref*xi_norm;
```

C.6.4 Thermal problem

According to Yago *et al.* [40], the implementation of the thermal compliance problem is rather analogous to the structural mean compliance problem, detailed in section C.3.5. In that case, the temperature, $\hat{\theta}$, is the only unknown per node (`n_unkn=1`) and the steady-state problem is used as the state equation. Therefore, the cost function (24) has to be replaced by

$$\mathcal{J}(\theta_\chi) \equiv \frac{1}{2}l(\theta_\chi) = \frac{1}{2}a_\chi(\theta_\chi, \theta_\chi) = \frac{1}{2} \left(\int_{\Omega} \nabla \theta_\chi \cdot \boldsymbol{\kappa}_\chi \cdot \nabla \theta_\chi d\Omega \right) = \int_{\Omega} \mathcal{U}_\chi d\Omega, \quad (52)$$

where $l(\theta_\chi)$ and $a_\chi(\theta_\chi, \theta_\chi)$ correspond to the bilinear forms of the thermal problem. Furthermore, $\nabla \theta_\chi$ and $\boldsymbol{\kappa}_\chi$ represent the thermal gradient vector and the symmetric second order thermal conductivity tensor, respectively. Unlike the elastic material behavior used in section C.3.2, the conductive material follows Fourier's law, i.e. the heat flux is proportional to the thermal gradient by $\mathbf{q}(\mathbf{x}, \chi) = -\boldsymbol{\kappa}(\mathbf{x}, \chi) \cdot \nabla \theta_\chi(\mathbf{x})$.

The state equation (14) must be also substituted by

$$\left[\begin{array}{l} \text{Find the temperature field } \boldsymbol{\theta}_\chi \in \mathcal{U}(\Omega) \text{ such that} \\ a(w, \boldsymbol{\theta}_\chi) = l(w) \quad \forall w \in \mathcal{V}(\Omega) \end{array} \right. \quad (53)$$

where

$$a(w, \boldsymbol{\theta}_\chi) = \int_{\Omega} \nabla w(\mathbf{x}) \cdot \boldsymbol{\kappa}_\chi(\mathbf{x}) \cdot \nabla \boldsymbol{\theta}_\chi(\mathbf{x}) \, d\Omega, \quad (54)$$

$$l(w) = - \int_{\partial_q \Omega} w(\mathbf{x}) \bar{q}(\mathbf{x}) \, d\Gamma + \int_{\Omega} w(\mathbf{x}) r_\chi(\mathbf{x}) \, d\Omega, \quad (55)$$

where $\mathcal{U}(\Omega)$ and $\mathcal{V}(\Omega)$ stand for the corresponding set of admissible temperature fields and the corresponding space of admissible virtual temperature fields, respectively. $r(\mathbf{x}, \chi)$ and $\bar{q}(\mathbf{x})$ correspond respectively to the heat source function and the prescribed heat flux on the boundaries of Ω .

After applying the RTD to equation (52), mimicking the procedure described in section C.3.5, the resultant *pseudo-energy*, $\xi(\hat{\mathbf{x}})$, is expressed as

$$\xi(\hat{\mathbf{x}}, \chi) = -m_\kappa (\chi_\kappa(\hat{\mathbf{x}}))^{m_\kappa - 1} \bar{\mathcal{U}}(\hat{\mathbf{x}}) \Delta \chi_\kappa(\hat{\mathbf{x}}), \quad (56)$$

with

$$\bar{\mathcal{U}}(\hat{\mathbf{x}}) = \frac{1}{2} (\nabla \boldsymbol{\theta}_\chi \cdot \bar{\boldsymbol{\kappa}} \cdot \nabla \boldsymbol{\theta}_\chi)(\hat{\mathbf{x}}) \geq 0. \quad (57)$$

Several modification to the provided code, based on equation (52) to (56), are required in order to solve thermal problems. The most relevant ones are listed next: the number of unknowns per node must be set to 1, the gradient matrix, \mathbf{B} , must be adjusted to be equal to the Cartesian derivatives, the material property is now the conductivity value of the high conductive material instead of E and ν and the constitutive tensor $\boldsymbol{\kappa}$ is now defined as

$$\boldsymbol{\kappa} = \kappa \begin{bmatrix} K_{11} & K_{12} \\ K_{21} & K_{22} \end{bmatrix}. \quad (58)$$

In addition, boundary condition must be defined accordingly to the thermal problem.

C.6.5 3D extension

The topology optimization code *UNVARTOP* can be readily extended to solve 3D problems. All the functions related to FE analysis must be rewritten, starting from the mesh, the shape matrices \mathbf{N} , the corresponding strain-displacement matrices \mathbf{B} and the constitutive tensor \mathbb{C} . Therefore, element stiffness matrices should be recomputed, along with the stiffness and mass matrices for the Laplacian regularization. It is recommended to use an iterative solver (e.g. `minres` solver) to compute the displacements, as employed for the Laplacian regularization (see section C.4.8), in order to reduce computational cost. Function `compute_volume` must be slightly adapted to hexahedral elements. In addition, functions `isosurface`, `isocaps` and `isonormals` must be used to represent the optimal topology.

It is important to notice that the algorithm inside the topology optimization does not require any modification.

C.7 Conclusions

This paper has presented the 2D implementation in Matlab of the unsmooth variational topology optimization approach, previously formulated for structural [22] and thermal [40] topology optimization problems. The paper described and implemented the approach for educational

purposes while demonstrating its capabilities and maintaining high computational efficiency and readability of the code. Furthermore, the implementation preserves the finite element analysis of the domain, thus introducing students to the numerical analysis as well as the topology optimization field.

The numerical examples performed in this work illustrate the potential and effectiveness of the technique to tackle a large set of different problems with a volume constraint, e.g. minimum mean compliance problems (section C.3.5), multi-load mean compliance problems (section C.3.6) and compliant mechanisms synthesis (section C.3.7). The set of numerical examples include a variety of boundary conditions, active and passive nodes, number of time-steps, along others. Additionally, section C.6.4 shows how to easily switch from the structural problem of minimum mean compliance to the thermal problem, where thermal compliance is minimized. Finally, section C.6.5 provides some guidelines for the extension of the code to the resolution of 3D problems.

The topologies obtained for these examples are comparable to those shown by other researchers using more established techniques (e.g. SIMP method or Level-set method). In addition, smooth topology configuration have been obtained in all the benchmarks with a relatively small number of iterations. That is a feature to be highlighted against more conventional techniques based on elemental densities, such as SIMP method.

In conclusion, the dissemination of this code will provide newcomers in this field a better understanding in how this new topology optimization approach works as well as to encourage future research of this technique for miscellaneous applications.

The Matlab code, detailed in appendix C.A, along with some variations of it, can be downloaded from the author's GitHub repository <https://github.com/DanielYago/UNVARTOP>. Additional online resources, such as figures and animations, are also stored in the repository.

C.8 Acknowledgements

This research has received funding from the European Research Council (ERC) under the European Union's Horizon 2020 research and innovation programme (Proof of Concept Grant agreement n 874481) through the project "Computational design and prototyping of acoustic metamaterials for target ambient noise reduction" (METACOUSTIC). The authors also acknowledge financial support from the Spanish Ministry of Economy and Competitiveness, through the research grant DPI2017-85521-P for the project "Computational design of Acoustic and Mechanical Metamaterials" (METAMAT) and through the "Severo Ochoa Programme for Centres of Excellence in R&D" (CEX2018-000797-S). D. Yago acknowledges the support received from the Spanish Ministry of Education through the FPU program for PhD grants.

Conflict of interest

The authors declare that they have no conflict of interest as regards this work.

C.A Matlab code

```

1 function [iter,J] = UNVARTOP_2D_compliance (nelx,nely,nsteps,Vol0,Vol1,k,tau)
2 n_dim = 2; n_unkn = 2; n_nodes = 4; n_gauss = 4; n = (nelx+1)*(nely+1); h_e
   = 1; alpha0 = 1e-3;
3 iter_max_step = 20; iter_min_step = 4; iter_max = 500;
4 opt = struct('Plot_top_iso',1,'Plot_vol_step',1,'EdgeColor','none','
   solver_Lap','direct');
5 %% Vector for assembling matrices
6 [X,Y] = meshgrid(0:nelx,nely:-1:0); coord = [X(:),Y(:)]; clear X Y
7 nodenrs = reshape(1:n,1+nely,1+nelx);
8 nodeVec = reshape(nodenrs(1:end-1,1:end-1)+1,nelx*nely,1); clear nodenrs;

```

```

9 connect = nodeVec+[0 nely+[1 0] -1]; clear nodeVec;
10 %% Loads and boundary setting for Cantilever beam
11 F = sparse(n_unkn*n,1);
12 U = zeros(n_unkn*n,1);
13 F(n_unkn*find(coord(:,2)==0 & coord(:,1)==nelx),1) = -0.01*nelx;
14 fixed_dofs = reshape(n_unkn*find(coord(:,1)==0)+(-n_unkn+1:0),1,[]);
15 active_node = []; passive_node = [];
16 free_dofs = setdiff(1:(n_unkn*n),fixed_dofs);
17 U(fixed_dofs,:) = 0;
18 %% Parameter definition
19 m = 5; E0 = 1; alpha = 1e-6; beta = nthroot(alpha,m); nu = 0.3;
20 %% Prepare animation
21 psi_vec = zeros(size(coord,1),nsteps+1);
22 chi_vec = zeros(size(connect,1),nsteps+1);
23 U_vec = zeros(n_unkn*size(coord,1),1,nsteps+1);
24 %% Finite element analysis preparation
25 [posgp4,W4] = gauss_points(n_gauss);
26 [posgp1,W1] = gauss_points(1);
27 [DE] = D_matrix_stress(E0,nu);
28 KE = zeros(n_nodes*n_unkn,n_nodes*n_unkn);
29 KE_i = zeros(n_nodes*n_unkn,n_nodes*n_unkn,n_gauss);
30 for i=1:n_gauss
31 [BE,Det_Jacobian] = B_matrix(posgp4(:,i),n_unkn,n_nodes);
32 KE_i(:, :, i) = BE'*DE*BE;
33 KE = KE + KE_i(:, :, i)*Det_Jacobian*W4(i);
34 end
35 [BE_cut,Det_Jacobian_cut] = B_matrix(posgp1,n_unkn,n_nodes);
36 K_cut = BE_cut'*DE*BE_cut;
37 KE_cut = K_cut*Det_Jacobian_cut*W1(1);
38 edofMat = kron(connect,n_unkn*ones(1,n_unkn)) + repmat(1-n_unkn:0,1,n_nodes)
;
39 iK = reshape(kron(edofMat,ones(n_nodes*n_unkn,1))',(n_nodes*n_unkn)^2*nelx*
nely,1);
40 jK = reshape(kron(edofMat,ones(1,n_nodes*n_unkn))',(n_nodes*n_unkn)^2*nelx*
nely,1);
41 %% Laplacian filter preparation
42 KE_Lap = 1/6* [ 4 -1 -2 -1;-1 4 -1 -2;-2 -1 4 -1;-1 -2 -1 4];
43 ME_Lap = 1/36*[ 4 2 1 2; 2 4 2 1; 1 2 4 2; 2 1 2 4];
44 KE_Lap = ME_Lap + (tau*h_e).^2*KE_Lap;
45 i_KF = reshape(kron(connect,ones(n_nodes,1))',n_nodes^2*nelx*nely,1);
46 j_KF = reshape(kron(connect,ones(1,n_nodes))',n_nodes^2*nelx*nely,1);
47 s_KF = reshape(KE_Lap(:)*ones(1,nelx*nely),n_nodes^2*nelx*nely,1); clear
KE_Lap ME_Lap;
48 K_Lap = sparse(i_KF,j_KF,s_KF);
49 if strcmp(opt.solver_Lap,'direct'); LF = chol(K_Lap,'lower'); clear K_Lap
i_KF j_KF s_KF;
50 else; LF = ichol(K_Lap, struct('type','ict','droptol',1e-3,'diagcomp',0.1));
clear i_KF j_KF s_KF; end
51 i_xi = reshape(connect',n_nodes*nelx*nely,1);
52 N_T = N_matrix(posgp4).*W4/4;
53 %% Loop over steps
54 psi = alpha0*ones(n,1); psi(passive_node) = -alpha0; psi(active_node) =
alpha0; psi_vec(:,1)=psi;
55 [~,chi] = compute_volume(psi,connect); chi0_step = chi; chi_vec(:,1) = chi
;
56 % Initialize variables
57 iter = 1; J_vec = []; vol_vec = []; lambda_vec = 0; lambda = 0; fhandle6 =
[];
58 [fhandle2,ohandle2] = plot_isosurface([],[],0,psi,coord,connect,1,opt);
59 for i_step = 1:nsteps
60 [t_ref] = set_reference_volume(i_step,Vol0,Vol,nsteps,k);
61 % Main loop by steps
62 Tol_chi = 1;
63 Tol_lambda = 1;
64 iter_step = 1;

```

```

65 while (((Tol_chi>1e-1 || Tol_lambda>1e-1) && iter_step<iter_max_step) ||
iter_step<=iter_min_step)
66 % FE-analysis
67 [K] = assmbeley_stiff_mat (chi,KE,KE_cut,beta,m,iK,jK,n_unkn,nelx,nely);
68 U(free_dofs,:) = K(free_dofs,free_dofs) \ (F(free_dofs,:) - K(free_dofs,
fixed_dofs)*U(fixed_dofs,:));
69 if iter == 1; U_vec(:, :, 1)=U; J_ref = full(abs(sum(sum(F.*U,1),2))); end;
J = full(sum(sum(F.*U,1),2))/J_ref;
70 % Calculate sensitivities
71 Energy = zeros(n_gauss,nelx*nely);
72 id = chi==1|chi==0; int_chi = interp_property (m,m-1,beta,chi(id));
73 u_e = reshape(U(edofMat(id,:)',1),n_nodes*n_unkn,[]); w_e = u_e;
74 for i=1:n_gauss; Energy(i,id) = sum(w_e.*(KE_i(:, :, i)*u_e),1); end
75 Energy(:,id) = int_chi.*Energy(:,id);
76 id = ~id; int_chi = interp_property (m,m-1,beta,chi(id));
77 u_e = reshape(U(edofMat(id,:)',1),n_nodes*n_unkn,[]); w_e = u_e;
78 Energy(:,id) = repmat(int_chi.*sum(w_e.*(K_cut*u_e),1),n_gauss,1);
79 if iter == 1; xi_shift = min(0,min(Energy(:))); xi_norm = max(range(Energy
(:)),max(Energy(:))); end
80 % Apply Laplacian regularization
81 xi_int = N_T*(Energy-xi_shift*chi)/xi_norm;
82 if strcmp(opt.solver_Lap,'direct')
83 xi = LF'\(LF\accumarray(i_xi,xi_int(:),[n 1]));
84 else
85 [xi,flag] = minres(K_Lap,accumarray(i_xi,xi_int(:),[n 1]),1e-6,500,LF,LF
'); assert(flag == 0);
86 end
87 % Compute topology
88 [lambda,chi_n,psi,vol] = find_volume (xi,connect,active_node,passive_node,
t_ref,lambda,alpha0);
89 lambda_vec = [lambda_vec,lambda];
90 Tol_lambda = (lambda_vec(iter+1)-lambda_vec(iter))/lambda_vec(iter+1);
91 % Plot topology
92 [fhandle2,ohandle2] = plot_isosurface(fhandle2,ohandle2,iter,psi,coord,
connect,J,opt);
93 % Update variables
94 Tol_chi = sqrt(sum((chi-chi_n).^2))/sqrt(sum(chi0_step.^2));
95 chi = chi_n;
96 fprintf(' Step:%5i It.:%5i Obj.:%11.4f Vol.:%7.3f \n',i_step,iter_step,J,
vol);
97 iter_step = iter_step+1; iter = iter+1;
98 drawnow;
99 end
100 chi0_step = chi;
101 if J<10
102 [fhandle6,J_vec,vol_vec] = plot_volume_iter(fhandle6,i_step,J_vec,J,
vol_vec,vol,opt.Plot_vol_step,6,'Cost function Step','#step','+-b');
103 psi_vec(:,i_step+1)=psi; chi_vec(:,i_step+1)=chi; U_vec(:, :, i_step+1)=U;
104 end
105 if iter_step >= iter_max_step; warning('VarTopOpt:Max_iter_step','Maximum
number of in-step iterations achieved.');
```

```

119 function [BE, Det_Jacobian, cart_deriv] = B_matrix(posgp, n_unkn, n_nodes)
120 dshape = 0.25*[-1 -1; 1 -1; 1 1; -1 1]'.* flip(1+[-1 -1; 1 -1; 1 1; -1 1]'.*posgp
    ,1);
121 Jacobian_mat = dshape*[0 0; 1 0; 1 1; 0 1];
122 Det_Jacobian = det(Jacobian_mat);
123 cart_deriv = Jacobian_mat\dshape;
124 BE = zeros(3, n_unkn*n_nodes); BE([1 3], 1:n_unkn:end) = cart_deriv; BE([3
    2], 2:n_unkn:end) = cart_deriv;
125 %%%% %%%% %%%% %%%% %%%% %%%% %%%% %%%% %%%% %%%%
126 function [DE] = D_matrix_stress(E, nu) %Planestress
127 DE = E/(1-nu^2)*[1 nu 0; nu 1 0; 0 0 (1-nu)/2];
128 %%%% %%%% %%%% %%%% %%%% %%%% %%%% %%%% %%%% %%%%
129 function [coeff] = interp_property (m, n, beta, chi)
130 coeff = chi + (1-chi).*beta;
131 coeff = double(m==n).*coeff.^m + double(m~=n).*m*coeff.^n*(1-beta);
132 %%%% %%%% %%%% %%%% %%%% %%%% %%%% %%%% %%%% %%%%
133 function [K] = assmely_stiff_mat (chi, KE, KE_cut, beta, m, iK, jK, n_unkn, nelx,
    nely)
134 sK = interp_property(m, m, beta, chi).*KE(:); sK(:, chi~=1&chi~=0) =
    interp_property(m, m, beta, chi(chi~=1&chi~=0)).*KE_cut(:);
135 K = sparse(iK, jK, sK, n_unkn*(1+nelx)*(1+nely), n_unkn*(1+nelx)*(1+nely)); K =
    (K+K')/2; clear sK;
136 %%%% %%%% %%%% %%%% %%%% %%%% %%%% %%%% %%%% %%%%
137 function [lambda, chi, psi, vol, Tol_constr] = find_volume (xi, connect,
    active_node, passive_node, t_ref, lambda, alpha0)
138 l1 = min(xi); c1 = t_ref; l2 = max(xi); c2 = t_ref-1; Tol_constr = 1; iter
    =1;
139 if lambda>l1 && lambda<l2
140 [chi, psi, vol, l1, l2, c1, c2, Tol_constr] = compute_volume_lambda(xi, connect,
    active_node, passive_node, t_ref, lambda, l1, l2, c1, c2, alpha0);
141 end
142 while (abs(Tol_constr)>1e-4) && iter<1000
143 lambda = 0.5*(l1+l2);
144 [chi, psi, vol, l1, l2, c1, c2, Tol_constr] = compute_volume_lambda(xi, connect,
    active_node, passive_node, t_ref, lambda, l1, l2, c1, c2, alpha0);
145 iter = iter + 1;
146 end
147 %%%% %%%% %%%% %%%% %%%% %%%% %%%% %%%% %%%% %%%%
148 function [chi, psi, vol, l1, l2, c1, c2, Tol_constr] = compute_volume_lambda(xi,
    connect, active_node, passive_node, t_ref, lambda, l1, l2, c1, c2, alpha0)
149 psi = xi - lambda; psi(passive_node) = -alpha0; psi(active_node) = alpha0;
150 [vol, chi] = compute_volume (psi, connect);
151 Tol_constr = -(vol-t_ref);
152 if Tol_constr > 0, l1 = lambda; c1 = Tol_constr; else; l2 = lambda; c2 =
    Tol_constr; end
153 %%%% %%%% %%%% %%%% %%%% %%%% %%%% %%%% %%%% %%%%
154 function [volume, chi] = compute_volume (psi, connect)
155 P = [-1 -1; 1 -1; 1 1; -1 1]; dvol = 1/4;
156 s = [-0.9324695142031521 -0.6612093864662645 -0.2386191860831969
    0.2386191860831969 0.6612093864662645 0.9324695142031521]; [s, t] =
    meshgrid(s, s);
157 W = [ 0.1713244923791704 0.3607615730481386 0.4679139345726910
    0.4679139345726910 0.3607615730481386 0.1713244923791704]; W=w'*w; W=W(:)
    ';
158 psi_n = psi(connect); chi = sum((sign(psi_n)+1), 2)'/8; id = chi~=1&chi~=0;
159 phi_x = psi_n(id, :).*((1+P(:, 1)*s(:)')*(1+P(:, 2)*t(:)'))/4;
160 chi(1, id) = (W*(phi_x>0)'+ 0.5*W*(phi_x==0)')*dvol;
161 volume = 1 - sum(chi) / size(connect, 1);
162 %%%% %%%% %%%% %%%% %%%% %%%% %%%% %%%% %%%% %%%%
163 function [fig_handle, obj_handle] = plot_isosurface(fig_handle, obj_handle,
    iter, psi, coord, connect, J, opt)
164 if opt.Plot_top_iso
165 if iter==0; fig_handle = figure(2); set(fig_handle, 'Name', 'Topology');
    caxis([-1 1]); colormap(flip(gray(2)));
166 axis equal tight; xlabel('x'); ylabel('y'); title(['J = ', num2str(J)]);

```

```

167 obj_handle = patch('Vertices', coord, 'Faces', connect, 'FaceVertexCData', psi,
    'EdgeColor', opt.EdgeColor, 'FaceColor', 'interp');
168 else
169 set(0, 'CurrentFigure', fig_handle); set(get(gca, 'Title'), 'String', ['J = '
    , num2str(J)]);
170 set(obj_handle, 'FaceVertexCData', psi);
171 end
172 end
173 %%%% %%%% %%%% %%%% %%%% %%%% %%%% %%%% %%%% %%%%
174 function [fig_handle, J_vec, vol_vec] = plot_volume_iter(fig_handle, iter, J_vec
    , J, vol_vec, vol, opt_plot, fig_num, fig_name, xlabel_name, linestyle)
175 J_vec = [J_vec, J]; vol_vec = [vol_vec, vol];
176 if opt_plot
177 if iter==1; fig_handle = figure(fig_num); set(fig_handle, 'Name', fig_name);
178 subplot(2,1,1); plot(J_vec, linestyle); ylabel('$\mathcal{J}_\chi$', '
    Interp', 'Latex'); xlabel(xlabel_name); grid; grid minor;
179 subplot(2,1,2); plot(vol_vec, linestyle); ylabel('\Omega^|');
    xlabel(xlabel_name); grid; grid minor;
180 else; set(0, 'CurrentFigure', fig_handle);
181 subplot(2,1,1); set(findobj(gca, 'Type', 'line'), 'Xdata', 1:numel(J_vec), '
    YData', J_vec);
182 subplot(2,1,2); set(findobj(gca, 'Type', 'line'), 'Xdata', 1:numel(vol_vec), '
    YData', vol_vec);
183 end
184 end
185 %%%% %%%% %%%% %%%% %%%% %%%% %%%% %%%% %%%% %%%%
186 function [vol] = set_reference_volume(iter, Vol0, Volf, nsteps, k)
187 if k==0; vol=Vol0+(Volf-Vol0)/nsteps*iter;
188 else; C1=(Vol0-Volf)/(1-exp(k)); C2=Vol0-C1; vol=C1*exp(k*iter/nsteps)+C2;
    end

```

Listing 1: UNVARTOP code written in Matlab

Replication of results

The Matlab codes provided in the paper, in Appendix C.A and [GitHub repository](#), are the same ones used for obtaining the results here presented (Section C.5). Therefore, they can be fully used as a replication tool, to reproduce those results, as well as to be used in additional numerical simulations.

References

- [1] G. Allaire, E. Bonnetier, G. Francfort, and F. Jouve, “Shape optimization by the homogenization method,” *Numerische Mathematik*, vol. 76, no. 1, pp. 27–68, 1997. DOI: [10.1007/s002110050253](https://doi.org/10.1007/s002110050253).
- [2] G. Allaire, F. Jouve, and A.-M. Toader, “A level-set method for shape optimization,” *Comptes Rendus Mathematique*, vol. 334, no. 12, pp. 1125–1130, Jan. 2002. DOI: [10.1016/s1631-073x\(02\)02412-3](https://doi.org/10.1016/s1631-073x(02)02412-3).
- [3] G. Allaire, F. Jouve, and A.-M. Toader, “Structural optimization using sensitivity analysis and a level-set method,” *Journal of Computational Physics*, vol. 194, no. 1, pp. 363–393, 2004. DOI: [10.1016/j.jcp.2003.09.032](https://doi.org/10.1016/j.jcp.2003.09.032).
- [4] N. Anderson and Å. Björck, “A new high order method of regula falsi type for computing a root of an equation,” *BIT*, vol. 13, no. 3, pp. 253–264, Sep. 1973. DOI: [10.1007/bf01951936](https://doi.org/10.1007/bf01951936).
- [5] E. Andreassen, A. Clausen, M. Schevenels, B. S. Lazarov, and O. Sigmund, “Efficient topology optimization in MATLAB using 88 lines of code,” *Structural and Multidisciplinary Optimization*, vol. 43, no. 1, pp. 1–16, Nov. 2010. DOI: [10.1007/s00158-010-0594-7](https://doi.org/10.1007/s00158-010-0594-7).

- [6] M. P. Bendsøe, “Optimal shape design as a material distribution problem,” *Structural Optimization*, vol. 1, no. 4, pp. 193–202, Dec. 1989. DOI: [10.1007/bf01650949](https://doi.org/10.1007/bf01650949).
- [7] M. P. Bendsøe and O. Sigmund, *Topology Optimization*. Springer Berlin Heidelberg, 2004. DOI: [10.1007/978-3-662-05086-6](https://doi.org/10.1007/978-3-662-05086-6).
- [8] E. Biyikli and A. C. To, “Proportional topology optimization: A new non-sensitivity method for solving stress constrained and minimum compliance problems and its implementation in MATLAB,” *PLOS ONE*, vol. 10, no. 12, Y. Shi, Ed., e0145041, Dec. 2015. DOI: [10.1371/journal.pone.0145041](https://doi.org/10.1371/journal.pone.0145041).
- [9] R. Bulirsch and J. Stoer, *Introduction to Numerical Analysis*. Springer New York, Dec. 1, 2010, 764 pp., ISBN: 144193006X.
- [10] V. J. Challis, “A discrete level-set topology optimization code written in matlab,” *Structural and Multidisciplinary Optimization*, vol. 41, no. 3, pp. 453–464, Sep. 2009. DOI: [10.1007/s00158-009-0430-0](https://doi.org/10.1007/s00158-009-0430-0).
- [11] D. Da, L. Xia, G. Li, and X. Huang, “Evolutionary topology optimization of continuum structures with smooth boundary representation,” *Structural and Multidisciplinary Optimization*, vol. 57, no. 6, pp. 2143–2159, Nov. 2017. DOI: [10.1007/s00158-017-1846-6](https://doi.org/10.1007/s00158-017-1846-6).
- [12] M. Dowell and P. Jarratt, “A modified regula falsi method for computing the root of an equation,” *BIT*, vol. 11, no. 2, pp. 168–174, Jun. 1971. DOI: [10.1007/bf01934364](https://doi.org/10.1007/bf01934364).
- [13] R. A. Feijoo, A. A. Novotny, E. Taroco, and C. Padra, “The topological-shape sensitivity method in two-dimensional linear elasticity topology design,” *Applications of Computational Mechanics in Structures and Fluids*, 2005.
- [14] S. M. Giusti, A. A. Novotny, and C. Padra, “Topological sensitivity analysis of inclusion in two-dimensional linear elasticity,” *Engineering Analysis with Boundary Elements*, vol. 32, no. 11, pp. 926–935, 2008. DOI: [10.1016/j.enganabound.2007.12.007](https://doi.org/10.1016/j.enganabound.2007.12.007).
- [15] J. K. Guest, J. H. Prévost, and T. Belytschko, “Achieving minimum length scale in topology optimization using nodal design variables and projection functions,” *International Journal for Numerical Methods in Engineering*, vol. 61, no. 2, pp. 238–254, 2004. DOI: [10.1002/nme.1064](https://doi.org/10.1002/nme.1064).
- [16] B. S. Lazarov and O. Sigmund, “Filters in topology optimization based on helmholtz-type differential equations,” *International Journal for Numerical Methods in Engineering*, vol. 86, no. 6, pp. 765–781, Dec. 2010. DOI: [10.1002/nme.3072](https://doi.org/10.1002/nme.3072).
- [17] Q. Q. Liang and G. P. Steven, “A performance-based optimization method for topology design of continuum structures with mean compliance constraints,” *Computer Methods in Applied Mechanics and Engineering*, vol. 191, no. 13-14, pp. 1471–1489, Jan. 2002. DOI: [10.1016/s0045-7825\(01\)00333-4](https://doi.org/10.1016/s0045-7825(01)00333-4).
- [18] K. Liu and A. Tovar, “An efficient 3d topology optimization code written in matlab,” *Structural and Multidisciplinary Optimization*, vol. 50, no. 6, pp. 1175–1196, 2014. DOI: [10.1007/s00158-014-1107-x](https://doi.org/10.1007/s00158-014-1107-x).
- [19] C. G. Lopes, R. B. dos Santos, and A. A. Novotny, “Topological derivative-based topology optimization of structures subject to multiple load-cases,” *Latin American Journal of Solids and Structures*, vol. 12, no. 5, pp. 834–860, May 2015. DOI: [10.1590/1679-78251252](https://doi.org/10.1590/1679-78251252).
- [20] D. G. Luenberger and Y. Ye, *Linear and Nonlinear Programming*. Springer International Publishing, 2016. DOI: [10.1007/978-3-319-18842-3](https://doi.org/10.1007/978-3-319-18842-3).
- [21] A. A. Novotny, R. A. Feijóo, E. Taroco, and C. Padra, “Topological sensitivity analysis,” *Computer Methods in Applied Mechanics and Engineering*, vol. 192, no. 7-8, pp. 803–829, 2003. DOI: [10.1016/s0045-7825\(02\)00599-6](https://doi.org/10.1016/s0045-7825(02)00599-6).

- [22] J. Oliver, D. Yago, J. Cante, and O. Lloberas-Valls, “Variational approach to relaxed topological optimization: Closed form solutions for structural problems in a sequential pseudo-time framework,” *Computer Methods in Applied Mechanics and Engineering*, vol. 355, pp. 779–819, Oct. 2019. DOI: [10.1016/j.cma.2019.06.038](https://doi.org/10.1016/j.cma.2019.06.038).
- [23] S. Osher and J. A. Sethian, “Fronts propagating with curvature-dependent speed: Algorithms based on hamilton-jacobi formulations,” *Journal of Computational Physics*, vol. 79, no. 1, pp. 12–49, 1988. DOI: [10.1016/0021-9991\(88\)90002-2](https://doi.org/10.1016/0021-9991(88)90002-2).
- [24] M. Otomori, T. Yamada, K. Izui, and S. Nishiwaki, “Matlab code for a level set-based topology optimization method using a reaction diffusion equation,” *Structural and Multidisciplinary Optimization*, vol. 51, no. 5, pp. 1159–1172, 2014. DOI: [10.1007/s00158-014-1190-z](https://doi.org/10.1007/s00158-014-1190-z).
- [25] G. Patanè and B. Falcidieno, “Computing smooth approximations of scalar functions with constraints,” *Computers & Graphics*, vol. 33, no. 3, pp. 399–413, Jun. 2009. DOI: [10.1016/j.cag.2009.03.014](https://doi.org/10.1016/j.cag.2009.03.014).
- [26] S. S. Rao, *The Finite Element Method in Engineering*. Butterworth-Heinemann, 2004, ISBN: 0-7506-7828-3.
- [27] O. Sigmund, “A 99 line topology optimization code written in matlab,” *Structural and Multidisciplinary Optimization*, vol. 21, no. 2, pp. 120–127, Apr. 2001. DOI: [10.1007/s001580050176](https://doi.org/10.1007/s001580050176).
- [28] O. Sigmund and J. Petersson, “Numerical instabilities in topology optimization: A survey on procedures dealing with checkerboards, mesh-dependencies and local minima,” *Structural Optimization*, vol. 16, no. 1, pp. 68–75, 1998. DOI: [10.1007/bf01214002](https://doi.org/10.1007/bf01214002).
- [29] J. Sokolowski and A. Zochowski, “On the topological derivative in shape optimization,” *SIAM Journal on Control and Optimization*, vol. 37, no. 4, pp. 1251–1272, Jan. 1999. DOI: [10.1137/s0363012997323230](https://doi.org/10.1137/s0363012997323230).
- [30] K. Suresh, “A 199-line matlab code for pareto-optimal tracing in topology optimization,” *Structural and Multidisciplinary Optimization*, vol. 42, no. 5, pp. 665–679, Jul. 2010. DOI: [10.1007/s00158-010-0534-6](https://doi.org/10.1007/s00158-010-0534-6).
- [31] A. Takezawa, S. Nishiwaki, and M. Kitamura, “Shape and topology optimization based on the phase field method and sensitivity analysis,” *Journal of Computational Physics*, vol. 229, no. 7, pp. 2697–2718, Apr. 2010. DOI: [10.1016/j.jcp.2009.12.017](https://doi.org/10.1016/j.jcp.2009.12.017).
- [32] R. Tavakoli and S. M. Mohseni, “Alternating active-phase algorithm for multimaterial topology optimization problems: A 115-line MATLAB implementation,” *Structural and Multidisciplinary Optimization*, vol. 49, no. 4, pp. 621–642, Oct. 2013. DOI: [10.1007/s00158-013-0999-1](https://doi.org/10.1007/s00158-013-0999-1).
- [33] L. J. van Vliet, I. T. Young, and G. L. Beckers, “A nonlinear laplace operator as edge detector in noisy images,” *Computer Vision, Graphics, and Image Processing*, vol. 45, no. 2, pp. 167–195, 1989. DOI: [10.1016/0734-189x\(89\)90131-x](https://doi.org/10.1016/0734-189x(89)90131-x).
- [34] M. Y. Wang, S. Zhou, and H. Ding, “Nonlinear diffusions in topology optimization,” *Structural and Multidisciplinary Optimization*, vol. 28, no. 4, pp. 262–276, 2004. DOI: [10.1007/s00158-004-0436-6](https://doi.org/10.1007/s00158-004-0436-6).
- [35] M. Y. Wang, S. Chen, and Q. Xia, *Toplsm, a 199-line matlab program*, Jul. 2004.
- [36] S. Y. Wang, K. M. Lim, B. C. Khoo, and M. Y. Wang, “An extended level set method for shape and topology optimization,” *Journal of Computational Physics*, vol. 221, no. 1, pp. 395–421, 2007. DOI: [10.1016/j.jcp.2006.06.029](https://doi.org/10.1016/j.jcp.2006.06.029).
- [37] S. Wang and M. Y. Wang, “Radial basis functions and level set method for structural topology optimization,” *International Journal for Numerical Methods in Engineering*, vol. 65, no. 12, pp. 2060–2090, 2006. DOI: [10.1002/nme.1536](https://doi.org/10.1002/nme.1536).

- [38] P. Wei, Z. Li, X. Li, and M. Y. Wang, “An 88-line MATLAB code for the parameterized level set method based topology optimization using radial basis functions,” *Structural and Multidisciplinary Optimization*, vol. 58, no. 2, pp. 831–849, Feb. 2018. DOI: [10.1007/s00158-018-1904-8](https://doi.org/10.1007/s00158-018-1904-8).
- [39] Y. M. Xie and G. P. Steven, *Evolutionary Structural Optimization*. Springer London, 1997. DOI: [10.1007/978-1-4471-0985-3](https://doi.org/10.1007/978-1-4471-0985-3).
- [40] D. Yago, J. Cante, O. Lloberas-Valls, and J. Oliver, “Topology optimization of thermal problems in a nonsmooth variational setting: Closed-form optimality criteria,” *Computational Mechanics*, vol. 66, no. 2, pp. 259–286, Jun. 2020. DOI: [10.1007/s00466-020-01850-0](https://doi.org/10.1007/s00466-020-01850-0).
- [41] T. Yamada, K. Izui, S. Nishiwaki, and A. Takezawa, “A topology optimization method based on the level set method incorporating a fictitious interface energy,” *Computer Methods in Applied Mechanics and Engineering*, vol. 199, no. 45-48, pp. 2876–2891, 2010. DOI: [10.1016/j.cma.2010.05.013](https://doi.org/10.1016/j.cma.2010.05.013).
- [42] X. Y. Yang, Y. M. Xie, G. P. Steven, and O. M. Querin, “Bidirectional evolutionary method for stiffness optimization,” *AIAA Journal*, vol. 37, pp. 1483–1488, Jan. 1999. DOI: [10.2514/3.14346](https://doi.org/10.2514/3.14346).
- [43] W. Zhang, J. Yuan, J. Zhang, and X. Guo, “A new topology optimization approach based on moving morphable components (MMC) and the ersatz material model,” *Structural and Multidisciplinary Optimization*, vol. 53, no. 6, pp. 1243–1260, Dec. 2015. DOI: [10.1007/s00158-015-1372-3](https://doi.org/10.1007/s00158-015-1372-3).
- [44] O. C. Zienkiewicz, R. L. Taylor, and J. Z. Zhu, *The Finite Element Method: Its Basis and Fundamentals*. Elsevier LTD, Oxford, Oct. 1, 2013, 768 pp., ISBN: 1856176339.
- [45] Z. H. Zuo and Y. M. Xie, “A simple and compact python code for complex 3d topology optimization,” *Advances in Engineering Software*, vol. 85, pp. 1–11, Jul. 2015. DOI: [10.1016/j.advengsoft.2015.02.006](https://doi.org/10.1016/j.advengsoft.2015.02.006).

Article D

Topology optimization methods for 3D structural problems: a comparative study



Original Paper | [Open Access](#) | [Published: 20 August 2021](#)

Topology Optimization Methods for 3D Structural Problems: A Comparative Study

[Daniel Yago](#), [Juan Cante](#), [Oriol Lloberas-Valls](#) & [Javier Oliver](#) 

[Archives of Computational Methods in Engineering](#) (2021) | [Cite this article](#)

560 Accesses | 1 Altmetric | [Metrics](#)

Abstract

The work provides an exhaustive comparison of some representative families of topology optimization methods for 3D structural optimization, such as the *Solid Isotropic Material with Penalization* (SIMP), the *Level-set*, the *Bidirectional Evolutionary Structural Optimization* (BESO), and the *Variational Topology Optimization* (VARTOP) methods. The main differences and similarities of these approaches are then highlighted from an algorithmic standpoint. The comparison is carried out via the study of a set of numerical benchmark cases using industrial-like fine-discretization meshes (around 1 million finite elements), and Matlab as the common computational platform, to ensure fair comparisons. Then, the results obtained for every benchmark case with the different methods are compared in terms of computational cost, topology quality, achieved minimum value of the objective function, and robustness of the computations (convergence in objective function and topology). Finally, some quantitative and qualitative results are presented, from which, an attempt of qualification of the methods, in terms of their relative performance, is done.

Topology optimization methods for 3D structural problems: a comparative study

D. Yago^{a,b}, J. Cante^{a,b}, O. Lloberas-Valls^{b,c}, J. Oliver^{b,c}

^a Escola Superior d'Enginyeries Industrial, Aeroespacial i Audiovisual de Terrassa (ES-EIAAT), Universitat Politècnica de Catalunya · BarcelonaTech (UPC), Campus Terrassa UPC, c/ Colom 11, 08222 Terrassa, Spain

^b Centre Internacional de Mètodes Numèrics en Enginyeria (CIMNE), Campus Nord UPC, Mòdul C-1 101, c/ Jordi Girona 1-3, 08034 Barcelona, Spain

^c Escola Tècnica Superior d'Enginyeria de Camins, Canals i Ports de Barcelona (ETSEC-CPB), Universitat Politècnica de Catalunya · BarcelonaTech (UPC), Campus Nord UPC, Mòdul C-1, c/ Jordi Girona 1-3, 08034 Barcelona, Spain

D.1 Abstract

The work provides an exhaustive comparison of some representative families of topology optimization methods for 3D structural optimization, such as the *Solid Isotropic Material with Penalization* (SIMP), the *Level-set*, the *Bidirectional Evolutionary Structural Optimization* (BESO), and the *Variational Topology Optimization* (VARTOP) methods. The main differences and similarities of these approaches are then highlighted from an algorithmic standpoint.

The comparison is carried out via the study of a set of numerical benchmark cases using industrial-like fine-discretization meshes (around 1 million finite elements), and Matlab as the common computational platform, to ensure fair comparisons. Then, the results obtained for every benchmark case with the different methods are compared in terms of computational cost, topology quality, achieved minimum value of the objective function, and robustness of the computations (convergence in objective function and topology). Finally, some quantitative and qualitative results are presented, from which, an attempt of qualification of the methods, in terms of their relative performance, is done.

Keywords: Topology optimization, Topological derivative, SIMP method, SOFTBESO method, VARTOP method, Level-set method, Comparative study, computational cost, topology quality

D.2 Introduction

In the past three decades, topology optimization has become an active research field to seek new optimal counterintuitive designs in a wide range of problems governed by different physics, i.e., solid mechanics [143, 125, 8, 23, 124, 31], fluid dynamics [18, 46, 51], thermal dynamics [69, 44, 138], acoustics [113, 37, 36, 72, 75, 99] and electromagnetism [61, 148, 147], among others. Furthermore, topology optimization of coupled multiphysics problems has been addressed in recent works, combining structural-thermal interaction [109, 107, 34], structural-fluid interaction [142, 84, 12, 63] or even thermal-fluid interaction [3, 21, 137, 81]. As a result of this substantial effort, the optimal design obtained from the minimization of a given topology optimization problem can be used by engineers as a first approximation in the development of new products in a wide range of applications.

All up-to-date approaches exhibit certain strengths and weaknesses. As a first approximation¹, optimization techniques can be grouped into two main blocks: (I) *methods based on trial-and-error schemes*, e.g., *Genetic Algorithms* or *Ant Colony Algorithms* [55, 2, 29, 56, 128, 76], and (II) *methods relying on the gradient computation* [15, 131, 93, 8, 6, 20, 126]. The main disadvantage of the former group is their extremely high computational cost as the number of unknowns increases. This computational cost may become prohibitive for current computational

¹For further discussion about the classification, the reader is referred to [100, 40, 33, 114, 35, 87].

systems since thousands of different layouts must be tested to find the optimal configuration. Consequently, the algorithms included in the second set are the most widespread algorithms, e.g., (a) *topology optimization within homogenization theory* [17], (b) *density-based optimization* (SIMP) techniques [15, 86, 16], (c) *evolutionary methodologies* (ESO)² [133, 140], (d) *Level-set approaches* [7, 8, 125], (e) *Topological Derivative method* [115], (f) *Phase field approach* [20, 123, 120], and (g) *Variational Topology Optimization (VARTOP) method* [90, 135], among others.

Starting with the seminal paper of Bendsøe and Kikuchi [17], numerical methods for topology optimization have been extensively developed. In particular, this article was the basis for a stream of *density-based approaches*, such as the *Solid Isotropic Material with Penalization* (SIMP) method [15, 86, 16], being nowadays one of the most widely used topology optimization methods. Simple continuous *element-wise design variables* are used in the formulation and resolution of the *topology optimization problem* in a fixed design domain, for which Young's modulus is defined as a polynomial function of the *element-wise density*, $\rho_e \in (0, 1)$. The *design variable* must be first penalized³ (normally a penalty exponent $p \geq 3$ is used) and later regularized, thus providing almost *black-and-white solutions* (with semi-dense elements) not ensuring manufacturability. On the other hand, a large number of regularization schemes have been suggested to be used regarding topology optimization, including: (1) *filtering*, via the classical sensitivity [110, 111, 108] or density [19, 23] filters, projection techniques [49, 50], morphology-based filters [112, 122] or Helmholtz-type filters [66, 65], among others, and (2) *geometric constraint techniques*, e.g., perimeter constraint [53, 42] or gradient constraints [94]. Through these mathematical techniques, significant numerical instabilities [108, 64] resulting from the ill-posedness of unconstrained topology optimization problems for continuous structures, including gray areas (semi-dense intermediate elements), checkerboard patterns, and mesh-dependency issues are alleviated. Finally, the solution to the topology optimization problem is obtained via the update of the *design variable*, through the *classical optimality criteria (OC) method* [17, 118]⁴, the *moving asymptotes (MMA) algorithm* [119] or other *mathematical programming-based optimization algorithms*, among others.

Besides the *SIMP method*, the *Evolutionary Structural Optimization* (ESO) method, firstly introduced by Xie and Steven [133, 131] although similar ideas were presented earlier [102, 83], is also one of the most used for industrial applications. In the recent years, the ESO approach has gained widespread popularity due its simplicity and ease of implementation in commercial FE codes. *ESO*, considered as a *hard-kill method*⁵, relies on a simple *heuristic criterion* to gradually remove inefficient material. The elements with low *rejection criterion* are gradually removed starting from a full stiff design domain, thus evolving towards an optimum. Contrary to *SIMP*, a *discrete element design variable*, $\chi \in \{0, 1\}$, is used to define the topology layouts, which are free of gray elements. This change in design variable results in convergence issues and a high dependency on the initial configuration, thus leading to local optimal solutions [146]. Despite these numerical issues, *ESO* has been applied to a large range of problems, from the well-known structural problems [134, 132, 144, 30], including non-linear problems [96, 80], to thermal problems [68, 69, 95], and contact problems [70, 71]. In addition, the above mentioned issues are mitigated in its later version, the *Bi-directional Evolutionary Structural Optimization* (BESO) method [97, 140, 98], which extends the approach to allow for new elements to be added, while inefficient elements are removed at the same time. The new material is added either in the locations near to those elements with a *high criterion function value* [97, 98] or in those void areas

²The *evolutionary approaches* appear also in the literature as *Sequential Element Rejection and Admission* (SERA), and henceforth they should be considered as synonyms.

³Although existing other interpolation schemes, such as the *Rational Approximation of Material Properties* (RAMP) material interpolation [117] or the SINH method [22], the SIMP scheme [15, 145] is the most popular one in structural optimization due to its simplicity. However, these alternative schemes may be of interest for topology optimization problems involving alternative physics, e.g., in dynamic problems.

⁴Other heuristic techniques have been proposed to tackle non-convex topology optimization problems, such as the *modified optimality criteria technique* (MOC) [79].

⁵The removed elements are not included in the subsequent finite element analysis. Consequently, no criterion function is computed for the void elements.

with higher criterion function values, computed via a linear interpolation of the displacement field [140]. However, these extrapolation techniques are not consistent with those used for the solid elements. As any other *density-based method*, the sensitivity is commonly regularized via a *checkerboard suppression filter* [67], a *mesh-independent filter* [62] or a *perimeter control* [141], similar to the ones used in *SIMP*, in order to reduce mesh-dependencies. Nevertheless, such *hard-kill BESO methods* fail to obtain convergent solutions. For that reason, in later revisions, Huang and Xie [62] proposed a *modified hard-kill BESO* to enhance the time-convergence via a *stabilization algorithm*, where the historical information is used, in addition to a new mesh-independent filter and nodal sensitivities. As an alternative to *hard-kill ESO/BESO methods*, *soft-kill approaches* retain the void elements as very soft elements, thus allowing the computation of the *criterion function* within the entire domain. Zhu *et al.* [149] and Huang and Xie [59] proposed independent approaches that used a *penalized density variable*. In particular, Huang and Xie [59] combined the *modified BESO method with SIMP material interpolation scheme*, improving the numerical stability and the potential of the methodology. An excellent overview of some recent developments in topology optimization using *ESO* is provided in [60].

The last major stream is constituted by *Level-set-based methods*. In contrast to the previous topology optimization approaches, the optimal layout is implicitly defined by a scalar function ϕ (with the sign). Additionally, the structural boundary of the design Γ is represented by the *zero-level iso-contour* (or iso-surface) of the *level-set function* (LSF) [92, 104, 91]. As a result, optimal designs with sharp and smooth edges are obtained, thus avoiding *semi-dense (gray) elements*, like those observed in *density-based methods*. Many formulations of *Level-set-based approaches* have been proposed over the years since Haber and Bendsoe [54] suggested its applications with topology optimization techniques, e.g., [105, 7, 125, 6]. The most important ones relying on a *level-set function* are the *Level-set* (based on shape derivative), the *Topological Derivative*, and the *Phase-field methods*.

Regarding the original *Level-set*, Osher and Santosa [93], Allaire *et al.* [7, 8] and Wang *et al.* [125] took up the idea of using the *level-set function* for topology optimization and combined it with a *shape-derivative-based* topology optimization framework. Therefore, only material boundaries are altered via shape-sensitivity analysis⁶ to seek the optimal design. As a consequence, this set of techniques can not nucleate new holes in the interior of the domain. Therefore, the resulting optimal solutions are heavily dependent on the initial layouts, which must be made up of many small holes evenly distributed throughout the domain [8]. This initial configuration ensures the merging and cancellation of holes via the propagation of the boundaries, while avoiding local optimal solutions. To overcome this limitation, a hole nucleation algorithm [39, 103], referenced as the *bubble technique*, was introduced in the *topology optimization approach*. This technique allows the creation of new holes in the material domain. Instead of the density variable used in *density-based methods* to define the topology design, the *level-set function* is used here, with the material domain being those points where the LSF is positive. The geometry in a fixed mesh is typically mapped to a mechanical model using either *immersed boundary techniques* (e.g., via X-FEM [38]) or *density-based mapping* (e.g., via relaxed Heaviside functions [125]) [130]. When using the second mapping, the stiffness coefficients are expressed in terms of the *level-set function* via approximated Heaviside functions, i.e., the *ersatz material approximation* is used [4, 32], where the void material is replaced with a soft material. In addition, the LSF is commonly updated using a *Hamilton-Jacobi (HJ) equation* [93, 125, 8]⁷, thus requiring the solution of a *pseudo-time PDE equation*. Although this updating scheme tends to converge to smooth topologies, it may require a huge number of iterations⁸, as well as the regular application of reinitialization algorithms to a signed-distance function. These reinitializations must be ap-

⁶The basis of this approach lies in computing the sensitivity of the functional when a normal infinitesimal deformation is applied on the boundaries of the domain [116].

⁷However, other updating schemes have been proposed over the years, such as the resolution of a set of ordinary differential equations in the approaches using *radial basis functions* (RBFs) [129, 127] or a *system of algebraic equations using compactly supported RBFs* (CSRBFs) [77, 78], among others.

⁸When an explicit scheme is performed, the time-step is limited by the CFL condition.

plied each time there are significant shape-changes or after a hole nucleation process [8, 125], thus reducing the efficiency of the approach. Nevertheless, it has been extensively used for a broad range of design problems, including structural problems [5], vibration problems [93, 5], thermal problems [52], among others. As an alternative to *HJ equations*, updating procedures based on mathematical programming are used, e.g., using the parameters of the discretized *level-set function* as optimization variables (for instance *radial basis functions* (RBF) and *spectral methods*) [129, 77]. Finally, as described for *density-based approaches*, the topology optimization problem must be regularized to ensure mesh-independence and improve convergence. It can be achieved either by a filtering procedure or a constraint equation, e.g., perimeter constraint [8, 85].

Alternatively to *Level-set* using the shape-derivative framework, and after the mathematical development of the *topological derivatives* [115, 27, 45], some researchers incorporated the concept of the *topological derivative* into a *shape-sensitivity-based Level-set method*, thus leading to the *Topological Derivative approach* [24, 6]. A similar algorithm as in classical *Level-set* is performed. However, in contrast to those prior methods, this topology optimization technique can nucleate holes in the interior of the material domain by using the *topological gradient* or *topological derivative*. The sensitivity is defined as the variation of the objective function due to the insertion of an infinitesimal spherical void at any point \mathbf{x} in the design domain Ω , thus avoiding the stagnation in local optimal solutions. Nevertheless, the *topological gradient* must be analytically derived through rather complex mathematics for each of the topology optimization problems, e.g., structural linear optimization [45, 47, 89], thermal orthotropic optimization [48, 82], microstructure topology optimization [14, 10], among others. This mathematical operator represents an extra step required to proceed with the optimization, burdening its potential against other techniques with sensitivities easier to compute. The *topological derivative* was first incorporated in conjunction with shape-derivative as a way to systematically nucleate holes [24, 6, 28, 43], similar as in *Level-set* with the *bubble technique*. In later revisions, the *topological derivative* was used exclusively to update the *level-set function* [27, 88]. Until then, only stiff material could be removed from the material domain, making it impossible to add new material. It was not until Amstutz and Andr a [11] and He *et al.* [57] that fully bi-directional *Topological Derivative approaches* were introduced. In these techniques, the optimal layout, expressed in terms of the LSF, is defined as a function of the *topological gradient*. To improve stability, reaction and diffusive terms can be added to the classical *HJ-equation*, leading to the so-called *Generalized HJ-equation*. The diffusive term smooths out the design and suppresses sharp corners, avoiding the ill-posedness of the topology optimization problem.

The last group of interest is the *Phase field topology optimization approach*, where the theory of phase transitions is adapted to the resolution of topology optimization problems [9, 26, 41]. The design variable corresponds to the *density*, as other *density-based approaches*, but, in this case, a linear material interpolation is considered, without any exponent factor. In addition, an extra term is added to the objective function that controls the interface thickness while penalizing intermediate values, thus solving one of the main disadvantages of *SIMP-like approaches*. The optimal solutions present smooth material domains, almost *black-and-white designs* separated by sharp thin finite thickness interfaces. The modified functional is minimized based on the *Cahn-Hilliard equation*, leading to the resolution of two coupled second-order equations without requiring a volume constraint, i.e., the volume stays constant through the optimization procedure. However, some researchers have solved directly the modified topology optimization problem with the inclusion of a volume constraint [20, 126, 25, 123], resembling *SIMP* with an explicit penalization in the density and a gradient regularization. The gradient regularization results in a smoothing similar to that obtained by the inclusion of diffusive terms in the *level-set-based methods*⁹. Connected with this concept, Yamada *et al.* [139] suggested a *Phase field approach* based on a *level-set function*, used as the design variable, and a *topological derivative* incorporating a *fictitious interface energy*. This last mathematical technique allows to control

⁹Alternatively, Takezawa *et al.* [120] used a *time-dependent reaction-diffusion equation* instead, called the *Allen-Cahn equation*, to evolve the phase function.

the complexity of the optimal layout. Although being applied to other problems [138, 73], it still resorts to a *Hamilton-Jacobi equation* to update the topology design, which may entail high computation resources to achieve convergence.

As an alternative to all these well-established techniques, the *Variational Topology Optimization* (VARTOP)¹⁰ approach [90] combines the mathematical simplicity of *SIMP-based methods*, while considering the *characteristic function* χ as the design variable. Thus a binary configuration (*black-and-white design*) is obtained. The domain, and so the *characteristic function*, is implicitly represented through a *0-level-set function*, termed as *discrimination function*, as in *level-set-based methods*. Nevertheless, the topology design is not updated neither via a *Hamilton-Jacobi equation* nor a *Reaction-Diffusion equation*, but via a *fixed-point, non-linear, closed-form algebraic system* resulting from the derivation of the topology optimization problem. In addition, an *approximated topological derivative*, in contrast to the *exact Topological Derivative methods*, is used in the formulation within an *ersatz material approach*, highly reducing the mathematical complexity independent of the tackled problem. The topology optimization problem is subjected to a volume constraint expressed in terms of a *pseudo-time variable*. This constraint equation is iteratively increased until the desired volume is achieved, thus obtaining converged topologies for intermediate volumes. By means of this procedure, referred to as *time-advancing scheme*, the corresponding *Pareto Frontier* is obtained. For each time-step, the *closed-form optimality criteria* has to be solved to compute both the *Lagrange multiplier* that fulfills the volume constraint and the optimal *characteristic function*. As for the regularization, a *Laplacian regularization*, similar to those used in SIMP and Phase-field approaches [20, 66, 65, 139], is applied to the *discrimination function*, providing not only smoothness in the optimal design but also mesh-size control. The technique has been already applied to linear static structural [90] and steady-state thermal [136] applications, considering the volume constraint as a single constraint equation, with promising results.

In the literature, there are plenty of articles that either theoretically compare several topology optimization methods as the ones presented above [33, 40, 87, 100, 101, 114, 35], or compare the results obtained with the topology optimization approach proposed by the corresponding authors with those computed using a recognized topology optimization approach. However, not many articles compare in a practical way a set of cases with a wide range of techniques under the same convergence criteria. This is one of the most relevant aspects of this work since the results of a set of widely used techniques are compared with each other: (1) *SIMP* (briefly described in Section D.4.1), (2) *BESO using a soft-kill criterion* (detailed in Section D.4.2), (3) *VARTOP* using a pure variational topological approach (presented in Section D.4.3), and (4) *Level-set* (detailed in section D.4.4). These three well-known methods have been selected among all existing ones due to their wide use both at the professional and research level, as well as for the convenience of implementation and their documentation, thus facilitating their verification and assuring a fair comparison. Following the implementations proposed by the different methods' authors, the studied topology optimization techniques have been implemented including as few modifications as possible in order to match the original approaches. The modifications are detailed throughout the document for each of the addressed methods. Although the chosen topology optimization techniques have been applied to a wide spectrum of different applications, the comparison in this article focuses at *minimizing the static structural problem*. The comparison of the results is addressed through a set of well-known benchmark cases, whose optimal layouts are easily recognized. Specifically, *minimum mean compliance*, *multi-load mean compliance*, and *compliant mechanism topology optimization problems* are carried out.

The remainder of this paper is organized as follows. The structural static problem as well as the three addressed topology optimization problems are defined in Section D.3, while in Section D.4, the considered approaches are reviewed in terms of their formulation and algorithms. In addition, specific comments are provided to address the studied topology optimization problems

¹⁰The method abbreviation *UNVARTOP* used in previous papers has been here rebranded as *VARTOP*, which should be taken as equals.

with each of the techniques. These techniques are compared with each other in terms of the objective function, the quality of topology design, and the computational cost via a set of benchmark cases detailed in Section D.5 and analyzed in Section D.6.

D.3 Theoretical aspects

D.3.1 Domain definition

Let the design domain, Ω , denote a fixed smooth open domain of \mathbb{R}^n for $n = \{2, 3\}$, composed by two smooth subdomains $\Omega^+, \Omega^- \subset \Omega$, with $\overline{\Omega}^+ \cup \overline{\Omega}^- = \overline{\Omega}$ and $\Omega^+ \cap \Omega^- = \emptyset$, as displayed in Figure D.1-(a) ¹¹. The boundary of the design domain, termed as $\partial\Omega$, is also composed of the boundaries corresponding to the two subdomains $\partial\Omega^+$ and $\partial\Omega^-$, satisfying $\partial\Omega^+ \cap \partial\Omega^- = \Gamma$. The material domain, Ω^+ , consists of a stiff material with a high Young's modulus, while the second subdomain, Ω^- , is formed by a soft material with a low Young's modulus. The stiffness ratio between both materials is given by the *contrast factor*, $\alpha \ll 1$.

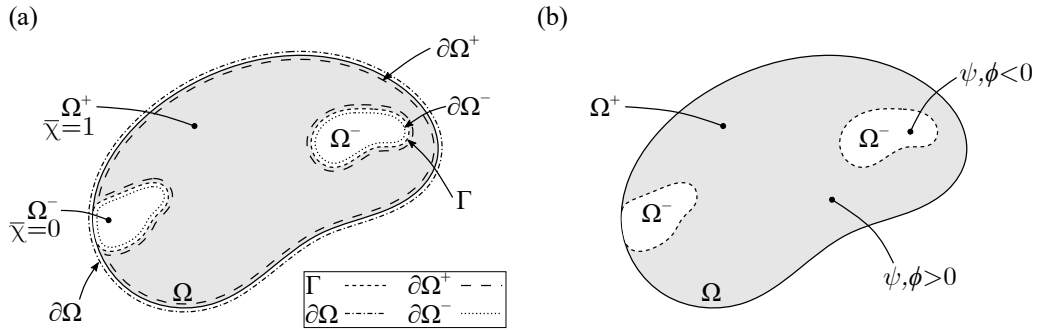


Figure D.1: Domain representation: (a) Representation of the design domain, Ω , comprising two disjoint sub-domains Ω^+ and Ω^- and (b) Implicit representation via the *level-set function* ϕ or the *discrimination function* ψ .

The topology layout of the design domain can be defined via a *characteristic function* $\bar{\chi}(\mathbf{x}) : \Omega \rightarrow \{0, 1\}$ as

$$\begin{cases} \Omega^+ := \{\mathbf{x} \in \Omega / \bar{\chi}(\mathbf{x}) = 1\} \\ \Omega^- := \{\mathbf{x} \in \Omega / \bar{\chi}(\mathbf{x}) = 0\} \end{cases}, \quad (1)$$

where $\bar{\chi}$ corresponds to the *Heaviside function* of $(\rho - \bar{\rho})$ in *density-based approaches (SIMP)*, the *Heaviside function* of the *level-set function* ϕ in *Level-set-based methods*, and the *characteristic function* χ itself in *VARTOP*. Notice that the term $\bar{\rho}$ must be computed in *density-based methods* so that the constraint equation is satisfied (normally the volume), thus obtaining a *white-and-black design*.

In particular, for *Level-set-based* and *VARTOP approaches*, the subdomains can be defined through a continuous function, $\varphi(\mathbf{x}) : \Omega \rightarrow \mathbb{R}$, $\varphi \in H^1(\Omega)$ (a *level-set function* ϕ or a *discrimination function* ψ , respectively) such that

$$\begin{cases} \Omega^+ := \{\mathbf{x} \in \Omega / \varphi(\mathbf{x}) > 0\} \\ \Omega^- := \{\mathbf{x} \in \Omega / \varphi(\mathbf{x}) < 0\} \end{cases}, \quad (2)$$

as illustrated in Figure D.1-(b). The *characteristic function* $\bar{\chi}$ can be then obtained as $\bar{\chi}(\mathbf{x}) = \mathcal{H}(\varphi(\mathbf{x}))$, where $\mathcal{H}(\cdot)$ stands for the *Heaviside function*.

D.3.2 The Topology Optimization problem. Contextual introduction

Topology optimization methods look for the optimal material distribution that minimizes a given *objective function*, \mathcal{J} , subjected to one or more *constraints* \mathcal{C}_k (e.g., a volume constraint, $\mathcal{C}_0 \leq 0$, and possibly other N design variable constraints, $\mathcal{C}_k \leq 0$, $k : 1 \dots N$) and governed by a linear or non-linear state equation. The material distribution is described by the *density variable* $\rho(\mathbf{x})$, the *characteristic function* $\chi(\mathbf{x})$ or the *level-set function* $\psi(\mathbf{x})$, depending on the topology approach used to carry out the optimization. To keep the definition of the topology optimization problem as general as possible, let us define $\zeta(\mathbf{x})$ as the *design variable* at point \mathbf{x} , which will be considered as $\rho(\mathbf{x})$, $\chi(\mathbf{x})$ or $\phi(\mathbf{x})$ for the *density-based*, *VARTOP*, and *level-set-based methods*, respectively. Based on this concept, the classical mathematical formulation of the corresponding *topology optimization problem* is given by

$$\left[\begin{array}{l} \min_{\zeta \in \mathcal{U}_{ad}} \mathcal{J}(\mathbf{u}(\zeta), \zeta) \equiv \int_{\Omega} j(\mathbf{u}(\zeta), \zeta, \mathbf{x}) d\Omega \quad (a) \\ \text{subject to:} \\ \mathcal{C}_0(\zeta) \equiv \int_{\Omega} c_0(\zeta, \mathbf{x}) d\Omega \leq 0 \quad (b-1), \quad (3) \\ \mathcal{C}_k(\zeta) \leq 0, \quad k : 1 \dots N \quad (b-2) \\ \text{governed by:} \\ \text{State equation} \quad (c) \end{array} \right.$$

where the *objective function* \mathcal{J} can be expressed as a volume integral of a local function $j(\mathbf{u}(\zeta), \zeta, \mathbf{x})$ over the entire domain, and the constraint functional \mathcal{C}_0 represents the *volume constraint* in terms of the design variable ζ . Additional *constraint equations* $\mathcal{C}_k(\zeta)$ can be incorporated into the topology optimization problem to explicitly include constraints to the design variables, particular to each approach.

The *state equation* gives as a solution the unknown field $\mathbf{u}(\zeta)$ for a specific optimal design ζ included in the admissible set of solutions, \mathcal{U}_{ad} . This unknown field must satisfy the boundary conditions applied to the design domain. In particular, the linear elasticity equilibrium problem, formulated as

$$\left[\begin{array}{l} \text{Find } \mathbf{u}(\zeta, \mathbf{x}) \text{ such that} \\ \left\{ \begin{array}{ll} \nabla \cdot \boldsymbol{\sigma}(\zeta, \mathbf{x}) + \mathbf{b}(\zeta, \mathbf{x}) = \mathbf{0} & \text{in } \Omega \\ \boldsymbol{\sigma}(\zeta, \mathbf{x}) \cdot \mathbf{n} = \mathbf{t}_n(\mathbf{x}) & \text{on } \partial_{\sigma}\Omega, \\ \mathbf{u}(\zeta, \mathbf{x}) = \bar{\mathbf{u}}(\mathbf{x}) & \text{on } \partial_u\Omega \end{array} \right. \end{array} \right. \quad (4)$$

¹¹($\bar{\cdot}$) corresponds to the closure of the open domain (\cdot).

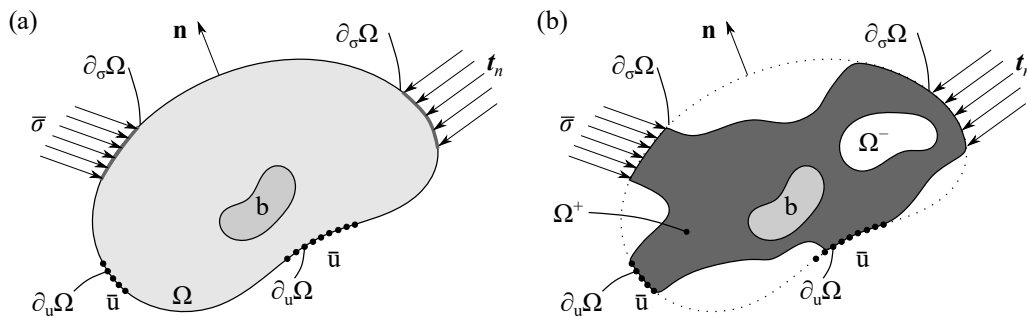


Figure D.2: Elastic problem sketch: (a) fixed analysis domain Ω with boundary conditions (in which the displacement $\bar{\mathbf{u}}(\mathbf{x})$ or the normal traction $\mathbf{t}_n(\mathbf{x})$ can be prescribed at $\partial_u\Omega$ and $\partial_{\sigma}\Omega$, respectively) and (b) Stiff and soft material domains, Ω^+ and Ω^- , respectively, with the same boundary conditions.

is considered as the state equation for all the topology optimization problems addressed in this paper. In the preceding equation, $\boldsymbol{\sigma}(\zeta, \mathbf{x})$ and $\mathbf{b}(\zeta, \mathbf{x})$ stand for the *second-order stress tensor field* and the *volumetric force*, respectively, which both depend on the topology layouts. Additionally, $\mathbf{t}_n(\mathbf{x})$ and $\bar{\mathbf{u}}(\mathbf{x})$ are respectively the boundary tractions applied on $\partial_\sigma\Omega \subset \partial\Omega$ and the displacements prescribed on $\partial_u\Omega \subset \partial\Omega$, and \mathbf{n} corresponds to the unit outward normal. As for the material behavior, the elastic material is governed by the Hooke's law, i.e., $\boldsymbol{\sigma} = \mathbb{C}_\zeta : \boldsymbol{\varepsilon}$, with $\boldsymbol{\varepsilon}$ being the *strain tensor* ($\boldsymbol{\varepsilon} = \nabla^S \mathbf{u}_\zeta(\mathbf{x})$) and \mathbb{C}_ζ being the *fourth-order, elastic constitutive tensor*. The *constitutive tensor* depends on the *design variable* ζ via the corresponding material interpolation of each topology optimization approach.

As depicted in Figure D.2, the boundary $\partial\Omega$ of the analysis domain Ω is made of two mutually disjoint subsets, $\partial_u\Omega$ and $\partial_\sigma\Omega$, where the displacements and tractions are prescribed, respectively, as detailed in the previous equation.

Alternatively, the variational form of the *linear elasticity problem* (4) becomes

$$\left[\begin{array}{l} \text{Find the displacement field } \mathbf{u}_\zeta \in \mathcal{U}(\Omega) \text{ such that} \\ a(\mathbf{w}, \mathbf{u}_\zeta) = l(\mathbf{w}) \quad \forall \mathbf{w} \in \mathcal{V}(\Omega) \end{array} \right. \quad (5)$$

where

$$a(\mathbf{w}, \mathbf{u}_\zeta) = \int_{\Omega} \nabla^S \mathbf{w}(\mathbf{x}) : \mathbb{C}_\zeta(\mathbf{x}) : \nabla^S \mathbf{u}_\zeta(\mathbf{x}) d\Omega, \quad (6)$$

$$l(\mathbf{w}) = \int_{\partial_\sigma\Omega} \mathbf{w}(\mathbf{x}) \cdot \mathbf{t}_n(\mathbf{x}) d\Gamma + \int_{\Omega} \mathbf{w}(\mathbf{x}) \cdot \mathbf{b}_\zeta(\mathbf{x}) d\Omega, \quad (7)$$

with \mathbf{u}_ζ and \mathbf{w} being the *displacement field* and the *virtual displacement field*, respectively.

The *linear elasticity problem* (equations (5) to (7)), discretized using the standard *finite element method*, reads

$$\left[\mathbb{K}_\zeta \hat{\mathbf{u}}_\zeta = \mathbf{f}_\zeta \right. \quad (8)$$

with

$$\mathbb{K}_\zeta = \int_{\Omega} \mathbf{B}^T(\mathbf{x}) \mathbb{C}_\zeta(\mathbf{x}) \mathbf{B}(\mathbf{x}) d\Omega, \quad (9)$$

$$\mathbf{f}_\zeta = \int_{\partial_\sigma\Omega} \mathbf{N}_u^T(\mathbf{x}) \mathbf{t}_n(\mathbf{x}) d\Gamma + \int_{\Omega} \mathbf{N}_u^T(\mathbf{x}) \mathbf{b}_\zeta(\mathbf{x}) d\Omega, \quad (10)$$

where the stiffness matrix and the external force vector are denoted by \mathbb{K}_ζ and \mathbf{f} , respectively. For the sake of clarity, the dependence of the force vector on the design variable will be neglected, considering a constant force scenario \mathbf{f} , independent of the topology layout, with null *volumetric forces*. The displacement field, $\mathbf{u}_\zeta(\mathbf{x})$, and its gradients, $\nabla^S \mathbf{u}_\zeta$, are approximated as follows

$$\mathbf{u}_\zeta(\mathbf{x}) \equiv \mathbf{N}_u(\mathbf{x}) \hat{\mathbf{u}}_\zeta \quad (11)$$

$$\nabla^S \mathbf{u}_\zeta(\mathbf{x}) \equiv \mathbf{B}(\mathbf{x}) \hat{\mathbf{u}}_\zeta \quad (12)$$

where $\mathbf{N}_u(\mathbf{x})$ and $\mathbf{B}(\mathbf{x})$ stand for the *displacement, shape function matrix* and the *strain-displacement matrix*, respectively, and $\hat{\mathbf{u}}_\zeta$ corresponds to the *nodal displacement vector*. Notice that the dependence on the design variable ζ is highlighted by the subscript $(\cdot)_\zeta$.

Minimum mean compliance

The *minimum mean compliance topology optimization problem* seeks the optimal topology layout that minimizes the global stiffness of the structure, or equivalently, maximizes the external work on the structure. The objective function $\mathcal{J}^{(I)}(\mathbf{u}_\zeta, \zeta)$, in variational form, is given by

$$\mathcal{J}^{(I)}(\mathbf{u}(\zeta), \zeta) \equiv l(\mathbf{u}_\zeta), \quad (13)$$

and the corresponding discretized *topology optimization problem* can be written as

$$\left[\begin{array}{l}
\min_{\zeta \in \mathcal{U}_{ad}} \mathcal{J}^{(I)}(\mathbf{u}(\zeta), \zeta) \equiv \int_{\Omega} \hat{\mathbf{u}}_{\zeta}^T \mathbf{B}^T(\mathbf{x}) \mathbb{C}_{\zeta}(\mathbf{x}) \mathbf{B}(\mathbf{x}) \hat{\mathbf{u}}_{\zeta} d\Omega \quad (a) \\
\text{subject to:} \\
\mathcal{C}_0(\zeta) \equiv \int_{\Omega} c_0(\zeta, \mathbf{x}) d\Omega \leq 0 \quad (b-1) \\
\mathcal{C}_k(\zeta) \leq 0, \quad k : 1 \dots N \quad (b-2) , \quad (14) \\
\text{governed by:} \\
\mathbb{K}_{\zeta} \hat{\mathbf{u}}_{\zeta} = \mathbf{f}, \text{ with} \quad \mathbb{K}_{\zeta} = \int_{\Omega} \mathbf{B}^T(\mathbf{x}) \mathbb{C}_{\zeta}(\mathbf{x}) \mathbf{B}(\mathbf{x}) d\Omega \quad (c) \\
\mathbf{f} = \int_{\partial_{\sigma}\Omega} \mathbf{N}_{\mathbf{u}}^T(\mathbf{x}) \mathbf{t}_n(\mathbf{x}) d\Gamma
\end{array} \right.$$

with $j(\mathbf{u}(\zeta), \zeta, \mathbf{x})$ being $\nabla^S \mathbf{u}_{\zeta}(\mathbf{x}) : \mathbb{C}_{\zeta}(\mathbf{x}) : \nabla^S \mathbf{u}_{\zeta}(\mathbf{x})$. The *mean compliance* can be also defined as $\mathbf{f}^T \hat{\mathbf{u}}_{\zeta}$, when nodal variables are used.

Multi-load mean compliance

Multi-load compliance topology optimization problems are a subfamily of *minimum mean compliance problems* (Section D.3.2), in which a set of elastic problems with different loading conditions are solved independently, instead of a single one with all the external loads applied at the same time. As a result, the topology optimization procedure aims at a trade-off between the optimal topology layouts for each specific loading state. Hence, the objective function (3-a) is computed as the weighted average sum of all individual compliances, i.e.,

$$\mathcal{J}^{(II)}(\mathbf{u}(\zeta), \zeta) \equiv \sum_{i=1}^{n_l} l(\mathbf{u}_{\zeta}^{(i)}) \equiv \sum_{i=1}^{n_l} \int_{\Omega} \nabla^S \mathbf{u}_{\zeta}^{(i)}(\mathbf{x}) : \mathbb{C}_{\zeta}(\mathbf{x}) : \nabla^S \mathbf{u}_{\zeta}^{(i)}(\mathbf{x}) d\Omega, \quad (15)$$

where i and n_l corresponds to the index of the i -th loading state¹² and the number of loading states, respectively. Consequently, the *topology optimization problem* (14) becomes

$$\left[\begin{array}{l}
\min_{\zeta \in \mathcal{U}_{ad}} \mathcal{J}^{(II)}(\mathbf{u}(\zeta), \zeta) \equiv \sum_{i=1}^{n_l} \int_{\Omega} \hat{\mathbf{u}}_{\zeta}^{(i)T} \mathbf{B}^T(\mathbf{x}) \mathbb{C}_{\zeta}(\mathbf{x}) \mathbf{B}(\mathbf{x}) \hat{\mathbf{u}}_{\zeta}^{(i)} d\Omega = \sum_{i=1}^{n_l} \mathbf{f}^{(i)T} \hat{\mathbf{u}}_{\zeta}^{(i)} \quad (a) \\
\text{subject to:} \\
\mathcal{C}_0(\zeta) \equiv \int_{\Omega} c_0(\zeta, \mathbf{x}) d\Omega \leq 0 \quad (b-1) \\
\mathcal{C}_k(\zeta) \leq 0, \quad k : 1 \dots N \quad (b-2) \cdot \quad (16) \\
\text{governed by:} \\
\mathbb{K}_{\zeta} \hat{\mathbf{u}}_{\zeta}^{(i)} = \mathbf{f}^{(i)}, \text{ with} \quad \mathbb{K}_{\zeta} = \int_{\Omega} \mathbf{B}^T(\mathbf{x}) \mathbb{C}_{\zeta}(\mathbf{x}) \mathbf{B}(\mathbf{x}) d\Omega \quad (c) \\
\mathbf{f}^{(i)} = \int_{\partial_{\sigma}\Omega^{(i)}} \mathbf{N}_{\mathbf{u}}^T(\mathbf{x}) \mathbf{t}_n^{(i)}(\mathbf{x}) d\Gamma, \quad i : 1 \dots n_l
\end{array} \right.$$

Notice that n_l independent *linear elastic problems* must be solved in order to obtain the displacement field $\hat{\mathbf{u}}_{\zeta}^{(i)}$ for each of the loading states.

¹²The displacements \mathbf{u}_{ζ} and the actual energy density \mathcal{U}_{ζ} for the i -th loading state are designated with the superscript $(\cdot)^{(i)}$.

Compliant mechanism synthesis

Contrary to the two previous sections where the main goal was to *maximize the mean stiffness* of the structure, the objective now is to design a flexible structure capable of transferring an action (force or displacement) from the *input port* to the *output port*, obtaining a desired force or displacement at that port. The corresponding objective function $\mathcal{J}^{(III)}(\mathbf{u}(\zeta), \zeta)$ can be expressed as

$$\mathcal{J}^{(III)}(\mathbf{u}(\zeta), \zeta) \equiv -l_2(\mathbf{u}_\zeta^{(1)}), \quad (17)$$

where $l_2(\mathbf{u}_\zeta^{(1)})$ corresponds to the rhs term (7) of the elastic problem (5) for $\mathbf{w} = \mathbf{u}_\zeta^{(1)}$ with the boundary traction $\mathbf{t}_n^{(2)}(\mathbf{x})$ being a *dummy constant force value* applied only at the *output port* in the desired direction.

Mimicking the procedure detailed for the other two topology optimization problems in Sections D.3.2 and D.3.2, the new mathematical problem is given by

$$\left[\begin{array}{l} \min_{\zeta \in \mathcal{A}_{ad}} \mathcal{J}^{(III)}(\mathbf{u}(\zeta), \zeta) \equiv - \int_{\Omega} \hat{\mathbf{u}}_\zeta^{(1)\top} \mathbf{B}^\top(\mathbf{x}) \mathbb{C}_\zeta(\mathbf{x}) \mathbf{B}(\mathbf{x}) \hat{\mathbf{u}}_\zeta^{(2)} d\Omega = -\mathbf{1}^\top \hat{\mathbf{u}}_\zeta^{(1)} \quad (a) \\ \text{subject to:} \\ \mathcal{C}_0(\zeta) \equiv \int_{\Omega} c_0(\zeta, \mathbf{x}) d\Omega \leq 0 \quad (b-1) \\ \mathcal{C}_k(\zeta) \leq 0, \quad k : 1 \dots N \quad (b-2) \quad (18) \\ \text{governed by:} \\ \mathbb{K}_\zeta \hat{\mathbf{u}}_\zeta^{(1)} = \mathbf{f}^{(1)}, \text{ with } \mathbf{f}^{(1)} = \int_{\partial_\sigma \Omega^{(1)}} \mathbf{N}_\mathbf{u}^\top(\mathbf{x}) \mathbf{t}_n^{(1)}(\mathbf{x}) d\Gamma \quad (c) \\ \mathbb{K}_\zeta \hat{\mathbf{u}}_\zeta^{(2)} = \mathbf{f}^{(2)}, \text{ with } \mathbf{f}^{(2)} = \mathbf{1} = \int_{\partial_\sigma \Omega^{(2)}} \mathbf{N}_\mathbf{u}^\top(\mathbf{x}) \mathbf{t}_n^{(2)}(\mathbf{x}) d\Gamma \end{array} \right.$$

As anticipated in expression (17), the *compliant mechanism problem* (18) is not self-adjoint, so an *auxiliary state problem* must be solved in addition to the *original state problem*. The additional system presents the same stiffness matrix \mathbb{K}_ζ but a different force vector $\mathbf{f}^{(2)}$, consisting in a *dummy constant force* at the output port, which solution is denoted as $\mathbf{u}_\zeta^{(2)}$. Additional springs, denoted by K_{in} and K_{out} , must be considered in the *input and output ports*, respectively, to ensure convergence.

D.3.3 General algorithm

The flowchart of the general algorithm, used to obtain the optimal topology layouts, is illustrated in Figure D.3. Note that each technique will present variations of this optimization algorithm, which will be specified in the corresponding sections (Sections D.4.1 to D.4.4). Nevertheless, the methods addressed in this paper exhibit a similar updating scheme.

The main part of the algorithm consists in solving the *state equation* (8) to obtain the *unknown field* $\mathbf{u}(\zeta)$, and computing the corresponding *sensitivities* along with the *objective function value* (equations (14)-a, (16)-a or (18)-a). After computing the topological derivatives of the objective function, some type of *regularization* must be applied to them (e.g., sensitivity filtering and/or temporal regularization) to improve numerical stability and ensure convergence. The topology ζ is then updated accordingly to each approach following a *optimality criterion* so that the objective function is minimized. For a given volume constraint, topology and objective function convergence is sought, thus obtaining the optimal topology design.

Depending on the topology optimization method, a set of intermediate optimal topologies is obtained when using *time-advancing schemes*, while a single optimal design is only obtained

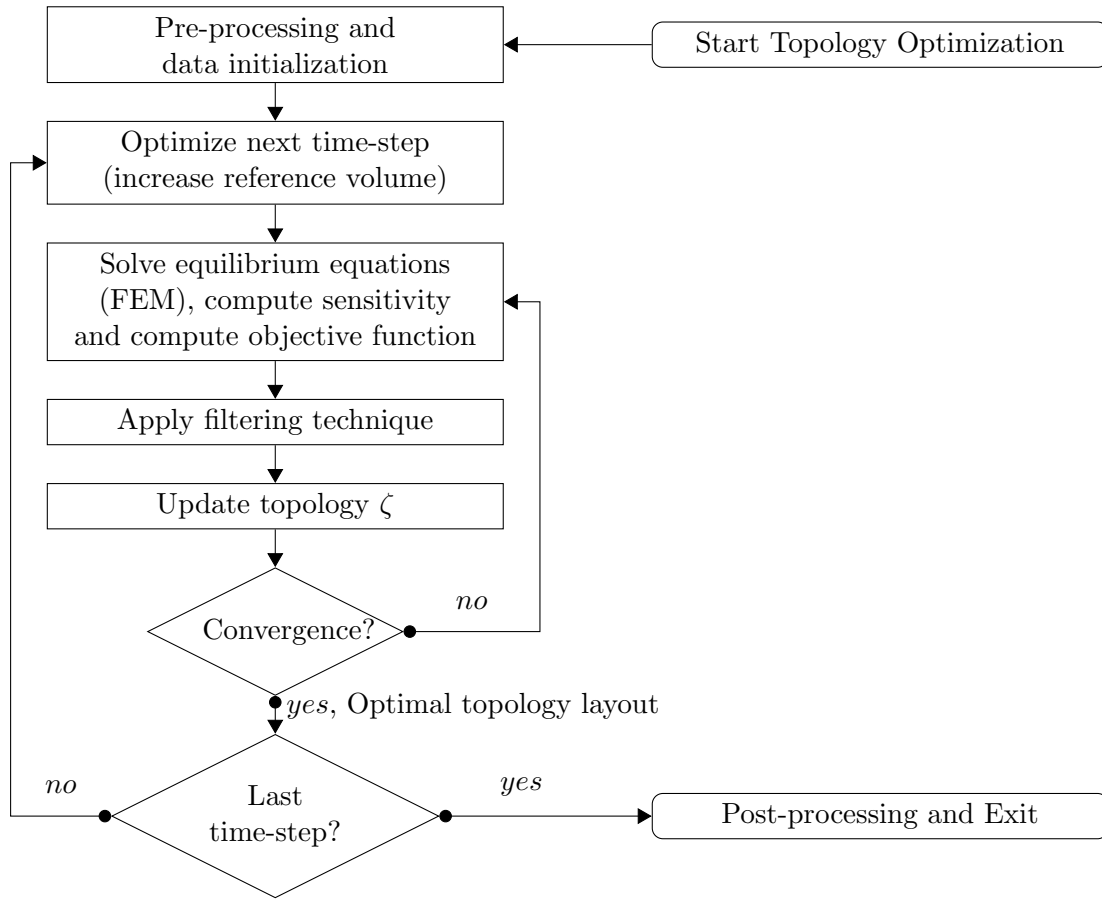


Figure D.3: The general flowchart for topology optimization approaches.

(the last one) for *single-time-step methods* (see Section D.2). For the first family of approaches, the algorithm previously described must be repeated for each time-step until the convergence criteria are met, thus obtaining a set of converged solutions over the *Pareto Frontier* of optimal solutions between the *objective function* and the *volume constraint*.

D.4 Topology Optimization methods

In the following subsections, the specific details of each considered topology optimization method are described, focusing on the differences among them.

D.4.1 SIMP method

As aforementioned, the SIMP approach employs *element-wise density variables* ρ_e as *design variables* to describe the topology layout. Therefore, the design domain Ω is discretized into cells or voxels¹³ and each element e is assigned a density ρ_e . Although ρ_e would ideally be equal to 1 for material and 0 for void, the design variable is here relaxed by allowing intermediate values $0 \leq \rho_e \leq 1$. As a consequence, additional constraints (3-b-2) must be added to the original *topology optimization problem* subject to the volume constraint. Furthermore, the material interpolation of the constitutive tensor \mathbb{C}_ρ is defined as

$$\mathbb{C}_\rho(\rho_e) = \mathbb{C}^- + \rho_e^p (\mathbb{C}^+ - \mathbb{C}^-), \quad \rho_e \in [0, 1], \quad (19)$$

where \mathbb{C}^+ and \mathbb{C}^- correspond to the constitutive tensor of the stiff and soft materials, respectively. In addition, the parameter p stands for the penalization factor (typically $p \geq 3$). For a

¹³Henceforth, both cells and voxels will be referred to as elements.

constant Poisson ratio, equation (19) can be written in terms of the Young's modulus E as

$$\mathbb{C}_\rho(\rho_e) = (E^- + \rho_e^p (E^+ - E^-)) \mathbb{C}_{(1)}, \quad (20)$$

where E^+ and E^- represent the Young's modulus for the stiff and soft materials, respectively, and $\mathbb{C}_{(1)}$ corresponds to the constitutive tensor with unit Young's modulus. Assuming that E^- can be defined proportional to the high Young's modulus, E^+ , via the *contrast factor* α , the resultant constitutive tensor $\mathbb{C}_\rho(\rho_e)$ is defined as \mathbb{C}^+ multiplied by a coefficient, which depends on the *design variable of the element*, i.e.,

$$\mathbb{C}_\rho(\rho_e) = (\alpha + \rho_e^p (1 - \alpha)) \mathbb{C}^+. \quad (21)$$

The global stiffness matrix \mathbb{K}_ρ is obtained via the assembly of element stiffness matrices defined as

$$\begin{aligned} \mathbb{K}_e(\rho_e) &= \int_{\Omega_e} \mathbf{B}^T(\mathbf{x}) \mathbb{C}_\rho(\mathbf{x}) \mathbf{B}(\mathbf{x}) d\Omega = \\ &= (\alpha + \rho_e^p (1 - \alpha)) \int_{\Omega_e} \mathbf{B}^T(\mathbf{x}) \mathbb{C}^+ \mathbf{B}(\mathbf{x}) d\Omega = \\ &= (\alpha + \rho_e^p (1 - \alpha)) \mathbb{K}_e^+, \end{aligned} \quad (22)$$

with \mathbb{K}_e^+ being the element stiffness matrix considering stiff material for element e .

Taking into account these two characteristics, the *topology optimization problem* (3) becomes

$$\left[\begin{array}{l} \min_{\rho \in \mathcal{U}_{ad}} \mathcal{J}(\mathbf{u}(\rho), \rho) \equiv \int_{\Omega} j(\mathbf{u}(\rho), \rho, \mathbf{x}) d\Omega \\ \text{subject to:} \\ \mathcal{C}_0(\rho) \equiv \frac{|\Omega(\rho)|}{|\Omega|} - f \leq 0 \\ \mathcal{C}_e(\rho_e) \leq 0 \rightarrow 0 \leq \rho_e \leq 1, e : 1 \dots N_e \\ \text{governed by:} \\ \mathbb{K}_\rho \hat{\mathbf{u}}_\rho^{(i)} = \mathbf{f}^{(i)} \end{array} \right. \quad \begin{array}{l} (a) \\ \\ (b-1) \\ (b-2) \\ \\ (c) \end{array} \quad (23)$$

where $|\Omega(\rho)|$ and $|\Omega|$ are respectively the stiff material volume and the design domain volume, and f is the prescribed volume fraction¹⁴.

The sensitivity of the objective function (23-a), $\partial \mathcal{J}(\mathbf{u}(\rho), \rho) / \partial \rho_e$, is obtained via the adjoint technique, so that the derivative of the unknown field \mathbf{u}_ρ with respect to the density ρ_e , $\partial \mathbf{u}(\rho) / \partial \rho_e$, is not required to be computed. Additionally, the sensitivity of the volume constraint (23-b-1) with respect to the density of the element e is equal to $|\Omega_e| / |\Omega|$. According to [16], the sensitivity of the objective function for the three *topology optimization problems* addressed in this work are given by

$$\frac{\partial \mathcal{J}^{(I)}(\mathbf{u}(\rho), \rho)}{\partial \rho_e} = -\omega_e(\rho_e) \hat{\mathbf{u}}_e(\rho) \mathbb{K}_e^+ \hat{\mathbf{u}}_e(\rho) \quad (24)$$

$$\frac{\partial \mathcal{J}^{(II)}(\mathbf{u}(\rho), \rho)}{\partial \rho_e} = -\omega_e(\rho_e) \sum_{i=1}^{n_l} \hat{\mathbf{u}}_e^{(i)}(\rho) \mathbb{K}_e^+ \hat{\mathbf{u}}_e^{(i)}(\rho) \quad (25)$$

$$\frac{\partial \mathcal{J}^{(III)}(\mathbf{u}(\rho), \rho)}{\partial \rho_e} = \omega_e(\rho_e) \hat{\mathbf{u}}_e^{(1)}(\rho) \mathbb{K}_e^+ \hat{\mathbf{u}}_e^{(2)}(\rho) \quad (26)$$

where $\omega_e(\rho_e) = p \rho_e^{p-1} (1 - \alpha)$ and $\hat{\mathbf{u}}_e^{(i)}(\rho)$ denotes the nodal displacements of element e and the state equation (i).

¹⁴The term $|(\cdot)|$ denotes the Lebesgue measure of (\cdot) .

As mentioned in Section D.2, a regularization technique must be applied to the original topology optimization problem to ensure the existence of a solution and avoid the formation of the so-called checkerboard patterns. Different filtering techniques modifying the element sensitivity are studied for the comparison, including a radial sensitivity filter computed using the convolution function (see Section D.4.1) and the filter based on *Helmholtz type differential equation* (Section D.4.1). The solution to the filtering technique is denoted by $\widetilde{(\cdot)}$ and replaces the non-filtered sensitivity.

Considering the sensitivities of the objective function and volume constraint, the corresponding *topology optimization problem* can be solved by means of the *Optimality Criteria* (OC) method. The *OC method* seeks the fulfillment of the Karush-Kuhn-Tucker (KKT) conditions

$$\frac{\widetilde{\partial \mathcal{J}}}{\partial \rho_e} + \lambda \frac{\partial \mathcal{C}_0}{\partial \rho_e} = 0, \quad e : 1 \dots N_e, \quad (27)$$

where λ is the *Lagrange multiplier* associated with the volume constraint $\mathcal{C}_0(\boldsymbol{\rho})$ such that the volume constraint is met, and must be computed via a root-finding algorithm (e.g., a bisection method). Note that the element density ρ_e must be in the range of 0 to 1. The *optimality conditions* can be expressed as $B_e = 1$, where

$$B_e = -\frac{\widetilde{\partial \mathcal{J}}}{\partial \rho_e} \left(\lambda \frac{\partial \mathcal{C}_0}{\partial \rho_e} \right)^{-1}. \quad (28)$$

A *heuristic updating scheme*, proposed by Bendsøe and Kikuchi [17], is used to update the design variables and achieve convergence. For *minimum mean compliance*, the scheme is defined as

$$\rho_e^{(k+1)} = \begin{cases} \max(0, \rho_e^{(k)} - m) & \text{if } \rho_e^{(k)} B_e^\eta \leq \max(0, \rho_e^{(k)} - m) \\ \min(1, \rho_e^{(k)} + m) & \text{if } \rho_e^{(k)} B_e^\eta \geq \min(1, \rho_e^{(k)} + m) \\ \rho_e^{(k)} B_e^\eta & \text{otherwise} \end{cases}, \quad (29)$$

where m is a positive move limit, η is a numerical damping coefficient and k represents the iteration counter. These two numerical parameters are typically set 0.2 and 0.5, respectively, for *minimum mean compliance*. Equation (28) is modified for *compliant mechanism optimization problems* to just account for positive sensitivities as

$$B_e = \max\left(\epsilon, -\frac{\widetilde{\partial \mathcal{J}}}{\partial \rho_e}\right) \left(\lambda \frac{\partial \mathcal{C}_0}{\partial \rho_e} \right)^{-1}, \quad (30)$$

with ϵ being a small positive value. Equivalently, the updating scheme (29) can be expressed as

$$\rho_e^{(k+1)} = \begin{cases} \max(0, \rho_e^{(k)} - m) & \text{if } \rho_e^{(k)} B_e^\eta \leq \max(\epsilon, \rho_e^{(k)} - m) \\ \min(1, \rho_e^{(k)} + m) & \text{if } \rho_e^{(k)} B_e^\eta \geq \min(1, \rho_e^{(k)} + m) \\ \rho_e^{(k)} B_e^\eta & \text{otherwise} \end{cases}, \quad (31)$$

with $m = 0.1$ and $\eta = 0.3$.

In the following subsections, three variations of the *SIMP approach* are introduced, mainly by changing the filter used to regularize the sensitivity (for instance, using a distance filter computed via a convolution function and a Helmholtz-type filter) or by trying a *time-advancing strategy* (with multiple steps).

SIMP method using PDE-like filter: SIMP^(I)

In this case, the sensitivities are regularized via a *Helmholtz-type PDE equation* with homogeneous Neumann boundary conditions, as detailed in [66, 13]. The *regularized sensitivities* $\widetilde{\partial\mathcal{J}/\partial\rho_e}$ correspond to the solution of

$$\begin{cases} \widetilde{\zeta} - R_{min}^2 \Delta_{\mathbf{x}} \widetilde{\zeta} = \zeta & \text{in } \Omega \\ \nabla_{\mathbf{x}} \widetilde{\zeta} \cdot \mathbf{n} = 0 & \text{on } \partial\Omega \end{cases}, \quad (32)$$

where ζ and $\widetilde{\zeta}$ are $\rho_e \partial\mathcal{J}/\partial\rho_e$ and $\rho_e \widetilde{\partial\mathcal{J}/\partial\rho_e}$, respectively, and $\Delta_{\mathbf{x}}(\mathbf{x}, \cdot)$ and $\nabla_{\mathbf{x}}(\mathbf{x}, \cdot)$ are the Laplacian and gradient operators. The filter radius R_{min} is equal to $r_{min}/(2\sqrt{3})$, with r_{min} being the filter radius of *distance-based filters* (see subsection D.4.1).

As reported by Lazarov and Sigmund [66], this type of filtering technique provides computational advantages when regularizing the sensitivities for complex non-uniform meshes in terms of memory storage and computational complexity when compared to classical filtering procedures. Although, for structured meshes, as in the cases addressed in this paper, this performance improvement may not be observed.

SIMP method using a time-advancing scheme: SIMP^(II)

An *incremental-time-advancing scheme* can be implemented on top of SIMP^(I). The volume reference of the volume constraint is iteratively updated, thus obtaining a set of intermediate converged solutions. Once the convergence is achieved, the *reference volume fraction* f in equation (23-(b-1)) is decreased and the topology optimization procedure is repeated for the new volume constraint. At the first iteration of each time-step, the volume constraint must be fulfilled, so that the *Helmholtz-type PDE filter* keeps the volume constant.

SIMP method using convolution filter: SIMP^(III)

The filter in this approach modifies the sensitivities $\partial\mathcal{J}/\partial\rho_e$ by means of a standard distance filter as follows

$$\frac{\widetilde{\partial\mathcal{J}}}{\partial\rho_e} = \frac{1}{\max(\gamma, \rho_e) \sum_{i \in N_{ei}} H_{ei}} \sum_{i \in N_{ei}} H_{ei} \rho_i \frac{\partial\mathcal{J}}{\partial\rho_i}, \quad (33)$$

where γ is a small positive number to avoid division by zero and N_{ei} denotes the set of elements i for which the center-to-center distance, $\text{dist}(e, i)$, of element i to element e is smaller than a filter radius r_{min} , defined by the user, i.e., $N_{ei} = \{i \in N_e / \text{dist}(e, i) \leq r_{min}\}$. The function H_{ei} corresponds to the weight factor function (of a linearly decaying filter kernel) given by

$$H_{ei} = \max(0, r_{min} - \text{dist}(e, i)). \quad (34)$$

This sensitivity filter can be mathematically written using a convolution product of the filter function $H(\mathbf{x} - \mathbf{y})$ and the sensitivity of the objective function $\partial\mathcal{J}/\partial\rho(\mathbf{x})$ as

$$\begin{aligned} \frac{\widetilde{\partial\mathcal{J}}}{\partial\rho}(\mathbf{x}) &= \frac{1}{\hat{\rho}(\mathbf{x})} \left(H * \left(\rho \frac{\partial\mathcal{J}}{\partial\rho} \right) \right) (\mathbf{x}) = \\ &= \frac{1}{\hat{\rho}(\mathbf{x}) \int_{\mathbb{B}_r} H(\mathbf{x} - \mathbf{y}) d\mathbf{y}} \int_{\mathbb{B}_r} H(\mathbf{x} - \mathbf{y}) \rho(\mathbf{y}) \frac{\partial\mathcal{J}}{\partial\rho}(\mathbf{y}) d\mathbf{y}, \end{aligned} \quad (35)$$

where \mathbb{B}_r is a sphere in 3D and a circle in 2D with center at \mathbf{x} , and radius r_{min} and $\hat{\rho}$ is equal to $\max(\gamma, \rho_e)$.

D.4.2 SOFTBESO method

The original *ESO* and *BESO methods* use a *discrete density variable* $\chi_e = \{0, 1\}$ as *design variable* in a *hard-kill topology optimization procedure* where elements with low *rejection criterion* are removed from the topology layout. In particular, in *BESO*, elements can be added in specific areas by using extrapolation techniques. However, as mentioned in Section D.2, this set of *hard-kill approaches* suffers from numerical instabilities failing in some circumstances to obtain convergent solutions. For that reason, this paper focuses on *soft-kill evolutionary techniques*, and in particular, in the *bi-directional evolutionary (BESO) approach* proposed by Huang and Xie [59].

In this context, the design variable, now termed as the *element-wise density variable* $\rho_e = \{\rho_{min}, 1\}$, is defined using the original *SIMP material interpolation*, thus relaxing the design variable with a penalization factor p . Therefore, the material interpolation of the constitutive tensor is given by

$$\mathbb{C}_\rho(\rho_e) = \rho_e^p \mathbb{C}^+ = \rho_e^p E^+ \mathbb{C}_{(1)}, \quad \rho_e = \{\rho_{min}, 1\}. \quad (36)$$

Assuming that the Young's modulus of the void material, E^- , can be expressed, in terms of α , as α times the Young's modulus of the stiff material E^+ , then ρ_{min} must be equal to $\sqrt[p]{\alpha}$. A similar procedure as the one defined for *SIMP-based approaches* is used here to compute the element stiffness matrix, i.e.,

$$\mathbb{K}_e(\rho_e) = \int_{\Omega_e} \mathbf{B}^T(\mathbf{x}) \mathbb{C}_\rho(\mathbf{x}) \mathbf{B}(\mathbf{x}) d\Omega = \rho_e^p \int_{\Omega_e} \mathbf{B}^T(\mathbf{x}) \mathbb{C}^+ \mathbf{B}(\mathbf{x}) d\Omega = \rho_e^p \mathbb{K}_e^+, \quad (37)$$

with \mathbb{K}_e^+ being the element stiffness matrix considering stiff material for element e .

The corresponding *topology optimization problem* (3) for *BESO* can be written as

$$\left[\begin{array}{l} \min_{\rho \in \mathcal{U}_{ad}} \mathcal{J}(\mathbf{u}(\rho), \rho) \equiv \int_{\Omega} j(\mathbf{u}(\rho), \rho, \mathbf{x}) d\Omega \quad (a) \\ \text{subject to:} \\ \mathcal{C}_0(\rho) \equiv \frac{|\Omega(\rho)|}{|\Omega|} - f \leq 0 \quad (b-1), \quad (38) \\ \mathcal{C}_e(\rho_e) \leq 0 \rightarrow \rho_e = \{\rho_{min}, 1\}, \quad e : 1 \dots N_e \quad (b-2) \\ \text{governed by:} \\ \mathbb{K}_\rho \hat{\mathbf{u}}_\rho^{(i)} = \mathbf{f}^{(i)} \quad (c) \end{array} \right.$$

where the volume fraction f is decreased at each iteration until the desired final fraction \bar{f} , following an exponential expression $f_{k+1} = \max(\bar{f}, (1 - ER)f_k)$. The evolutionary volume ratio $ER \ll 1$ corresponds to the maximum volume fraction decreased at each iteration. Notice that the convergence in topology and objective are not met until the desired final fraction \bar{f} is reached.

As detailed in Section D.4.1, the sensitivities of the objective function (38-a) $\partial \mathcal{J} / \partial \rho_e$ for the considered topology optimization problems are defined as

$$\frac{\partial \mathcal{J}^{(I)}(\mathbf{u}(\rho), \rho)}{\partial \rho_e} = -\omega_e(\rho_e) \hat{\mathbf{u}}_e(\rho) \mathbb{K}_e^+ \hat{\mathbf{u}}_e(\rho), \quad (39)$$

$$\frac{\partial \mathcal{J}^{(II)}(\mathbf{u}(\rho), \rho)}{\partial \rho_e} = -\omega_e(\rho_e) \sum_{i=1}^{n_l} \hat{\mathbf{u}}_e^{(i)}(\rho) \mathbb{K}_e^+ \hat{\mathbf{u}}_e^{(i)}(\rho), \quad (40)$$

$$\frac{\partial \mathcal{J}^{(III)}(\mathbf{u}(\rho), \rho)}{\partial \rho_e} = \omega_e(\rho_e) \hat{\mathbf{u}}_e^{(1)}(\rho) \mathbb{K}_e^+ \hat{\mathbf{u}}_e^{(2)}(\rho), \quad (41)$$

with $\omega_e(\rho_e)$ being equal to $p\rho_e^{p-1}$.

For the regularization procedure, a *linear distance-based filter*, similar as the one used in $SIMP^{(III)}$, is applied to the sensitivities $\partial\mathcal{J}/\partial\rho_e$. The filtered sensitivities are obtained as

$$\frac{\widetilde{\partial\mathcal{J}}}{\partial\rho_e} = \frac{1}{\sum_{i \in N_{ei}} H_{ei}} \sum_{i \in N_{ei}} H_{ei} \frac{\partial\mathcal{J}}{\partial\rho_i}, \quad (42)$$

which can also be computed using the convolution function of H_{ei} (34) and the non-regularized sensitivities $\partial\mathcal{J}/\partial\rho_e$. In addition to the spatial filtering (used to address the mesh-dependency problem), a temporal filtering is also applied by averaging the sensitivity numbers with historical information, thus improving convergence. The temporal filter can be expressed as

$$\frac{\widetilde{\partial\mathcal{J}}}{\partial\rho_e} \Big|_{e,k} = \frac{1}{2} \left(\frac{\widetilde{\partial\mathcal{J}}}{\partial\rho_e} \Big|_{e,k} + \frac{\widetilde{\partial\mathcal{J}}}{\partial\rho_e} \Big|_{e,k-1} \right), \quad (43)$$

where k corresponds to the iteration number. Notice that the *temporal-filtered sensitivity* used in the *optimality criteria* (44) replaces the spatial-filtered sensitivity.

The optimality criterion for the *topology optimization problem* (38) can easily be derived if no restriction is imposed on the design variable, i.e.,

$$\frac{\widetilde{\partial\mathcal{J}}}{\partial\rho_e} + \lambda \frac{\partial\mathcal{C}_0}{\partial\rho_e} = 0, \quad e : 1 \dots N_e, \quad (44)$$

where the *Lagrange multiplier* λ must be computed so that the volume constraint $\mathcal{C}_0(\boldsymbol{\rho})$ is fulfilled. For *minimum mean compliance problem*, the corresponding updating scheme can be expressed as

$$\rho_e^{k+1} = \begin{cases} 1 & \text{if } \left(-\frac{\widetilde{\partial\mathcal{J}}}{\partial\rho_e} / \frac{\partial\mathcal{C}_0}{\partial\rho_e} - \lambda \right) \geq 0 \\ \rho_{min} & \text{if } \left(-\frac{\widetilde{\partial\mathcal{J}}}{\partial\rho_e} / \frac{\partial\mathcal{C}_0}{\partial\rho_e} - \lambda \right) < 0 \end{cases}, \quad (45)$$

although the number of elements changing from the void domain to the material domain (or equivalently a volume fraction) is limited by a factor AR_{max} . Consequently, if the number of elements changing from the void domain to the material domain is greater than the *maximum volume addition ratio*, only the AR_{max} elements from the void domain with the highest sensitivity are added to the material domain. In the material domain, the $AR_{max} + ER$ elements with the lowest sensitivity are removed from the material domain and replaced with void material, thus satisfying the volume constraint. This procedure ensures that not many elements are added in a single iteration, causing the structure to loose its integrity.

For *compliant mechanism synthesis* [60, 58], the updating equation (45) is relaxed to

$$\rho_e^{k+1} = \begin{cases} \min(\rho_e^{(k)} + m, 1) & \text{if } \left(-\frac{\widetilde{\partial\mathcal{J}}}{\partial\rho_e} / \frac{\partial\mathcal{C}_0}{\partial\rho_e} - \lambda \right) \geq 0 \\ \max(\rho_e^{(k)} - m, \rho_{min}) & \text{if } \left(-\frac{\widetilde{\partial\mathcal{J}}}{\partial\rho_e} / \frac{\partial\mathcal{C}_0}{\partial\rho_e} - \lambda \right) < 0 \end{cases} \quad (46)$$

with $m = 0.1$, where the design variable ρ_e can now take intermediate values.

D.4.3 VARTOP method

As in *Level-set*, the zero-level of the *level-set function* is used to precisely define the boundaries of the material domain, although no updating equation is defined in terms of the *discrimination function* ψ . Instead, the *characteristic function* $\bar{\chi}(\mathbf{x}) = \{\beta, 1\}$ is employed as the design variable, which is computed from the *discrimination function* at each iteration via the Heaviside function

$\mathcal{H}_\beta(\psi(\mathbf{x}))$ ¹⁵ (see Figure D.1). As result, the material interpolation of the constitutive tensor \mathbb{C}_χ is given by

$$\mathbb{C}_\chi(\mathbf{x}) = \chi^m(\mathbf{x})\mathbb{C}^+, \quad \chi(\mathbf{x}) \in [\beta, 1], \quad (47)$$

with β being the *relaxation factor*. It is important to stress that, once the domain is discretized by finite elements, the *characteristic function* will take 1 or β in the majority of the domain, whereas it will only take values ranging 1 to β in the elements bisected by the material boundary Γ . The relaxation factor β is defined such that the Young's modulus for the void material is α times that of the stiff material, i.e.,

$$\mathbb{C}_\chi^-(\mathbf{x}) = \alpha\mathbb{C}^+ = \beta^m\mathbb{C}^+ = \beta^m E^+ \mathbb{C}_{(1)} \quad \text{for } \mathbf{x} \in \Omega^-, \quad (48)$$

with β being

$$\beta = {}^m\sqrt{\alpha}, \quad (49)$$

where m is an *exponential factor* defined by the user and α is the *contrast factor* for the Young's modulus. The element stiffness matrix $\mathbb{K}_e(\chi(\mathbf{x}), \mathbf{x})$ is obtained as

$$\mathbb{K}_e(\chi(\mathbf{x}), \mathbf{x}) = \int_{\Omega_e} \mathbf{B}^T(\mathbf{x}) \mathbb{C}_\chi(\mathbf{x}) \mathbf{B}(\mathbf{x}) d\Omega = \int_{\Omega_e} \mathbf{B}^T(\mathbf{x}) \chi^m(\mathbf{x})\mathbb{C}^+ \mathbf{B}(\mathbf{x}) d\Omega. \quad (50)$$

The *topology optimization problem* (3) is now written as

$$\left[\begin{array}{l} \min_{\chi \in \mathcal{U}_{ad}} \mathcal{J}(\mathbf{u}(\chi), \chi) \equiv \int_{\Omega} j(\mathbf{u}(\chi), \chi, \mathbf{x}) d\Omega \quad (a) \\ \text{subject to:} \\ \mathcal{C}_0(\chi) \equiv \frac{|\Omega^-|}{|\Omega|} - \frac{1}{|\Omega|} \int_{\Omega} \frac{1 - \chi(\mathbf{x})}{1 - \beta} d\Omega = t - \frac{|\Omega^-(\chi)|}{|\Omega|} = 0 \quad (b-1), \quad (51) \\ \text{governed by:} \\ \mathbb{K}_\chi \hat{\mathbf{u}}_\chi^{(i)} = \mathbf{f}^{(i)} \quad (c) \end{array} \right.$$

where the volume constraint $\mathcal{C}_0(\chi)$ has been expressed in terms of the soft material fraction in contrast to equations (23) and (38). The term t stands for the *pseudo-time variable*, used as *time-advancing parameter*.

The *relaxed topological derivative* (RTD), used as an approximation to the *exact geometric topological derivative*, for a functional $\mathcal{F}(\chi) : L^2(\Omega) \rightarrow \mathbb{R}$ is defined as

$$\frac{\delta \mathcal{F}(\chi)}{\delta \chi}(\hat{\mathbf{x}}) = \left[\frac{\partial j(\mathbf{u}(\chi), \chi, \mathbf{x})}{\partial \chi} \right]_{\mathbf{x}=\hat{\mathbf{x}}} \Delta \chi(\hat{\mathbf{x}}), \quad \text{with } \Delta \chi(\hat{\mathbf{x}}) = \begin{cases} -(1 - \beta) < 0 & \text{for } \hat{\mathbf{x}} \in \Omega^+ \\ (1 - \beta) > 0 & \text{for } \hat{\mathbf{x}} \in \Omega^- \end{cases}, \quad (52)$$

where $\Delta \chi(\hat{\mathbf{x}})$ is termed the *exchange function* and stands for the signed variation of $\chi(\hat{\mathbf{x}})$, due to that material exchange. The sensitivity of the volume constraint (51-b-1) with respect to the *characteristic function* is equal to $\text{sgn}(\Delta \chi(\hat{\mathbf{x}}))/|\Omega|$, where $\text{sgn}(\cdot)$ denotes the sign function of (\cdot) . The optimality condition for the *constrained topology optimization problem* can be written as

$$\left(\frac{\partial j(\mathbf{u}(\chi), \chi, \hat{\mathbf{x}})}{\partial \chi} \Delta \chi(\hat{\mathbf{x}}) + \lambda \frac{\text{sgn}(\Delta \chi(\hat{\mathbf{x}}))}{|\Omega|} \right) > 0 \quad \forall \hat{\mathbf{x}} \in \Omega, \quad (53)$$

where λ stands for a *Lagrange multiplier* enforcing volume constraint $\mathcal{C}_0(\chi) = 0$. Therefore, the *closed-form non-linear solution* for the *topology optimization problem* (51), termed as *cutting&bisection* algorithm, can be expressed as

$$\begin{cases} \psi_\chi(\mathbf{x}, \lambda) := \xi(\mathbf{u}(\chi), \chi, \mathbf{x}) - \lambda/|\Omega| \\ \chi(\mathbf{x}, \lambda) = \mathcal{H}_\beta[\psi_\chi(\mathbf{x}, \lambda)] \\ \mathcal{C}_0(\chi(\mathbf{x}, \lambda)) = 0 \end{cases}, \quad (54)$$

¹⁵The image set $\{1, 0\}$ of the *Heaviside function* is relaxed to $\{1, \beta\}$, this being highlighted with the subscript $(\cdot)_\beta$ in the *Heaviside function* symbol.

where $\xi(\mathbf{u}(\chi), \chi, \mathbf{x})$ is termed the *pseudo-energy* and depends on the specific objective function. The Lagrange multiplier λ is computed using an efficient bisection algorithm and its value fulfils the volume constraint, as in the previous approaches.

For the three *topology optimization problems*, the *pseudo-energies* at point $\hat{\mathbf{x}}$ are given by

$$\xi^{(I)}(\mathbf{u}(\chi), \chi, \hat{\mathbf{x}}) = \omega(\hat{\mathbf{x}}) \hat{\mathbf{u}}(\chi, \hat{\mathbf{x}}) \check{\mathbb{K}}^+(\hat{\mathbf{x}}) \hat{\mathbf{u}}(\chi, \hat{\mathbf{x}}), \quad (55)$$

$$\xi^{(II)}(\mathbf{u}(\chi), \chi, \hat{\mathbf{x}}) = \omega(\hat{\mathbf{x}}) \sum_{i=1}^{n_l} \hat{\mathbf{u}}^{(i)}(\chi, \hat{\mathbf{x}}) \check{\mathbb{K}}^+(\hat{\mathbf{x}}) \hat{\mathbf{u}}^{(i)}(\chi, \hat{\mathbf{x}}), \quad (56)$$

$$\xi^{(III)}(\mathbf{u}(\chi), \chi, \hat{\mathbf{x}}) = -\omega(\hat{\mathbf{x}}) \hat{\mathbf{u}}^{(1)}(\chi, \hat{\mathbf{x}}) \check{\mathbb{K}}^+(\hat{\mathbf{x}}) \hat{\mathbf{u}}^{(2)}(\chi, \hat{\mathbf{x}}), \quad (57)$$

for non-bisected elements, with $\omega(\hat{\mathbf{x}})$ being equal to $m\chi^{m-1}(\hat{\mathbf{x}})(1 - \beta)$ ¹⁶ and $\check{\mathbb{K}}^+$ being the integrand of the stiffness matrix at point $\hat{\mathbf{x}}$. However, the *pseudo-energy* must be first shifted and normalized, according to

$$\hat{\xi}(\mathbf{u}(\chi), \chi, \hat{\mathbf{x}}) = \frac{\xi(\mathbf{u}(\chi), \chi, \hat{\mathbf{x}}) - \chi(\hat{\mathbf{x}})\Delta_{shift}}{\Delta_{norm}}, \quad (58)$$

thus obtaining a *modified energy density* $\hat{\xi}(\mathbf{u}(\chi), \chi, \hat{\mathbf{x}})$. The terms Δ_{shift} and Δ_{norm} correspond, respectively, to the shifting and normalization parameters defined at the first iteration¹⁷. This variable must be later regularized using a Laplacian regularization (similar as the one described in Section D.4.1 for SIMP^(I)). The *pseudo-energy density* actually used in the *closed-form solution* (54) comes from the resolution of

$$\begin{cases} \hat{\xi}_\tau - (\tau h_e)^2 \Delta_{\mathbf{x}} \hat{\xi}_\tau = \hat{\xi} & \text{in } \Omega \\ \nabla_{\mathbf{x}} \hat{\xi}_\tau \cdot \mathbf{n} = 0 & \text{on } \partial\Omega \end{cases}, \quad (59)$$

where, $\Delta_{\mathbf{x}}(\mathbf{x}, \cdot)$ and $\nabla_{\mathbf{x}}(\mathbf{x}, \cdot)$ are respectively the Laplacian and Gradient operators, and \mathbf{n} is the outward normal to the boundary of the design domain, $\partial\Omega$. τ and h_e stand for the dimensionless *regularization parameter* and the typical size of the finite element mesh, respectively.

Contrary to the common *SIMP implementations* (SIMP^(I) and SIMP^(III)) or the *BESO method*, the *VARTOP* is formulated under a *time-advancing framework*, where the *pseudo-time* t in equation (51-b-1) is iteratively increased, thus obtaining intermediate converged solutions, which are local minima and provide a Pareto Frontier in terms of the volume fraction. Notice that, at every time-step, convergence is achieved unlike the algorithm used for *BESO*.

D.4.4 Level-set method via a Hamilton-Jacobi equation

As previously mentioned in the introduction, *Level-set methods* use a *level-set function* (LSF) to implicitly represent the optimal material domain via equation (2), and the material boundary via the 0-level of the *level-set function*. It is important to note that originally *Level-set approaches* only updated the material boundary based on a differential equation, preventing them from creating new voids. This drawback was first overcome by inserting new voids every certain iteration. However, Yamada *et al.* [139], among other researchers, suggested an approach in which a *Level-set method* was used to update not only the boundary of the material domain, but also the material domain itself, thus allowing to nucleate new voids. This specific approach will be taken as the reference in this article in conjunction with the *relaxed topological derivative* (RTD), defined in equation (52), to obtain the sensitivity function.

¹⁶For points in the boundary material, the *characteristic function* and the element stiffness matrix should be replaced with the corresponding ones, as detailed in [90].

¹⁷The terms Δ_{shift} and Δ_{norm} are defined as $\min(\xi_0, 0)$ and $\max(\text{range}(\xi_0), \max(\xi_0))$, respectively.

In contrast to *VARTOP*, the LSF is updated via a *time-dependent updating equation*, typically using a *Hamilton-Jacobi equation*, although other updating schemes can be used. From the *level-set function*, a *characteristic function* $\bar{\chi}$ can be defined as

$$\bar{\chi}(\mathbf{x}, \phi(\mathbf{x})) = \mathcal{H}_\beta(\phi(\mathbf{x})) = \begin{cases} 1 & \text{for } \phi(\mathbf{x}) \geq 0 \\ \beta & \text{for } \phi(\mathbf{x}) < 0 \end{cases} \quad (60)$$

with β being the *relaxation factor*. Based on the preceding definition of the *characteristic function*, the corresponding material interpolations (equations (47) to (50)) are defined. The *topology optimization problem* (3), in terms of the *level-set function*, becomes

$$\left[\begin{array}{l} \min_{\phi \in \mathcal{U}_{ad}} \mathcal{J}(\mathbf{u}(\phi), \bar{\chi}(\phi)) \equiv \int_{\Omega} j(\mathbf{u}(\phi), \bar{\chi}(\phi), \mathbf{x}) d\Omega \quad (a) \\ \text{subject to:} \\ \mathcal{C}_0(\phi) \equiv t - \frac{|\Omega^-(\bar{\chi}(\phi))|}{|\Omega|} = 0 \quad (b-1) \\ \mathcal{C}_n(\hat{\phi}_n) \leq 0 \rightarrow -1 \leq \hat{\phi}_n \leq 1, n : 1 \dots N_n \quad (b-2) \\ \text{governed by:} \\ \mathbb{K}_\phi \hat{\mathbf{u}}_\phi^{(i)} = \mathbf{f}^{(i)} \quad (c) \end{array} \right. , \quad (61)$$

where the nodal *level-set function* $\hat{\phi}_n$ must be bounded between -1 and 1 , for convergence reasons. From equation (61), the *Lagrangian function* can be expressed as

$$\mathcal{L}(\mathbf{u}(\bar{\chi}(\phi)), \bar{\chi}(\phi), \lambda) = \mathcal{J}(\mathbf{u}(\bar{\chi}(\phi)), \bar{\chi}(\phi)) + (\lambda + \frac{1}{2}s \mathcal{C}_0(\bar{\chi}(\phi))) \mathcal{C}_0(\bar{\chi}(\phi)), \quad (62)$$

when an *Augmented Lagrangian method* is used to fulfill the volume constraint. Therefore, the *optimality condition* (53) for the *characteristic function* $\bar{\chi}(\mathbf{x}, \phi(\mathbf{x}))$ reads

$$\frac{\delta \mathcal{L}(\mathbf{u}(\bar{\chi}(\phi)), \bar{\chi}(\phi), \lambda)}{\delta \bar{\chi}}(\hat{\mathbf{x}}) = \left(\frac{\partial j(\mathbf{u}(\bar{\chi}(\phi)), \bar{\chi}(\phi), \hat{\mathbf{x}})}{\partial \bar{\chi}} \Delta \bar{\chi}(\hat{\mathbf{x}}) + (\lambda + s \mathcal{C}_0(\bar{\chi}(\phi))) \frac{\text{sgn}(\Delta \bar{\chi}(\hat{\mathbf{x}}))}{|\Omega|} \right) > 0 \quad \forall \hat{\mathbf{x}} \in \Omega, \quad (63)$$

where λ and s stand for the *Lagrange multiplier* and the penalty factor of the *Augmented Lagrangian method*. Notice that the same *pseudo-energy functions* as in *VARTOP* (equations (55) to (57)) are obtained for the three topology optimization methods.

Instead of the *closed-form non-linear solution* described in Section D.4.3, for each time-step the topology in this approach, ϕ , is updated via a *Hamilton-Jacobi equation*, i.e.,

$$\frac{\partial \phi}{\partial t} = \kappa \frac{\delta \mathcal{L}(\mathbf{u}(\bar{\chi}(\phi)), \bar{\chi}(\phi), \lambda)}{\delta \bar{\chi}} \quad \text{in } \Omega, \quad (64)$$

where the *shape derivative* of the Lagrangian has been replaced with the corresponding *relaxed topological derivative* (52), and κ corresponds to a coefficient of proportionality. Substituting equation (63) to the preceding equation gives

$$\phi_{k+1} = \phi_k + \Delta t \kappa \left(\frac{\partial j(\mathbf{u}(\bar{\chi}(\phi_k)), \bar{\chi}(\phi_k), \hat{\mathbf{x}})}{\partial \bar{\chi}} \Delta \bar{\chi}(\hat{\mathbf{x}}) - \frac{\lambda_k + s \mathcal{C}_0(\bar{\chi}(\phi_k))}{|\Omega|} \right) \quad (65)$$

with

$$\lambda_k = \lambda_{k-1} + s \mathcal{C}_0(\bar{\chi}(\phi_k)). \quad (66)$$

The new *level-set function* ϕ_{k+1} is then regularized via the *Laplacian regularization* (59), and the corresponding *characteristic function* $\bar{\chi}_{\phi, k+1}(\mathbf{x}, \phi_{\tau, k+1}(\mathbf{x}))$ is computed based on the regularized LSF, $\phi_{\tau, k+1}(\mathbf{x})$, using equation (60).

As defined in equation (61), a *time-advancing framework* can be formulated, thus obtaining a set of intermediate, converged optimal solutions. However, in addition to the topology and objective function criteria, the volume constraint must be checked to ensure convergence for every time-step, since it is no longer enforced at each iteration.

D.5 Benchmark cases

A set of four numerical examples in 3D problems is used to compare the six different implementations with each other. The set of benchmark cases contains two *minimum compliance problems* (Section D.3.2), one *multi-load compliance problem* (Section D.3.2) and one *compliant mechanism synthesis* (Section D.3.2). In all cases and methods, eight-node hexahedral (Q_1) finite elements¹⁸ are used in the solution of the state equation (8).

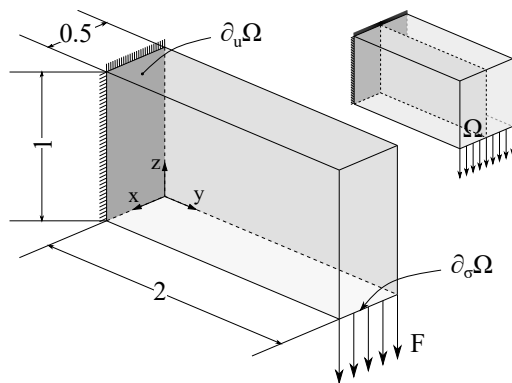
This set of 3D problems has been carefully selected to be used as benchmark cases using a variety of topology optimization techniques, which have been widely used for this purpose by different researchers. All of them exhibit a high geometric complexity and represent a significant challenge for the considered methods when solving the optimization problems. They are defined in the following subsections.

D.5.1 Cantilever beam

This first numerical example refers to the minimization of the *structural mean compliance* of a cantilever beam in a prismatic domain subjected to specific Dirichlet and Neumann boundary conditions. The displacements are prescribed on the left face of the design domain and a distributed vertical load is applied on the bottom-right edge of it. The analysis domain Ω , displayed in Figure D.4, corresponds to a prism of (relative) dimensions 1x2x1, with the largest dimension oriented in the y -axis. Thanks to the symmetry with respect to the $y - z$ plane, half of the domain is discretized with 50x200x100 unit cubic hexahedral elements.

This benchmark will be used to check the correctness of the implementations as well as to have a first comparison of the results obtained with each technique in terms of the number of iterations, objective function and topology quality. Some optimal layouts for different volume fractions can be found in [1, 66].

Figure D.4: Cantilever beam: topology optimization domain with boundary conditions and dimensions. A distributed vertical load F is applied on the bottom-right edge while the displacements \mathbf{u} are prescribed to $\mathbf{0}$ on the left surface of the domain. The rear surface of the domain, in soft gray, represents the surface of symmetry.



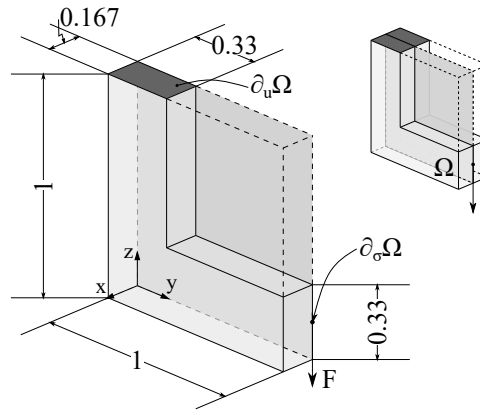
D.5.2 L-shaped structure

This second example tackles the optimization of a simplified version of a hook, as it is shown in Figure D.5. This optimization problem, as the previous one, also corresponds to the minimization of the *mean compliance* (14). The analysis domain is split into two regions: 1) the L-shaped structure, which corresponds to the design domain Ω , and 2) a prismatic volume prescribed as void in the top right area, defined by $y \geq \frac{1}{3}$ and $z \geq \frac{1}{3}$. A single vertical load is applied as illustrated in Figure D.5 at point $x = 0$, $y = 1$ and $z = \frac{1}{6}$ and the displacements at the top side, near the left edge, are prescribed (i.e., $y \leq \frac{1}{3}$ and $z = 1$). The design domain, with symmetry in the $y - z$ plane, is discretized with a structured mesh of 30x180x180 hexahedral elements.

¹⁸The design domains are assumed to be prismatic domains discretized with hexahedral unit cubic finite elements, i.e., a regular finite element mesh. Consequently, some of the advantages of *Laplacian filters* over *distance-based filters* may not be noticed.

Similarly to the previous problem, this example will provide a comparison between the approaches, but now with a more complex design domain (a rough edge domain with a point-wise load), thus showing the performance of the methods against point loads and non-rectangular design domains. The reader is sent to [74] for the reference optimal solution.

Figure D.5: L-shaped structure: topology optimization domain with boundary conditions. A point-wise vertical force F is applied on the right-bottom surface while the displacements \mathbf{u} are prescribed on the top-left boundary of the design domain. The rear boundary corresponds to the $y - z$ symmetry surface. A considerable fraction of the domain (on the top-right side of the domain) is prescribed to void material.



D.5.3 Multi-load cantilever beam

A multi-load topology optimization problem with two different loading conditions not applied at once is optimized in this example. Both the dimensions of the prismatic domain, Ω , and the discretization mesh are the same ones as in the first example (see Section D.5.1). However, in this case, the displacements of all the nodes on the left side are imposed and two loading conditions are applied on the top and bottom-right edges. In the first loading condition, a vertical distributed downward force is applied on the bottom-right edge while in the second one, a distributed force with the same magnitude is applied upwards on the upper-right edge, as displayed in Figure D.6.

Through this numerical case, it is aimed at determining whether the methods are capable of obtaining symmetric designs when two opposite forces are applied in the design domain, as well as to compare the topology quality and computational cost of the resultant optimal topologies with all the considered techniques.

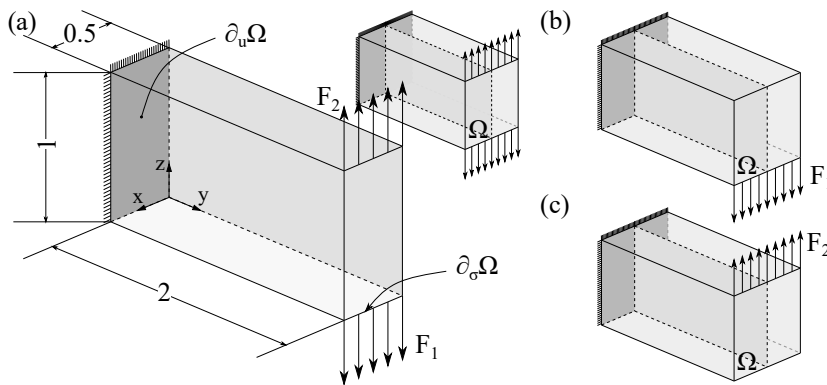
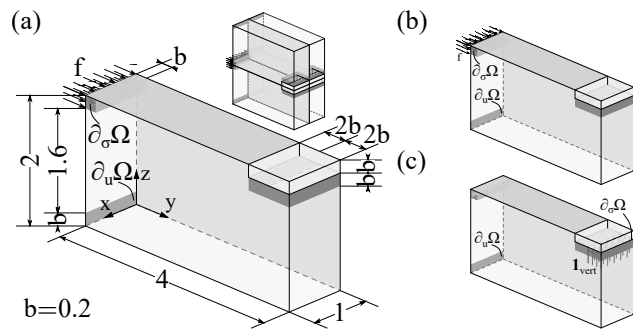


Figure D.6: Multi-load Cantilever beam: (a) topology optimization domain with boundary conditions. The displacements are prescribed on the left surface of the domain, and a vertical distributed downward force F_1 is applied in the first loading case (b), whereas a vertical distributed upward force F_2 , in the second loading case (c). The rear boundary of the domain corresponds to the symmetry surface.

D.5.4 Gripper compliant mechanism

In this last numerical example, a *compliant mechanism* is designed where the vertical displacement at the *output port* is maximized. The displacements are prescribed near the bottom edge at the left side of the domain ($y = 0$ and $z \leq 0.2$). As illustrated in Figure D.7, a positive, horizontal distributed load is applied at the *input port* ($y = 0$ and $z \geq 1.8$), while a vertical upward *dummy load* is applied at the *output port* ($z = 1.8$ and $y \geq 3.6$). The analysis domain Ω , whose (relative) dimensions are $2 \times 4 \times 4$, is discretized with a mesh of $100 \times 200 \times 200$ hexahedral elements. However, thanks to the two existing symmetries, only a quarter of the domain is analyzed, thus leading to 1.000.000 finite elements. In addition, two regions near the *input* and *output ports* are prescribed to stiff material to guarantee stiff material in those areas ($\Delta z = 0.2$).

Figure D.7: Gripper (*compliant mechanism*): (a) topology optimization domain with boundary conditions. The displacements are prescribed at the bottom part of the left surface of the domain, and a positive, horizontal distributed load is applied at the top of the left surface for the state equation (b), while a positive, vertical distributed dummy load is applied at the jaws of the gripper for the *additional state equation* (c). The top and rear surfaces correspond to the $x - y$ and $x - z$ symmetries, respectively.



Additionally, surface distributed springs are included in the *input* and *output ports* (in the same direction as the target displacement) to restrict the displacement amplitude at these areas and simulate both the input work of the actuator and the elastic reaction work at the output port. The corresponding numerical values for the springs are $K_{in} = 1.5 \cdot 10^{-1} N/m^3$ and $K_{out} = 1.5 N/m^3$, while the distributed forces are $f_1 = 3.81 \cdot 10^{-3} N/m^2$ and $f_2 = 3.81 \cdot 10^{-4} N/m^2$, respectively. Note that the optimal solution will heavily depend on the ratios of these parameters, however not all parameter combinations will ensure a convergent admissible solutions. For that reason and due to the non-semi-definite *topological derivative*, this last example will provide an analysis of the performance of the different techniques with respect to the *design of compliant mechanisms*, produced either with localized hinges or deformable bars (for optimal reference solutions refer to [120, 139, 58]).

D.6 Comparison of methods

D.6.1 Comparison settings

In the following subsections, the basis of the comparison will be detailed, specifying the platform on which Matlab will be executed, the versions for the Matlab codes of each approach as well as the specific parameters used in each method and numerical example. In addition, it is important to define equivalent convergence criteria for the different techniques in order to guarantee a fair comparison in terms of the computational cost.

Computing cluster features

The benchmark cases are solved on a cluster, in which each node consists of two AMD EPYC 7451 with 24 cores (48 threads) each one at 2.9 GHz and 1 TB DDR4 RAM memory at 2666 MHz. Each example is solved using eight cores and 99 GB of RAM memory to ensure enough

memory for each of the numerical benchmarks. In this way, a greater number of cases can be solved at once without affecting the result of each approach. All these cases are computed using modified codes in Matlab 2018b under Scientific Linux 7.2 (based on RedHat Enterprise 7.2).

Matlab codes

All the codes used in this paper are 3D extensions of the respective 2D codes, already published by their respective developers, preserving the original algorithmic structure.

Firstly, *SIMP-based method* codes are based on the 2D implementation initially introduced by Sigmund [106] in the 99-line program for two-dimensional topology optimization. This program was later improved by Andreassen *et al.* [13], who vectorized the element loops in the assembly and filtering strategies. The code in Matlab was later extended to three-dimensional topology optimization problems by Liu and Tovar [74], who provided the analytical element stiffness matrix for a cubic hexahedral element. Therefore, the *SIMP method with PDE-filtering* ($SIMP^{(I)}$) and *SIMP method with convolution filter* ($SIMP^{(II)}$) take the basic scheme from the 82-line program (using a PDE filter) and the 71-line program (with the `conv2` function) from [121], respectively, and implement the formulation for the 3D elastic problem from [74]. Both approaches use the *optimality criteria (OC) method* combined with a *sensitivity filtering* ($ft = 1$) to solve the corresponding *topology optimization problem*. It is worth noticing that the L_∞ norm of the design variable has been replaced by a L_2 norm normalized with the size of the domain. In addition, some minor changes to the OC Matlab function have been done to correctly consider active and passive elements. As mentioned, the *SIMP method using time-advancing scheme* ($SIMP^{(II)}$) employs the same scheme as the *SIMP method with PDE-filtering* ($SIMP^{(I)}$), but this time using a *time-advancing scheme*, similar as the one implemented in *VARTOP* [90, 135].

Secondly, a *Soft-kill BESO* code, implemented in Matlab, has been adapted from the one presented by Huang and Xie [60] in chapter 4 for *2D topological stiffness optimization*. This code has been extended to three-dimensional problems mimicking the Matlab code for $SIMP^{(III)}$, since they share most of the general scheme of the algorithm. Some modifications have been done to adapt the specific updating scheme, the sensitivity filtering along with the corresponding temporal filtering (the so-called *averaging scheme* in [60]). Additional minor changes must be implemented in the sensitivity and stiffness computations, since the original SIMP material interpolation is used instead of the one implemented in [13], with two unique discrete values: $\rho = \{1, \rho_{min}\}$ for the *minimum mean compliance problem* (see Section D.4.2). In this particular scenario, the minimum value ρ_{min} is imposed to elements in the void domain to avoid *zero stiffness elements*. Additionally, a similar L_2 norm of the topology, implemented for *SIMP-based methods*, is here also used to check if the topology has converged in addition to the existing one in objective function.

Thirdly, the Matlab code for *VARTOP* is a 3D extension of the corresponding program for 2D topology optimization problems provided in [135]. The element stiffness matrices, as a product of the strain-displacement matrix with the nominal constitutive tensor, are precomputed for the non-bisected and bisected elements, here termed *mixed elements*. In this way, once the type of element has been determined, the global stiffness matrix can be quickly computed and assembled. In addition, the *pseudo-energy density* is also easily computed from the matrices calculated with the reference element. In this case, a *Laplacian smoothing*, applied to the *pseudo-energy density* at each iteration, is precomputed at the first iteration as implemented in $SIMP^{(I)}$. Finally, the *Lagrange multiplier* is computed using the *closed-form optimality method* in conjunction with a *modified marching cubes method* to compute the volume, explained in Oliver *et al.* [90]. The convergence criteria defined in [90] are replaced with the objective function criterion and the topology criterion in terms of a *relaxed design variable*, in addition to the volume constraint.

Finally, the *Level-set* method using the *Relaxed Topological Derivative* (RTD) corresponds to a modification of the previous code for *VARTOP*, where the updating scheme is changed. Instead of the original *closed-form optimality criteria*, a *Hamilton-Jacobi* equation is used to

update the *level-set function* with a given Δt , as detailed in Oliver *et al.* [90]. An *Augmented Lagrangian method* is used to ensure the volume constraint equation \mathcal{C}_0 . The stiffness matrices as well as the different terms required to compute the *pseudo-energy density* are precomputed at the initial iteration. The same *Laplacian smoothing* as in *VARTOP* is here applied to the *level-set function* at each iteration. In addition to the two existing convergence criteria, the volume constraint must be also considered in the outer loop.

Guidelines for the comparison

The general guidelines for a fair comparison are listed below:

1. Benchmark cases: the same numerical benchmark cases and finite element meshes must be used for every topology optimization approach. Four benchmark cases will be carried out using dense meshes (around 1 million finite element) in order to obtain *high-quality designs*.
2. Target volume fraction: the same ratio of the final material domain is imposed by the constraint equation in each approach, which is fulfilled through different techniques. The desired volume fraction corresponds to a small ratio of material with respect to the initial design domain, so that a large material reduction is achieved throughout the topology optimization. For three-dimensional problems using high dense meshes, this value will commonly be between 80% and 95% of the design domain, Ω , depending on user requirements. Nevertheless, it will depend on each specific numerical example and its respective boundary conditions as connections between the different boundary conditions areas must be preserved. This ensures a stiff connection between the nodes in which the loads are applied and those where the displacements are prescribed in the elastic problem.
3. Objective function normalization: since not all the methods start from a full material configuration, an initial iteration with this material layout is computed in all Matlab codes as a reference iteration. The objective function value at this iteration, \mathcal{J}_0 , is used to normalize the subsequent iterations in each method, thus obtaining equivalent values for each numerical example, technique and volume fraction. However, the use of different design variables, nodal¹⁹ versus element²⁰ variables, produces huge discrepancies in the actual objective function value since the stiffness of semi-dense elements is underestimated [112]. For that reason, an additional final iteration is computed with an element *black-and-white* configuration, i.e $\chi, \rho = \{1, 10^{-9}\}$, thus obtaining a fully equivalent objective function value. Nevertheless, it is important to point out that this configuration is not practical from a design standpoint as the smoothness of the design is lost in the projection. The reader is addressed to Appendix D.B for further details.
4. Contrast factor: since each compared topology optimization approach defines a different material interpolation for the constitutive tensor \mathbb{C}_ζ , it is important to ensure the same contrast factor α , so that the same Young's modulus is used for the soft material when using the *ersatz material approach*. This parameter may strongly affect the objective function value and the convergence of the topology optimization. A preliminary study has revealed that topology convergence can be achieved for contrast factors up to $\alpha = 10^{-6}$, for *minimum mean compliance problems*. Thus, this value will be used as *contrast factor* for this type of problems.

¹⁹The *characteristic function*, defined through the *discrimination function*, is used as design variable in the *Level-set* and *VARTOP methods*. Therefore, the material interface is precisely defined by the *level-set function* or *discrimination function*, respectively.

²⁰The density is defined for each element either using a continuous material interpolation for the *SIMP-like approaches* or a discrete solution for the *Soft-kill BESO method*.

5. Convergence criteria: in order to guarantee a fair comparison, the convergence criteria of each approach must be replaced with the same equivalent conditions:

- Volume constraint: the same tolerance $Tol_{c_0} = 10^{-3}$ in the volume constraint (3-b-1) is assumed for all the topology optimization approaches, except in *Level-set*. In this approach, the tolerance is slightly relaxed to $5 \cdot 10^{-3}$, in order to improve convergence when using the *Augmented Lagrangian method*.
- Objective function criterion: a (weighted) moving mean of the relative objective function \mathcal{J} is evaluated along n consecutive iterations as

$$\Delta \mathcal{J}_k = \frac{1}{n} \sum_{i=k-n}^{i=k} \frac{|\mathcal{J}_i - \mathcal{J}_{i-1}|}{\mathcal{J}_0}, \quad (67)$$

where the parameter k denotes the k -th iteration and \mathcal{J}_0 stands for the objective function at the initial iteration. The appropriate number of iterations n depends on the topology optimization technique, as the number of iterations per time-step will not be the same. Notice that, for *time-advancing schemes*, the $n + 1$ iterations correspond to the same time-step, thus avoiding variations in the objective function due to the change of volume constraint. For all the benchmark cases, a tolerance $Tol_{\mathcal{J}} = 10^{-3}$ in the objective function is prescribed.

- Topology criterion: a L_2 norm between two consecutive iterations is evaluated in a *relaxed design variable* ρ as

$$\Delta \rho_k = \frac{1}{|\Omega_0|^{1/2}} \left(\int_{\Omega} (\rho_k - \rho_{k-1})^2 d\Omega \right)^{1/2}, \quad (68)$$

where k represents the iteration number and $|\Omega_0|$ stands for the material volume at the first iteration. The design variable ρ_k corresponds to a *relaxed characteristic function* for discrete design variables (for instance, in the *VARTOP*, *SOFTBESO*, and *Level-set methods*) or to the density variable for the *SIMP approaches*. In Appendix D.A, the reader can find the exact definition of this topology criterion for discrete design variables. For this criterion, the convergence tolerance is $Tol_{\zeta} = 2.5 \cdot 10^{-3}$.

For *incremental time-advancing methods*, such as the *VARTOP*, *SIMP^(II)*, and *Level-set methods*, a linear variation of the tolerances in cost and topology is defined, starting from a higher value for the first time-step (around one order of magnitude higher) to the value established in the last time-step. Consequently, all approaches obtain the convergence with the same criteria for the last increment (i.e., for the same stiff material fraction), thus resulting in a fair comparison.

It is important to stress that the objective function criterion is not a reliable indicator of convergence in *compliant mechanism synthesis problems*. The normalized objective function oscillates significantly more than in *minimum mean compliance problems* in all methods, thus preventing to obtain an optimal solution. This oscillation may be related to this specific type of problem, and, in particular, to the initial value of the objective function which may be null. As a consequence, the normalization of the objective function can not be performed, thus invalidating this convergence criterion. For these reasons, the objective function criterion has not been considered in the last numerical benchmark of this paper. However, it can be used in the other three benchmark cases since a proportionality between the objective and topology criteria is observed, both monotonously converging to the optimal values. In addition, the normalization problem is not detected in *minimum mean compliance problems* as the external work is different from 0 in any case. In case it would also be omitted in these examples, no substantial change would be observed with respect to the obtained results, just resulting in minimal variations in the number of iterations to converge.

Parameter definition

For each topology optimization method and benchmark case, a specific set of parameters must be defined. These parameters define the material behavior (via the *contrast factor* or minimum Young's modulus), the volume fraction, the convergence tolerances, the exact updating parameters for the design variable, and the the ones for the regularization technique.

Whenever possible, common values in material properties, volume fraction, and convergence tolerances will be imposed for the different benchmark cases and topology optimization methods. However, the specific updating parameters depend on each approach and numerical example due to convergence issues. In particular, a consistent difference is noticed regarding the definition of the parameters for *minimum mean compliance* and *compliant mechanism synthesis problems*, as already commented.

Regarding the target volume fraction, a 10% volume fraction of stiff material and a *contrast factor* $\alpha = 10^{-6}$ are imposed for *minimum mean compliance* problems. As for *compliant mechanism synthesis problem*, the volume constraint is applied for a 15% volume fraction, while *contrast factor* is increased to $\alpha = 10^{-2}$. In both problems, a linear isotropic material with a Young's modulus $E = 1$ and Poisson's ratio $\nu = 0.3$ is used.

The updating and regularization parameters depend on each approach, and in certain cases, on the optimization problem. The exact values of these parameters are detailed in Appendix D.C. In general, the parameters of each method are given as follows:

- **SIMP-based methods:** the penalty value and the minimum radius are prescribed to $p = 3$ and $r_{min} = 3$, respectively. A sensitivity filtering ($ft = 1$) is used for the topology optimization, as aforementioned. The updating parameters m and η are defined according to the optimization problem, corresponding to 0.2 and 0.5 for *minimum compliance problems*, and 0.1 and 0.3, respectively, for *compliant mechanism design problem*.
- **SOFTBESO:** the same values for the penalty factor and minimum radius as those in SIMP are used. The *evolutionary ratio* ER and the *maximum volume addition ratio* AR_{max} are prescribed to 0.01 and 0.1, respectively.
- **VARTOP:** the number of steps n_{steps} , the exponential factor m and the regularization factor τ depend on each problem. However, the same value of time-steps as SIMP^(II) is used for each benchmark case.
- **Level-set:** in contrast to SIMP^(II) and VARTOP, the optimizations are carried out with a single time-step. However, the same exponential factors as the ones in VARTOP are employed, and the regularization factor τ is set to 1. In addition, the time-increment Δt and the penalty coefficient s of the *Augmented Lagrangian method* also change with the optimization problem.

For *incremental time-advancing techniques* with multiple time-steps, the volume fraction of stiff material at each step is reduced following an exponential evolution

$$f_j = f_0 + \frac{\bar{f} - f_0}{1 - e^k} \left(1 - e^{k \frac{j}{n_{steps}}} \right), \quad j : 1 \dots n_{steps} \quad (69)$$

with factor $k = -2$.

D.6.2 Results

The results obtained from the six topology optimization approaches are now compared with each other for every of the numerical benchmarks (see Section D.5). The comparison is carried out in terms of the optimal topology, objective function value, and the computational cost, discussing the relative objective function values and the relative computation costs. In addition, an analysis of the convergence is also performed. Finally, an overall comparison of the different methods is made according to the results.

General discussion of results

The optimal topology layout for the required material volume is here compared for the six different approaches from a quantitative and qualitative standpoint. In particular, the quality of the optimal solution is discussed together with the minimum filament size of the resulting (linear) pieces of the final design (bars), the computational cost in terms of the iterations, and the normalized value of the objective function for the four addressed benchmark cases.

Cantilever beam The final solutions of the Cantilever beam problem for each topology optimization technique are displayed in Table D.1. Although the resultant topologies are quite different, all methodologies except for $SIMP^{(II)}$ obtain a similar overall optimal design consisting of two separated webs. However, these webs present a different internal layout and topology complexity. The designs obtained from $SIMP^{(I)}$, $SIMP^{(III)}$, $VARTOP$, and $Level-set$ illustrate a much simpler design based on bars, while $SOFTBESO$ produces an optimal design with a thin web (or a high number of close bars), with almost constant thickness. On the other side, $SIMP^{(II)}$ finds a different optimal layout with a single continuous central web.

The mean bar width value \bar{h} , computed as the ratio between the stiff volume and the surface area of the solution, provides feedback on the complexity of the optimal design. For low \bar{h} values, as in $SOFTBESO$, the optimal solution is made of a large number of thin bars, making it more difficult to manufacture and more likely to buckle. As this number increases, the width of the bars tends to increase, thus simplifying the complexity of the design, as in $SIMP^{(I)}$, $VARTOP$, or $Level-set$. Furthermore, these topologies are less prone to buckling effects.

The topologies can be also compared in terms of the corresponding value of the objective function. It can be noted that as the number of bars increases and/or the size of these bars decreases (tending to a single continuous web in the limit), the value of the objective function decreases, as it is observed in the $SOFTBESO$ and $SIMP^{(II)}$ approaches. On the contrary, $Level-set$ and $VARTOP$ optimize the design layout using thicker bars, thus obtaining a higher compliance value²¹. Similar designs and objective function values are obtained via $SIMP^{(I)}$ and $SIMP^{(III)}$.

Finally, the techniques can be compared in terms of the number of iterations (i.e., a computational cost-measure). As detailed in Table D.1, $VARTOP$ requires fewer iterations (116) to achieve the optimal topology layout while not being so far from the optimal topologies obtained by the other approaches. It is closely followed by $SIMP^{(III)}$ with 124 iterations, and with a few iterations more one can find $SIMP^{(I)}$, $SIMP^{(II)}$, and $SOFTBESO$ with 175, 231 and 272 iterations, respectively. The $Level-set$ method takes many more iterations (1266) to converge.

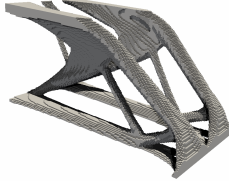
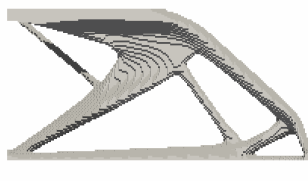
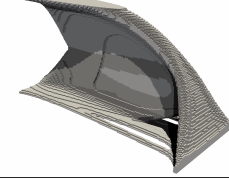
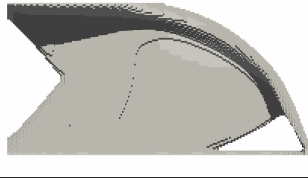
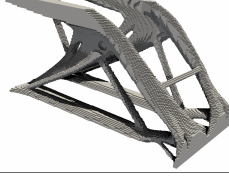
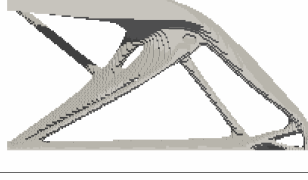
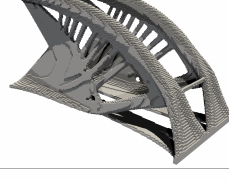
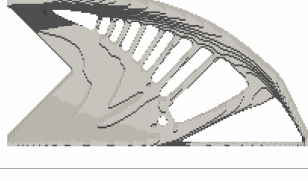
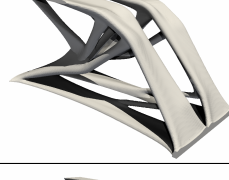

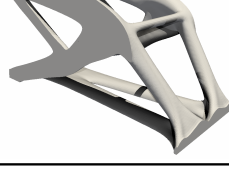

L-shaped structure The obtained results for the L-shaped structure are presented in Table D.2. As it can be noticed, the overall design of the structure is similar in all the methods. The vertical part, at the left, is almost identical in all the solutions. The most significant differences are found in the lower part of the structure, in which the topological complexity changes with the method. In this case, designs with 2 or 3 webs are obtained according to the approach, which connects the vertical part of the structure with the load application point. In particular, all the methods present a 2 web design except for the solutions of $SIMP^{(II)}$, which displays an internal central structure. Additionally, all the designs are mainly constituted by bars, being thinner in $SIMP^{(II)}$ and $SOFTBESO$, as displayed by the mean bar width value \bar{h} .

Regarding the objective function value, the values for all the solutions are around a compliance value of 2.40-2.60 with respect to the initial reference compliance²². $SIMP^{(II)}$ achieves the topology design with the lowest objective function value, while other approaches produce solutions with a value closer to 2.5. $SOFTBESO$ obtains the solution with the highest objective function value (2.6).

²¹The bar width could be reduced by modifying the value of the regularization parameter, τ .

²²An initial iteration with a full stiff material is computed. The passive elements/nodes are accounted for in this initial design.

Table D.1: Comparison of the results of topology optimization methods for the Cantilever beam. The number of iterations, objective function values, and mean bar widths \bar{h} are given for each of the addressed approaches. The optimal topology is also illustrated in the last two columns, via an isometric view and a side view.

Method	Total iter.	\mathcal{J}	\bar{h}	Optimal solutions	
SIMP ^(I)	175	6.4710	2.1012		
SIMP ^(II)	231	5.9609	1.7888		
SIMP ^(III)	124	6.7285	1.9700		
SOFTBESO	272	6.4369	1.4586		
VARTOP	116	6.3981	2.2783		
Level-set	1266	6.9494	2.8121		

Finally, a comparison of the number of iterations shows that, again, *VARTOP* requires fewer iterations than the other considered topology optimization techniques. There is not a large difference in the number of iterations with *SIMP^(I)* or *SIMP^(III)* (66 and 76 versus 62 of the *VARTOP*), although the difference in iterations increases when compared to *SIMP^(II)*, *SOFTBESO* or *Level-set* techniques, as observed in the previous example.

Multi-load Cantilever beam Table D.3 presents the results obtained regarding the *multi-load problem* for the corresponding approaches. In contrast to the previous cases, the resultant optimal solutions are quite different from each other. Although all six methodologies find symmetrical optimal solutions (with respect to the horizontal midplane of the domain), the resulting topologies do not correspond to the symmetrical solutions obtained for the first example (see table D.1), which could be intuitively presumed.

Most of the solutions are based on bar designs except for the *SOFTBESO* approach, which consists of a continuous core. For this reason, the mean bar size \bar{h} is the lowest of all techniques. Nevertheless, the solutions obtained with *VARTOP*, *SIMP^(I)*, and *SIMP^(III)* have many similarities, being the design of these last two techniques practically the same. Furthermore, the optimal layout achieved with *SIMP^(II)* is made of 3 webs with thinner bars, having a similar overall design. It is important to stress that the solutions obtained using *VARTOP* and *Level-set* present the highest mean bar width, thus achieving the best designs from a manufacturing standpoint and buckling resistance. However, the solution of the *Level-set* method corresponds to a different local minimum than the previous ones.

The lowest objective function values are obtained by *SOFTBESO* and *SIMP^(II)* even though the designs are quite complex and can not be easily manufactured. Conversely, *Level-set* finds the topology layout with the highest value. The other approaches (*VARTOP*, *SIMP^(III)*, and *SIMP^(I)*) provide sufficiently manufacturable (low complexity) solutions with intermediate values. Similar to the previous cases, methods *SIMP^(I)*, *SIMP^(III)* and *VARTOP* are the ones with the lowest computational cost, method *SIMP^(I)* being 30% faster than the other two methods.

Gripper compliant mechanism The results of this last numerical example are summarized in Table D.4. The optimal solutions exhibit resemblance to each other, obtaining the desired mechanism. However, the topology layouts can be grouped into two groups: obtaining 3D-like designs for *SIMP* and *SOFTBESO* methods, while almost 2D-extruded designs are obtained for *VARTOP* and *Level-set*. The considered approaches can also be split into two main groups depending on their capability to generate the mechanism either by creating localized hinges or deformable bars. All methods except *SOFTBESO* achieve a design based on localized hinges, thus significantly increasing the value of the objective function. In other words, the same force applied at the *input port* results in a smaller displacement in the target direction at the *output port*. For this reason, it is concluded that *SOFTBESO* has not fully converged to the same local minimum under the given parameters. Regarding the mean bar width, the values for all approaches range between 2.4 and 2.5, being equal to 2.7 for *SIMP^(I)* as the design is based on a smaller number of thicker bars.

Except for the *SOFTBESO*, the objective function values of the other approaches range between -260 and -331 , showing a larger discrepancy than in the previous benchmark cases. On the other hand, unlike the previous benchmark cases, the best topology design is obtained using the *Level-set method*, even though the layout almost resembles a 2D-extruded design.

Finally, the comparison of the number of iterations reveals that *VARTOP* requires much fewer iterations than the other methods. The other topology optimization techniques require between 200 and 300 iterations. Therefore, the considered methods can be sorted according to the number of iterations, in increasing order, as follows: *VARTOP*, *Level-set*, *SOFTBESO*, *SIMP^(III)*, *SIMP^(II)* and *SIMP^(I)*.

After analyzing all the results, it can be stated that topologies resulting from *Level-set* and *VARTOP* have smooth and accurate interfaces since the solution is defined via a *level-set* or a

Table D.2: Comparison of the results of topology optimization methods for the L-shaped structure. The number of iterations, objective function values, and mean bar widths \bar{h} are given for each of the addressed approaches. The optimal topology is also illustrated in the last two columns.

Method	Total iter.	\mathcal{J}	\bar{h}	Optimal solutions	
SIMP ^(I)	66	2.4823	2.1194		
SIMP ^(II)	140	2.4229	1.7722		
SIMP ^(III)	76	2.4882	2.1108		
SOFTBESO 190		2.6171	1.5100		
VARTOP	62	2.4811	2.4903		
Level-set	1071	2.5163	2.4532		

Table D.3: Comparison of the results of topology optimization methods for the Multi-load cantilever beam. The number of iterations, objective function values, and mean bar widths \bar{h} are given for each of the addressed approaches. The optimal topology is also illustrated in the last two columns.

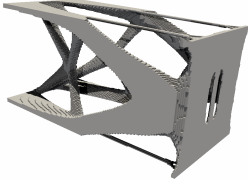
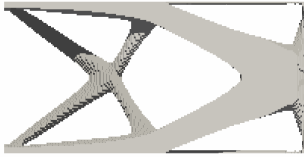
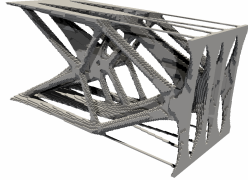
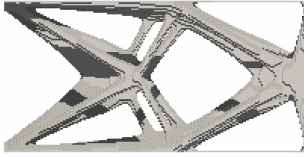
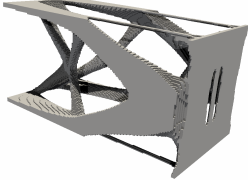
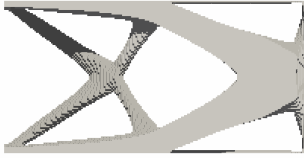
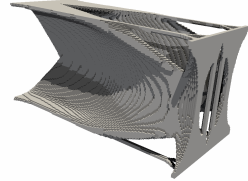
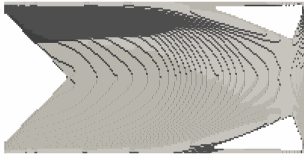
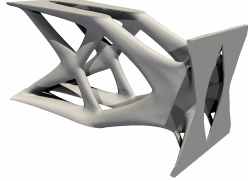
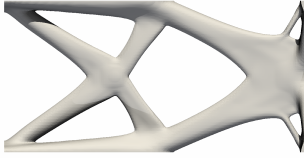
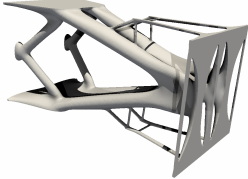
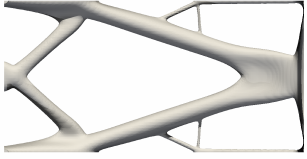
Method	Total iter.	\mathcal{J}	\bar{h}	Optimal solutions	
SIMP ^(I)	81	7.4271	1.8343		
SIMP ^(II)	208	6.7774	1.4312		
SIMP ^(III)	111	7.3156	1.8300		
SOFTBESO	249	6.6406	1.3108		
VARTOP	115	7.0459	2.5573		
Level-set	694	8.2108	2.5669		

Table D.4: Comparison of the results of topology optimization methods for the Gripper compliant mechanism. The number of iterations, objective function values, and mean bar widths \bar{h} are given for each of the addressed approaches. The optimal topology is also illustrated in the last two columns.

Method	Total iter.	\mathcal{J}	\bar{h}	Optimal solutions	
SIMP ^(I)	325	-261.6980	2.7041		
SIMP ^(II)	297	-305.3930	2.5020		
SIMP ^(III)	264	-297.0620	2.4805		
SOFTBESO	207	-135.7380	2.5441		
VARTOP	32	-269.4409	2.4553		
Level-set	176	-331.0203	2.5128		

discrimination function. Thus, low complexity topology designs are obtained. On the contrary, *SIMP-based* and *SOFTBESO methods* produce element-wise discontinuous designs. In addition, *SIMP-based approaches* require special post-processing as the design has *semi-dense elements*, thus requiring an extra projection procedure to determine the density value that defines the material interface. In this procedure, bars might be disconnected or broken up, giving as solution non-optimal topologies. Additionally, a smoothing post-processing should be done to achieve crisp and smooth edges from these two family of approaches.

Objective function value

In Figure D.8, the objective function values for each example and topology optimization method are illustrated. The values are normalized with respect to $SIMP^{(I)}$. As aforementioned, the objective function for each of the numerical benchmarks does not differ much from one approach to another. The values are between a range of $\pm 15\%$ of the ones obtained using $SIMP^{(I)}$.

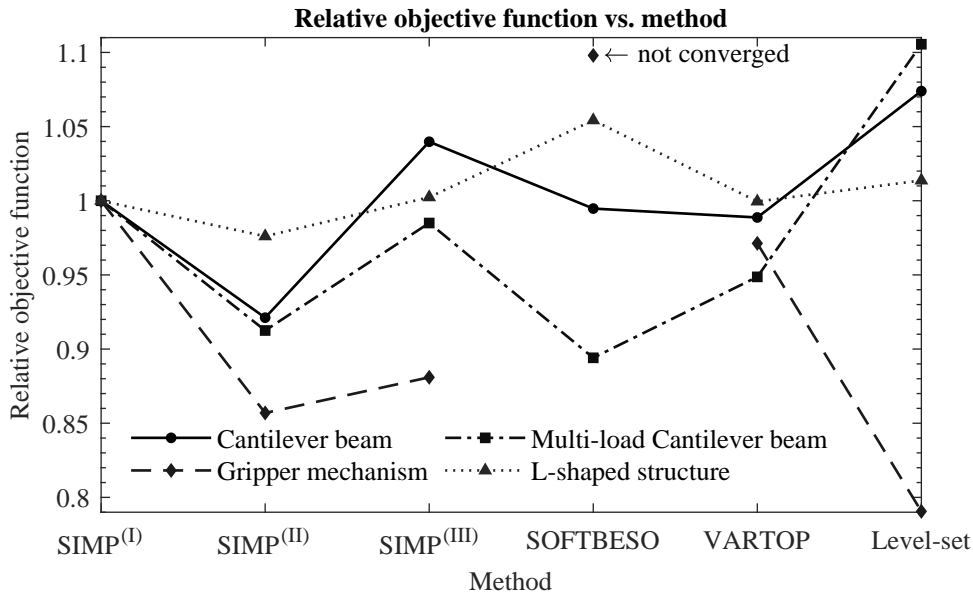


Figure D.8: Objective function value for each example and topology optimization approach normalized with the results obtained with the $SIMP^{(I)}$ method. Legend: (1) the Cantilever case is represented with a solid black line, (2) the L-shaped case, with a dotted black line, (3) the Cantilever multi-load case, with a dash-dotted line and (4) the Gripper mechanism with a dashed line, which is interrupted for the *SOFTBESO* method due to lack of convergence.

As observed in the graphic, $SIMP^{(II)}$ achieves consistently the optimal solutions with the lowest objective function value as a consequence of the larger number of thin straight bars (high topology complexity), as detailed in Section D.6.2. Nevertheless, two exceptions are observed, the first one for the *multi-load cantilever* problem where *SOFTBESO* achieves a solution with a lower objective function, and the second one for the Gripper case and the *Level-set*.

It is important to emphasize that a greater variance is only observed in the *Gripper* due to the fact that there is a greater difference in topology among the different approaches. Each technique achieves a characteristic compliant design with the exception of *SOFTBESO*. This approach obtains a topology layout with an objective function value that is almost two times higher than the one obtained using $SIMP^{(I)}$.

CPU computation cost: iterations

The computational cost is assessed in this paper according to the number of iterations instead of the computational time. In this way, it is possible to decouple the solution from the platform

used to run the topology optimization technique (i.e., OS, programming language, and hardware, among others) as well as from the solver used to solve the state problem. It has been observed that the selection of a specific iterative solver may significantly increase the computational time of some approaches with respect to others. Therefore, to remain as unbiased as possible, and in the hypothetical case that all methods would use a direct solver with equivalent computational cost per iteration, the computational cost could be evaluated with the number of iterations, thus obtaining a fair comparison.

The comparison of the computation cost in terms of the number of iterations is shown in Table D.5. The values of the computational cost, normalized with respect to $SIMP^{(I)}$, are illustrated in Figure D.9. As can be seen, the relative computational cost depends on each numerical example. However, it keeps a certain tendency along the considered approaches for *minimum mean compliance* problems.

Regarding the Cantilever beam, $VARTOP$ and $SIMP^{(III)}$ are up to 1.4 times faster than $SIMP^{(I)}$, and up to 2 times faster than $SIMP^{(II)}$ or $SOFTBESO$. $Level-set$ turns out to be 7 times more computationally expensive than $SIMP^{(I)}$. In addition, it is important to stress that $VARTOP$ is 7% faster than $SIMP^{(III)}$, even though it provides not only the optimal solution but a set of solutions for different volume fractions (Pareto Frontier).

For the L-shaped structure and the multi-load cantilever beam optimizations, the relative computation costs increase from the previous example, except in $VARTOP$. Its relative computational cost becomes almost 1 for the L-shaped structure and even 1.4 for the multi-load cantilever case. $SIMP^{(I)}$ results in the the fastest approach for this latter benchmark. The advantage over the $SOFTBESO$, $Level-set$, and $SIMP^{(II)}$ methods is still present, although no significant improvement in computational cost is obtained with respect to $SIMP^{(III)}$ and $VARTOP$.

As for the *compliant mechanism example*, the previously observed trend does not apply any more. In this case, $VARTOP$ is the fastest approach by far (almost an order of magnitude faster), followed by the $Level-set$ and $SOFTBESO$ approaches. Both methods require approximately half as many iterations as $SIMP^{(I)}$. $SIMP^{(III)}$ and $SIMP^{(II)}$ techniques are respectively 20%

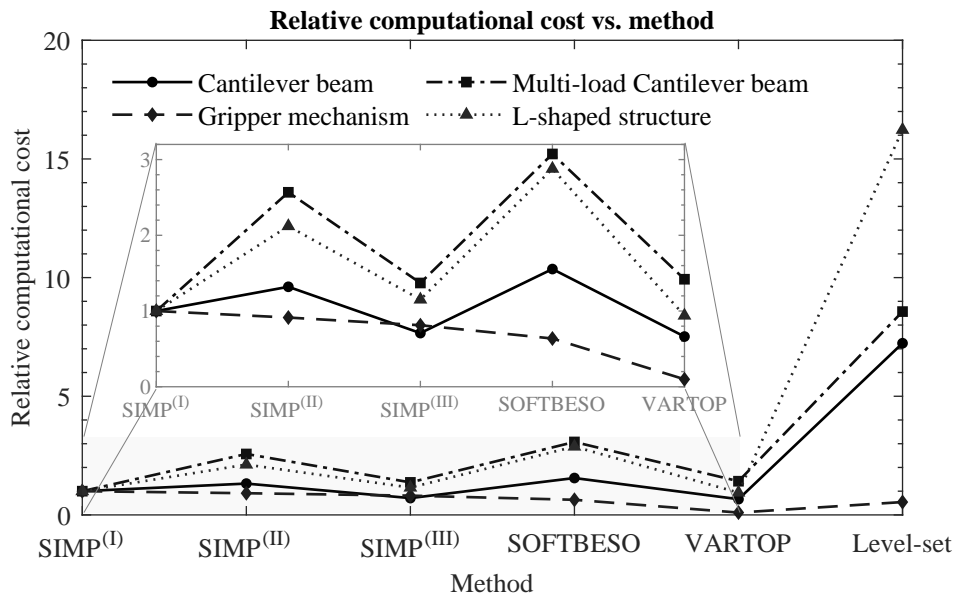


Figure D.9: Relative computational cost in terms of the number of iterations. Each numerical example is normalized with the number of iterations of the $SIMP^{(I)}$. Legend: (1) the Cantilever case is represented with a solid black line, (2) the L-shaped case, with a dotted black line, (3) the Cantilever multi-load case, with a dash-dotted line and (4) the Gripper mechanism with a dashed line.

and 10% faster than the reference method. This trend change in the computational cost may be caused by the change in the topology optimization problem (i.e., the non self-adjoint character of the *problem*).

Table D.5: Comparison of computational cost in terms of iterations of the considered topology optimization methods.

Numerical Example	SIMP ^(I)	SIMP ^(II)	SIMP ^(III)	BESO	VARTOP	Level-set
Cantilever beam	175	231	124	272	116	1266
L-shaped structure	66	140	76	190	62	1071
Multi-load cantilever beam	81	208	111	249	115	694
Gripper	325	297	264	207	32	176

Robustness: monotonic convergence degree

The convergence robustness is analyzed through the evolution of the objective function and volume fraction, and the criteria in topology and objective function throughout the optimization. For each technique, the analysis of these variables determine the monotonic convergence degree of every method. The discussion is performed only through the first two examples, since they are representative enough to provide a complete overview of the issue of robustness.

The evolution of the objective function for the Cantilever beam is illustrated in Figure D.10. *Single-time-step methods* are represented in the first column while *incremental time-advancing techniques* (i.e., SIMP^(II), VARTOP, and Level-set) are depicted in the second column. Each time-step is shaded with a different color to improve its visualization. The normalized objective function value $\mathcal{J}/\mathcal{J}_0$ (solid line colored in black) is illustrated in the left y-axis, while the stiff material fraction (dash-dotted line, colored in gray) is associated with the right y-axis.

Based on the convergence, the following features can be highlighted: (1) SIMP^(I) and SIMP^(III) prescribe a constant stiff material fraction (i.e., $f = 0.1$) from the initial iteration, and the objective function converges monotonically to a value close to 7.8²³, (2) in *SOFTBESO*, the stiff material fraction is gradually reduced from the initial value 1 to the target value 0.1, consequently, the objective function increases until the target volume is achieved, (3) in SIMP^(II) and VARTOP, the target stiff material fraction is reduced from 1 to 0.1 in 12 time-steps, thereby the objective function is minimized at each time-step, and (4) *Level-set*, which even though it can also be an *incremental time-advancing method*, it has a particular response since the volume constraint is not strictly enforced on each iteration, but it oscillates ruled by an *Augmented Lagrangian method*.

As illustrated in Appendix D.D, the *order of convergence* of the objective function is close to 1 for all the techniques. Therefore, all topology optimization methods have a linear convergence in the objective function.

The convergence curves of the objective function and topology criteria are depicted in Figure D.11. The objective function criterion (solid black line) is represented in the left y-axis, while the topology criterion (gray dash-dotted line) in the right y-axis. As in Figure D.10, the previous four different groups can be distinguished, but now in terms of the convergence criteria. Both SIMP^(II) and VARTOP show a strictly monotonous convergence within each time-step, only noticing some small oscillations in the second last time-step where a change in topology has taken place. As for the other methods, SIMP^(I) and SIMP^(III) present monotonous convergence with small amplitude oscillations, while some important variations are noticed in *SOFTBESO* once the final stiff material fraction is achieved. Finally, the convergence criterion in the *Level-set method* mimics the trend detected in the objective function and volume fraction with small amplitude oscillations. As a global comment, it can be stated that the objective function criterion

²³Note that the objective function value in the graph does differ from Table D.1, since different contrast factor α are used in the optimization and in the post-processing iteration.

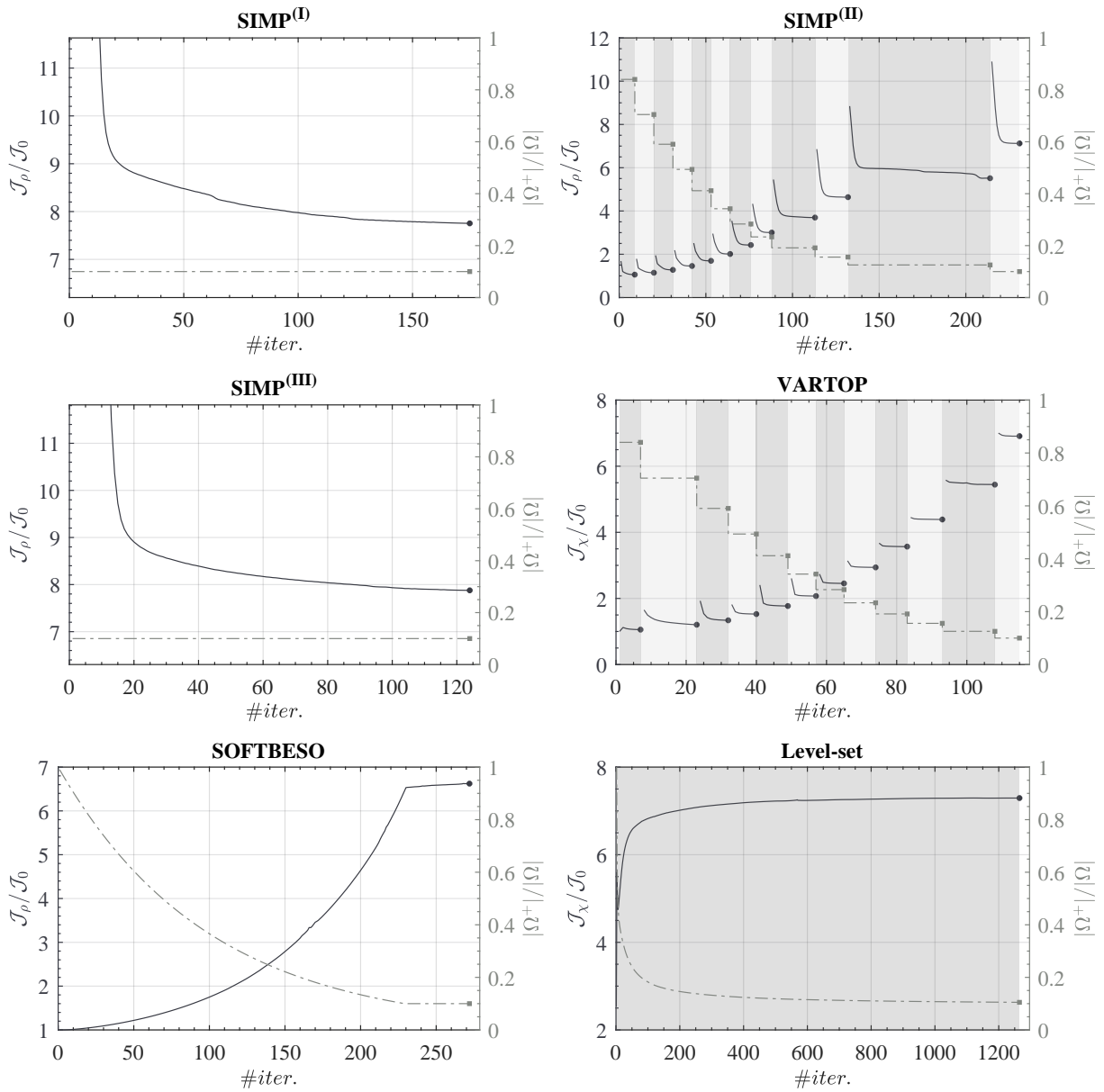


Figure D.10: Evolution histories of the values of the objective function and volume fraction throughout the iterations of the Cantilever beam topology optimization for the six considered methods. *Single-time-step approaches* are illustrated in the first column, while *incremental time-advancing techniques* are depicted in the second column, each time-step being shaded with a different color. The normalized objective function \mathcal{J}_ρ or \mathcal{J}_χ is associated with the left y-axis and represented with a solid black line. On the other side, the volume fraction (i.e., the stiff material fraction) $\frac{|\Omega^+|}{|\Omega|}$ is represented by a dash-dotted gray line in the right y-axis of each graphic.

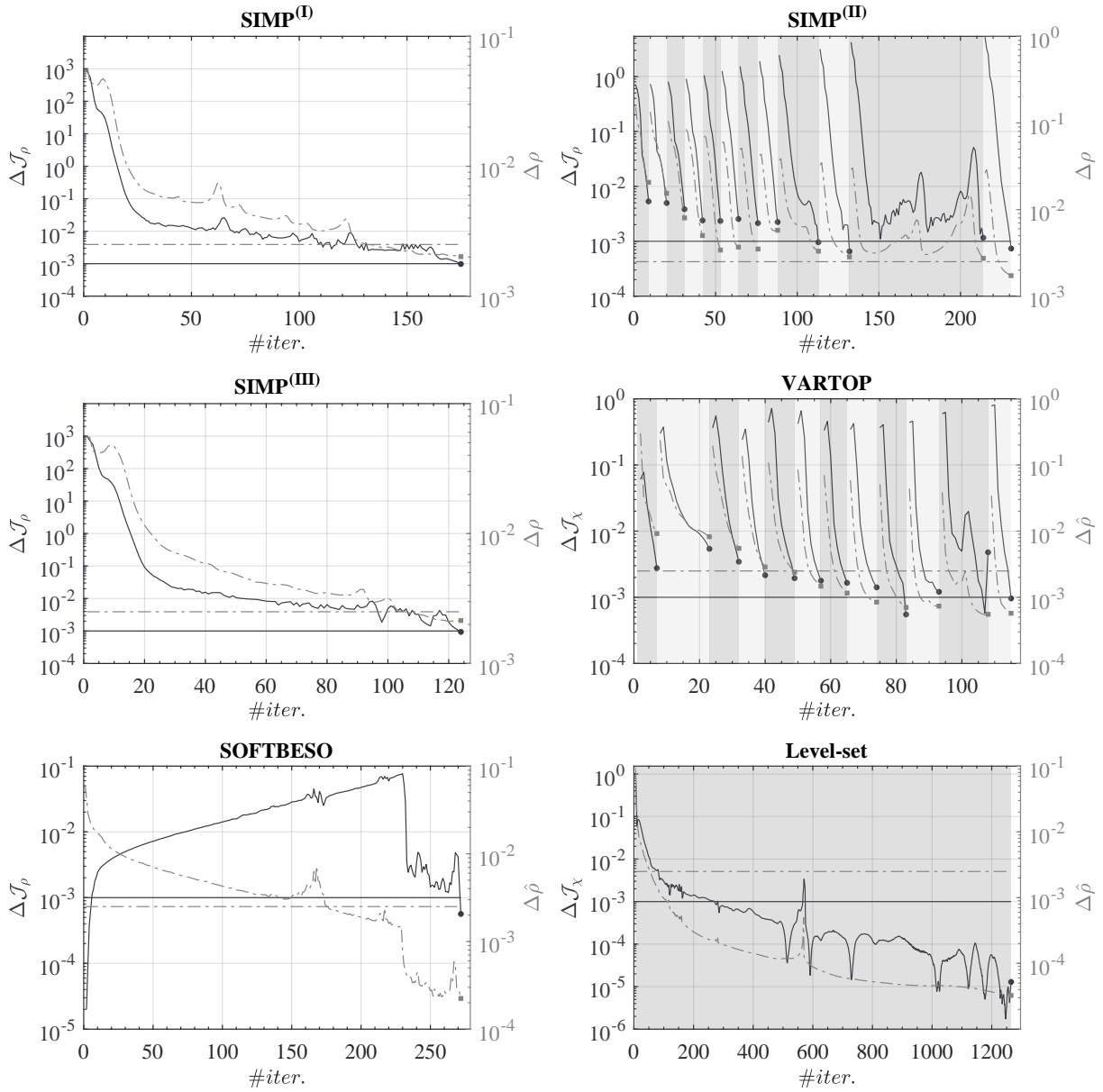


Figure D.11: Evolution histories of the criteria values in the objective function and in the topology throughout iterations of the Cantilever beam topology optimization for the six considered methods. *Single-time-step approaches* are illustrated in the first column, while *incremental time-advancing techniques* are depicted on the second column, each time-step being shaded with a different color. The criterion in objective function, associated with the left y-axis, is represented with a solid black line, while the criterion in the topology is represented by a dash-dotted gray line in the right y-axis of each graphic. In addition, the corresponding maximum tolerances $Tol_{\mathcal{J}}$ and Tol_{ζ} allowed in the last time-step (or in the entire optimization for *single-time-step methods*) are also displayed in every graphic as horizontal lines with the same properties.

corresponds to the most restrictive criterion in all topology optimization approaches, except in the *Level-set method*, in which the volume constraint is the limiting one.

The convergences corresponding to the other examples have been also analyzed in detail. The graphics do not present any significant difference with respect to those already analyzed for the Cantilever beam. However, for completeness reasons the corresponding graphics of the second example are depicted in Appendix D.E.

Overall performance

In this last subsection, instead of comparing the different methods in a quantitative and analytical way, a more qualitative comparison is presented according to the following aspects: (1) Surface smoothness, (2) Topology complexity, (3) Objective function, and (4) Computational cost.

The first aspect refers to the surface smoothness required by several manufacturing techniques. In these technologies, sharp edges and noise shells (i.e., abrupt continuous changes) must be avoided in the boundary of the optimal solution. The second criterion takes into account the complexity of the optimal design obtained by each technique, considering other mechanical properties not directly included in the optimization. For instance, designs based on thick bars will have a better structural behavior in buckling or fatigue compared to designs with a greater number of thin bars. These two aspects will also have an impact on the manufacturing challenges, which will decrease as the design becomes smoother and less complex. The third one considers the value of the objective function, or equivalently the efficiency of each method of finding a better local minimum. This criterion gathers the information shown in Figure D.8 regarding the relative objective function values. The last point of comparison globally assesses the computational cost of each method to perform the optimization. Analogous to the last aspect, this criterion gathers the information represented in Figure D.9 with respect to the relative computational cost.

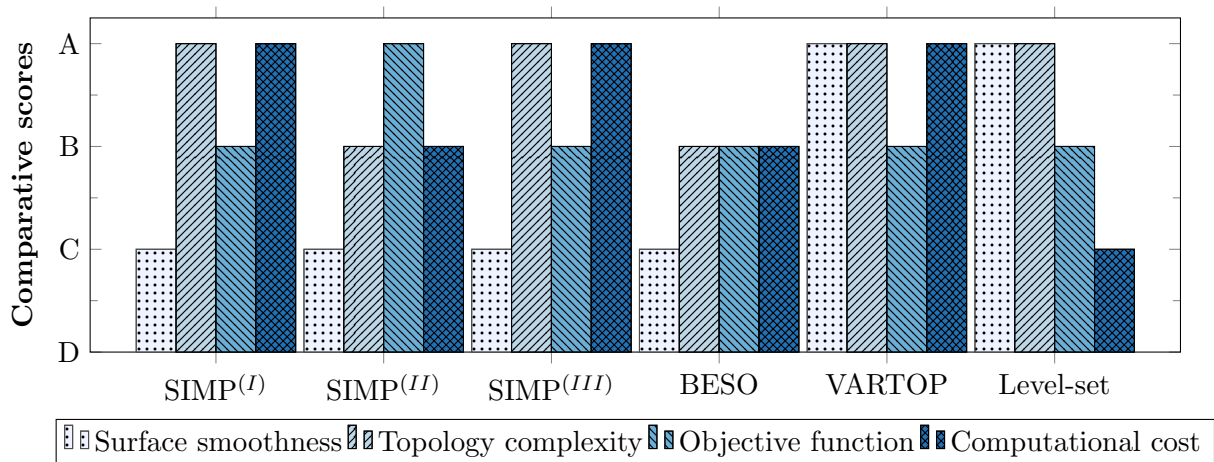


Figure D.12: Qualitative comparison of the studied methods regarding the smoothness of the design (dotted column), the topology complexity (right-inclined lines pattern), the value of the objective function (left-inclined lines pattern) and the computational cost in terms of iterations (column with crosshatch pattern). Each one of the areas is rated qualitatively with the levels A, B, C, or D, being A the best qualification and D the worst one.

In Figure D.12, each one of the aspects is represented with a column bar rated between A and D, with A being the best qualification in that section and D being the worst one. For each approach, four bars of different colors and patterns are represented, each one corresponding to an analyzed aspect.

Regarding the surface smoothness, *VARTOP* and *Level-set* provide designs whose surfaces are smooth. On the contrary, all other approaches only achieve element-wise optimal designs,

thus the boundary of the solution is defined through abrupt continuous changes. Consequently, additional post-processing procedures are required to manufacture these solutions with smooth boundaries. For this reason, *VARTOP* and *Level-set* are evaluated with an A, while the others are rated with a C grade.

Concerning the topology complexity, it has been noticed in Section D.6.2 that the quality of the solutions is reasonably high in almost all the techniques, being this slightly lower for *SIMP^(II)* and *BESO methods*. In these two techniques, the complexity of the optimal topology increases, obtaining designs based on thinner bars (i.e. lower bar width) with lower buckling prevention. Accordingly, this two approaches are rated with a B while the others, with an A.

In terms of the objective function, all approaches obtain a similar optimal value, although *SIMP^(II)* consistently obtains marginally lower values than the other techniques, as detailed in section D.6.2. For this reason, *SIMP^(II)* obtains an A qualification, while the other methods are left with a B. Finally, the comparison of the computational cost, discussed in section D.6.2, is represented in the last column. The computational cost is lower and of similar magnitude for *SIMP^(I)*, *SIMP^(III)* and *VARTOP*, followed by the *SIMP^(II)* and *BESO* approaches, and finally by *Level-set*. These three groups are respectively rated with an A, B, and C.

Figure D.12 can be further simplified by combining the two topology-related features in a single criterion referred to as *topology quality*, and the two criteria related to the objective function and the computational cost in a single criterion called *computational efficiency*. These two criteria are equivalently represented by a bar chart in Figure D.13. From this figure, it can be concluded that *VARTOP*, although not being the best approach in all considered aspects in Figure D.12, is presented as a competitive technique to more conventional *topology optimization approaches*, such as *SIMP^(I)* and *SIMP^(III)*. On the other hand, *SOFTBESO* and *Level-set* do not provide any significant advantages, exhibiting mostly deficiencies in topology complexity or computational cost, respectively, for the cases studied in this paper.

D.7 Concluding remarks

This contribution presents a thorough comparison among most of the well-established *topology optimization approaches*, i.e. the *SIMP*, *Level-set*, and *SOFTBESO methods*, and the *VARTOP approach*. A set of well-known 3D numerical benchmarks in the field of structural topology

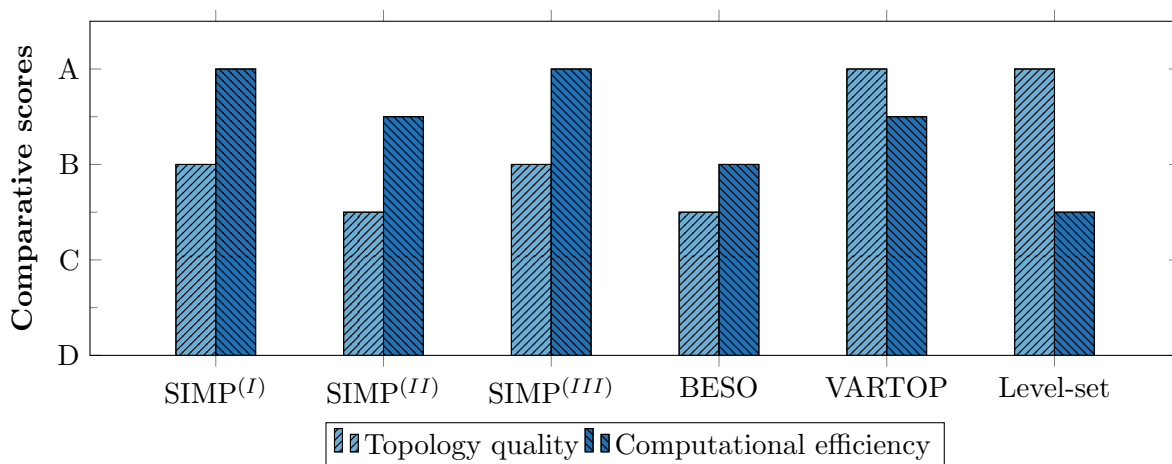


Figure D.13: Qualitative comparison of the studied methods, combining the topology related properties and the computational ones in a single bar. The topology quality is represented with a light blue colored bar and a right tilted line pattern, while the computational efficiency is represented using a dark blue bar with a left tilted line pattern. Each of the criteria is rated qualitatively with the levels A, B⁺, B, C⁺, C, D⁺ or D, being A the best qualification and D the worst one.

optimization has been addressed to analyze their performance. The corresponding results have been assessed in terms of the optimal topology, the robustness in convergence, the objective function, and the computational cost.

Regarding the topology, a quality dependence has been observed among the assessed methods, being slightly lower for $SIMP^{(II)}$ and *BESO methods*. The quality and complexity of the topologies can depend on the type of design variable: continuous vs discrete and nodal vs element, as well as the approach to impose the volume constraint.

Regarding the design variable, the methods can be split into three groups:

- *Level-set* and *VARTOP* use *nodal scalar functions* to precisely describe the interface, as well as a *discrete characteristic function* to define sharp *white-and-black* configurations.
- *SOFTBESO* uses an *element-wise discrete functions* to define the topology layout²⁴. Although obtaining *white-and-black* designs, the material boundary is only defined through elements.
- *SIMP-based methods* use an *element-wise continuous variable*. Consequently, these techniques can not precisely define the boundary, but instead get a blurred interface with *gray semi-dense elements*. By using a projection technique, *white-and-black* designs can be obtained, which interface is defined through elements.

As a consequence, *SOFTBESO* and *SIMP* techniques may not obtain the best possible optimal solution and would require post-processing techniques to obtain smooth designs which could be easily manufactured. However, there is no guarantee that the resultant topologies are actually optimal layouts.

As aforementioned, the volume constraint methodology may also affect the resultant topology. In those techniques where the volume constraint is gradually imposed using *element-wise variables* (e.g. *SOFTBESO* and $SIMP^{(II)}$), the final topologies tend to be more complex and consist of a larger number of thin bars. As a result, these topologies have worse mechanical behavior and are more challenging and expensive to manufacture.

In terms of the topology, it can be concluded that both a combination of nodal scalar design variables with a gradual incremental volume constraint, and a combination of a continuous element-wise variable with a constant volume constraint provide optimal topologies with high quality. In the comparison, $SIMP^{(I)}$, $SIMP^{(III)}$, *VARTOP*, and *Level-set* achieve optimal designs that are based on thicker bars (with higher mean bar size), thus improving manufacturability with high-quality optimal designs and reducing the buckling proneness.

Concerning the robustness of each method, it has been confirmed that all the techniques have a linear convergence in the objective function regardless of the methodology used to impose the volume constraint. This fact supports the selection of the techniques for the comparison, and the independence with respect to the filtering technique (i.e. spatial or Helmholtz-type filtering) and the updating scheme of the design variable (i.e. incremental or absolute). These two differences may have an effect on the optimal solution, but not on the *order of convergence*.

In regard to the objective function value, a small variation of $\pm 15\%$ is observed in the four numerical benchmarks among the studied methods with the exception of two tests in the Gripper mechanism. However, $SIMP^{(II)}$ achieves systematically the lowest objective function values, as the majority of its optimal designs are based on smaller, thinner bars (i.e., high complex designs), as mentioned before. Due to this characteristic, these designs are proclive to buckling.

For the first three examples, all studied techniques can be sorted according to a descending number of required iterations as follows: *Level-set*, *SOFTBESO*, $SIMP^{(II)}$, *VARTOP*, $SIMP^{(III)}$ and $SIMP^{(I)}$. However, the relative computational cost depends on each example and technique, but the same trend is observed. It is important to emphasize that *incremental time-advancing techniques* such as $SIMP^{(II)}$ and *VARTOP* obtain not only the final optimal solution but also a set of intermediate converged solutions at almost the same computational cost (Pareto frontier for the volume fraction). In this scenario, *VARTOP* is up to 1.5 times faster than the

²⁴As aforementioned, a *relaxed characteristic function* (or density variable) is used for *compliant mechanism synthesis*.

corresponding $SIMP^{(II)}$ implementation. As for the Gripper compliant mechanism, the tendency in computational cost completely changes from the previous examples, observing a very significant reduction with $VARTOP$ compared to $SIMP^{(I)}$. Contrary to the other numerical examples, $SOFTBESO$ and $Level-set$ also require a lower number of iterations than $SIMP$ -based implementations.

In conclusion, the $VARTOP$, $SIMP^{(I)}$, and $SIMP^{(III)}$ approaches present topology layouts with a higher topology quality than the other methods at a lower computational cost, even though their objective function is not minimized as much as in other approaches.

The authors are aware that, in spite of the efforts done for a fair comparison, a certain degree of subjectivity can still remain in this kind of studies, but they also think that those studies should be presented to the community of structural topology optimization even to be argued and discussed with the aim of the progress of computational topology optimization.

Acknowledgements

This research has been funded by the European Research Council (ERC) under the European Union's Horizon 2020 research and innovation programme (Proof of Concept Grant agreement n 874481) through the project "Computational design and prototyping of acoustic metamaterials for target ambient noise reduction" (METACOUSTIC). The authors also acknowledge financial support from the Spanish Ministry of Economy and Competitiveness, through the research grant DPI2017-85521-P for the project "Computational design of Acoustic and Mechanical Metamaterials" (METAMAT) and through the "Severo Ochoa Programme for Centres of Excellence in R&D" (CEX2018-000797-S). D. Yago acknowledges the support received from the Spanish Ministry of Education through the FPU program for PhD grants.

Conflict of interest

The authors declare that they have no conflict of interest as regards this work.

D.A Convergence criteria

Convergence is evaluated in terms of the volume constraint, the objective function, and the topology design, as mentioned in Section D.6.1. In particular, the topology criterion must be analyzed in detail, since this criterion must be standardized in all methods, each one using a different design variable.

For *density-based methods*, such as $SIMP$, the topology criterion can be written as a L_2 norm of the *element density variable* ρ_e between two consecutive iterations as

$$\Delta\rho_k = \frac{1}{|\Omega_0|^{1/2}} \left(\int_{\Omega} (\rho_k - \rho_{k-1})^2 d\Omega \right)^{1/2} = \frac{1}{|\Omega_0|^{1/2}} \left(\sum_{e=1}^{N_e} (\rho_{e,k} - \rho_{e,k-1})^2 |\Omega_e| \right)^{1/2}, \quad (70)$$

where e corresponds to the element number and k to the iteration number, and $|\Omega_e|$ is the volume of element e .

However, for the other approaches, a relaxed *characteristic function* must be used to compute the topology criterion. The element *density variable* or the corresponding element *characteristic function* are regularized via a *Laplacian regularization* (32). Therefore, the topology criterion is computed as

$$\Delta\hat{\rho}_k = \frac{1}{|\Omega_0|^{1/2}} \left(\int_{\Omega} (\mathbf{N}\hat{\rho}_k - \mathbf{N}\hat{\rho}_{k-1})^2 d\Omega \right)^{1/2} = \frac{\sqrt{(\hat{\rho}_k - \hat{\rho}_{k-1})^T \mathbb{M} (\hat{\rho}_k - \hat{\rho}_{k-1})}}{|\Omega_0|^{1/2}}, \quad (71)$$

with $\hat{\rho}_k$ being the solution to

$$(\mathbb{M} + (\tau h)^2 \mathbb{K}) \hat{\rho}_k = \int_{\Omega} \mathbf{N}^T \varphi_e d\Omega. \quad (72)$$

The element variable φ_e corresponds to element *density variable* ρ_e , the element *characteristic function* $\bar{\chi}_{e,\psi}$ or the element *characteristic function* $\bar{\chi}_{e,\phi}$ for the *BESO*, *VARTOP*, or *Level-set methods*, respectively. The matrices \mathbf{N} , \mathbb{M} and \mathbb{K} stand for the shape function matrix, the mass matrix and the stiffness matrix, and τ corresponds to the *regularization parameter* of the topology criterion. It is important to stress that the regularization parameter τ must be chosen thoroughly so that the two topology criteria are equivalent. Based on the authors' experience, it has been prescribed to $\tau = 8$.

D.B Post-processing iteration

Due to the discrepancies in the design variables (nodal vs element and continuous vs discrete) and the existence of *semi-dense elements*, the objective function value \mathcal{J} can not be directly compared between topology optimization approaches. For that reason, once the optimal topology has converged, an additional iteration must be computed using a *black-and-white* element-wise design with a uniform small *contrast factor* $\alpha = 10^{-9}$ for all the studied methods. In this scenario, the topology design is expressed via the *characteristic function* $\bar{\chi}_e = \{1, \beta\}$, as defined in equation (1), with β depending on each method so that a constant soft Young's modulus is used throughout the methods, as detailed in Section D.4.

Bear in mind that a projection technique on the *density* or on the *characteristic function* (based on its element definition) is required to obtain an optimal topology layout represented only by elements completely contained in the stiff material domain or in the soft material domain. In this projection technique, the volume must be kept unmodified so that the objective function is computed with the same stiff material fraction. Depending on the topology optimization approach, the element-wise *characteristic function* $\bar{\chi}_e$ is computed as

- For *VARTOP* and *Level-set*, a *Heaviside function* with the *actual characteristic function* $\hat{\chi}_{e,\psi}$ (or $\hat{\chi}_{e,\phi}$ for the *Level-set method*) and a reference value computed via a bisection algorithm, i.e.,

$$\bar{\chi}_e = \mathcal{H}_{\beta} (\hat{\chi}_{e,\psi} - \gamma) \quad \text{for } \forall e \in N_e, \quad (73)$$

with $\beta < \gamma < 1$ being computed such that the volume constraint $\mathcal{C}_0(\bar{\chi}_e)$ in the entire domain is enforced (equations (51-b-1) and (61-b-1)).

- For *density-based approaches* (including *Soft-kill BESO*), a *Heaviside function* with the element density variable ρ_e and a reference value $\bar{\rho}$ computed via a bisection algorithm, i.e.,

$$\bar{\chi}_e = \mathcal{H}_{\beta} (\rho_e - \bar{\rho}) \quad \text{for } \forall e \in N_e, \quad (74)$$

with β being 0 for *SIMP methods* or $\sqrt[p]{\alpha}$ for *BESO*.

D.C Parameter definition

In order to ensure replicability, all the relevant parameters are provided in Tables D.C.6 and D.C.7. Table D.C.6 details the values related to the tolerances as well as the values for the contrast factor and the volume fraction for each topology optimization. On the other hand, Table D.C.7 provides the specific parameters for updating and regularizing the design variable.

Table D.C.6: Global parameters and tolerances used for each benchmark case and topology optimization method. *Volume fraction*, *contrast factor*, and *objective function tolerance* are detailed for each benchmark, while tolerances in *volume fraction* and *topology* are defined for each method.

Method	Benchmark			
	Cantilever	L-shaped structure	Multiload Cantilever	Gripper
SIMP ^(I) , SIMP ^(II) , SIMP ^(III) , BESO	$Tol_{c_0} = 10^{-3}$, $Tol_{\zeta} = 2.5 \cdot 10^{-3}$, $n = 3$			
	$\alpha = 10^{-6}$,	$ \Omega^+ = 0.1 \Omega $,	$Tol_{\mathcal{J}} = 10^{-3}$	$\alpha = 10^{-2}$, $ \Omega^+ = 0.15 \Omega $, $Tol_{\mathcal{J}} = 10^0$
VARTOP	$Tol_{c_0} = 10^{-3}$, $Tol_{\zeta} = 2.5 \cdot 10^{-3}$, $n = 2$			
	$\alpha = 10^{-6}$,	$ \Omega^+ = 0.1 \Omega $,	$Tol_{\mathcal{J}} = 10^{-3}$	$\alpha = 10^{-2}$, $ \Omega^+ = 0.15 \Omega $, $Tol_{\mathcal{J}} = 10^0$
Level-set	$Tol_{c_0} = 5 \cdot 10^{-3}$, $Tol_{\zeta} = 2.5 \cdot 10^{-3}$, $n = 5$			
	$\alpha = 10^{-6}$,	$ \Omega^+ = 0.1 \Omega $,	$Tol_{\mathcal{J}} = 10^{-3}$	$\alpha = 10^{-2}$, $ \Omega^+ = 0.15 \Omega $, $Tol_{\mathcal{J}} = 10^0$

D.D Order of convergence

In this appendix, the *order of convergence* of the objective function for the different methods will be evaluated to define an additional parameter regarding the computational robustness (Section D.6.2). As a result, it will be possible to verify whether one method stands out from the others in terms of the *order of convergence*.

The *order of convergence*, p , for the objective function can be computed from the sequence of iterative values $\mathcal{J}_n/\mathcal{J}_0$ (from $n = 0$ to $n = \infty$) that converges to $\mathcal{J}^*/\mathcal{J}_0$, when

$$\lim_{n \rightarrow \infty} \frac{|e_{n+1}|}{|e_n|^p} = \mu, \quad (75)$$

with $p > 0$ and $\mu \neq 0$ corresponding to the *order of convergence* and *rate of convergence*. The e_{n+1} and e_n denote the errors of the objective function at n -th and $(n + 1)$ -th iterations, respectively, with respect to the converged one, $\mathcal{J}^*/\mathcal{J}_0$. The error at each iteration is evaluated as

$$e_n = \frac{\mathcal{J}_n}{\mathcal{J}_0} - \frac{\mathcal{J}^*}{\mathcal{J}_0}, \quad (76)$$

with $\mathcal{J}^*/\mathcal{J}_0$ being approximated to the normalized objective function value for the last converged optimal solution. For *incremental time-advancing techniques*, the *order of convergence* can be evaluated for each time-step using the corresponding converged objective function value.

The iterative sequence of the error in the objective function e_n is illustrated in Figure D.D.14 for the Cantilever beam benchmark case. As in Figures D.10 to D.11, *single-time-step methods* are displayed in the first column while *incremental time-advancing techniques* are depicted in the second column, the *order of convergence* being computed for an intermediate time-step. The corresponding linear regression, used to compute the *order of convergence*, is represented in all the graphics with a dashed line. The exact value for the *order of convergence* is displayed at the top-left corner. As can be observed, the *order of convergence* for all the approaches is close to 1, thus all the addressed methods have a linear convergence in the objective function.

Table D.C.7: Parameters used for each benchmark case and topology optimization method.

Method	Benchmark			
	Cantilever	L-shaped structure	Multiload Cantilever	Gripper
SIMP ^(I)	$p = 3, \quad r_{min} = 3, \quad ft = 1$			
	$m = 0.2, \quad \eta = 0.5$			$m = 0.1, \quad \eta = 0.3$
SIMP ^(II)	$p = 3, \quad r_{min} = 3, \quad ft = 1, \quad k = -2$			
	$m = 0.2, \quad \eta = 0.5, \quad n_{steps} = 12$	$m = 0.2, \quad \eta = 0.5, \quad n_{steps} = 8$	$m = 0.2, \quad \eta = 0.5, \quad n_{steps} = 12$	$m = 0.1, \quad \eta = 0.3, \quad n_{steps} = 8$
SIMP ^(III)	$p = 3, \quad r_{min} = 3, \quad ft = 1$			
	$m = 0.2, \quad \eta = 0.5$			$m = 0.1, \quad \eta = 0.3$
BESO	$r_{min} = 3, \quad ER = 0.01, \quad AR_{max} = 0.1$			
	$p = 3$			$p = 2, \quad m = 0.1$
VARTOP	$m = 3, \quad \tau = 1, \quad n_{steps} = 12, \quad k = -2$	$m = 5, \quad \tau = 1.5, \quad n_{steps} = 8, \quad k = -2$	$m = 3, \quad \tau = 1.5, \quad n_{steps} = 12, \quad k = -2$	$m = 100, \quad \tau = 0.5, \quad n_{steps} = 8, \quad k = -2$
Level-set	$m = 3, \quad \tau = 1, \quad n_{steps} = 1, \quad \Delta t = 0.1, \quad s = 10^{-4}$	$m = 5, \quad \tau = 1, \quad n_{steps} = 1, \quad \Delta t = 0.1, \quad s = 5 \cdot 10^{-7}$	$m = 3, \quad \tau = 1, \quad n_{steps} = 1, \quad \Delta t = 0.1, \quad s = 10^{-3}$	$m = 100, \quad \tau = 0.5, \quad n_{steps} = 1, \quad \Delta t = 0.05, \quad s = 10^{-2}$

D.E Robustness of L-shaped structure

Mimicking Figures D.10 and D.11, the evolution of the objective function and the stiff material fraction is illustrated in Figure D.E.15, while the evolution of the criteria is depicted in Figure D.E.16.

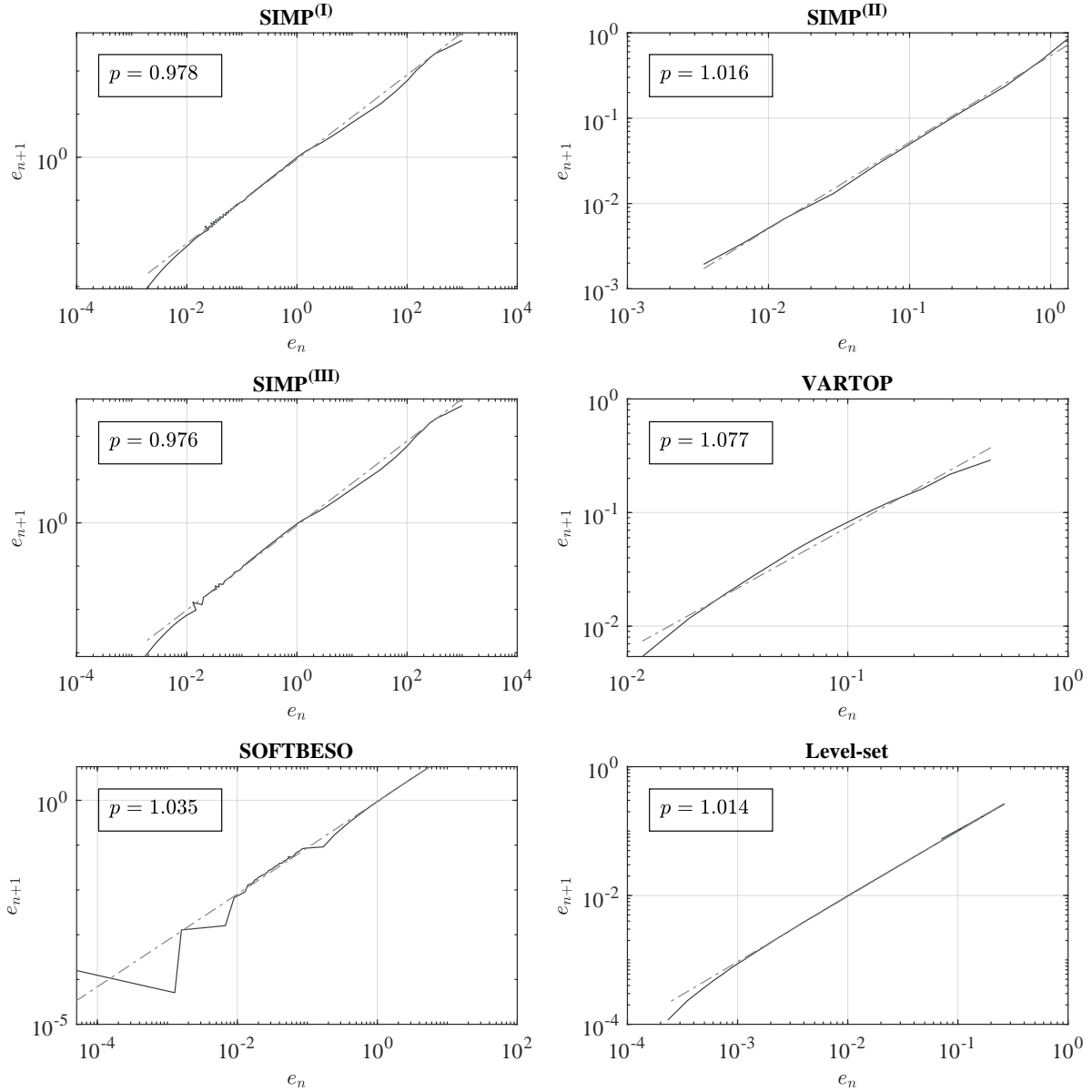


Figure D.D.14: Iterative sequence of the objective function errors throughout the iterations of the Cantilever beam topology optimization for the six considered methods. *Single-time-step approaches* are illustrated in the first column, while *incremental time-advancing techniques* are depicted in the second column. The objective function error e_n is represented with a solid black line, while the corresponding linear regression is represented with a dashed gray line. The order of convergence is included in the top-left corner.

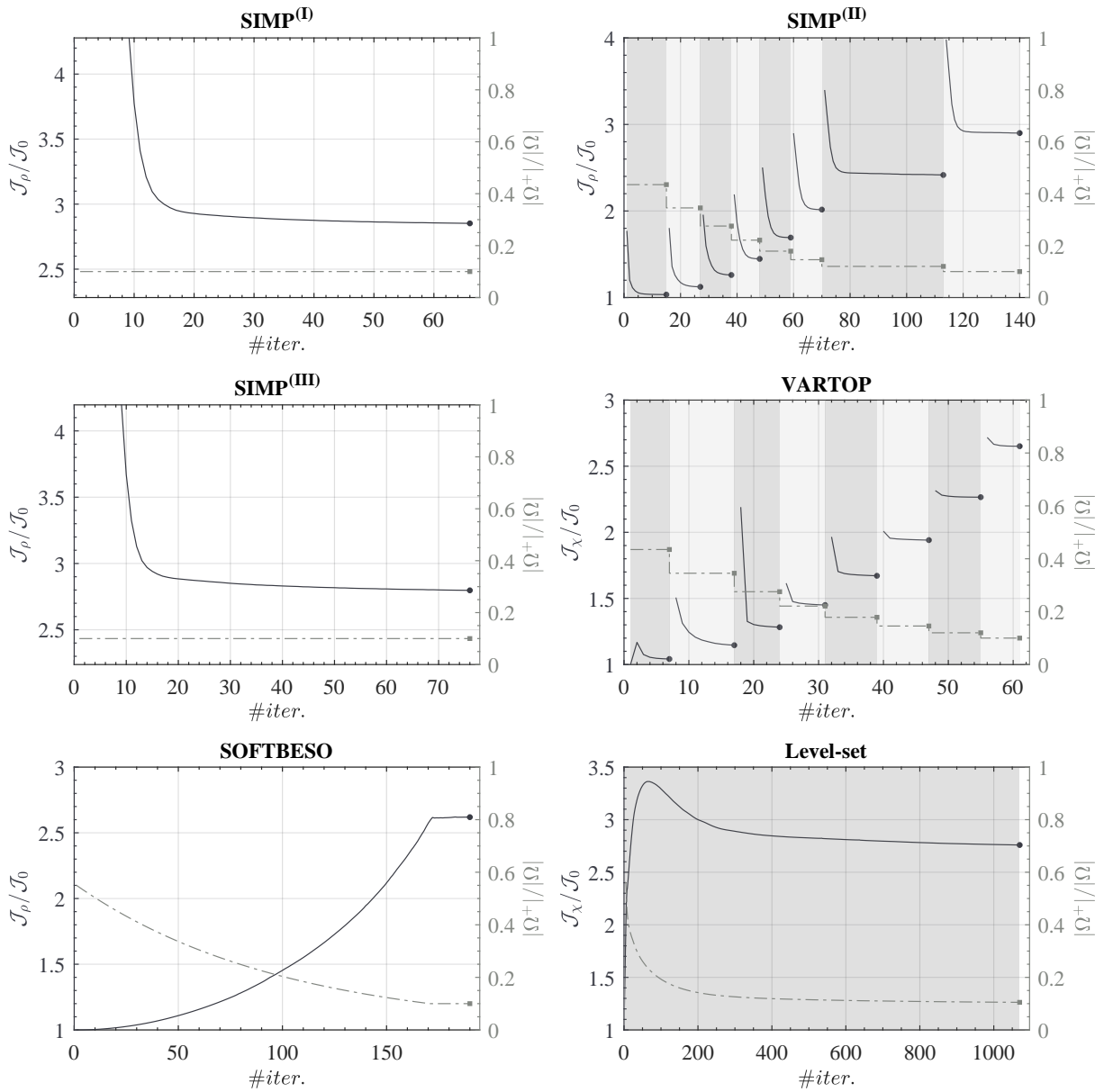


Figure D.E.15: Evolution histories of the values of the objective function and volume fraction throughout the iterations of the L-shaped structure topology optimization for the six considered methods. *Single-time-step approaches* are illustrated in the first column, while *incremental time-advancing techniques* are depicted in the second column, each time-step being shaded with a different color. The normalized objective function \mathcal{J}_ρ or \mathcal{J}_χ is associated with the left y-axis and represented with a solid black line. On the other side, the volume fraction (i.e., the stiff material fraction) $\frac{|\Omega^+|}{|\Omega|}$ is represented by a dash-dotted gray line in the right y-axis of each graphic.

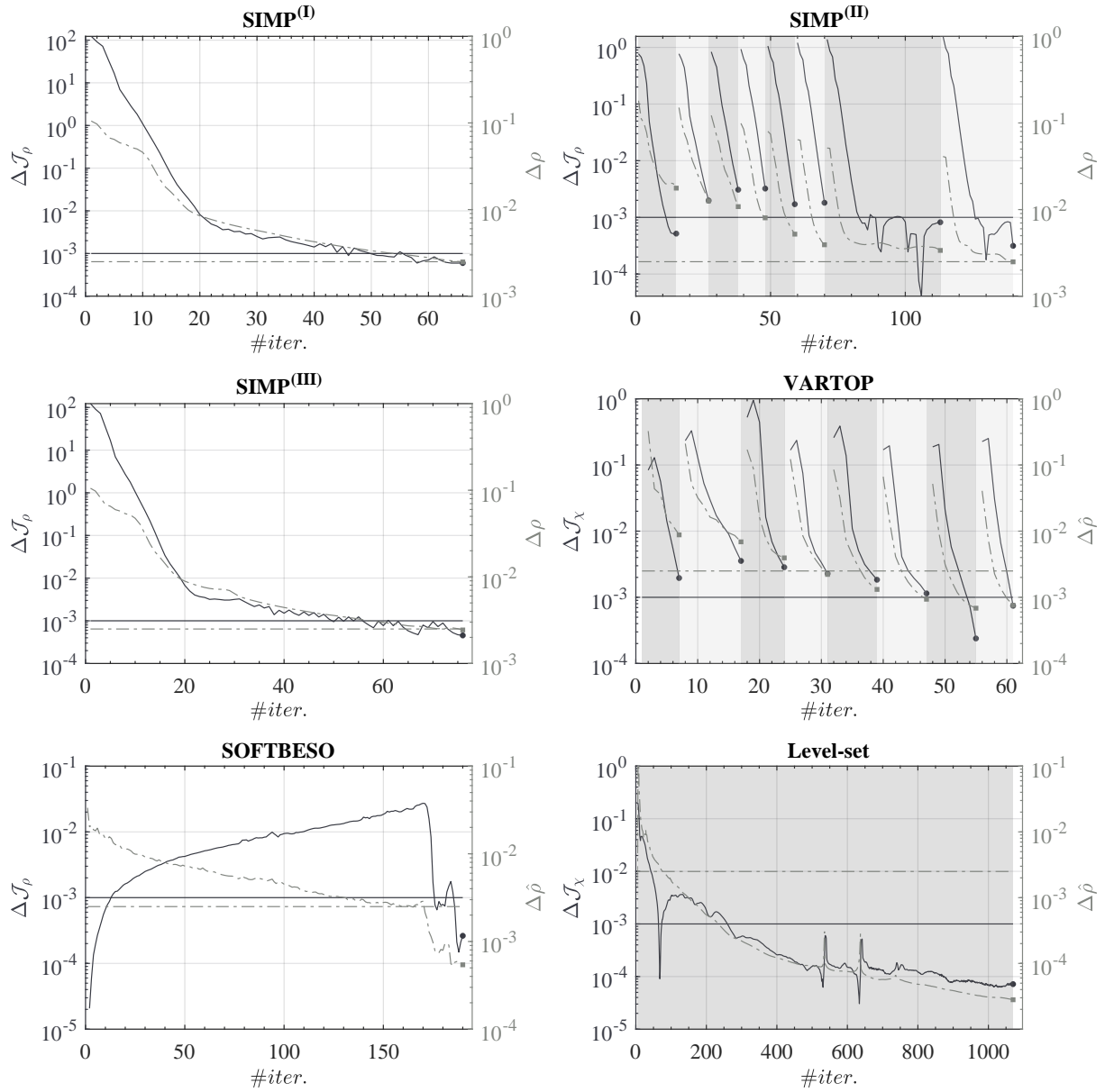


Figure D.E.16: Evolution histories of the criteria values in the objective function and in the topology throughout iterations of the L-shaped structure topology optimization for the six considered methods. *Single-time-step approaches* are illustrated in the first column, while *incremental time-advancing techniques* are depicted on the second column, each time-step being shaded with a different color. The criterion in objective function, associated with the left y-axis, is represented with a solid black line, while the criterion in the topology is represented by a dash-dotted gray line in the right y-axis of each graphic. In addition, the corresponding maximum tolerances $Tol_{\mathcal{J}}$ and Tol_{ζ} allowed in the last time-step (or in the entire optimization for single-time-step methods) are also displayed in every graphic as horizontal lines with the same properties.

References

- [1] N. Aage, E. Andreassen, and B. S. Lazarov, “Topology optimization using PETSc: An easy-to-use, fully parallel, open source topology optimization framework,” *Structural and Multidisciplinary Optimization*, vol. 51, no. 3, pp. 565–572, Aug. 2014. DOI: [10.1007/s00158-014-1157-0](https://doi.org/10.1007/s00158-014-1157-0).
- [2] H. Adeli and N.-T. Cheng, “Augmented lagrangian genetic algorithm for structural optimization,” *Journal of Aerospace Engineering*, vol. 7, no. 1, pp. 104–118, Jan. 1994. DOI: [10.1061/\(asce\)0893-1321\(1994\)7:1\(104\)](https://doi.org/10.1061/(asce)0893-1321(1994)7:1(104)).
- [3] J. Alexandersen, O. Sigmund, and N. Aage, “Large scale three-dimensional topology optimisation of heat sinks cooled by natural convection,” *International Journal of Heat and Mass Transfer*, vol. 100, pp. 876–891, Sep. 2016. DOI: [10.1016/j.ijheatmasstransfer.2016.05.013](https://doi.org/10.1016/j.ijheatmasstransfer.2016.05.013).
- [4] G. Allaire, E. Bonnetier, G. Francfort, and F. Jouve, “Shape optimization by the homogenization method,” *Numerische Mathematik*, vol. 76, no. 1, pp. 27–68, 1997. DOI: [10.1007/s002110050253](https://doi.org/10.1007/s002110050253).
- [5] G. Allaire, F. de Gournay, F. Jouve, and A.-M. Toader, “Structural optimization using topological and shape sensitivity via a level set method,” *Control and Cybernetics*, vol. 34, 2005.
- [6] G. Allaire and F. Jouve, “A level-set method for vibration and multiple loads structural optimization,” *Computer Methods in Applied Mechanics and Engineering*, vol. 194, no. 30–33, pp. 3269–3290, 2005. DOI: [10.1016/j.cma.2004.12.018](https://doi.org/10.1016/j.cma.2004.12.018).
- [7] G. Allaire, F. Jouve, and A.-M. Toader, “A level-set method for shape optimization,” *Comptes Rendus Mathématique*, vol. 334, no. 12, pp. 1125–1130, Jan. 2002. DOI: [10.1016/s1631-073x\(02\)02412-3](https://doi.org/10.1016/s1631-073x(02)02412-3).
- [8] G. Allaire, F. Jouve, and A.-M. Toader, “Structural optimization using sensitivity analysis and a level-set method,” *Journal of Computational Physics*, vol. 194, no. 1, pp. 363–393, 2004. DOI: [10.1016/j.jcp.2003.09.032](https://doi.org/10.1016/j.jcp.2003.09.032).
- [9] S. M. Allen and J. W. Cahn, “A microscopic theory for antiphase boundary motion and its application to antiphase domain coarsening,” *Acta Metallurgica*, vol. 27, no. 6, pp. 1085–1095, Jun. 1979. DOI: [10.1016/0001-6160\(79\)90196-2](https://doi.org/10.1016/0001-6160(79)90196-2).
- [10] S. Amstutz, S. M. Giusti, A. A. Novotny, and E. A. de Souza Neto, “Topological derivative for multi-scale linear elasticity models applied to the synthesis of microstructures,” *International Journal for Numerical Methods in Engineering*, vol. 84, no. 6, pp. 733–756, 2010. DOI: [10.1002/nme.2922](https://doi.org/10.1002/nme.2922).
- [11] S. Amstutz and H. Andrä, “A new algorithm for topology optimization using a level-set method,” *Journal of Computational Physics*, vol. 216, no. 2, pp. 573–588, 2006. DOI: [10.1016/j.jcp.2005.12.015](https://doi.org/10.1016/j.jcp.2005.12.015).
- [12] C. S. Andreasen and O. Sigmund, “Topology optimization of fluid–structure-interaction problems in poroelasticity,” *Computer Methods in Applied Mechanics and Engineering*, vol. 258, pp. 55–62, May 2013. DOI: [10.1016/j.cma.2013.02.007](https://doi.org/10.1016/j.cma.2013.02.007).
- [13] E. Andreassen, A. Clausen, M. Schevenels, B. S. Lazarov, and O. Sigmund, “Efficient topology optimization in MATLAB using 88 lines of code,” *Structural and Multidisciplinary Optimization*, vol. 43, no. 1, pp. 1–16, Nov. 2010. DOI: [10.1007/s00158-010-0594-7](https://doi.org/10.1007/s00158-010-0594-7).
- [14] C. Barbarosie and A.-M. Toader, “Shape and topology optimization for periodic problems,” *Structural and Multidisciplinary Optimization*, vol. 40, no. 1–6, pp. 381–391, Apr. 2009. DOI: [10.1007/s00158-009-0378-0](https://doi.org/10.1007/s00158-009-0378-0).

- [15] M. P. Bendsøe, “Optimal shape design as a material distribution problem,” *Structural Optimization*, vol. 1, no. 4, pp. 193–202, Dec. 1989. DOI: [10.1007/bf01650949](https://doi.org/10.1007/bf01650949).
- [16] M. P. Bendsøe and O. Sigmund, *Topology Optimization*. Springer Berlin Heidelberg, 2004. DOI: [10.1007/978-3-662-05086-6](https://doi.org/10.1007/978-3-662-05086-6).
- [17] M. P. Bendsøe and N. Kikuchi, “Generating optimal topologies in structural design using a homogenization method,” *Computer Methods in Applied Mechanics and Engineering*, vol. 71, no. 2, pp. 197–224, Nov. 1988. DOI: [10.1016/0045-7825\(88\)90086-2](https://doi.org/10.1016/0045-7825(88)90086-2).
- [18] T. Borrvall and J. Petersson, “Topology optimization of fluids in stokes flow,” *International Journal for Numerical Methods in Fluids*, vol. 41, no. 1, pp. 77–107, 2002. DOI: [10.1002/flid.426](https://doi.org/10.1002/flid.426).
- [19] B. Bourdin, “Filters in topology optimization,” *International Journal for Numerical Methods in Engineering*, vol. 50, no. 9, pp. 2143–2158, 2001. DOI: [10.1002/nme.116](https://doi.org/10.1002/nme.116).
- [20] B. Bourdin and A. Chambolle, “Design-dependent loads in topology optimization,” *ESAIM: Control, Optimisation and Calculus of Variations*, vol. 9, pp. 19–48, Jan. 2003. DOI: [10.1051/cocv:2002070](https://doi.org/10.1051/cocv:2002070).
- [21] T. E. Bruns, “Topology optimization of convection-dominated, steady-state heat transfer problems,” *International Journal of Heat and Mass Transfer*, vol. 50, no. 15-16, pp. 2859–2873, Jul. 2007. DOI: [10.1016/j.ijheatmasstransfer.2007.01.039](https://doi.org/10.1016/j.ijheatmasstransfer.2007.01.039).
- [22] T. Bruns, “A reevaluation of the SIMP method with filtering and an alternative formulation for solid–void topology optimization,” *Structural and Multidisciplinary Optimization*, vol. 30, no. 6, pp. 428–436, Aug. 2005. DOI: [10.1007/s00158-005-0537-x](https://doi.org/10.1007/s00158-005-0537-x).
- [23] T. E. Bruns and D. A. Tortorelli, “Topology optimization of non-linear elastic structures and compliant mechanisms,” *Computer Methods in Applied Mechanics and Engineering*, vol. 190, no. 26-27, pp. 3443–3459, Mar. 2001. DOI: [10.1016/s0045-7825\(00\)00278-4](https://doi.org/10.1016/s0045-7825(00)00278-4).
- [24] M. Burger, B. Hackl, and W. Ring, “Incorporating topological derivatives into level set methods,” *Journal of Computational Physics*, vol. 194, no. 1, pp. 344–362, 2004. DOI: [10.1016/j.jcp.2003.09.033](https://doi.org/10.1016/j.jcp.2003.09.033).
- [25] M. Burger and R. Stainko, “Phase-field relaxation of topology optimization with local stress constraints,” *SIAM Journal on Control and Optimization*, vol. 45, no. 4, pp. 1447–1466, Jan. 2006. DOI: [10.1137/05062723x](https://doi.org/10.1137/05062723x).
- [26] J. W. Cahn and J. E. Hilliard, “Free energy of a nonuniform system. I. interfacial free energy,” *The Journal of Chemical Physics*, vol. 28, no. 2, pp. 258–267, Feb. 1958. DOI: [10.1063/1.1744102](https://doi.org/10.1063/1.1744102).
- [27] J. Céa, S. Garreau, P. Guillaume, and M. Masmoudi, “The shape and topological optimizations connection,” *Computer Methods in Applied Mechanics and Engineering*, vol. 188, no. 4, pp. 713–726, 2000. DOI: [10.1016/s0045-7825\(99\)00357-6](https://doi.org/10.1016/s0045-7825(99)00357-6).
- [28] V. J. Challis, “A discrete level-set topology optimization code written in matlab,” *Structural and Multidisciplinary Optimization*, vol. 41, no. 3, pp. 453–464, Sep. 2009. DOI: [10.1007/s00158-009-0430-0](https://doi.org/10.1007/s00158-009-0430-0).
- [29] C. D. Chapman, K. Saitou, and M. J. Jakiela, “Genetic algorithms as an approach to configuration and topology design,” *Journal of Mechanical Design*, vol. 116, no. 4, pp. 1005–1012, Dec. 1994. DOI: [10.1115/1.2919480](https://doi.org/10.1115/1.2919480).
- [30] D. Chu, Y. Xie, A. Hira, and G. Steven, “Evolutionary structural optimization for problems with stiffness constraints,” *Finite Elements in Analysis and Design*, vol. 21, no. 4, pp. 239–251, Apr. 1996. DOI: [10.1016/0168-874x\(95\)00043-s](https://doi.org/10.1016/0168-874x(95)00043-s).

- [31] P. G. Coelho, P. R. Fernandes, J. M. Guedes, and H. C. Rodrigues, “A hierarchical model for concurrent material and topology optimisation of three-dimensional structures,” *Structural and Multidisciplinary Optimization*, vol. 35, no. 2, pp. 107–115, Jun. 2007. DOI: [10.1007/s00158-007-0141-3](https://doi.org/10.1007/s00158-007-0141-3).
- [32] M. Dambrine and D. Kateb, “On the ersatz material approximation in level-set methods,” *ESAIM: Control, Optimisation and Calculus of Variations*, vol. 16, no. 3, pp. 618–634, 2009. DOI: [10.1051/cocv/2009023](https://doi.org/10.1051/cocv/2009023).
- [33] J. D. Deaton and R. V. Grandhi, “A survey of structural and multidisciplinary continuum topology optimization: Post 2000,” *Structural and Multidisciplinary Optimization*, vol. 49, no. 1, pp. 1–38, 2013. DOI: [10.1007/s00158-013-0956-z](https://doi.org/10.1007/s00158-013-0956-z).
- [34] J. Deng, J. Yan, and G. Cheng, “Multi-objective concurrent topology optimization of thermoelastic structures composed of homogeneous porous material,” *Structural and Multidisciplinary Optimization*, vol. 47, no. 4, pp. 583–597, Nov. 2012. DOI: [10.1007/s00158-012-0849-6](https://doi.org/10.1007/s00158-012-0849-6).
- [35] N. P. van Dijk, K. Maute, M. Langelaar, and F. van Keulen, “Level-set methods for structural topology optimization: A review,” *Structural and Multidisciplinary Optimization*, vol. 48, no. 3, pp. 437–472, 2013. DOI: [10.1007/s00158-013-0912-y](https://doi.org/10.1007/s00158-013-0912-y).
- [36] H.-W. Dong, S.-D. Zhao, Y.-S. Wang, and C. Zhang, “Topology optimization of anisotropic broadband double-negative elastic metamaterials,” *Journal of the Mechanics and Physics of Solids*, vol. 105, pp. 54–80, Aug. 2017. DOI: [10.1016/j.jmps.2017.04.009](https://doi.org/10.1016/j.jmps.2017.04.009).
- [37] J. Du and N. Olhoff, “Minimization of sound radiation from vibrating bi-material structures using topology optimization,” *Structural and Multidisciplinary Optimization*, vol. 33, no. 4-5, pp. 305–321, Jan. 2007. DOI: [10.1007/s00158-006-0088-9](https://doi.org/10.1007/s00158-006-0088-9).
- [38] P. Duysinx, L. V. Miegroet, T. Jacobs, and C. Fleury, “Generalized shape optimization using x-FEM and level set methods,” in *Solid Mechanics and Its Applications*, Springer Netherlands, 2006, pp. 23–32. DOI: [10.1007/1-4020-4752-5_3](https://doi.org/10.1007/1-4020-4752-5_3).
- [39] H. A. Eschenauer, V. V. Kobelev, and A. Schumacher, “Bubble method for topology and shape optimization of structures,” *Structural Optimization*, vol. 8, no. 1, pp. 42–51, Aug. 1994. DOI: [10.1007/bf01742933](https://doi.org/10.1007/bf01742933).
- [40] H. A. Eschenauer and N. Olhoff, “Topology optimization of continuum structures: A review,” *Applied Mechanics Reviews*, vol. 54, no. 4, pp. 331–390, Jul. 2001. DOI: [10.1115/1.1388075](https://doi.org/10.1115/1.1388075).
- [41] D. J. Eyre, “Systems of cahn–hilliard equations,” *SIAM Journal on Applied Mathematics*, vol. 53, no. 6, pp. 1686–1712, Dec. 1993. DOI: [10.1137/0153078](https://doi.org/10.1137/0153078).
- [42] P. Fernandes, J. M. Guedes, and H. Rodrigues, “Topology optimization of three-dimensional linear elastic structures with a constraint on “perimeter”,” *Computers & Structures*, vol. 73, no. 6, pp. 583–594, 1999. DOI: [10.1016/s0045-7949\(98\)00312-5](https://doi.org/10.1016/s0045-7949(98)00312-5).
- [43] P. Fulmański, A. Laurain, J.-F. Scheid, and J. Sokołowski, “A level set method in shape and topology optimization for variational inequalities,” *International Journal of Applied Mathematics and Computer Science*, vol. 17, no. 3, pp. 413–430, Oct. 2007. DOI: [10.2478/v10006-007-0034-z](https://doi.org/10.2478/v10006-007-0034-z).
- [44] T. Gao, W. H. Zhang, J. H. Zhu, Y. J. Xu, and D. H. Bassir, “Topology optimization of heat conduction problem involving design-dependent heat load effect,” *Finite Elements in Analysis and Design*, vol. 44, no. 14, pp. 805–813, Oct. 2008. DOI: [10.1016/j.finel.2008.06.001](https://doi.org/10.1016/j.finel.2008.06.001).
- [45] S. Garreau, P. Guillaume, and M. Masmoudi, “The topological asymptotic for PDE systems: The elasticity case,” *SIAM Journal on Control and Optimization*, vol. 39, no. 6, pp. 1756–1778, 2001. DOI: [10.1137/s0363012900369538](https://doi.org/10.1137/s0363012900369538).

- [46] A. Gersborg-Hansen, O. Sigmund, and R. Haber, “Topology optimization of channel flow problems,” *Structural and Multidisciplinary Optimization*, vol. 30, no. 3, pp. 181–192, Jun. 2005. DOI: [10.1007/s00158-004-0508-7](https://doi.org/10.1007/s00158-004-0508-7).
- [47] S. M. Giusti, A. Ferrer, and J. Oliver, “Topological sensitivity analysis in heterogeneous anisotropic elasticity problem. theoretical and computational aspects,” *Computer Methods in Applied Mechanics and Engineering*, vol. 311, pp. 134–150, 2016. DOI: [10.1016/j.cma.2016.08.004](https://doi.org/10.1016/j.cma.2016.08.004).
- [48] S. M. Giusti, A. A. Novotny, and J. Sokołowski, “Topological derivative for steady-state orthotropic heat diffusion problem,” *Structural and Multidisciplinary Optimization*, vol. 40, no. 1-6, pp. 53–64, Feb. 2009. DOI: [10.1007/s00158-009-0359-3](https://doi.org/10.1007/s00158-009-0359-3).
- [49] J. K. Guest, J. H. Prévost, and T. Belytschko, “Achieving minimum length scale in topology optimization using nodal design variables and projection functions,” *International Journal for Numerical Methods in Engineering*, vol. 61, no. 2, pp. 238–254, 2004. DOI: [10.1002/nme.1064](https://doi.org/10.1002/nme.1064).
- [50] J. K. Guest, A. Asadpoure, and S.-H. Ha, “Eliminating beta-continuation from heaviside projection and density filter algorithms,” *Structural and Multidisciplinary Optimization*, vol. 44, no. 4, pp. 443–453, Jul. 2011. DOI: [10.1007/s00158-011-0676-1](https://doi.org/10.1007/s00158-011-0676-1).
- [51] J. K. Guest and J. H. Prévost, “Topology optimization of creeping fluid flows using a darcy–stokes finite element,” *International Journal for Numerical Methods in Engineering*, vol. 66, no. 3, pp. 461–484, 2006. DOI: [10.1002/nme.1560](https://doi.org/10.1002/nme.1560).
- [52] S.-H. Ha and S. Cho, “Topological shape optimization of heat conduction problems using level set approach,” *Numerical Heat Transfer, Part B: Fundamentals*, vol. 48, no. 1, pp. 67–88, Jul. 2005. DOI: [10.1080/10407790590935966](https://doi.org/10.1080/10407790590935966).
- [53] R. B. Haber, C. S. Jog, and M. P. Bends Bendsøe, “A new approach to variable-topology shape design using a constraint on perimeter,” *Structural Optimization*, vol. 11, no. 1-2, pp. 1–12, 1996. DOI: [10.1007/bf01279647](https://doi.org/10.1007/bf01279647).
- [54] R. Haber and M. Bendsoe, “Problem formulation, solution procedures and geometric modeling - key issues in variable-topology optimization,” in *7th AIAA/USAF/NASA/ISSMO Symposium on Multidisciplinary Analysis and Optimization*, American Institute of Aeronautics and Astronautics, Sep. 1998. DOI: [10.2514/6.1998-4948](https://doi.org/10.2514/6.1998-4948).
- [55] P. Hajela, E. Lee, and C.-Y. Lin, “Genetic algorithms in structural topology optimization,” in *Topology Design of Structures*, Springer Netherlands, 1993, pp. 117–133. DOI: [10.1007/978-94-011-1804-0_10](https://doi.org/10.1007/978-94-011-1804-0_10).
- [56] W. Hare, J. Nutini, and S. Tesfamariam, “A survey of non-gradient optimization methods in structural engineering,” *Advances in Engineering Software*, vol. 59, pp. 19–28, May 2013. DOI: [10.1016/j.advengsoft.2013.03.001](https://doi.org/10.1016/j.advengsoft.2013.03.001).
- [57] L. He, C.-Y. Kao, and S. Osher, “Incorporating topological derivatives into shape derivatives based level set methods,” *Journal of Computational Physics*, vol. 225, no. 1, pp. 891–909, 2007. DOI: [10.1016/j.jcp.2007.01.003](https://doi.org/10.1016/j.jcp.2007.01.003).
- [58] X. Huang, Y. Li, S. Zhou, and Y. Xie, “Topology optimization of compliant mechanisms with desired structural stiffness,” *Engineering Structures*, vol. 79, pp. 13–21, Nov. 2014. DOI: [10.1016/j.engstruct.2014.08.008](https://doi.org/10.1016/j.engstruct.2014.08.008).
- [59] X. Huang and Y. M. Xie, “Bi-directional evolutionary topology optimization of continuum structures with one or multiple materials,” *Computational Mechanics*, vol. 43, no. 3, pp. 393–401, Jul. 2008. DOI: [10.1007/s00466-008-0312-0](https://doi.org/10.1007/s00466-008-0312-0).
- [60] X. Huang and Y. M. Xie, *Evolutionary Topology Optimization of Continuum Structures*. John Wiley & Sons, Ltd, Apr. 2010. DOI: [10.1002/9780470689486](https://doi.org/10.1002/9780470689486).

- [61] X. Huang, Y. M. Xie, B. Jia, Q. Li, and S. W. Zhou, “Evolutionary topology optimization of periodic composites for extremal magnetic permeability and electrical permittivity,” *Structural and Multidisciplinary Optimization*, vol. 46, no. 3, pp. 385–398, Jan. 2012. DOI: [10.1007/s00158-012-0766-8](https://doi.org/10.1007/s00158-012-0766-8).
- [62] X. Huang and Y. Xie, “Convergent and mesh-independent solutions for the bi-directional evolutionary structural optimization method,” *Finite Elements in Analysis and Design*, vol. 43, no. 14, pp. 1039–1049, Oct. 2007. DOI: [10.1016/j.finel.2007.06.006](https://doi.org/10.1016/j.finel.2007.06.006).
- [63] N. Jenkins and K. Maute, “Level set topology optimization of stationary fluid-structure interaction problems,” *Structural and Multidisciplinary Optimization*, vol. 52, no. 1, pp. 179–195, Mar. 2015. DOI: [10.1007/s00158-015-1229-9](https://doi.org/10.1007/s00158-015-1229-9).
- [64] C. S. Jog and R. B. Haber, “Stability of finite element models for distributed-parameter optimization and topology design,” *Computer Methods in Applied Mechanics and Engineering*, vol. 130, no. 3-4, pp. 203–226, Apr. 1996. DOI: [10.1016/0045-7825\(95\)00928-0](https://doi.org/10.1016/0045-7825(95)00928-0).
- [65] A. Kawamoto, T. Matsumori, S. Yamasaki, T. Nomura, T. Kondoh, and S. Nishiwaki, “Heaviside projection based topology optimization by a PDE-filtered scalar function,” *Structural and Multidisciplinary Optimization*, vol. 44, no. 1, pp. 19–24, Aug. 2010. DOI: [10.1007/s00158-010-0562-2](https://doi.org/10.1007/s00158-010-0562-2).
- [66] B. S. Lazarov and O. Sigmund, “Filters in topology optimization based on helmholtz-type differential equations,” *International Journal for Numerical Methods in Engineering*, vol. 86, no. 6, pp. 765–781, Dec. 2010. DOI: [10.1002/nme.3072](https://doi.org/10.1002/nme.3072).
- [67] Q. Li, G. Steven, and Y. Xie, “A simple checkerboard suppression algorithm for evolutionary structural optimization,” *Structural and Multidisciplinary Optimization*, vol. 22, no. 3, pp. 230–239, Oct. 2001. DOI: [10.1007/s001580100140](https://doi.org/10.1007/s001580100140).
- [68] Q. Li, G. P. Steven, O. M. Querin, and Y. M. Xie, “Structural topology design with multiple thermal criteria,” *Engineering Computations*, vol. 17, no. 6, pp. 715–734, Sep. 2000. DOI: [10.1108/02644400010340642](https://doi.org/10.1108/02644400010340642).
- [69] Q. Li, G. P. Steven, O. M. Querin, and Y. Xie, “Shape and topology design for heat conduction by evolutionary structural optimization,” *International Journal of Heat and Mass Transfer*, vol. 42, no. 17, pp. 3361–3371, Sep. 1999. DOI: [10.1016/s0017-9310\(99\)00008-3](https://doi.org/10.1016/s0017-9310(99)00008-3).
- [70] W. Li, G. Steven, and Y. Xie, “Shape design for elastic contact problems by evolutionary structural optimization,” in *7th AIAA/USAF/NASA/ISSMO Symposium on Multidisciplinary Analysis and Optimization*, American Institute of Aeronautics and Astronautics, Sep. 1998. DOI: [10.2514/6.1998-4851](https://doi.org/10.2514/6.1998-4851).
- [71] W. Li, Q. Li, G. P. Steven, and Y. Xie, “An evolutionary shape optimization for elastic contact problems subject to multiple load cases,” *Computer Methods in Applied Mechanics and Engineering*, vol. 194, no. 30-33, pp. 3394–3415, Aug. 2005. DOI: [10.1016/j.cma.2004.12.024](https://doi.org/10.1016/j.cma.2004.12.024).
- [72] Y. fan Li, X. Huang, F. Meng, and S. Zhou, “Evolutionary topological design for phononic band gap crystals,” *Structural and Multidisciplinary Optimization*, vol. 54, no. 3, pp. 595–617, Mar. 2016. DOI: [10.1007/s00158-016-1424-3](https://doi.org/10.1007/s00158-016-1424-3).
- [73] S. Lim, T. Yamada, S. Min, and S. Nishiwaki, “Topology optimization of a magnetic actuator based on a level set and phase-field approach,” *IEEE Transactions on Magnetics*, vol. 47, no. 5, pp. 1318–1321, May 2011. DOI: [10.1109/tmag.2010.2097583](https://doi.org/10.1109/tmag.2010.2097583).
- [74] K. Liu and A. Tovar, “An efficient 3d topology optimization code written in matlab,” *Structural and Multidisciplinary Optimization*, vol. 50, no. 6, pp. 1175–1196, 2014. DOI: [10.1007/s00158-014-1107-x](https://doi.org/10.1007/s00158-014-1107-x).

- [75] L. Lu, T. Yamamoto, M. Otomori, T. Yamada, K. Izui, and S. Nishiwaki, “Topology optimization of an acoustic metamaterial with negative bulk modulus using local resonance,” *Finite Elements in Analysis and Design*, vol. 72, pp. 1–12, Sep. 2013. DOI: [10.1016/j.finel.2013.04.005](https://doi.org/10.1016/j.finel.2013.04.005).
- [76] G.-C. Luh and C.-Y. Lin, “Structural topology optimization using ant colony optimization algorithm,” vol. 9, no. 4, pp. 1343–1353, Sep. 2009. DOI: [10.1016/j.asoc.2009.06.001](https://doi.org/10.1016/j.asoc.2009.06.001).
- [77] Z. Luo, L. Tong, M. Y. Wang, and S. Wang, “Shape and topology optimization of compliant mechanisms using a parameterization level set method,” *Journal of Computational Physics*, vol. 227, no. 1, pp. 680–705, Nov. 2007. DOI: [10.1016/j.jcp.2007.08.011](https://doi.org/10.1016/j.jcp.2007.08.011).
- [78] Z. Luo, M. Y. Wang, S. Wang, and P. Wei, “A level set-based parameterization method for structural shape and topology optimization,” *International Journal for Numerical Methods in Engineering*, vol. 76, no. 1, pp. 1–26, Oct. 2008. DOI: [10.1002/nme.2092](https://doi.org/10.1002/nme.2092).
- [79] Z. .-. Ma, N. Kikuchi, and I. Hagiwara, “Structural topology and shape optimization for a frequency response problem,” *Computational Mechanics*, vol. 13, no. 3, pp. 157–174, Dec. 1993. DOI: [10.1007/bf00370133](https://doi.org/10.1007/bf00370133).
- [80] D. Manickarajah, Y. Xie, and G. Steven, “An evolutionary method for optimization of plate buckling resistance,” *Finite Elements in Analysis and Design*, vol. 29, no. 3-4, pp. 205–230, Jun. 1998. DOI: [10.1016/s0168-874x\(98\)00012-2](https://doi.org/10.1016/s0168-874x(98)00012-2).
- [81] G. Marck, M. Nemer, and J.-L. Harion, “Topology optimization of heat and mass transfer problems: Laminar flow,” *Numerical Heat Transfer, Part B: Fundamentals*, vol. 63, no. 6, pp. 508–539, Jun. 2013. DOI: [10.1080/10407790.2013.772001](https://doi.org/10.1080/10407790.2013.772001).
- [82] R. J. Marczak, “Topology optimization and boundary elements—a preliminary implementation for linear heat transfer,” *Engineering Analysis with Boundary Elements*, vol. 31, no. 9, pp. 793–802, Sep. 2007. DOI: [10.1016/j.enganabound.2007.01.005](https://doi.org/10.1016/j.enganabound.2007.01.005).
- [83] C. Mattheck and S. Burkhardt, “A new method of structural shape optimization based on biological growth,” *International Journal of Fatigue*, vol. 12, no. 3, pp. 185–190, May 1990. DOI: [10.1016/0142-1123\(90\)90094-u](https://doi.org/10.1016/0142-1123(90)90094-u).
- [84] K. Maute and M. Allen, “Conceptual design of aeroelastic structures by topology optimization,” *Structural and Multidisciplinary Optimization*, vol. 27, no. 1-2, pp. 27–42, May 2004. DOI: [10.1007/s00158-003-0362-z](https://doi.org/10.1007/s00158-003-0362-z).
- [85] X. W. Michael Yu Wang, “Pde-driven level sets, shape sensitivity and curvature flow for structural topology optimization,” *Computer Modeling in Engineering & Sciences*, vol. 6, no. 4, pp. 373–396, 2004, ISSN: 1526-1506. DOI: [10.3970/cmcs.2004.006.373](https://doi.org/10.3970/cmcs.2004.006.373). [Online]. Available: <http://www.techscience.com/CMES/v6n4/24856>.
- [86] H. P. Mlejnek, “Some aspects of the genesis of structures,” *Structural Optimization*, vol. 5, no. 1-2, pp. 64–69, Mar. 1992. DOI: [10.1007/bf01744697](https://doi.org/10.1007/bf01744697).
- [87] D. J. Munk, G. A. Vio, and G. P. Steven, “Topology and shape optimization methods using evolutionary algorithms: A review,” *Structural and Multidisciplinary Optimization*, vol. 52, no. 3, pp. 613–631, May 2015. DOI: [10.1007/s00158-015-1261-9](https://doi.org/10.1007/s00158-015-1261-9).
- [88] J. A. Norato, M. P. Bendsøe, R. B. Haber, and D. A. Tortorelli, “A topological derivative method for topology optimization,” *Structural and Multidisciplinary Optimization*, vol. 33, no. 4-5, pp. 375–386, 2007. DOI: [10.1007/s00158-007-0094-6](https://doi.org/10.1007/s00158-007-0094-6).
- [89] A. Novotny, R. Feijóo, E. Taroco, and C. Padra, “Topological sensitivity analysis for three-dimensional linear elasticity problem,” *Computer Methods in Applied Mechanics and Engineering*, vol. 196, no. 41-44, pp. 4354–4364, Sep. 2007. DOI: [10.1016/j.cma.2007.05.006](https://doi.org/10.1016/j.cma.2007.05.006).

- [90] J. Oliver, D. Yago, J. Cante, and O. Lloberas-Valls, “Variational approach to relaxed topological optimization: Closed form solutions for structural problems in a sequential pseudo-time framework,” *Computer Methods in Applied Mechanics and Engineering*, vol. 355, pp. 779–819, Oct. 2019. DOI: [10.1016/j.cma.2019.06.038](https://doi.org/10.1016/j.cma.2019.06.038).
- [91] S. Osher and R. Fedkiw, *Level Set Methods and Dynamic Implicit Surfaces*. Springer New York, 2003. DOI: [10.1007/b98879](https://doi.org/10.1007/b98879).
- [92] S. Osher and J. A. Sethian, “Fronts propagating with curvature-dependent speed: Algorithms based on hamilton-jacobi formulations,” *Journal of Computational Physics*, vol. 79, no. 1, pp. 12–49, 1988. DOI: [10.1016/0021-9991\(88\)90002-2](https://doi.org/10.1016/0021-9991(88)90002-2).
- [93] S. J. Osher and F. Santosa, “Level set methods for optimization problems involving geometry and constraints,” *Journal of Computational Physics*, vol. 171, no. 1, pp. 272–288, Jul. 2001. DOI: [10.1006/jcph.2001.6789](https://doi.org/10.1006/jcph.2001.6789).
- [94] J. Petersson and O. Sigmund, “Slope constrained topology optimization,” *International Journal for Numerical Methods in Engineering*, vol. 41, no. 8, pp. 1417–1434, Apr. 1998. DOI: [10.1002/\(sici\)1097-0207\(19980430\)41:8<1417::aid-nme344>3.0.co;2-n](https://doi.org/10.1002/(sici)1097-0207(19980430)41:8<1417::aid-nme344>3.0.co;2-n).
- [95] Y. M. X. Qing Li Grant P. Steven, “Thermoelastic topology optimization for problems with varying temperature fields,” *Journal of Thermal Stresses*, vol. 24, no. 4, pp. 347–366, Apr. 2001. DOI: [10.1080/01495730151078153](https://doi.org/10.1080/01495730151078153).
- [96] O. Querin, G. Steven, and Y. Xie, “Topology optimisation of structures with material and geometric non-linearities,” in *6th Symposium on Multidisciplinary Analysis and Optimization*, American Institute of Aeronautics and Astronautics, Sep. 1996. DOI: [10.2514/6.1996-4116](https://doi.org/10.2514/6.1996-4116).
- [97] O. Querin, G. Steven, and Y. Xie, “Evolutionary structural optimisation (ESO) using a bidirectional algorithm,” *Engineering Computations*, vol. 15, no. 8, pp. 1031–1048, Dec. 1998. DOI: [10.1108/02644409810244129](https://doi.org/10.1108/02644409810244129).
- [98] O. Querin, V. Young, G. Steven, and Y. Xie, “Computational efficiency and validation of bi-directional evolutionary structural optimisation,” *Computer Methods in Applied Mechanics and Engineering*, vol. 189, no. 2, pp. 559–573, Sep. 2000. DOI: [10.1016/s0045-7825\(99\)00309-6](https://doi.org/10.1016/s0045-7825(99)00309-6).
- [99] D. Roca, D. Yago, J. Cante, O. Lloberas-Valls, and J. Oliver, “Computational design of locally resonant acoustic metamaterials,” *Computer Methods in Applied Mechanics and Engineering*, vol. 345, pp. 161–182, Mar. 2019. DOI: [10.1016/j.cma.2018.10.037](https://doi.org/10.1016/j.cma.2018.10.037).
- [100] G. I. N. Rozvany, “A critical review of established methods of structural topology optimization,” *Structural and Multidisciplinary Optimization*, vol. 37, no. 3, pp. 217–237, 2008. DOI: [10.1007/s00158-007-0217-0](https://doi.org/10.1007/s00158-007-0217-0).
- [101] G. Rozvany, “Aims, scope, methods, history and unified terminology of computer-aided topology optimization in structural mechanics,” *Structural and Multidisciplinary Optimization*, vol. 21, no. 2, pp. 90–108, Apr. 2001. DOI: [10.1007/s001580050174](https://doi.org/10.1007/s001580050174).
- [102] E. Schnack, *Gradientless shape optimization with FEM*. Düsseldorf: VDI-Verl, 1988, ISBN: 3188506473.
- [103] A. Schumacher, “Topologieoptimierung von bauteilstrukturen unter verwendung von lochpositionierungskriterien,” Ph.D. dissertation, Forschungszentrum für Multidisziplinäre Analysen und Angewandte Strukturoptimierung, Institut für Mechanik und Regelungstechnik, Siegen, Germany, 1996.
- [104] J. A. Sethian, *Level Set Methods and Fast Marching Methods*. Cambridge University Press, 1999, 404 pp., ISBN: 0521645573.
- [105] J. A. Sethian and A. Wiegmann, “Structural boundary design via level set and immersed interface methods,” *Journal of Computational Physics*, vol. 163, no. 2, pp. 489–528, 2000. DOI: [10.1006/jcph.2000.6581](https://doi.org/10.1006/jcph.2000.6581).

- [106] O. Sigmund, “A 99 line topology optimization code written in matlab,” *Structural and Multidisciplinary Optimization*, vol. 21, no. 2, pp. 120–127, Apr. 2001. DOI: [10.1007/s001580050176](https://doi.org/10.1007/s001580050176).
- [107] O. Sigmund, “Design of multiphysics actuators using topology optimization – part i: One-material structures,” *Computer Methods in Applied Mechanics and Engineering*, vol. 190, no. 49-50, pp. 6577–6604, Oct. 2001. DOI: [10.1016/s0045-7825\(01\)00251-1](https://doi.org/10.1016/s0045-7825(01)00251-1).
- [108] O. Sigmund and J. Petersson, “Numerical instabilities in topology optimization: A survey on procedures dealing with checkerboards, mesh-dependencies and local minima,” *Structural Optimization*, vol. 16, no. 1, pp. 68–75, 1998. DOI: [10.1007/bf01214002](https://doi.org/10.1007/bf01214002).
- [109] O. Sigmund and S. Torquato, “Design of materials with extreme thermal expansion using a three-phase topology optimization method,” *Journal of the Mechanics and Physics of Solids*, vol. 45, no. 6, pp. 1037–1067, Jun. 1997. DOI: [10.1016/s0022-5096\(96\)00114-7](https://doi.org/10.1016/s0022-5096(96)00114-7).
- [110] O. Sigmund, “Design of material structures using topology optimization,” Ph.D. dissertation, Technical University of Denmark, 1994.
- [111] O. Sigmund, “On the design of compliant mechanisms using topology optimization,” *Mechanics of Structures and Machines*, vol. 25, no. 4, pp. 493–524, 1997. DOI: [10.1080/08905459708945415](https://doi.org/10.1080/08905459708945415).
- [112] O. Sigmund, “Morphology-based black and white filters for topology optimization,” *Structural and Multidisciplinary Optimization*, vol. 33, no. 4-5, pp. 401–424, Jan. 2007. DOI: [10.1007/s00158-006-0087-x](https://doi.org/10.1007/s00158-006-0087-x).
- [113] O. Sigmund and J. S. Jensen, “Systematic design of phononic band-gap materials and structures by topology optimization,” *Philosophical Transactions of the Royal Society of London. Series A: Mathematical, Physical and Engineering Sciences*, vol. 361, no. 1806, R. T. Bonnecaze and G. J. Rodin, Eds., pp. 1001–1019, Mar. 2003. DOI: [10.1098/rsta.2003.1177](https://doi.org/10.1098/rsta.2003.1177).
- [114] O. Sigmund and K. Maute, “Topology optimization approaches,” *Structural and Multidisciplinary Optimization*, vol. 48, no. 6, pp. 1031–1055, 2013. DOI: [10.1007/s00158-013-0978-6](https://doi.org/10.1007/s00158-013-0978-6).
- [115] J. Sokolowski and A. Zochowski, “On the topological derivative in shape optimization,” *SIAM Journal on Control and Optimization*, vol. 37, no. 4, pp. 1251–1272, Jan. 1999. DOI: [10.1137/s0363012997323230](https://doi.org/10.1137/s0363012997323230).
- [116] J. Sokolowski and J.-P. Zolesio, *Introduction to Shape Optimization*. Springer Berlin Heidelberg, 1992. DOI: [10.1007/978-3-642-58106-9](https://doi.org/10.1007/978-3-642-58106-9).
- [117] M. Stolpe and K. Svanberg, “An alternative interpolation scheme for minimum compliance topology optimization,” *Structural and Multidisciplinary Optimization*, vol. 22, no. 2, pp. 116–124, Sep. 2001. DOI: [10.1007/s001580100129](https://doi.org/10.1007/s001580100129).
- [118] K. Suzuki and N. Kikuchi, “A homogenization method for shape and topology optimization,” *Computer Methods in Applied Mechanics and Engineering*, vol. 93, no. 3, pp. 291–318, Dec. 1991. DOI: [10.1016/0045-7825\(91\)90245-2](https://doi.org/10.1016/0045-7825(91)90245-2).
- [119] K. Svanberg, “The method of moving asymptotes—a new method for structural optimization,” *International Journal for Numerical Methods in Engineering*, vol. 24, no. 2, pp. 359–373, Feb. 1987. DOI: [10.1002/nme.1620240207](https://doi.org/10.1002/nme.1620240207).
- [120] A. Takezawa, S. Nishiwaki, and M. Kitamura, “Shape and topology optimization based on the phase field method and sensitivity analysis,” *Journal of Computational Physics*, vol. 229, no. 7, pp. 2697–2718, Apr. 2010. DOI: [10.1016/j.jcp.2009.12.017](https://doi.org/10.1016/j.jcp.2009.12.017).
- [121] TOPOPT Group, *Efficient topology optimization in matlab using 88 lines of code*, Webpage, Accessed: 2020-04-28, Jul. 2018. [Online]. Available: <http://www.topopt.mek.dtu.dk/Apps-and-software/Efficient-topology-optimization-in-MATLAB>.

- [122] F. Wang, B. S. Lazarov, and O. Sigmund, “On projection methods, convergence and robust formulations in topology optimization,” *Structural and Multidisciplinary Optimization*, vol. 43, no. 6, pp. 767–784, Dec. 2010. DOI: [10.1007/s00158-010-0602-y](https://doi.org/10.1007/s00158-010-0602-y).
- [123] M. Y. Wang, S. Zhou, and H. Ding, “Nonlinear diffusions in topology optimization,” *Structural and Multidisciplinary Optimization*, vol. 28, no. 4, pp. 262–276, 2004. DOI: [10.1007/s00158-004-0436-6](https://doi.org/10.1007/s00158-004-0436-6).
- [124] M. Y. Wang and X. Wang, ““Color” level sets: A multi-phase method for structural topology optimization with multiple materials,” *Computer Methods in Applied Mechanics and Engineering*, vol. 193, no. 6-8, pp. 469–496, Feb. 2004. DOI: [10.1016/j.cma.2003.10.008](https://doi.org/10.1016/j.cma.2003.10.008).
- [125] M. Y. Wang, X. Wang, and D. Guo, “A level set method for structural topology optimization,” *Computer Methods in Applied Mechanics and Engineering*, vol. 192, no. 1-2, pp. 227–246, 2003. DOI: [10.1016/s0045-7825\(02\)00559-5](https://doi.org/10.1016/s0045-7825(02)00559-5).
- [126] M. Y. Wang and S. Zhou, “Phase field: A variational method for structural topology optimization,” *Computer Modeling in Engineering and Sciences*, vol. 6, no. 6, pp. 547–566, 2004.
- [127] S. Y. Wang, K. M. Lim, B. C. Khoo, and M. Y. Wang, “An extended level set method for shape and topology optimization,” *Journal of Computational Physics*, vol. 221, no. 1, pp. 395–421, 2007. DOI: [10.1016/j.jcp.2006.06.029](https://doi.org/10.1016/j.jcp.2006.06.029).
- [128] S. Y. Wang, K. Tai, and M. Y. Wang, “An enhanced genetic algorithm for structural topology optimization,” vol. 65, no. 1, pp. 18–44, 2005. DOI: [10.1002/nme.1435](https://doi.org/10.1002/nme.1435).
- [129] S. Wang and M. Y. Wang, “Radial basis functions and level set method for structural topology optimization,” *International Journal for Numerical Methods in Engineering*, vol. 65, no. 12, pp. 2060–2090, 2006. DOI: [10.1002/nme.1536](https://doi.org/10.1002/nme.1536).
- [130] F. Wein, P. D. Dunning, and J. A. Norato, “A review on feature-mapping methods for structural optimization,” *Structural and Multidisciplinary Optimization*, vol. 62, no. 4, pp. 1597–1638, Aug. 2020. DOI: [10.1007/s00158-020-02649-6](https://doi.org/10.1007/s00158-020-02649-6).
- [131] Y. M. Xie and G. P. Steven, “A simple evolutionary procedure for structural optimization,” *Computers & Structures*, vol. 49, no. 5, pp. 885–896, Dec. 1993. DOI: [10.1016/0045-7949\(93\)90035-c](https://doi.org/10.1016/0045-7949(93)90035-c).
- [132] Y. M. Xie and G. P. Steven, “A simple approach to structural frequency optimization,” *Computers & Structures*, vol. 53, no. 6, pp. 1487–1491, Dec. 1994. DOI: [10.1016/0045-7949\(94\)90414-6](https://doi.org/10.1016/0045-7949(94)90414-6).
- [133] Y. M. Xie and G. P. Steven, *Evolutionary Structural Optimization*. Springer London, 1997. DOI: [10.1007/978-1-4471-0985-3](https://doi.org/10.1007/978-1-4471-0985-3).
- [134] Y. Xie and G. Steven, “Optimal design of multiple load case structures using an evolutionary procedure,” *Engineering Computations*, vol. 11, no. 4, pp. 295–302, Apr. 1994. DOI: [10.1108/02644409410799290](https://doi.org/10.1108/02644409410799290).
- [135] D. Yago, J. Cante, O. Lloberas-Valls, and J. Oliver, “Topology optimization using the unsmooth variational topology optimization (UNVARTOP) method: An educational implementation in MATLAB,” *Structural and Multidisciplinary Optimization*, vol. 63, pp. 955–981, Nov. 2020. DOI: [10.1007/s00158-020-02722-0](https://doi.org/10.1007/s00158-020-02722-0).
- [136] D. Yago, J. Cante, O. Lloberas-Valls, and J. Oliver, “Topology optimization of thermal problems in a nonsmooth variational setting: Closed-form optimality criteria,” *Computational Mechanics*, vol. 66, no. 2, pp. 259–286, Jun. 2020. DOI: [10.1007/s00466-020-01850-0](https://doi.org/10.1007/s00466-020-01850-0).

- [137] K. Yaji, T. Yamada, S. Kubo, K. Izui, and S. Nishiwaki, “A topology optimization method for a coupled thermal–fluid problem using level set boundary expressions,” *International Journal of Heat and Mass Transfer*, vol. 81, pp. 878–888, Feb. 2015. DOI: [10.1016/j.ijheatmasstransfer.2014.11.005](https://doi.org/10.1016/j.ijheatmasstransfer.2014.11.005).
- [138] T. Yamada, K. Izui, and S. Nishiwaki, “A level set-based topology optimization method for maximizing thermal diffusivity in problems including design-dependent effects,” *Journal of Mechanical Design*, vol. 133, no. 3, p. 031011, 2011. DOI: [10.1115/1.4003684](https://doi.org/10.1115/1.4003684).
- [139] T. Yamada, K. Izui, S. Nishiwaki, and A. Takezawa, “A topology optimization method based on the level set method incorporating a fictitious interface energy,” *Computer Methods in Applied Mechanics and Engineering*, vol. 199, no. 45–48, pp. 2876–2891, 2010. DOI: [10.1016/j.cma.2010.05.013](https://doi.org/10.1016/j.cma.2010.05.013).
- [140] X. Y. Yang, Y. M. Xie, G. P. Steven, and O. M. Querin, “Bidirectional evolutionary method for stiffness optimization,” *AIAA Journal*, vol. 37, pp. 1483–1488, Jan. 1999. DOI: [10.2514/3.14346](https://doi.org/10.2514/3.14346).
- [141] X. Yang, Y. Xie, J. Liu, G. Parks, and P. Clarkson, “Perimeter control in the bidirectional evolutionary optimization method,” *Structural and Multidisciplinary Optimization*, vol. 24, no. 6, pp. 430–440, Dec. 2002. DOI: [10.1007/s00158-002-0256-5](https://doi.org/10.1007/s00158-002-0256-5).
- [142] G. H. Yoon, J. S. Jensen, and O. Sigmund, “Topology optimization of acoustic–structure interaction problems using a mixed finite element formulation,” vol. 70, no. 9, pp. 1049–1075, 2007. DOI: [10.1002/nme.1900](https://doi.org/10.1002/nme.1900).
- [143] M. Yulin and W. Xiaoming, “A level set method for structural topology optimization and its applications,” *Advances in Engineering Software*, vol. 35, no. 7, pp. 415–441, 2004. DOI: [10.1016/j.advengsoft.2004.06.004](https://doi.org/10.1016/j.advengsoft.2004.06.004).
- [144] C. Zhao, G. Steven, and Y. Xie, “Evolutionary natural frequency optimization of two-dimensional structures with additional non-structural lumped masses,” *Engineering Computations*, vol. 14, no. 2, pp. 233–251, Mar. 1997. DOI: [10.1108/02644409710166208](https://doi.org/10.1108/02644409710166208).
- [145] M. Zhou and G. Rozvany, “The COC algorithm, part II: Topological, geometrical and generalized shape optimization,” *Computer Methods in Applied Mechanics and Engineering*, vol. 89, no. 1–3, pp. 309–336, Aug. 1991. DOI: [10.1016/0045-7825\(91\)90046-9](https://doi.org/10.1016/0045-7825(91)90046-9).
- [146] M. Zhou and G. Rozvany, “On the validity of ESO type methods in topology optimization,” *Structural and Multidisciplinary Optimization*, vol. 21, no. 1, pp. 80–83, Mar. 2001. DOI: [10.1007/s001580050170](https://doi.org/10.1007/s001580050170).
- [147] S. Zhou, W. Li, Y. Chen, G. Sun, and Q. Li, “Topology optimization for negative permeability metamaterials using level-set algorithm,” *Acta Materialia*, vol. 59, no. 7, pp. 2624–2636, Apr. 2011. DOI: [10.1016/j.actamat.2010.12.049](https://doi.org/10.1016/j.actamat.2010.12.049).
- [148] S. Zhou, W. Li, G. Sun, and Q. Li, “A level-set procedure for the design of electromagnetic metamaterials,” *Optics Express*, vol. 18, no. 7, p. 6693, Mar. 2010. DOI: [10.1364/oe.18.006693](https://doi.org/10.1364/oe.18.006693).
- [149] J. H. Zhu, W. H. Zhang, and K. P. Qiu, “Bi-directional evolutionary topology optimization using element replaceable method,” *Computational Mechanics*, vol. 40, no. 1, pp. 97–109, Jun. 2006. DOI: [10.1007/s00466-006-0087-0](https://doi.org/10.1007/s00466-006-0087-0).